

# Proceedings

## 22<sup>nd</sup> International Symposium on Space Terahertz Technology

April 25-28, 2011

Loews Ventana Canyon Resort, Tucson, AZ USA



The 22<sup>nd</sup> International Symposium on Space Terahertz Technology was held from April 25 to April 28 in Tucson, Arizona, USA at the Loews Ventana Canyon resort. There were ~110 registered participants at the conference. Engineers and scientists from the United States, the European Union, Japan, Russia, Chile and China attended.

The local organizing committee would like to thank the conference manager Brian Duffy and his staff for making the 22<sup>nd</sup> ISSTT an enjoyable and smooth event. Their many hours of hard work made the conference possible.

All submitted manuscripts have been included in these proceedings. For presentations without a submitted manuscript, the presentation abstract has been included in the proceedings. Authors at this ISSTT had the opportunity to submit their paper to a special issue of the IEEE Transactions on Terahertz Science and Technology. Papers accepted by the TST journal through this process will be published in the January 2012 issue of the TST. Digest versions of these papers are included in these conference proceedings.

51 oral, 31 poster and 7 invited presentations were given at the conference in five broad categories:

Coherent Detectors:	20
Direct Detectors:	11
THz Sources:	11
Components and Optics:	17
Systems:	22
Invited:	7

The 23<sup>rd</sup> International Symposium on Space Terahertz Technology will be held in Tokyo, Japan from April 2-4 2012. Further details are available at <http://atc.mtk.nao.ac.jp/ISSTT2012/index.htm>.

Chris Walker and Chris Groppi  
Conference Co-Chairs

### **Conference Location**

Loews Ventana Canyon Resort  
7000 North Resort Drive  
Tucson, Arizona, 85750  
Phone: (520) 299-2020  
Reservations: (800) 234-5117  
Fax: (520) 299-6832  
ventanareservations@loewshotels.com

### **Local Organizing Committee**

Christopher Walker, U. Arizona (Co-Chair)  
Christopher Groppi, Arizona State (Co-Chair)  
Christian d'Aubigny, TeraVision Inc.  
Craig Kulesa, U. Arizona  
Gene Lauria, U. Arizona

### **Scientific Organizing Committee**

Christopher Walker, U. Arizona  
Christopher Groppi, Arizona State  
Christian d'Aubigny, TeraVision Inc.  
David Chuss, NASA Goddard Spaceflight Center  
Jon Kawamura, NASA Jet Propulsion Laboratory  
Victor Belitsky, Chalmers University of Technology  
Imran Mehdi, NASA Jet Propulsion Laboratory

### **Corporate Sponsors**

Rohde & Schwartz  
Toll free: 1-888-Test-RSA (1-888-837-8772)  
Info@rsa.rohde-schwarz.com  
[www.rohde-schwarz.com/USA](http://www.rohde-schwarz.com/USA)

Universal Cryogenics, Inc.  
+1 (520) 622-6277  
[kirby@ucryo.com](mailto:kirby@ucryo.com)  
<http://ucryo.com>

Virginia Diodes Inc.  
+1-434-297-3257  
[vdirfq@vadiodes.com](mailto:vdirfq@vadiodes.com)  
<http://vadiodes.com/>

TeraVision Inc.  
1-800-670-8357  
[info@teravision-inc.com](mailto:info@teravision-inc.com)  
<http://www.teravision-inc.com>

## **ISSTT 2011 Program**

### **Monday, April 25, 2011**

19:00-21:00: Welcome gathering and registration, Hotel main lobby patio

### **Tuesday, April 26, 2011**

8:00-8:30: Continental breakfast and registration

8:30-8:50: Announcements and Conference Welcome: Prof. Christopher Walker

8:50-10:10: Session 1 Terahertz Systems I (Chair: Christopher Groppi)

<b>Paper</b>	<b>Abstract Title</b>	<b>Presenter</b>
1-1	THz Interferometers in Geosynchronous Orbit,- status and results	Anders Emrich
1-2	Liquid-cryogen free frontend for a 2.5-THz heterodyne receiver	Heinz-Wilhelm Huebers
1-3	Towards Multi- Pixel Heterodyne Terahertz Receivers	Victor Belitsky
1-4	Antenna coupled KIDs for NIKA	Lorenza Ferrari

10:10-10:30 Coffee Break

10:30-11:00 Invited Talk: "Millimeter and Submillimeter Observations of Asteroids and Comets With the MIRO Instrument on the Rosetta Spacecraft"

Dr. Samuel Gulkis, NASA JPL

11:00-12:20: Session 2: Coherent Detectors I (Chair: Jacob Kooi)

<b>Paper</b>	<b>Abstract Title</b>	<b>Presenter</b>
2-1	Radiation mixer based on the 2DEG in a GaN heterostructure	Boris Karasik
2-2	Integrated Balanced SIS Mixer at 500 GHz	Marc Westig
2-3	Performance of a twin slot antenna coupled NbN hot electron bolometer mixer at 2.5 THz	Wen Zhang
2-4	Nb/Al-AlOx/Nb junction properties' variations due to storage and mounting	Alexey Pavolotsky

12:20-13:20: Lunch Break

Meeting of ISSTT Steering Committee (continue on Wednesday if necessary)

13:20-15:00: Session 3: THz Sources I (Chair: Tom Crowe)

<b>Paper</b>	<b>Abstract Title</b>	<b>Presenter</b>
3-1	Steady-State and Transient Thermal Analysis of High-Power Planar Schottky Diodes	Aik-Yean Tang
3-2	Design of a high-power 1.6 THz Schottky tripler using ‘on-chip’ power-combining and Silicon micro-machining	Jose Siles
3-3	Fundamental-Mode Operation of Superlattice Electronic Devices in D-Band (110–170 GHz)	Heribert Eisele
3-4	Power Combined Gallium Nitride Amplifier with 3 Watt Output Power at 87 GHz	Andy Fung
3-5	A 2.5-2.7 THz room temperature electronic source	Alain Maestrini

15:00-15:20: Coffee Break

15:20-15:50: Invited Talk: “Future Incoherent Detector Arrays”

Dr. Harvey Moseley, NASA GSFC

15:50-17:10: Session 4: Incoherent Detectors I (Chair: Teunis Klapwijk)

<b>Paper</b>	<b>Abstract Title</b>	<b>Presenter</b>
4-1	Lumped Element Kinetic Inductance Detectors for NIKA	Markus Roesch
4-2	The SPICA-SAFARI Detector System: TES Detector Arrays with Frequency Division Multiplexed SQUID Readout	P. De Korte
4-3	A Study on Photon Counting Interferometry in Terahertz Frequencies	Hiroshi Matsuo
4-4	Optical characterization at 1.5-3 THz of high sensitivity TES detectors designed for future Far-Infrared Space missions	Phil Mauskopf

17:30-19:00: Poster Session and Reception

<b>Paper</b>	<b>Abstract Title</b>	<b>Presenter</b>
P-1	Kilopixel Superconducting Bolometer Arrays for Near-Space Astrophysics Applications	Dominic Benford
P-2	Performance of first ALMA band 5 production cartridge	Bhushan Billade
P-3	Receiver Optics and 1.9 THz HEB Mixers for STO	Michael Brasse
P-4	Compact Micromachined Infrared Bandpass Filters for Planetary Spectroscopy	Ari Brown
P-5	Measure the beam wavefronts of a terahertz source	Morris Cui
P-6	Light-tight cryogenic test facility development for the SAFARI instrument on-ground calibration	Pieter Dieleman

P-7	Development of planar Schottky diodes	Vladimir Drakinskiy
P-8	Design, Fabrication and Alignment of the SuperCam Telescope Relay Optics	Christian Drouet d'Aubigny
P-9	Phocus radiometer payload	Anders Emrich
P-10	Spectrometers for THz radiometers	Anders Emrich
P-11	STEAMR breadboard results and demonstrator status	Anders Emrich
P-12	ALMA WVR final report	Anders Emrich
P-13	Antenna lens array for large scale M-KIDs camera	Lorenza Ferrari
P-14	Optical test facility for SAFARI bolometers	Lorenza Ferrari
P-15	The Supercam 8-pixel integrated focal plane unit	Christopher Groppi
P-16	The Supercam Local Oscillator Multiplexing Unit: Design, fabrication and measured performance	Christopher Groppi
P-17	Terahertz response of YBCO HEB homodyne detectors	Arvid Hammar
P-18	YBCO HEB THz mixers	Arvid Hammar
P-19	“32-channel Multi-Chip-Module” The Cryogenic Readout System for Submillimeter/Terahertz Cameras	Yasunori Hibi
P-20	1.1 THz Multi-pixel Heterodyne Receiver for APEX	Norma Hurtado
P-21	Development of THz Quantum Cascade Laser as a Local Oscillator for Heterodyne Receivers	Yoshihisa Irimajiri
P-22	In-orbit Performance and Current Status of the SMILES Mission	Kenichi Kikuchi
P-23	Operating of the superconducting integrated receiver channel of the TELIS atmospheric sounder.	Oleg Kiselev
P-24	Dual-Chip Power Combiner using 300 GHz Tripler with Diamond Heat-Spreaders	Choonsup Lee
P-25	Initial Terahertz Probing of Carbon Nanofiber Composite Coatings as Potential Quasi-Optical THz Shielding and Attenuation Devices	Lei Liu
P-26	A Truncated Waveguide Phase Shifter	N.P. Lourie
P-27	Advances Towards an ALMA Band-1 Receiver	Patricio Mena
P-28	Test of a Waveguide OMT for the 385-500 GHz Band	Alessandro Navarrini
P-29	TES Bolometers with High-Frequency Readout Circuit	Sergey Shitov
P-30	Status of ALMA Band 7 Cartridge Production	Sylvain Mahieu
P-31	A 230 GHz Unilateral Finline Mixer on Silicon Substrate	Yangjun Zhou
P-32	3.5 THz Quantum Cascade Laser at 70 K as local oscillator	Ren Yuan

20:00-22:00: Community Forum: Research Opportunities in Terahertz Astronomy

## Wednesday, April 27, 2011

8:00-8:30: Continental Breakfast and Registration

8:30-9:00: Invited Talk: “The South Pole Telescope: Operations and Early Results”

Dr. Antony Stark, Harvard-Smithsonian CfA

9:00-10:20 Session 5: Incoherent Detectors II (Chair: Harvey Moseley)

<b>Paper</b>	<b>Abstract Title</b>	<b>Presenter</b>
5-1	Doped Lead Telluride-Based Alloys – a New Type of Sensitive Detectors of Terahertz Radiation	Dmitry Kokhlov
5-2	Optical sensitivity measurements in nano-HEB detectors	Boris Karasik
5-3	Low Noise Transition Edge Sensor (TES) for the SAFARI Instrument on SPICA	Pourya Khosropanah
5-4	Optical characterization of high sensitivity TES detectors designed for the SPICA/SAFARI 30-60 mm channel	D. Morozov

10:20-10:40: Coffee Break

10:40-12:20 Session 6: Coherent Detectors II (Chair: Patrick Puetz)

<b>Paper</b>	<b>Abstract Title</b>	<b>Presenter</b>
6-1	Scalable terahertz-frequency HEB mixers	Faouzi Boussaha
6-2	A quasi-optical NbN mixer with 800K DSB noise temperature at 2.5 THz	Yan Delorme
6-3	560 GHz, 664 GHz and 1.2 THz Schottky based MMIC sub-harmonic mixers for planetary atmospheric remote sensing	Thomas Bertrand
6-4	First Results of the Sideband-Separating Mixer for ALMA Band 9 Upgrade	Andrey Khudchenko
6-5	High Sensitivity Waveguide HEB Mixers at 2.5 THz	Patrick Puetz

12:20-13:20: Lunch Break

13:20-13:50: Invited Talk: “CCAT”

Dr. Jonas Zmuidzinas, Caltech/JPL

13:50-14:50 Session 7: Optics and Components (Chair: Christian d'Aubigny)

<b>Paper</b>	<b>Abstract Title</b>	<b>Presenter</b>
7-1	The experimental demonstration of a low-cost 37-horn focal-plane array consisting of smooth-walled multiple-flare angle horns fabricated by direct drilling	Jamie Leech
7-2	Effect of Phase Slippage and Higher Order Beam Modes in a 340GHz Focal Plane Array Optics	Axel Murk
7-3	VNA Measurements in the 0.75-1.1 THz Band	Jeffrey Hesler

14:50-15:10 Session 8: THz Systems II (Chair: Victor Belitsky)

<b>Paper</b>	<b>Abstract Title</b>	<b>Presenter</b>
8-1	A Multibeam 2SB SIS Receiver at 3mm Wavelength	Wenlei Shan

15:10-15:30: Coffee Break

15:30-16:00 Invited Talk: "SOFIA"

Dr. Erick Young

16:00-17:20 Session 8: THz Systems II continued

<b>Paper</b>	<b>Abstract Title</b>	<b>Presenter</b>
8-2	Development of the 1.3-1.5 THz Band Superconducting HEB Mixer Receivers for ASTE 10 m Telescope	Tatsuya Shiino
8-3	Heterodyne molecular spectroscopy measurement at 3.5 THz using a tunable quantum cascade laser	Ren Yuan
8-4	Antenna Coupled MKID test camera on APEX telescope: on sky performance	Andrey Baryshev
8-5	The Kilopixel Array Pathfinder Project (KAPPA): A 16 pixel 660 GHz pathfinder instrument with an integrated heterodyne focal plane detector	Christopher Groppi

18:30 Reception and Conference Dinner

Invited Talk: "THz Astronomy, Past, Present and Future,"

Dr. Thijs de Graaw, ALMA



## Thursday, April 28

8:00-8:30: Registration and Continental Breakfast

8:30-9:00: Invited Talk: "Exploring the Terahertz Universe: Capabilities and Early Science Results of the Herschel Space Observatory"

Paul Goldsmith, NASA JPL

9:00-10:40 Session 9: THz Systems III (Chair: Andrey Baryshev)

Paper	Abstract Title	Presenter
9-1	The Stratospheric Terahertz Observatory	Christopher Walker
9-2	A progress update on Supercam, a 64-pixel heterodyne imaging spectrometer	Jenna Kloosterman
9-3	HEAT: The High Elevation Antarctic THz Telescope	Craig Kulesa
9-4	Status report on the Caltech Submillimeter Observatory Receiver Upgrade	Jacob Kooi
9-5	First results from GREAT on SOFIA	Jurgen Stutzki

10:40-11:00: Coffee Break

11:00-12:20 Session 10: Coherent Detectors III (Chair: Gene Lauria)

Paper	Abstract Title	Presenter
10-1	Next Generation of Hot-Electron Bolometer Mixers for Future Heterodyne Missions	Sergey Ryabchun
10-2	Characterisation of broadband unilateral finline SIS mixers with sideband separation at 700GHz	Boon-Kok Tan
10-3	670 GHz Schottky Diode Based Subharmonic Mixer with CPW Circuits and 70 GHz IF	Goutam Chattopadhyay
10-4	Cryogenic MMIC Low Noise Amplifiers for W-Band and Beyond	Lorene Samoska

12:20-13:20: Lunch Break

13:20-13:50: Invited Talk: "THz Transistors"

Bill Deal, Northrop Grumman Corporation

13:50-14:30 Session 10: Coherent Detectors III Continued

<b>Paper</b>	<b>Abstract Title</b>	<b>Presenter</b>
10-5	Upgrade of EMIR's band 3 and band 4 mixers	Doris Maier
10-6	A 340 GHz 2SB Schottky Receiver for Earth Observation Applications	Peter Sobis

14:30-15:30 Session 11: THz sources II (Chair: Imran Mehdi)

<b>Paper</b>	<b>Abstract Title</b>	<b>Presenter</b>
11-1	Frequency locking of a 3.5 THz quantum cascade laser using a gas cell	Ren Yuan
11-2	High power room temperature, compact, narrow line THz source as a local oscillator for THz receivers	M. Scheller
11-3	Development and Characterization of a 2.7THz LO Source	Thomas Crowe

15:30-15:50: Coffee Break

15:50-16:30 Session 11: THz Sources II continued

<b>Paper</b>	<b>Abstract Title</b>	<b>Presenter</b>
11-4	Toward a Terahertz Local Oscillator for SOFIA Based on a Quantum-Cascade Laser	Heiko Richter
11-5	Verification of Spectral Purity in the HIFI Local Oscillator	John Pearson

16:30-17:10 Session 12: Components and Optics II (Chair: Christian d'Aubigny)

<b>Paper</b>	<b>Abstract Title</b>	<b>Presenter</b>
12-1	Experimental Demonstration of a New Technique for Characterizing the Full Optical Behavior of Multimode Detectors	Chris Thomas
12-2	Silicon Micromachining Technology for THz applications: Development of Silicon Based Integrated Receivers	Cecile Jung

17:10-17:30 Closing remarks and adjourn

## List of Registered Participants

Joost Adema	Grigori Goltsman
Maestrini Alain	Christopher E. Groppi
Jan Barkhof	Samuel Gulkis
Andrey Baryshev	Arvid Hammar
Victor Belitsky	Darren J. Hayton
Menno van de Bemt	Jeffrey Hesler
Bhushan Billade	Ronald Hesper
Faouzi Boussaha	Yasunori Hibi
Michael Brasse	Matt Hollister
Ari D. Brown	Heinz-Wilhelm Huebers
Eric Bryerton	Norma Hurtado
Robbie M. Burton	Yoshihisa Irimajiri
Thomas Crowe	Brian D. Jackson
Morris Cui	Jeanne Treuttel
Thijs de Graauw	Cecile Jung
William R. Deal	Boris Karasik
Yan Delorme	Alexandre Karpov
Pieter Dieleman	Jonathan Kawamura
Jack East	Dmitry Khokhlov
Heribert Eisele	Kenichi Kikuchi
Anders Emrich	Oleg Kiselev
Lorenza Ferrari	Teun Klapwijk
Andy Fung	Jacob Kooi
Jian-Rong Gao	Eugene F. Lauria
Paul Goldsmith	Choonsup Lee

Jamie Leech

Robert Lin

Sarah Lipsey

Lei Liu

Sylvain Mahieu

Doris Maier

Dan P. Marrone

Hiroshi Matsuo

Imran Mehdi

Willie C. Merrell

Raquel Monje

Tetsuo Mori

Axel Murk

Alessandro Navarrini

Shing-Kuo Pan

Alexey Pavolotsky

Patrick Puetz

Theodore Reck

George P. Reiland

Yuan Ren

Heiko Richter

Markus Roesch

Karwan Rostem

Kamaljeet Saini

Lorene Samoska

Yutaro Sekimoto

Wenlei Shan

Sheng-Cai Shi

Jerry Shiao

Tatsuya Shiino

Jose Siles

Brian A. Stalder

Antony A. Stark

Juergen Stutzki

Boon Kok Tan

Aik Yean Tang

David J. Thoen

Christopher N. Thomas

Todd Veach

Caleb Wheeler

Erick T. Young

Jonas Zmuidzinas

## THz Interferometers in Geosynchronous Orbit, - status and results

A. Emrich<sup>1\*</sup>, E. Ryman<sup>1</sup>, J. Embretsén<sup>1</sup>, A. Carlström<sup>2</sup>, J. Christensen<sup>2</sup> and J. Riesbeck<sup>1</sup>

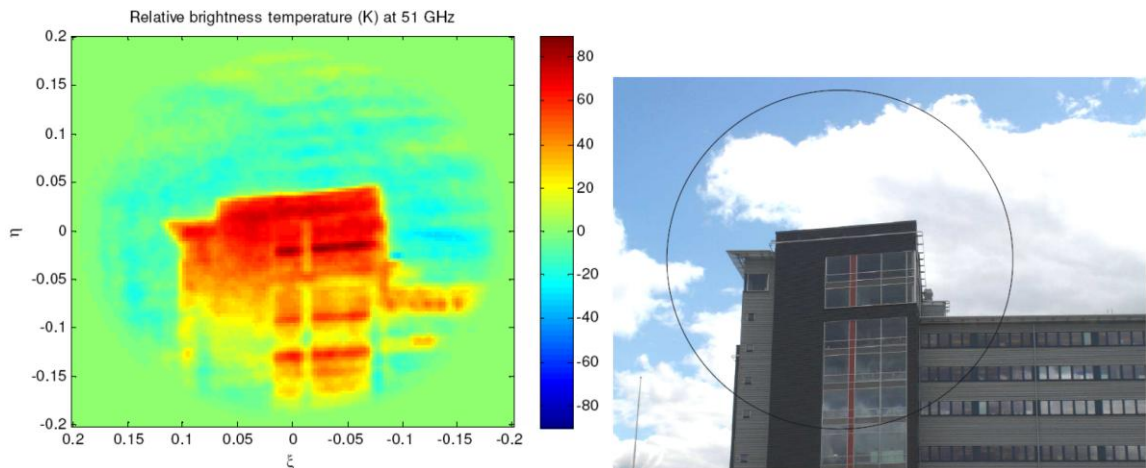
*1 Omnisys Instruments AB\*, Västra Frölunda, Sweden*

*2 RUAG Space AB, Göteborg, Sweden*

\* Contact: ae@omnisys.se, phone +46-31-7343401

**Abstract**—This paper presents the development of a demonstrator for the Geostationary Atmospheric Sounder (GAS) instrument and test results. GAS utilizes synthetic aperture radiometry to obtain desired spatial (30 km) and temporal (nowcasting) resolution for measurement of atmospheric temperature and humidity profiles under all weather conditions. These parameters are decisively important to meteorological and climate models at all time scales. The instrument development project includes on-ground demonstration of both the imaging performance and the mechanical concept. This activity was concluded in October 2010 with a final presentation at ESTEC and all test results agreed with predictions and verified that such an instrument could be developed and meet the end user requirements. The design and implementation of the demonstrator will be presented with some system level test results. Ruag Space AB has been the prime for the demonstration phase and responsible for the post processing, analyses and demonstrator system level tests. Omnisys has been responsible for the electronics, i.e. front-ends, cross correlator back-end, LO system etc.

The plan for the next phase is still uncertain on the European side, but there is an ongoing development at JPL for a similar instrument, GEOSTAR. Omnisys are now working together with this team and are concentrating on the cross correlator part. A full custom ASIC in 65 nm CMOS has been developed and is currently being tested. The first test results are very encouraging with clock speeds ( $> 2.5$  GHz) and power consumption ( $< 0.13$  mW/ch/GHz) as expected. Full performance predictions will be disclosed at the conference. Full custom samplers are also being developed with a planned tape-out in mid 2011. Expected performance of these devices will be presented together with a preliminary design of a full cross correlate system.



## Liquid-cryogen free frontend for a 2.5-THz heterodyne receiver

H.-W. Hübers<sup>\*1,5</sup>, H. Richter<sup>1</sup>, S. G. Pavlov<sup>1</sup>, A. D. Semenov<sup>1</sup>, L. Mahler<sup>2</sup>, A. Tredicucci<sup>2</sup>,  
H. E. Beere<sup>3</sup>, D. A. Ritchie<sup>3</sup>, K. Il'in<sup>4</sup>, and M. Siegel<sup>4</sup>

<sup>1</sup>*Institute of Planetary Research, German Aerospace Center (DLR), Rutherfordstr. 2, 12489 Berlin, Germany\**

<sup>2</sup>*NEST CNR-INFM and Scuola Normale Superiore, Piazza dei Cavalieri 7, 56126 Pisa, Italy*

<sup>3</sup>*Cavendish Laboratory, University of Cambridge, Madingley Road, Cambridge CB3 0HE, United Kingdom*

<sup>4</sup>*Institute of Micro- and Nano-Electronic Systems, Karlsruhe Institute of Technology, 76187 Karlsruhe, Germany*

<sup>5</sup>*Institut für Optik und Atomare Physik, Technische Universität Berlin, Hardenbergstraße 36,  
10623 Berlin, Germany*

\* Contact: heinz-wilhelm.huebers@dlr.de, phone +49-30-67055596

**Abstract**— The terahertz (THz) portion of the electromagnetic spectrum bears an amazing scientific potential in astronomy. High resolution spectroscopy in particular heterodyne spectroscopy of molecular rotational lines and fine structure lines of atoms or ions is a powerful tool, which allows obtaining valuable information about the observed object such as temperature and dynamical processes as well as density and distribution of particular species. Examples are the OH rotational transitions at 2.5 THz, the HD rotational transition at 2.7 THz, and the OI fine structure line at 4.7 THz. These lines are, for example, major targets to be observed with GREAT, the German Receiver for Astronomy at Terahertz Frequencies, which will be operated on board of SOFIA. For SOFIA, a heterodyne receiver which does not require cooling by liquid cryogenics will ease operation significantly, because the complexity and limitation of the operating time due to the use of cryo-liquids can be overcome.

As part of a study for a second generation heterodyne receiver on SOFIA we are developing a 2.5-THz frontend which is implemented in a pulse-tube cooler (PTC). It consists of a quantum-cascade laser (QCL) as local oscillator and a phonon-cooled NbN hot electron bolometric mixer [1]. The QCL is mounted on the first stage of the PTC and operates at a temperature of about 50 K while the HEB is mounted on the second stage of the PTC (temperature ~5 K). Frequency stabilization to below 300 kHz full width at half maximum is achieved by locking to a molecular absorption line [2]. While the gas absorption cell is outside the PTC the Ge:Ga detector, which is necessary for the locking scheme, is mounted on the second cold stage. We will present the design and performance of the frontend and discuss the prospects for an application on board of SOFIA.

- [1] H. Richter, A. D. Semenov, S. Pavlov, L. Mahler, A. Tredicucci, K. Il'in, M. Siegel, and H.-W. Hübers, *Appl. Phys. Lett.* **93**, 141108 (2008).
- [3] H. Richter, S. G. Pavlov, A. D. Semenov, L. Mahler, A. Tredicucci, H. E. Beere, D. A. Ritchie, and H.-W. Hübers, *Appl. Phys. Lett.* **96**, 071112 (2010).

# Towards Multi-Pixel Heterodyne Terahertz Receivers

Victor Belitsky, Vincent Desmaris, Dimitar Dochev, Denis Meledin, Alexey Pavolotsky

**Abstract**— Terahertz multi-pixel heterodyne receivers introduce multiple challenges for their implementation, mostly due to the extremely small dimensions of all components and even smaller tolerances in terms of alignment, linear dimensions and waveguide component surface quality. In this manuscript, we present a concept of terahertz multi-pixel heterodyne receiver employing optical layout using polarization split between the LO and RF. The frontend is based on a waveguide balanced HEB mixer for the frequency band 1.6 – 2.0 THz. The balanced HEB mixer follows the layout of earlier demonstrated APEX T2 mixer. However for the mixer presented here, we implemented split-block layout offering minimized lengths of all waveguides and thus reducing the associated RF loss. The micromachining methods employed for producing the mixer housing and the HEB mixer chip are very suitable for producing multiple structures and hence are in-line with requirements of multi-pixel receiver technology. The demonstrated relatively simple mounting of the mixer chip with self-aligning should greatly facilitate the integration of such multi-channel receiver.

**Index Terms**— Instrumentation, Multi-pixel, Terahertz, Waveguide Balanced Mixer.

## I. INTRODUCTION

AN airborne observatory such as SOFIA [1], or a space observatories as Herschel [2] and Plank [3] allow to reduce or eliminate atmospheric absorption for observations in the terahertz frequency band. Moreover, high altitude and dry sites such as Dome C in Antarctica [4], Llano de Chajnantor [5, 6] and Cerro Chajnantor [7] in Chile could provide reasonable atmospheric transmission at THz frequencies thus making them suitable for technology testing and radio astronomical observations from the ground [5, 8] over limited periods of time when PWV is less than 0.1 mm giving possibilities to observe in the 1.5 THz frequency window from the ground.

The current generation of Terahertz receivers installed at the radio-telescopes uses single-pixel heterodyne instruments. Aiming increased observation efficiency through use of multi-pixel heterodyne instruments, called sometimes “science

multipliers”, become an actual option for new ground-based telescopes such as Dom C or CCAT [9]. Such multi-pixel Terahertz heterodyne instruments should allow doing more science during very limited time available for effective Terahertz observations from the ground and use flight time of SOFIA efficiently.

Heterodyne instrumentation for the THz ground-based telescopes, airborne and space observatories has made remarkable progress during the last two decades bringing SIS and HEB mixer technology to its ultimate state [10-12]. Often above 1 THz, a quasioptical HEB mixer design with planar antenna and substrate lens [13, 14] is used. Alternatively, waveguide HEB mixers have been also demonstrated [5, 8, 15, 16] offering superior efficiency of the receiver-antenna coupling via a corrugated horn. Furthermore, waveguide designs present a natural filtering for the out-of-the-band background noise, feature especially useful for easily saturated HEB mixers. When installed at the ground-based telescopes, the atmospheric contribution to the background noise remains close to 300 K at terahertz frequencies and could cause saturation with rather weak control over RF band as in, e.g., quasioptical HEB mixers. Additionally, THz receivers have to cope with the relatively low attainable power of local oscillator (LO) sources and its sufficiently high sideband noise [17], problems, which are multiplied by a number of pixels, at least, for a multi-pixel system. These problems could be circumvented by employing a balanced layout, which offers extremely high efficiency of using the LO power (around 3 dB loss only) and provides improved receiver stability by intrinsic cancellation of the LO amplitude noise as it was demonstrated in [5].

The dimensions of all components are scaled down with the frequency and for Terahertz frequencies, e.g., around 1.3 THz the waveguide dimensions are  $90 \times 180 \mu\text{m}$  [5] and required even smaller, nearly sub-micron, design tolerances. The size of the corrugated feed becomes smaller too and comparable with e.g. the size of the SMA contact. This implies a demand to find new approaches for the optical layout where the RF/LO part of the receiver could be separated from IF/DC interface.

Micrometer scale dimensions and tolerances introduce increasing challenges for fabrication using conventional machining and call for applying a micro machining technology, e.g., terahertz all-metal waveguides [18, 19].

In this manuscript, we present a concept of terahertz multi-pixel heterodyne receiver employing optical layout using polarization split between the LO and RF. The frontend is based on a waveguide balanced HEB mixer for the frequency

Manuscript received June 19, 2011. This work was partly supported by the European Commission Framework Programme 7 via RadioNet, JRA AMSTAR+, Grant No. 227290.

Authors are with the *Group for Advanced Receiver Development*, Department of Earth and Space Sciences with Onsala Space Observatory, Chalmers University of Technology, Gothenburg, SE 412 96, Sweden (corresponding author Victor.Belitsky@chalmers.se, phone +46-31-772 1000).

band 1.6 – 2.0 THz. Additionally, we investigate possibilities for a simplified and accurate mounting, and electrical interfacing of the HEB mixer substrate by utilizing a novel HEB mixer chip layout [20].

## II. TERAHERTZ MULTI-PIXEL RECEIVER CONCEPT

### A. Optical Layout

Focal plane heterodyne multi-pixel systems are not background limited and that implies specific pitch for placing the feeds of each pixel while each pixel's optics should be matched to the antenna [21]. With the given feed size, at Terahertz frequencies, physical dimensions of the array following optimal pitch leave no room for the IF system assuming realistic dimensions of SMA connectors and IF amplifiers. As discussed in the introduction, we need a receiver layout that provides a possibility to separate optics, with pixel feed corrugated horn and LO distributing and injection system, and the IF/DC system with its bulky (compare to Terahertz mixers) IF amplifiers and DC and IF connectors.

Additional problem to consider is potential complexity of the LO distribution and injection system. Most likely, the LO power of a few tens of microwatt could be expected from Terahertz LO source [22]. In order to preserve as much LO power as possible, such system should have individual LO feed for each pixel. For LO injection, using a beam-splitter option either leads to an unacceptable LO power loss (under-pumped mixers) or increased RF signal damping (high optical RF loss). In either case it would be detrimental to the receiver performance. On our view, a possible solution of combining the LO and RF at the optical path would be using a grid polarizer; this will produce the input beam with orthogonally polarized LO and RF while providing virtually no insertion loss at RF and no injection loss for the LO. Such system depicted in Figure 1.

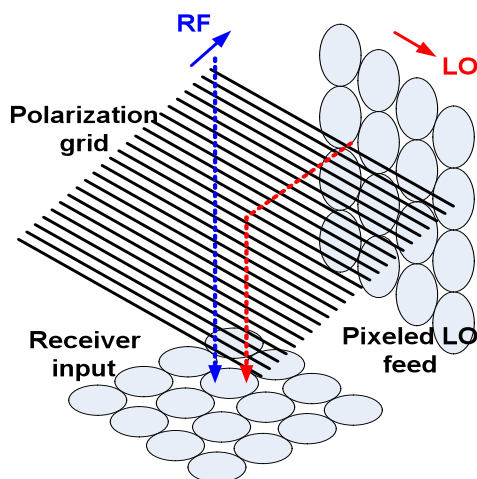


Fig. 1. Proposed optical layout for Terahertz multi-pixel receiver. In order to preserve the LO power, the LO feed is has RF-signal-matched pixel structure. A polarization grid is used to combine the LO and RF with minimum loss. The incoming signal has the LO and RF orthogonally polarized.

The advantages of the system depicted in Figure 1 are the

following:

- Separation of the RF/LO and IF/DC interfaces that ease design, and integration of the entire receiver;
- Minimum insertion loss for RF and LO in the quasioptical part;
- Physical separation of the RF and LO feed systems that ease design and integration;

### B. Frontend Concept for Single Pixel

In order to use such optical layout, the frontend design should be modified to receive both polarizations; each pixel mixer should have polarization splitter (e.g., OMT) to separate the RF and LO; the mixer should have two separate inputs for the RF and LO signals. The latter is an inherent feature of the waveguide balanced mixer demonstrated earlier [5] and has additional advantage of very effective use of the LO power while suppressing the LO AM noise. Schematically, the single pixel frontend with the feed and the LO/RF separation and injection part is presented in Figure 2.

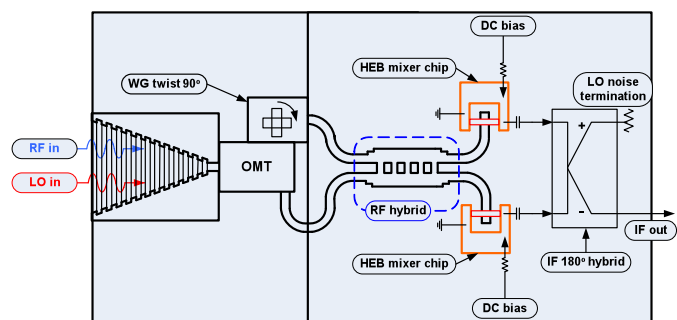


Fig. 2. Proposed pixel layout for Terahertz multi-pixel receiver. Input corrugated horn converts both LO and RF input beams into orthogonal waveguide modes; the waveguide modes are separated by OMT; balanced waveguide mixer is connected to the OMT outputs either directly or via 90-degree waveguide twist.

Clearly, in order to accommodate two orthogonally polarized RF and LO signals, the pixel frontend should have more complex design - as depicted in the Figure 2; the LO/RF separation scheme would introduce insertion loss for both RF and LO; additional components such as OMT and 90-degree waveguide twist should be fabricated and integrated with the mixer for each pixel. The latter two components were of interest for other research groups and their results [23 – 25] show good compatibility with micromachining approach [18, 19] and thus give a hope for successful implementation.

### C. Waveguide Balanced HEB Mixer for 1.6 – 2.0 THz

As discussed above and demonstrated in [5], a balanced mixer layout gives several important advantages:

- Balanced design preserves most of the LO power;
- Balanced design has separate LO port, which is convenient and is required for the LO injection scheme suggested here;
- Balanced scheme rejects the LO AM noise and background additive noise and that is increasingly important assuming the LO multiplication stages are pumped extremely heavily at Terahertz frequencies.

For multi-pixel application, the balanced waveguide mixer



should preferably have split-block layout. This is especially important in the view of reproducing many pixels where the split-block should provide a possibility of simultaneous access to several pixels in contrast to, e.g., end-piece configuration. In split-block layout all lead waveguides could be made of minimum length to minimize insertion loss and thus contributing to the system noise performance. Finally, in the split-block configuration, it is easier to achieve a compact design reducing the mixer foot-print required due to a smaller physical size of the feed and, consequently, enabling a tighter pixel packing at Terahertz frequencies.

Mounting and electrical connections of the chip in the mixer block and an easy way of integrating active mixer component, e.g., HEB mixer, have strong effect on the ability to build multi-pixel heterodyne receiver at Terahertz frequencies. A very tiny, thin and fragile substrate of a HEB mixer precludes using wire-bonding and introduces a great challenge of mounting. In order to circumvent these problems, we use novel layout [20] comprising supporting  $\Pi$ -frame for electrical contacts and used as mechanical reference for mounting in the mixer block. Figure 3 depicts the  $\Pi$ -frame chip compatible with the split-block layout.

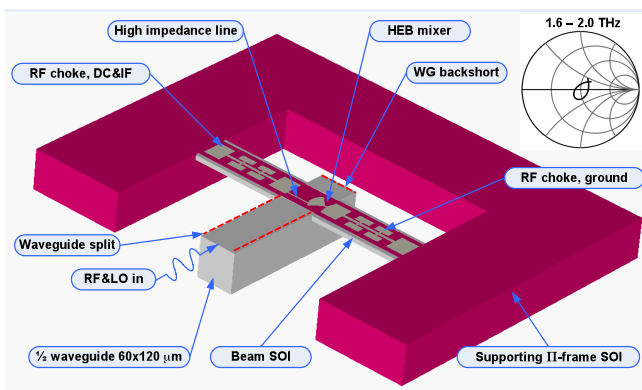


Fig. 3. An illustration of the HEB mixer chip with supporting  $\Pi$ -frame. This layout is fully compatible with the split-block technique and dramatically eases mounting and electrical contacting to the mixer chip allowing, e.g., a wire-bonding to the contact pads (not shown) deposited on the beam supporting frame. The insert shows matching of the probe to the waveguide over the 1.6 to 2.0 THz band.

In order to fabricate such structure, we used double-bonded SOI (silicon-on-insulator) substrate. The top layer, of 2.0  $\mu\text{m}$  thick high-resistivity silicon, defines the thickness of the beam where the HEB mixer is placed. In order to pattern the mixer and shape the substrate, we used optical- and E-beam lithography, sputter thin film deposition and Si dry etching. Details of the processing and NbN film deposition could be found in [20]. As a result, the structure depicted in Figure 3 was fabricated and integrated into the waveguide balanced mixer block designed for 1.6–2.0 THz band and manufactured using all-metal Terahertz waveguide technique, GARD-process [17, 18, 5]. After mounting the mixer chips their alignment was checked using SEM imaging: the accuracy of the mixer chip placement was within  $\pm 2 \mu\text{m}$  and the mounting was performed within less than 10 min per chip. Figure 4 shows SEM picture of the mixer chip mounted into

the mixer mount, the waveguide dimensions are  $60 \times 120 \mu\text{m}$ .

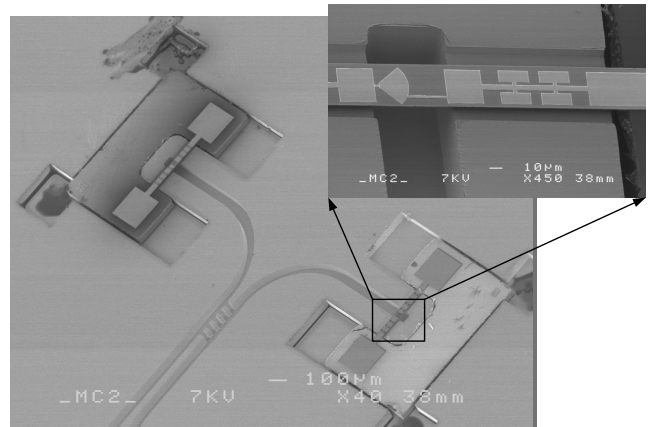


Fig. 4. SEM picture of the fabricated mixer mount with layout presented in Figure 2 and the two HEB mixer chips integrated. No wire bonding for DC/IF interfacing was made. The insert shows SEM picture with magnified view of the HEB mixer beam crossing the waveguide.

It is worth mentioning that the presented mixer layout greatly facilitates mounting and aligning of the HEB devices in the mixer block. Alignment relies on photo-lithography-defined dimensions of the HEB beam, frame and the mixer block structure. Through this, the entire mounting procedure becomes self-aligning. The GARD-process, used for the fabrication of all-metal waveguide structure, is a lithographic process with inherent dimension accuracy better than  $1 \mu\text{m}$ , and hence can replicate identical waveguide mixer block structures over, e.g., a 4'' wafers. Its combination with the novel type of HEB chips provides easy handling and alignment possibilities and opens the way for realization of multi-pixel THz waveguide receivers.

### III. CONCLUSION

In this paper, we presented a concept of multi-pixel heterodyne receiver employing a grid polarizer to inject LO signal into the receiver RF beam. Such scheme offers convenience of designing and building optics and IF/DC interfaces. This approach however requires additional waveguide circuitry comprising an OMT and a waveguide 90-degree twist for each pixel and could be manufactured using micro-fabrication and micro-machining techniques. For the mixers, we suggest using a balanced waveguide hot-electron bolometer mixer. A technology demonstrator employing a novel layout for the HEB mixer with supporting  $\Pi$ -frame and operating in the 1.6 - 2.0 THz band was presented. The design combines several key technologies: all-metal THz waveguide micromachining, ultra-thin NbN deposition and a micromachining of SOI substrate to manufacture the HEB mixer. Integration of the chip into the mixer relies on self-aligning and provides mounting accuracy within  $\pm 2 \mu\text{m}$  confirmed via SEM measurements. As it looks from the mixer fabrication point of view, the number of pixels would be rather constrained by a possibility to generate enough LO power. Given achieved dimensions' accuracy, mounting and alignment tolerances, the demonstrated approach should be

suitable for building multi-pixel and single-end deep-terahertz mixers operating at up to 5 THz.

#### ACKNOWLEDGMENTS

Authors would like to thank S.-E. Ferm for his remarkable fine-mechanic work in this project.

Onsala Space Observatory, Swedish National Facility for Radio Astronomy, contributing 50% of the funds for these studies via RadioNet AMSTAR+.

#### REFERENCES

- [1] SOFIA: Stratospheric Observatory for Infrared Astronomy, <http://www.sofia.usra.edu/index.html>.
- [2] Herschel Observatory, <http://herschel.esac.esa.int/>.
- [3] Planck Observatory, <http://www.esa.int/esaMI/Planck/index.html>.
- [4] N. Schneider, V. Minier, G. Durand, P. Tremblin, J. Urban, and P. Baron, "Atmospheric Transmission at Dome C between 0 and 10 THz," EAS Publications Series, vol. 40, pp. 327–332, 2010.
- [5] D. Meledin, A. Pavolotsky, V. Desmaris, I. Lapkin, C. Risacher, V. P. Robles, D. Henke, O. Nyström, E. Sundin, D. Dochev, M. Pantaleev, M. Fredrixon, M. Strandberg, B. Voronov, G. Gol'tsman, and V. Belitsky, "A 1.3 THz balanced waveguide HEB mixer for the APEX telescope," IEEE Trans. Microwave Theory Tech., vol. 57, pp. 89–98, 2009.
- [6] J. R. Pardo, E. Serabyn, and J. Cernicharo, "Submillimeter atmospheric transmission measurements on Mauna Kea during extremely dry El Nino conditions: implications for broadband opacity contributions," J. Quant. Spectrosc. Radiat. Transf., vol. 68, pp. 419–433, 2001.
- [7] S. Paine, R. Blundell, D. C. Papa, and J. W. Barrett, "A Fourier transform spectrometer for measurement of atmospheric transmission at submillimeter wavelengths," PASP, vol. 112, pp. 108–118, 2000.
- [8] D. P. Marrone, R. Blundell, E. Tong, S. N. Paine, D. Loudkov, J. H. Kawamura, D. Lühr, and C. Barrientos, "Observations in the 1.3 and 1.5 THz atmospheric windows with the receiver lab telescope," in 16<sup>th</sup> Int. Symp. Space Terahertz Technol. Göteborg, Sweden, 2005.
- [9] The Cornell Caltech Atacama Telescope (CCAT), <http://submm.org/>.
- [10] G. de Lange, "Development of the HIFI band 3 and 4 mixer units," Proc. SPIE Int. Soc. Opt. Eng., vol. 5498, pp. 267–277, 2004.
- [11] G. H. Tan, "The ALMA front ends: an overview," in Proc. 19<sup>th</sup> Int. Symp. Space Terahertz Technol., Groningen, 2008.
- [12] V. Belitsky, I. Lapkin, V. Vassilev, R. Monje, A. B. Pavolotsky, D. Meledin, D. Henke, O. Nyström, V. Desmaris, C. Risacher, M. Svensson, M. Olberg, E. Sundin, M. Fredrixon, D. Dochev, S.-E. Ferm, and H. Olofsson, "Facility Heterodyne Receiver for the Atacama Pathfinder Experiment Telescope," in Joint 32<sup>nd</sup> Int. Conf. Infrared Millimeter Waves and 15<sup>th</sup> Int. Conf. Terahertz Electronics Cardiff, UK, 2007.
- [13] P. Khosropanah, J. R. Gao, W. M. Laauwen, M. Hajenius, and T. M. Klapwijk, "Low noise NbN hot electron bolometer mixer at 4.3 THz," Appl. Phys. Lett., vol. 91, p. 221111, 2007.
- [14] S. Cherednichenko, V. Drankinskiy, T. Berg, P. Khosropanah, and E. Kollberg, "Hot-electron bolometer terahertz mixers for the Herschel Space Observatory," Rev. Sci. Instr., vol. 79, p. 034501, 2008.
- [15] D. Meledin, D. P. Marrone, C.-Y. E. Tong, H. Gibson, R. Blundell, S. N. Paine, et al, "A 1 THz superconducting Hot Electron Bolometer receiver for astronomical observations," IEEE Trans. Microwave Theory and Techniques, vol. 52, no.10, pp. 2338–2343, Oct. 2004.
- [16] E. Tong, J. Kawamura, D. Marrone, D. Loudkov, S. Paine, R. Blundell, C. Barrientos, and D. Lühr, "A 1.5 THz hot electron bolometer receiver for ground-based terahertz astronomy in northern Chile," Proc. SPIE, vol. 6373, 2006.
- [17] J. W. Kooi and V. Ossenkopf, "HIFI instrument stability as measured during the thermal vacuum tests of the Herschel space observatory," Proc. 20<sup>th</sup> Int. Symp. Space THz Technol., 2009.
- [18] A. Pavolotsky, D. Meledin, C. Risacher, M. Pantaleev, and V. Belitsky, "Micromachining approach in fabricating of THz waveguide components," Microelectron. J., vol. 36, p. 636, 2005.
- [19] V. Desmaris, D. Meledin, A. Pavolotsky, R. Monje, and V. Belitsky, "All-metal micromachining for the fabrication of sub-millimetre and THz waveguide components and circuits," J. Micromech. Microeng., vol. 18, p. 095994, 2008.
- [20] D. Dochev, V. Desmaris, D. Meledin, A. Pavolotsky, V. Belitsky, "A Technology Demonstrator for a 1.6 – 20 THz Waveguide HEB Receiver with a Novel Mixer Layout", Int. Journal of Infrared, Millimeter and Terahertz Waves, vol. 32, No. 4, pp 451-465, April 2011. (doi: 10.1007/s10762-011-9774-9).
- [21] J.F. Johansson, "Millimetre Wave Imaging – Theory and Experiments", Research Report No. 151, Department of Radio and Space Science, Chalmers Univ. of Technology, Gothenburg, Sweden, May 1986.
- [22] J. V. Siles, B. Thomas, G. Chattopadhyay, A. Maestrini, C. Lee, E. Schlecht, C. Jung and I. Mehdi, "Design of a high-power 1.6 THz Schottky tripler using 'on-chip' power-combining and Silicon micro-machining", Proceedings of 22<sup>nd</sup> International Symposium on Space Terahertz Technology, Tucson, 26-28 April 2011.
- [23] Christopher E. Groppi, Christian Y. Drouet d'Aubigny, Arthur W. Lichtenberger, Christine M. Lyons, Christopher K. Walker, "Broadband Finline Ortho-Mode Transducer for the 750-1150 GHz Band", Proceedings of 16th International Symposium on Space Terahertz Technology, pp.513-518, May 2-4, 2005, Chalmers University of Technology, Göteborg, Sweden.
- [24] G. Chattopadhyay, J. Ward, N. Llombert, and K. Cooper, "Submillimeterwave 90. Polarization twists for integrated waveguide circuits," IEEE Microw. Wireless Compon. Lett., vol. 20, no. 11, pp. 592–594, Nov. 2010.
- [25] Lihan Chen, Alex Arsenovic, James R. Stanec, Theodore J. Reck, Arthur W. Lichtenberger, "A Micromachined Terahertz Waveguide 90 Twist", IEEE Microw. Wireless Compon. Lett., vol. 21, no. 5, pp. 234–236, May 2011.

## **NIKA: a dual band KIDs camera**

L. Ferrari<sup>1\*</sup>, A. Benoit<sup>4</sup>, A. Bideaud<sup>4</sup>, L. J. Swenson<sup>4</sup>, M. Roesch<sup>8</sup>, F.X. De'sert<sup>6</sup>, S. Doyle<sup>5</sup>, A. Endo<sup>3</sup>, A. Cruciani<sup>4,9</sup>, P. Ade<sup>5</sup>, A.M. Baryshev<sup>1,11</sup>, J.J.A. Baselmans<sup>2</sup>, O. Bourrion<sup>7</sup>, P. Camus<sup>4</sup>, C. Giordano<sup>10</sup>, C. Hoffmann<sup>4</sup>, S. Leclercq<sup>6</sup>, J. Macias Perez<sup>7</sup>, P. Mauskopf<sup>5</sup>, K.F. Schuster<sup>6</sup>, C. Tucker<sup>5</sup>, C. Vescov<sup>7</sup>, S.J.C. Yates<sup>2</sup>

*1 SRON, Netherlands Institute for Space Research\*, Groningen, 9747 AD, The Netherlands*

*2 SRON, Netherlands Institute for Space Research\*, Utrecht, 3584 CA, The Netherlands*

*3 Kavli Institute of NanoScience, Delft University of Technology, Delft, 2628 CJ, The Netherlands*

*4 Institut Neel, CNRS & University Joseph Fourier, Grenoble, 38042, France*

*5 Cardiff School of Physics and Astronomy, Cardiff University, Cardiff, CF24 3AA, Wales*

*6 Laboratoire d'Astrophysique, Observatoire de Grenoble, Grenoble, 38041, France*

*7 Laboratoire de Physique Subatomique et le Cosmologie (LPSC), Grenoble, 38026, France*

*8 Institut de RadioAstronomie Millimetrique, Saint Martin d'Herès, 38406, France*

*9 Dipartimento di Fisica, Università di Roma La Sapienza, Rome, 00185, Italy*

*10 Fondazione Bruno Kessler, Povo (TN), I-38123, Italy*

*11 Kapteyn Astronomical institute, University of Groningen, Groningen, 9747 AD, The Netherlands*

\* Contact: lorenza@sron.nl, phone +31-50-363 8321

**Abstract**—The Neel IRAM KIDs Array (NIKA) is a kinetic inductance detectors based instrument developed for millimeter wave astronomy. The instrument includes dual-band optics opening two observational windows at 150 and 220 GHz. The detectors mounted on the 150 GHz are lumped-element KIDs. The array mounted on the other frequency range is composed by 256 antenna coupled KIDs arranged in rectangular pattern. We present the results of the test-run made in October 2010 at the Institute for Millimetric Radio Astronomy (IRAM) 30-meter telescope at Pico Veleta. We will focus on the antenna coupled KIDs detectors results in particular on the optimization of the detector chip, design of lens array and on the sky measurements.

## Radiation mixer based on the 2DEG in a GaN heterostructure

B. S. Karasik<sup>1,\*</sup>, J. J. Gill<sup>1</sup>, T. J. Crawford<sup>1</sup>, I. Mehdi<sup>1</sup>, and A. V. Sergeev<sup>2</sup>

*1 Jet Propulsion Laboratory, California Institute of Technology\*, Pasadena, CA 91109*

*2 SUNY at Buffalo, Dept. of Electrical Engineering, Buffalo, NY 14260*

\* Contact: boris.s.karasik@jpl.nasa.gov, phone +1 (818) 393-4438

**Abstract**—Radiation THz mixer utilizing the hot-electron effect in the two-dimensional electron gas (2DEG) has several important features (microwatt level local oscillator (LO) power, ~ 100 K operating temperature, multi-GHz IF bandwidth) making it attractive for the space applications where cryogenic cooling is unacceptable (e.g., planetary missions). Enhancement of this mixer sensitivity to the level similar or better than that of the Schottky mixer may lead to significant advancements in the future instrument architecture enabling single-pixel and array receivers up to the highest frequency available for the solid-state multiplier LOs (currently, close to 3 THz). An AlGaAs/GaAs based 2DEG mixer has been pursued in past with a limited success because of the somewhat unfavorable for realization of the strong Drude absorption combination of the material parameters (high electron mobility, low electron density) found in typical GaAs heterostructures. In particular, the intrinsic kinetic inductance of the mixer was large that leads to the high reactive component in the THz impedance.

We are revisiting the 2DEG mixer approach, this time utilizing a GaN based heterostructure. This relatively new material has become quite popular due to its importance for blue LED and high-power HEMT transistor technologies. A favorable for the 2DEG THz mixing combination of the mobility  $< 1000 \text{ V cm}^2 (\text{V sec})^{-1}$  and the electron density  $> 10^{13} \text{ cm}^{-2}$  is readily available in these heterostructures. Initial FTS transmission tests have shown a significant THz absorption in the GaN heterostructures grown on sapphire substrates. More FTS low-temperature (down to 77 K) tests are under way followed by the proof-of-concept demonstration using a quasioptical 0.6-2 THz mixer design. The 2DEG mixer analysis and experimental results will be presented at the meeting.

## Integrated Balanced SIS Mixer at 500 GHz

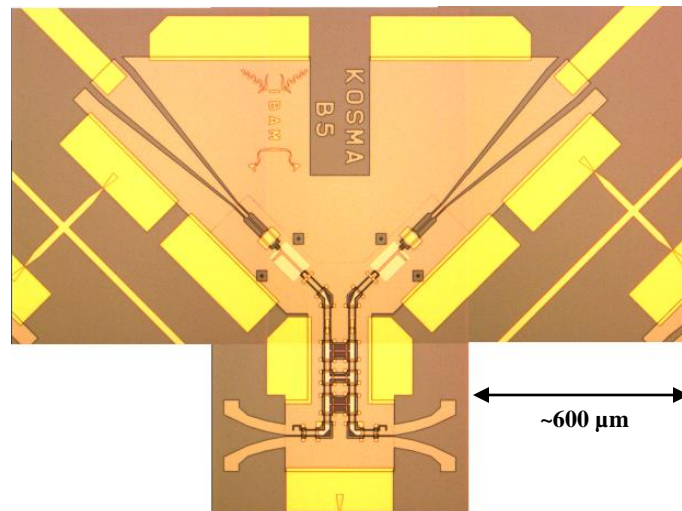
M. P. Westig<sup>1\*</sup>, C. E. Honingh<sup>1</sup>, K. Jacobs<sup>1</sup>

*1 KOSMA, I. Physikalisches Institut, Universität zu Köln\*, Köln, Germany*

\* Contact: westig@ph1.uni-koeln.de, phone +49-221-470-3489

This work is funded by BMBF Verbundforschung Astronomie, contract 05A08PK2.

**Abstract**—We present the design and measurement results of a balanced SIS mixer for the 400-500 GHz band fully integrated on a thin Silicon substrate. A superconducting coplanar waveguide circuit with two broadband waveguide probes, a 90° hybrid coupler and two pairs of SIS junctions with integrated tuning was extensively simulated using CST and Sonnet. The coplanar waveguides use capacitive bridges to suppress odd mode propagation. The circuit is deposited on a 9 micrometer thick Silicon substrate shaped with deep reactive ion etching from a Silicon-On-Insulator wafer. IF and ground connections to a waveguide block are made via integrated beam lead contacts, enhancing the RF and IF performance as well as the device cooling. We show details of the RF design and measurement results which show excellent performance over the RF band measured within a 4-8 GHz IF band.



On-wafer photo of an Integrated Balanced Mixer (IBAMI) device

# Performance of a Twin-Slot Antenna Coupled NbN Hot Electron Bolometer Mixer at 2.5 THz

Wen Zhang, Jian- Rong Gao, Merlijn Hajenius, Wei Miao, Pourya Khosropanah, Teun M. Klapwijk, Sheng-Cai Shi, and Darren Hayton

**Abstract**—We demonstrate a quasi-optical NbN hot electron bolometer (HEB) mixer using a twin-slot antenna on a Si lens to couple terahertz radiation. The mixer shows a receiver noise temperature of 1150 K at 2.5 THz, which is expected based on a model that includes quantum noise. The measured direct response is understood by taking into account the main beam efficiency and the parasitic reactance due to the geometric change between bolometer and transmission line. The measured beam of the mixer is nearly collimated and has a Gaussian beam efficiency of 90 % with side-lobes below -16 dB.

**Index Terms**—hot electron bolometer, direct response, receiver noise temperature, beam pattern.

## I. INTRODUCTION

TERAHERTZ quasi-optical mixers [1] combining a superconducting NbN hot electron bolometer (HEB) with a dielectric lens-planar antenna coupling scheme for radiation have played a crucial role in astronomy in the THz frequency region. Such mixers offer not only low noise but also a high radiation coupling efficiency. Among different planar antennas, a twin-slot antenna [2] becomes preferred for astronomic applications because of the following expected characteristics: a high coupling efficiency, a Gaussian beam, linear polarization, and a reasonably wide RF bandwidth. Quasi-optical mixers of superconductor-insulator-superconductor (SIS) [3] and HEB [4]

using twin-slot antennas were successfully applied to the high frequency bands ( $\leq 1.9$  THz) in the Heterodyne Instrument for the Far Infrared (HIFI) on the Herschel Space Observatory<sup>1</sup>. Although twin-slot antennas have been reported at 2.5 THz for Nb HEB mixers [5]-[7] and NbN HEB mixers [8]-[10], they showed lower sensitivities than spiral antenna coupled HEB mixers. Although similar sensitivities have been observed at 1.6 THz [11], where both types of HEB mixers were fabricated in the same way and in the same wafer, it is unclear whether the lower sensitivities at 2.5 THz are due to the twin-slot antenna or the detector. The (far-field) beam pattern of a quasi-optical mixer is also a crucial performance parameter particularly when it has to match the incoming beam from a telescope and when it is for a mixer array. The beam pattern study was pioneered in [6], however, the result is not conclusive.

In this letter we report on a twin-slot antenna coupled NbN HEB mixer at 2.5 THz that demonstrates low noise temperature, excellent beam pattern, and direct response, which are in agreement with predictions. Such a mixer is suitable for observations of the astronomically-interesting lowest rotational transition of HD at 2.7 THz, which can be observed with Stratospheric THz Observatory (STO) [12], Stratospheric Observatory for Infrared Astronomy (SOFIA) [13], and future space observatories [14].

## II. HEB DEVICE AND MEASUREMENT SETUP

Figure 1 shows a lens-twin slot antenna coupled HEB mixer. The HEB consists of a 1.5  $\mu\text{m}$  wide, 0.2  $\mu\text{m}$  long, and 5.5 nm thick NbN bridge on a highly resistive Si substrate. The bridge is connected to the central conductor of a coplanar waveguide (CPW) transmission line by NbTiN-Au superconducting bilayer contact pads [15]-[17]. The HEB has a normal-state resistance ( $R_N$ ) of 124  $\Omega$  at 11 K, a superconducting transition temperature of 10 K, and a critical current of 133  $\mu\text{A}$  at 4.2 K. To have a center frequency at 2.8 THz, we designed a twin-slot antenna with the following dimensions: the slot length  $L$  is  $0.3\lambda_0$  with  $\lambda_0$  ( $=107 \mu\text{m}$ ) the free space wavelength; the slot separation  $S$  is  $0.17\lambda_0$ ; and the slot width  $W$  is  $0.02\lambda_0$ . The CPW line has a central conductor with a width of 2.8  $\mu\text{m}$  and two gaps of 1.4  $\mu\text{m}$ , yielding a characteristic impedance of 51  $\Omega$ . To avoid leakage of the RF signal via the intermediate frequency (IF) output line, a RF choke filter is used with three sections consisting of three alternating high (75  $\Omega$ ) and low impedance

Manuscript received July 7, 2011. The work was supported in part by the NSFC under Grant Nos. 10803021, 10933005 and 10621303, the Ministry of Science and Technology under Grant No. 2010CB327401, CAS KeyLab for Radio Astronomy, KNAW China Exchange Programme, NWO, and the AMSTAR<sup>+</sup> project of RadioNet under FP7.

W. Zhang, W. Miao, S. C. Shi are with Purple Mountain Observatory, Chinese Academy of Sciences, Nanjing, Jiangsu 210008, China (e-mail: wzhang@pmo.ac.cn; miaow@mwlab.pmo.ac.cn; scshi@pmo.ac.cn).

J. R. Gao, and H. Hajenius are with SRON Netherlands Institute for Space Research, 3584 CA Utrecht, and also with the Kavli Institute of Nanoscience, Delft University of Technology, 2628 CJ Delft, the Netherlands (e-mail: j.r.gao@tudelft.nl; hajenius@gmail.com).

P. Khosropanah and D. Hayton are with SRON Netherlands Institute for Space Research, the Netherlands (e-mail: p.khosropanah@sron.nl, and D.J.Hayton@sron.nl).

T. M. Klapwijk is with the Kavli Institute of Nanoscience, Delft University of Technology, 2628 CJ Delft, the Netherlands (e-mail: t.m.klapwijk@tudelft.nl).

<sup>1</sup><http://sci.esa.int/science-e/www/object/index.cfm?fobjectid=34691>

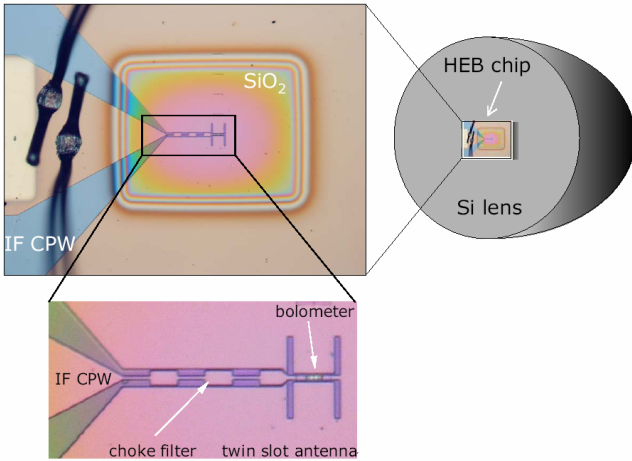


Fig. 1. Schematic drawing of a quasi-optical mixer where a HEB chip is glued to the backside of a Si ellipsoidal lens. As shown in the optical micrograph the NbN HEB consists of a twin slot antenna, a coplanar waveguide (CPW) transmission line (in the center), a choke filter, and a wide CPW line for intermediate frequency (IF) output.

(34  $\Omega$ ) segments, each being a quarter wavelength (10.7  $\mu\text{m}$ ) long.

To determine the double sideband receiver noise temperature ( $T_{N,rec}$ ), we performed the measurements in a vacuum setup [see Fig. 2(a)] as described in [18]. The HEB chip is glued to the backside of a Si ellipsoidal lens without antireflection coating, mounted in a mixer block that is placed in a liquid helium cryostat. A hot (295 K) and cold (77 K) load can be selected by rotating a mirror. The radiation from the hot/cold load is combined with that from the LO by a 3- $\mu\text{m}$  Mylar beam splitter. Before reaching the HEB, the radiation passes through the metal-mesh heat filter at 4.2 K that blocks infrared radiation.

The LO is an optically pumped Far Infrared (FIR) ring gas laser, operated at a frequency of 2.523 THz using  $\text{CH}_3\text{OH}$  gas. The LO power coupled to the mixer is regulated by rotating a wire grid in front of the gas laser.

The IF signal, resulting from the mixing of the LO and the hot/cold load signal, first passes through a bias-T, a circulator, and then a cryogenic low noise amplifier (Berkshire 1.3-1.7 GHz) operated at 4.2 K, followed by room-temperature amplifiers. This signal is filtered at 1.5 GHz within a band of 80 MHz. Between each two components in the IF chain, an attenuator is added to avoid standing waves. The entire IF chain has a gain of about 80 dB and a noise temperature of 7 K.

To verify the antenna design, the direct response  $\Delta I(f)$  of the mixer as a function of frequency is measured by operating it as a direct detector using an evacuated Fourier-transform spectrometer (FTS) [7]. The beam splitter used inside the FTS is a 12.5  $\mu\text{m}$  thick Mylar sheet. Additionally, there is a high density polyethylene (HDPE) thin lens inside the FTS to collimate radiation. It is worthy to note that the optics are different from  $T_{N,rec}$  measurement and contain a 2-mm thick HDPE window and a heat filter of two layers of Zitex G104.

We also characterize the beam pattern of the same mixer using a computer controlled measurement setup [6], [19],

where the gas laser at 2.5 THz is applied as a signal source as shown in Fig. 2(b). The HEB is heated to a temperature that is slightly below the superconducting transition temperature of the NbN bridge. At a fixed bias voltage (0.6 mV), a lock-in amplifier is used to record the current changes due to the modulated defocused laser beam as a function of the tilt and rotation angle of the HEB cryostat. The dynamic range of the current signal is about 25 dB. The twin-slot antenna is positioned in such a way that its E plane is horizontal, and the H

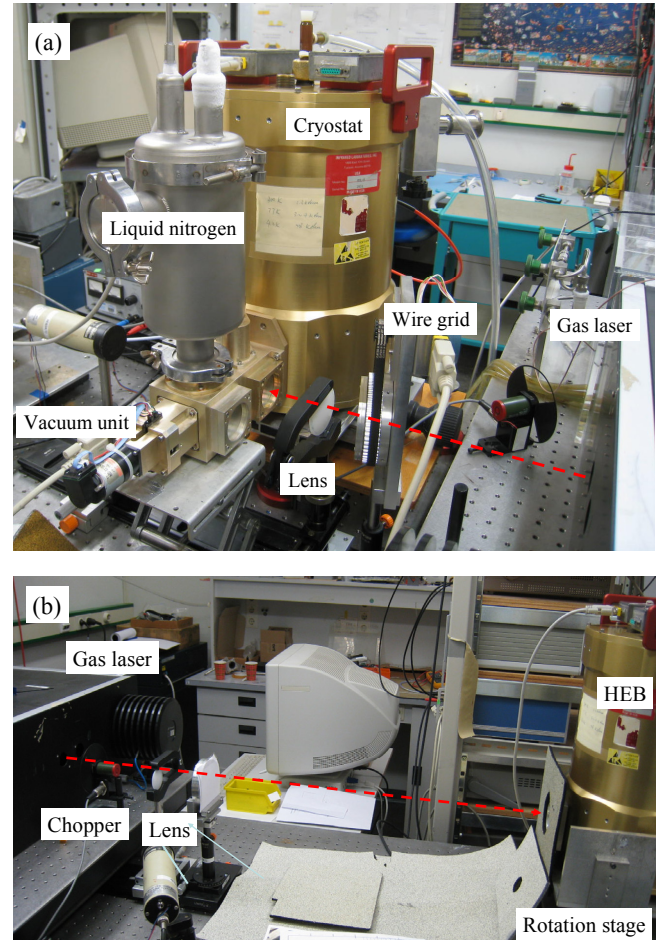


Fig. 2. (a) Receiver noise temperature measurement setup, where vacuum unit consisting of hot/cold loads, beamsplitter, and rotating mirror is directly connected to the HEB cryostat. Hot and cold loads can be selected by rotating the mirror. (b) Beam pattern measurement setup, where gas laser works as a signal source. The current change due to the modulated laser beam as functions of tilt and rotation angles of the HEB cryostat is recorded using a lock-in amplifier.

plane is vertical.

### III. DIRECT RESPONSE

$\Delta I(f)$  is measured using a lock-in amplifier at a constant bias voltage and at a temperature close to the transition temperature of NbN bridge. Fig. 3(a) shows the measured normalized direct response of the mixer. We find a peak response at 1.8 THz, and other two lower peaks at 2.7 and 1.2 THz, respectively. The former is the designed center frequency, relative to the slot

length (half-wavelength), and the latter might be due to full-wavelength resonance. The dip at 2.2 THz is due to the absorption of the HDPE thin lens inside the FTS and 2 mm HDPE vacuum window of HEB cryostat.  $\Delta I(f)$  should be governed by the multi-factors expressed as  $S\eta_{int}\eta_{opt}\eta_{FTS}P_l$ , where  $S$  is the frequency independent current responsivity;  $\eta_{int}$  the intrinsic coupling efficiency for THz radiation power transmitted from the antenna to the bridge;  $\eta_{opt}$  the transmission due to the HDPE thin lens, HDPE window, and heat filter;  $\eta_{FTS}$  the power transfer function of the FTS;  $P_l$  the power spectrum of the lamp in the FTS, which is virtually constant within the frequency range of interest [7]. The transmission of the Si lens is not included since the absorption loss is negligible based on our measurement. Thus the measured relative response reflects the product of  $\eta_{int}$ ,  $\eta_{opt}$ , and  $\eta_{FTS}$ . Fig. 3a also shows the product of  $\eta_{opt}\eta_{FTS}$ , where  $\eta_{opt}$  is obtained based on measured power transmission data and  $\eta_{FTS}$  is calculated for Mylar beam splitter. To derive  $\eta_{int}$  we divide  $\Delta I(f)$  by the product of  $\eta_{opt}\eta_{FTS}$ . The result is a relative  $\eta_{int}$  that is plotted in Fig. 3(b). We find the 3 dB intrinsic response bandwidth to be approximately 2.1 THz, which is relatively wide.

To simulate  $\eta_{int}$ , each slot of the antenna is considered as a voltage generator in series with the antenna impedance [21]. The RF choke filter is assumed in series with one voltage generator/antenna impedance. Furthermore, the NbN bridge sees an impedance equal to both the added choke filter and the slot impedance transformed by the CPW transmission line on one side, while seeing only the transformed slot impedance on the other side. In addition, a capacitance  $C$  in parallel and an inductance  $L$  in series with the bolometer are added to the embedding impedance ( $Z_{embed}$ ) to take into account the electromagnetic current crowding effects due to the abrupt change between the bridge and the central conductor [21]. We took a calculated  $C$  of 0.4 fF and a fitted  $L$  of 10 pH for the calculation. The impedance of the twin-slot antenna as a function of frequency is calculated using a simulator ‘‘PILRAP’’ [22].  $\eta_{int}$  is derived by the impedance mismatch between the embedding impedance ( $Z_{embed}$ ) seen at the bridge terminals and the bolometer impedance  $Z_{HEB}$  (equal to its  $R_N$ )

$$\eta_{int}(f) = 1 - \left| \frac{Z_{HEB} - Z_{embed}}{Z_{HEB} + Z_{embed}} \right|^2 \quad (1)$$

In addition to Eq. 1, we also consider the effect of main beam efficiency in the final result of  $\eta_{int}(f)$ . When the frequency is much higher than the design frequency, the main beam efficiency suppresses the response due to the second antenna resonance. The calculated  $\eta_{int}(f)$  is also plotted in Fig. 3b for comparison and shows good agreement with the measured one with respect to the frequency dependence and the overall shape.

#### IV. RECEIVER NOISE TEMPERATURE

Double sideband receiver noise temperature ( $T_{N,rec}$ ) of the

mixer was measured by fixing the bias voltage of the HEB, but varying the LO power [18], [23]. At a bias voltage of 0.6 mV, we measured the receiver output power as a function of bias current, which is the result of varying LO power. Two such data sets are recorded,  $P_{out,hot}$  responding to the hot load and  $P_{out,cold}$  to the cold load. The Y-factor can be obtained by  $Y(I) = P_{out,hot}(I)/P_{out,cold}(I)$  at the same current using the fitted polynomial curves to the  $P_{out,hot}$  and  $P_{out,cold}$  data points. The derived  $T_{N,rec}$  as a function of bias current is plotted in Fig. 4(a), where the lowest  $T_{N,rec}$  is  $1150 \pm 50$  K at a current of 24  $\mu$ A, found from a broad minimum. As discussed in [18], a clear advantage of this method is that the  $T_{N,rec}$  can be determined without suffering from the effect of direct detection. We also estimated the total conversion loss at the same operating point using a known method in [25] and find it to be 12.2 dB. The total loss in front of bolometer is 4.52 dB, in which the optics contribute 1.9 dB and the intrinsic coupling efficiency of the antenna contributes 2.62 dB, obtained from  $\eta_{int}$  [see Fig. 3(b)]. The optimum LO power absorbed in the HEB is 130 nW.

For comparison,  $T_{N,rec}$  was also obtained in a conventional way, in which we measured the receiver output power,  $P_{out,hot}$  and  $P_{out,cold}$ , responding to the hot and cold load as a function of bias voltage under a constant optimum LO power. The results are plotted in Fig. 4(b). The lowest  $T_{N,rec}$  is  $1250 \pm 300$  K, which is 9 % higher than the previously determined 1150 K due to the direct detection effect. Note that at the optimum operation point the bias current changes  $\sim 0.3$   $\mu$ A when the hot and cold load is switched. Because of the limited RF bandwidth, the influence on  $T_{N,rec}$  for the twin-slot antenna coupled HEB mixer is, as expected, considerably smaller than that for a spiral antenna coupled NbN HEB mixer [19].

$T_{N,rec}$  can be predicted using the quantum noise theory for terahertz HEB mixers based on a distributed hot-spot model

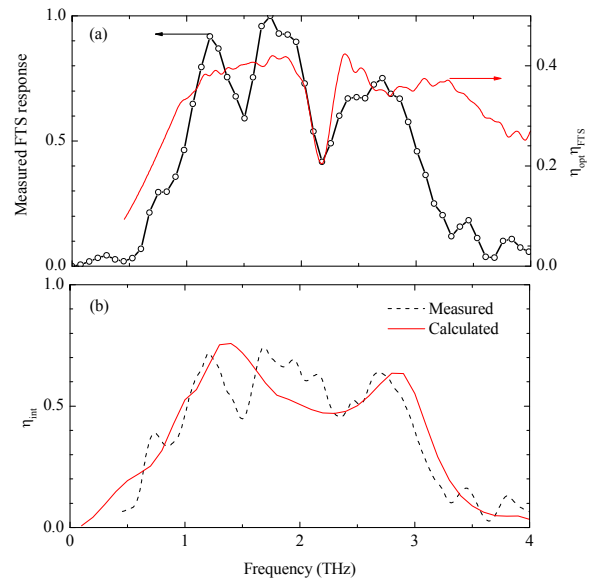


Fig. 3. (a) Measured, normalized direct response  $\Delta I(f)$  of the twin-slot antenna coupled NbN HEB mixer and product of measured power transmission of HDPE lens, HDPE window, and heat filter ( $\eta_{opt}$ ) and calculated power transfer function of the FTS ( $\eta_{FTS}$ ) as a function of frequency; (b) Measured and calculated intrinsic direct response ( $\eta_{int}$ ).



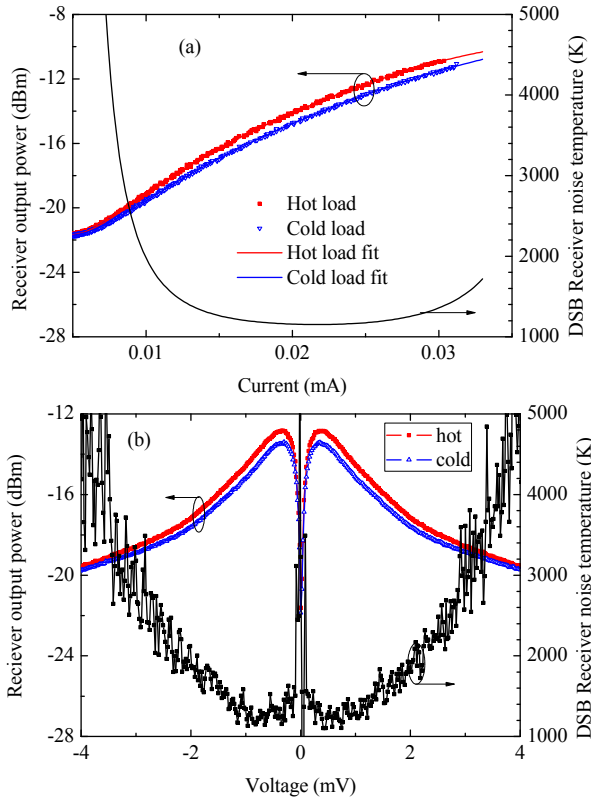


Fig. 4. (a) Measured receiver output powers (left axis) at the optimum bias voltage of 0.6 mV and the polynomial fit responding to the hot and cold load as a function of bias current of the HEB, which is varied by changing LO power. Double sideband receiver noise temperature  $T_{N,rec}$  (right axis) of the HEB mixer is also shown as a function of bias current; (b) Measured receiver output power (left axis) responding to the hot and cold load at optimum LO power as a function of bias voltage.  $T_{N,rec}$  is also plotted (right axis) vs. bias voltage.

[25], which includes the contribution of quantum noise (QN). We use the empirical values for the classical output noise and the quantum efficiency  $\beta$ -factor found in [23] to calculate  $T_{N,rec}$ . The calculated  $T_{N,rec}$  is 1170 K, for which 40 % is contributed by QN. The result agrees well with the measured one (1150 K).

The measured  $T_{N,rec}$  is comparable to the one found using a similar HEB but coupled with a spiral antenna at the same frequency [23], however, strictly speaking, is 25 % higher if we could have the same optical loss (see table 1). We attribute this difference to the parasitic reactance due to the abrupt change between the bridge and the CPW line, causing a slightly lower intrinsic coupling [21]. We also noticed that a new result of 600

TABLE I

Comparison between spiral antenna and twin-slot antenna coupled HEB mixers at 2.5 THz, measured in vacuum setup. All the relevant parameters are also listed: optical loss of the 3- $\mu$ m Mylar beam splitter at 300 K ( $L_{BS}$ , calculated), the IR filter at 4 K ( $L_{filter}$ , measured), the uncoated Si lens at 4 K ( $L_{lens}$ , reflection loss calculated; absorption loss is negligible based on our measurements on a Si wafer from the same material as used for our Si lens), intrinsic coupling between HEB and antenna ( $L_{coup}$ , from FTS response), and DSB receiver noise temperature ( $T_{N,rec}$ , measured).

	$L_{BS}$ (dB)	$L_{filter}$ (dB)	$L_{lens}$ (dB)	$L_{coup}$ (dB)	$L_{total}$ (dB)	$T_{N,rec}$ (K)
Spiral antenna HEB	0.2	0.73	1.5	0.07	2.5	974
Twin slot antenna HEB	0.2	0.2	1.5	2.62	4.52	1150

K at 2.5 THz was very recently reported in [26], and 630 K in [27] using spiral antenna coupled NbN HEBs.

## V. BEAM PATTERN

Fig. 5a shows the measured beam patterns in E and H planes at 2.5 THz. The main beams in E and H planes overlap exactly, indicating a symmetric beam. The full width at -10 dB level is 1.4°, implying that the main beam is well collimated. The side lobes are 16 dB below the main lobe, which is generally adequate for THz astronomical applications. For comparison, a calculated beam pattern using the PILRAP [22] is also plotted in Fig. 5a, which shows good agreement with the measured ones. Fig. 5b illustrates the same beam pattern, but in a two-dimensional plot. The Gaussian beam efficiency, defined as the coupling efficiency between the measured beam of an antenna and a fundamental Gaussian mode [28], is found to be 90 %.

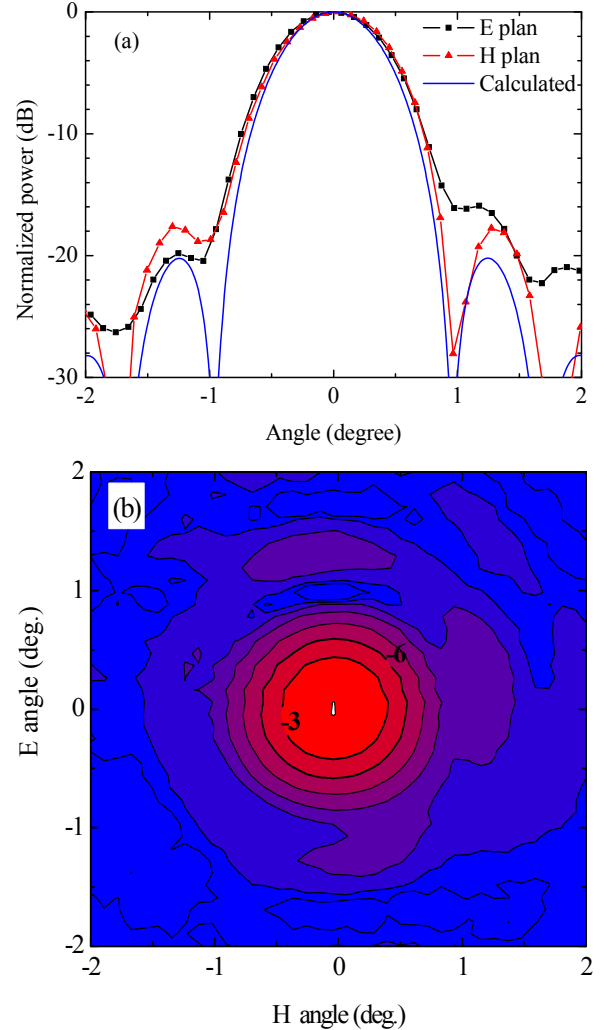


Fig. 5. (a) Measured and simulated far-field beam patterns of the quasi-optical mixer shown in figure 1 at 2.5 THz. (b) the same beam pattern, but plotted in two-dimensions.

## VI. CONCLUSION

In summary we have demonstrated a practical quasi-optical NbN HEB mixer using a twin-slot antenna, which has a measured  $T_{N,rec}$  of 1150 K at 2.5 THz (this can become 800 K if a lens with an antireflection coating were employed [20]), the main beam with a high Gaussian beam coupling efficiency and with sidelobes more than 16 dB below the boresight response, and an expected direct response. Our results are extremely encouraging for pushing the operating frequency of a twin slot antenna even higher, such as to 4.7 THz in order to study the OI fine structure transition.

## ACKNOWLEDGMENT

We acknowledge L. de Jong, W.J. Vreeling, W. M. Laauwen, W. Horinga, and J. N. Hovenier for their technical support.

## REFERENCES

- [1] J. Zmuidzinis, and P. L. Richards, "Superconducting detectors and mixers for millimeter and submillimeter astrophysics," *Proc. IEEE*, vol. 92, no.10, pp.1597-1616, Oct. 2004.
- [2] D. F. Filipovic, S. S. Gearhart, and G. M. Rebeiz, "Double-slot antennas on extended hemispherical and elliptical silicon dielectric lenses," *IEEE Trans. Microw. Theory Techn.*, vol.41, no.10, pp. 1738-1749, Oct. 1993.
- [3] A. Karpov D. Miller, F. Rice, J. Zmuidzinis, J.A. Stern, B. Bumble, and H.G. leDuc, "Development of 1.25 THz SIS mixer for Herschel space observatory," *Proc. SPIE*, vol. 6275, 62751U, 2006.
- [4] S. Cherednichenko, V. Drakinskiy, T. Berg, P. Khosropanah, and E. Kollberg, "Hot-electron bolometer terahertz mixers for the Herschel Space Observatory," *Rev. Sci. Instrum.* 79, 2008, 034501.
- [5] B. S. Karasik, M. C. Gaidis, W. R. McGrath, B. Bumble, and H. G. LeDuc, "Low noise in a diffusion-cooled hot-electron mixer at 2.5 THz," *Appl. Phys. Lett.*, vol.71, pp.1567-1569, Sep. 1997.
- [6] R. A. Wyss, B. S. Karasik, W. R. McGrath, B. Bumble, and H. LeDuc, "Submillimeter-wave spectral response of twin-slot antennas coupled to hot electron bolometers," in *Proc. 10<sup>th</sup> Int. Space Terahertz Technol. Symp., Charlottesville*, Virginia, 1999, pp.215-224.
- [7] W. F. M. Ganzevles, L. R. Swart, J. R. Gao, P. A. J. de Korte, and T. M. Klapwijk, "Direct response of twin-slot antenna-coupled hot-electron bolometer mixers designed for 2.5 THz radiation detection," *Appl. Phys. Lett.*, vol.76, no.22, 2000, pp. 3304-2206.
- [8] A. D. Semenov, H. Richter, H.-W. Hubers, B. Gunther, A. Smirnov, L. S. Il'in, M. Siegel, and J. P. Karamarkovic, "Terahertz performance of integrated lens antennas with a hot-electron bolometer," *IEEE Trans. Microwave Theory Techn.*, vol. 55, no.2, pp. 239-247, 2007.
- [9] D. Loudkov, P. Khosropanah, S. Cherednichenko, A. Adam, H. Merkel, E. Kollberg, and G. Gol'tsman, "Broadband fourier transform spectrometer (FTS) measurements of spiral and double-slot planar antennas at THz frequencies," in *Proc. 13<sup>th</sup> Int. Space Terahertz Technology Symp.*, Cambridge, Massachusetts, March 26-28, 2002, pp.373-381.
- [10] Z. Q. Yang, M. Hajenius, J. N. Hovenier, A. B. Baryshev, J. J. A. Baselmans, J. R. Gao, T. M. Klapwijk, A. J. L. Adam, T. O. Klaassen, B. S. Williams, S. Kumar, Q. Hu, and J. L. Reno, "Compact heterodyne receiver at 2.8 THz based on a quantum cascade laser and a superconducting bolometer," *Proc. Joint 30th Int. Infrared Millim. Waves/13th Int. Terahertz Electron. Conf.*, vol.2, pp.465-466, 2005.
- [11] J. R. Gao, M. Hajenius, Z. Q. Yang, T. M. Klapwijk, W. Miao, S. C. Shi, B. Voronov, and G. Gol'tsman, "Direct comparison of the sensitivity of a spiral and a twin-slot antenna coupled HEB mixer at 1.6 THz," in *Proc. 17<sup>th</sup> Int. Space Terahertz Technology Symp.*, Paris, France, May 10-12, 2006, pp.59-62.
- [12] C. Walker, C. Kulesa, J. Kloosterman, T. Cottam, D. Lesser, P. Bernasconi, H. Eaton, N. Rolander, D. Neufeld, C. Lisse, C. Groppi, C. Martin, A. Stark, D. Hollenbach, J. Kawamura, P. Goldsmith, W. Langer, H. Yorke, J. Sterne, A. Skalare, I. Mehdi, S. Weinreb, J. Kooi, J. Stutzki, U. Graf, M. Brasse, C. Honingh, R. Simon, M. Akyilmaz, P. Puetz, and M. Wolfire, "The statospheric THz observatory (STO)," *Proc. SPIE*, vol. 7733, 77330N, 2010.
- [13] R. Guesten, P. Hartogh, H.-W. Huebers, U.U. Graf, J. Jacobs, H.-P. Roeser, F. Schaefer, R.T. Schieder, R. Stark, J. Stutzki, P. Van der Wal, and A. Wunsch, "GREAT: the first-generation German heterodyne receiver for SOFIA," *Proc. SPIE*, vol.4014, pp.23-30, 2000.
- [14] F. P. Helmich, and R. J. Ivison, "FIRI-a far-infrared interferometer," *Exp. Astron.* 23, pp.245-276, 2009.
- [15] M. Hajenius, J. J. A. Baselmans, J. R. Gao, T. M. Klapwijk, P. A. J. de Korte, B. Voronov, and G. Gol'tsman, "Low noise NbN superconducting hot electron bolometer mixers at 1.9 and 2.5 THz," *Supercond. Sci. Technol.* 17, S224-S228, 2004.
- [16] J. J. A. Baselmans, M. Hajenius, J. R. Gao, T. M. Klapwijk, P. A. J. de Korte, B. Voronov, and G. Gol'tsman, "Doubling of sensitivity and bandwidth in phonon cooled hot electron bolometer mixers," *Appl. Phys. Lett.*, vol.84, no.11, pp.1958-1961, 2004.
- [17] M. Hajenius, J. J. A. Baselman, A. Baryshev, J. R. Gao, T. M. Klapwijk, J. W. Kooi, W. Jellema, and Z. Q. Yang, "Full characterization and analysis of a terahertz heterodyne receiver based on a NbN hot electron bolometer," *J. Appl. Phys.*, 100, 074507, 2006.
- [18] P. Khosropanah, J. R. Gao, W. M. Laauwen, M. Hajenius, and T.M. Klapwijk, "Low noise NbN hot electron bolometer mixer at 4.3 THz," *Appl. Phys. Lett.*, 91, 2007, 221111.
- [19] W. Zhang, P. Khosropanah, J. R. Gao, T. Bansal, T. M. Klapwijk, W. Miao, and S. C. Shi, "Noise temperature and beam pattern of an NbN hot electron bolometer mixer at 5.25 THz," *J. Appl. Phys.*, 108, 093102, 2010.
- [20] P. Focardi, A. Neto, and W.R. McGrath, "Coplanar-waveguide-based terahertz hot-electron-bolometer mixers-improved embedding circuit description," *IEEE Trans. Microwave Theory Techn.*, vol.50, no.10, pp. 2374-2383, Oct. 2002.
- [21] P. Focardi, W. R. McGrath, and A. Neto, "Design guidelines for terahertz mixers and detectors," *IEEE Trans. Microwave Theory Techn.*, vol.53, no.5, pp. 1653-1661, May 2005.
- [22] M. J. M. van der Vorst, Integrated lens antennas for submillimeter-wave applications, Ph. D thesis, Eindhoven University of Technology, The Netherlands, 1999.
- [23] W. Zhang, P. Khosropanah, J. R. Gao, E. L. Kollberg, S. K. Yngvesson, T. Bansal, R. Barends, and T. M. Klaowijk, "Quantum noise in a terahertz hot electron bolometer mixer," *Appl. Phys. Lett.*, 96, 111113, 2010.
- [24] S. Cherednichenko, M. Kroug, H. Merkel P. Khosropanah, A. Adam, E. Kollberg, D. Loudkov, G. Gol'tsman, B. Voronov, H. Richter, and H.-W. Huebers, "1.6 THz heterodyne receiver for the far infrared space telescope," *Physica C*, 372-376, pp.427-431, 2002.
- [25] E. L. Kollberg and K. S. Yngvesson, "Quantum noise theory for terahertz hot electron bolometer mixers," *IEEE Trans. Microwave Theory Techn.*, vol.54, no.5, pp.2077-2089, 2006.
- [26] I. Tretyakov, S. Ryabchun, M. Finkel, A. Maslennikova, N. Kaurova, A. Lobastova, B. Voronov, and G. Gol'tsman, "Low noise and wide bandwidth of NbN hot-electron bolometer mixers," *Appl. Phys. Lett.*, 98, 033507, 2011,
- [27] D. J. Hayton et al, an unpublished result.
- [28] M. J. M. van der Vosrt, P. J. I. de Maagt, A. Neto, A. L. Reynolds, R. M. Heeres, W. Luinge, and M. H. A. J. Herben, "Effect of international reflections on the radiation properties and input impedance of integrated lens antennas-comparison between theory and measurements," *IEEE Trans. Microwave Theory Techn.*, vol.49, no.6, pp.1118-1125, 2001.

# $Nb/Al-AlO_x/Nb$ junction properties' variations due to storage and mounting

A. Pavolotsky, D. Dochev, V. Belitsky *Senior Member, IEEE*

**Abstract**—We report studies of room temperature aging and annealing of  $Nb/Al-AlO_x/Nb$  tunnel junctions with a  $2...3\ \mu m^2$  size. We observed a noticeable drop of the junction normal resistance  $R_n$  unusually combined with increase of subgap resistance  $R_j$  as a result of aging. Changes of  $R_j$  occur at sufficiently shorter time scale than that of  $R_n$ . Variation of both  $R_n$  and  $R_j$  depend on the junction size. An effect of aging history on the junction degradation after consequent annealing was discovered. We suggest that the observed junction aging and annealing behavior could be explained by diffusional ordering and structural reconstruction in the tunnel  $AlO_x$  barrier. The diffusion driving such structural ordering and reconstruction of the  $AlO_x$  tunnel layer is enhanced due to the intrinsic stress relaxation (creep) processes in the underlying  $Al$  layer. Also, we discuss the influence of dicing the wafer into the single mixer chip on the junction aging behavior.

**Index Terms**—Superconducting devices, superconducting tunnel junctions, superconducting device reliability, superconducting device thermal stability

## I. INTRODUCTION

FOR many applications [1], [2], long-term stability of the of  $Nb$ -SIS junction properties has a particular importance. During the projected service time (e.g., up to 20 years for ALMA), junctions may experience long storage periods at room conditions, multiple thermal cycling and possible re-mounting, the latter requiring exposure to moderate elevated temperatures. For years, since introduction of  $Nb/Al-AlO_x/Nb$  tunnel junctions [3], [4], variation of their properties under room temperature aging and annealing at elevated temperatures has been extensively discussed [5]–[12]. However, no consistent explanation for the observed effects has been proposed. This work presents some new experimental results along with a new interpretation of the properties and its changes for the  $Nb/Al-AlO_x/Nb$  tunnel junctions.

An increase of the junction normal state resistance  $R_n$  (decrease of critical current  $I_c$ ) followed by further degradation of its characteristics at even higher temperatures, seemed to be a commonly agreed trend. General understanding behind the increase of the normal state resistance of  $Nb/Al-AlO_x/Nb$  junctions is that during the annealing at lower temperature range, below  $250...275\ ^\circ C$ , the tunnel barrier gets thicker either due to (additional) oxidation of the  $Al$  layer by chemisorbed oxygen [9], [14], or by adsorbed water molecules (hydroxyl groups) [5], [15]–[17]. This was supported by Raman spectroscopy study [18], showing decay

of Al-OH peak and corresponding rise of Al-O peak as a result of  $Nb/Al-AlO_x/Nb$  junction annealing. At higher annealing temperatures, above  $250...275\ ^\circ C$ ,  $AlO_x$  barrier apparently grows due to diffusion of oxygen through the junction's counter electrode [5], [6].

However, there are experimental facts, which do not fit the suggested trend and cannot be explained within the same approach. In the number of studies, unusual drop of  $R_n$  value of  $Nb/Al-AlO_x/Nb$  [10]–[12] and  $Al/Al-AlO_x/Al$  [13], [16], [19] junctions with annealing or aging has been observed.

In this study, partly reported earlier in [22], we experimentally observed a reduction of  $R_n$  of  $Nb/Al-AlO_x/Nb$  junctions with aging similarly to [10]–[12]. Unusually, this  $R_n$  reduction was accompanied with an increase of the subgap resistance,  $R_j$ . Furthermore, we observe the junction size affecting the  $R_n$  and  $R_j$  changes with aging. In addition, we experimentally detect a difference in persistence of the  $Nb/Al-AlO_x/Nb$  junctions recently fabricated and long time aged at room temperature. These phenomena hardly could find explanation within the concept of further oxidation of  $AlO_x$  barrier layer with adsorbed oxygen or water vapor. Below, we present a discussion in attempt to interpret all mentioned effects related to aging and annealing in terms of diffusion and stress-related processes in the vicinity of the tunnel barrier.

## II. EXPERIMENT

The  $Nb/Al-AlO_x/Nb$  junctions studied in this work have been processed using dedicated equipment placed in class 100 clean-room environment. The junctions used in this studies were fabricated at the different stages of the SIS mixer development for the APEX Band 3 (385...500 GHz) receiver, which has recently been installed at the APEX telescope [20], [21]. The nominal junction areas were  $A = 3\ \mu m^2$  (wafers R5.1, R6.1, R7.1, R8.2 and D1.2) and  $A = 2\ \mu m^2$  (wafer D1.2), with the  $\pm 10\%$  typical spread of the junction size due to the processing-specific variation. The  $Nb/Al-AlO_x/Nb$  trilayer growth and processing parameters (please, see [22] for the details) were the same for all wafers discussed in the paper.

Each fabricated wafer contained 203 SIS mixer chips, out of which, 30 were connected to the wafer external contact pads, allowing dc characterization of the junctions before dicing wafer into single mixer chips. Each chip had a pair of junctions connected in parallel [20]. For junction characterization, we measured their current-voltage characteristics (IVC) at 4.2 K. Analyzing the recorded IVCs, we extracted the values of junction normal resistance,  $R_n$  and subgap resistance  $R_j$  (please, see [22] for the details). Normal state

Authors are with the Group for Advanced Receiver Development, Department of Earth and Space Sciences with Onsala Space Observatory, University of Technology, Gothenburg, SE 412 96, Sweden e-mail: Alexey.Pavolotsky@chalmers.se

resistance  $R_n$  corresponds to the resistance of normal electrons tunneling through  $AlO_x$  barrier at bias voltage higher than the junction superconducting gap voltage,  $V_g$ .  $R_n$  is considered as a measure of transparency of the tunnel barrier transparency. Another important parameter is the subgap resistance  $R_j$ , which corresponds to the resistance of quasiparticles tunneling through the barrier at bias voltages below  $V_g$ . There are very little of quasiparticles in niobium at 4.2 K. Therefore, the  $R_j$  value is very sensitive to the presence and quantity of the tunnel barrier defects and hence used as an indicator of the  $Nb/Al-AlO_x/Nb$  tunnel junction quality.

As fabricated, all wafers demonstrated high-quality of the junctions and yield of about 90%. The junction parameters are  $R_n A \approx 20 \Omega \mu m^2$ ,  $R_j/R_n \approx 15 \dots 25$  and the superconducting gap voltage  $V_g \approx 2.87$  mV.

The aging of the wafers carried out in a controlled environment at room temperature  $19 \dots 23^\circ C$  in an air-conditioned laboratory room. The wafers were stored in standard anti-static trays and no additional measures were taken to protect the wafers from environmental factors during the storage period. The junction IVCs were recorded and changes in their  $R_n$  and  $R_j$  values due to aging were analyzed as a function of their area. Assuming the  $AlO_x$  barrier of  $Nb/Al-AlO_x/Nb$  trilayer is uniform across the wafer area, the measure for the junction area is the recorded as-fabricated values of the  $R_n$ .

The junction annealing experiments were performed as a sequence of hot-plate baking steps at the range of temperatures  $120^\circ C \dots 250^\circ C$  for 1 hour in the atmosphere of  $42 \pm 2\%$  RH room air, with the temperature increased by a  $10^\circ C$  -increment at each step. Each baking step followed by recording of the junction IVCs.

Some wafers were diced into the single chips right after the fabrication. Diced chips experienced aging under the same conditions, as described above.

### III. RESULTS AND DISCUSSION

Junctions from different wafers experience similar type of changes after long aging at room temperature. The normal state resistance of the junctions decays, which agrees with results reported in [10]–[12]. Furthermore, we have observed the junction size effect on  $R_n$  aging behavior, similar to that, reported in [12]. Fig. 1 depicts relative changes of the junction normal resistance, defined as  $(R_n - R_{n0})/R_{n0}$ , versus their normalized values of as-fabricated normal resistances  $R_{n0}/R_{n0}^{max}$  normalized by  $R_{n0}^{max}$ ; here  $R_{n0}^{max}$  is maximum  $R_{n0}$  for the given wafer. There is a noticeable tendency that the more resistive junctions experience higher relative drop of the normal resistance. That indicates that the smaller area junctions exhibit relatively stronger decrease of their normal resistance due to aging as compared to the junctions of a bigger size on the same substrate. Interestingly, we did not observe similar aging behavior for the junctions located at the diced chips.

The reduction of  $R_n$  due to aging and the junction size effect are attempted to be explained in [10]–[12] by suggesting out-diffusion of hydrogen, trapped in the niobium electrodes during the junction fabricating. Following this explanation, one

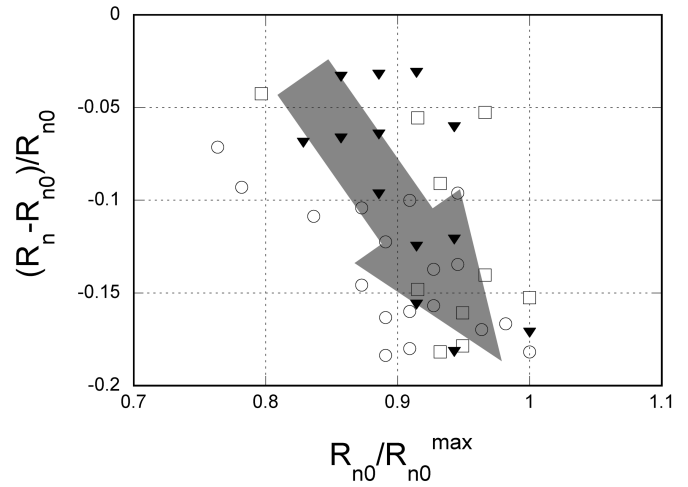


Fig. 1. Room temperature aging effect on the normal resistance of the junctions from wafers R5.1 (circles, aged for 655 days), R6.1 (squares, 597 days) and R7.1 (triangles, 428 days).  $R_{n0}$ ,  $R_{n0}^{max}$ , and  $R_n$  - junction normal resistance as-deposited, maximal for the given wafer and after aging, correspondingly. Gray arrow illustrates the trend and guides eye.

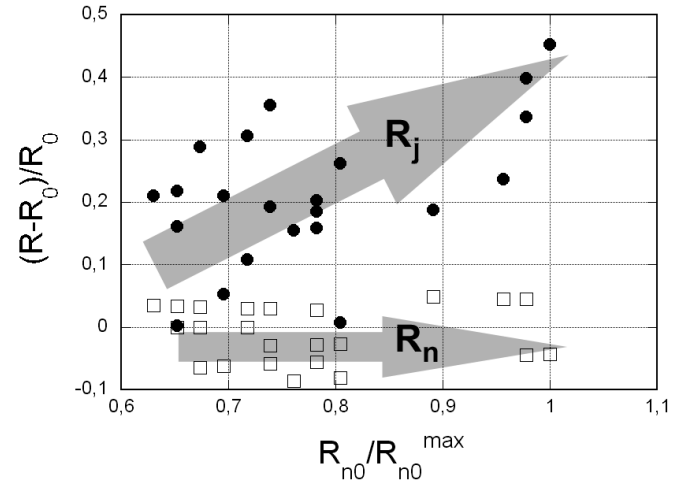


Fig. 2. Room temperature aging effect on the subgap (circles) and normal resistance (squares) of the junctions from the wafer D1.2 (aged for 63 days).  $R_{n0}^{max}$ , and  $R_n$  - junction normal resistance as-deposited, maximal for the given wafer and after aging, correspondingly. Gray arrows illustrate the trend and guide eye.

should expect similar behavior of the junction subgap resistance  $R_j$  with aging. However, we observe the tendency just opposite to the  $R_n$  changes:  $R_j$  increases with aging (Fig. 2). The wafers R5.1, 6.1 and R7.1 demonstrate a similar tendency of the  $R_j$  increasing and the results are earlier presented in [23]. It is worth to notice that the wafer D1.2 (measurements at Fig. 2) experienced about an order shorter aging, compared to the wafers R5.1, R6.1 and R7.1 ((measurements at Fig. 1)). While aging effect on  $R_j$  is clearly seen at the moderate aging times, the  $R_n$  changes are nearly not noticeable at shorter aging time. However, being exposed to annealing at  $120^\circ C$  for 30 minutes, the junction normal resistance  $R_n$  changes, Fig. 3, showing the similar junction size effect and very much alike as after the long room temperature aging (Fig. 1). This

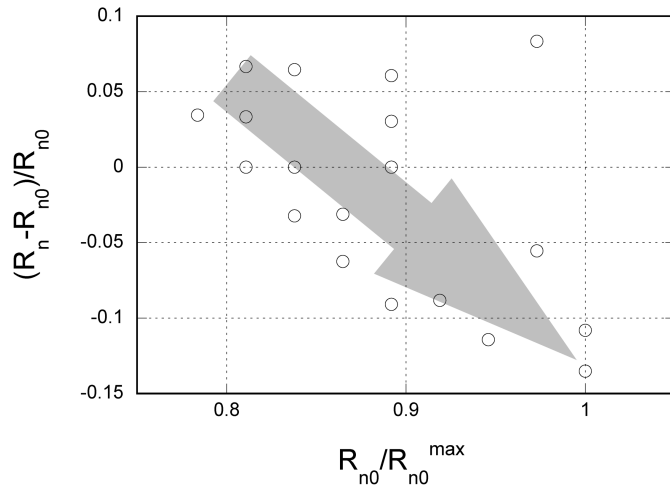


Fig. 3. Effect of annealing at  $120^{\circ}\text{C}$  on the normal resistance of the  $3\ \mu\text{m}$  size junctions from the wafer D1.2 (aged for 63 days before annealing).  $R_n^{\text{max}}$ , and  $R_n$  - junction normal resistance as-deposited, maximal for the given wafer and after aging, correspondingly. Gray arrow illustrates the trend and guides eye.

points out to the fact that aging processes affecting  $R_j$  occur at a shorter time scale than those, causing  $R_n$  changes, and that fact could hardly be explain within the concept of hydrogen-induced aging effects.

After room temperature aging, the junctions were annealed at elevated temperatures, which effects their normal and sub-gap resistances as presented in [22] and, partially, in [23]. The changes, both for  $R_n$  and  $R_j$ , follow the same trend for the junctions experienced room temperature aging with different durations (batches R8.2 and D1.2). However, depending on the aging history, the junctions were able to survive annealing up to different temperatures. Fig. 4 compares the fraction of the failed junctions with respect to the annealing temperature for the wafers that were subject to pre-aging with different duration. Under the term "failed junction", we consider either a short-circuited junction or a junction with sufficiently degraded IVC. From this plot, we could suggest that the junctions subjected to a longer room temperature aging survive higher annealing temperature. Compared to the earlier presented data [5], [6], [8], [9], the longer pre-aged junctions (batch R8.2) demonstrate similar ability to persist annealing conditions. Worth mentioning though, the junctions used in the present work have substantially thinner tunnel barrier, then those reported in [5], [6], [8], [9]. This makes the junctions more susceptible to the intrinsic stress. This is discussed in more detail further in the paper.

Any direct studies of the processes in  $\text{AlO}_x$  tunnel barrier and adjacent to it layers are extremely difficult, as it is a structure of about one nm thick, sandwiched in between rather thick (200...500 nm) layers of niobium. However, in this discussion, we could greatly benefit from the recent results on *in-situ* studies of the growth kinetics and crystal state of the ultra-thin oxide film over the atomically clean single-crystal  $\text{Al}$  surfaces at the low temperatures between  $80^{\circ}\text{C}$  and  $380^{\circ}\text{C}$ , ref. [24]–[26]. The conditions of the  $\text{Al}$ -oxide film growing in [24]–[26] largely resemble the conditions and

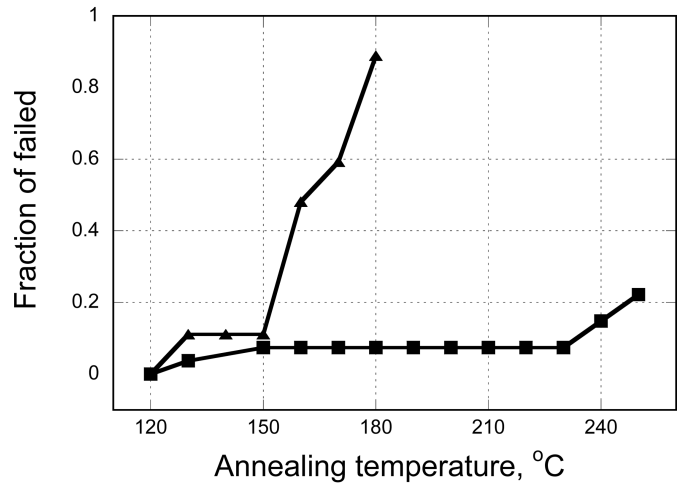


Fig. 4. Annealing temperature effect on the fraction of failed junctions, which experience long room temperature aging (wafer R8.2, aged for 391 days, *squares*), compared to that of junctions, experienced shorter aging (wafer D1.2, aged for 63 days, *triangles*).

thus the properties of the  $\text{AlO}_x$  tunnel barrier grown over the  $\text{Al}$  layer during fabrication of  $\text{Nb/Al-ALOX/Nb}$  junctions. The authors of these papers conclude that various processes of structural ordering in the oxygen sublattice of  $\text{AlO}_x$ , namely, an annihilation of the vacancy-type defects and even crystallization of initially amorphous oxide layer [24], [26], occur in the above mentioned interval of temperatures and  $\text{AlO}_x$  thickness about 1 nm. Applying these conclusions to the  $\text{Al-ALOX}$  layer of the tunnel barrier, we speculate that the same processes should certainly cause a decrease of the "leakage" component of the subgap current. This could explain the observed increase of  $R_j$  after room temperature aging. From the other hand, the structural ordering reduces the material volume [24], [26], and consequently causes thinning of the tunnel barrier and hence could explain a decrease of the  $R_n$  after a long aging.

Within the very same concept, the difference in the time scales of changes for both  $R_j$  and  $R_n$  could also be explained. The process of curing of minor structural defects that should lead to a raise of  $R_j$ , requires relatively little diffusion to occur, as discussed above. Whereas decreasing of  $R_n$  requires sufficient re-arrangement of the film structure and diffusion processes in the  $\text{AlO}_x$  film being developed in a very much longer time scale.

The studied room temperature aging of the  $\text{Nb/Al-ALOX/Nb}$  junctions occurs at noticeably lower temperature as compared to the conditions of ultra-thin oxide film growth presented in [24]–[26]. Nevertheless, we believe that even the aging effects could be explained through the  $\text{AlO}_x$  layer structure ordering. However in the case of the room temperature aging, a non-thermal enhancement of diffusion and consequent curing of the structural defects should exist. An indication of such non-thermal diffusion enhancement mechanism comes from observed dependance of  $R_n$  and  $R_j$  on junction area. The fact that the smaller junctions demonstrate a stronger aging effect points out to the intrinsic stress that always is accumulated in  $\text{Nb}$  film of the wiring layer during its growth. Our fabricating

process is calibrated in such way that the wiring layer  $Nb$  film typically characterized by slight compressive stress of about 100 MPa. Similarly, the fact that junctions on the diced chips did not demonstrate any noticeable aging changes also speaks for the role of the intrinsic stress in  $Nb$  film of the wiring layer. Sufficient fraction of stress is released during dicing, because long  $Nb$  wires connecting chips with anodization and testing terminals get cut.

In order to understand how the stress affects the tunnel junction, we assume perfect adhesion at the  $Nb/Al-AlO_x/Nb$  /  $Nb_{wiring}$  interfaces and account that the yield strength value is 100...200 MPa for a deposited  $Al$  material [27], that is comparable with the intrinsic stress of the niobium film. For  $Al$ , the room temperature corresponds to a moderate homologous temperature  $\Theta_{Al} = T/T_m^{Al} \simeq 0.32$ , where  $T_m^{Al}$  is melting temperature of  $Al$ . Altogether, this leads to a conclusion that the intrinsic stress in  $Nb$  wiring layer could be partly relaxed via creep deformation (stress relaxation process) of the aluminum layer of  $Nb/Al-AlO_x/Nb$  trilayer at room temperature. This hypothesis is supported by an experimental observation of the stress relaxation in a free-standing microstructures made of sputtered  $Al$  films occurred at room temperature, when originally loaded with a 50 MPa stress [28]. Furthermore, whatever mechanism of stress relaxation process takes place in  $Al$  layer of  $Nb/Al-AlO_x/Nb$  trilayer, either diffusion creep [29], [30], or dislocation climb creep [30], [31], it should be associated with diffusional flows of vacancies in the  $Al$  layer. Vacancy flow in the vicinity of the  $AlO_x$  layer provides an additional diffusion path that in a non-thermal way enhances diffusion needed for structural ordering of  $AlO_x$  barrier layer.

Moreover, following the same concept, the difference in temperature dependence of the failed junctions ratio after annealing could be explained. The diffusion ordering of the  $AlO_x$  layer is far more slower than deformation (stress relaxation) of the  $Al$  layer. At higher annealing temperature, the  $Al$  layer deformation occurs quicker and tears  $AlO_x$  layer out, whereas the diffusion reconstruction cannot catch up creep of  $Al$  layer. Alternatively, a very long room temperature aging allows the major part of the  $Al$  layer relaxation to happen at low deformation speed, making the  $AlO_x$  layer reconstruction able to follow. Consequently, the annealing at elevated temperatures does not lead to tearing oxide layer out up to noticeably higher temperatures.

#### IV. CONCLUSION

We have studied long-term stability of  $Nb/Al-AlO_x/Nb$  junctions of a  $2...3 \mu m^2$  size, when stored at room temperature conditions. We observe reduction of the normal resistance  $R_n$  and increase of the subgap resistance  $R_j$  of the tested junctions as a result of room temperature aging. Changes of  $R_j$  occur at sufficiently shorter time scale than that of  $R_n$ . Room temperature storage (aging) effects for both  $R_n$  and  $R_j$  are subject to the junction size effect. Interestingly, junctions on the diced chips did not demonstrate any noticeable aging effects. Finally, we observed effect of aging history on the temperature dependence of the junction failure after consequent annealing.

We suggest that the observed junction aging and annealing behavior could be explained by diffusional ordering and structural reconstruction in the  $AlO_x$  layer. The diffusion driving the structural ordering and reconstruction of the  $AlO_x$  tunnel layer is enhanced due to the intrinsic stress relaxation (creep) processes in the underlying  $Al$  layer.

#### ACKNOWLEDGMENT

This work was partly supported by the Swedish Research Council under a grant. Authors are thankful to professor A. V. Lubenchenko for the fruitful discussions. Authors would like to acknowledge Dr. V. Desmaris for reading of the paper and the useful comments.

#### REFERENCES

- [1] Th. de Grauw, N.D. Whyborn, H. van de Stadt, G. Beaudin, D.A. Beintema, V. Belitsky, et.al., "Heterodyne instrument for FIRST (HIF): Preliminary design," *Proc. SPIE*, vol. 3357, pp. 336 - 347, 1998.
- [2] R. S. Booth, "ALMA, the Atacama Large Millimetre Array," *Proceedings of the Conference "Darwin and Astronomy — The Infrared space Interferometer"*, Stockholm, Sweden, 17 - 19 November 1999, European Space Agency, 2000, ESA SP, vol. 451, ISBN 92-9092-645-7., pp.107 - 114.
- [3] J. M. Rowell, M. Gurvitch, J. Geerk, "Modification of tunneling barriers on Nb by a few monolayers of Al," *Physical Review B*, vol. 24, No. 4, pp. 2278 - 2281, 1981.
- [4] M. Gurvitch M. A. Washington and H. A. Huggins, "High quality refractory Josephson tunnel junctions utilizing thin aluminium layers," *Applied Physics Letters*, vol. 42, No. 5, pp. 472 - 474, 1983.
- [5] J. V. Gates, M. A. Washington and M. Gurvitch, "Critical current uniformity and stability of Nb/Al-oxide-Nb Josephson junctions," *Journal of Applied Physics*, vol. 55, No. 5, pp. 1419 - 1421, 1984.
- [6] T. Shiota, T. Imamura, and S. Hasuo, "Fabrication of high quality  $Nb/Al-AlO_x/Nb$  Josephson junctions: III - Annealing Stability of  $AlO_x$  tunneling barriers," *IEEE Transactions on Applied Superconductivity*, vol. 2, No. 4, pp. 222 - 227, 1992.
- [7] S. Morohashi, Y. Kataoka, T. Imamura, and S. Hasuo, "Secondary ion mass spectrometry study for Josephson junction with  $Nb/Al-AlO_x/Nb$  structure," *Applied Physics Letters*, vol. 62, No. 10, pp. 1164 - 1166, 1993.
- [8] A. Oliva and R. Monaco, "Annealing properties of high quality  $Nb/Al-AlO_x/Nb$  tunnel junctions," *IEEE Transactions on Applied Superconductivity*, vol. 4, No. 1, pp. 25 - 32, 1994.
- [9] T. Lehnert, D. Billon, C. Grassl, and K. H. Gundlach, "Thermal annealing properties of  $Nb/Al-AlO_x/Nb$  tunnel junctions," *Journal of Applied Physics*, vol. 72, No. 7, pp. 3165 - 3168, 1992.
- [10] S. K. Tolpygo and D. Amparo, "Fabrication-process-induced variations of  $Nb/Al-AlO_x/Nb$  Josephson junctions in superconductor integrated circuits," *Superconducting Science and Technology*, vol. 23, 034024, 2010.
- [11] K. Hinode, T. Satoh, S. Nagasawa, and M. Hidaka, "Hydrogen-inclusion-induced critical current deviation of  $Nb/Al-AlO_x/Nb$  Josephson junctions in superconducting integrated circuits," *IEEE Transactions on Applied Superconductivity*, vol. 19, No. 3, pp. 131 - 134, 2009.
- [12] K. Hinode, T. Satoh, S. Nagasawa, and M. Hidaka, "Origin of hydrogen-inclusion-induced critical current deviation in  $Nb/Al-AlO_x/Nb$  Josephson junctions," *Journal of Applied Physics*, vol. 107, 073906, 2010.
- [13] H. Scherer, Th. Weimann, A. B. Zorin, and J. Niemeyer, "The effect of thermal annealing on the properties of  $Al/Al-AlO_x/Al$  single electron tunneling transistors," *Journal of Applied Physics*, vol. 90, No. 5, pp. 2528 - 2532, 2001.
- [14] P. J. Koppinen, L. M. Väistö, and I. J. Maasilta, "Complete stabilization and improvement of the characteristics of tunnel junctions by thermal annealing," *Applied Physics Letters*, vol. 90, 053503, 2007.
- [15] A. L. Geiger, B. S. Chandrasekhar, J. G. Adler, "Inelastic electron tunneling in Al-Al-Oxide-Metal systems," *Physical Review*, vol. 188, No. 3, pp. 1130 - 1138, 1969.
- [16] M. K. Konkin and J. G. Adler, "Annealing effects in tunnel junctions (thermal annealing)," *Journal of Applied Physics*, vol. 50, No. 12, pp. 8125 - 8128, 1979.

- [17] M.K. Konkin and J. G. Adler, "Annealing effects in tunnel junctions (voltage annealing)," *Journal of Applied Physics*, vol.51, No.10, pp. 5450 - 5454, 1980.
- [18] S.Morohashi, "Raman spectroscopic study of *Nb/Al-AlO<sub>x</sub>/Nb* josephson junctions," *Japanese Journal of Applied Physics*, vol.33, Part 2, No. 2A, pp. L170 - L172, 1994.
- [19] T.Holmqvist, M.Meschke ,and J.P. Pekola, "Double oxidation scheme for tunnel junction fabrication," *Journal of Vacuum Science and Technology B*, vol.B26, No.1, pp. 28 - 31, 2008.
- [20] R.R. Monje, V. Belitsky, V. Vassilev, A. Pavolotsky, I. Lapkin, V. Desmaris, D. Meledin, D. Henke, D. Dochev, "A 0.5 THz Sideband Separation SIS Mixer for APEX Telescope," *19th International symposium on space terahertz technology*, April 28 - 30, Groningen, The Netherlands, pp. 439 - 443, 2008.
- [21] Latest status and technical details at [http://gard04.rss.chalmers.se/APEX\\_web/SHeFI.htm](http://gard04.rss.chalmers.se/APEX_web/SHeFI.htm)
- [22] A. B. Pavolotsky, D. Dochev, V. Belitsky, "Aging- and annealing-induced variation in *Nb/Al-AlO<sub>x</sub>/Nb* tunnel junction properties," *Journal of Applied Physics*, vol. 109, No. 2, 024502, 2011.
- [23] D. Dochev, A.B. Pavolotsky, Z. Lai and V. Belitsky, "The influence of aging and annealing on the properties of *Nb/Al-AlO<sub>x</sub>/Nb* tunnel junctions," *Journal of Physics: Conference Series*, vol.234, 042006, 2010.
- [24] P.C. Snijders, L.P.H. Jeurgens, W.G. Sloof, "Structural ordering of ultra-thin, amorphous aluminium-oxide films," *Surface Science*, vol. 589, pp. 98 - 105, 2005.
- [25] F. Reichel, L.P.H. Jeurgens, E. J. Mittemeijer, "The effect of substrate orientation on the kinetics of ultra-thin oxide-film growth on Al single crystals," *Acta Materialia*, vol.56, pp. 2897 - 2907, 2008.
- [26] F. Reichel, L.P.H. Jeurgens, G. Richter, and E. J. Mittemeijer, "Amorphous versus crystalline state for ultrathin *Al<sub>2</sub>O<sub>3</sub>* overgrowths on Al substrates," *Journal of Applied Physics*, vol. 103, 093515, 2008.
- [27] F.-J. Lee, P. Zhang and J. C. Bravman, "Study on the strength and elongation of free-standing Al beams for microelectromechanical systems applications," *Applied Physics Letters*, vol. 84, pp. 915 - 917, 2004.
- [28] F.-J. Lee, G. Cornella and J. C. Bravman, "Stress relaxation of of free-standing Al beams for microelectromechanical systems applications," *Applied Physics Letters*, vol.76, pp. 3415 - 3417, 2000.
- [29] C. Herring, "Diffusional viscosity of a polycrystalline solid," *Journal of Applied Physics*, vol. 21, pp. 437 - 445, 1950.
- [30] B. Ya. Pines, "Diffusion and the mechanical properties of solids," *Soviet Physics Uspekhi*, vol.5, pp. 251 - 271, 1962.
- [31] J. Weertman, "Theory of steady-state creep based dislocation climb," *Journal of Applied Physics*, vol. 26, pp. 1213 - 1217, 1955.

# Steady-State and Transient Thermal Analysis of High-Power Planar Schottky Diodes

Aik Yean Tang, Erich Schlecht, Goutam Chattopadhyay, Robert Lin, Choonsup Lee, John Gill, Imran Mehdi and Jan Stake

**Abstract**— In this paper, we present the thermal analysis of high frequency planar Schottky diode based multiplier chips, for high power applications. In order to optimize the thermal characteristic of the multiplier chip, several chip layout and fabrication options are explored. Both the steady-state and transient thermal characteristic of a multiplier chip are analyzed by solving the heat equation via the 3D finite element method, taking into account the temperature-dependent material properties. The result shows that the multiplier chips exhibit thermal resistances in the order of  $10^3$  K/W and thermal time-constants in the order of milliseconds. The analysis also indicates that bonding agents with a better thermal conductivity is required in order to fully exploit benefits of the heat spreader. On the other hand, a GaN-on-Si-based multiplier chip demonstrates a better thermal handling capability compared to the GaAs-based chip. Experimental verification of the simulation result is performed using IR microscopy, showing a reasonable match of the measured and simulated result. The transient characteristic of the measured junction temperature is modeled by two time-constants, i.e. 11 and 3.3 ms.

**Index Terms**—Frequency multiplier, Gallium Arsenide, Gallium Nitride, heat spreader, high power submillimeter-wave generation, Schottky diodes, thermal conductivity, thermal analysis.

## I. INTRODUCTION

Advancement in terahertz applications, such as radio astronomy, astrophysics and earth observations, as well as imaging and sensing applications [1-5] has generated an increasing demand on the output power of terahertz sources. To date, planar Schottky diode based multiplier chains have been demonstrated to be promising, compact and reliable terahertz sources [6],[7]. Nevertheless, the output power of the multiplier chain is within the micro-watt range for operating frequencies beyond 1 THz. Therefore,

Manuscript received August 12, 2011. This work was carried out at the Jet Propulsion Laboratory, California Institute of Technology, Pasadena, CA, under contract with National Aeronautics and Space Administration. The research has received funding from the VINNOVA, Security Link, Ericsson's Research Foundation, Solveig och Karl G Eliassons Minnesfond, and Chalmersska Forskningsfonden 2010.

A.Y. Tang and J. Stake are with the Department of Nanoscience and Microtechnology, Chalmers University of Technology, SE-42196, Göteborg, Sweden. (phone: +46 (0)31 772 1739; fax:+46 (0)31 164513; e-mail: aik-yeen.tang@chalmers.se).

E. Schlecht, G. Chattopadhyay, R. Lin, C. Lee, J. Gill and I. Mehdi are with the Jet Propulsion Laboratory, California Institute of Technology, Pasadena, CA 91125 USA.

continuous technology development of the multiplier chain is required toward delivering high power terahertz sources.

Recent progress in power amplifier technology has made it possible to construct W-band (75 – 110 GHz) sources capable of producing powers in the 1-Watt range [8]. These sources are required in order to build multiplier based local oscillator chains in the frequency range of 2-3 THz. However, it becomes imperative that the multipliers, in particular the initial stage multipliers, be able to withstand the large input power without degrading electrical performance or burning out. Therefore, the chip thermal management is nontrivial in optimizing the multiplier performance for high power applications.

To date, literature regarding thermal analysis and modeling of transistors [9-13], heterostructure barrier varactors [14],[15] and Gunn diodes [16-18] abound. For planar Schottky diode, the work on thermal analysis is limited. Thus far, a 1-D 'series-resistor' [19] and a 2-D heat flow model [20] have been reported. However, these models are not sufficiently flexible to be implemented to explore various chip layouts, as well as material systems in improving the thermal management of the multiplier chip.

In this paper, we present a 3D thermal analysis of the planar Schottky diode based multiplier chip. Both the steady-state and transient thermal characteristic of a multiplier chip are analyzed by solving the heat equation in a 3D calculation domain. The solution is acquired numerically via the finite element method (FEM). The objective of this work is to understand the thermal constraints of conventional multiplier chips and explore possible options to optimize the chip thermal characteristics. Various layout and fabrication options, such as thickness of the metal traces, substrate width and thickness, bonding to a heat spreader, are explored. In addition to the conventional Gallium Arsenide (GaAs)- based multiplier chip, the thermal characteristics of Gallium Nitride (GaN)-based diode on Silicon (Si) substrates are also studied.

The layout of the multiplier chip analyzed in this work and the thermal simulation setup are described in Section II. The experimental verification performed using infrared (IR) microscopy is explained in Section III. The steady-state and transient thermal analysis results are then discussed in Section IV. With this, an effective and flexible method to analyze the thermal behavior of the multiplier chip is demonstrated.



## II. THE MULTIPLIER CHIP LAYOUT AND SIMULATION SETUP

The chip layout analyzed in this work is based on the 200 GHz substrate-less frequency doubler chip developed by the Jet Propulsion Laboratory (JPL). The multiplier chip is designed based on a balanced configuration, where 3 diodes are connected in series at each branch. The series connection of diodes in the design aims at improving the chip power handling capability. Details of the chip design are described in [21]. Fig 1 shows the top view and the cross section of the multiplier chip.

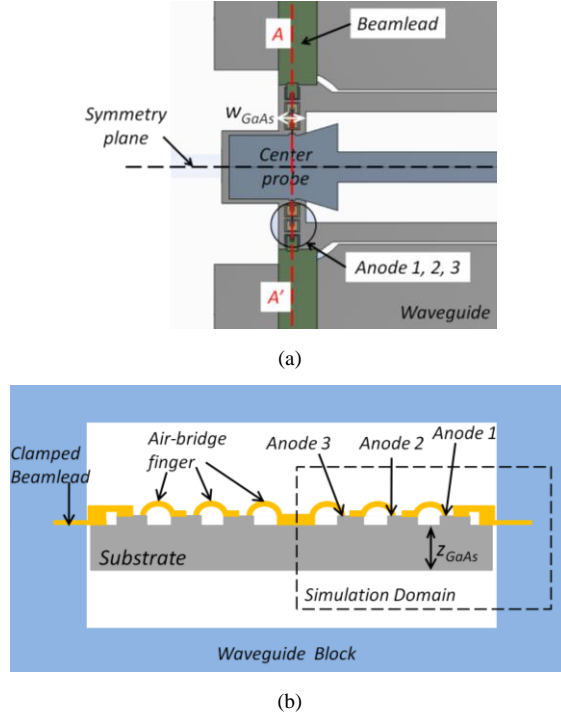


Fig. 1 Schematic of the substrateless multiplier chip (a) a top view of the chip mounted on a half waveguide split block; (b) the A-A' cross section of the multiplier chip in the full waveguide block. NB! The drawing is not to scale.

For the thermal analysis, the 3D FEM solution is acquired via the Ansys Mechanical [22] simulation tool. Due to the twofold symmetry of this chip, only half of the chip is simulated. The simulation domain is outlined in Fig. 1. The default chip layout and variation of layout parameters are summarized in TABLE I.

TABLE I  
LAYOUT AND FABRICATION OPTIONS

Parameter	Symbol	Variable
Thickness of GaAs <sup>a</sup> or Si substrate	$z_{GaAs}, z_{Si}$	3 <sup>b</sup> , 5, 10, 25, 50 <sup>a</sup> $\mu\text{m}$
Thickness of gold	$z_{gold}$	1 <sup>a</sup> , 2 $\mu\text{m}$
Width of substrate	$w_{GaAs}$	70 <sup>a</sup> , 120 $\mu\text{m}$
Thickness of CVD diamond	$z_{diamond}$	0 <sup>a</sup> , 10, 25 $\mu\text{m}$
Thickness of bonding agent	$z_{bond}$	0 <sup>a</sup> , 1 $\mu\text{m}$

<sup>a</sup> Default layout parameter of the multiplier chip analyzed in this paper.

<sup>b</sup> Only simulated for the GaAs-based multiplier.

In the FEM analysis, a similar heat load is applied directly beneath each of the anode contacts. All the non-contact surfaces of the waveguide block, except the facet facing toward the inner channel and the chip, are configured to be at the ambient temperature ( $T_{amb}$ ), i.e. 300 K. The remaining surfaces are assumed to be adiabatic, i.e. assuming the effect of convection and radiation cooling mechanisms are negligible.

The temperature dependent thermal properties of the material are taken into account in this analysis. For simplicity, the thermal properties of the top junction layer and highly-doped buffer-layer are assumed to be similar. The material thermal properties used in this analysis are listed in TABLE II.

TABLE II  
MATERIAL THERMAL PROPERTIES

Material	Thermal conductivity, $\kappa \left( \frac{W}{mK} \right)$	Thermal capacity, $c_p \left( \frac{J}{kg K} \right)$	Mass density, $\rho \left( \frac{kg}{m^3} \right)$
GaAs	$51 \times \left( \frac{300}{T} \right)^{1.28}$	Tabulated data in [23]	5317
Gold	310	130	19320
Brass	109	377	8500
CVD diamond	1100	-	-
Bonding agent	0.52	-	-
GaN	$157 \times \left( \frac{300}{T} \right)^{1.9}$	-	-
Si	$160 \times \left( \frac{300}{T} \right)^{1.5}$	-	-

Upon setting up the proper simulation boundaries and material thermal properties, the conduction heat equation as stated in (1) is solved.

$$\rho \times c_p(T) \times \left( \frac{\partial T(x, y, z, t)}{\partial t} \right) = (\nabla \bullet (\kappa(T) \times \nabla T(x, y, z, t))) + g \quad (1)$$

where  $\rho$  is the material mass density,  $c_p(T)$  is the temperature-dependent thermal capacity,  $T(x, y, z, t)$  is the time- and spatial-dependent temperature,  $\kappa(T)$  is the temperature-dependent thermal conductivity and  $g$  is the heat generation rate per unit volume.

## III. EXPERIMENTAL VERIFICATION

For the experimental characterization, a QFI [24] IR microscope (InfraScope<sup>TM</sup>) with the capability of recording

the steady-state as well as the transient thermal characteristic was used. The 200 GHz multiplier chip is mounted on a waveguide split block, where the block is heated to an ambient temperature of 80 °C. The diodes are DC biased and the total power dissipation is estimated from the DC voltage and current.

### A. Steady-state Thermal Characterization

In this measurement, the total DC power dissipation level is estimated to be 7.02 mW, i.e. 1.17 mW per anode. A similar power level is then applied to the anodes in the FEM simulations. For the steady-state thermal imaging, the spatial resolution is approximately 3 μm, allowing the temperature of each individual anode to be resolved. Fig. 2 shows the measured and simulated temperature distribution for the multiplier chip. A comparison of the measured and simulated anode temperatures is summarized in TABLE III.

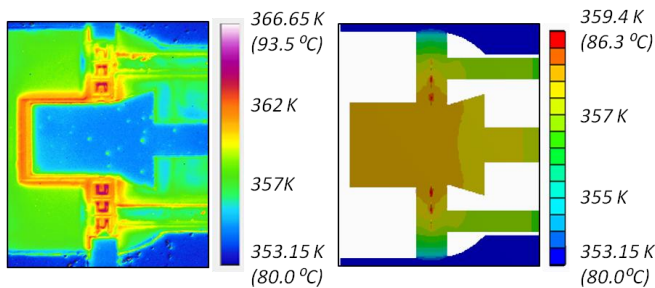


Fig. 2 Measured and simulated temperature distribution of the multiplier chip.

TABLE III  
ANODE TEMPERATURE COMPARISON BETWEEN THE IR  
MEASUREMENT AND FEM SIMULATION

Anode #	IR Microscopy (°C)	Simulation (°C)	Max ΔT (°C)
1 / 6	87.0 / 88.0	85.0	3.0
2 / 5	88.0 / 89.0	86.0	3.0
3 / 4	89.0 / 89.5	86.0	3.5

By comparing the temperature at the anode area, the differences between measured and simulated temperatures are less than 3.5 °C. For a temperature rise of approximately 10 °C, the temperature difference contributes toward a maximum error of ~ 35%. The high error percentage is related to the relatively small temperature rise, due to a relatively low DC equivalent forward biased power dissipation in the chip. Nevertheless, the error is below 5 % in the absolute temperature scale (in °C).

For the ohmic contacts, the measured temperature is higher than the temperature at anode contacts. On the other hand, the measured temperature at center probe is lower compared to the simulation. The discrepancies between the measurement and simulation result are related to the geometrical anisotropic radiation and the lack of material spectral radiance correction. Thus, the dependency of material surface emissivity on temperature, emission angle and wavelength should be taken into consideration for further temperature characterization. Alternatively, the radiance correction problem could be circumvented by coating a thin layer of black paint as discussed in [11].

### B. Transient Thermal Characterization

For transient thermal characterization, a single pixel, high-speed temperature detector is used in conjunction with the steady-state microscope. The multiplier is subjected to a 5 Hz square pulse, where the on-state equivalent power is estimated to be 9.2 mW, i.e. 1.53 mW per anode. Due to a lack of sufficient spatial resolution in this measurement setup, the recorded temperature is inherently an average temperature of the total imaging area. The imaging area and recorded temperature are shown in Fig. 3.

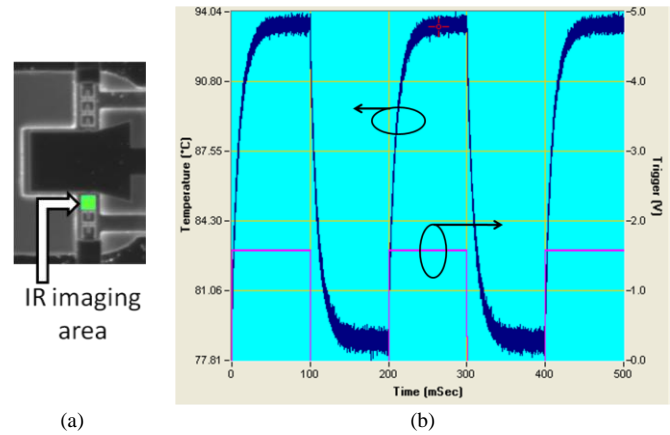


Fig. 3 (a) Imaging area of the chip during transient characterization; (b) The recorded average temperature and the measurement synchronization pulse during transient characterization.

Analysis of the measured temperature for the first on-state pulse, i.e. the first 100 ms, shows that modeling the transient characteristic of the temperature requires more one time-constant. The time-constants of the temperature transient characteristic are estimated by fitting (2) to the measured temperature. In this analysis, the temperature data below 1 ms is excluded. A plot of the measured temperature rise and the corresponding fitted curve for the period of 100 ms is shown in Fig. 4.

$$T(t) = T_1 + T_2 \times \left(1 - \exp\left(-\frac{t}{\tau_1}\right)\right) + T_3 \times \left(1 - \exp\left(-\frac{t}{\tau_2}\right)\right) \quad (2)$$

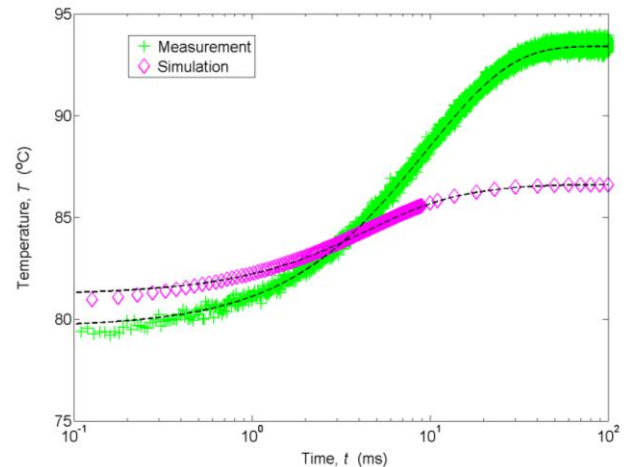


Fig. 4 A comparison of the measured and simulated transient temperature. The corresponding fitted curves are plotted in dashed lines. (Note: temperature data below 1ms is excluded from the curve-fit).

A transient simulation of the multiplier chip subjected to a similar heat pulse is performed. In order to compare with the measured temperature, a total of twelve temperature points within the imaging area are resolved. The average of these twelve temperatures is then used to estimate the coefficients of interest. The coefficients, estimated from the measurement and simulation, are compared in TABLE IV.

TABLE IV  
COEFFICIENTS OF THE FITTED CURVE

Coefficient	IR Microscopy	Simulation
$T_1$ (°C)	79.6	81.2
$T_2$ (°C)	12.0	1.2
$T_3$ (°C)	1.8	4.2
$\tau_1$ (ms)	11.0	14.0
$\tau_2$ (ms)	3.3	4.0

The result shows that the IR measured temperature settled at 94 °C whereas the simulated temperature settled at 87 °C. The estimated coefficient  $T_2$  and  $T_3$  are differing between the measured and simulated data. The discrepancy could be related to the lack of sufficient spatial resolution ( $\sim 30 \mu\text{m}$ ) as well as spectral radiance correction. The anomalously higher temperature at the ohmic contact, as discussed in Section III.A, is averaged into the measurement data, increasing the overall temperature. Thus, transient characterization with higher spatial resolution and more sophisticated spectral radiance correction is required. Nevertheless, there is a reasonable match for the estimated time-constants (i.e.  $\tau_1$  and  $\tau_2$ ) between the measurement and simulation.

#### IV. RESULT

For semiconductor device operation at room temperature, a junction temperature range between 300 K and 500 K is considered reasonable. Therefore, all of the thermal analysis performed in this work is limited to this temperature range. In this section, the result of the steady-state thermal analysis is first presented and discussed, followed by the transient thermal analysis.

##### A. Steady-state Thermal Analysis

###### 1) The Hot Spot

Due to the temperature-dependent thermal conductivity of the GaAs, the temperature exhibits a non-linear behavior as a function of power dissipation. Thus, thermal resistance ( $R_{th}$ ), as defined in (3), is explicitly power dissipation dependent.

$$R_{th\_i} = \frac{T_{anode\_i} - T_{amb}}{P_{dis\_i}} \quad (3)$$

where  $i$  is the anode number.

Fig. 5 shows the steady-state anode junction temperatures for the multiplier chip with the default layout parameters. At a lower power dissipation level, such as 5 mW per anode, the temperatures of all the anodes are similar. However, it is observed that the temperature between anodes deviates as the power dissipation level is increased. The hot spot in the chip is located at the anode closest to the symmetry plane, i.e. anode

3. Thus, the analysis herein after is based on the thermal characteristic of anode 3.

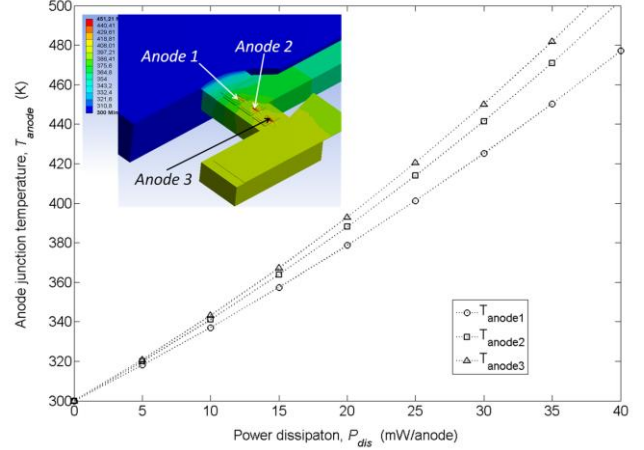


Fig. 5 A comparison of the anode temperatures in the multiplier chip as a function of power dissipation level. (Inset: A temperature distribution plot for the chip at power dissipation level of 30 mW per anode.)

##### 2) Thermal Constraints

In order to optimize the chip layout, the thermal constraints for the chip have to be identified. Fig. 6 shows the temperature profile along the surface of a chip substrate. This figure indicates that the thermal bottleneck (i.e. high temperature gradient) is located at the transition area between the waveguide block to chip substrate, as well as the diode mesa areas close to the anode heat source.

By considering these constraints, the chip layout could be optimized by improving the heat path from the anode junction area to the substrate, and the beam lead connection from the substrate to the waveguide block. A better heat extraction from the top of the anode junction contributes to a reduced temperature gradient close to the junction area. This could be achieved by increasing the thickness of metal (i.e. gold) connection between the diodes, the center probe and the waveguide. On the other hand, a wider or thicker substrate would lower the overall thermal resistance of the chip. The suppression of the thermal gradient by increasing the thickness of gold and the width of the substrate is illustrated in Fig. 6.

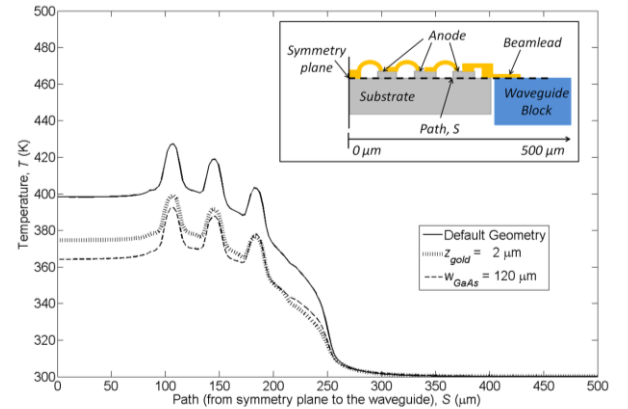


Fig. 6 A plot of the temperature profile along the surface of the substrate at a power dissipation level of 30 mW for each anode. (Inset: Schematic of the simulation domain indicating the physical location of the path,  $S$ . NB! The drawing is not to scale.)

### 3) Thermal Characteristic Optimization for a Thin Substrate

For high frequency electronic operation, a thinner substrate is favored in order to reduce dielectric loading losses. On the contrary, a thicker substrate is preferred to optimize the chip thermal conductance. A thinner substrate exhibits a larger thermal resistance. It is also subjected to a larger thermal coupling effect from adjacent diodes, which could be enhanced by the poor and temperature-dependent material thermal conductivity of the substrate material.

Intuitively, the larger thermal resistance for a thin substrate could be compensated by attaching a heat spreader at the bottom of the substrate. Thus, use of CVD diamond substrates, which possess approximately 30 times better thermal conductivity than GaAs, has been investigated. A comparison of the effect of bonding the CVD diamond to the chip on the thermal behavior for several configurations is shown in Fig. 7. Considering a power dissipation level of 10 mW per anode, the thermal resistance for a 3  $\mu\text{m}$  thick GaAs substrate is approximately four times larger than the resistance for a 50  $\mu\text{m}$  thick substrate.

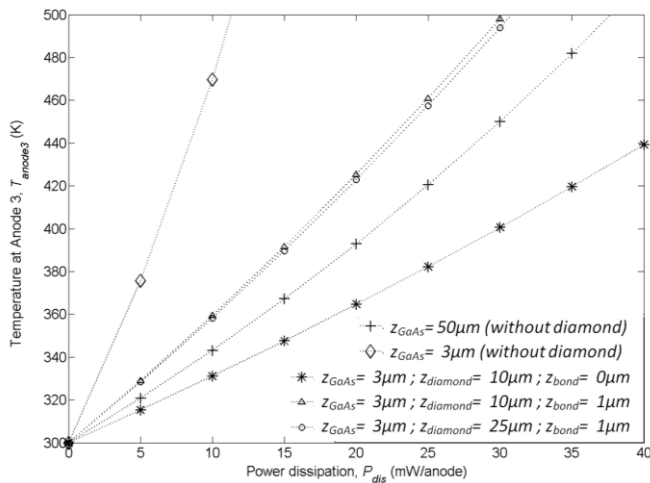


Fig. 7 A plot of the maximum junction temperature as a function of power dissipation.

Ideally, attachment of a 10  $\mu\text{m}$  thick CVD diamond beneath the thin substrate results in a lower thermal resistance compared to the 50  $\mu\text{m}$  thick substrate. For these two configurations, the thermal resistance is  $3.4 \times 10^3$  K/W and  $5 \times 10^3$  K/W, respectively, at a power dissipation level of 30 mW per anode. However, in practice, the CVD diamond is attached to the substrate via a thin layer of bonding agent. Due to the low thermal conductivity of the bonding agent, the thermal resistance is observed to be approximately two times higher compared to the values in the ideal case (without bonding agent). Moreover, with a layer of bonding agent, the effect of the CVD diamond layer thickness is minimal (see the plot for 10 and 25  $\mu\text{m}$  thick CVD diamond layers in Fig. 7).

Fig. 8 illustrates the temperature profile from the top of anode to the bottom of substrate or heat spreader. The plot shows that the advantage of utilizing the CVD diamond is impeded by the bonding agent, which exhibits a high thermal resistance. Thus, it is concluded that the thermal behavior of the 3  $\mu\text{m}$  thick substrate chip could be improved by bonding it

to the CVD diamond. However, the thermal behavior of this configuration is not as optimal as a 50  $\mu\text{m}$  thick substrate chip. In order to fully exploit the benefits of the heat spreader, a bonding agent with better thermal conductivity is required. One possibility is to load the bonding agent with diamond beads which helps to reduce the thermal resistance in the bonding layer. Alternatively, fabrication process incorporating ion-beam deposited CVD diamond layer on the semiconductor substrate could be considered.

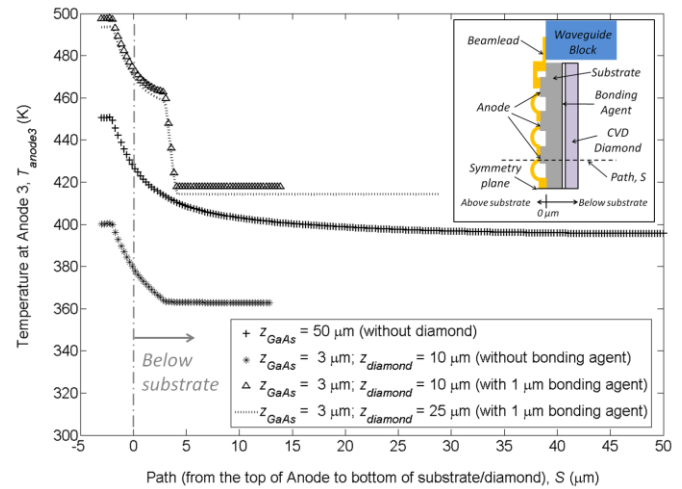


Fig. 8 Temperature gradient from the top of anode contact to the bottom of the chip (Inset: Schematic of the simulation domain indicating the physical location of the path,  $S$ . NB! The drawing is not to scale. ).

From the material system point of view, progress in the Gallium Nitride (GaN) grown on Silicon (Si) substrate [25] has provided an opportunity to develop GaN-based diodes on Si-substrate. This material system possesses a better heat handling capability than GaAs, providing an alternative to GaAs for developing high power diode-based multipliers. Since the GaN layer is grown directly on the Si substrate, the thermal conductance of the substrate is not reduced by the bonding agent. Thus, the thermal behavior of this material system is also investigated.

Fig. 9 shows a comparison the thermal behavior of the GaAs and the GaN-on-Si-based multiplier chip. In this figure, a piecewise cubic hermite polynomial is used to interpolate the temperature as a function of substrate thickness for each power dissipation level (i.e. 0 to 40 mW at the interval of 5 mW). For both of these material systems, it is observed that the nonlinear temperature rise prevails for a thinner substrate, as a consequence of the non-linear temperature coupling effect. However, the result shows that the level of temperature elevation is lower for the GaN-on-Si based chip. For a 10  $\mu\text{m}$  thick substrate, the temperature of the hot spot reached 500 K at the power level of 20 mW per anode for the GaAs-based multiplier, compared to the power level of 40 mW per anode for GaN-on-Si-based multiplier.

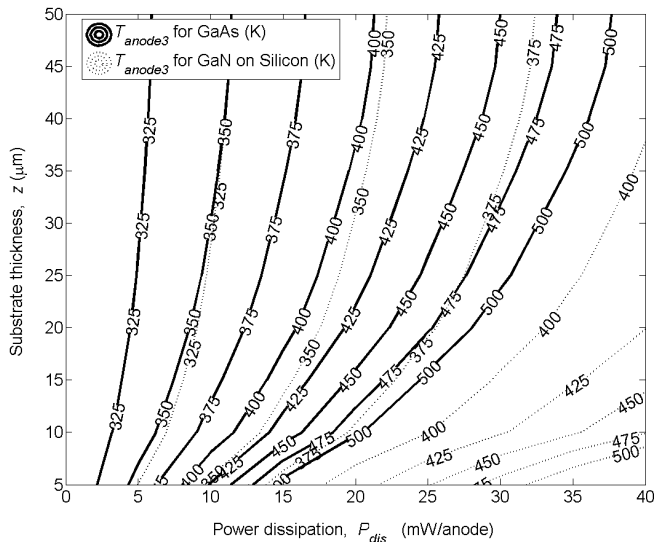


Fig. 9 A contour plot of the temperature of anode 3 as a function of substrate thickness and power dissipation for GaAs- and GaN-on-Si-based multiplier chip.

### B. Transient Thermal Analysis

A transient thermal analysis is also performed on the multiplier chip with the default layout parameters for 2 power dissipation levels, i.e. 10 and 30 mW per anode. In order to compare the transient behavior of a thinner substrate, the multiplier chip with a 5  $\mu\text{m}$  thick substrate is simulated. In these simulations, the temperatures at the anode junctions are monitored. Fig. 10 shows the simulation result for the transient characteristic of anode 3.

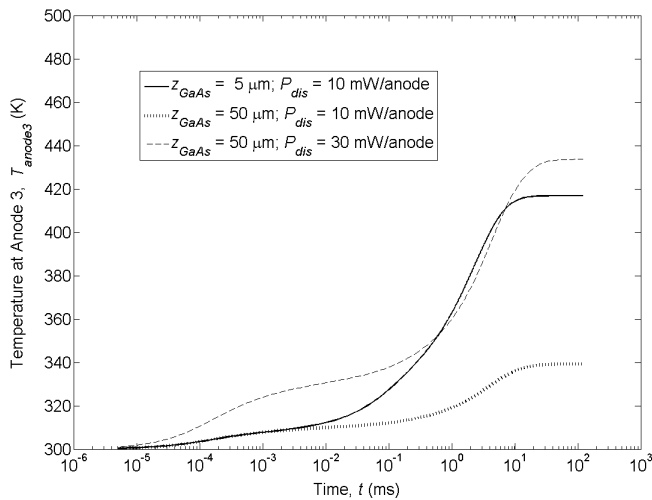


Fig. 10 Transient thermal characteristic of the multiplier chip.

At the diode junction, a sharp temperature rise occurs at the initial state. This is followed by a long slow rise to the steady-state. For a multiplier chip with a similar substrate thickness, the initial temperature rise differs for different power dissipation level. On the other hand, the initial temperature rises are similar for multiplier chips with different substrate thickness but subjected to a similar power dissipation level. This indicates that a similar thermal mass is experienced by the heat front at the instant when the power is dissipated. As

time progresses, the heat front encountered a different thermal mass, due to the difference in the substrate thickness. In addition, the transient behavior for the multiplier chip could also be attributed to the thermal coupling effect, where the temperature rise is enhanced by the ambient heat from other anodes.

From the analysis, it is concluded there exists multi time-constants in the transient characteristics. The overall thermal time constant for the multiplier chip is large, exhibiting a settling time in the order of tens millisecond.

## V. CONCLUSION

In this paper, a flexible and effective way of performing 3D thermal analysis of multiplier chips has been demonstrated using the FEM method. A 200 GHz frequency doubler chip is analyzed, taking into account the non-linear temperature response of the chip. The chip beamlead and the substrate thickness are identified as the two bottlenecks for thermal management. Optimization of the substrate thickness and material can result in better multiplier chip performance.

For the transient thermal analysis, the multiplier chip exhibits a slow and multi time-constants thermal response. This indicates that the temperature is almost constant for high frequency continuous wave (CW) application. However, further investigation on the transient behavior could be beneficial for applications where the multipliers are operated in pulse mode, such as radar imaging and sensing applications.

## ACKNOWLEDGMENT

The authors would like to thank Dr. J. Vukusic (Chalmers University of Technology) for the useful feedback.

## REFERENCES

- [1] P. Siegel, "Terahertz technology," *IEEE Transactions on Microwave Theory and Techniques*, vol. 50, 2002, pp. 910-928.
- [2] M. Shur, "Terahertz technology: devices and applications," *Proceedings of 35th European Solid-State Device Research Conference*, 2005, pp. 13-21.
- [3] A. Maestrini, B. Thomas, H. Wang, C. Jung, J. Treuttel, Y. Jin, G. Chattopadhyay, I. Mehdi, and G. Beaudin, "Schottky diode-based terahertz frequency multipliers and mixers," *Comptes Rendus Physique*, vol. 11, Aug. 2010, pp. 480-495.
- [4] D. Woolard, R. Brown, M. Pepper, and M. Kemp, "Terahertz Frequency Sensing and Imaging: A Time of Reckoning Future Applications?," *Proceedings of the IEEE*, vol. 93, 2005, pp. 1722-1743.
- [5] D.T. Hodges, E.E. Reber, F.B. Foote, and R.L. Schellenbaum, *Safeguards applications of far infrared radiometric techniques for the detection of contraband*, 1980.
- [6] I. Mehdi, G. Chattopadhyay, E. Schlecht, J. Ward, J. Gill, F. Maiwald, and A. Maestrini, "Terahertz Multiplier Circuits," *IEEE MTT-S International Microwave Symposium Digest*, 2006, pp. 341-344.
- [7] G. Chattopadhyay, E. Schlecht, J. Ward, J. Gill, H. Javadi, F. Maiwald, and I. Mehdi, "An all-solid-state broad-band frequency multiplier chain at 1500 GHz," *IEEE Transactions on Microwave Theory and Techniques*, vol. 52, 2004, pp. 1538-1547.
- [8] D. Ingram, Y. Chen, I. Stones, D. Yamauchi, B. Brunner, P. Huang, M. Biedenbender, J. Ellion, R. Lai, D. Streit, K. Lau, and H. Yen, "Compact W-band solid-state MMIC high power sources," *Microwave Symposium Digest, 2000 IEEE MTT-S International*, 2000, pp. 955-

958 vol.2.

- [9] D.J. Walkey, T.J. Smy, T. Macelwee, and M. Maliepaard, "Compact representation of temperature and power dependence of thermal resistance in Si, Inp and GaAs substrate devices using linear models," *Solid-State Electronics*, vol. 46, Jun. 2002, pp. 819-826.
- [10] P. Baureis, "Electrothermal modeling of multi-emitter heterojunction-bipolar-transistors (HBTs)," *Third International Workshop on Integrated Nonlinear Microwave and Millimeterwave Circuits*, 1994, pp. 145-148.
- [11] J. Wilson and K. Decker, "GaAs MMIC thermal modeling for channel temperatures in accelerated life test fixtures and microwave modules," *Proceedings of IEEE/CPMT 10th Semiconductor Thermal Measurement and Management Symposium*, 1994, pp. 121-128.
- [12] C. Snowden, "Large-signal microwave characterization of AlGaAs/GaAs HBT's based on a physics-based electrothermal model," *IEEE Transactions on Microwave Theory and Techniques*, vol. 45, 1997, pp. 58-71.
- [13] D. Dawson, "Thermal modeling, measurements and design considerations of GaAs microwave devices," *Technical Digest 16th Annual Gallium Arsenide Integrated Circuit (GaAs IC) Symposium*, 1994, pp. 285-290.
- [14] J. Stake, L. Dillner, S. Jones, C. Mann, J. Thornton, J. Jones, W. Bishop, and E. Kollberg, "Effects of self-heating on planar heterostructure barrier varactor diodes," *IEEE Transactions on Electron Devices*, vol. 45, 1998, pp. 2298-2303.
- [15] M. Ingvarson, B. Alderman, A. Olsen, J. Vukusic, and J. Stake, "Thermal constraints for heterostructure barrier varactors," *IEEE Electron Device Letters*, vol. 25, 2004, pp. 713-715.
- [16] X. Tang, M. Rousseau, C. Dalle, and J.C. De Jaeger, "Physical analysis of thermal effects on the optimization of GaN Gunn diodes," *Applied Physics Letters*, vol. 95, 2009, p. 142102.
- [17] F. Hasegawa and Y. Aono, "Thermal limitation for CW output power of a Gunn diode," *Solid-State Electronics*, vol. 16, Mar. 1973, pp. 337-344.
- [18] R.P. Joshi, S. Viswanadha, P. Shah, and R.D. del Rosario, "Monte Carlo analysis of GaN-based Gunn oscillators for microwave power generation," *Journal of Applied Physics*, vol. 93, 2003, p. 4836.
- [19] E. Schlecht, G. Chattopadhyay, A. Maestrini, D. Pukala, J. Gill, S. Martin, F. Maiwald, and I. Mehdi, "A high-power wideband cryogenic 200 GHz Schottky 'substrateless' multiplier: Modeling, design and results," *Proceedings of the Ninth International Conference on Terahertz Electronics*, Charlottesville, VA, USA: 2001, pp. 485-494.
- [20] D. Porterfield, "Millimeter-Wave Planar Varactor Frequency Doublers," University of Virginia, 1998.
- [21] J. Bruston, "Development of 200-GHz to 2.7-THz multiplier chains for submillimeter-wave heterodyne receivers," *Proceedings of SPIE*, Munich, Germany: 2000, pp. 285-295.
- [22] ANSYS Mechanical, ANSYS Inc, Southpointe, 275 Technology Drive, Canonsburg, PA 15317, USA.
- [23] S. Adachi, *GaAs and related materials: bulk semiconducting and superlattice properties*, World Scientific, 1994.
- [24] Quantum Focus Instruments Corporation, 2385 La Mirada Drive, Vista, CA 92081 USA.
- [25] S. Pal and C. Jacob, "Silicon - A new substrate for GaN growth," *Bulletin of Materials Science*, vol. 27, 2004, pp. 501-504.

# Design of a High-Power 1.6 THz Schottky Tripler Using ‘On-chip’ Power-Combining and Silicon Micromachining

José V. Siles, *Member IEEE*, Bertrand Thomas, Goutam Chattopadhyay, *Fellow IEEE*, Alain Maestrini, *Member IEEE*, Choonsup Lee, Erich Schlecht, *Member IEEE*, Cécile Jung and Imran Mehdi, *Fellow IEEE*

**Abstract**— In this work, we present a novel concept for power-combined high-power frequency multipliers consisting of four multiplying structures integrated on a single-chip with the input and output waveguides perpendicular to the waveguide channels, where the diodes are located, by using silicon micromachining techniques. The input power is equally divided in-phase by four E-probes located at the input waveguide. The produced output power is recombined at the output using the same concept. A 1.6 THz tripler has been designed using this architecture. The expected conversion efficiency of the tripler is  $\sim 2\text{-}3\%$  efficiency over a  $\sim 20\%$  bandwidth for a 32 mW of total input pump power.

**Index Terms**—Terahertz technology, frequency multipliers, local oscillator sources, Schottky diodes, power-combining, silicon micromachining.

## I. INTRODUCTION

THE availability of increasing output power at W-band together with the use of power-combining schemes and high-thermal conductivity substrates have led to record measured output power of terahertz sources in recent years. Recently, 1.4 mW of output power at 0.9 THz with two cascaded Schottky based frequency triplers driven with a 400-500 mW W-band HEMT power module has been reported [1]. Moreover, power levels up to 10 mW at 600 GHz and 0.1 mW at 1.9 THz are envisioned using this W-band source. The tremendous progress in GaN-based power amplifier technology, with output power levels in excess of 5 W recently demonstrated at W-band, makes it now possible to conceive solid-state multiplied sources beyond 3 THz [2], as well as to develop multi-pixel heterodyne instruments for ground and space based applications in the THz range [3].

In this work, we report on the design of a novel power-combined 1.6 THz Schottky frequency tripler intended to handle around a 30 mW input power to produce  $\sim 1$  mW at

1.6 THz. The design of Schottky based triplers at these frequency ranges is mainly constrained by the shrinkage of the waveguide dimensions with frequency and the minimum diode mesa sizes, which limits to two the maximum number of diodes per chip. Hence, multiple chip power-combined schemes become necessary to increase the power-handling capabilities of high frequency multipliers. However, the use of traditional power-combining topologies already demonstrated at frequencies below 1 THz [1, 4] presents several challenges for frequencies beyond 1 THz. On the one hand, the use of several Y-junctions or hybrid couplers to divide/combine the input/output power at these frequency bands increases unnecessarily the electrical path of the signal at a range of frequencies where the waveguide losses are considerably high. On the other hand, guarantying a perfect alignment of the very small chips during assembly in order to preserve the balanced nature of the multiplier is practically impossible, with the subsequent impact on the multiplier performance. The novel concept presented herein (see Fig. 1) overcomes these difficulties by performing the power-combining directly ‘on-chip’ instead of using 4 different chips. Four E-probes are located at a single input waveguide in order to drive 4 multiplying structures (with 2 diodes each). The produced output power is then recombined at the output using the same concept. The four multiplying structures are physically connected on one-chip so the alignment and symmetry of the circuits can be very well preserved since that is controlled by the high accuracy of MMIC lithography. Contrarily to traditional frequency triplers, in this design the input and output waveguides are perpendicular to the waveguide channels where the diodes are located. Therefore, the multiplier block can be more easily fabricated using Silicon micro-machining technology [5] instead of regular metal machining.

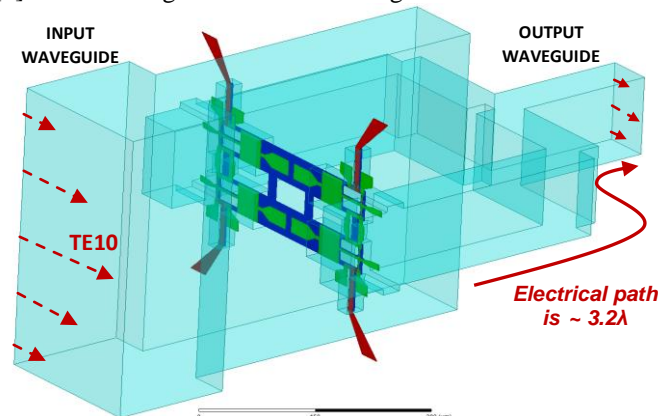


Fig. 1. ‘On-chip’ power combining scheme for frequency multipliers.

This research is supported by the Fulbright Program, sponsored by the U.S. Department of State. The work herein was carried out at the Jet Propulsion Laboratory, California Institute of Technology, under a contract with the National Aeronautics and Space Administration. Government sponsorship acknowledged.

J. V. Siles, G.Chattopadhyay, C. Lee, E. Schlecht, C. Jung and I. Mehdi are with NASA Jet Propulsion Laboratory, California Institute of Technology, Pasadena, CA 91109 USA (phone: 818-354-4006; fax: 818-354-0000; e-mail: Jose.V.Siles@jpl.nasa.gov).

B. Thomas, was with NASA Jet Propulsion Laboratory. He is now with Radiometer Physics GmbH, 53340 Meckenheim, Germany.

A. Maestrini is with Université Pierre et Marie Curie, Paris 6 and with the Observatory of Paris-LERMA, 75014 Paris, France.

Copyright © 2011 NASA Jet Propulsion Laboratory, California Institute of Technology. All rights reserved.

## II. DESCRIPTION OF THE ON-CHIP POWER COMBINED FREQUENCY TRIPLER TOPOLOGY

Based on the frequency multiplier topology described in [1,6], this novel concept exploits the 3D capabilities of the Silicon micromachining techniques in order to place the MMIC multiplier chip perpendicular to the E-plane of both the input and output waveguides. With this strategy, four identical E-probes can be used in-phase with the electric field lines of the exciting  $TE_{10}$  mode to equally divide the input signal into four ways directly on-chip as can be seen in Fig. 2. The same concept is applied to recombine the power at the output. This prevents the need of using waveguide-based power dividing structures that would add undesired excess losses to the circuit. In addition, the balance and symmetry of the circuit with this new approach, which is crucial to obtain a good performance in any power-combined frequency multiplier at terahertz frequencies [4, 7], lies on the superior accuracy of the lithographic fabrication of the MMIC chip and Silicon micro-machined blocks ( $<1 \mu\text{m}$ ) rather than on the tolerances involved with manual assembly and traditional metal milling (5-10  $\mu\text{m}$ ). This could represent a big step for future multipliers operating beyond 1 THz where dimensions of critical elements of the device can be as low as 10-20  $\mu\text{m}$  between 1-2 THz, and 5-10  $\mu\text{m}$  beyond 2 THz.

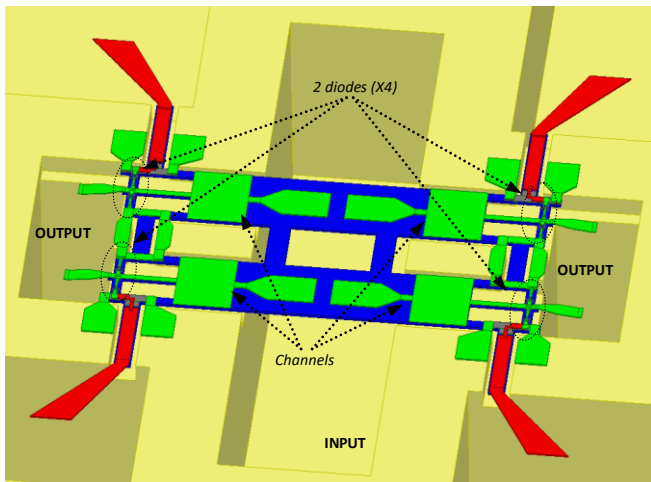


Fig. 2. Close-up view of the 1.6 THz on-chip power-combined MMIC device. Four beamleads (in red) provide independent bias to each diode branch. If fine tuning of the tripler performance is not required, only a single bias line would be necessary.

Note that this topology inherently provides two independent outputs that can be either combined together using a Y-junction, as shown in Fig. 1) or used to feed two independent frequency mixers in order to enable direct multi-pixel operation.

### III. 1.6 THz TRIPLER DESIGN

The complete power-combined tripler was designed using the methodology presented in detail in [2], which is based on an iterative process that involves the use of Ansoft HFSS for the electromagnetic simulation of the multiplier architecture and Agilent ADS for nonlinear simulation of the Schottky diode device and the harmonic balance optimization of the matching circuitry.

Once the input power has been split at the input probe level, the topology in Fig. 2 can be seen as four identical frequency triplers located at four independent small waveguide channels between the input and output waveguides. Each of these multiplying structures features two Schottky planar varactor diodes of approximately 1.2 fF of zero bias junction capacitance and has several stripline sections of low and high impedance used to match the diodes at the input and output frequencies and to prevent the third harmonic from leaking into the input waveguide. In order to balance the circuit, the dimensions of both the channel and the circuit are chosen to cut off the TE-mode at the second (idler) frequency. The dimensions of the output waveguide ensure that the first and second harmonics are cut off at the output, and the balanced configuration of the diodes ensures that the power levels from all the even harmonics of the input signal are strongly suppressed. The design is completed with a series of waveguide sections to provide broadband input matching to the diodes.

The predicted performance of the on-chip power combined frequency tripler for a 32 mW input power is presented in Fig. 3. A conversion efficiency of  $\sim 2-3 \%$  is expected over a  $\sim 20 \%$  bandwidth.

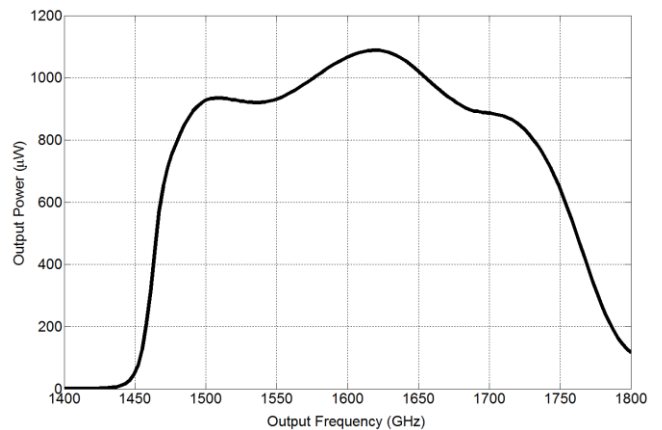


Fig. 3. Predicted performance of the on-chip power combined 1.6 THz frequency tripler for an input power of 32 mW.

### IV. COMPARISON BETWEEN ON-CHIP POWER COMBINING AND TRADITIONAL QUAD-CHIP POWER COMBINING

In order to evaluate the advantages of the proposed multiplier scheme over other power-combining techniques, an equivalent quad-chip frequency tripler has been designed following the same specifications and identical number of diodes and anode sizes. In this case, two levels of Y-junctions at the input and output waveguides have been employed to divide/combine the input/output signals. The scheme is similar to that proposed in [7]. The main constraint for this quad-chip design is the necessity to use at least two dc bias feed through. This sets a minimum distance between the multiplier chips and leads to an undesired increase in the electrical path of the output signal (17 wavelengths) as can be seen in Fig. 4. However, for the on-chip power-combined topology, the complexity of the bias circuitry is greatly reduced since it can be placed on a plane perpendicular to the input and output waveguides. The electrical path is then around 3 wavelengths (see Fig. 1), which implies a reduction of more than a factor of 5 in the output waveguide losses.



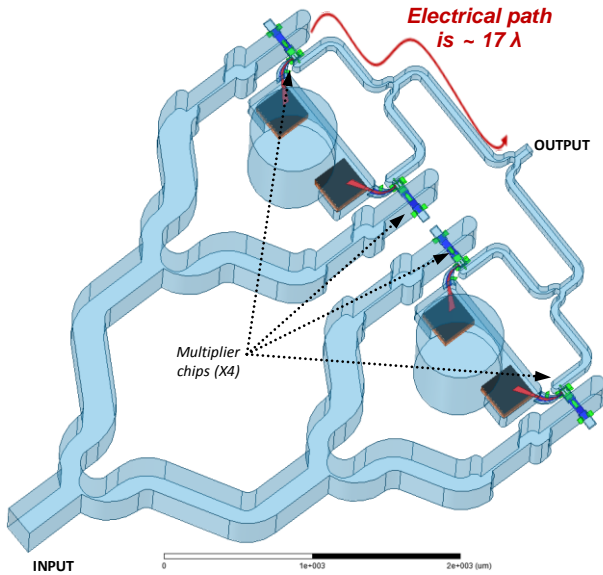


Fig. 4. Quad-chip power-combined 1.6 THz Schottky diode tripler.

The comparison between the two architectures are plotted in Fig. 5, together with the simulated performance of a single-chip 1.6 THz tripler designed for 8 mW, one fourth of the input power of the power-combined multiplier. This single chip corresponds to one of the branches shown in Fig. 4. It can be clearly seen the degradation in the conversion efficiency of the quad-chip tripler mainly due to the waveguide losses connected with the necessity of using a number of Y-junctions to power-combine the input and output signals (red dashed line). However, the on-chip power-combined tripler (black solid line) exhibits an efficiency very close to the single-chip multiplier design (dashed blue curve), which would set the reference for an ideal power-combined multiplier. Only the bandwidth is slightly reduced due to the fact of having kept the same dimensions for the reduced-height input waveguide in all the three cases, which made it necessary to reduce the lengths of the four E-probes so they could still fit together within the input waveguide. A better optimization of both the E-probes and the input waveguide dimensions in the on-chip power combined tripler would allow recovering the lost bandwidth with regards to the single-chip tripler.

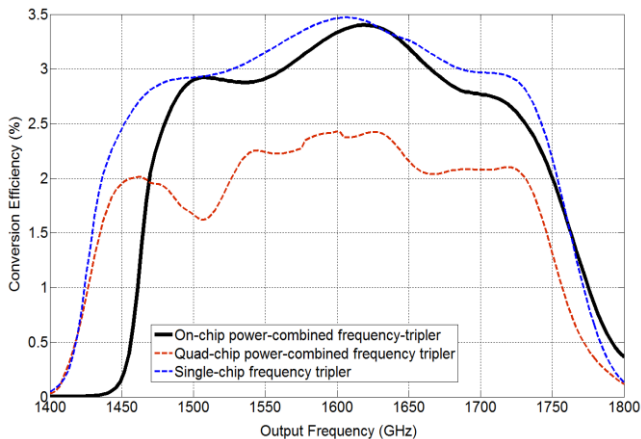


Fig. 5. Conversion efficiency of the single-chip, quad-chip power-combined, and on-chip power-combined 1.6 THz Schottky diode triplers.

## V. SILICON-MICROMACHINED BLOCK DESIGN

As already mentioned, the block design is based on the 3D integration of Silicon micromachined waveguide circuits. The concept is similar to tradition split-waveguide block designs but a number of very thin Silicon wafers are stuck together in order to define both the waveguide channels where the diodes are located and the input and output matching sections. Eight 245  $\mu\text{m}$ -thick Silicon wafers needs to be employed to fit the matching sections, the waveguide channel where the chip is placed, and the Y-junction to recombine the signal at the output. Wafer to wafer alignment is performed using Silicon alignment pins of diameters between 0.5 and 1 mm. The length and width of the Silicon wafers (20 x 20 mm) are chosen to coincide with the standard metal block dimensions used in our laboratory at JPL. The total thickness of the block is 1.96 mm, which represents a reduction of 5-10 times with regards to the metal block dimensions that would be necessary for a traditional split-waveguide metal block design, like the structure presented in Fig. 4.

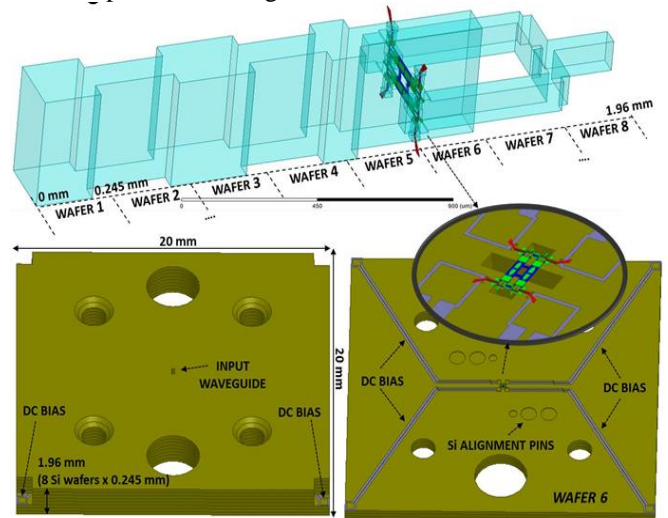


Fig. 6. Final scheme of the on-chip power combined 1.5 THz Schottky tripler including the input matching and output Y-junction (top). Block design for Silicon micromachining featuring eight 0.245 mm-thick Silicon wafers (bottom left). Detailed view of the Silicon wafer where the chips is located (bottom right). The full block dimensions are 20x20x1.96 mm.

## VI. CONCLUSION

The novel on-chip power-combining topology for high-frequency multiplier design presented herein allows the power handling capabilities of traditional frequency multipliers by a factor of four. The advantage of this approach with regard to other power-combining techniques involving multiple chips is that additional losses or performance degradation due to circuit imbalances are avoided. The topology is presented through the design of a 1.6 THz frequency tripler for a nominal input power of 32 mW. The use of Silicon micromachining instead of metal milling also makes it possible to considerably reduce the mass and volume of the multipliers.

The final goal of this work is to develop high-power all-solid state terahertz local oscillator sources to enable multi-pixel spectroscopy at 1.9 THz and 2.7 THz and to extend the use of Schottky technology up to 4.7 THz.

## REFERENCES

- [1] A. Maestrini, J. Ward, J. Gill, C. Lee, B. Thomas, R. Lin, G. Chattopadhyay and I. Mehdi, "A frequency-multiplied source with more than 1mW of power across the 840-900-GHz band", *IEEE Trans. on Microwave Theory and Tech.*, Vol. 58, No. 7, pp. 1925-1931, Jul. 2007.
- [2] I. Mehdi, B. Thomas, R. Lin, A. Maestrini, J. Ward, E. Schlecht, J. Gill, C. Lee, G. Chattopadhyay, and F. Maiwald, "High-power local oscillator sources for 1-2 THz", in *Proc. SPIE*, 7741, 774112 (2010).
- [3] G. Chattopadhyay, I. Mehdi, J. Ward, E. Schlecht, A. Skalare, and P. H. Siegel, "Development of Multi-Pixel Heterodyne Array Instruments at Submillimeter Wavelengths," *Proc. of the Asia Pacific Microw. Conf.*, Dec. 2004.
- [4] J. V. Siles, A. Maestrini, B. Alderman, S. Davies, H. Wang, J. Treuttel, E. Leclerc, T. Narhi and C. Goldstein, "A single-waveguide in-phase power-combined frequency doubler at 190 GHz", *IEEE Microwave and Wireless Components Letters*, Vol.21, No. 6, pp. 332-334, Jun 2011
- [5] C. Jung, C. Lee, B. Thomas, G. Chattopadhyay, A. Peralta, R. Lin, J. Gill and I. Mehdi, "Silicon micro-machining technology for THz applications", 35<sup>th</sup> Int. Conf. on Infrared, Millimeter and Terahertz waves, Sep. 2010.
- [6] A. Maestrini, J. Ward, J. Gill, H. Javadi, E. Schlecht, C. Tripon-Canseliet, G. Chattopadhyay and I. Mehdi, "A 540-640 GHz High Efficiency Four Anode Frequency Tripler," *IEEE Trans. Microwave Theory Tech*, Vol. 53, pp. 2835 – 284, Sep. 2005.
- [7] A. Maestrini, J. Ward, C. Tripon-Canseliet, J. Gill, C. Lee, H. Javadi, G. Chattopadhyay, and I. Mehdi, "In-Phase Power-Combined Frequency Triplers at 300 GHz", *IEEE Microwave and Wireless Component Letters*, Vol. 18, no. 3, pp. 218-220, March 2008

## Fundamental-Mode Operation of Superlattice Electronic Devices in D-Band (110–170 GHz)

H. Eisele\*, S. P. Khanna, E. H. Linfield, and L. H. Li

University of Leeds, School of Electronic and Electrical Engineering, Leeds LS2 9JT, United Kingdom

\* Contact: h.eisele@leeds.ac.uk +44-113-343-7074

This work was in part supported by the US Army and UK EPSRC.

**Abstract**—In 1970, Esaki and Tsu proposed a device structure where the Bragg reflection of miniband electrons in a semiconductor superlattice (SL) gives rise to regions of negative differential velocity [1]. Superlattice electronic devices (SLEDs) are based on this proposed device structure and have received much attention since the 1990s [2] because the underlying physical process, the Bloch effect, is associated with time constants that are much shorter than those of the transferred-electron effect in, for example, GaAs Gunn devices [3].

Devices on integral heat sinks were evaluated from three wafers grown at Leeds. Their structures had 110 SL periods and each period consisted of two monolayers of GaAs for the quantum well, and 11 or 12 monolayers of AlAs for the barrier, to achieve estimated miniband widths [4] of more than 100 meV for fundamental-mode operation in D-band (110–170 GHz). Device fabrication followed the same process steps as described in [5] except that smaller SLEDs, with nominal diameters of 15–40  $\mu\text{m}$ , were selected for packaging and RF testing. These SLEDs were mounted in the same type of package that had been employed previously [5] and were tested in the same type of top-hat WR-6 waveguide cavity as fundamental-mode InP Gunn devices at D-band frequencies [6]. Although operation in a second-harmonic mode below 190 GHz has never been observed in the more than 20 years of the cavities' use with GaAs impact ionization transit-time diodes and InP Gunn devices, the same procedure as in [5] was employed to verify fundamental-mode operation at D-band: These SLEDs could, at constant bias, be mechanically tuned with the back short by more than 1 GHz around their D-band frequencies, and their corresponding second-harmonic frequencies were confirmed to be in the range 240–310 GHz. Examples of measured record output powers are 5.0 mW at 123.3 GHz, 2.2 mW at 134.9 GHz, 0.62 mW at 151.5 GHz, and 1.1 mW at 155.1 GHz, all in the fundamental mode, and 0.52 mW at 252.8 GHz in a second-harmonic mode.

The fundamental-mode oscillation frequencies of these GaAs/AlAs SLEDs are the highest reported to date and approximately twice as high as those that have been observed with GaAs Gunn devices [7]. The oscillation frequencies and also the output powers around 150 GHz are higher than those of InGaAs/InAlAs SLEDs [8], which confirms the strong potential of SLEDs for achieving power generation up to at least 1 THz [5]. Very similar to the at least six- to ten-fold performance improvements in InP Gunn devices above 100 GHz [6], substantial increases in output power of SLEDs are expected from optimized thermal management.

### References

- [1] L. Esaki and R. Tsu, *IBM J. Res. Develop.*, vol. 14, no. 1, pp. 61–65, Jan. 1970.
- [2] E. Schomburg, *et al.*, *Appl. Phys. Lett.*, vol. 74, no. 15, pp. 2179–2181, Apr. 1999.
- [3] R. Scheuerer, *et al.*, *Appl. Phys. Lett.*, vol. 81, no. 8, pp. 1515–1517, Aug. 2002.
- [4] G. Bastard, *Phys. Rev. B*, vol. 24, no. 10, pp. 5693–5697, Nov. 1981.
- [5] H. Eisele, S. P. Khanna, and E. H. Linfield, *Applied Physics Letters*, vol. 96, no. 7, Feb. 2010, pp. 072101-1–072101-3.
- [6] H. Eisele and G. I. Haddad, *IEEE Microwave and Guided Wave Letters*, vol. 5, no. 11, Nov. 1995, pp. 385–387.
- [7] H. Eisele and G. I. Haddad, John Wiley & Sons, New York, 1997, pp. 343–407.
- [8] E. Schomburg, *et al.*, *Electron. Lett.*, vol. 35, no. 17, pp. 1491–1492, Aug. 1999.

# Power Combined Gallium Nitride Amplifier with 3 Watt Output Power at 87 GHz

A. Fung, J. Ward, G. Chattopadhyay, R. Lin, L. Samoska, P. Kangaslahti, I. Mehdi, B. Lambrigtsen, P. Goldsmith, M. Micovic, A. Kurdoghlian, K. Shinohara, I. Milosavljevic, and D. H. Chow

**Abstract** — Many terahertz frequency signal sources that are derived from frequency multiplication with Schottky diodes utilize W-band power amplifiers. In this report we present measured results for powered combined gallium nitride (GaN) W-band power amplifier modules. An individual module contains a single three stage GaN MMIC. GaN modules are power combined separately with 2-way and 4-way WR10 waveguide hybrid couplers to increase output power. At a drain operating bias of 12 V, the highest measured output power from a single MMIC module, 2-way power combined modules, and 4-way power combined modules are 0.78, 1.29, and 2.28 W, respectively. Further increasing drain bias to 15 V on the 4-way power combined module produced 3 W peak output power. We discuss the GaN package module, the modular WR10 waveguide power combiners, the power characterization test set, and our measured results.

**Index Terms** — gallium nitride, W-band, MMIC, power amplifier, power combining.

## I. INTRODUCTION

W-band power amplifiers are currently used in many high frequency local oscillator (LO) sources for terahertz heterodyne receivers to study molecular spectra. Information obtained can be used to remotely detect the presence and quantity of molecules, and to determine the pressure, temperature, and Doppler velocity of gases (see ref. 1 and 2 for a review of terahertz technology and applications). The availability of higher W-band power amplifiers can simplify future array heterodyne systems that will require more LO power, and enable new higher frequency radar and communication systems.

W-band power amplifiers have been largely developed from technologies such as gallium arsenide (GaAs) pseudomorphic high electron mobility transistors (pHEMTs) [3] and indium phosphide (InP) HEMTs [4]. Advances in gallium nitride (GaN) HEMTs have demonstrated W-band operation with output power density per unit gate width surpassing that

of GaAs and InP HEMTs by about a factor of 7.5 [5]. Recent progress in GaN amplifiers have now demonstrated output power over a watt level from single chip MMICs; 1.3 W at 75 GHz [6] and 1.7 W at 91 GHz [7] have been measured. By power combining MMIC chips in waveguide, earlier efforts using GaAs pHEMTs and InP HEMTs in an 8-way waveguide power combiner have demonstrated output power levels of 2.4 W and 2.24 W. These correspond to power density per unit gate width of the output PA stage of 0.23 and 0.175 W/mm, respectively [8]. Recent efforts in a 12-way radially power combined GaN PA produced 5.2 W at 95 GHz while operating the output stage at a power density of 0.72 W/mm [9]. In this effort, we report on a 4-way power combined GaN PA that resulted in 3 W of output power at 87 GHz with a higher output stage power density of 1.25 W/mm. These new GaN efforts demonstrate state-of-the-art W-band operation of GaN PAs with greater output power and greater power density capability than other compound semiconductor technologies that we are aware of to date. Additional benefits of GaN are that it is mechanically more robust and can operate at higher temperatures than GaAs and InP [10-12].

## II. MMIC AND MODULE

The GaN MMIC chip we use has 0.15  $\mu\text{m}$  T-gate length transistors with  $f_T$  and  $f_{\text{max}}$  of 90 and 200 GHz, respectively. The basic transistor unit cell consists of 4 x 37.5  $\mu\text{m}$  wide gate fingers. The MMIC PA has three stages. Stage 1, 2 and 3 have 1, 2, and 4 transistor units each, respectively. Optimum

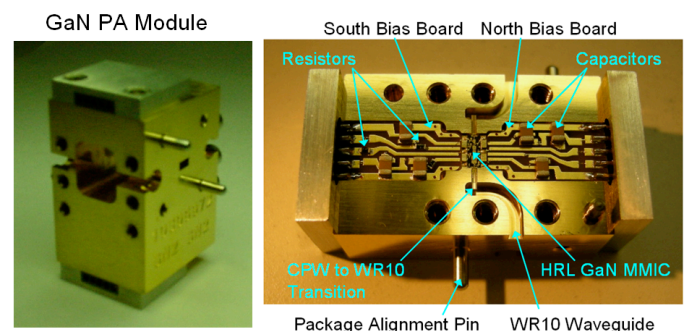


Fig. 1. The GaN PA module is a split block package with RF input and output WR10 ports compatible with MIL Spec MIL-F-3922/67B-010.

Manuscript received August 1, 2011. This research was carried out in part at the Jet Propulsion Laboratory, California Institute of Technology, under a contract with the National Aeronautics and Space Administration. A. Fung, G. Chattopadhyay, R. Lin, L. Samoska, P. Kangaslahti, I. Mehdi, B. Lambrigtsen, and P. Goldsmith are with the Jet Propulsion Laboratory, California Institute of Technology, Pasadena, CA 91109 USA (phone: 818-354-1832; fax: 818-393-4683; e-mail: andy.fung@jpl.nasa.gov). J. Ward is now with Raytheon Co., Fort Wayne, IN, 46808, USA. M. Micovic, A. Kurdoghlian, K. Shinohara, I. Milosavljevic, and D. H. Chow are with HRL Laboratories, LLC, Malibu, CA 90265, USA.

gain 50 ohm inter-stage matching is used to minimize potential issues from uncertainties in the transistor model. The net output stage gate periphery is  $600 \mu\text{m}$ . The MMIC PA was designed and fabricated by HRL Laboratories under HRL internal research and development efforts [13]. The single chip GaN PA MMIC is packaged in a split block W-band amplifier module. The module has two separate bias boards for the drain (north side) and gate (south side) bias lines of the MMIC. Figure 1 shows the general layout of the package. The GaN MMIC chip resides in a cavity in which waveguide modes are ideally cut off. Off-chip bias line capacitors and resistors are added near the MMIC and on the DC bias boards for decoupling. The bias boards are fitted with a socket receptacle for easy connection to voltage bias supplies. For transmitting RF signal from the MMIC to the input and output WR10 waveguides of the module, microstrip to waveguide transitions are used. Wirebonds complete all chip to RF transitions and DC bias board connections.

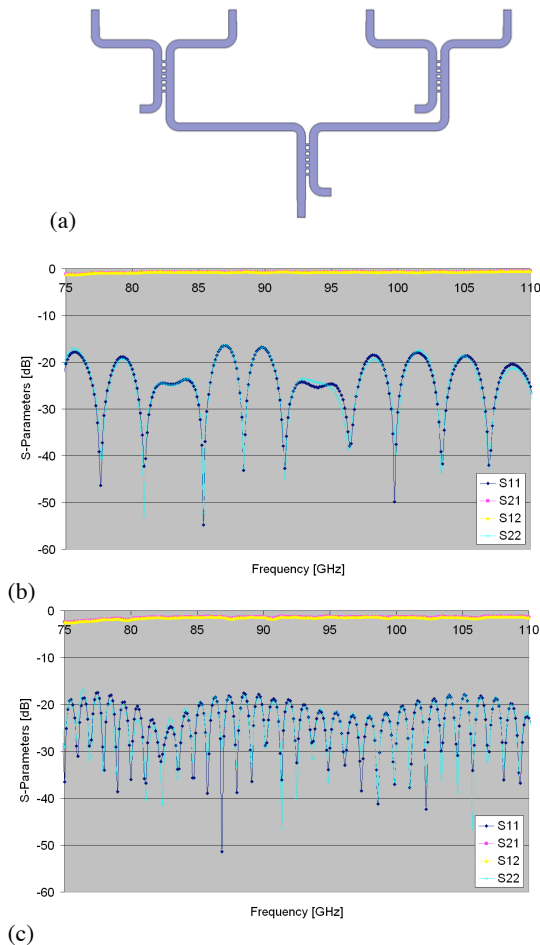


Fig. 2. Characteristics of the 2- and 4-way power combiners (splitters). (a) Diagram of the 4 to 1 port power combiner (splitter). Internal ports are terminated by matched absorber loads. The 2 to 1 port power combiner (not shown) is a special case of the 4 to 1 port design. (b) S-Parameters of the back-to-back 2 to 1 port combiners. (c) S-Parameters of the back-to-back 4 to 1 port combiners.

### III. WAVEGUIDE HYBRID COUPLER POWER COMBINERS

The 2- and 4-way power combiners (splitters) examined in this study utilize waveguide hybrids [14] and are designed to function over the full W-Band. A waveguide hybrid is a four-port directional coupler. Ideally, power incident on any port is divided equally between two other ports with a  $90^\circ$  phase difference, and the fourth port is isolated. The waveguide form of quadrature hybrid consists of two parallel waveguides coupled through a series of apertures or branch waveguides. The number of waveguide branches determines the fractional bandwidth of the coupler. Hybrid couplers used as power splitters and combiners have an advantage over traditional waveguide Y-splitters in that the hybrid couplers are balanced and offer better return loss.

In the 2- and 4-way waveguide hybrid coupler power combiners (splitters), 6-branch couplers allow for full W-band (75-110 GHz) operation. The designs are optimized using a 3-D electromagnetic simulator (Ansoft's High Frequency Structure Simulator – HFSS) and Agilent's linear circuit simulator (Advanced Design System – ADS) using an iterative technique known as space mapping [15]. The parameters that are optimized in the two hybrid coupler designs are the amplitude and phase imbalance at the output ports and the return loss performance at all the ports. We designed the couplers to have less than  $\pm 0.5$  dB of amplitude imbalance and  $90^\circ \pm 1^\circ$  phase shift over the entire W-band. Figure 2 shows the schematic of the 4-way hybrid coupler power combiner and measured S-parameters of both the 2- and 4-way combiners measured back-to-back in pairs. For the 2 to 1 hybrid coupler combiner measured back-to-back, insertion loss is less than 1.2 dB and return loss is greater than 16.4 dB across the band. For the 4 to 1 hybrid coupler combiner measured back-to-back, insertion loss is less than 2.5 dB and return loss is greater than 17.5 dB.

### IV. POWER PERFORMANCE MEASUREMENTS

The power-in versus power-out (PiPo) characterization test set consists of a frequency multiplied signal source. An Agilent 20 GHz signal synthesizer is used as the initial signal generator. A Millitech sextupler is used to multiply the synthesizer signal to W-band frequency. Different custom JPL packaged PAs are used to provide adequate input test power at various W-band frequencies. A variable attenuator is used to change the test signal power level. An isolator is used to improve matching for the test PA output and the GaN PA device under test (DUT) input. Couplers allow for the input and output test signal power levels to and from the DUT to be sampled. An Agilent W-band and an Erickson broadband power meter monitor the input and output power levels of the DUT. A high power load terminates the output of the test set.

Output power as a function of frequency has been measured at various input power levels for the 2- and 4-way power combined GaN PAs that are constructed from multiple units of the single chip module. The power combined PA's saturated

output power increases while the unsaturated gain remains essentially the same as a single amplifier module except for slight losses due to non-ideal amplitude and phase combining, and passive losses in the combiner waveguides themselves.

The 2- and 4-way power combined GaN PAs are shown in Figures 3 (a) and 4 (a). Operating at 12 V drain bias, for the 2- and 4-way power combined GaN PAs respectively, the maximum output powers are 1.29 and 2.28 W; corresponding gains are 8.1 and 6.7 dB; and power added efficiencies (PAEs) are 13.7 and 11.2 %. The maximum output power achieved in this study is 3 W with 6.6 dB gain and 10.2 % PAE at 15 V drain bias with the 4-way GaN PA (see Fig. 4 (c)).

2-Way Combiner GaN PA Module

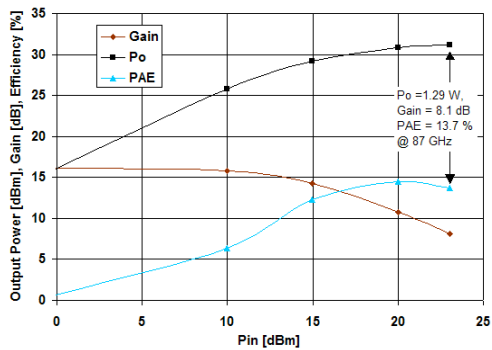
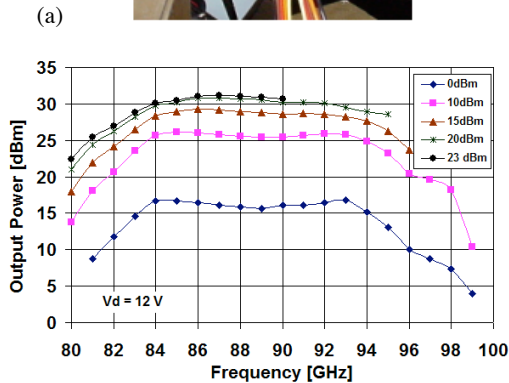
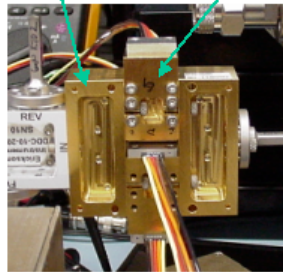


Fig. 3. 2-way waveguide power combined GaN PA results. (a) Photo of the power combined GaN PA. (b) Output power measured at input power levels of 0, 10, 15, 20 and 23 dBm as a function of frequency. (c) PiPo, gain and PAE of the 2-way power combined PA at 87 GHz.

4-Way Combiner GaN PA Module

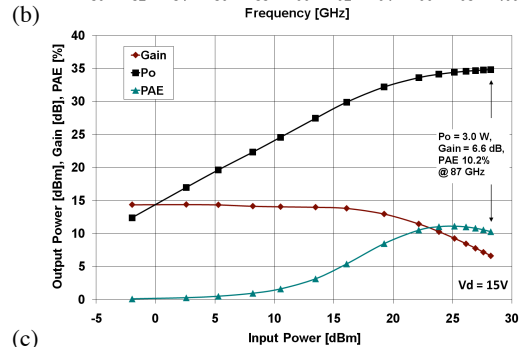
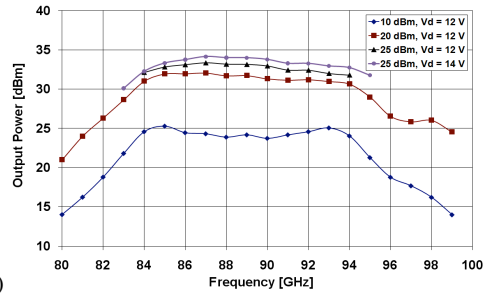
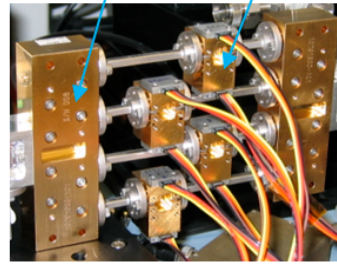


Fig. 4. 4-way waveguide power combined GaN PA results. (a) Photo of the power combined GaN PA. Individual amplifier modules are staggered with waveguide sections to prevent mechanical interference and are not intended to add any net phase shifts at the input of the power combiners. (b) Output power measured at input power levels of 10, 20 and 25 dBm as a function of frequency. (c) PiPo, gain and PAE of the 4-way power combined PA at 87 GHz.

### V. THREE MONTH POWER-ON TEST

We examined the characteristics of a single MMIC chip module under continuous input power at ambient temperature. The amplifier was DC biased where the gain S21 is approximately optimized, peaking slightly at 86 GHz. For the extended time power-on response test, the amplifier is driven into compression with 22 dBm at 86 GHz. During the test, output power, input power, and the bias conditions of each of the three stages of the MMIC amplifier are recorded (see Fig. 5). Measurements indicate there is a settling time for the output power of the amplifier to reach a steady value from the initial power on value. The packaged amplifier MMIC was not subjected to a burn-in period prior to the test. Output power and also PAE show some fluctuations that coincide in time with drain current bias fluctuation changes. The cause of the drain current bias fluctuations is still under

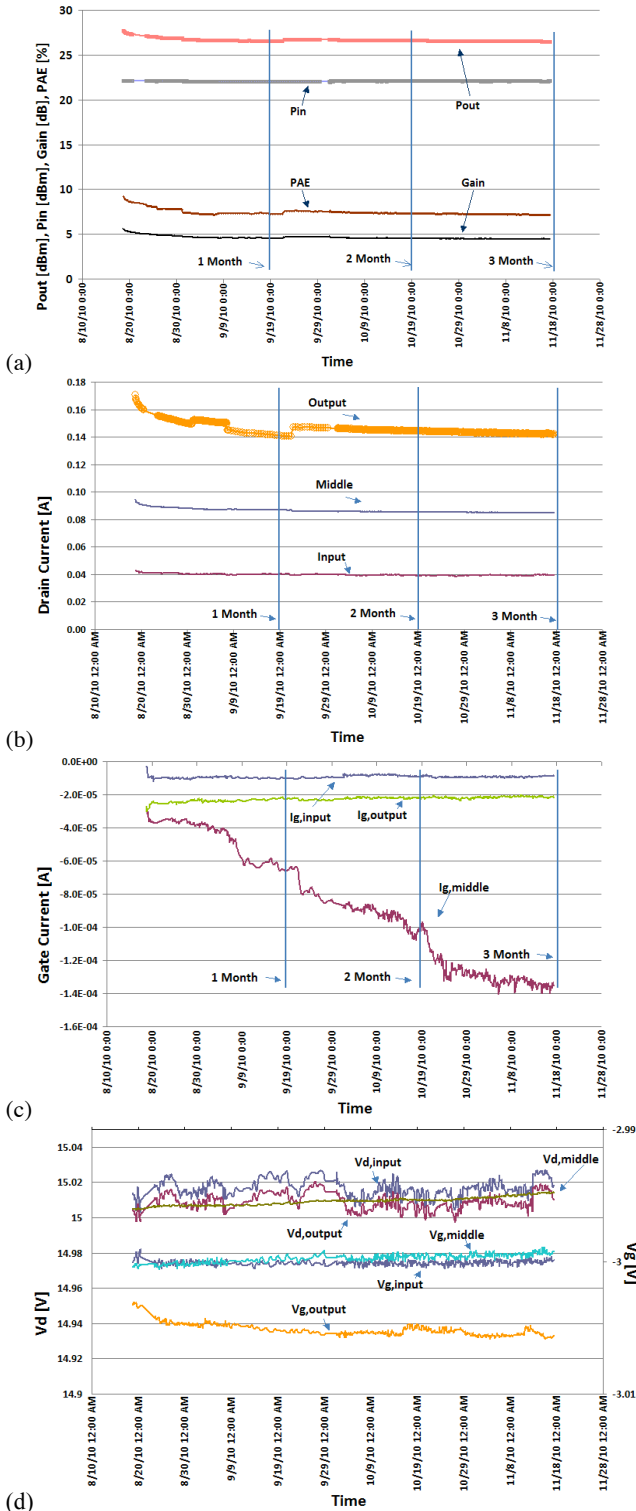


Fig. 5. Extended time power-on test results for a packaged single MMIC chip module. (a) Plot of output power, input power, PAE and gain versus time. (b) Plot of drain current of each of the three stages of the MMIC amplifier versus time. (c) Plot of gate current of each of the three stages of the MMIC amplifier versus time. (d) Plot of drain and gate voltage supply values versus time.

investigation. Gate current of the middle stage of the amplifier increases in magnitude while the input and output stages remain essentially constant during the three-month test. The output power level doesn't appear to be greatly affected by the measured bias changes and remains fairly constant after the initial settling period. The test data we present here is our first examination of extended power-on performance of one amplifier module. More effort in accelerated lifetime testing at elevated temperatures with additional test samples would benefit determination of mean time to failure (see ref. [10] for more discussions).

## VI. CONCLUSION

We report results on waveguide power combined GaN MMIC modules for W-band operation. By power combining four GaN modules with waveguide hybrid couplers, a maximum output power of 3 W, with 6.6 dB gain and 10.2 % PAE was measured. An extended power on-test of three months duration was performed on a single MMIC chip module. After an initial settling period of the output power level and drain currents, the output power remained essentially constant. It is expect future W-band PAs will migrate towards GaN based semiconductors from other III-V compound semiconductors as the technology matures in terms of reliability and cost.

## ACKNOWLEDGMENT

The authors thank Mary Soria, Joelle Cooperrider, and Peter Bruneau of JPL, and Dr. William Jeffrey and Dr. Conilee Kirkpatrick of HRL for their support.

## REFERENCES

- [1] P. H. Siegel, "Terahertz Technology," *IEEE Trans. Microwave Theory & Tech.*, vol. 50, no. 3, pp. 910-928, March 2002.
- [2] P. H. Siegel, "THz Instruments for Space," *IEEE Trans. Antennas Propagat.*, vol. 55, no. 11, Part 1, pp. 2957-2965, November 2007.
- [3] H. Wang, L. Samoska, T. Gaier, A. Peralta, H. Liao, Y. C. Leong, S. Weinreb, Y. C. Chen, M. Nishimoto, and R. Lai, "Power-amplifier modules covering 70-113 GHz using MMICs," *IEEE Trans. Microwave Theory & Tech.*, vol. 49, no. 1, pp. 9-16, January 2001.
- [4] Y. C. Chen, D. L. Ingram, R. Lai, M. Barsky, R. Grunbacher, T. Block, H. C. Yen, and D. C. Streit, "A 95-GHz InP HEMT MMIC amplifier with 427-mW power output," *IEEE Microwave Guided Wave Lett.*, vol. 8, no. 11, pp. 399-401, November 1998.
- [5] M. Micovic, A. Kurdoghlian, H. P. Moyer, P. Hashimoto, M. Hu, M. Antcliffe, P. J. Willadsen, W. S. Wong, R. Bowen, I. Milosavljevic, Y. Yoon, A. Schmitz, M. Wetzel, C. McGuire, B. Hughes, and D. H. Chow, "GaN MMIC PAs for E-Band (71 GHz - 95 GHz) Radio," *IEEE Compound Semi. IC Symp. Dig.*, pp. 1-4, October 2008.
- [6] Y. Nakasha, S. Masuda, K. Makiyama, T. Ohki, M. Kanamura, N. Okamoto, T. Tajima, T. Seino, H. S., K. Imanishi, T.

- Kikkawa, K. Joshin, and Naoki Hara, "E-Band 85-mW Oscillator and 1.3-W Amplifier IC's using 0.12-mm GaN HEMTs for Millimeter-wave Transceivers," *IEEE Compound Semi. IC Symp. Dig.*, October 2010.
- [7] A. Brown, K. Brown, J. Chen, K. C. Hwang, N. Koliass, and R. Scott, "W-band GaN Power Amplifier MMICs," *IEEE MTT-S International Microwave Symposium Dig.*, vol. , pp. -, June 2011.
- [8] D. L. Ingram, Y. C. Chen, I. Stones, D. Yamauchi, B. Brunner, P. Huang, M. Biedenbender, J. Elliot, R. Lai, D. C. Streit, K. F. Lau, and H. C. Yen, "Compact W-Band Solid-State MMIC High Power Sources," *IEEE MTT-S International Microwave Symposium Dig.*, vol. 2, pp. 955-958, June 2000.
- [9] J. Schellenberg, E. Watkins, M. Micovic, B. Kim, and K. Han, "W-Band, 5W Solid-State Power Amplifier/Combiner," *IEEE MTT-S International Microwave Symposium Digest, May 2010*.
- [10] U. K. Mishra, L. Shen, T. E. Kazior, Y.-F. Wu, "GaN-Based RF Power Devices and Amplifiers," *Proceedings of the IEEE*, vol. 96, no. 2, pp. 287-305, February 2008.
- [11] D. Maier, M. Alomari, N. Grandjean, J-F Carlin, M-A Diforte-Poisson, C. Duan, A. Chuvilin, D.Troadec, C. Gaquiere, U. Kaiser, S. Delage, E. Kohn, "Above 500°C Operation of InAlN/GaN HEMTs," *IEEE Int. Electron Device Meeting. Dig.*, December 2009.
- [12] F. Medjdoub, J-F Carlin, M. Gonschorek, E. Feltin, M.A. Py, D. Ducatteau, C. Gaquiere, N. Grandjean, E. Kohn, "Can InAlN/GaN be an alternative to high power / high temperature AlGaIn/GaN devices?" *IEEE Int. Electron Device Meeting. Dig.*, vol., no., pp.1-4, 11-13 Dec. 2006.
- [13] M. Micovic, A. Kurdogklian, K. Shinohara, S. Burnham, I. Milosavljevic, A. Corrion, M. Hu, W.S. Wong, A. Schmitz, P. Hashimoto, P. J. Willadsen, D. H. Chow, A. Fung, R. Lin, L. Samoska, P. Kangaslahti, B. Lambrigsten, and P. Goldsmith, "W-Band GaN MMIC with 842mW Output Power at 88 GHz," *IEEE MTT-S International Microwave Symposium Digest, May 2010*.
- [14] S. Srikanth and A. R. Kerr, "Waveguide Quadrature Hybrids for ALMA Receivers," *ALMA Memo 343*, January 2001.
- [15] J. W. Bandler, R. M. Biernacki, S. H. Chen, and Y. F. Huang, "Design Optimization of Interdigital Filters Using Aggressive Space Mapping and Decomposition," *IEEE Trans. Microwave Theory & Tech.*, vol. 49, no. 5, pp. 761-769, May 1997.



# A 2.5-2.7 THz Room Temperature Electronic Source

Alain Maestrini, Imran Mehdi, Robert Lin, José Vicente Siles, Choonsup Lee, John Gill, Goutam Chattopadhyay, Erich Schlecht, Bertrand Thomas, and John Ward

**Abstract**—We report on a room temperature 2.5 to 2.7 THz electronic source based on frequency multipliers. The source utilizes a cascade of three frequency multipliers with W-band power amplifiers driving the first stage multiplier. Multiple-chip multipliers are utilized for the two initial stages to improve the power handling capability and a sub-micron anode is utilized for the final stage tripler. Room temperature measurements indicate that the source can put out a peak power of about 14 microwatts with more than 4 microwatts in the 2.5 to 2.7 THz range.

**Index Terms**—Frequency multipliers, Schottky diode multipliers, Submillimeter-wave technology, Power combining, Varactor diodes.

## I. INTRODUCTION

SUBMILLIMETER-WAVE spectrometry is a proven flight technique that is essential for NASA's unique goals, such as atmospheric remote sensing, study of cosmic water profiles, comet characterization [1], and investigation of cosmological phenomena with radio telescopes [2]. Recent results obtained from the Heterodyne Instrument for Far-Infrared (HIFI) on the Herschel Space Observatory have shown spectacular emission and absorption spectra with unprecedented resolution [3]. The highest frequency band on HIFI is 1.9 THz. High-resolution radiometry beyond this range has been severely limited due to the lack of robust sources.

In this paper we will briefly discuss the development and characterization of a  $3 \times 3 \times 3$  based frequency multiplier chain that provides microwatts of output power in the 2.5 to 2.7 THz range. The target for our LO subsystem development is the 2.7 THz ground-state transition in HD, a molecule with immense

cosmological significance. Deuterium was formed in the Big Bang, and because of its relatively weak nuclear binding, its abundance provides strong constraints on the physical conditions during the first few minutes of the universe's expansion and hence the density of baryons [4]. Subsequently, deuterium is lost during nucleo-synthesis when material is cycled through stars in the course of galactic chemical evolution. Understanding the abundance of deuterium is essential for probing the origin and evolution of the universe as well as its star formation history. In the molecular interstellar medium deuterated molecular hydrogen is the dominant reservoir of deuterium [5]. Spectroscopic measurements of the ground-state transition of HD (at 112  $\mu\text{m}$ , 2.675 THz) should allow us to take a census of deuterium in our Galaxy. Although an instrument on the Infrared Space Observatory (ISO) already detected the transition of HD in emission with low spectral resolution [6], HD can exist in a variety of regions having different densities and temperatures, so high-velocity resolution heterodyne observations are the only way to be certain of where any HD seen in absorption or emission is located.

## II. DESIGN ARCHITECTURE

Schottky diode based multipliers have proven to be an excellent choice as local oscillators in the submillimeter-wave range due to their compactness, electronic tunability and stability. The approach used for the HIFI instrument was based on single chip frequency multipliers cascaded together. However, to reach 2.7 THz with enough power to pump HEB

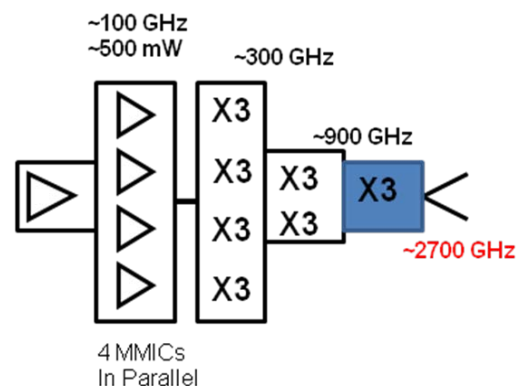


Fig. 1: Block diagram of the 2.5-2.7 THz source is shown. A scheme utilizing in-phase power combining is used to generate power at the 900 GHz driver stage, allowing for sufficient pump power to the last stage tripler.

The research presented in this letter was carried out at the Jet Propulsion Laboratory, California Institute of Technology, under a contract with the National Aeronautics and Space Administration, at the Université Pierre et Marie Curie-Paris6, and at the Observatoire de Paris, France.

A. Maestrini is with the Université Pierre et Marie Curie-Paris6, Paris, France, and with the Observatoire de Paris, LERMA, France. (e-mail: alain.maestrini@obspm.fr)

I. Mehdi, R. Lin, J.V. Siles, C. Lee, J. Gill, G. Chattopadhyay, and E. Schlecht are with the Jet Propulsion Laboratory, California Institute of Technology, Pasadena, CA, USA. (e-mail: imran.mehdi@jpl.nasa.gov)

B. Thomas was with the Jet Propulsion Laboratory. He is now with Radiometer Physics GmbH, Germany.

J. Ward was with the Jet Propulsion Laboratory. He is now with Raytheon Company, Fort Wayne, Indiana, USA.

mixers a slightly different approach comprised of more powerful driver stages has been utilized. The resulting scheme used for the 2.5 to 2.7 source is shown in Fig. 1.

### A. W-Band Power amplifiers

In order to have sufficient drive power at  $\sim 900$  GHz we start with a  $\sim 500$  mW source at  $\sim 100$  GHz. While a number of recent results have been presented with GaN based power amplifier chips that can produce these power levels [7], we utilized GaAs based HEMT device power amplifiers. A four-chip waveguide based block was designed and fabricated. 90-degree quadrature hybrid couplers are utilized at the input and output of this construction. The drain voltages for each MMIC are tied together and the resultant output power as a function of frequency for different drain voltages is shown in Fig. 2.

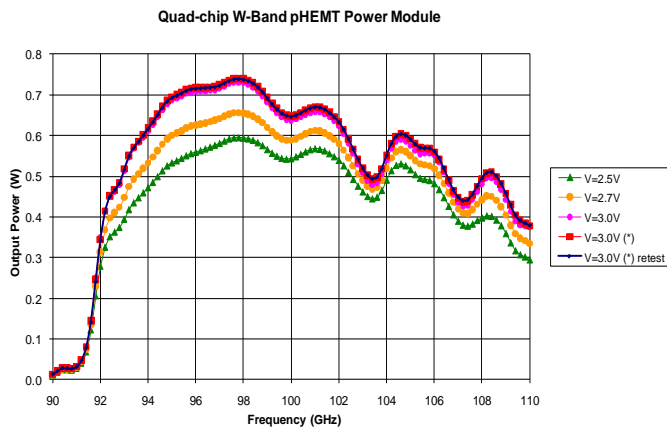


Fig. 2: Measured performance of a four-chip power combined power amplifier module as a function of various drain voltages.

### B. Power-Combined Multipliers

The large amount of available power at W-band now puts the onus on the multiplier designer to successfully harness this power. A number of approaches have been identified to achieve this goal. For a given multiplier design, as the input power is increased, the multiplier will either experience thermal heating or reverse breakdown, both of which will result in catastrophic failure. To improve the thermal handling of multiplier chips, an approach utilizing diamond substrates has been previously reported [8]. The second limitation to frequency multiplier power-handling occurs when the input signal to the multiplier becomes large enough to drive the diodes into reverse breakdown. Increasing anode area, increasing the number of anodes per chip, optimizing doping levels, and moving to a high thermal conductivity substrate or GaN will allow additional improvements in single-chip power handling.

However, chip thickness and number of anodes per chip can only be increased up to a limit. In order to avoid unwanted waveguide modes, both of these design parameters are eventually constrained. Enhancing power handling capabilities beyond this point requires novel approaches such as

sandwiching dual chips within a single-waveguide, as suggested in [9]. A simpler to implement approach is to power combine multiplier circuits in a waveguide based topology [10]. This approach offers a number of advantages: It is a straightforward concept and does not require any new technology development at the chip level; in fact, existing chips can be utilized. The power combining and dividing functionality is accomplished in the waveguide, allowing for a low-loss transmission media. Moreover, this approach provides an easily scalable design, both in frequency as well as in power. Traditional designs such as the Y-junction and the 90-degree hybrid couplers have been utilized for this approach.

A quad-chip power combined tripler has been designed and characterized for this task, as shown in Figure 3. The power-combined version is based on two mirror-image tripler chips that are power-combined in-phase in a single waveguide block using a compact Y-junction divider at the input waveguide and a Y-junction combiner at the output waveguide. The complete power-combined tripler was designed using the methodology presented in detail in [11].

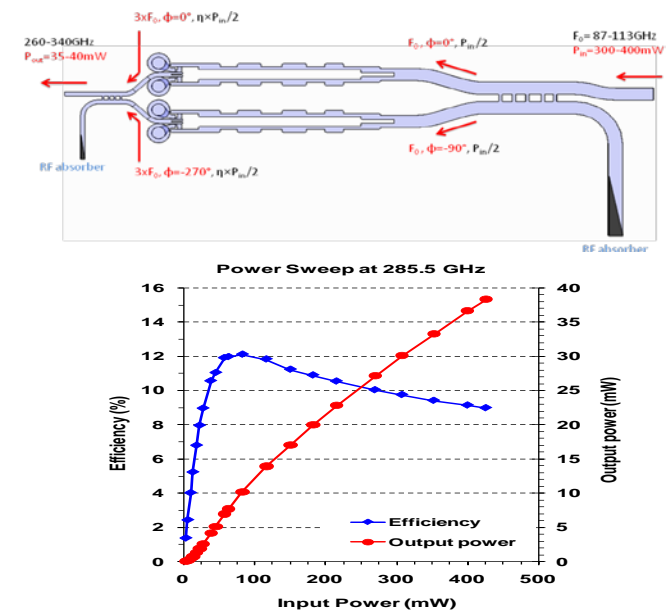


Fig. 3: Approach used to power combine four tripler chips in the first stage multiplier is shown above. The results obtained from such a quad-chip tripler are shown in the plot below for a fixed frequency of 286.6 GHz. This measurement is done at room temperature.

Fig. 3 shows an overall schematic view of the tripler including the input matching circuit. The tripler uses a split-block waveguide design with four independent DC bias lines. The input waveguide is split in four ways by a hybrid coupler followed by a Y-junction to evenly feed four multiplying circuits featuring six Schottky planar varactor diodes of about 16 fF each. The chips are mounted in four independent channels that run between their respective input and the output waveguides. The four reduced-height output waveguides are combined by a Y-junction and a hybrid coupler using the same

concept as at the input.

On each chip, an E-plane probe located in the input waveguide couples the signal at the input frequency to a suspended microstrip line. This line has several sections of low and high impedance used to match the diodes at the input and output frequencies and to prevent the third harmonic from leaking into the input waveguide. The third harmonic produced by the diodes is coupled to the output waveguide by a second E-plane probe. In order to balance the circuit, the dimensions of both the channel and the circuit are chosen to cut off the TE-mode at the second (idler) frequency and third harmonic within the channel. The dimensions of the output waveguide ensure that the first and second harmonics are cut off at all frequencies measured, and the balanced geometry of the chips ensures that powers at the even harmonics of the input are strongly suppressed outside the diode loop. The output power achieved from this chip is shown in Fig. 3 as a function of input power. As can be seen, this provides sufficient pump power to drive the second stage multiplier for the 2.7 THz LO subsystem.

The second stage tripler, designed to cover the 850-970 GHz range, uses a similar power combining technique based on a dual-chip configuration. Details of the 900 GHz chip and chain have been presented previously [12]. The final stage tripler is based on a single balanced tripler configuration that has been successfully demonstrated in the THz range. The chip is fabricated on a very thin membrane to reduce parasitic loading. A close-up of the chip inside the waveguide block is shown in Fig. 4.

### III. MEASUREMENTS

#### A. Test Setup

A commercial synthesizer followed by an active sextupler and a WR10 isolator is used to drive the power amplifier module. This serves as the driver for the LO chain as shown in Figure 1. The chain to 900 GHz was first calibrated and has been described in detail elsewhere [12]. When pumped with 330-500 mW at W-band, this driver chain delivers more than 1 mW in the 840-900 GHz band at room temperature as shown in Figure 5. However, for most of the tests presented in this paper, the input power at W-band was limited to 350 mW. Thus the power delivered by the driver chain to the last stage multiplier was in the range of 0.25-1 mW.

A VDI-Erickson PM4 power meter was used to record output power levels. Goly cells and cryogenic semi-conductor bolometers were also initially used to fine tune the LO chain as they provide a much faster time constant. However their calibration is more problematic, requiring an external calibrator to determine the responsivity of the sensor. The Thomas Keating power meter is easier to calibrate, but is limited to power levels above about 5  $\mu$ W due to its high level of noise. In addition, the Thomas Keating meter has a large optical window, which is prone to pick up parasitic signals coming from lower-frequency leaks in the local oscillator chain (same as the Goly cell and bolometers).

The VDI-Erickson PM4 meter has the advantage of a wave-

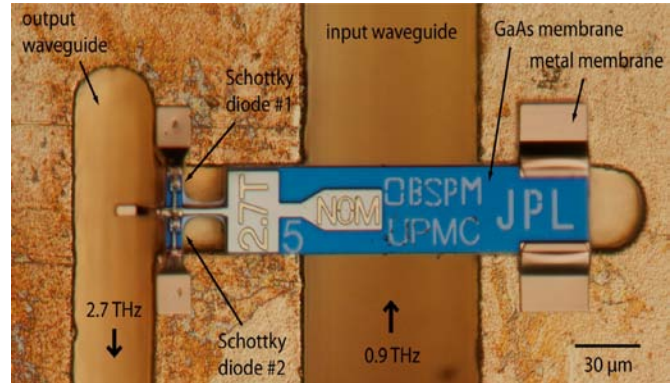


Fig. 4: Close-up of the last stage tripler circuit. This chip design is based on a balanced tripler configuration successfully used in the THz range.

guide coupling that shields the THz signal from any lower-frequency parasitic radiation. The WR10 input waveguide is oversized for THz frequencies, so a small THz horn is used to radiate inside it and the beam is coupled to the sensor with little reflection. Cross-comparison with Thomas Keating power meters has shown good agreement (within 1 dB or less) between the two sensors at 1 THz.

A 2.5 cm-long circular to WR10-rectangular waveguide transition was attached to the feed-horn using a standard UG387 flange. We found that the circular-to-rectangular waveguide transition did slightly improve the matching of the output beam of the 2.7 THz tripler to the sensor (our power head did not have an integrated waveguide extension like in the current series of PM4 power meters, so a piece of WR10 waveguide was needed to connect the power head to the frequency multiplier.) The multiplier chain and the VDI-Erickson power meter were placed in a vacuum chamber that was purged and then filled with pure nitrogen gas at a pressure of 0.80 bar. The powers were first recorded by the

PM4 power meter set on the 2 mW scale and a calibration

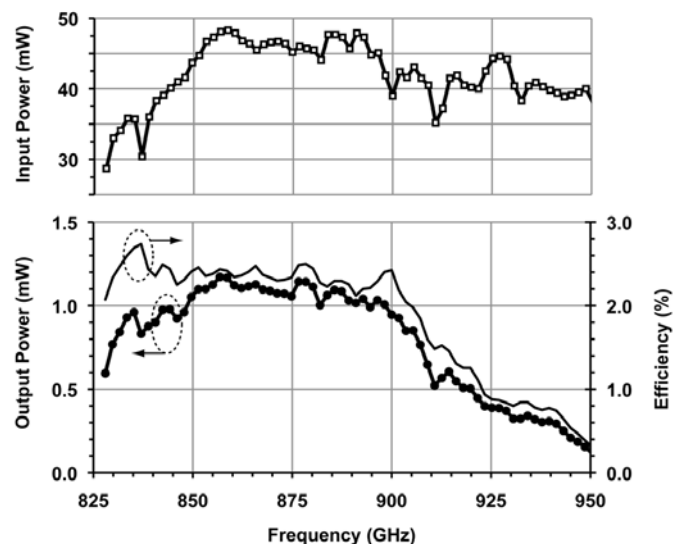


Figure 5: Performance of the first two multipliers is shown in this figure. The top plot shows the output power from the quad-chip 300 GHz tripler while the bottom plot shows the output from the dual-chip 900 GHz tripler.

factor of 100%, and later corrected by a factor of 1.15 (0.6 dB) to take into account the RF losses of the 2.5 cm long internal WR10 waveguide and of the circular to rectangular waveguide transition [per PM4 Instructional Manual].



Figure 6: Performance of the LO chain at room temperature. Measured power under ambient conditions shows loss due to water absorption. In a nitrogen environment, a peak power of 14 microwatts at 2580 GHz has been measured. This is a record for a solid-state tunable room-temperature source at this frequency.

### B. Frequency Sweep

The bias voltages of the 300 GHz and 900 GHz frequency triplers were found to be almost constant across the 2480-2750 band, and needed very little adjustment. The bias voltage applied to the 300 GHz stage was thus left constant at -12 V in all of the data presented in this paper. The voltage applied to the 900 GHz stage was set to -2 V for frequencies above 2540 GHz and between -1 V and -0.2 V for frequencies in the 2480-2540 GHz band. The input power at W-band was kept to a flat 350 mW for frequencies above 2530 GHz and was limited to 155-350 mW in the 2480-2530 GHz band due to the power roll-off of the W-band power amplifier module.

The complete chain was first characterized under ambient conditions. The measured output power is shown in Fig. 6. Even though the distance between the output horn of the chain and the waveguide of the power meter is less than 5 cm the strong water absorption line at 2640.4 GHz (strongest H<sub>2</sub>O line in this region of the electromagnetic spectrum) can considerably attenuate the output power. The chain was then placed inside a vacuum chamber with pure nitrogen. The power meter in this setup is also placed inside the vacuum chamber. Results obtained are also shown in Fig. 6.

This chain achieved an unprecedented output power level and bandwidth for an electronic source working in this frequency range at room temperature. Peak power of 14 microwatts at 2580 GHz has been measured. A number of chains have since been built with output powers in a similar range.

## IV. CONCLUSION

A compact, broadband and robust electronic source based on frequency multipliers covering the 2.5 to 2.7 THz range has

been presented. Output power from this source is sufficient to pump HEB mixers in this frequency range. The performance of the chain can be further improved upon cooling and optimizing each multiplier stage if desired. The system can be adapted for network analysis, time domain studies, coherent transmitters used in laboratory spectroscopy, or as local oscillators in remote sensing.

## ACKNOWLEDGMENT

We acknowledge technical discussions with Dr. Peter Siegel and Dr. John Pearson, and superb waveguide fabrication work by Peter Bruneau (all at JPL).

## REFERENCES

- [1] Seungwon Lee, Samuel Gulkis, Mark Hofstadter, Paul von Allmen, Jacques Crovisier, Nicolas Biver, and Dominique Bockelee-Morvan, "Submillimeter Spectroscopic Observations of Asteroid (21) Lutetia with MIRO Instrument on the ESA Rosetta Spacecraft, Geophysical Research Abstracts Vol. 13, EGU2011-5009-2, 2011 EGU General Assembly 2011.
- [2] T. de Graauw, N. Whyborn, E. Caux, T. Phillips, J. Stutzki, A. Tielens, R. Guesten, F. Helmich, W. Luinge, J. Martin-Pintado, J. Pearson, P. Planesas, P. Roelfsema, P. Saraceno, R. Schieder, K. Wildeman, and K. Wafelbakker, "The Herschel-heterodyne instrument for the far-infrared (HIFI)," EAS Pub. Series, vol. 34, pp. 3-20, 2009.
- [3] Paul Goldsmith, Herschel Oxygen Project Team, American Astronomical Society, AAS Meeting #217, #202.06; Bulletin of the American Astronomical Society, Vol. 43, 2011.
- [4] T. P. Walker, G. Steigman, H.-S. Kang, D. M Schramm, and K. A. Olive, "Primordial nucleosynthesis redux," ApJ, 376, 51-69, 1991.
- [5] A. Dalgarno, J. H. Black, and J. C. Weisheit, "Ortho-Para Transitions in H<sub>2</sub> and the Fractionation of HD," ApJ Letters, 14, 77, 1973.
- [6] F. Bertoldi, R. Timmermann, D. Rosenthal, S. Drapatz, and C. M. Wright, "Detection of HD in the Orion molecular outflow," A&A, 346, 267-277, 1999.
- [7] M. Micovic, A. Kurdoghlian, K. Shinohara, S. Burnham, I. Milosavljevic, M. Hu, A. Corrión, A. Fung, R. Lin, L. Samoska, P. Kangaslahti, B. Lambbrigtsen, P. Goldsmith, W. S. Wong, A. Schmitz, P. Hashimoto, P. J. Willadsen, and D. H. Chow, "W-Band GaN MMIC with 842 mW output power at 88 GHz," IEEE MTT-S Microwave Symposium Digest, pp. 237-239, 2010.
- [8] C. Lee, J. Ward, R. Lin, E. Schlecht, G. Chattopadhyay, J. Gill, B. Thomas, A. Maestrini, I. Mehdi, and P. Siegel, "A wafer-level diamond bonding process to improve power handling capability of submillimeter-wave Schottky diode Frequency Multipliers," IEEE MTT-S Microwave Symposium Digest, pp. 957-960, 2009.
- [9] J. V. Siles, A. Maestrini, B. Alderman, S. Davies, H. Wang, J. Treuttel, E. Leclerc, T. Närhi and C. Goldstein, "A single-waveguide in-phase power-combined frequency doubler at 190 GHz," IEEE Microwave and Wireless Components Letters, Vol.21, No. 6, pp. 332-334, Jun 2011.
- [10] A. Maestrini, J. Ward, G. Chattopadhyay, E. Schlecht, J. Gill, C. Lee, H. Javadi, and I. Mehdi, "In-phase power combining of submillimeter-wave multipliers," Proceedings of the 33<sup>rd</sup> International Conference on Infrared, Millimeter and Terahertz Waves, 2008.
- [11] A. Maestrini, J. Ward, J. Gill, H. Javadi, E. Schlecht, C. Tripon-Canseliet, G. Chattopadhyay and I. Mehdi, "A 540-640 GHz High Efficiency Four Anode Frequency Tripler," IEEE Trans. Microwave Theory Tech, Vol. 53, pp. 2835 - 284, September 2005.
- [12] A. Maestrini, J.S. Ward, J.J. Gill, C. Lee, B. Thomas, R.H. Lin, G. Chattopadhyay, and Imran Mehdi, "A Frequency-Multiplied Source with more than 1 mW of Power across the 840-900 GHz Band," IEEE-MTT Special Issue on "THz Technology: Bridging the Microwave-to-Photonics Gap", Vol. 58, no. 7, pp. 1925-1932, July 2010.

# Development of Lumped Element Kinetic Inductance Detectors for NIKA

M. Roesch, A. Benoit, A. Bideaud, N. Boudou, M. Calvo, A. Cruciani, S. Doyle, H.G. Leduc, A. Monfardini, L. Swenson, S. Leclercq, P. Mauskopf and K.F. Schuster for the NIKA collaboration

**Abstract**— Lumped-element kinetic inductance detectors (LEKIDs) have recently shown considerable promise as direct-absorption mm-wavelength detectors for astronomical applications. One major research thrust within the Néel Iram Kids Array (NIKA) collaboration has been to investigate the suitability of these detectors for deployment at the 30-meter IRAM telescope located on Pico Veleta in Spain.

Compared to microwave kinetic inductance detectors (MKID), using quarter wavelength resonators, the resonant circuit of a LEKID consists of a discrete inductance and capacitance coupled to a feedline. A high and constant current density distribution in the inductive part of these resonators makes them very sensitive. Due to only one metal layer on a silicon substrate, the fabrication is relatively easy.

In order to optimize the LEKIDs for this application, we have recently probed a wide variety of individual resonator and array parameters through simulation and physical testing. This included determining the optimal feed-line coupling, pixel geometry, resonator distribution within an array (in order to minimize pixel cross-talk), and resonator frequency spacing. Based on these results, a 144-pixel Aluminum array was fabricated and tested in a dilution fridge with optical access, yielding an average optical NEP of  $\sim 2 \times 10^{-16}$  W/Hz<sup>1/2</sup> (best pixels showed NEP =  $6 \times 10^{-17}$  W/Hz<sup>1/2</sup> under 4-8 pW loading per pixel). In October 2010 the second prototype (NIKA2) of LEKIDs has been tested at the IRAM 30 m telescope. A new LEKID geometry for 2 polarizations will be presented. Also first optical measurements of a titanium nitride array will be discussed.

**Index Terms**—superconducting resonators, kinetic inductance.

## I. INTRODUCTION

IN 2003, the use of the kinetic inductance effect [1] was considered for the first time as a detector application for

M. Roesch, S. Leclercq and K.F. Schuster are with IRAM (Institut de Radioastronomie Millimétrique), St. Martin d'Herès, France (e-mail: [roesch@iram.fr](mailto:roesch@iram.fr), [leclercq@iram.fr](mailto:leclercq@iram.fr), [schuster@iram.fr](mailto:schuster@iram.fr)).

A. Benoit, A. Bideaud, N. Boudou, M. Calvo and A. Monfardini are with the Institut NEEL, Grenoble, France (e-mail: [alain.benoit@grenoble.cnrs.fr](mailto:alain.benoit@grenoble.cnrs.fr), [aurelien.bideaud@grenoble.cnrs.fr](mailto:aurelien.bideaud@grenoble.cnrs.fr), [nicolas.boudou@grenoble.cnrs.fr](mailto:nicolas.boudou@grenoble.cnrs.fr), [martino.calvo@grenoble.cnrs.fr](mailto:martino.calvo@grenoble.cnrs.fr), [alessandro.monfardini@grenoble.cnrs.fr](mailto:alessandro.monfardini@grenoble.cnrs.fr)).

L. Swenson was with the Institut NEEL, Grenoble France. He is now with Caltech, Pasadena, CA, USA (e-mail: [swenson@astro.caltech.edu](mailto:swenson@astro.caltech.edu)).

A. Cruciani is with the Dipartimento di Fisica Università di Roma, Rom, Italy (e-mail: [angelo.cruciani@grenoble.cnrs.fr](mailto:angelo.cruciani@grenoble.cnrs.fr)).

S. Doyle and P. Mauskopf are with the Cardiff School of Physics and Astronomy, Cardiff University, Cardiff, UK (e-mail: [simon.doyle@astro.cf.ac.uk](mailto:simon.doyle@astro.cf.ac.uk), [philip.mauskopf@astro.cf.ac.uk](mailto:philip.mauskopf@astro.cf.ac.uk)).

H. G. Leduc is with the Jet Propulsion Laboratory, California Institute of Technology, Pasadena, CA 91109 (e-mail: [Henry.G.Leduc@jpl.nasa.gov](mailto:Henry.G.Leduc@jpl.nasa.gov)).

mm and sub-mm astronomy [2]. Photons, with energy higher than the gap energy ( $E = \hbar \cdot \nu > 2\Delta$ ), break Cooper pairs in a superconducting film. This leads to an increase in number of quasi particles, which changes the surface reactance (kinetic inductance) of the superconductor (kinetic inductance effect).

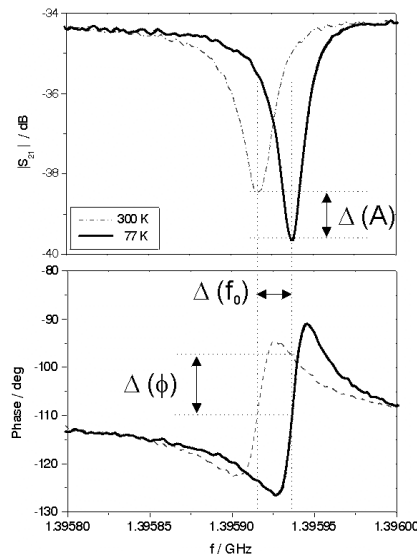


Fig. 1. Principle of KIDs. Solid lines: under dark conditions; dashed line: optical load of 300 K.

One possibility to make advantage of this effect is to use a superconducting resonant circuit as detecting element. A measurement of such a resonator coupled to a transmission line is shown in Fig. 1. An illumination of the detector leads to a shift in resonance frequency  $f_0$ , which can be measured in a change in amplitude and phase. One advantage of KIDs is the relative easy fabrication process. Due to only one metallization layer on a substrate, it is less complicated compared to bolometer fabrication. Another advantage of KIDs represents the readout system. Frequency multiplexing allows the readout of a large number of resonators. Packed in a limited bandwidth, a single transmission line is sufficient to read out several hundreds of pixel [3,4].

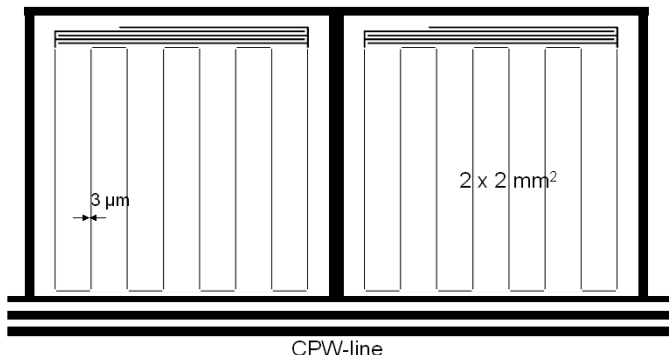


Fig. 2. Schematic of 2 LEKIDs. The resonators are coupled to a cpw-line. The line width is  $3 \mu\text{m}$  and the pixel size is around  $2 \times 2 \text{ mm}^2$ .

In Fig 2, one resonator design, a so-called lumped element kinetic inductance detector (LEKID) is shown. This type of resonator was first proposed as alternative to the quarter wavelength resonators in 2007 [5]. Compared to quarter wavelength resonators [6], this type consists of a long meandered line, the inductive part, and an interdigital capacitor. A very high and constant current density over the whole length of the meander makes this part a very sensitive direct detection area. The optical efficiency can be optimised by changing the grid of the meander geometry. Therefore, there are no lenses or antenna structures necessary to couple the incoming microwaves into the resonator. The resonators are surrounded a ground plane to reduce the cross talk between the pixels.

The NEEL IRAM KIDs array (NIKA) is a collaboration of several groups to develop a multi pixel camera based on kinetic inductance detectors for the IRAM 30m telescope located in Spain. NIKA saw first light in October 2009 [7]. A second test run with a dual band optic took place in October 2010 [8]. Here we present the development of a LEKID array for NIKA. Measurement results of electrical and optical characterization are demonstrated in this paper.

## II. LAB MEASUREMENTS

### A. Electrical and optical characterization

We recently tested LEKID arrays with 132 pixels (see Fig. 3). The used aluminum is deposited via magnetron dc sputtering on high resistivity silicon substrate. The thickness of the aluminum is 20 nm. The arrays have been characterized electrically and optically. The arrays are measured in an H3H4-dilution cryostat with optical window. The base temperature is 80 mK. In the cryostat several filters are mounted to provide the frequency bandwidth of the 2 and 1.3 mm band. A polarizer at the 80 mK stage allows the measurement of 2 arrays at the same time, one for the 2 mm and a second for the 1.3 mm band. With this configuration the pixels respond to only one polarization of the signal, which means that the response of the detector is smaller. In Fig. 4 a VNA scan of the scattering parameter S21 of a 132-pixel aluminum array is shown. One of the problems is still the cross-talk between the pixels. There are lots of double

resonances and a non-homogenous distribution which is caused mainly by the cross-talk. The variations in attenuation along the scan are due to standing waves along the feedline and the gain of the cold amplifier. The intrinsic quality factor  $Q_0$  was measured to be around 100 000 under an optical load of 300 K.

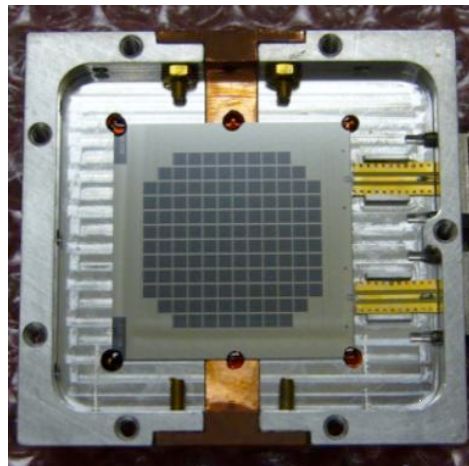


Fig. 3. Picture of a mounted 132-pixel aluminum array for the 2 mm band of NIKA.

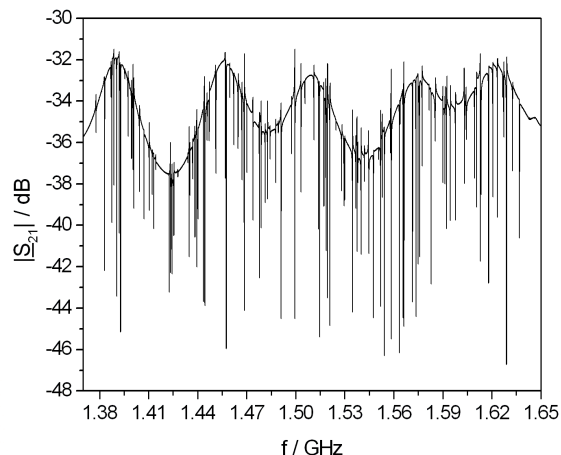


Fig. 4. VNA scan of the transmission scattering parameter S21 of the 132-pixel aluminum array at 100 mK.

To characterize the LEKIDs optically, a so-called sky simulator built at the Institute NEEL is used [9]. A picture of the simulator is shown in Fig. 5a. It is a pulse tube cryostat with a 24 cm absorber cold plate in it. The absorber can be cooled down to 50 K, which correspond almost to the background we have at the telescope. The simulator is equipped with a resistance to heat the cold plate. In Fig 5b the whole setup is shown. We use a high  $\epsilon$  ball that is mounted on a XY-arm in front of the sky simulator. This setup allows simulating on the fly measurements as they are done at the telescope.

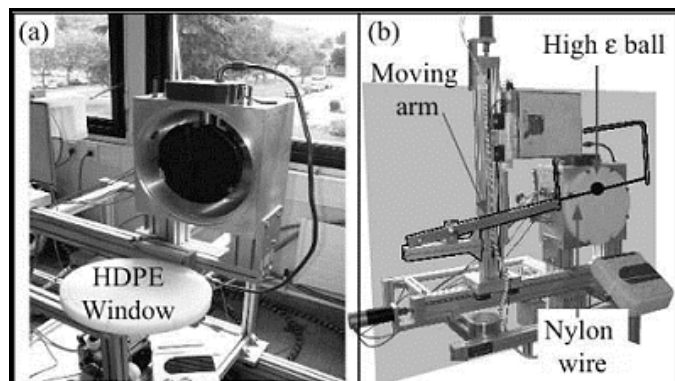


Fig. 5. Picture of the sky simulator used for the measurements in the lab. a) open pulse tube cryostat with view to the 24 cm absorber cold plate; b) complete system with high  $\epsilon$  ball for planet simulation.

The second telescope run of NIKA took place in October 2010. More information on the telescope run can be seen in [8]. The noise spectrum shown in Fig. 6 was taken at the telescope under excellent sky conditions. The spectrum is very flat ( $\sim f^{-0.15}$ ). The noise increases below 0.2 Hz due to sky fluctuations. The sensitivity was calculated giving an average  $NEP = 2.3 \cdot 10^{-16}$  W/ $\sqrt{\text{Hz}}$  @ 1 Hz per pix and a NEFD = 37 mJy/s per beam for the LEKIDs at 2 mm. For some best pixels a NEP of  $6 \cdot 10^{-17}$  W/ $\sqrt{\text{Hz}}$  @ 1 Hz per pix was calculated. Remember that all the tests have been done with a polarizer that decreases the signal by a factor of 2.

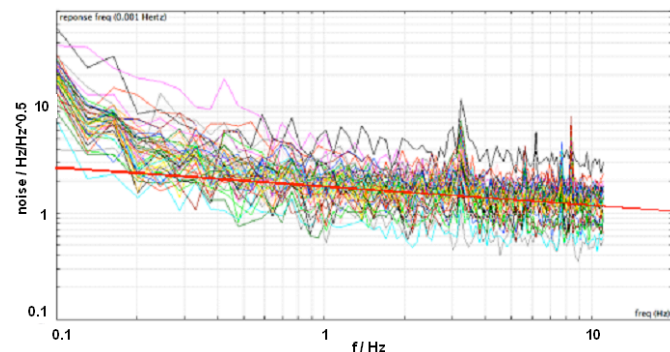


Fig. 6. Noise spectrum taken at the IRAM 30 m telescope with LEKIDs at 2mm.

### B. Optical absorption

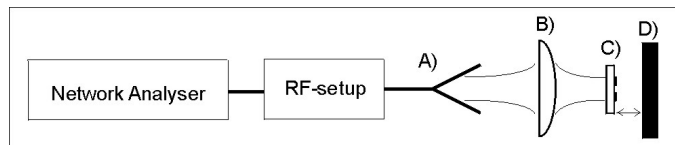


Fig. 7. Schematic of the setup for the measurement of the optical absorption of LEKIDs at room temperature. A) corrugated feed horn, B) corrugated lens, C) sample, D) back-short cavity.

To optimize the optical coupling of the LEKID structure we did room temperature measurements with the setup shown in Fig. 7. It consists of a network analyzer, an rf-setup to provide the frequency band of 120 to 180 GHz, a feed horn, a corrugated lens and the sample with its back-short. This reflection measurement setup allows tests at room temperature, which saves much time compared to cryogenic

measurements. The resistivity of the aluminum was adapted to room temperature by changing the thickness by the residual resistance ration (RRR) to measure under the same conditions.

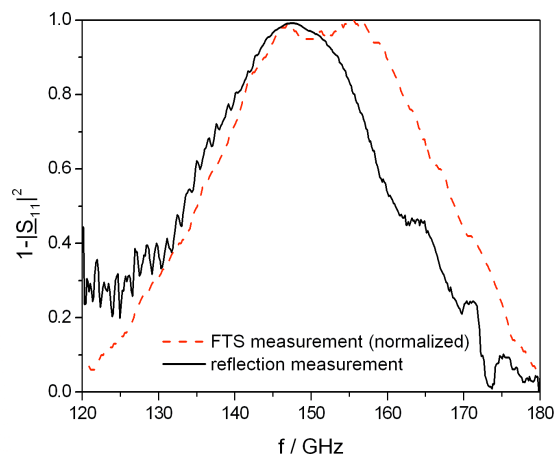


Fig. 8. Comparison of the reflections measurement results (solid black line) and FTS measurement with a Martin-Puplet interferometer (dashed red line).

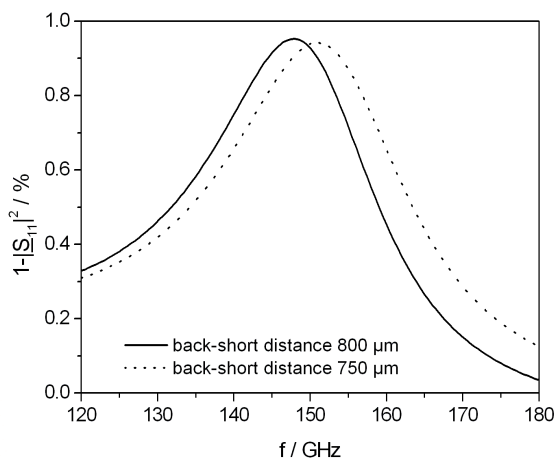


Fig. 9. Simulation of the back-short dependence of two identical structures. Solid line: back-short of 800  $\mu\text{m}$ ; dotted line: back-short of 750  $\mu\text{m}$ .

Fig. 8 shows the results of the reflection measurements of a 132-pixel aluminum array (see Fig. 3). The thickness of the aluminum is 90 nm and the back-short distance is 800  $\mu\text{m}$ . The absorbed frequency band is well centered at 150 GHz with a 3dB band of around 30 GHz. For comparison a second measurement, done with a Martin-Puplet interferometer at low temperatures has been done. The result is also shown in Fig. 8. The two measurements show a good agreement. The frequency band of the Martin-Puplet measurements is slightly shifted to higher frequency. The explanation for that is a smaller back-short distance of 750  $\mu\text{m}$ . This smaller back-short was found by simulation and the room temperature measurements to guarantee an optimal absorption. To demonstrate the back-short dependence of the absorption, simulations have been done with a transmission line model. The result of two simulations for identical structures but different back-short is shown in Fig. 9. The results show that

the characterization of the optical coupling at room temperature is a feasible alternative to the time intensive cold measurements. More information about the absorption measurements at room temperature and the transmission line model for these structures will be published elsewhere [10].

### III. LEKID-GEOMETRY FOR 2 POLARIZATIONS

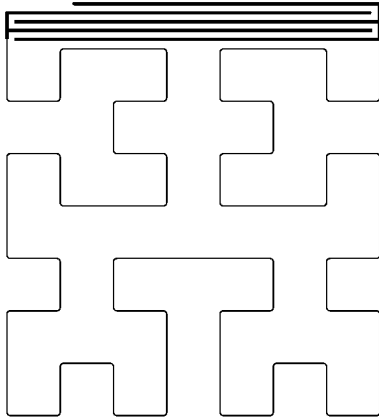


Fig. 10. The picture shows a design for a LEKID that is sensitive to 2 polarizations. The Structure is a Hilbert curve of the 3<sup>rd</sup> order.

In the next setup of the NIKA cryostat, the polarizer is replaced by a dichroic. This allows the use of pixels that are sensitive to 2 polarizations, which increases the optical response of the detector. For this application a symmetric design with a constant filling factor over the whole direct detection area is needed to guarantee the same absorption for the 2 polarizations. One possible design is shown in Fig. 9. It is a so-called Hilbert fractal curve of the 3<sup>rd</sup> order. This geometry is a well-known for patch antennas [11]. However for the LEKID application we use the geometry as a direct absorption area. In this case the antenna behavior is less important. It is a geometry that fulfills the conditions for the 2-polarization detection mentioned above [12].

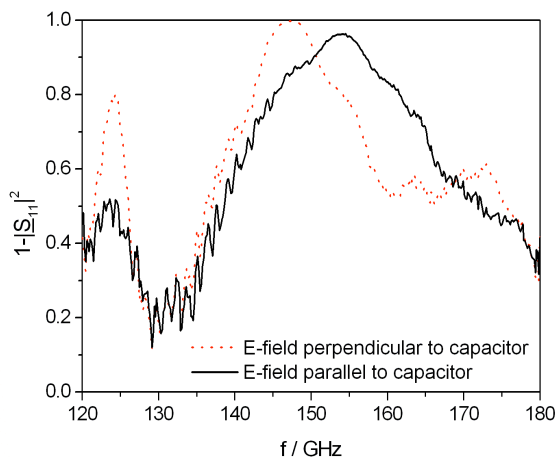


Fig. 11. The plot shows the absorption in the two polarizations of the geometry shown in Fig. 9. The measurements have been done with at room temperature with the setup shown above.

In Fig. 11 the reflection measurement results for the Hilbert geometry is shown. A back-short distance of 700  $\mu\text{m}$  was

found to guarantee an optimal optical absorption. The results show an almost identical absorption for the 2 polarizations. Around 150 GHz a maximum absorption of almost 100 % was measured.

After the room temperature measurements we mounted a 132-pixel array into the cryostat to characterize the detectors under real observing conditions. The results of the sensitivity of the 2-polarization sample are shown in Fig. 12. Three optical measurements have been done. The first one was done without polarizer in front of the cryostat (black squares). The second one has been done with a polarizer in front of the cryostat with a vertical orientation (blue triangles). For the third one, the polarizer was mounted with a horizontal orientation (red stars). The results show clearly almost the same sensitivity for both polarizations. Assuming that the noise is the same for both polarizations, the responses are almost identical. The better NET without the polarizer is due to the same noise level but a much higher response. The green line in Fig. 11 indicates the average value of the NET for all the pixels of the sample. It was calculated to be around 2.5  $\text{mK}/\text{Hz}^{0.5}$  @ 1 Hz per beam. Some best pixels even have shown a NET = 0.8  $\text{mK}/\text{Hz}^{0.5}$  @ 1 Hz per beam.

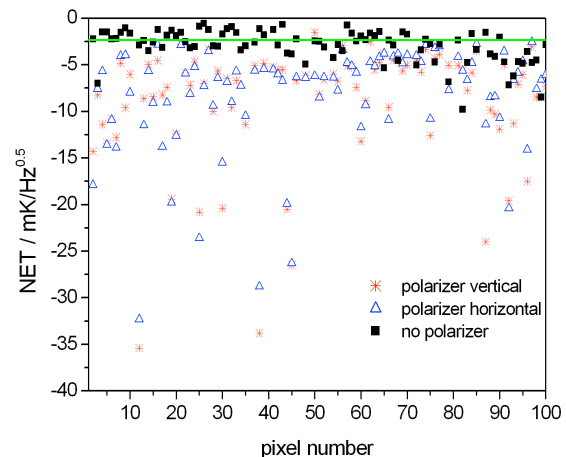


Fig. 12. Sensitivity measurement for a 132-pixel array sensitive to 2 polarizations. The measurements have been done with and without a polarizer in front of the cryostat. Black squares: no polarizer; blue triangles: polarizer horizontal; red stars: polarizer vertical.

### IV. TITANIUM NITRIDE LEKIDS

In 2010, titanium nitride was proposed as promising new material for KIDs [13]. The kinetic inductance is higher compared to aluminum, which increases the response of the detector. Moreover, the normal resistivity is higher, allowing thicker films and larger lines, which decreases problems due to lithography. We designed a mask, adapted to the much higher resistivity and kinetic inductance, for a 132-pixel TiN array for 1.3 mm. The TiN was deposited via sputtering at JPL by H. G. Leduc on a 350  $\mu\text{m}$  thick silicon substrate. The film thickness is about 70 nm with a square resistance of around 30 ohms per square. The Tc was measured to be around 1.25 K. We mounted the array in the cryostat and measured it under different optical loads at 80 mK. The array was mounted at the



2mm band instead of the 1.3 mm band. The results of these measurements are shown in Fig. 13 for one resonator.

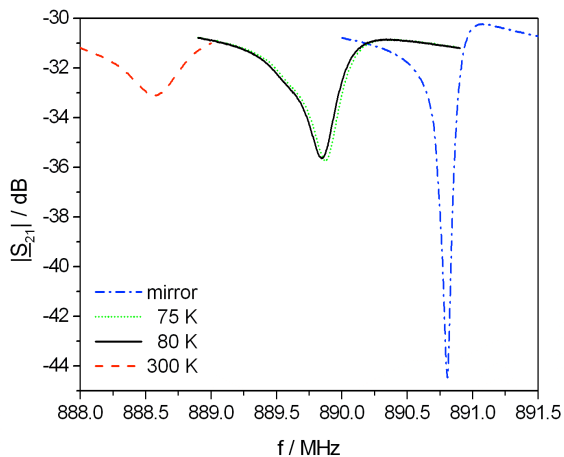


Fig. 13. Response of a TiN LEKID resonator to different optical loads. Dashed red line: 300 K; solid black line: 80 K; dotted green line: 75 K; dashed dotted blue line: mirror in front of cryostat (cryostat closed).

The shift in frequency, comparing a closed cryostat and a 300 K load, is around 2 MHz. The response of the TiN LEKIDs is around a factor of 10 higher compared to the usual aluminum arrays (200 KHz). Using the sky simulator we measured a shift in frequency of 30 kHz between 75 and 80 K background loading (see Fig. 12). The problem with this big response is that the resonances are almost destroyed under a 300 K load. Also the resonances have been found at lower frequencies than expected (700-900MHz). The cold amplifier we have used is optimized for the 1.2 – 1.8 GHz band. From the amplifier specifications, the noise is 4 to 5 times higher when at 900 MHz, and even worse below. There is thus room for improving just by using an amplifier designed for lower frequencies. In order to study the sensitivity under smaller loading, we have reduced the optical load from around 6 pW to 0.1 pW by applying a diaphragm to the pupil. A first estimation gives NEPs per pixel better than  $5 \cdot 10^{-17}$  W/ $\sqrt{\text{Hz}}$  @ 1 Hz. This is already an encouraging result for a first test with TiN, that will surely improve considering that we are sensitive to only one polarization with the meandered geometry, and we are well out of the amplifier bandwidth.

## V. CONCLUSION

We demonstrated in this paper the high potential of lumped element kinetic inductance detectors as mm-wave detectors, in particular at 2 mm wavelength. The results of the two telescope runs show that we are competitive now to existing bolometer arrays. The good agreement between the observations at the telescope and the measurements done with the lab setup, validates the used sky simulator. The new NIKA cryostat setup with a dichroic filter allows now measuring the optical response of pixels that are sensitive to two polarizations. Some best pixels of the presented design in this paper show a sensitivity of  $\text{NET} = 0.8 \text{ mK}/\sqrt{\text{Hz}} @ 1 \text{ Hz}$  per beam. This is the best result achieved with kinetic inductance

detectors, in particular for LEKIDs, at 2 mm so far. The first measurements with titanium nitride resonators show very promising results regarding the sensitivity of the pixels. Future work will address remaining issues such as pixel cross talk. We are also investigating in aluminum and TiN arrays for 1mm. First samples have been measured but the sensitivity is not satisfactory yet.

Currently we are able to readout 112 pixels in a 230 MHz bandwidth. We are currently working on readout electronics that will allow the readout of more pixels in a larger bandwidth.

A third telescope run at the IRAM 30m is foreseen for September 2011.

## ACKNOWLEDGMENT

This work was supported in part by the French National Research Agency Grant No. ANR-09-JCJC-0021-01.

Part of this work was supported by the Keck Institute for Space Studies (KISS).

## REFERENCES

- [1] M. Tinkham, Introduction to Superconductivity, Krieger Pub Co, 1975.
- [2] P.K. Day, H.G. LeDuc, B.A. Mazin, A. Vayonakis and J. Zmuidzinas, "A broadband superconducting detector suitable for use in large arrays," *Nature*, 425, 817, 2003.
- [3] L.J. Swenson, J. Minet, G.J. Grabovskij, et al., in AIP Proc., 2009, paper 1185, p. 84.
- [4] S.J.C. Yates, J.J.A. Baselmans, A.M. Baryshev, et al., in AIP Proc., 2009, paper 1185, p. 249.
- [5] S. Doyle, "Lumped Element Kinetic Inductance Detectors," thesis, Cardiff University, Cardiff, Wales, April. 2008.
- [6] B.A. Mazin, "Microwave Kinetic Inductance Detectors," thesis, California Institute of Technology, Pasadena, California, USA, 2004.
- [7] A. Monfardini, et al. NIKA: A Millimeter-Wave Kinetic Inductance Camera, *Astronomy & Astrophysics*, 521, A29, 2010.
- [8] A. Monfardini et al., A dual-band millimeter-wave kinetic inductance camera for the IRAM 30m telescope, *ApJS*, Volume 194, Issue 2, article id. 24 (2011)
- [9] A. Bideaud, dissertation, 2010 (in French).
- [10] M. Roesch et al, "Optimisation of the direct detection area of LEKIDs for NIKA", in preparation
- [11] K.J. Vinoy, K. A. Jose, V. K. Varadan and V.V. Varadan, "Hilbert curve fractal antenna: A small antenna for VHF/UHF applications", *Microwave Opt Technol Lett* 29 (2001), 215-219.
- [12] M. Roesch et al., "New LEKID design for two polarizations", in preparation.
- [13] H. G. Leduc, et al., "Titanium nitride films for ultrasensitive microresonator detectors", *Appl. Phys. Lett.* 97, (2010)

# The SPICA-SAFARI Detector System: TES Detector Arrays with Frequency Division Multiplexed SQUID Readout

B. D. Jackson, P. A. J. de Korte, J. van der Kuur, P. D. Mauskopf, J. Beyer, M. P. Bruijn, A. Cros, J.-R. Gao, D. Griffin, R. den Hartog, M. Kiviranta, G. de Lange, B.-J. van Leeuwen, C. Macculi, L. Ravera, N. Trappe, H. van Weers, and S. Withington

**Abstract**—The SAFARI instrument is a far-infrared imaging Fourier transform spectrometer for JAXA’s SPICA mission. Taking advantage of the low emission of SPICA’s 5 K telescope, SAFARI will provide background-limited, Nyquist-sampled spectroscopic imaging of a 2’x2’ field-of-view over 34-210  $\mu\text{m}$ , revolutionizing far-infrared astronomy.

SAFARI’s aggressive science goals drive the development of a unique detector system combining large-format Transition Edge Sensor arrays and frequency division multiplexed SQUID readout with a high 160x multiplexing factor. The detectors and their cold readout electronics are packaged into 3 focal plane arrays that will be integrated into SAFARI’s focal plane unit.

This paper presents the preliminary design concept for the SAFARI detector system.

**Index Terms**— Astrophysics, Bolometers, Frequency division multiplexing, Superconducting devices, System-level design

Manuscript received July 29, 2011. This work was supported in part by the European Space Agency under ESA TRP contracts number 22559/09/NL/CP and 22559/09/NL/CP.

B.D. Jackson and G. de Lange are with the SRON Netherlands Institute for Space Research, Landleven 12, 9747 AD, Groningen, The Netherlands. (corresponding author, phone: +31-50-363-4074, fax: +31-50-363-4033, e-mail: B.D.Jackson@sron.nl).

P.A.J. de Korte, J. van der Kuur, M.P. Bruijn, J.-R. Gao, R. den Hartog, B.-J. van Leeuwen, and H. van Weers are with SRON Netherlands Institute for Space Research, Sorbonnelaan 2, 3584 CA, Utrecht, The Netherlands.

P.D. Mauskopf is with the Dept. of Physics and Astronomy, University of Cardiff, 5, The Parade, P.O. Box 913, Cardiff, CF24 3YB, UK.

J. Beyer is with the Physikalisch-Technische Bundesanstalt (PTB), Abbestrasse 2-12, D-10587 Berlin, Germany.

A. Cros and L. Ravera are with the Universite de Toulouse (UPS-OMP), Institut de Recherche en Astrophysique et Planétologie and CNRS, UMR 5277, 9, Av. colonel Roche, BP 44346, F 31028 Toulouse Cedex 4, France.

J.-R. Gao is with the Kavli Institute of Nanoscience, Faculty of Applied Sciences, Delft University of Technology, Lorentzweg 1, 2628 CJ Delft, The Netherlands.

D. Griffin is with the Space Science and Technology Department, Rutherford Appleton Laboratory, Chilton, Didcot, Oxon, UK.

M. Kiviranta is with VTT, The Technical Research Centre of Finland, Tietotie 3, 02150 Espoo, Finland.

C. Macculi is with the Istituto di Astrofisica Spaziale e Fisica Cosmica, INAF, Roma, Italy.

N. Trappe is with the Experimental Physics Department, National University of Ireland, Maynooth, Co Kildare, Ireland.

S. Withington is with the Cavendish Laboratory, University of Cambridge, JJ Thomson Avenue, Cambridge, CB3 0HE, UK.

## I. INTRODUCTION

Far-infrared (far-IR) observations are critical to answering some of the most fundamental questions in astronomy:

- What is the universe made of and how does it evolve?
- Are we alone in the universe?
- How do galaxies, stars and planets form and evolve?

However, far-IR observations also face major challenges. To start with, the atmosphere is virtually opaque in the far-IR, requiring space or stratospheric observatories. Developing these observatories is further complicated by two factors: 1) diffraction requires large telescopes at long wavelengths; and 2) thermal emission from all but deep cryogenic telescopes is orders of magnitude brighter than the far-IR signals of interest.

To-date, space observatories have addressed one or the other of these challenges, but not both. Small ( $< 1$  m) cryogenic telescopes like ISO [1] and Spitzer [2] provided high sensitivities but limited spatial resolution. In contrast, while ESA’s Herschel Space Observatory is revolutionizing far-IR astronomy with its 3.5-m telescope [3], its passively cooled 80-K telescope’s thermal emission is  $\sim 10^6$  times brighter than the far-IR sky background.

The Japanese Space Agency’s proposed SPICA mission will be the first to address both of these challenges by actively cooling a large (3.25-m) telescope to below 6 K to enable sky-background-limited observations at 4-210  $\mu\text{m}$  [4]. In doing so, SPICA offers the potential for orders of magnitude higher sensitivity than is achieved in Herschel.

When considering SPICA’s potential sensitivity improvements versus the Herschel photometers, it is noted that SPIRE [5,6] and PACS’ 160  $\mu\text{m}$  channel [7] are confusion-limited – deeper integrations will not detect weaker sources because they will not be resolved by the telescope. However, because PACS’ 110 and 70  $\mu\text{m}$  channels are not confusion-limited, SPICA’s higher sensitivity will increase mapping speeds and enable larger-area surveys. This being said, the real far-IR niche for SPICA is in spectroscopy, as the PACS spectrometer is sensitivity-limited – while it benefits from Herschel’s large telescope, it is limited to observations of relatively few and strong sources, and to narrow-band spectroscopic mapping. Thus, while Herschel’s photometric maps reveal not-before-seen structure in the interstellar

TABLE I  
KEY SAFARI PERFORMANCE REQUIREMENTS

Characteristic	Requirement
Wavelength range	34-210 $\mu\text{m}$
Instantaneous field of view	$2^\circ \times 2^\circ$
Angular resolution	Diffraction-limited above 40 $\mu\text{m}$
Spatial sampling	Per wavelength band, Nyquist-sampled at band-center <sup>a</sup>
Focal plane fill factor	80% (goal)
Spectral resolution	
- photometric imaging	R ~ 2-3
- low-resolution mode	R ~ 100 @ 100 $\mu\text{m}$
- medium-resolution mode	R ~ 2000 @ 100 $\mu\text{m}$
Sensitivity	
- photometric	< 50 $\mu\text{Jy}$ ( $5\sigma$ -1 hr) <sup>a</sup>
- spectral (med. res. mode)	< few $\times 10^{-19}$ W/m <sup>2</sup> ( $5\sigma$ -1 hr) <sup>a</sup>
Maximum signal level	0.5 Jy (10 Jy <sup>b</sup> for 34-57 $\mu\text{m}$ )

<sup>a</sup> This required spatial sampling may be achieved post-processing (i.e. with a dither mode).

<sup>b</sup> Instrument sensitivity may be degraded (eg. by the use of neutral density filters) for input signal levels greater than 0.5 Jy.

medium in our galaxy and resolve large numbers of extragalactic sources, the spectrometers only touch the tip of this iceberg. Being able to extend this mapping capability to spectroscopy will enable blind, wide-field spectroscopic surveys to characterize the chemistry and dynamics of many sources. This is the next far-IR revolution that SPICA will enable, and it is this goal that drives the design of SAFARI – the SPICA Far-Infrared Instrument.

This paper summarizes the preliminary design concept for the detector system at the heart of SAFARI.

## II. THE SAFARI INSTRUMENT CONCEPT

SAFARI is a far-IR imaging Fourier transform spectrometer (FTS) being developed by a consortium of European and Canadian institutes. An FTS concept similar to SPIRE [8] has been selected based on achievable detector sensitivities – an FTS in SPICA will reach background-limited sensitivities for detector Noise Equivalent Powers (NEPs) of  $\sim 2 \times 10^{-19}$  W/Hz<sup>1/2</sup>, which should be achievable within the available time (for detectors operating at 50 mK base temperature).

Table I summarizes key SAFARI instrument performance requirements. When combined with operational and calibration aspects of a fast-scan FTS instrument, these result in a unique and challenging set of detector requirements, as summarized in Table II. Beyond these performance requirements, the system is further defined by extremely tight constraints from the SAFARI instrument and SPICA spacecraft. SPICA's thermal budget is a particular detector system design driver, with  $\sim 3$  and 0.5 mW of dissipation allowed at 4.5 and 1.7 K, and only  $\sim 2.5$  mW of passive heat-load at 4.5 K from the detector system's cryo-harness.

## III. THE SAFARI DETECTOR SYSTEM

The SAFARI detector system includes three large-format detector arrays, detector control and readout electronics

TABLE II  
KEY SAFARI DETECTOR SYSTEM PERFORMANCE REQUIREMENTS

Characteristic	Requirement
Wavelength bands	34-60, 60-110, 110-210 $\mu\text{m}$ <sup>a</sup>
Number of pixels	61x61, 34x34, 18x18 <sup>a,b</sup>
Sensitivity	
- goal	$2 \times 10^{-19}$ W/Hz <sup>1/2</sup> <sup>b</sup>
- requirement	4.5, 3.6, $3.5 \times 10^{-19}$ W/Hz <sup>1/2</sup> <sup>a,b</sup>
Focal plane fill factor	80% (goal)
Coupling efficiency x fill factor	64% (goal)
Minimum system response speed	40, 28, 13 Hz <sup>a</sup>
Saturation power	$\sim 4$ fW <sup>a,b</sup>

<sup>a</sup> Where 3 values are given, these apply to the system's short, medium, and long wavelength bands, in that order.

<sup>b</sup> The NEP goals and requirements assume a Nyquist-sampled focal plane. For filled arrays with less-than-Nyquist sampling, NEP figures scale with pixel dimension and saturation powers with pixel area.

(including both room-temperature and cryogenic elements), and infrastructure that is required to package the ultra-sensitive electronics in SAFARI's Focal Plane Unit. These elements are divided over the following main units:

- 3 "Focal Plane Arrays" (FPAs), each containing one detector array, its multiplexed SQUID amplifier readout electronics, and shielding and filtering needed to operate these components within the SPICA environment;
- a 136 K Low-Noise Amplifier (LNA) that amplifies the weak outputs from the cryogenic electronics; and
- the Detector Control Unit (DCU) containing room-temperature control and readout electronics.

The development of this system is divided into three main focus areas that are addressed in the sections that follow:

- the detector arrays;
- multiplexed detector readout electronics; and
- the packaging and shielding for the detector arrays and their cold readout electronics in the focal plane arrays.

## IV. DETECTOR ARRAY CONCEPT

The SAFARI detectors combine superconducting Transition Edge Sensor (TES) thermometers with horn-coupled absorbers on SiN suspension structures to realize SAFARI's unique requirements for large-format arrays of small, fast detectors with low noise, high optical coupling efficiency, and moderate saturation power [9].

SiN-suspended TES detectors are used on many ground-based sub-mm and mm-wave telescopes [10-13]. However, SPICA's cryogenic telescope reduces the detectors' background load by orders of magnitude. This requires a revolutionary step in detector sensitivity, moving from typical NEPs of a few  $\times 10^{-17}$  W/Hz<sup>1/2</sup> for ground-based observatories to a goal of  $2 \times 10^{-19}$  W/Hz<sup>1/2</sup> for SAFARI. Achieving very-low detector NEP's requires extremely low-conductivity thermal suspensions, which can be realized with high aspect-ratio SiN membrane structures. For the nominal 850  $\mu\text{m}$  size of SAFARI's mid-wavelength band pixels, the classical diagonal

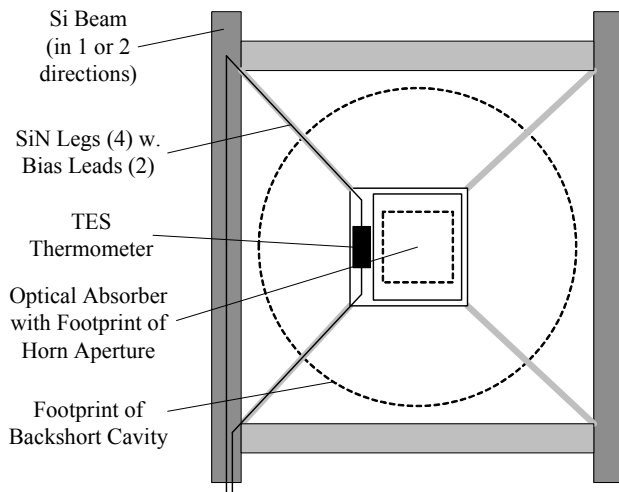


**Figure 1** - Schematic of a SiN-suspended, absorber-coupled TES bolometer pixel in classical “diagonal-leg” geometry. Low NEP devices require very low thermal conductivity of the SiN suspension. See Ref. [14] for alternative low-conductivity geometries.

leg suspension geometry (see Fig. 1) allows 450  $\mu\text{m}$  long SiN legs, which must be  $\sim 1 \mu\text{m}$  wide and 250 nm thick to reach the desired low conductivity.

The second critical requirement for the detector design is the optical absorption efficiency. The current design baseline combines an impedance-matched absorber in a non-resonant cavity with a multi-mode pyramidal horn that concentrates light into the cavity. This non-resonant design should offer high coupling efficiency over the nearly octave-wide bands in which the SAFARI detectors must operate.

TES detector arrays for SAFARI are being developed at SRON [14] and Cambridge [15], with both groups typically measuring detector sensitivities of  $NEP_d \sim 4\text{-}5 \times 10^{-19} \text{ W/Hz}^{1/2}$  for single pixels and small arrays of detectors with  $T_c \sim 100 \text{ mK}$  operating at  $\sim 50 \text{ mK}$ . This is within a factor of  $\sim 2$  of SAFARI’s goal sensitivities. Ref. 16 presents preliminary measurements of the optical coupling efficiency of these detectors. Coupling efficiencies of  $\sim 50\%$  are obtained, but with the horn-absorber-cavity geometry still to be optimized.

## V. MULTIPLEXED DETECTOR READOUT

A SQUID amplifier chain is used to read-out the weak analog signals from SAFARI’s low-impedance TES detectors, without degrading the detector noise. The gain that is required to bridge the long cables between the instrument’s focal plane unit and warm electronics will be realized using two SQUID amplifier stages inside the focal plane arrays [17], followed by a semi-conductor amplifier in the cable harness [18].

In order to minimize the complexity and heat-loads in the cryostat’s cable harness, multiplexing is used to connect many TES detectors to a single SQUID amplifier. For SAFARI, a frequency division multiplexing [19] concept is used in which each detector within a readout channel is biased by a different AC carrier frequency. After modulation by the optical signals,

the carriers are added to create a comb of amplitude-modulated signals that is coupled to a single SQUID amplifier.

The multiplexing ratio that can be realized by this scheme is limited by the dynamic range of the SQUID amplifier. However, this limitation can be overcome by applying negative feedback to suppress the signals at the input of the SQUID. Baseband feedback ensures a stable feedback loop despite the long cables between the warm and cold electronics. Based on past developments for IXO [20], an FDM system with a multiplexing factor of 160 is baselined for SAFARI.

## VI. THE FOCAL PLANE ARRAYS

The third major development item for the SAFARI detector system is the focal plane arrays that package and shield the ultra-sensitive detectors and cold electronics for each of the three wavelength bands. Critical elements are the mounting, shielding, and thermal isolation of the 50 mK electronics, plus the high-density electrical interconnects that couple the 1000’s of detector pixels to the LC filter and SQUID amplifier chips. Moreover, this functionality must be realized within the tight space and mass constraints of a flight instrument.

The FPA must protect the detectors and SQUID amplifiers from DC magnetic fields; high-frequency radiated E-fields (eg. from the downlink antennas); and straylight from the surrounding 4.5 K radiation environment. The requirements on this shielding are set by the  $\sim 1 \text{ aW}$  noise levels and  $\sim 4 \text{ fW}$  saturation powers of the TES detectors.

The detectors and first-stage SQUID amplifiers (at 50 mK) are isolated from the 1.7 K environment of the instrument’s cold optical box by a two-layer Kevlar suspension system that minimizes the load on the SAFARI cooler (which provides 1  $\mu\text{W}$  of heat-lift at 50 mK), while also surviving launch.

Fig. 2 shows a block diagram of the preliminary design concept for the SAFARI focal plane array.

## VII. CONCLUSION

The SAFARI detector system combines large-format TES arrays with frequency division multiplexed SQUID readout to realize low-noise operation of up to 6000 pixels in three wavelength bands covering 34-210  $\mu\text{m}$ . This system addresses the challenging performance requirements of a background-limited FTS spectrometer behind a cryogenic telescope, within SPICA’s tight resource constraints.

Absorber-coupled TES thermometers on SiN membrane suspensions already offer sensitivities within a factor of 2 of SAFARI’s goal sensitivity of  $NEP_{\text{elec}} = 2 \times 10^{-19} \text{ W/Hz}^{1/2}$ . Ongoing work aims to verify the detectors’ optical coupling and demonstrate the design’s scalability to large arrays.

Readout of 1000’s of TES detectors within SPICA’s interface constraints is a major challenge. A frequency division multiplexing system with baseband feedback is being developed for SAFARI to enable operation of 160 detectors per SQUID amplifier chain. The next step in this development is to integrate FDM readout with low-NEP TES bolometers in

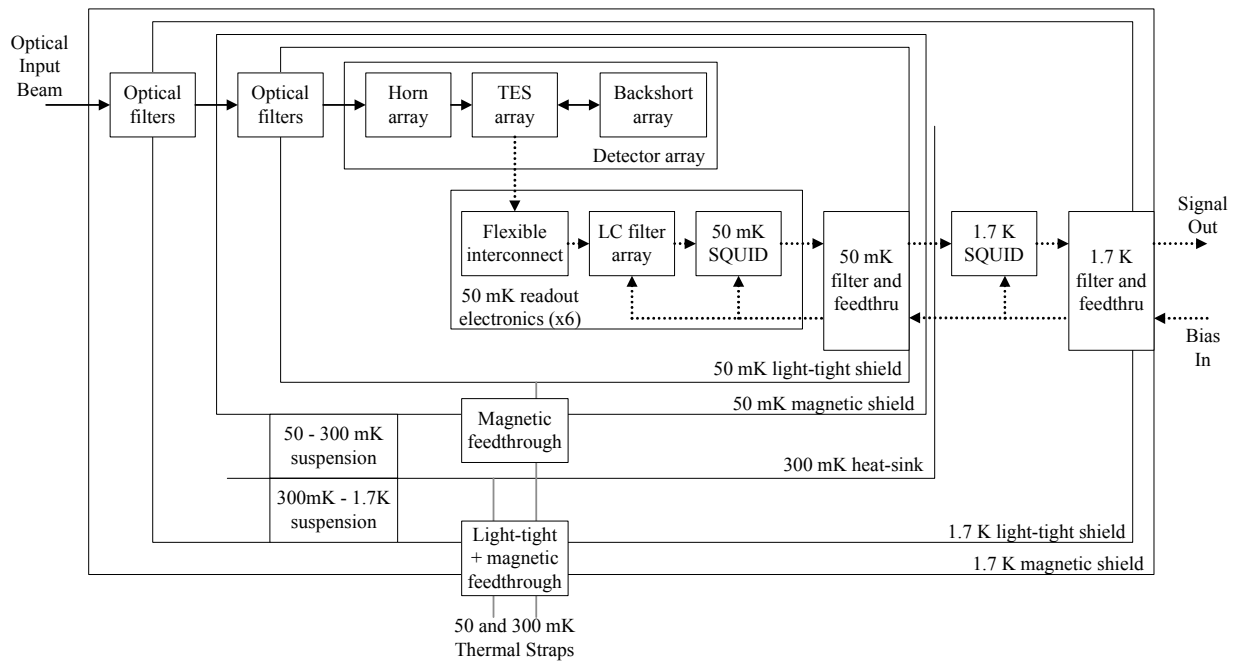


Figure 2 - SAFARI Focal Plane Array block diagram.

a 64-pixel experiment that confirms the system's scalability.

The third major challenge in this system is to package and shield the sensitive detectors and cold electronics within Focal Plane Arrays that isolate the 50 mK electronics from the 1.7 and 4.5 K environments of the SAFARI instrument and SPICA spacecraft. A preliminary concept has been developed and the next step is to demonstrate critical technologies such as the shielding and filtering needed to operate extremely low-noise detectors within a spacecraft environment.

#### ACKNOWLEDGMENT

The authors are only part of the international SAFARI detector system development team, which includes: D. Audley, D. Boersma, L. Ferrari, D. Glowacka, R. Hijmering, H. Hoevers, P. Khosropanah, P.P. Kooijman, D. van Loon, D. Morozov, A. Murphy, J.-H. Nieland, C. O'Sullivan, and M. Ridder. The authors also thank W. Jellema, B. Swinyard, S. Bandler, and J. Baselmans for inputs to the system design; and P. Ade and C. Tucker for filters for optical testing.

#### REFERENCES

- [1] M.F. Kessler, J.A. Steinz, M.E. Anderegg, *et al.*, "The Infrared Space Observatory (ISO) mission," *Astronomy & Astrophysics* 315, 27 (1996).
- [2] M. W. Werner, *et al.*, "The Spitzer Space Telescope Mission," *The Astrophysical Journal Supplement Series*, 154:1-9, Sept., 2004.
- [3] G. L. Pilbratt, *et al.*, "Herschel Space Observatory An ESA facility for far-infrared and submillimetre astronomy," *Astronomy & Astrophysics*, vols. 518 and 521 (2010).
- [4] B. Swinyard, T. Nakagawa, *et al.*, "The space infrared telescope for cosmology and astrophysics: SPICA A joint mission between JAXA and ESA," *Experimental Astronomy*, vol. 23, pp. 193-219 (2009).
- [5] M. J. Griffin, *et al.*, "The Herschel-SPIRE instrument and its in-flight performance," *Astronomy and Astrophysics*, vol. 518, L3 (2010).
- [6] H. T. Nguyen, *et al.*, "Hermes: The SPIRE confusion limit," *Astronomy & Astrophysics*, vol. 518, L5 (2010).
- [7] A. Poglitsch, *et al.*, "The Photodetector Array Camera and Spectrometer (PACS) on the Herschel Space Observatory," *Astronomy & Astrophysics*, vol. 518, L2 (2010).
- [8] B. M. Swinyard, *et al.*, "The FIRST-SPIRE spectrometer a novel imaging FTS for the sub-millimetre," in *Proc. SPIE Vol. 4013*, Munich, 27-31 March (2000).
- [9] P. D. Mauskopf, *et al.*, "A TES focal plane for SPICA-SAFARI," in *Proc. 21<sup>st</sup> Int. Symp. On Space THz Technology*, Oxford, UK, 23-25 March, 2010, pp. 246-255.
- [10] W. Holland, *et al.*, "SCUBA-2: a 10,000-pixel submillimeter camera for the James Clerk Maxwell Telescope," *SPIE Vol. 6275*, 62751E (2006).
- [11] J. Mehl, *et al.*, "TES bolometer array for the APEX-SZ camera," *J. Low Temp. Phys.*, vol. 151, pp. 697-702 (2008).
- [12] J. E. Ruhl, *et al.*, "The South Pole Telescope," in *Proc. SPIE Vol. 5498*:11 (2004).
- [13] J. G. Staguhn, *et al.*, "Instrument performance of GISMO, a 2 millimeter TES bolometer camera used at the IRAM 30 m Telescope," in *Proc. SPIE Vol. 7020*, 702004 (2008).
- [14] P. Khosropanah, *et al.*, "Low noise transition edge sensor (TES) for the SAFARI instrument on SPICA," *22<sup>nd</sup> Int. Symp. on Space THz Technology*, Tucson, AZ, USA, April 26-28, 2011.
- [15] D. J. Goldie, *et al.*, "Ultra-low-noise MoCu transition edge sensors for space applications," *J. App. Phys.*, vol. 109, 083105 (2011).
- [16] P. D. Mauskopf, *et al.*, "Optical characterization at 1.5-3 THz of high sensitivity TES detectors designed for future far-infrared space missions," *22<sup>nd</sup> Int. Symp. on Space THz Tech.*, Tucson, AZ, USA, April 2011; and D. Morozov, *et al.*, "Optical characterization of high sensitivity TES detectors designed for the SPICA/SAFARI 30-60 mm channel," *22<sup>nd</sup> Int. Symp. on Space THz Tech.*, Tucson, AZ, USA, April 2011.
- [17] D. Drung, *et al.*, "Novel SQUID current sensors with high linearity at high frequencies," *IEEE Trans. Appl. Supercond.*, vol. 19, no. 3, pt. 1, pp. 772-777 (2009).
- [18] G. Torrioli, *et al.*, "A cryo-amplifier working in a double loop-flux locked loop scheme for SQUID readout of TES detectors," *Proc. SPIE Vol. 7732*, 77324I (2010); doi:10.1117/12.856430.
- [19] H. Spieler, "Frequency domain multiplexing for large scale bolometer arrays," in *Monterey Far-IR, Sub-mm and mm Detector Technology Workshop proceedings*, J. Wolf, J. Farhoomand, and C. McCreight, eds., pp. 243-249 (2002). NASA/CP-2003-21140 and LBNL-49993.
- [20] P. A. J. de Korte, *et al.*, "EURECA: a European-Japanese micro-calorimeter array," in: *Proc. SPIE Vol. 6266*(1) (2006).

# A Study on Photon Counting Interferometry in Terahertz Frequencies

H. Matsuo<sup>1\*</sup>, T. Matsuo<sup>2</sup>, I.S. Ohta<sup>2</sup>

*1 National Astronomical Observatory of Japan\*, Tokyo 181-8588, Japan*

*2 Kinki University, Osaka 577-8502, Japan*

\* Contact: h.matsuo@nao.ac.jp, phone +81-422-34-3915

*Abstract*—A new interferometer technology is proposed that is based on intensity interferometry. In terahertz frequencies photon statistics is not random but there is some coherence in intensity, or photon bunching, is expected when brightness temperatures of thermal sources are higher than about 100 K. Although standard intensity interferometer cannot measure phase information, when photon counting detectors are introduced, it will be possible to measure delay time of bunched photon arrival and complex visibility can be measured.

Some case study is made to estimate feasibility of the photon counting interferometry; one for far-infrared fine structure line observations from Antarctic plateau and another for observing exo-planets in far-infrared wavelengths from space platforms. In both cases, it is estimated that we can measure photon arrivals and complex visibilities can be used to make aperture synthesis images of the sources.

## Optical characterization at 1.5-3 THz of high sensitivity TES detectors designed for future Far-Infrared Space missions

P. D. Mauskopf<sup>1\*</sup>, D. Morozov<sup>1</sup>, P. A. R. Ade<sup>1</sup>, D. Griffin<sup>2</sup>, D. Goldie<sup>3</sup>, D. Glowacka<sup>3</sup>, A. Velichko<sup>3</sup> and S. Withington<sup>3</sup>

*1 Cardiff University, School of Physics and Astronomy\*, Cardiff, UK CF24 3AA*

*2 Rutherford Appleton Laboratory, Harwell Science and Innovation Campus, Didcot OX11 0QX*

*3 Cambridge University, Astrophysics Group, Cavendish Laboratory, Cambridge, UK CB3 0HE*

\* Contact: Philip.mauskopf@astro.cf.ac.uk, phone +44-2920-876 170

**Abstract**—High sensitivity TES detectors are being developed for use in future Far-Infrared (FIR) space missions such as SPICA, FIRI, SAFIR, SPIRIT and SPECS. These missions plan on implementing actively cooled telescope optics to minimize the level of background radiation in the instrument and allow several orders of magnitude increase in sensitivity over current space missions such as HERSCHEL and SPITZER. The combination of low emission from the cooled telescope and the low-background environment from space results in a photon flux of on order several thousands of photons per second in a 50% bandwidth and a level of photon noise equivalent power (NEP) in the range  $\text{NEP}=10^{-20} - 10^{-18} \text{ W}/\sqrt{\text{Hz}}$  depending on the details of the instrument design. In this paper, we describe the optical characterization of high-sensitivity TES detectors designed for operation in the wavelength range from 100-200  $\mu\text{m}$  (1.5-3 THz). A detector consists of a TES thermometer (MoCu or MoAu) and an optical absorber fabricated from a thin Tantalum (Ta) film deposited on a thermally isolating silicon nitride (SiN) structure. The TES thermometers have a transition temperatures of approximately 100 mK and the measured thermal conductance agrees with the design values of  $G = 0.2\text{-}0.5 \text{ pW/K}$  corresponding to a phonon limited detector  $\text{NEP} < 10^{-18} \text{ W}/\sqrt{\text{Hz}}$ . We measure the absorbed optical power from a blackbody source as a function of source temperature through a set of two high pass and two low pass filters defining a pass band from 1.5-3 THz. The radiation from the blackbody source is coupled to an integrating cavity containing the TES and absorber using an electroformed conical horn. We find that this system has good optical performance and the dependence of absorbed power on blackbody temperature agrees with the values calculated from the combination of the blackbody emission spectrum and the measured filter transmission. We compare the measured optical efficiencies for different absorber geometries and impedances.

## Kilopixel Superconducting Bolometer Arrays for Near-Space Astrophysics Applications

Dominic J. Benford<sup>\*1</sup>, Christine A. Jhabvala<sup>1</sup>,  
Nikhil S. Jethava<sup>1,2</sup>, Timothy M. Miller<sup>1</sup>, S. Harvey Moseley<sup>1</sup>, Elmer H. Sharp<sup>1,2</sup>,  
Johannes G. Staguhn<sup>1,3</sup>, Edward J. Wollack<sup>1</sup>, Kent D. Irwin<sup>4</sup>, Gene C. Hilton<sup>4</sup>

1. NASA/Goddard Space Flight Center, Greenbelt, MD 20771 USA;

2. Global Science & Technology, 7855 Walker Drive, Suite 200, Greenbelt, MD 20770

3. Johns Hopkins University, 3400 N. Charles Street, Baltimore, MD 21218

4. NIST, Mail Stop 814.03, 325 Broadway, Boulder, CO 80305, USA

\* Contact: Dominic.Benford@nasa.gov, phone +1.301.286.8771

**Abstract**— We are producing a matured 1,280 pixel, high-filling-factor backshort-under-grid bolometer arrays for efficient operation at the wavelengths between 30 $\mu$ m and 2mm. The arrays employ leg-isolated superconducting transition edge sensor bolometers operated at 128 mK; tuned resonant backshorts for efficient optical coupling; and a second-generation superconducting quantum interference device (SQUID) multiplexer readout. We describe the design, development, and performance of this bolometer array technology to achieve background-limited sensitivity for cryogenic balloon-borne telescopes and for airborne imagers and spectrometers. The first flight use of these detector arrays will be in the Primordial Inflation Polarization Explorer (PIPER), a balloon-borne experiment to measure the polarization of the cosmic microwave background (CMB) and search for the imprint of gravity waves produced during an inflationary epoch in the early universe. PIPER will fly four times in 2013 to observe at wavelengths of 1500, 1100, 850, and 500  $\mu$ m in order to separate CMB from foreground emission. Similar (although smaller) arrays will be operated on BETTIL, the Balloon-borne Experimental Twin Telescope Infrared Interferometer, operating at a wavelength of 30 $\mu$ m-90 $\mu$ m, shortly thereafter. These arrays were also developed with the intent of operating them on the SOFIA airborne observatory, where the large format can increase the facility's scientific return from imagers and spectrometers.



# Performance of the first ALMA Band 5 production cartridge.

Bhushan Billade, Olle Nyström, Denis Meledin, Erik Sundin, Igor Lapkin, Mathias Fredrixon, Vincent Desmaris, Hawal Rashid, Magnus Strandberg, Sven-Erik Ferm, Hui Wang, Hui Xu, Monika Obrocka, Brian Ellison, Alexey Pavolotsky and Victor Belitsky.

**Abstract**—We present performance of the first ALMA Band 5 production cartridge, covering RF frequencies from 163 GHz to 211 GHz. ALMA Band 5 is a dual polarization, sideband separation (2SB) receiver based on all Niobium (Nb) Superconductor-Insulator-Superconductor (SIS) tunnel junction mixer, providing 16 GHz of instantaneous RF bandwidth for the astronomy observations. The 2SB mixer for each polarization employs a quadrature layout. The sideband separation occurs at the output of the IF hybrid that has integrated bias-T for biasing the mixers, and is produced using superconducting thin film technology.

Experimental verification of the Band 5 cold cartridge performed together with warm cartridge assembly, confirms the system noise temperature below 45 K, less than five quantum noise (5 hf/k) over most of the RF band, which is to our knowledge, the best results at these frequencies. The measurement of the sideband rejection indicates that the sideband rejection better than 10 dB over 90% of the observational band.

**Index Terms**—Terahertz System, Astronomy instruments, ALMA, Superconducting devices, Millimeter wave mixers, Superconductor-insulator-superconductor mixers, Thin film circuits.

## I. INTRODUCTION

THE Atacama Large Millimetre/sub-millimeter Array (ALMA) is a radio interferometer under construction by an international consortia consisting of European countries (ESO), USA, Canada, Chile and Japan. ALMA is located at 5000 meters above sea level in the Atacama desert in Chile, where the earth's atmosphere provide the most favorable conditions for radio astronomy observations at these frequencies. ALMA will cover the frequencies from 31 GHz to 950 GHz split up into ten different frequency bands. With its more than 60 antennas of 12 m diameter and a reconfigurable baseline ranging from 150 m to 18 Km, ALMA will offer unprecedented sensitivity and resolution.

The work presented here concerns the design and development of the ALMA Band 5 receiver, one of the 10 frequency bands of the ALMA project. ALMA Band 5 is funded by European Commission's Framework Program 6 (FP6), an

infrastructure enhancement project. In this framework program, the project considers to supply 6 receiver cartridges to the ALMA project for integration into the ALMA frontend receiver. Similar to other ALMA bands, the Band 5 receiver is also divided into two separate units, a warm cartridge assembly (WCA) and a cold cartridge assembly (CCA).

The Group for Advanced Receiver Development at Chalmers University with Onsala Space Observatory is responsible for the design and development of the cold cartridge assembly (CCA) and the STFC Rutherford Appleton Laboratory, UK, is responsible for the design and development of the Band 5 warm cartridge assembly (WCA) and the local oscillator (LO) chain.

The CCA is a unit which is cryogenically cooled using a three stage cryo-cooler of the ALMA front end cryostat. Different components of the cartridge are thermally connected to different temperature stages of the cooler. The cold cartridge assembly hosts, receiver optics, orthomode transducer (OMT), SIS mixers, IF hybrid, IF low noise amplifiers, mixer bias and ESD protection circuitry and x6 local oscillator stage. The x6 (times six) local oscillator stage is delivered by RAL.

The warm cartridge assembly is a unit which resides outside the cryo-cooler and provides a blind mate interface to the cold cartridge assembly. The warm cartridge assembly hosts the local oscillator source operating in the frequency range from 14 GHz to 17 GHz, a x2 (times two) multiplier, phase lock loop for LO after the x2 (times two) multiplier stage, warm IF amplifiers and bias and control circuitry.

## II. ALMA BAND 5 COLD CARTRIDGE

The ALMA Band 5 receiver is a dual polarization, sideband separating, heterodyne receiver, covering the RF frequencies from 163 GHz to 211 GHz, with 4-8 GHz down converted intermediate frequency (IF) for each channel. Band 5 receiver employs sideband separation quadrature layout (2SB) based on all Niobium (Nb) superconducting tunnel junction (SIS) mixers [1]. The separation of two orthogonal polarizations is realized using a waveguide orthomode transducer [2]. For each polarization branch, the receiver will provide 8 GHz instantaneous RF band for observations. Among the other frequency bands of the ALMA project, Band 5 is the lowest frequency band that uses all cold optics. Consequently, the physical dimensions for all the optics components for Band 5 are largest compared to all other ALMA bands. All these relatively big optics components packed inside a limited space

Manuscript received on August 01, 2011. This work was supported by EC Framework Program 6 (FP6), under infrastructure enhancement contract 515906

Bhushan Billade, Igor Lapkin, Olle Nyström, Erik Sundin, Denis Meledin, Vincent Desmaris, Hawal Rashid, Alexey Pavolotsky and Victor Belitsky are with the *Group of Advanced Receiver Development (GARD)* at Chalmers University of Technology, Gothenburg, Sweden. (phone: +46 31 772 1851, e-mail: [bhushan.billade@chalmers.se](mailto:bhushan.billade@chalmers.se)).

Hui Wang, Hui Xu, Monika Obrocka and Brian Ellison are with STFC, Rutherford Appleton Laboratory, UK.

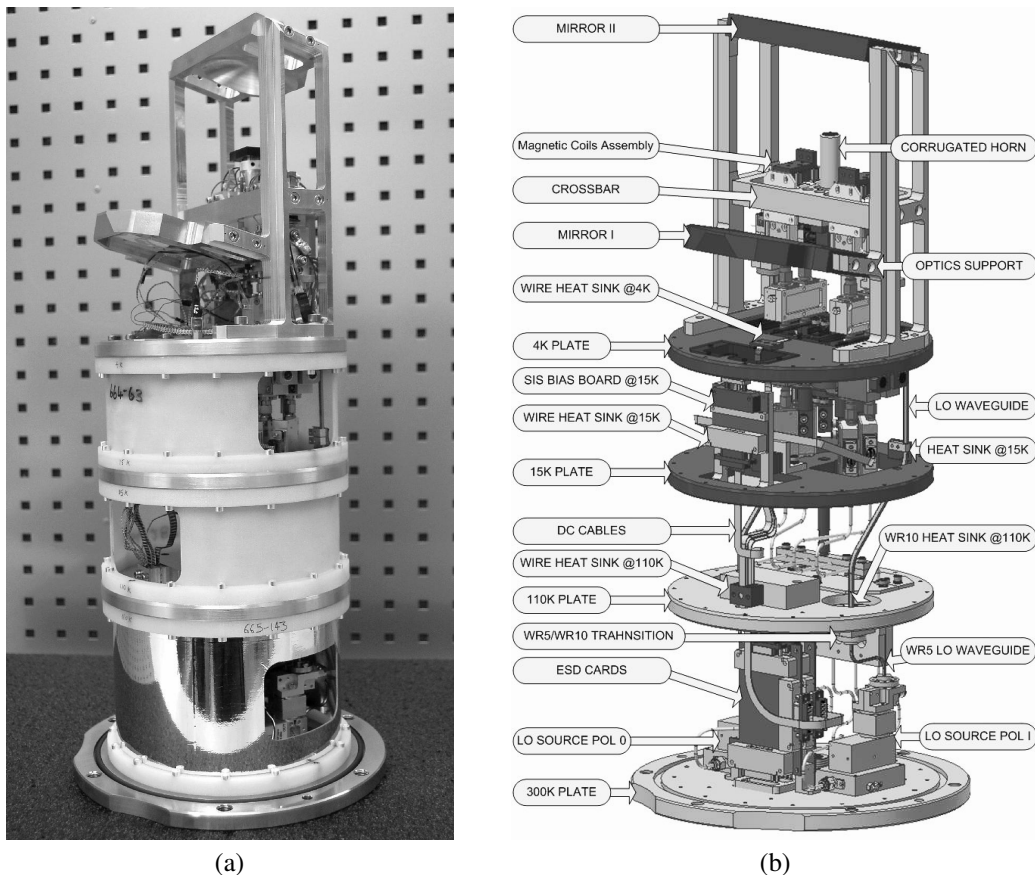


Fig. 1. Band 5 CCA 01 (a) Picture of the first Band 5 cold cartridge assembly (b) a CAD drawing of the CCA, showing different temperature stages and arrangement of receiver components inside the cartridge envelop, the fiber glass supports separating different temperature stages are removed for visibility of components inside.

of  $\emptyset$  170 mm, which leaves very little space for the other receiver components.

Fig. 1 shows a CAD drawing of the cold cartridge, the fiber glass support is removed for better visibility. It can be seen from the figure that the mirrors along with the optics supports occupy much of the space on the 4 K temperature stage. The design parameters of Band 5 mirrors and corrugated horn are based on the design proposed by M. Carter et al., [3] and has been verified using physical optics simulation by M. Whale et al., [4]. The optics dimensions put strong constraints on the sizes of all the receiver components and demands a very compact design. Furthermore, the arrangement of the components in the cartridge is such that we have to direct the IF output of the mixers pointing down along the cartridge axis. In such a configuration, the mixer design with a split block technique becomes too big to fit inside the cartridge. We have found that the only possible solution is to use a mixer block configuration with waveguide back piece [5], [6]. This layout allows very compact design of the mixer block and also the IF output pointing in desirable direction. Furthermore, to avoid extra cables, all the components in the chain are directly attached to each other with matched SMA connectors. Keeping compactness of all the components in mind and to take advantage of cold temperature, we chose a custom made superconducting IF hybrid that fits the distance between the SMA connectors of the 2SB mixer IF outputs avoiding any

unnecessary cabling. Apart from tight constraints on the size of all the receiver components, we have very limited cooling capacity at 4 K stage, restricting the total power dissipation at 4 K stage to merely 36 mW. These 36 mW are shared between the four SIS mixers, magnetic coils, low noise amplifiers and thermal load due to heat conduction. A lot of efforts have been put to reduce contribution from each of these components but still it does not allow us to integrate the DC bias circuitry for the SIS mixers at 4 K stage [7]. Therefore, in our design, as shown in Fig. 1 the DC biasing to the mixer is done using a bias circuitry placed at the 15 K plate and integrating a bias-T with the IF hybrid; the DC biasing is thus achieved through the output SMA connector of the mixers. The hybrid is followed by a 4-8 GHz isolator and a cryogenic HEMT low noise amplifier.

Part of the local oscillator chain resides inside the cold cartridge assembly and is placed on the 300 K plate of the cartridge. The LO signal is then guided from the 300 K stage to 4 K stage to the mixers using WR10 (over-sized) waveguide. In order to reduce the thermal coupling between the different temperature stages, we use stainless steel waveguide with heat sinks at all the corresponding temperature stages.

### III. ALMA BAND 5 WARM CARTRIDGE

Fig. 2 shows the picture of the Band 5 warm cartridge produced by the Band 5 WCA team at the Rutherford Appleton

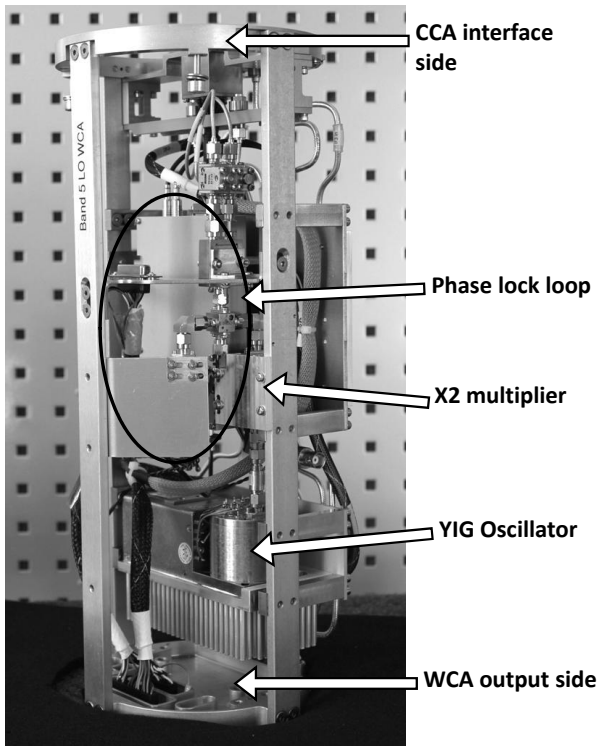


Fig. 2. A picture of the entire warm cartridge assembly (WCA), showing different components of the cartridge.

Laboratory in UK. Warm cartridge assembly consists of a YIG oscillator source in the frequency range of 14-17 GHz followed by a frequency doubler. The frequency doubler is then followed by a phase lock loop operating in the range of 28-34 GHz. In its final operational state, the reference signal for the phase locking will be provided by mixing two lasers in a photo-mixer producing a down converted reference in the frequency range of 28-34 GHz. In our measurement setup in the lab, we use a frequency synthesizer to obtain the required 28-34 GHz reference for the phase lock.

The warm cartridge assembly provides a blind mate interface to the cold cartridge. The blind mate interface consist of two input K-type connectors for the LO signals for both the polarizations, DC biasing for frequency doublers and multipliers for the LO stages inside CCA through Fisher connector, and biasing for the CCA through Glen-air connectors. The blind mate interface also includes four IF outputs from the CCA.

Fig. 3 shows the cold cartridge base plate, which hosts part of the LO multiplier chain and provides hermetically tight blind mate interface to the WCA. The part of the LO chain inside the CCA consists of a active frequency tripler (x3) followed by a frequency doubler (x2). The biasing to the tripler and doubler is provided through a fisher connector. Similar to all other ALMA bands, the DC biasing of different CCA components - the mixers, amplifiers, coils, and temperature sensors is done through a standard double 51 pin Glenair connector.

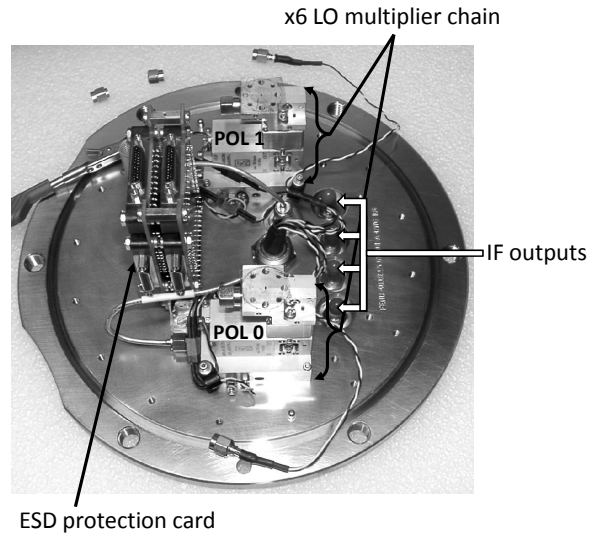


Fig. 3. A picture of 300 K CCA base plate showing, multiplier stages, ESD protection circuitry and IF outputs.

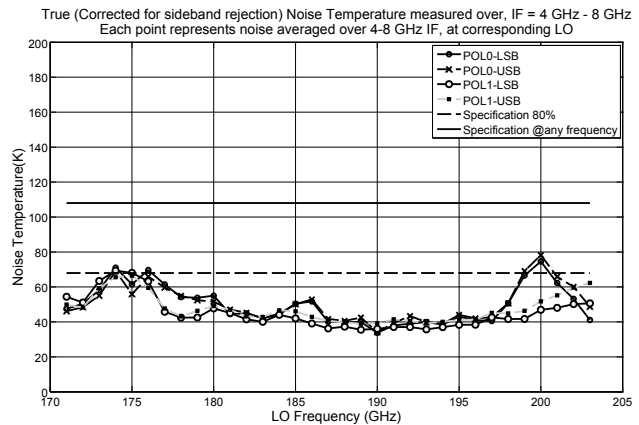


Fig. 4. Measurement of noise temperature for ALMA Band 5 CCA 01, for both sidebands and polarization, measured over the 4-8 GHz IF band.

#### IV. MEASUREMENT RESULTS

##### A. Noise temperature measurement

The performance verification of the Band 5 cold cartridge was performed together with the warm cartridge assembly delivered by the Rutherford Appleton Laboratory, UK. To perform these tests we used NAOJ cartridge test cryostat [8]. Most of the measurements are done using an automated computerized system, built around the test cryostat [9].

The noise specifications for the ALMA Band 5 project requires the system noise temperature to be below 65 K over 80% of the band and less than 108 K at any frequency. Fig. 4 shows the measured noise performance of the first Band 5 production cartridge. The noise was measured over the 4-8 GHz IF band for both sidebands and polarizations and includes the contribution from the dewar windows, IR filters and takes into account all the noise contributions up to the IF output ports of warm cartridge assembly. The noise measurements were carried out using standard Y-factor method. The presented noise temperature also takes into account the correction for

the sideband rejection [10]. Our measurements confirm that the receiver performance meets all the noise specification for the Band 5 project, and in most cases better than the specifications with a good margin.

### B. Sideband rejection measurement

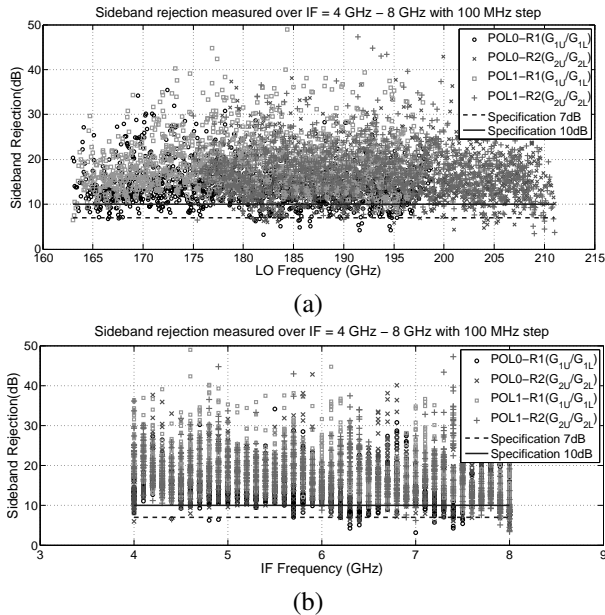


Fig. 5. Measurement of sideband rejection/image rejection for ALMA Band 5 CCA 01, for both polarization, (a) Sideband rejection vs. RF frequency (b) Sideband rejection vs. IF frequency.

In sideband separation millimeter wave receiver knowledge of image rejection is very important. Unless the image rejection is ideal, a correction term is required in estimation of the system noise temperature. We use the technique proposed by A. Kerr [10] to estimate the sideband rejection. Fig. 5 (a) shows the sideband rejection measurement results, performed at RF frequencies from 163 to 211 GHz with 100 MHz frequency steps and Fig. 5 (b) shows the same measurements plotted across the IF band for all RF frequencies. The measurements confirm that the sideband rejection is better than 10 dB over 90% of the band and better than 7 dB over 99%.

## V. CONCLUSION

We have designed and built the first ALMA Band 5 production cartridge and fully characterized it. The characterization of the cold cartridge was performed with integrated warm cartridge assembly. Performance verification of the entire system including, cryostat window, IF filters and all the IF components, confirms that the first Band 5 production cartridge meets all ALMA project specifications.

The measurement of 2SB configuration confirms that the system noise temperature less than 45 K over most of the RF band, which is less than five quantum noise (5 hf/K) and less than 65 K (7 hf/K) over the entire RF band. This is to our knowledge best results so far at these frequencies. The sideband separation for both polarizations is better than 10

dB over 90% of the band and better than 7 dB over 99% of the RF band.

The first ALMA Band 5 cartridge is delivered to the European ALMA Integration Center at RAL in UK and is expected to be in operation at the ALMA cite in Chile during year 2012.

## ACKNOWLEDGMENT

This project is funded by EC Framework Program 6 (FP6), under infrastructure enhancement contract 515906.

The author would like to thank Dr. Jacob Kooi (Caltech, USA), Doug Henke (currently at HIA, Victoria, Canada), Richardo Finger (DAS, University of Chile, Santiago) and Dr. Raquel Monje (Caltech, USA) for their contribution at earlier stages of the project.

The author would also like to thank Gert Johnsen and Dr. Dimitar Dochev.

## REFERENCES

- [1] B. Billade, V. Belitsky, A. Pavolotsky, I. Lapkin, and J. Kooi, "Alma band 5 (163-211 ghz) sideband separation mixer," in *20th International Symposium on Space Terahertz Technology*, April 2009, pp. 19–23.
- [2] S. Asayama and M. Kamikura, "Development of double-ridged waveguide orthomode transducer for the 2 mm band," *Journal of Infrared, Millimeter and Terahertz Waves*, vol. 30, no. 6, pp. 573–579, June 2009.
- [3] M. Carter *et al.*, "Alma front-end optics design report," available from ALMA project documentation server, Tech. Rep. FEND-40.02.00.00-035-B-REP.
- [4] M. Whale, N. Trappe, and V. Belitsky, "Physical optics analysis of the alma band 5 front end optics," in *Proceedings of the 19th International Symposium on Space Terahertz Technology*, Groningen, April 2008, pp. 368–372.
- [5] B. Billade, "Design of dual polarisation sideband separation mixer for alma band 5," Licentiate Thesis, Chalmers University of Technology, Gothenburg, Sweden, September 2009.
- [6] R. Monje, V. Belitsky, C. Risacher, V. Vassilev, and A. Pavolotsky, "Sis mixer for 385-500 ghz with on chip lo injection," in *Proceedings of the 18th International Symposium on Space Terahertz Technology*, USA, March 2007, pp. 44–49.
- [7] M. Strandberg, "Analysis, simulation and cryogenic/mechanical design for alma band 5 cartridge," Licentiate Thesis, Chalmers University of Technology, Gothenburg, Sweden, June 2011.
- [8] Y. Sekimoto *et al.*, "Cartridge test cryostats for alma front end," National Astronomical Observatory of Japan, ALMA Memo 455, April 2003.
- [9] O. Nyström *et al.*, "Integrated setup for thz receiver characterization," in *Proceedings of the 21st International Symposium on Space Terahertz Technology*, Oxford, UK, March 2010, pp. 4–6.
- [10] A. Kerr, S. K. Pan, and J. E. Effland, "Sideband calibration of millimeter-wave receiver," ALMA Memo 357, March 2001.

## Receiver Optics and 1.9 THz HEB Mixers for STO

M. Brasse\*, U. U. Graf, C. E. Honingh, K. Jacobs, M. Justen, P. Pütz, M. Schultz, and J. Stutzki  
*Kölner Observatorium für Submm Astronomie (KOSMA), I. Physikalisches Institut, Universität zu Köln,  
Zülpicher Str. 77, 50937 Köln, Germany*

\* Contact: [brasse@ph1.uni-koeln.de](mailto:brasse@ph1.uni-koeln.de), phone +49-221-470 7338

This work was supported through STO by NASA grant number NNX08AG39G and by the German Space Agency (DLR) through grant 50 OK 0801.

**Abstract**—We present results of our work on the receiver optics and the 1.9 THz waveguide hot electron bolometer (HEB) mixers for the Stratospheric Terahertz Observatory (STO). The balloon-borne STO is a 0.8 m telescope using 4-pixel HEB mixer focal plane arrays to survey selected regions of the Galactic Plane in the [NII] and [CII] spectral lines at 1.461 THz and 1.901 THz, respectively. The receiver optics and the 4 HEB mixers at 1.9 THz are the KOSMA hardware contribution to the STO project.

The cold optics unit provides the mounting point of the two focal plane units (FPU), each with four HEB mixers, to the integrated imaging optics and employs a cryogenic polarizer grid for overlay of both array beams.

The warm receiver optics unit includes the LO mounts and the Fourier grating mirrors, which split the LO beam into an array of four beams. Instead of a more common Martin-Puplett Interferometer (MPI), we use a multi-beam Fabry-Perot Interferometer (FPI) with polarizer grids as diplexer for each frequency. Compared to the MPI, the FPI, centered at 1.5 GHz, provides a larger IF bandwidth for the receiver. Both optical units including the mirrors are machined from one piece or assembled from as few parts as possible. This monolithic approach ensures sufficient alignment accuracy of the optics.

The FPU and a single pixel prototype FPI are characterized at 1.9 THz with waveguide mixers developed at KOSMA for STO. These mixers utilize a NbTiN HEB on a 2  $\mu\text{m}$  SiN membrane. The design is similar to the KOSMA 2.5 THz mixer, presented in a separate contribution to this conference, and uses beam leads for electrical contacts and registration to the waveguide environment. The waveguides have been made exclusively by stamping with different specially made carbon steel tools in CuTe blocks.

# Compact Micromachined Infrared Bandpass Filters for Planetary Spectroscopy

A. D. Brown<sup>1\*</sup>, S. Aslam<sup>1</sup>, J. A. Chervenak<sup>1</sup>, W. C. Huang<sup>1</sup>, W. Merrell<sup>1</sup>, and M. Quijada<sup>1</sup>

*1 NASA Goddard Space Flight Center\*, Greenbelt, MD 20771*

\* Contact: ari.d.brown@nasa.gov, phone +1-301-286 2293

*Abstract*—The thermal instrument strawman payload of the Jupiter Europa Orbiter on the Europa Jupiter Science Mission will map out thermal anomalies, the structure, and atmospheric conditions of Europa and Jupiter within the 7-100 micron spectral range. One key requirement for the payload is that the mass cannot exceed 3.7 kg. Consequently, a new generation of light-weight miniaturized spectrometers needs to be developed. On the path toward developing these spectrometers is development of ancillary miniaturized spectroscopic components. In this paper, we present a strategy for making radiation hard and low mass FIR band pass metal mesh filters. Our strategy involves using MEMS-based fabrication techniques, which will permit the quasi-optical filter structures to be made with micron-scale precision. This will enable us to achieve tight control over both the pass band of the filter and the micromachined silicon support structure architecture, which will facilitate integration of the filters for a variety of applications.

## Measure the beam wavefronts of a terahertz source

M. Cui<sup>1,2</sup>, J.N. Hovenier<sup>2</sup>, Y. Ren<sup>2,4</sup>, J.R. Gao<sup>1,2</sup>, and T.M. Klapwijk<sup>2</sup>

<sup>1</sup>*SRON Netherlands Institute for Space Research, Sorbonnelaan 2, 3584 CA Utrecht, The Netherlands*

<sup>2</sup>*Kavli Institute of NanoScience, Delft University of Technology, Lorentzweg 1, 2628 CJ Delft, The Netherlands*

<sup>3</sup>*Purple Mountain Observatory (PMO), Chinese Academy of Sciences, 2 West Beijing Road, Nanjing, JiangSu 210008, China.*

<sup>4</sup>*Graduate School, Chinese Academy of Sciences, 19A Yu Quan Road, Beijing 100049, China*

\* Contact: m.cui@tudelft.nl, phone +31-15-278-4099

Terahertz (THz) quantum cascade lasers (QCL) are one of the most promising THz sources as local oscillators (LO) for heterodyne receivers at super-THz frequencies. To effectively couple the radiation from a THz QCL to a lens-antenna-coupled THz mixer, which usually has a Gaussian beam pattern, understanding the beam pattern of the QCL is crucial. The beam pattern of a THz QCL with regard to the intensity has been studied extensively. However, the wavefront of the beam has never been measured. The latter can be more crucial for the use as a LO in a receiver because the mixer is a phase sensitive, coherent detector,

Here we propose a measurement technique for the phase front in the THz domain by adapting the Shack-Hartmann wavefront sensors (SH-WFS) in the optical wavelengths. SH-WFS can provide accurate measurements of the wavefronts of beams. It is made of a panel of lens array, which creates a spot field from the incident wavefront on the detection plane, located at the focus plane of the lenses. The wavefront of the beam can be reconstructed from the locations of the spots.

We start our experiment by using an array of holes (Hartmann mask) instead of the lens array. The diameter of each hole in our Hartmann mask is 1 mm and the separation between adjacent holes is 3 mm. The detection plane is located 10 mm behind the mask. The displacement of the intensity spots from the holes in the mask, measured at the detection plane, can indicate a distorted wavefront of the THz beam. To prove the measurement principle, we start with the beams generated by a gas laser operated at 2.5 THz. We also measured the beam through a Fresnel lens, which is expected to distort the wavefront. We observed the distorted wavefront from the deviations of spot positions from those in the mask.

# Test facility development for the SPICA-SAFARI instrument

Pieter Dieleman, Bart Vandenbussche, Bruce M. Swinyard, Willem Jellema, Marc Ferlet, Lenze Meinsma, Wouter M. Laauwen, Lorenza Ferrari, Heino Smit, and Martin Eggens

**Abstract**— In this article the main characteristics of the SAFARI instrument onboard SPICA are described, as well as a proposed setup to verify function and performance of the instrument. A major challenge is the required low background light level, which excludes the use of cryostat windows and hence all test sources need to be inside the cryostat. The maximum allowed temperature for any unit inside the 4K compartment is 8K to minimize heat radiation affecting the detector NEP. A concept for a calibration source is introduced which operates up to 200 K with an attenuation factor of  $10^6$ . A beam quality test method is proposed as well. Finally, a total system concept is presented.

**Index Terms**— Submillimeter wave receivers, infrared spectroscopy, system testing, submillimeter wave measurements, cryogenics.

## I. INTRODUCTION

SAFARI (SpicA Far-infraRed Instrument) is an imaging Fourier Transform Spectrometer with a  $2' \times 2'$  instantaneous field of view (FoV) for the 34 – 210  $\mu\text{m}$  wavelength region. The architectural design of the instrument is similar to that of the Herschel/SPIRE instrument [1],[2]. The instrument is being developed by a European consortium led by SRON, the Netherlands Institute for Space Research. It is scheduled for launch in 2018 onboard the SPace Infrared telescope for Cosmology and Astrophysics (SPICA) satellite, developed jointly by JAXA and ESA. The main advantage of SPICA over Herschel is its actively cooled mirror, allowing orders of magnitude more sensitive detectors to be used. SAFARI offers imaging spectroscopy and imaging photometry in the far infrared with detector NEP of  $2 \cdot 10^{-19}$  W/ $\sqrt{\text{Hz}}$  and a spectral resolution of  $R = \sigma/\Delta\sigma = 2000$ . To reach this sensitivity the SAFARI instrument uses TES (Transition Edge Sensor) detectors[3] operated at 50 mK. This temperature is

reached by a combination of a sorption cooler and ADR inside the Focal Plane Unit (FPU). The FPU, including the optics and mechanisms, is cooled to 4.5K. The SAFARI wavelength range is split into 3 bands: 34 – 60, 60 – 110, and 110 – 210  $\mu\text{m}$ . To allow for direct sky mapping without jiggling, Nyquist sampling of the FoV is required, leading to a total number of pixels of about 4000. Efficient readout is obtained by Frequency Division Multiplexing (FDM), using 1 SQUID amplifier per channel consisting of 160 pixels.

In this article we describe the considerations in designing a cryogenic test facility for SAFARI on-ground calibration and characterization. A major challenge will be to meet the required low background (a few attoWatts per pixel) whilst providing the SAFARI Focal Plane Unit with the necessary calibration sources. The layout of this article is as follows: in section 2 the tests to be performed are described as well as the requirements for the Optical Ground Support Equipment (OGSE), the test equipment inside the cryostat. Section 3 describes the optical design of the OGSE as well as the status of the design of the various OGSE elements. Section 4 will go in on the status and development approach of light tightness measures.

## II. SAFARI GROUND TESTS

The characterization of a sensitive imaging spectrometer primarily focuses on the following aspects: Radiometry - to measure the sensitivity of the detectors and calibrate the calibration source internal to the instrument, Image quality – to measure the corresponding sky position of each pixel, Frequency resolution and frequency accuracy – to calibrate the spectrometer function of SAFARI. Critical issues specific for SAFARI are thermal and EMC compatibility of the TES detector system with the ADR cooler and FPU mechanisms. The critical SPICA interfaces with SAFARI are mechanical, thermal, electrical and optical: High launch loads of 20g sine, microphonics[4], temperature stability and cooling power, EMC and stray light. The AIV (Assembly Integration and Verification) program aims at an early optimization and verification of these critical items. The tests required and resulting hardware are presented in Table 1. Since these aspects require both development and qualification, a 3-model philosophy is chosen: A Demonstration model (DM) to show

Manuscript received July 29, 2011.

P.Dieleman, W. Jellema, L. Meinsma, W.M. Laauwen, L. Ferrari, H. Smit, M. Eggens are with the SRON Netherlands Institute for Space Research, Landlevan 12, 9700 AV Groningen, the Netherlands (Phone: +31503638286, email: P.Dieleman@sron.nl).

B. Vandenbussche is with the Institute of Astronomy K.U. Leuven, Celestijnenlaan 200B, 3001 Leuven, Belgium.

B.M. Swinyard and M. Ferlet are with the Rutherford Appleton laboratory, Chilton, Didcot OX11 0QX, united Kingdom.

L. Meinsma is with Annex, Bellingeweer 16, 9951 AM Winsum, the Netherlands.



TABLE I  
SAFARI TESTS AND RESULTING HARDWARE

Category	Test method	Test equipment
<i>Image quality</i>		
- Sky mapping	Point source scan in OFP <sup>a</sup>	Cryo XY stage, pinholes, broadband source
- Beam direction	Multiple scan planes	Z-axis in OFP scanner
- FTS wander	Scan FTS	Stable pinhole mask in OFP
- Pupil quality	Point scan in OPP <sup>b</sup>	X(Y) stage, pinhole in OPP
- Stray light	scan beyond OFP and OPP diameters	scan range 3 x plane size
- Cross talk	Point source mask in OFP	Representative reimager, pinhole masks
<i>Linearity</i>		
- Continuum	Increasing background with chopped weak line	Instrument Flasher with calibration source + etalon
- Line	Line strength variation	Chopper external laser with power tuning (grid)
<i>Radiometry</i>		
- calibration	Test internal against external calibrator	OGSE calibration source
- flatness	Measure NEP, gain	OGSE flatfield source
- source size	Measure NEP versus point source size	Back-illuminated pinhole wheel
<i>Spectrometry</i>		
- frequency	Known line source, FTS scans	External laser, calibrated cryo etalon, gas cell
- resolution	Narrow line source, FTS scans	External laser
<i>Stability</i>		
- noise, gain	Measure stable line signal for tbd period	Internal calibration source with etalon

<sup>a</sup>OFP stands for Object Focal Plane, the reimaged focal plane of the SAFARI FPU. <sup>b</sup>OPP stands for Object Pupil Plane, the reimaged pupil plane internal to the SAFARI FPU.

that the planned performance will be achievable and to find functional issues, a Qualification Model (QM) to verify SAFARI will survive the launch and space environment, and the Flight Model (FM), to be launched after full verification.

### III. OGSE DESCRIPTION

The equipment common for all tests are: A reimager with similar optical properties as the SPICA telescope, a pupil scanner, a calibration source in the reimaged focal plane (OFP), and a mask plate in the OFP back-illuminated by a wide-band and spectral source. Fig. 1 shows the OGSE assembly with all units mentioned in Table 1.

#### A. Reimager

The reimager consists of a flat folding mirror and 2 off-axis parabolas. The layout is similar to that of the PACS OGSE [5], although optimized for shorter wavelengths and lower geometric distortion by reducing the angles of incidence. Spot diagrams below indicate geometric spot size well below the Airy pattern size over the full FoV. The reimager used for the instrument level tests has a significantly smaller wavefront error than the SPICA telescope specification.

The magnification is determined by the limited size of a back-illuminating integrating sphere, and by the requirement

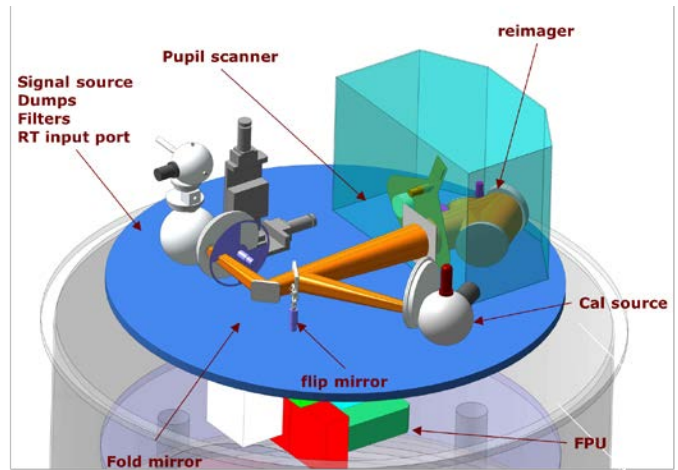


Fig. 1. OGSE layout inside the SAFARI test cryostat. The blue plate is the optical bench, the FPU is hanging upside-down at the lower side. The FPU beam goes through the optical bench, via a reimager into the OGSE space. The OGSE pupil stop acts as an additional stray light baffle, and at this position the pupil scanner is located. The beam is deflected by a flip mirror towards the cryogenic calibration source, or continues toward an XY scanner system with a pinhole mask wheel back-illuminated by an integrating sphere. This sphere is fed by an internal source directly, or via filters or etalons, and can be fed by a room temperature source via a light pipe as well. Both the FPU and OGSE will be enclosed by 4K light tight shield (not shown)

that the point source size must be larger than a wavelength for proper transmission while still be much smaller than the OFP Airy disk for accurate PSF scanning. The optimum lateral magnification is found to be 1.86, hence the 10x10 mm focal plane is reimaged on an 18.6x18.6 mm grid.

Similarly, the FPU pupil stop is reimaged in a plane in the OGSE space. In order to determine both position and direction of the FPU beam, the position of the reimaged beam on the OGSE pupil plane as well as field plane needs to be measured.

#### B. Pupil Plane beam measurement

The image of the FPU pupil in the OGSE has a diameter of 80 mm, the position of this plane is shown in Fig. 1 The f-number of the optics for this plane is 30, which gives an airy disk radius of  $1.22 F \cdot \lambda = 1.4$  mm for the shortest SAFARI wavelength, hence an appropriate pinhole size is 1 mm. For stray light measurements the point source needs to move out of the plane by 40 mm in all directions, hence the total pupil diameter to be scanned is 160 mm.

#### C. Focal Plane beam measurement

The types of measurements performed with the FP scanner are pixel spatial response, focal plane geometry and stray light (ghosts). The purpose of spatial response measurements is to verify the image quality, field curvature, and image distortion. The focal plane geometry gives information about the number of the pixels and the pitch. The strategy is to scan the focal plane with a pinhole mask, back-illuminated by an integrating sphere [6]. The pinhole size differs for the different bands to keep the pinhole diameter larger than the wavelength which avoids spectral power differences, but significantly smaller than the pixel size. The focal plane is curved; the instrument optics maps a flat TES aperture plane to a curved image with a

radius of curvature of about 550 mm. During a final XY scan the scanner will follow in Z the curved focal plane.

The source power should be high enough to obtain sufficient signal to noise ratio, but low enough to avoid nonlinearities due to saturation. The saturation power  $P_0 = V_0 \cdot 2R_0$  where  $R_0$  is the resistance value on the bias point and  $V_0$  is the voltage across the TES. Assuming a normal TES resistance of  $R_N = 100 \text{ m}\Omega$  and a bias point of 40 % of the superconducting to normal transition  $R_0$  is equal to 40 mΩ. The voltage across the TES is calculated from the relation  $NEP = V_0 \cdot \sqrt{S_I}$  with  $\sqrt{S_I}$  is the current to noise responsivity and  $NEP = 2 \cdot 10^{-19} \text{ W}/\sqrt{\text{Hz}}$ . The TES noise is 16 pA/ $\sqrt{\text{Hz}}$  in the electro thermal feedback (ETF) bandwidth. The voltage across the TES is equal to 12.5 nV and the saturation power is 4 fW. The signal source power chosen for beam measurements is 50% of the saturation power.

To correct for drift and 1/f noise, the signal is modulated, either by a dedicated chopper or by the instrument FTS mechanism movement. The signal to noise ratio S/N is required to be 1000. From this value the integration time is calculated: The noise N is  $2\pi \text{ NEP} / \sqrt{0.5\tau}$  where  $2\pi$  is the crest factor,  $1/\tau$  is the bandwidth and the factor 0.5 comes from the chopper duty cycle. With a signal power of 2 fW per pixel a S/N of 1000 is reachable with 1 s of integration time. This enables “on the fly” scans rather than step and integrate, which would lead to unwanted vibrations and dissipation in the system.

The pinhole size can be calculated from the convolution between the Airy function and a box car function corresponding to a pinhole disk (see Fig. 2).

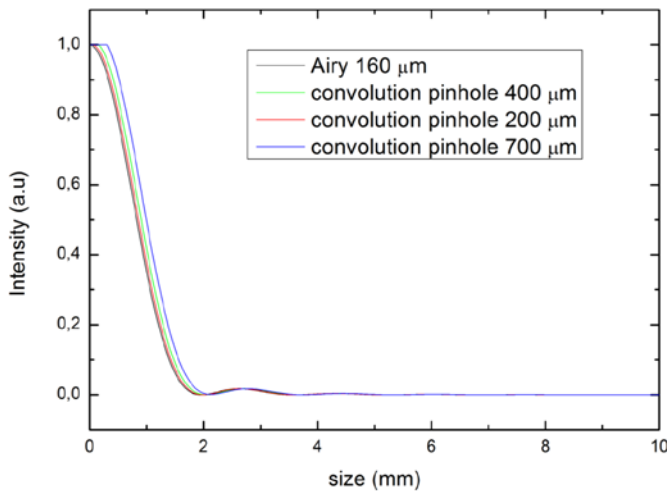


Fig. 2. Convolution of the Airy disk and a pinhole of different sizes for LW band.

The optimum pinhole diameters are 109, 198 and 372  $\mu\text{m}$  for the SW, MW and LW bands respectively. The Airy disk will be oversampled (about 150 samples) to measure the FWHM and the Airy rings position within an accuracy of 5%. The scan speed is determined by the integration time and the allowed spatial smearing due to on the fly integration. The planned speed is one pinhole radius per second, corresponding to 50  $\mu\text{m}/\text{s}$  for the SW band. The required relative accuracy of

the pinhole position with respect to the SAFARI FPU beam is 10  $\mu\text{m}$  for the SW band.

For the beam direction and focal plane geometry scans a back-illuminated mask is used rather than a single pinhole, to shorten the test duration. The size of the mask is 20 x 20 mm, similar to the focal plane size. The distance between two pinholes on the same mask is determined from the Airy disk size and the expected cross-talk levels

The stray light test in the object focal plane is performed with a single pinhole rather than a mask, to ensure that a stray light path can be uniquely determined. Since this pinhole for stray light tests needs to move out of the object focal plane by 20 mm on all sides, the travel for the scanner is 60mm x 60 mm.

#### D. Calibration source

For the radiometry tests of SAFARI a calibration source is designed. It is coupled to the instrument via the reimager and a flip mirror in the OGSE optical path, see Fig. 1. The output port of the calibration source is positioned in the reimaged focal plane. The calibration source must offer a homogeneous field over the entire reimaged focal plane with well-known frequency and power. Homogeneous illumination can be achieved by making use of an integrating sphere with an output port diameter at least 5 times smaller than the sphere diameter, in order to produce sufficient reflections inside before the light escapes. In order to keep the spectrum of the input signal unperturbed, the reflectivity of the inner surface must be close to 99% and the sphere needs to be cooled to 1.7K.

To obtain the required spectrum as well as a stable output power a black body is used with a temperature of around 100K. The black body consists of a spherical cavity coated on the inside with black absorber. It has a small opening, thus approaching a perfectly black cavity.

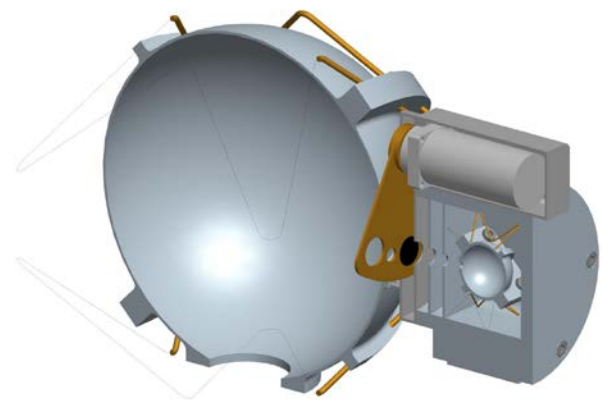


Fig. 3. Calibration source conceptual design.

The power level is reduced by a factor  $10^6$  to match SAFARI’s operational range of  $10^{-19}$  to  $10^{-14} \text{ W}$  per pixel. This reduction is achieved by geometric dilution: The coupling between the black body and the input of the integrating sphere is determined via the sizes of the two ports and their separation,

see Fig. 3. This determines the fraction of the solid angle  $\pi$  from the output of the black body that is coupled to integrating sphere. The remaining power is absorbed in the baffles, requiring a high absorption of the absorbing coatings on these baffles. A mechanism on the input port of the integrating sphere allows the choice of various opening diameters, expanding the power range in steps without altering the spectrum. By fast opening and closing the source can be used as a flasher. Optionally a frequency selective element like an etalon can be inserted to create well known spectral features. The loading per pixel of the SAFARI instrument can be calculated as a function of the black body temperature. Fig. 4 plots these values for the three detector bands.

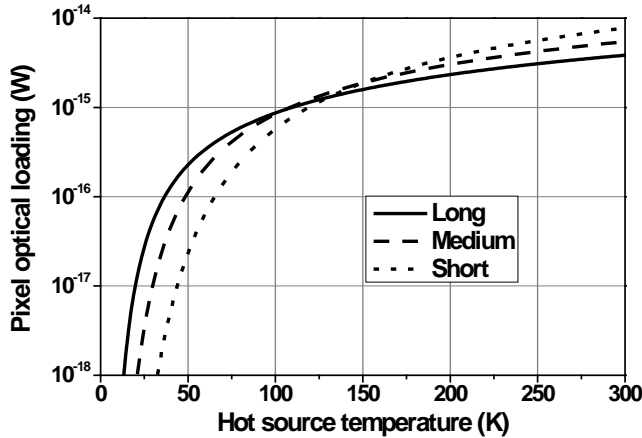


Fig. 4. Pixel loading versus black body temperature.

#### IV. STRAY-LIGHT CONTROL

The requirement on the background power level in the 4K compartment of the test cryostat is specified as the radiance level at the focal plane causing an increase in the SAFARI NEP of less than 20%. In order to reach this level, a combination of light tightness and stray light control measures is taken and a limit on the maximum temperatures inside the 4K OGSE space is set.

##### A. Absorber area

To model the effect of absorber in the 4K compartment, the test cryostat is treated as an integrating sphere which is coupled to the instrument via the pupil stop. The input signal is a hot source, e.g. the scanner actuator with a certain surface area, emissivity and temperature and corresponding IR power. If the sphere would be perfectly reflective all power from the source will make it to the exit port and from there will couple to the detector. Therefore a low-background environment requires absorbers in the OGSE compartment. Fig. 5 shows the loading of the TES pixels as a function of the fractional absorbing area. For the model a 1 meter diameter cryostat is used with emissivity 0.01. The absorber is modeled to have an emissivity of 0.99. Inside the cryostat the warm element is modeled by sphere of 40 mm diameter at a temperature of 20K and an emissivity of 0.1. The warm element is not in direct line of sight to the instrument.

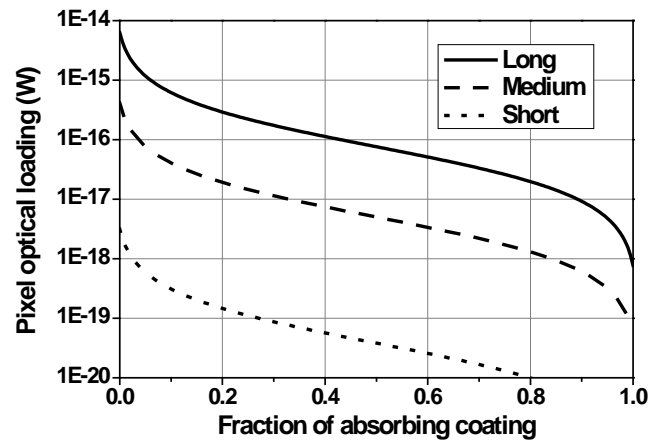


Fig. 5. Pixel loading versus fraction absorbing coating.

The attenuation versus fraction of absorbing coating is highly non-linear. The first 15% absorbing coverage of the 4K compartment wall already gives 10 dB of attenuation. The maximum temperature inside can be calculated as well: Assuming an absorbing coating fraction of 20% the NEP is increased by 20% for a 20mm diameter sphere with an emissivity of 0.1 and a temperature of 8K.

##### B. Light tightness measures

To ensure light from higher temperature shields does not reach the 4K compartment tongue and groove structures filled with carbon-loaded Stycast are used for mechanical connections that require regular mounting/demounting. The cable harness is led through Stycast filled meandering feedthroughs as well.

#### V. SUMMARY

The test setup of the SAFARI instrument is in a definition phase. Preliminary modeling has resulted in requirements for the calibration source and beam measurement equipment. The stray light control measures are being designed.

#### ACKNOWLEDGMENT

We thank the PACS team at Max-Planck-Institut für extraterrestrische Physik for helpful discussions on design choices.

#### REFERENCES

- [1] G.L. Pilbratt et al, "Herschel Space Observatory: An ESA facility for far-infrared and submillimetre astronomy", *Astronomy & Astrophysics*, vol. 518, July 2010, pp L1.
- [2] M.J. Griffin et al, "The Herschel-SPIRE instrument and its in-flight performance", *Astronomy & Astrophysics*, vol. 518, July 2010, pp L3.
- [3] P.D. Mauskopf et al, "Development of transition edge superconducting bolometers for the SAFARI Far-Infrared spectrometer on the SPICA space-borne telescope", in *Millimeter and Submillimeter detectors for astronomy IV*, SPIE 70200N (2008)
- [4] R.S. Bhatia et al, "The effects of cryocooler microphonics, EMI, and temperature variations on bolometric detectors", *Cryogenics* vol 41, 2002 pp 851–863.
- [5] G. Jacob et al, "Herschel –PACS Ground Calibration: the MPE Cryogenic Test Facility", *Astronomical Telescopes and Instrumentation*, SPIE 5487-106 (2004)
- [6] T. Belenguer et al, "MIRI Telescope Simulator", SPIE 7010-39 (2008)

## Development of planar Schottky diodes

V. Drakinskiy<sup>1\*</sup>, P. Sobis<sup>1,2</sup>, A.-Y. Tang<sup>1</sup>, T. Bryllert<sup>1,3</sup>, and J. Stake<sup>1</sup>

<sup>1</sup> Chalmers University of Technology\*, SE-412 96 Göteborg, Sweden

<sup>2</sup> Omnisys Instruments AB, Västra Frölunda, Sweden

<sup>3</sup> Wasa Millimeter Wave AB, Göteborg, Sweden

\*Contact: vladimir.drakinskiy@chalmers.se, phone +46 31 772 1848

**Abstract**— We present the development of an air-bridged planar Schottky diode process at Chalmers University of Technology for use in submillimeter wave mixer and multiplier circuits. As a first step evaluation has been targeted for heterodyne receivers (atmosphere sounders) operation at 340 GHz. The aim is to develop a reliable and repeatable discrete Schottky diode process, with good electrical and mechanical characteristics, which also can be scaled to smaller anodes and extended to integrated diode circuits for THz frequencies.

Air-bridged Schottky structures were demonstrated in the late 1980's as a reliable, high quality alternative to whisker contacted diodes. This approach gives a mechanically stable structure and still low parasitic capacitances. The Chalmers diode process is based on electron beam lithography, with a beam spot less than 5 nm, which allows for precise anode and airdridge formation. Hence, this process module can also be utilized for submicron size anodes and terahertz monolithic integrated circuits (TMICs).

Several batches with different shapes of anodes have been fabricated and evaluated with respect to DC/RF-performance. Repeatability of the diode's characteristics indicates good control of the diode fabrication process. We will present the main fabrication route, optimization and repeatability of the diodes as well as RF results from mixer and multiplier measurements up to 340 GHz.



Fig1. Microscopic image of the doubler chip with fabricated at MC2 Chalmers.

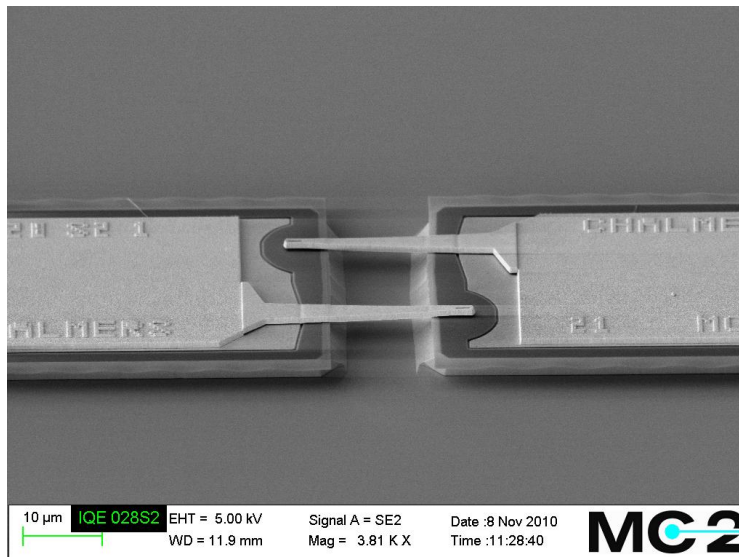


Fig2. SEM image of the antiparallel diodes with the anode area  $0.8 \mu\text{m}^2$  fabricated at MC2 Chalmers.

This work was supported by the European Space Agency (ESA) under contract no. 21867/08/NL/GLC.

# Design, Fabrication, and Alignment of the SuperCam Telescope Relay Optics

M. Borden<sup>1</sup>, D. Golish<sup>1,2</sup>, C. Drouet d'Aubigny<sup>1,2</sup>, C. Groppi<sup>3</sup>, J. Kloosterman<sup>1</sup>, T. Cottam<sup>1</sup>, X. Xu<sup>1</sup>, D. Lesser<sup>1</sup>, S. Silva<sup>1</sup>, C. Kulesa<sup>1</sup>, C. Walker<sup>1,2</sup>, B. Cuerden<sup>1</sup>

<sup>1</sup>Steward Observatory, University of Arizona, Tucson, AZ 85721 USA

<sup>2</sup>TeraVision Inc., Tucson, AZ 85705 USA

<sup>3</sup>School of Earth and Space Exploration, Arizona State University, Tempe, AZ 85287 USA

**Abstract**— SuperCam is a 64 pixel,  $\lambda=870\ \mu\text{m}$ , superheterodyne camera designed to work with the 10m diameter Heinrich Hertz Telescope on Mount Graham, Arizona. Large imaging arrays were not anticipated when the telescope was originally designed. As a result, complex relay optics are required to adequately re-image the telescope focus on the detector array. After a brief review of SuperCam's optical and environmental requirements, we present the approach selected, along with novel modeling methods used to validate the design. The optical tolerances which drove the opto-mechanical design are presented. New metrology and optical alignment methods developed for SuperCam, but equally applicable to other THz optical systems, are also discussed.

## I. INTRODUCTION

### 1.1 SuperCam Science and Instrument Design

SuperCam has been designed to operate in the astrophysically rich  $870\ \mu\text{m}$  atmospheric window. The Heinrich Hertz Submillimeter Telescope has a  $15\ \mu\text{m}$  RMS surface, making it one of the most accurate large submillimeter telescopes currently in operation. In addition, the 10,500ft elevation site on Mt. Graham offers weather sufficient for observing in this window more than 50% of the observing season, 24 hours per day. The receiver is an 8x8 array constructed from integrated 1x8 mixer modules, with state of the art mixer, local oscillator, low noise amplifier, cryogenic and digital signal processing technologies. In the past, all heterodyne focal plane arrays have been constructed using discrete mixers, arrayed in the focal plane. SuperCam reduces cryogenic and mechanical complexity by integrating multiple mixers and amplifiers into a single array module with a single set of DC and IF connectors. These modules are housed in a closed-cycle cryostat with a 1.5W capacity 4K cooler.

SuperCam has four times the number of pixels of any existing spectroscopic imaging array at submillimeter wavelengths. The exceptional mapping speed provided by 64 pixels,

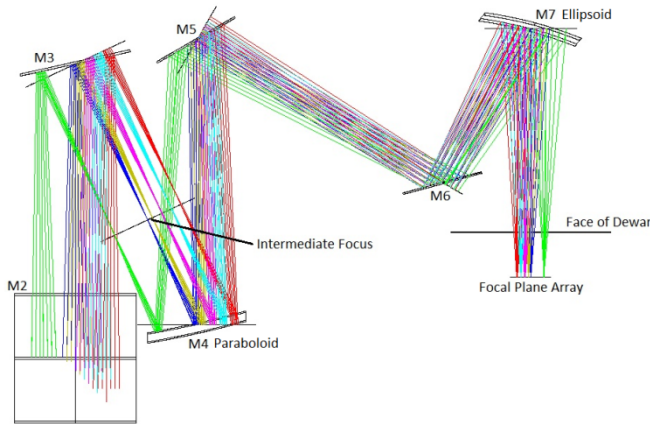
combined with the efficiency and angular resolution provided by the HHT will make SuperCam a uniquely powerful instrument for probing the history of star formation in our Galaxy and nearby galaxies. SuperCam will be used to answer fundamental questions about the physics and chemistry of molecular clouds in the Galaxy and their direct relation to star and planet formation. Through Galactic surveys, particularly in CO and its isotopomers, the impact of Galactic environment on these phenomena will be realized [1].

### 1.2 Environmental Constraints at the Telescope

The HHT was constructed before submillimeter array receivers became common. The instruments designed for the HHT typically reside at the Nasmyth foci to either side of the primary optical axis. The Nasmyth foci are located along the elevation axis of the telescope. A rotating tertiary in the apex room (which rotates with the telescope in elevation) allows instruments to be mounted on either side. However, the clear apertures of the elevation bearings on either side of the apex room are only 100 and 300 mm in diameter. Unfortunately, the size of SuperCam's beam footprint precludes putting the receiver past these narrow openings. The remaining option is to install the receiver in the apex room itself, which, among other challenges, limits the size of the system.

## II. DESCRIPTION OF THE SUPERCAM OPTICAL DESIGN

The HHT's secondary provides Nasmyth instruments with an  $f/13.8$  beam. The desired number of pixels for SuperCam requires a lower  $f/\#$  if they are to fit in a reasonably-sized cryostat. One of the goals of our optics is to transform the incoming  $f/13.8$  beams into  $f/5$  beams that will couple efficiently with the receiver feedhorns.



only the optics mounted on the wall are shown.

The SuperCam optical design, schematically pictured in Figure 1, is relatively simple. The system has two powered mirrors. The first is a parabolic mirror which essentially collimates the light from the telescope after it has come to a focus, the second is an elliptical mirror that focuses the beams to match the  $f/\#$  of the feedhorns. Practical constraints force the system to include a number of flat mirrors, first to provide enough optical path for the telescope beam to come into focus, and then to provide the distance between the two powered mirrors which is required to provide adequate pixel separation and maintain image space telecentricity. The first flat mirror moves into the beam to direct it to the back wall of the apex room where the SuperCam optical support structure is mounted. The next two flat mirrors provide optical path length to let the beams come to focus before they reflect off the parabolic mirror. Two additional flats provide optical path between the parabolic and elliptical mirrors to set the beam spacing and image space telecentricity [1,2]. A CAD model of the receiver and its optics mounted in the apex room is shown in Figure 2.

### III. OPTICAL TOLERANCES

For SuperCam to achieve adequate optical performance, an error budget was used to allocate error throughout the system. This budget includes the alignment tolerances of the SuperCam relay optics, the mirror fabrication errors, design residuals of the relay optics, errors associated with Optical Support Structure (OSS) deformation and errors in the alignment procedure, errors corresponding to FARO Arm measurement accuracy, and errors from the telescope. This error budget is shown below in Table 1.

Table 1: Error Budget for SuperCam Optical Tolerancing

Source of Error	Resulting WFE
Mirror Alignment	$\lambda/33.6$
Mirror Fabrication	$\lambda/34.1$
Design Residuals	$\lambda/34.2$
OSS Deflection / Alignment Procedure Errors	$\sim 0$
FARO Arm Measurement Accuracy (Alignment)	$\lambda/31$
HHT Errors	$\lambda/30$
Total	$\lambda/17.75$

When added in quadrature the collective errors were  $\lambda/17.75$ , which met the allowable error requirement.

### IV. TESTING OF OPTICAL COMPONENTS

#### 4.1 Measurement and Data Processing

A portable CMM was used in this application. The FARO Quantum Arm, which has a measurement range of 8' in diameter, is an articulated metrology arm capable of measuring complex objects and assemblies in a single dataset to a volumetric accuracy better than 30  $\mu\text{m}$ . It was used to measure the surface of each THz optic. The mirror was

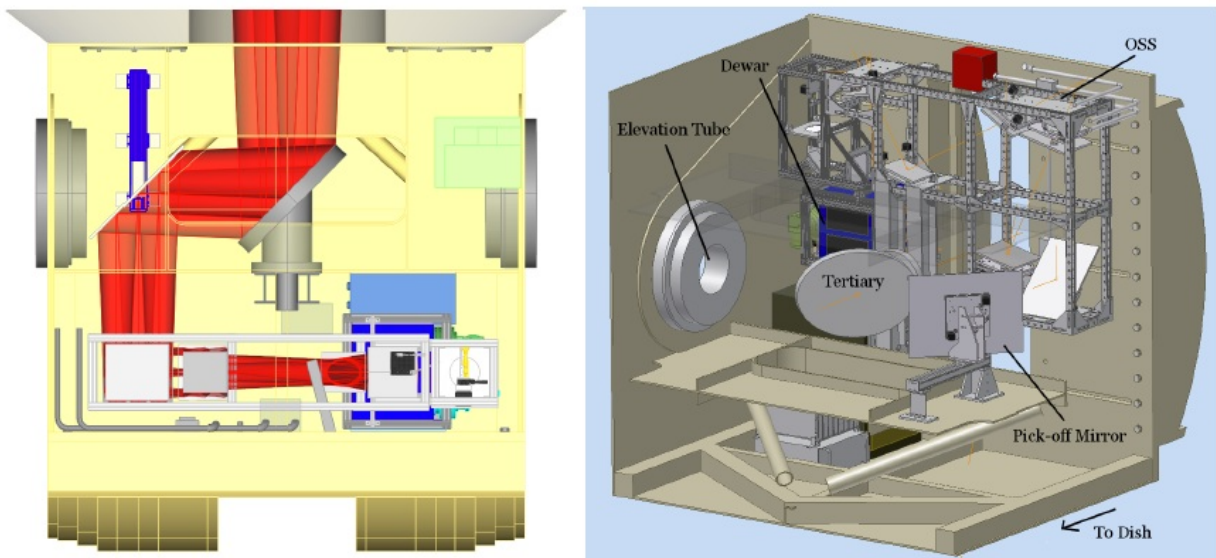
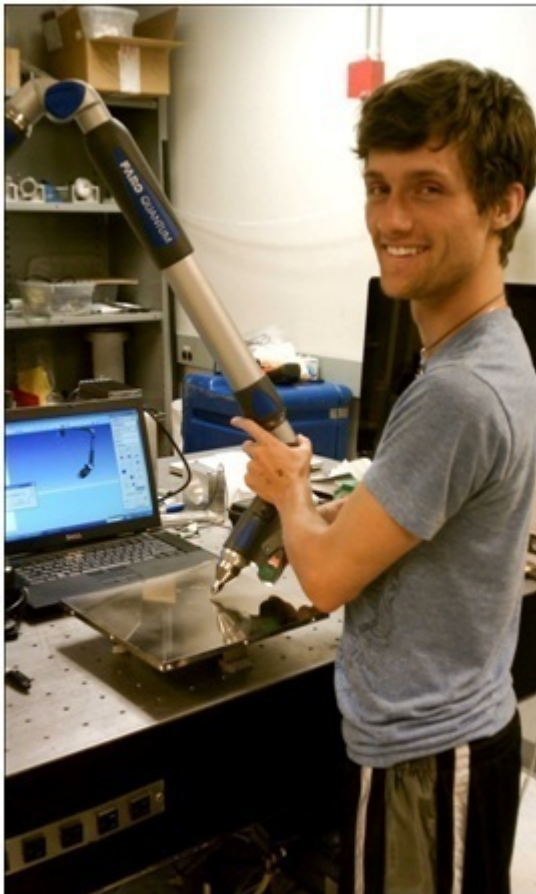


Figure 2: CAD model of SuperCam and its optics mounted on the back wall of the SMT apex room. Left – Top view showing the beam bundles (in red) passing through the SMT primary mirror and into the apex room. Right – SuperCam relay optics seen within apex room. (Groppi 2009)

mounted rigidly and data points were collected covering the entire surface of the optic.

As is common with CMMs, each measured coordinate is taken at the center of the spherical metrology probe. The result is a point which is offset by an amount equal to the radius of the probe along a vector normal to the surface. This was corrected using an algorithm in MATLAB. The resulting dataset represented the as-built optical surface. The theoretical surface was exported from Zemax. Using an optimizer in Spatial Analyzer® to best-fit the as-built optical surface to the theoretical optical surface, a dataset representing the difference between the two was generated. This difference dataset represented the fabrication errors associated with the as-built optical surface.

It was found that both mirrors were fabricated with an imperfect radii of curvature. The resulting fabrication error was found to be 26.5  $\mu\text{m}$  rms for mirror M7 and 21.1  $\mu\text{m}$  rms for mirror M4.



**Figure 3:** Author using FARO Arm to measure optical surface of mirror

#### 4.2 Evaluation of effect of Mirror Fabrication Errors on Optical Performance

Zernike polynomials were used to represent the fabrication error dataset. These Zernike polynomials were incorporated into the original optical model in Zemax. We determined that these surface figure inaccuracies degraded the optical

performance of the system from the design residuals of  $\lambda/34$  to  $\lambda/32.25$  in RMS wavefront error. Though the two powered mirrors were not fabricated perfectly, the resulting errors associated with their as-built surface figures were acceptable.

## V. OPTICAL ALIGNMENT

### 5.1 Creating Reference Fiducials and Updating Mirror CAD Models

Using the FARO Arm as a tool for aligning THz optics has two major advantages: the surfaces of the optics do not need to be polished to optical quality and the loose tolerances allowed by THz optical systems is conducive to using an articulated metrology arm. A challenge of using an articulated metrology arm for alignment is that constraining the position of the measuring probe on the optical surface of each mirror is difficult making it an undesirable reference surface for alignment. To compensate for this, a set of mechanical reference fiducials were created to fully constrain the probe. This ensures repeatable measurements. These fiducials were machined into the sides of each mirror in the system and their positions in relation to the optical surface were measured. The position of these fiducials between mirrors thus became the new reference for mirror alignment.

The measured reference fiducials were then added to the CAD models of each mirror. This was done using the Spatial Analyzer® optimization which best-fits the as-built surface of the mirror to its theoretical surface. The as-built surface dataset included the measured fiducial positions. Thus the best-fit procedure coupled the positions of the fiducials to the theoretical surface of the mirror.

### 5.2 Using FARO Arm and Spatial Analyzer® for Mirror Alignment

The FARO Arm was then registered to the optical assembly by measuring the accessible fiducials of one mirror, which was considered the reference mirror of the system (in our case the elliptical mirror). Theoretical points were then created in Spatial Analyzer® corresponding to each of these measured fiducials. The measured fiducials were best fit to their theoretical positions using Spatial Analyzer®. The remaining mirrors in the system were then one by one, iteratively aligned to this first mirror. Three reference fiducials from each mirror were measured and compared to their theoretical position as determined by the CAD model. The difference between the two was minimized to an acceptable level by adjusting the position of the mirror. It should be noted that as each mirror is aligned, it is aligned with respect to the first mirror in the system, not the mirror next to it in the mirror assembly. This prevents alignment errors from accumulating between mirrors. We found this procedure provided an accurate and simple quantitative feedback mechanism for aligning THz mirrors.

## VI. CONCLUSION

We found the FARO Arm to be an effective metrology tool for both verifying the surface of and aligning THz optics. Using the FARO Arm and the developed surface verifying

procedure, the surface figure of both powered mirrors was found to have imperfect radii of curvature. The resulting wavefront error at the pixel array as a result of these imperfect mirrors was  $\lambda/32.25$ .

Using the FARO Arm as an alignment instrument was very successful. The reach of our 8' Arm was adequate for aligning every mirror in the system to our reference mirror. The fiducials that were machined into each mirror provided a feature that was measured with consistency. Using these fiducials as alignment points, each mirror was referenced to the alignment mirror. This alignment process was iterative and was used until each reference fiducial being measured fell within adequate alignment tolerance for that mirror.

The remaining sources of error are the design residuals of the relay optics, the deflections of the Optical Support Structure and errors in the alignment procedure, errors corresponding to FARO Arm measurement accuracy, and the telescope figure and alignment errors. These errors together with the mirror fabrication errors and those associated with the alignment procedure account for a total error of  $\lambda/17.75$ .

#### REFERENCES

- [1] Groppi, C., Walker, C., Kulesa, C., Golish, D., Kloosterman, J., Weinreb, S., Jones, G., Barden, J., Mani, H., Kuiper, T., Kooi, J., Lichtenberger, A., Cecil, T., Puetz, P., Narayanan, G., Hedden, A. "Testing and Integration of Supercam, a 64-Pixel Array Receiver for the 350 GHz Atmospheric Window." 2009. *SPIE*, Vol 7741.
- [2] Groppi, C., Walker, C., Kulesa, C., Golish, D., Kloosterman, J., Weinreb, S., Jones, G., Barden, J., Mani, H., Kuiper, T., Kooi, J., Lichtenberger, A. "Testing and Integration of Supercam, a 64-Pixel Array Receiver for the 350 GHz Atmospheric Window." 2010. *International Symposium on Space Terahertz Technology. 21<sup>st</sup> Annual ISSTT Proceedings*. 23-25



# PHOCUS Radiometer Payload

O. Nyström<sup>1</sup>, T. Ekebrand<sup>2</sup>, C. Emrich<sup>2</sup>, M. Krus<sup>2</sup>

A. Emrich<sup>2</sup>, D. Murtagh<sup>1</sup>, V. Belitsky<sup>1</sup>

<sup>1</sup> Earth and Space Sciences, Chalmers University of Technology, Sweden

<sup>2</sup> Omnisys Instruments AB\*, Västra Frölunda, Sweden

\* Contact: olle.nystrom@chalmers.se, phone +46-31-772 1838

**Abstract**— PHOCUS – **P**articles, **H**ydrogen and **O**xygen **C**hemistry in the **U**pper **S**ummer **M**esosphere is a Swedish sounding rocket experiment with the main goal of investigating the upper atmosphere in the altitude range 50-110 km. This paper describes the radiometer instruments (SondRad) in the PHOCUS payload, which are intended to explore the water vapour concentration in connection with the appearance of noctilucent (night shining) clouds. The design of the radiometer system has been done in collaboration between Omnisys Instruments AB and the Group for Advanced Receiver Development (GARD) at Chalmers University of Technology where Omnisys was responsible for the design, implementation, and verification of the radiometers and backend and GARD was responsible for the optics and calibration systems.

The radiometers cover the water absorption lines at 183 GHz and 557 GHz with 67 kHz backend resolution. The 183 GHz channel is a side-looking radiometer while the 557 GHz radiometer is placed along the rocket axis looking in the forward direction. Both channels employ sub-harmonically pumped Schottky mixers and FFT spectrometer back-ends. The 183 GHz channel employs a CW-pilot signal calibrating the entire receiving chain while the IF-chain of the 557 GHz channel is calibrated by injecting a signal from a calibrated noise source through a directional coupler.

The instrument will collect complete spectra for both the 183 and 557 GHz with 300 Hz rate for the 183 GHz channel and 10 Hz for the 557 GHz channel for about 60 seconds reaching the apogee of the flight trajectory and 100 seconds after that. With lossless data compression using variable resolution over the spectrum, the data set is reduced to 2 x 12 MByte.

**Index Terms**—Radiometer, calibration, water vapour, and Noctilucent clouds.

## I. INTRODUCTION

PHOCUS – Particles, Hydrogen and Oxygen Chemistry in the Upper Summer Mesosphere is a Swedish<sup>1</sup> sounding rocket experiment with the goal of investigating the upper atmosphere in the altitude region 50-110 km and in particular the circumstances under which noctilucent (night shining) clouds (NLC) appear [1]. The NLC are restricted to a thin layer around 82 km, the highest clouds in our atmosphere, and are only present during the summer months and at high latitudes. The clouds are known to consist of water ice but the exact details of their formation are uncertain. Three criteria are needed to form ice clouds: cold temperatures, water vapour, and condensation nuclei. The nature of the condensation

<sup>1</sup> PHOCUS rocket experiment is funded by the Swedish National Space Board. The radiometer instrument was funded by the Swedish Research Council, Vetenskapsrådet.

nuclei is not fully understood but two important suggestions are meteoric smoke particles and ions [2].

Measurements of the water vapour amount in the tenuous atmosphere at 82 km altitude is challenging. The heterodyne technique is probably the only method that can provide these measurements in the presence of sunlight. The water vapour measurements on board PHOCUS are performed by two microwave radiometers (SondRad) shown in Figure 1, operating at the 183 GHz and 557 GHz water absorption lines. The PHOCUS payload carries in total 18 instruments from 8 different research groups, investigating different properties of the mesosphere. The instruments measure optical (spectral-, angular- and polarization) properties, chemical composition (O- and H-probes), charged particles, temperature and pressure, and water vapour, to mention a few [2].

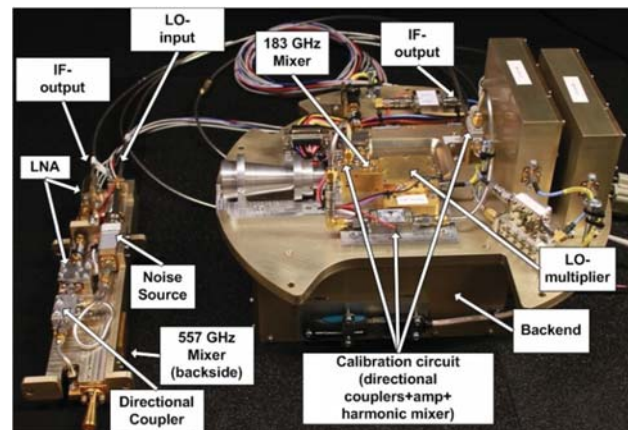


Figure 1. Picture of the two radiometers (557 GHz left). The backend with FFT-spectrometer located under the 183 GHz receiver (right).

## II. TECHNICAL DESCRIPTION

SondRad comprises two radiometers covering the water absorption lines at 183.31 GHz and 556.936 GHz. The 183 GHz receiver is side-looking and is placed in the middle section of the rocket, Figure 2. Approximately 2 m above, the 557 GHz receiver is placed, pointed along the rocket axis looking in the forward direction, Figure 2. Both radiometers employ sub-harmonically pumped Schottky mixers where the 183 GHz mixer is provided by RPG [3] and the 557 GHz mixer is provided by VDI [4]. The LO sources at 85 GHz and 95 GHz for both radiometers employ active multiplier chains that have been developed by Omnisys Instruments AB [5]. The active 85 GHz multiplier pumps the 183 GHz mixer directly whereas

the 91 GHz chain is followed by a power amplifier with x3 multiplier stage that sub-harmonically pumps the 557 GHz mixer.

The FFT-spectrometer backend provided by Omnisys Instruments AB, processes a 275 MHz band with 4096 channels.

The two radiometers employ two different calibration techniques described in section III. A block diagram of the complete system is shown in Figure 3, with the 557 GHz radiometer located in the so called “Particle module” and the 183 GHz frontend located below the “Mid recovery module” (Figure 3). The backend, with the FFT spectrometer, and the control unit is placed on the same platform as the 183 GHz receiver.

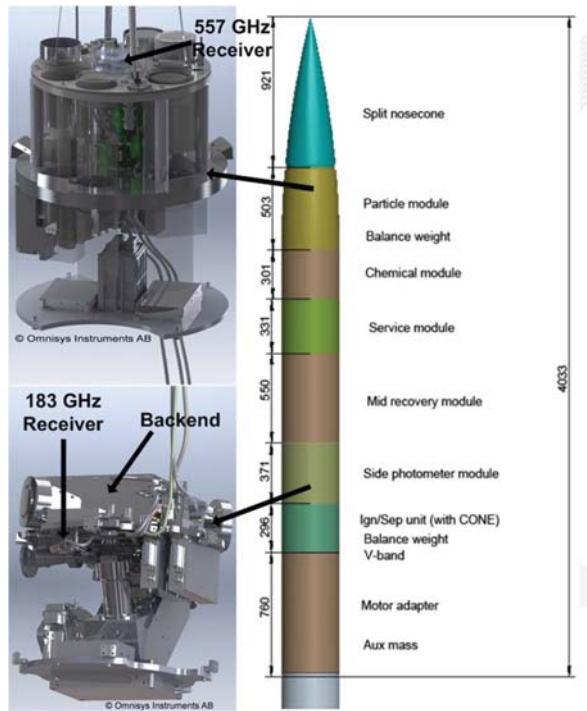


Figure 2. 3D-drawings of the 557 GHz and the 183 GHz radiometers and their respective placement on the rocket. The rocket figure is provided by SSC [6].

During the observation, starting at nose cone ejection, about 60 seconds after liftoff until reaching the apogee, and 100 seconds on the returning flight trajectory, the instrument will collect data with 300 Hz sampling rate for the 183 GHz receiver and 10 Hz sampling rate for the 557 GHz receiver. For the 183 GHz channel 183.310 GHz ±19.3 MHz will be saved of the FFT backend data and in addition 182.264 GHz ±0.5 MHz for the calibration signal. For the 557 GHz channel, 556.936 GHz ±19.3 MHz will be saved of the FFT backend data. The reason for limiting the spectral width is to reduce the amount of the data stored. Initially the data are stored locally in SDRAM, with limited capacity, and are dumped to non-volatile data storage at the apogee, as well as after the return to an observation stop altitude. A further step

to reduce the amount of data is to vary the spectral bandwidth of the channels by keeping a high resolution, 67 kHz, at the centre of the band and decrease the resolution by combining channels towards the band edges. By doing this, the number of channels is reduced from 576 to 184. With lossless data compression using the variable resolution over the spectrum, the recorded data set is reduced to approximately 12 MByte/100s observation.

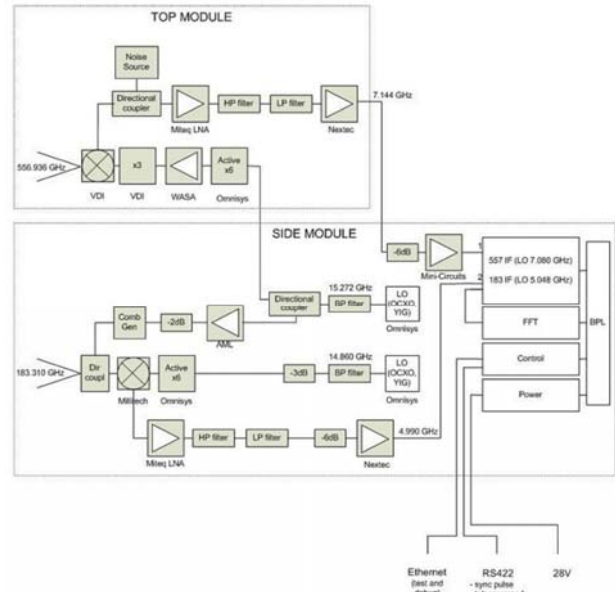


Figure 3. Block diagram of the complete system with the 557 GHz module at the top. LOs for both receivers are located at the 183 GHz base plate as well as the FFT-backend [7].

### III. RECEIVER CALIBRATION

A typical application for a radiometer in atmospheric or radio astronomical observation is to detect very weak signals, buried in noise. If the system noise is completely uncorrelated, i.e. white noise, signal integration over time will reduce the noise according to the radiometric equation [8]:

$$\sigma = \frac{T_{System}}{\sqrt{B \tau}} \quad (1)$$

where  $T_{system}$  is the total system noise ( $T_{antenna} + T_{receiver}$ ),  $B$  is the detection bandwidth,  $\tau$  is the integration time, and  $\sigma$  is the resulting standard deviation. In reality, the noise in a radiometer is a combination of white noise, the DC drift, and 1/f noise. The DC drift and 1/f noise limit the possibility of reducing the noise by integration and an optimum integration time can be calculated from the Allan variance [9]. This means that further integration will not improve the signal-to-noise ratio. Apart from the noise-originated instability of the receiver, the gain of the receiver varies over time. This can, for instance, vary if the physical temperature of the receiver changes and it implies that a calibration of the receiver is needed in order to be able to compensate for the gain drift over the entire observation period. The time periods between

calibration sequences should be well within the characteristic time of the gain instability.

The most common calibration technique for radiometers is use of a Dicke-switch [10], where the reference signals are radiation from a black body at two different and specific temperatures,  $P_{Hot}/P_{Cold}$ . The received power can be calculated according to Planck’s black body radiation law in the Rayleigh-Jeans limit [8], and, assuming a perfectly matched single-mode waveguide, the received power can be calculated as

$$P = k_B BT \tag{2}$$

where  $k_B$  is the Boltzmann’s constant,  $B$  is the detection bandwidth, and  $T$  is the brightness temperature of the black body. The receiver noise temperature is then calculated according to a well-known relation

$$T_e = \frac{T_{Hot} - Y * T_{Cold}}{Y - 1} \tag{3}$$

where  $Y$  is the ratio  $P_{Hot}/P_{Cold}$ , i.e. the IF output power of the radiometer when exposed to the different loads. This technique calibrates the entire receiver chain (optics, mixer, and LNAs) and is usually implemented by employing a chopper wheel or a mechanical switch placed in the receiver input beam. A common problem of the standard Dicke-switch calibration technique is that no measurements can be performed during the calibration cycle, hence precious observation time has to be sacrificed.

However, due to a very harsh environment on board the rocket, in terms of shock and vibration, as well as space constraints and extremely short observing time, a calibration system without any moving parts, a fully electronic calibration system, is preferred for PHOCUS. For example, a signal from a broadband calibrated noise source, instead of the hot load, could be injected through a directional coupler between the RF-horn and the mixer as in [11], but unfortunately at 183 GHz and 557 GHz such noise source is not commercially available.

The driver for the 183 GHz calibration system on the PHOCUS rocket was to consider the above mentioned criteria, e.g. no moving parts and the space constraints. To achieve this, a calibration system with a stable pilot signal injected through a directional coupler [12] (-13dB coupling) between the RF-horn antenna and the mixer was introduced. The pilot signal is placed 40 MHz away from the 183.31 GHz water absorption line, the target for the observation, and thus allows continuous calibration without any loss of observation time. With this calibration technique it is assumed that all receiver back-end channels experience the same gain variations in the time domain. The pilot signal is generated from the LO source for the 557 GHz radiometer, which has a base frequency of 15.727 GHz. The reference signal is extracted from the LO through a 20 dB directional coupler, amplified and fed to a harmonic mixer generating the pilot signal at 183.264 GHz (12<sup>th</sup> harmonic). The block diagram of the radiometer with its calibration system can be seen in Figure 4. The amplifier

operates in saturation in order to keep the amplitude of the generated output calibration signal insensitive to small fluctuations in the reference signal supplied.

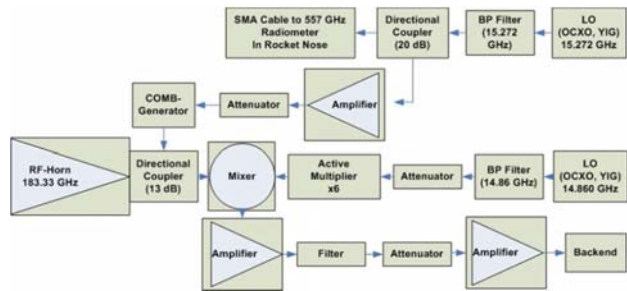


Figure 4. Layout of the 183 GHz system with the calibration signal extracted from the LO-path for the 557 GHz radiometer.

Right before the launch, the receiver noise temperature is measured by standard Y-factor technique in order to obtain an absolute temperature reference. This is done by placing a hot and cold load outside the rocket at the signal window. During this calibration, the level of the pilot signal referenced to the noise floor (ratio should be the same for hot- and cold loads) is recorded. During the flight, any drift of the gain in the receiver chain will result in a level change in the pilot signal relative to the baseline noise level.

The receiver temperature and the pilot signal measurements performed in the laboratory are presented in Figure 5 and Figure 6. The mean value and standard deviation are plotted together with the noise temperature, where the mean is calculated for the central channels where the resolution is the highest, 67 kHz. At the band edges, the channels are combined in order to reduce the data storage. The data in Figure 5 and Figure 6 are integrated over 10 seconds and the calibration accuracy (repeatability) is estimated to less than 2 % and is calculated as

$$\Delta = (Peak\ Hot - Baseline\ Hot) - (Peak\ Cold - Baseline\ Cold) \tag{4}$$

$$Uncertainty\ (\%) = \frac{\Delta}{Peak - Baseline} \times 100 \tag{5}$$

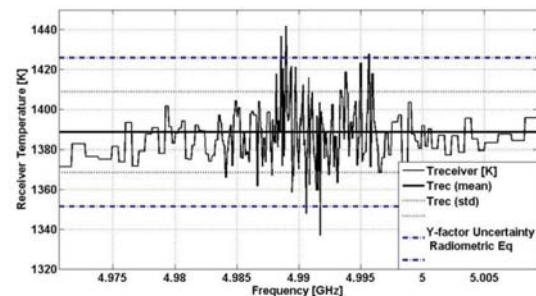


Figure 5. Laboratory measurements of the 183 GHz receiver noise temperature.

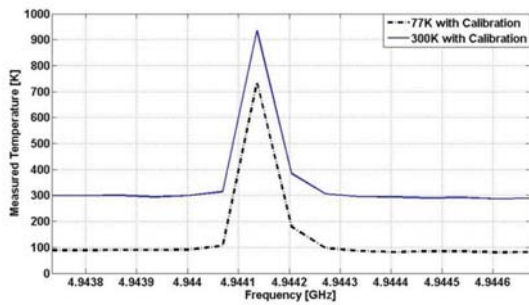


Figure 6. Pilot signal with liquid nitrogen and room temperature loads.

During the observation period the measurement rate is 300 Hz, resulting in an integration time of 3 ms per spectrum. Notice that the integration time in order to obtain a stable pilot signal is independent on the integration time used for the observation data, which might be shorter in order to dissect the mesosphere and obtain the desired altitude profile. The observations will typically be in blocks of 0.1 s, i.e. integration over 30 spectra.

The 557 GHz radiometer calibration utilizes a different technique. Also this calibration system is fully electronic for the same reasons as pointed out in the previous section. The much higher frequency of this channel makes it more difficult and expensive to generate signals that could be used as a pilot signal while, most importantly, introducing a directional coupler with its associated loss in front of the mixer would substantially increase the system noise. Following these considerations, the 557 GHz radiometer calibration is done by injecting broadband noise from a calibrated noise source, [13], through a directional coupler between the mixer output and the first IF Amplifier (LNA), Figure 7. This scheme limits calibration of the 557 GHz receiver channel to the gain of the IF and back-end parts, the parts probably mostly affected by changing the ambient temperature.

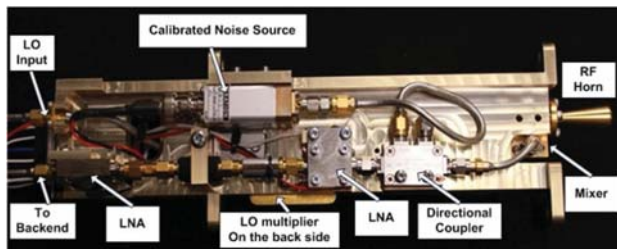


Figure 7. Picture of the 557 GHz radiometer with the horn, noise source, coupler, and LNAs. The mixer and LO-multiplier is located on the back side.

Since any measurements during the calibration would not be feasible, in contrast to the calibration system for the 183.31 GHz radiometer, the calibration is performed before the rocket reaches the altitude where the measurements should start. A second calibration is performed at the trajectory apogee, and the third calibration sequence is done once the rocket has reached an altitude below the region of interest. The drift in the receiver gain is measured between the calibration

periods by measuring the difference between the baseline (independent on the load temperature) and the level with the calibration noise source is switched on. A decrease in the receiver gain would result in a smaller difference between the on/off calibration signal cases. Figure 8 and Figure 9 show the receiver noise temperature of the 557 GHz receiver and the measured temperature levels with the noise source switched on/off for liquid nitrogen and room temperature loads.

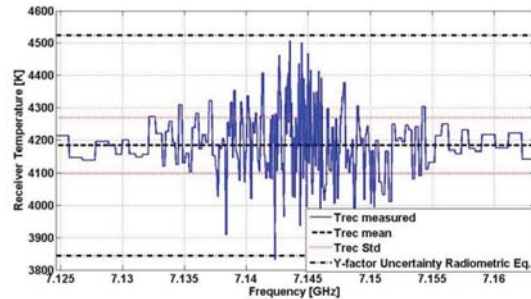


Figure 8. Laboratory measurement of the 557 GHz receiver noise temperature.

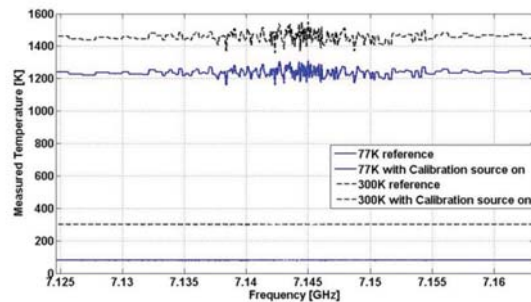


Figure 9. Measured temperatures with calibration source on/off for liquid nitrogen and room temperature loads.

#### IV. CONCLUSION

In this paper, we present the 183 GHz and 557 GHz radiometers for the PHOCUS sounding rocket experiment, with launch date between 4 July - 4 August, 2011. The receiver system together with its specific calibration techniques is described.

#### ACKNOWLEDGMENT

The authors would like to acknowledge Thomas Karlsson and Krister Sjölander at SSC for useful discussion on the instrument-rocket interface design.

#### REFERENCES

- [1] M. Gadsden and W. Schröder, "Noctilucent Clouds (Physics & Chemistry in Space)," Springer-Verlag (November 1989) ISBN: 978-0387506852.
- [2] J. Gumbel, "PHOCUS - Experiment Description" Department of Meteorology (MISU) Stockholm University, 2007.
- [3] Radiometer Physics GmbH, Available at: [www.radiometer-physics.de](http://www.radiometer-physics.de).
- [4] Virginia Diodes Inc. Available at: [www.Vadiodes.com](http://www.Vadiodes.com).
- [5] Omnisys Instruments AB, Available at: [www.Omnisys.se](http://www.Omnisys.se).
- [6] Swedish Space Cooperation (SSC), Available at: [www.sscspace.com](http://www.sscspace.com).

- [7] T. Ekebrand, *SondRad Operation Manual*, 2011-04-04.
- [8] K. Rohlf, and T. Wilson, *Tools of Radio Astronomy, 3rd ed.*, ed. S.-V.B. Heidelberg 2000.
- [9] D.W. Allan, *Statistics of atomic frequency standards*. Proceedings of the IEEE, 1966. **54**(2): p. 221-230.
- [10] R.H. Dicke, *The Measurement of Thermal Radiation at Microwave Frequencies*. Review of Scientific Instruments, 1946. **17**(7): p. 268-275.
- [11] T. Rose, et. al. "Microwave Radiometer Systems for Profiling of Low Water Vapour Concentrations and Temperature in Antarctica and for Polarized Observations of Rain: Instruments, Retrievals and Results. in *8th Int. Symp. On Tropospheric Profiling*", Delft, The Netherlands, 2009.
- [12] P. Meyer and J.C. Kruger, "Wideband crossed-guide waveguide directional couplers", in *Microwave Symposium Digest, IEEE MTT-S International*, 1998.
- [13] Wireless Telecom Group, Inc., Available at: [www.noisecom.com](http://www.noisecom.com).

## Spectrometers for THz radiometers

M. Krus<sup>1</sup>, J. Embretsén<sup>1</sup>, A. Emrich<sup>1</sup>, and S. Back-Andersson<sup>1</sup>

*1 Omnisys Instruments AB\*, Västra Frölunda, Sweden*

\* Contact: ae@omnisys.se, phone +46-31-7343401

**Abstract**—To meet the wide spectrum of requirements in THz radiometers, Omnisys has developed state of the art back-end spectrometers based on Filterbank, Autocorrelation and FFT techniques.

The FilterBank (FB) solution may be optimum for wideband spectrometer requirements with few channels and was selected for the ALMA WVR instrument, covering 0.5-8 GHz divided on four detection channels. Meeting stability requirements, both absolute and relative between channels, is the major challenge for implementing a FB spectrometer. For the ALMA WVR, Omnisys deployed several techniques to meet the very stringent specification and these will be presented.

For high resolution spectroscopy, the FFT based technology is a natural selection. Omnisys is today developing a FFT module capable of processing 5 GHz continuous bandwidth with more than 16 k channels. The module will be 200x120x20 mm and consume 15-25 W depending on configuration (preliminary). This design will be presented.

For wide bandwidth / medium resolution requirements with limited resources, the autocorrelation spectrometer has few competitors. The HIFAS ASIC developed by Omnisys now enable spectrometer designs with up to 6 GHz bandwidth and 1024 channel resolution with only a few watts of power consumption in a very compact package. The ASIC itself is 5x6 mm in size. Examples of complete spectrometer and spectrometer systems will be presented, including the STEAMR 12 GHz wide system, a METOP back-end for 56 GHz line observation and the GUSSTO system with 3x16 spectrometers for balloon based THz observation, each of the 48 pixels being processed with more than 2 GHz bandwidth.

## STEAMR breadboard results and demonstrator status

A. Emrich<sup>1\*</sup>, P.Sobis<sup>1</sup>, J. Embretsén<sup>1</sup>, and K. Kempe<sup>1</sup>

<sup>1</sup> Omnisys Instruments AB\*, Västra Frölunda, Sweden

\* Contact: ae@omnisys.se, phone +46-31-7343401

**Abstract**—Omnisys is responsible for the design and demonstration of the STEAMR instrument hardware. The breadboard phase was concluded in December 2010 and the Demonstration / Engineering Model phase has started in January 2011. The presentation will be on system implementation, test results and expected performance for Flight.

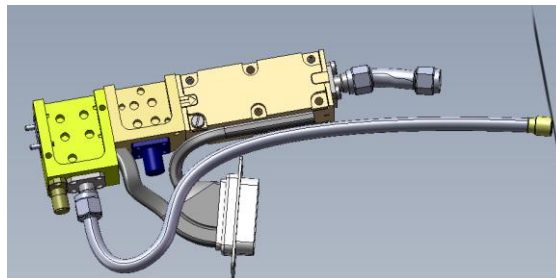
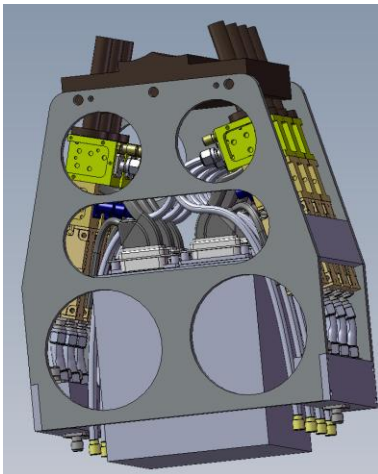
STEAMR is a limb sounding instrument and an array of receivers cover different altitudes without scanning, thus providing an order of magnitude performance improvement compared to a scanned single receiver implementation. STEAMR consist of 14 receivers covering 320-360 GHz with 12 GHz spectrometer bandwidth each.

The upper receiver channels will be based on the DSB principle while Sideband Separation has been considered for the lower altitudes. The pros and cons of using SSB versus DSB are considered from scientific view, based on demonstrated and estimated performance of different SSB implementations. To first order, the SSB implementation implies twice the complexity and power consumption compared to DSB and promise less confusion in the separation of line responses in the two sidebands, while the sensitivity impact is not clear today. Test results used as an input for estimation of scientific impact on different topologies will be presented..

For front-ends, this include planar diode based DSB and IQ mixers (used for SSB) with embedded custom LNA's and different types of LO generation chains. Excellent results have been achieved with both Chalmers/MC2 produced diodes as well as with VDI supplied diodes. These will be presented both for DSB as well as IQ mixer implementations.

For back-ends, this will include the first presentation of a spectrometer covering 6 GHz bandwidth based on a single chip autocorrelator with integrated ADC's. Two has been operated in parallel to meet the 12 GHz specified STEAMR bandwidth. With 14 receivers operating in the array, 168 GHz spectrometer bandwidth will be covered and we are now entering into the THz domain in bandwidth, not only operating frequency. Omnisys has currently >200 ASIC's in storage and about 40-50 is needed for the complete project, including spares.

The front-end's and back-end's have been tested in linearity, stability as well as sensitivity. For the sensitivity, both the Y-method has been used to determine  $T_{rec}$ , complemented with noise estimation in the computed spectra, enabling a determination of impact on sensitivity as a function of autocorrelation efficiency, system stability and other effects on the complete instrument. These effects increase the noise with a factor between 1.08-1.14, i.e. the effective  $T_{rec}$  would rather be about 1540 K with a  $T_{rec}$  determined by the Y-method to 1400 K.



## ALMA WVR final report

M. Wannerbratt<sup>1</sup>, T. Ekebrand<sup>1</sup>, A. Emrich<sup>1</sup>, P.Sobis<sup>1</sup>, U. Krus<sup>1</sup>, S. Back-Andersson<sup>1</sup>, D. Runesson<sup>1</sup> and  
M. Krus<sup>1</sup>

*1 Omnisys Instruments AB\*, Västra Frölunda, Sweden*

\* Contact: ae@omnisys.se, phone +46-31-7343401

**Abstract**—Omnisys is responsible for the design and production of 58 ALMA Water Vapor Radiometers. The design phase was 18 months followed by a production phase of 18 months.

The ALMA design and performance verification will briefly be presented but the focus on the presentation will be on production and test aspects, including optical and radiometric performance. As of December 2010, all 58 radiometers have been shipped to the ALMA site and passed on site acceptance tests.

The radiometers are tested for optical performance as well as radiometric performance in frequency response, stability, sensitivity, linearity and accuracy. The production verification data will be presented and conclusions drawn. This should give good insight for future THz radiometer design, including many aspects such as optical design, calibration system aspects etc.



## Antenna lens array for large scale M-KIDs camera

L. Ferrari<sup>1\*</sup>, A. M. Baryshev<sup>1,3</sup>, J.J.A. Baselmans<sup>2</sup>, and S.J.C. Yates<sup>2</sup>

*1 SRON, Netherlands Institute for Space Research\*, Groningen, 9747 AD, The Netherlands*

*2 SRON, Netherlands Institute for Space Research\*, Utrecht, 3584 CA, The Netherlands*

*3 Kapteyn Astronomical institute, University of Groningen, Groningen, 9747 AD, The Netherlands*

\* Contact: [lorenza@srn.nl](mailto:lorenza@srn.nl), phone +31-50-363 8321

**Abstract**— We are developing antenna-coupled Kinetic Inductance Detectors for large cameras like APEX and NIKA. The basic KID consists of a quarter-wave coplanar waveguide (CPW) resonator. One end of the resonator is coupled to the transmission line while the other one is shorted to ground. A twin-slot antenna focuses incident radiation on the shorted end. The radiation is concentrated and focused on the antenna by silicon elliptical lens segments glued on the back side of the KID sample. Due to Nyquist spatial sampling requirement, the individual lens dimensions are close to the wavelength, which makes geometrical optics approach insufficient. Physical optics calculations are required to achieve a good accuracy. We present the simulations performed with microwave studio CST in order to optimize the antenna and lens design increasing the optical efficiency.

## Optical test facility for SAFARI bolometers

L. Ferrari<sup>1\*</sup>, M.D. Audley<sup>1</sup>, G. De Lange<sup>1</sup>, J. R. Gao<sup>2,3</sup>, D. Griffin<sup>4</sup>, G. Keizer<sup>1</sup>, P. Khosropanah<sup>2</sup>, and P. Mauskopf<sup>5</sup>

*1 SRON Netherlands Institute for Space Research\*, Landleven 12, Groningen, 9747 AD The Netherlands*

*2 SRON Netherlands Institute for Space Research, Sorbonnelaan 2, Utrecht, 3584 CA, The Netherlands*

*3 Delft University of Technology, Lorentzweg 1, Delft, 2628 CJ, The Netherlands*

*4 Rutherford Appleton Laboratory, Harwell Science and Innovation Campus, Didcot OX11 0QX*

*5 Cardiff University, School of Physics and Astronomy, 5 The Parade, Cardiff, CF24 3AA, Wales*

\* Contact: lorenza@srn.nl, phone +31-50-363 8321

**Abstract**— We have developed an optical test facility for Transition Edge Sensor (TES) bolometers for the FIR. This activity is part of the program to develop TES-detectors for the SAFARI instrument, which is an imaging spectrometer on the SPICA satellite. For SAFARI, bolometers for three bands spanning from 30 to 210  $\mu\text{m}$  are required to exhibit a noise performance limited by the celestial background that translates into a detector NEP requirement of  $2 \times 10^{-19} \text{ W}/\sqrt{\text{Hz}}$ . Because of this extreme sensitivity and the limited dynamic range of the TES detectors, optical access to calibration sources operating at room temperature is excluded. We therefore have developed a low temperature, pass-band limited calibration source. Our optical test facility is set up in a dilution refrigerator providing a detector-plate base temperature of 10 mK. FIR radiation is generated by means of a black-body source that can be temperature controlled between 3 K and 35 K. Radiation is coupled to the 5 x 5 detector array using feedhorns. The radiation bands are defined by metal mesh filters. The TES signal readout is performed using lownoise SQUID current sensors. We present the mechanical and thermal design of the detector plate / black body assembly and we hope to present the optical measurements performed on low-power (fW level) TES bolometers.

## The Supercam 8-pixel integrated focal plane unit

C. Groppi<sup>1</sup>, D. Golish<sup>2</sup>, C. Walker<sup>2</sup>, B. Love<sup>2</sup>, C. Kulesa<sup>2</sup>, S. Weinreb<sup>3</sup>, J. Kooi<sup>3</sup>, A. Lichtenberger<sup>4</sup>

(1) Arizona State University, PO Box 871404, Tempe, AZ, 85287, USA

(2) University of Arizona, 933 N. Cherry Ave. Tucson, AZ, 85721, USA

(3) California Institute of Technology, 1200 Colorado Blvd., Pasadena, CA 91125, USA

(4) University of Virginia, 351 McCormick Road, Charlottesville, VA 22904, USA

\* Contact: cgroppi@asu.edu, phone 1-480-965-6436

*Abstract*— The SuperCam 64 beam focal plane is constructed from eight linear array modules with eight pixels each. Each pixel consists of a sensitive, single ended SIS mixer optimized for operation from 320-380 GHz, with measured noise temperatures of ~75K. The array mixers utilize SIS devices fabricated on Silicon-On-Insulator (SOI) substrates, with beam lead supports and electrical contacts. The 1x8 mixer subarrays are constructed from tellurium copper using the splitblock technique. Stainless steel guide pins and screws are used to ensure proper alignment and good contact between parts. A diagonal feedhorn extension block is bolted to the front of the mixer array assembly, extending the diagonal horns to 11mm aperture size. This eliminates the need for dielectric lenses and their associated manufacturing and alignment difficulties. The waveguide environment is designed around full height rectangular waveguide, with a fixed quarter wave backshort. IF outputs from the SIS devices are bonded directly to the input matching networks of low-noise, InP MMIC amplifier modules located in the array mixers. The IF center frequency of the array is 5 GHz. The MMIC chip is contained in an 11mm x 11mm amplifier module that contains integrated bias tees for the SIS device and the amplifier chip. The module achieves noise temperature of ~5 K and delivers 32 dB of gain while consuming only 8 mW of power. Several tests have been performed with these modules to ensure oscillation free operation, low noise, high stability, and no heating effects on the SIS device. Modules have been integrated into both single pixel and 1x8 array mixers, and have shown performance as good or better than expected with connectorized amplifiers. No heating effects are visible, although care must be taken to avoid oscillation due to feedback. Short lengths of semi-rigid cable inside each mixer block ensure that the output from the LNA cannot radiate into the mixer block cavity, preventing oscillations. We present the design, fabrication and measured performance of the Supercam 1x8 FPU modules, along with the design and performance of the integrated LNA modules and SIS devices.

## The Supercam Local Oscillator Multiplexing Unit

C. Groppi<sup>1</sup>, D. Golish<sup>2</sup>, B. Love<sup>2</sup>, C. Kulesa<sup>2</sup>, C. Walker<sup>2</sup>

(1) Arizona State University, PO Box 871404, Tempe, AZ, 85287, USA

(2) University of Arizona, 933 N. Cherry Ave. Tucson, AZ, 85721, USA

\* Contact: cgroppi@asu.edu, phone 1-480-965-6436

*Abstract*— With an array receiver, LO power must be efficiently distributed among pixels. Depending on the mechanical and optical constraints of the array, a balanced distribution can be achieved using quasioptical techniques or waveguide injection. With the quasioptical approach, dielectric beam splitters or holographic phase gratings are used to divide the LO energy between array pixels. We have chosen to use a hybrid waveguide/quasioptical LO power injection scheme. The LO power for the Supercam is provided by a single solid-state, synthesizer-driven source from Virginia Diode Inc. The active multiplier chain consists of a high power solid-state amplifier followed by a series of tunerless, broadband multipliers. The output of the chain is coupled to an eight-way waveguide corporate power divider with splitblock machineable waveguide twists. Each of the eight outputs provides the drive power for a 1x8 subarray via an identical 8 way corporate divider with diagonal waveguide feedhorn outputs. The complete 64-way power divider was constructed with the Kern micromilling machine at the University of Arizona, and consists of 17 waveguide splitblocks. The measured beampattern of the complete LO unit with optics shows that LO power is divided evenly to within 10% over all 64 pixels, with good optical quality and high efficiency. We present the design, fabrication and measured performance of this waveguide multiplexer and its associated LO source and optics unit.

## Terahertz response of YBCO HEB homodyne detectors

A. Hammar\*, S. Cherednichenko, and S. Bevilacqua

*Terahertz and Millimetre Wave Laboratory, Department of Microtechnology and Nanoscience,  
Chalmers University of Technology, SE-41296 Göteborg, Sweden*

\* Contact: arvidh@chalmers.se

We report on the direct response of hot electron bolometers (HEB) used as homodyne detectors. These bolometers were tested at frequencies 0.1-1.6 THz and for a range of temperatures around 77 K. A logarithmic spiral antenna on a silicon lens was used, providing a broad frequency coverage (well above 1 THz). The measured responsivity ranged from 100 to 500 V/W depending on temperature and RF signal frequency, with RF signal power referenced at the input of the silicon lens. Corrections were made for losses in the cryostat window and polarization losses between the signal and antenna. The response time was about 3 ns. With the room temperature readout we estimate the noise equivalent power to be about 1 nW/Hz<sup>1/2</sup>. The bolometer bridges have nominal dimensions 1 μm x 2 μm x 50 nm and are fabricated on sapphire substrates using UV photolithography. A gas laser was used as source for 1.6 and 0.7 THz RF signals, backward wave oscillators at 0.5 THz and Gunn diodes at 0.1 THz. The obtained results show that YBCO bolometers have good prospects for various applications in the terahertz range as fast direct detectors as well as broadband mixers.

## YBCO HEB THz mixers

A. Hammar\*, S. Cherednichenko, and S. Bevilacqua

*Terahertz and Millimetre Wave Laboratory, Department of Microtechnology and Nanoscience,  
Chalmers University of Technology, SE-41296 Göteborg, Sweden*

\* Contact: arvidh@chalmers.se

We report on an experimental investigation of high-Tc superconducting hot electron bolometer (HEB) mixers of YBCO. These mixers were tested at 100 and 530 GHz LO for a range of temperatures around 77 K. The conversion gain of -32 dB was measured at an LO power of about 1 mW (530 GHz) and 0.3 GHz IF. The mixers were integrated with a logarithmic spiral antenna on a silicon lens, providing a broad frequency coverage (well above 1 THz). To measure the incident RF signal power we used the homodyne responsivity (see abstract "*Terahertz response of YBCO HEB homodyne detectors*") which is referenced to the input of the silicon lens where the bolometers were glued. Corrections were made for losses in the cryostat window and polarization losses between the signal and antenna. We made the measurements at different temperatures and different LO power levels which were measured using a quasi optical detector at room temperature. The 3 dB gain bandwidth was measured to be about 0.2 GHz. The bolometer bridges have nominal dimensions 1  $\mu\text{m}$  x 2  $\mu\text{m}$  x 50 nm and are fabricated on sapphire substrates using UV photolithography. Backward wave oscillators sources were used at 530 GHz and Gunn diodes at 100 GHz.

# “32-channel Multi-Chip-Module” The Cryogenic Readout System for Submillimeter/Terahertz Cameras

Yasunori Hibi, Hiroshi Matsuo, Taishi Ookawa, Hirohisa Nagata, Hirokazu Ikeda, and Mikio Fujiwara

**Abstract**— We have been investigating the submillimeter/terahertz camera with the large format SIS (Superconductor - Insulator - Superconductor) photon detector array. To realize the submillimeter/terahertz camera, a cryogenic readout system matching to the SIS detector properties is necessary.

For this readout system, we have developed several kind of ICs (Integrated Circuits) constructed with n-channel GaAs-JFETs. We also have designed and manufactured 32-channel multi-chip-modules with these ICs. These modules can make 32-channel parallel input photo current signals into one or two serial output voltage signal(s). Size of these is 40mm x 30mm x 2mm. The estimated total power dissipation is about 400  $\mu$ W.

**Index Terms**—Application specific integrated circuits, Cryogenics, Gallium arsenide JFETs, Image sensors, Multichip modules,

## I. INTRODUCTION

OBSERVATIONAL astronomers desire to obtain submillimeter/terahertz astronomical observational data comparable to other wavelength/frequency data. To response these desires, developments of various high sensitivity submillimeter/terahertz cameras with many superconductive detector pixels are advancing. In these cameras, trans-edge sensor (TES) bolometers [1], kinetic inductance detectors (KIDs) [2], and superconducting tunnel junction (STJ) detectors [3]-[5] are employed. These superconductive detectors are used in deep cryogenic temperature. Therefore, to realize high performance submillimeter/terahertz cameras with such detectors, the multi-channel readout system workable in cryogenic temperature are required.

Since TES detectors and KIDs detectors are low impedance type detectors, the cryogenic readout system for these detectors must be suitable for low impedance type detectors.

Manuscript received July 31, 2011. This work was partly supported by the Grant-in-Aid for the Scientific Research from the Japan Society for the Promotion of Science (No. 18206042).

Yasunori Hibi, Hiroshi Matsuo, and Taishi Ookawa are with National Astronomical Observatory of Japan, 2-21-1, Osawa, Mitaka, Tokyo 1818588 Japan (corresponding author to provide phone: +81-422-34-3932; fax: +81-422-34-3864; e-mail: yasunori.hibi@nao.ac.jp).

Hirohisa Nagata and Hirokazu Ikeda are with Institute of Space and Astronautical Science, 3-1-1, Yoshinodai, Sagamihara, Kanagawa 2298510 Japan.

Mikio Fujiwara is with National Institute of Information and Communications Technology, 4-2-1, Nukui-Kitamachi, Koganei, Tokyo 1847895 Japan.

Therefore, those readout systems constructed by low input impedance devices such as superconducting quantum interference devices (SQUIDs) or high frequency amplifiers with high electron mobility transistors (HEMTs) have been developed. On the other hand, STJ detectors are relatively high impedance type detectors, the cryogenic readout system for STJ detectors must be suitable for high impedance type detectors.

We planned a cryogenic multi-channel readout system referred to the CMOS camera readout system; one of the room temperature readout system for high impedance type detectors [6]-[9]. To realize this cryogenic readout system, we have developed and investigated some functional cryogenic integrated circuits (ICs) constructed with n-channel GaAs JFETs [10]-[12].

## II. THE N-CHANNEL GAAS JFETS CRYOGENIC PERFORMANCES

As reported in Fujiwara, Sasaki, and Akiba 2002 [13], the n-type GaAs JFETs offer good cryogenic performance. At 4.2K, they show good statistic characteristics even their power dissipation below 1  $\mu$ W. Typical cryogenic characteristics are shown in Fig. 1. Furthermore, GaAs JFETs are also can easily work even at 0.3K [14]. Especially about input referred voltage noise, the value is around  $3 \mu\text{V}_{\text{rms}}/\text{Hz}^{0.5}@1\text{Hz}$  and this value can be suppressed by thermal cure [15] or infrared irradiation [16]. Except performances of these, the gate capacitance which a gate width of 5  $\mu\text{m}$  and a gate length of 100  $\mu\text{m}$  is smaller than 50 fF and the EFET OFF resistance which a gate width of 5  $\mu\text{m}$  width and a gate length of 5  $\mu\text{m}$  is larger than 100 T $\Omega$  [12]. These facts indicate that GaAs JFETs are very suitable for electric switches. In addition, Fujiwara and Sasaki 2004 [15] showed that the FET gate leakage current of these devices is  $10^{-18}$  A or smaller. This suggests that GaAs JFETs may be excellent choice to be combined with high impedance detectors such as STJ detectors. However, p-type GaAs JFETs do not exist commercially, so extra care must be taken when designing the circuits.

## III. THE GAAS JFETS INTEGRATED CIRCUITS

### A. 16-Channel AC-coupled CTIAs

The capacitive trans-impedance amplifier (CTIA) transforms input current signal into low impedance voltage signal. The circuit concept of the AC-coupled CTIA is shown in Fig. 2 a). The reason of taking the “AC-coupled”

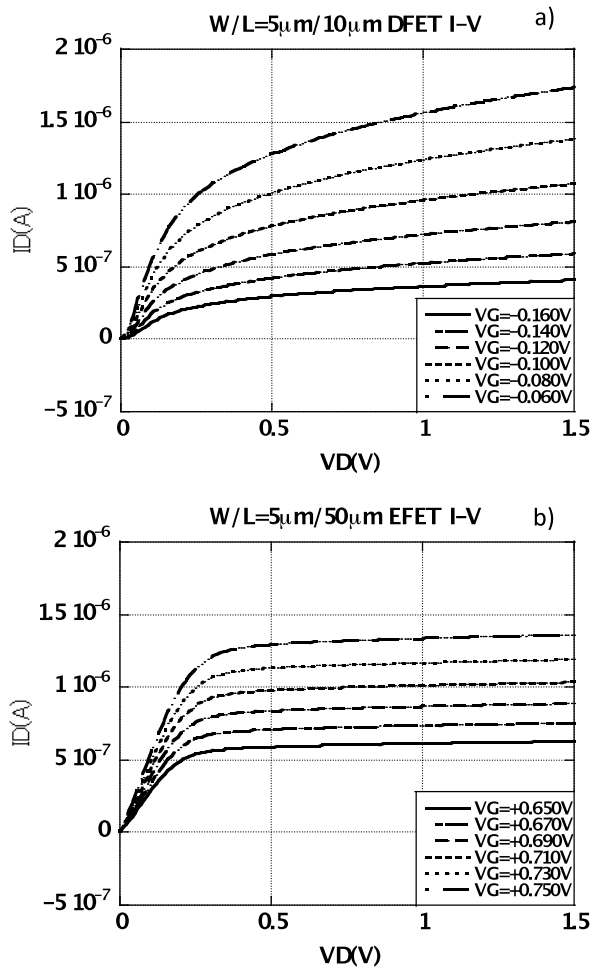


Fig. 1. Typical cryogenic (4.2 K) “ID-VDS” of the GaAs-JFETs when  $V_S=0V$ . The gate size of a) is width of  $5\ \mu m$  and length of  $10\ \mu m$ . And a) is depletion type (when  $V_G=0V$ ,  $I_D \neq 0A$ ) FET. The gate size of b) is width of  $5\ \mu m$  and length of  $50\ \mu m$ . And b) is enhancement type (when  $V_G=0V$ ,  $I_D=0A$ ) FET.

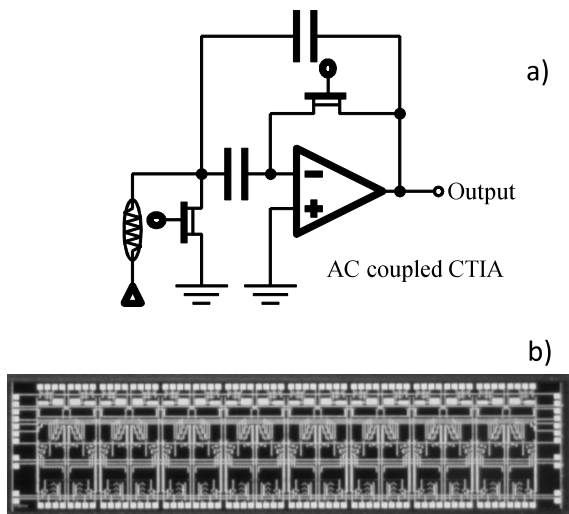


Fig. 2. The circuit concept of the AC-coupled CTIA (a) and the picture of 16-ch AC-coupled CTIAs IC (b).

mechanism is to suppress input offset voltage distribution when many amplifiers are integrated.

From our previous developments, we got 16-channel AC-coupled CTIAs. The power dissipation of this IC is about  $50\ \mu W$  and input offset voltage distribution is lower than  $3\ mV_{p-p}$ . Fig. 2b) shows a picture of 16-ch AC-coupled CTIA. The physical chip size is  $2\ mm \times 8\ mm \times 0.2\ mm$ .

### B. 32:1 Multiplexer with Sample-and-Holds

A multiplexer transforms parallel signals into serial signal. By combining sample-and-holds with the multiplexer, data sampling timings and data output timings can be settled voluntarily. A part of circuit diagram of the multiplexer with sample-and-holds is shown in Fig. 3 a).

We have developed 32:1 multiplexers with sample-and-holds and show this IC in Fig. 3 b). The power dissipation of this IC is about  $30\ \mu W$ . The physical chip size is  $2\ mm \times 8\ mm \times 0.2\ mm$ , too.

### C. 32-Channel Shift Register

A shift register is one of the simple digital memory circuits. We have developed the cryogenic shift register for generating multiplex timings. The circuit diagram of the flip-flop, which is one unit of the shift register, is shown in Fig. 4 a).

There are D (depletion)-type and E (enhancement)-type FETs in the n-type GaAs JFET. Then, one of the simplest digital logic circuit called DCFL (Direct Coupled FET Logic) is able to be realized by GaAs JFETs [19]. By combining such basic logic circuits, we designed and investigated a master-slave type shift register. We have developed 32-channel shift registers and show this IC in Fig. 4 b). The physical chip size is also  $2\ mm \times 8\ mm \times 0.2\ mm$ . The design power dissipation of this IC was  $16\ \mu W$  and the real power dissipation is larger than  $80\ \mu W$ . This is because that device parameter selection is too conservative.

### D. 32-Channel Voltage Distributer

The voltage distributor can distribute differential level voltage signals to each output terminal. Our aim to use the cryogenic voltage distributors is to keep each AC-coupled

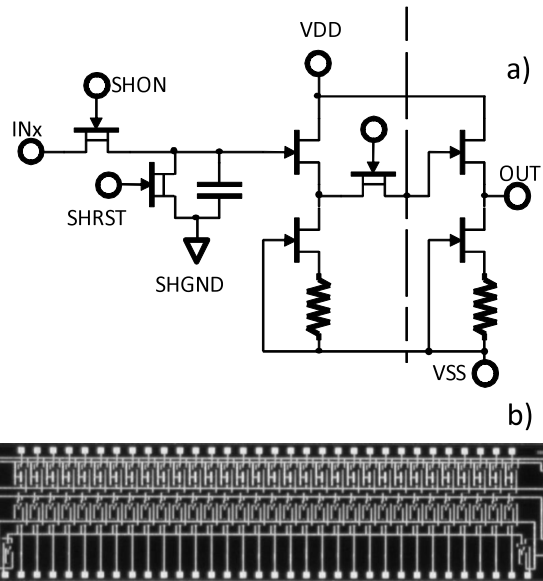


Fig. 3. A part of circuit diagram of the multiplexer with sample-and-holds (a) and the picture of 32:1 multiplexer with sample-and-holds IC (b).



IV. CRYOGENIC READOUT SYSTEM

A. Design Concept

We show the concept of the cryogenic multi-channel readout system in Fig. 6. We referred the multi-channel readout system of the CMOS camera and designed this cryogenic readout system. Operational outline of this system is following. Firstly, parallel input current signals are exchanged to parallel voltage signals by AC-coupled CTIAs. Secondly, the parallel voltage signals are sampled and held by sample-and-holds. Thirdly, the held parallel signals are transformed serial voltage signal by multiplexer operated by shift-register. The unique point of this system is the following. By including shift registers in this cryogenic system, the number of digital addressing lines from warm electronics is reduced. And by inserting two multiplexers operated by shift-registers, the operational dead time can be minimized.

B. The 32-Channel Multitip Module

Based on above concept, we designed and manufactured a 32-channel multi-chip module. This module can transform 32-channel parallel input current signal to 2-channel serial output voltage signals. We show the photograph of this in Fig. 7. This module is made of low temperature co-fired ceramics (LTCC) with 4 wiring layers and 2 ground layers. The size of this module is 40 mm x 30 mm x 2 mm. The estimated total power dissipation of this is around 400  $\mu$ W.

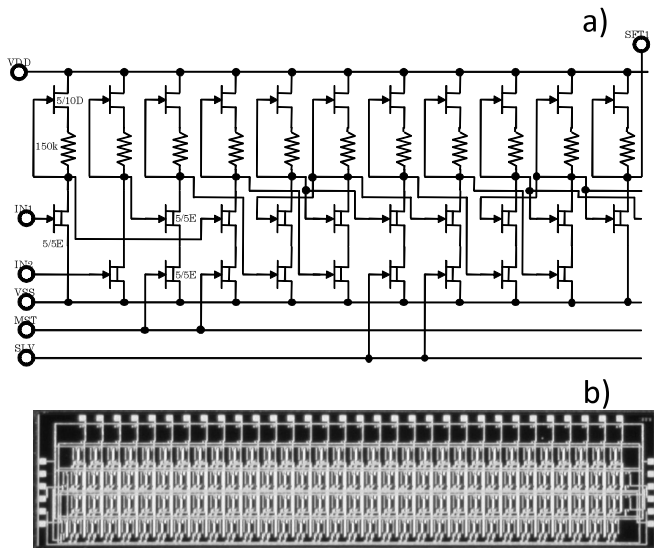


Fig. 4. The circuit diagram of the flip-flop (a) and the picture of 32-channel shift register IC (b). “5/10D” means it is depletion type JFET which gate size is width of 5  $\mu$ m and a gate length of 10  $\mu$ m. And “5/5E” means it is enhancement type JFET which gate size is width of 5  $\mu$ m and a gate length of 5  $\mu$ m.

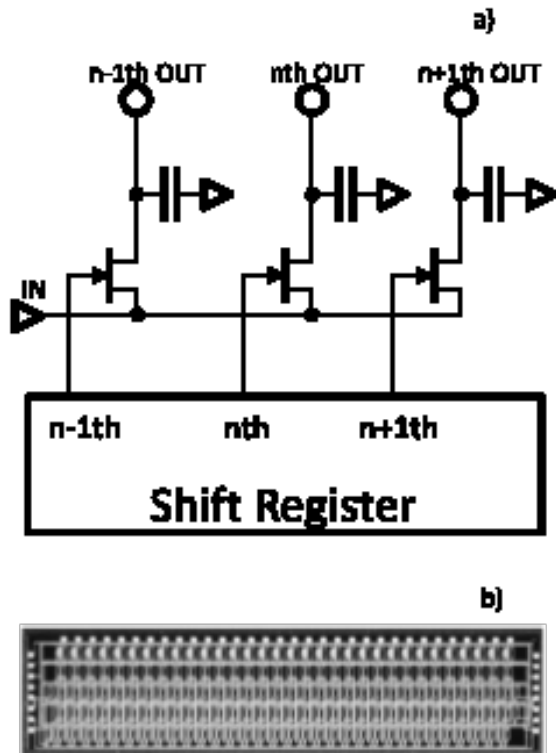


Fig. 5. The circuit concept of the voltage distributor (a) and the picture of 32-channel voltage distributor IC (b).

CTIAs in optimal operating conditions. The circuit concept of the voltage distributor is shown in Fig. 5 a).

We have designed and investigated the 32-channel voltage distributor constructing from the 32-channel shift register and sample-and-holds. We show this IC in Fig. 5 b). The physical chip size is same as previous three ICs. The total power dissipation is about 30  $\mu$ W.

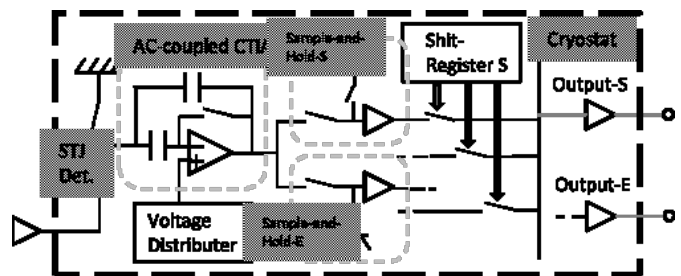


Fig. 6. Schematic of the cryogenic multi-channel readout system. This system has 2 sample-and-holds per 1 AC-coupled CTIA.

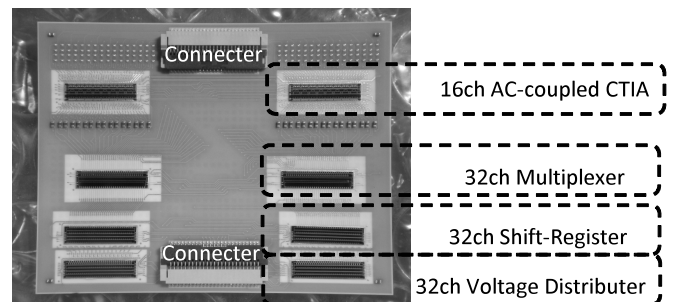


Fig. 7. The picture of the 32-ch cryogenic multichip module. 32-channel parallel input current signals input from upward connector. Output serial voltage signal, supply sources, and digital signals input from downward.

## V. CRYOGENIC TEST ENVIRONMENTS

As shown in Fig. 8 a), we set the multi-chip module into wet type cryostat. For signal input and output, we designed a flexible printed circuit (FPC) with 50 lines. This FPC is shown in Fig. 8 b). The DC power source of this module is generated and supplied by the exclusive room temperature electronics shown in Fig. 8c). And the digital signals for the module operation are generated by the other device and supplied through the electronics. In this test, we used 910 k $\Omega$  metal film resistances for dummy detectors.

## VI. SUMMARY

For realization of a multi-pixel sub-millimeter/terahertz camera, we have developed the multi-channel cryogenic readout system. N-channel GaAs-JFETs offer good cryogenic performances. In particular, the gate leakage current of these JFETs at cryogenic temperatures are extremely low ( $<10^{-18}$  A). This property makes the devices attractive for use with high-impedance cryogenic sub-millimeter/terahertz detectors. Therefore, we have designed and investigated several kinds of cryogenic circuits with GaAs-JFETs: AC-coupled CTIAs, shift registers, multiplexers with sample-and-holds, and voltage distributors. For connecting these circuits, we designed and manufactured the 32-channel multichip module. And we have prepared test devices for cryogenic test of the modules. Just now, we start investigating the 32-channel multichip modules for the submillimeter/terahertz cameras.

## ACKNOWLEDGMENT

We thank SONY Co., Ltd for supporting our development of GaAs JFET electronics.

## REFERENCES

- [1] K. D. Irwin and G. C. Hilton, "Trans-Edge Sensors," *Appl. Phys.*, vol. 99, pp. 63–149, 2005
- [2] S. Doyle, P. Mauskopf, J. Naylor, and A. Porch, "Lumped Element Kinetic Inductance Detectors," *J. of Low Temp. Phys.*, vol. 151, pp. 530–536, 2008
- [3] J. Zmuidzinas and P. L. Richards, "Superconducting Detectors and Mixers for Millimeter and Submillimeter Astrophysics," *Proc. IEEE*, vol. 92, pp. 1597–1616, 2004
- [4] H. Matsuo, H. Nagata, Y. Mori, J. Kobayashi, T. Okaniwa, T. Yamakura, C. Otani, and S. Ariyoshi, "Performance of SIS Photon Detectors for Superconductive Imaging Submillimeter-wave Camera (SISCAM)," *Proc. SPIE*, vol. 6275, 627504-1–627504-9, 2006
- [5] Y. Mori, T. Okaniwa, M. Nakahashi, S. Ariyoshi, C. Otani, H. Sato, and H. Matsuo, "Development of Superconductive Imaging Submillimeter-wave Camera with Nine Detector Elements (SISCAM-9)," *Proc. SPIE*, vol. 6275, 627523-1–627523-12, 2006
- [6] H. Matsuo, Y. Mori, Y. Murakoshi, S. Ariyoshi, H. Ezawa, Y. Hibi, J. Kobayashi, H. Nagata, M. Nakahashi, and C. Otani, "Realization of Submillimeter-wave Imaging Array with Superconductive Direct Detectors," *J. of Low Temp. Phys.*, vol. 151, pp. 304–309, 2008
- [7] H. Matsuo, Y. Hibi, H. Nagata, M. Nakahashi, Y. Murakoshi, H. Arai, S. Ariyoshi, C. Otani, H. Ikeda, and M. Fujiwara, "System Design of Submillimeter-wave Imaging Array SISCAM," *Proc. SPIE*, vol. 7020, 702015-1–702015-9, 2008
- [8] Y. Hibi, H. Matsuo, H. Nagata, H. Ikeda, and M. Fujiwara, "The Cryogenic Digital Readout Module with GaAs JFET ICs," *AIP Conf. Proc.*, vol. 1185, pp. 290–293, 2009
- [9] Y. Hibi, H. Matsuo, H. Nagata, H. Ikeda, and M. Fujiwara, "The Cryogenic Readout System with GaAs JFETs for Multi-pixel Cameras," *Proc. SPIE*, vol. 7854, 78541Z-1–78541Z-11, 2010
- [10] H. Nagata, J. Kobayashi, H. Matsuo, M. Nakahashi, K. Kobayashi, H. Ikeda, and M. Fujiwara, "Fabrication of Cryogenic Readout Circuits with N-Type GaAs-JFETs for Low Temperature Detectors," *J. of Low Temp. Phys.*, vol. 151, pp. 1022–1027, 2008
- [11] H. Nagata, H. Matsuo, Y. Hibi, J. Kobayashi, M. Nakahashi, H. Ikeda, and M. Fujiwara, "GaAs Cryogenic Readout Electronics for High

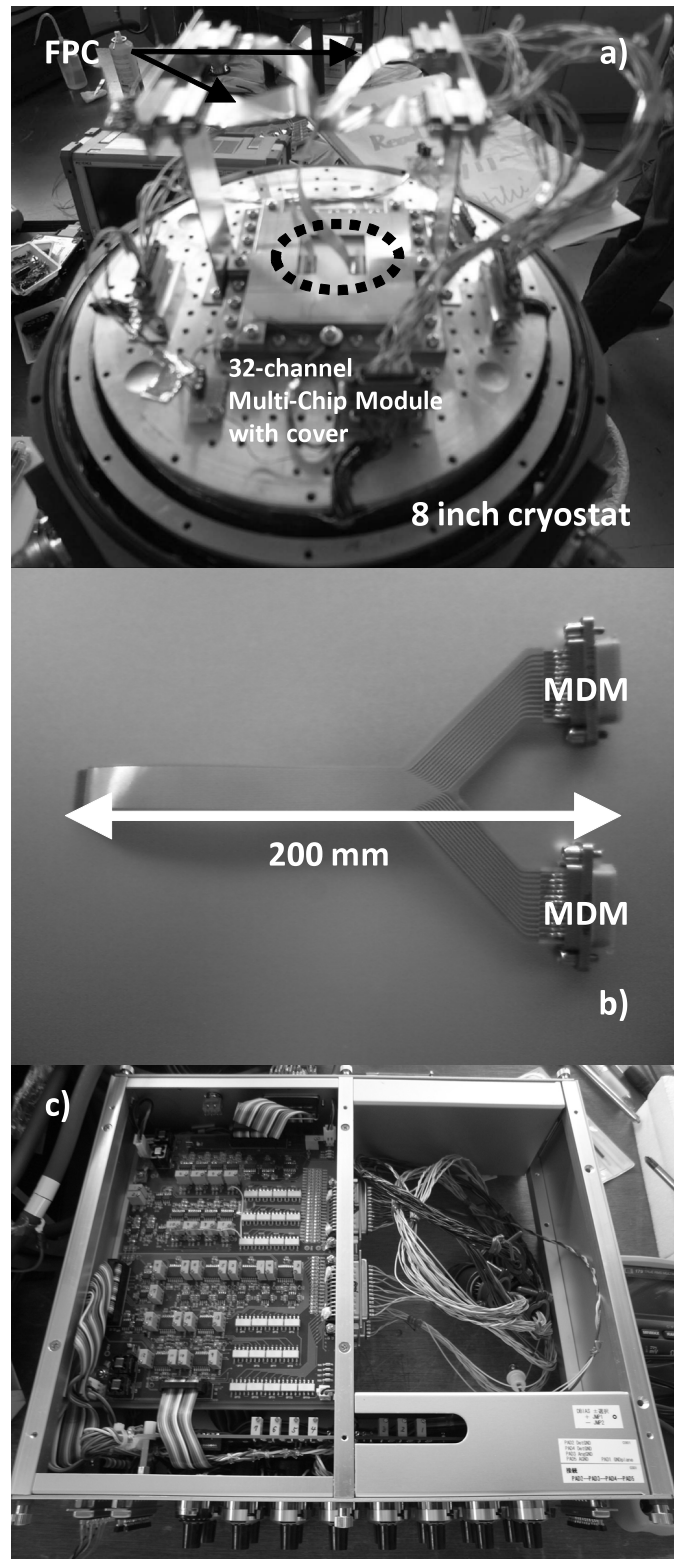


Fig. 8. Photographs of measurement environments. a) Inside of the wet type cryostat. b) FPC itself. c) The exclusive room temperature electronics.

- Impedance Detector Arrays for Far-Infrared and Submillimeter Wavelength Region,” *Cryogenics*, vol. 49, 676–679, 2009
- [12] Y. Hibi, H. Matso, H. Arai, H. Nagata, H. Ikeda, and M. Fujiwara, “The Cryogenic Multiplexer and Shift Register for Submillimeter-wave Digital Camera,” *Cryogenics*, vol. 49, 672–675, 2009
- [13] Fujiwara, M., Sasaki, M., Akiba, M., “Reduction Method for Low-Frequency Noise of GaAs Junction Field-Effect Transistor at a Cryogenic Temperature,” *Appl. Phys. Lett.*, vol. 80, 1844–1846, 2002
- [14] Nagata, H., Kobayashi, J., Matsuo, H., Fujiwara, M., “Progress on GaAs Cryogenic Readout Circuits for SISCAM,” *Proc. SPIE*, vol. 6275, 627527-1–627527-10, 2006
- [15] Fujiwara, M., Sasaki, M., “Performance of GaAs JFET at a Cryogenic Temperature for Application to Readout Circuit of High-Impedance Detectors,” *IEEE Trans. Electron. Dev.*, vol. 51, 2042–2047, 2004
- [16] Fujiwara, M., Sasaki, M., Nagata, H., Matsuo, H., “Optical Control of Low Frequency Noise Behavior in Cryogenic GaAs Junction Field Effect Transistor,” *Cryogenics*, vol. 49, 626–629, 2009

## 1.1 THz Multi-pixel Heterodyne Receiver for APEX

N. Hurtado<sup>1\*</sup>, U. U. Graf<sup>1</sup>, C. E. Honingh<sup>1</sup>, K. Jacobs<sup>1</sup>, M. P. Westig<sup>1</sup>, R. Güsten<sup>2</sup> and J. Stutzki<sup>1</sup>

<sup>1</sup> KOSMA, I. Physikalisches Institut, Universität zu Köln, Zùlpicher Str. 77, 50937 Köln, Germany

<sup>2</sup> Max-Planck-Institut für Radioastronomie (MPIfR), Auf dem Hügel 69, 53121 Bonn, Germany

\* Contact: hurtado@ph1.uni-koeln.de, phone +49-221-470 3549

This program is supported by the BmbF Verbundforschung under grant number 05A08PK2.

*Abstract*— We present the current development of a 9 pixel 1.1 THz heterodyne receiver for APEX in the Atacama Desert, Chile. The multi-pixel receiver greatly enhances the science output under the difficult observing conditions in this wavelength regime.

In a heterodyne array receiver, each detector beam has to be collimated individually before combining the beams in the common optics. This task is performed by the focal plane unit (FPU) modeled after the CHARM (Compact Heterodyne Array Receiver Module)<sup>1</sup> concept. The FPU consists of 3x3 pixels, each of them formed by a two mirror collimator arranged as an off-axis Cassegrain system and a feed horn. We employ a monolithic integrated optics approach, so no internal optics alignment is required.

The 1.1 THz focal plane array optics has been designed and is being built in our workshop. We performed simulations of the beams at the current frequency. We are confident that the simulations predict the performance correctly, because a similar design of the focal plane for 345 GHz was successfully built and tested. Its near field pattern simulations and measurements agreed very well. In this setup the large collimation mirrors and thus the beams, are arranged on a rectangular grid, with the feed horns and small illumination mirrors located in the gaps between the individual collimation mirrors/beams. The collimator was optimized to keep the mirrors as flat as possible; this together with the small reflection angles of 38° minimizes optical aberrations.

The LO power distribution is accommodated behind the FPU. A collimating Fourier grating<sup>2</sup> splits the LO beam in three identical beams which get coupled to three feed horns in the LO distribution plate at the rear side of the FPU. Each horn feeds a coupler structure, that supplies the LO power for a row of 3 mixers, thus supplying LO signal to all 9 pixels of the array. Different possibilities of the LO coupling design/fabrication are being analyzed and will be based on in-house hybrid waveguide/planar technology. The LO coupler is interfaced with balanced mixers, probably of a similar design as the on chip balanced SIS mixer at 490 GHz that is developed in our institute.

Two similar self-contained 3x3 beam receiver cartridges - one per polarization - will be installed in the cryostat and thus form the entire receiver. To accommodate the cartridges in the cryostat, we are developing a new simple thermal link<sup>3,4</sup> without screws to connect the cartridges to the cryostat.

---

<sup>1</sup> T. Lüthi, D. Rabanus, U. U. Graf, C. Granet, and A. Murk. Expandable fully reflective focalplane optics for millimeter- and submillimeter-wave array receivers. Review of Scientific Instruments, 77:4702, January 2006.

<sup>2</sup> U. U. Graf and S. Heyminck. Fourier Gratings as Submillimeter Beam Splitters. IEEE Trans. AP, 49(4):542–546, April 2001.

<sup>3</sup> A. Orłowska, M. Harman, B. Ellison, 2002, ALMA Project Book, chapter 6, Receiver Cryogenics System in <http://www.alma.nrao.edu/>

<sup>4</sup> M. S. Yokogawa, Y. Sekimoto, M. Sugimoto et al. 2003 PASJ, Vol. 55, pp. 519-525 “Plug-in Cryogenic System for Cartridge-Type SIS Receivers”/

# Development of THz Quantum Cascade Laser as a Local Oscillator for Heterodyne Receivers

Y. Irimajiri<sup>1\*</sup>, S. Shiba<sup>1,2</sup>, N. Sekine<sup>1</sup>, I. Hosako<sup>1</sup>, T. Koyama<sup>1,3</sup>, T. Yamakura<sup>4</sup>, H. Maezawa<sup>3</sup>, and S. Yamamoto<sup>2</sup>

<sup>1</sup> National Institute of Information and Communications Technology\*, Koganei, Tokyo, Japan

<sup>2</sup> Dept. of Physics, The University of Tokyo, Bunkyo-ku, Tokyo, Japan

<sup>3</sup> Solar-Terrestrial Environment Laboratory, Nagoya University, Chikusa-ku, Nagoya, Japan

<sup>4</sup> University of Tsukuba, Department of Physics, Tsukuba, Ibaragi Japan

\* Contact: irimaji@nict.go.jp, phone +81-42-327 6089

**Abstract**— We are developing THz-QCL (quantum cascade laser) as a local oscillator for heterodyne receivers. THz-QCLs are made of GaAs/Al<sub>0.15</sub>Ga<sub>0.85</sub>As using resonant LO phonon scattering depopulation scheme, and processed in a metal-metal waveguide using gold-gold thermo compression wafer bonding technique. CW mode operation of the THz-QCL has been achieved up to a heat-sink temperature of 74 K at the lasing frequency of 3.1 THz using a device with the size of 40 μm wide and 1.5 mm long fabricated by dry-etching method. The peak output power was measured to be about 34 μW at a heat-sink temperature of 15 K. We have also detected the QCL output with an HEB (Hot Electron Bolometer) mixer as a change in the I-V characteristic of the HEB mixer. The HEB mixers using an NbTiN ultra thin film as the superconducting material are coupled with the THz radiation by a quasi-optics twin slot antenna. The receiver noise temperature was measured to be 5600K in DSB.

## I. INTRODUCTION

THz-QCLs (Quantum cascade lasers) are compact, high output power and high frequency purity coherent CW sources and are promising THz radiation sources as a local oscillator for heterodyne receivers. THz-QCLs have potential for various applications such as security, foods inspection, medical, non-destructive inspection, imaging, and spectroscopic observation in astronomy or atmospheric science from a balloon-borne [1] or a space-borne [2], [3] system in THz region (0.1 – 10 THz).

In the frequency range from millimeter wave up to ~2 THz, combination of a solid state oscillator and frequency multiplier chains can be used as a local oscillator for heterodyne receivers. However, this method can no longer provide enough power for operation of HEB mixers above that frequency. THz-QCLs are promising solution for this problem, because it has good spectral purity and enough output power (order of mW) to drive HEB mixers. For this purpose, THz-QCLs have to be operated in the

continuous wave (CW) mode under the relatively high-temperature operation by liquid nitrogen or Peltier cooling. Stabilization of the frequency and the line width for THz-QCLs of the order of  $\Delta f/f \sim 10^{-7} \sim 10^{-8}$  is required for spectrum measurements. With these in mind, we are developing THz-QCLs for heterodyne receivers. So far we have succeeded in developing THz-QCL that can be operated in the CW mode at 3.1 THz up to heat-sink temperature of 74 K, and evaluating a performance of HEB mixer combined with the THz-QCL.

## II. DESIGN AND FABRICATION OF THz-QCL

In this study, metal-metal type waveguide structure was selected because this type of THz-QCLs has low threshold current (i.e. low power consumption). The output power is expected to be an order of 10 mW, which is lower than that of SISP (semi-insulation surface plasmon) type. However, the output power of the metal-metal type THz-QCLs should practically be enough for driving the HEB mixer because the required power for the HEB mixer is an order of 100 nW [4]. In practical use, the necessary power is about 10 μW in minimum there are various losses due to imperfect optical alignments and the beam splitter coupling efficiency of 10 % or less.

The design of the QC structure is referred to the GaAs/Al<sub>0.15</sub>Ga<sub>0.85</sub>As resonant LO phonon scattering scheme, which achieved the CW operation up to 117 K at 3.0 THz [5], [6]. The thickness of each layers are **4.9**/**7.9**/**2.5**/**6.6**/**4.1**/**15.6**/**3.3**/**9** (nm) (bold fonts represent Al<sub>0.15</sub>Ga<sub>0.85</sub>As). The THz-QCL are fabricated in Photonic Device Lab. of NICT. First, we grow 178 periods of the QC structure about 10 μm thick on a semi insulating GaAs substrate by Molecular Beam Epitaxy (MBE), and confirm that the error is less than 1 % from the design by X-ray diffraction measurement. For the metal-metal waveguide structure, we deposit a 350 nm thick gold film both on this epi-wafer and the n-GaAs substrate, and bond them by using the gold-gold thermo

compression wafer bonding method. After removing the substrate of the epi-wafer side, we fabricate a Fabry-Perot resonator whose size is 40  $\mu\text{m}$  in width and 1.5 mm in length by using a dry etching process. Finally we wrap the n-GaAs substrate down to about 180  $\mu\text{m}$  thickness to improve thermal conduction. Figure 1 shows a SEM image of the device, where the side surface is etched almost vertically. The fabricated THz-QCL is mounted on a chip carrier using Au-Sn eutectic alloy, and is wire-bonded with  $\phi 18 \mu\text{m}$  gold wire.

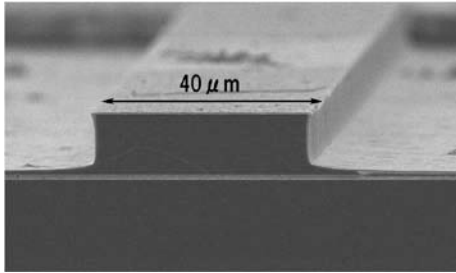


Fig. 1. SEM image of the fabricated THz-QCL device.

### III. MEASUREMENT RESULTS

#### A. IVL characteristics

Figure 2 shows a measurement setup of IVL characteristics of the THz-QCL. The device is cooled in a flow-type liquid helium dewar, where the temperature is controlled by a heater. The output power of the THz-QCL is detected by a liquid-helium-cooled Ge bolometer or a Pyro electric detector. The THz-QCL is operated in CW mode and the output power is modulated by an optical chopper and is measured with a lock-in detection. Prior to the measurements, the optical alignment is tuned as much as possible with the aid of the He-Ne laser. Figure 3 shows the IV (current-voltage), IL (current-laser power), and differential resistance characteristics of the THz-QCL measured under various heat-sink temperatures. This device has achieved the maximum output power of about 34  $\mu\text{W}$  at a heat-sink temperature of 15 K. Both the threshold current density (147  $\text{A}/\text{cm}^2$ ) and output power are relatively low in comparison with the results given in the earlier studies [5, 6], which may come from insufficient optimization of doping density in our case and so on. It should be noted that the laser oscillation threshold seems fairly higher than differential resistance jump. Hence there is a possibility that a low-level output power which is undetectable with the present detection system may come out even below the oscillation threshold down to the differential resistance jump position. The consuming power of this device is about 1 W. The IL curve exhibits hysteresis; it differs between

increasing and decreasing bias current. The laser output was measured up to the heat-sink temperature of 74 K, and the characteristic temperature  $T_0$  is derived to be 14 K. The temperature of the THz-QCL device should be higher than the heat-sink temperature due to the high thermal resistance at the metal bonding surface.

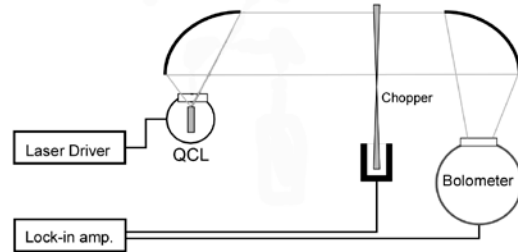


Fig. 2. Measurement setup of IVL characteristics of the THz-QCL.

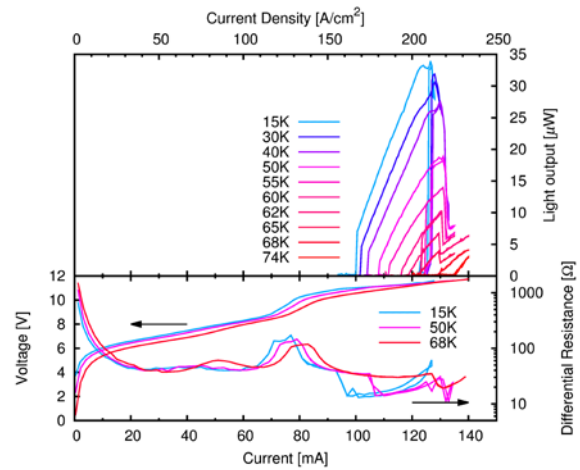


Fig. 3. Measured IVL characteristics of the THz-QCL.

#### B. Spectra characteristics

We measured the THz-QCL spectrum using a Fourier transform spectrometer. Figure 4 shows examples of the measured spectra. The longitudinal mode oscillating frequencies for the main modes are 3.07 THz and 3.09 THz, which are close to the designed frequency. The frequency difference of 25 GHz corresponds to Fabry-Perot mode for the resonance length of 1.5 mm and the refraction index of 4. The oscillating frequency can be changed by varying the operating temperature or the bias current. Although the frequency resolution of FTIR is about 3 GHz, we can actually see the change by determining the center frequency of the spectrum carefully through the Gaussian fit (Figure 5). Tuning sensitivities by the heat-sink temperature and the bias current are roughly estimated to be 90 MHz/K and 30 MHz/mA, respectively, although the dependences on the heat-sink temperature and the bias current are not linear. This frequency variation is caused by change

of refractive index or cavity length by temperature difference [7], [8]. We also see the mode hopping during the temperature and bias tuning.

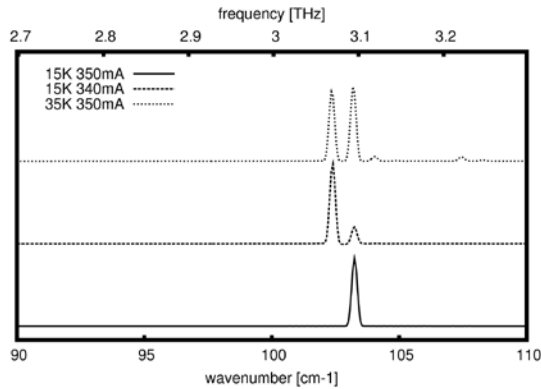


Fig. 4. Measured spectrum of the THz-QCL at different heat-sink temperature and bias current.

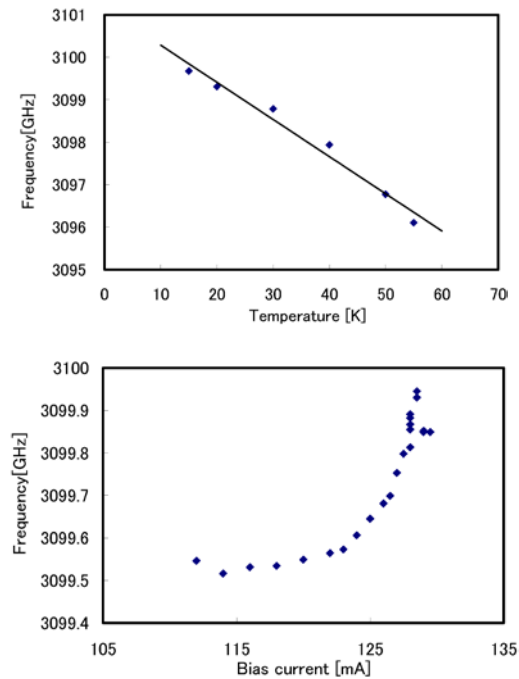


Fig. 5. Oscillation frequency dependence of the THz-QCL within a Fabry-Perot mode at 3.09 THz on the operation temperature (upper) and the bias current (bottom).

### C. Combination of the THz-QCL with the HEB mixer

The output power of the THz-QCL is fed into the HEB mixer, where the HEB mixer and the THz-QCL are mounted on the different dewar and cooled by liquid helium. The HEB mixer was cooled to 4 K and the operating temperature of THz-QCL was around 25 K by its own heat in the CW mode operation.

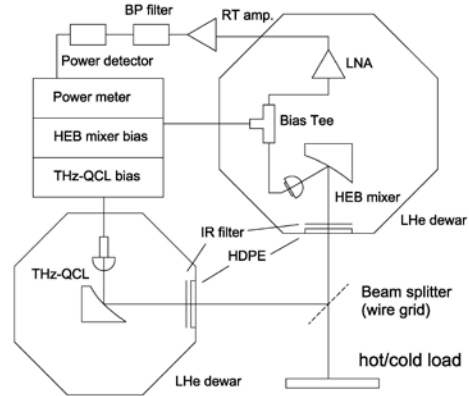


Fig. 6. Measurement setup of combination of the THz-QCL with the HEB mixer.

Each dewar has a window of high density polyethylene with 1 mm thickness and an infrared filter of Zitex G104. The transmission of these films is estimated to be about 90 % on the basis of the FTIR measurement. To focus the THz-QCL beam, an anti-reflection coated hyper hemispherical Si lens made of high resistivity silicon (10 kΩ/cm) is attached [9]. The measurement setup is shown in Figure 6.

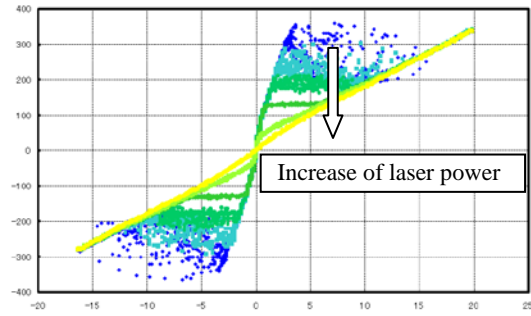


Fig. 7. IV characteristics of the HEB mixer with different laser input. The critical current decreases with increasing the laser input power.

The HEB mixer employed utilizes the superconducting NbTiN film with thickness of about 10 nm deposited on the Si substrate. The HEB device is fabricated in the University of Tokyo [10]. The size of the micro bridge structure is 2 μm in width and 0.3 μm in length. For the coupling with the THz radiation, a quasi-optical twin-slot antenna pattern is used. The laser output is vertically polarized and we used a wire grid as a beam splitter to couple the THz-QCL output to the HEB mixer, where the coupling efficiency is controlled by its tilt angle. As shown in Figure 7, the critical current of the HEB mixer decreased with increasing input laser power, which indicates that the laser power was detected by the HEB mixer. The receiver noise temperature was measured by using Y-factor method. The Y-factor of

about 0.15 dB is obtained, which corresponds to the receiver noise temperature of 5600 K (DSB) considering Callen & Welton's law [11]. This value is not so good in comparison with the other reports [12]-[14], because the HEB mixer and the antenna pattern are not designed for the THz-QCL frequency (3.1 THz) but for the 2.5 THz band. Furthermore we need to optimize the optics between the THz-QCL and the HEB mixer. When these effects are corrected, the receiver noise temperature becomes 2100 K. Because only the optical loss is considered in this correction, this performance can be achieved if higher LO power is available and the optical path is evacuated.

Furthermore our result is obtained with the NbTiN HEB mixer. So far, the NbN superconducting film is always used for the HEB mixer in the frequency region higher than 1.5 THz. Our result demonstrates for the first time that the HEB mixer using the NbTiN superconducting film can achieve the comparable performance in such a high frequency region.

## V. SUMMARY

We have developed THz-QCL which can be operated at 3.1 THz in the continuous wave mode up to a heat-sink temperature of 74 K. The receiver noise temperature in DSB was demonstrated to be 5600 K by using the THz-QCL as a local oscillator combined with the HEB mixer. Phase-locking of the THz-QCL and further improvements such as higher power and higher operation temperature for the THz-QCL are necessary.

## REFERENCES

- [1] Irimajiri, T. Manabe, S. Ochiai, H. Masuko, T. Yamagami, Y. Saito, N. Izutsu, T. Kawasaki, M. Namiki, I. Murata, "BSMILES—A Balloon-Borne Superconducting Submillimeter-Wave Limb-Emission Sounder for Stratospheric Measurements," *Geosci. Remote Sensing Lett.*, vol.3, no.1, pp.88-92, 2006.
- [2] S. Ochiai, S. Tsujimaru, Y. Irimajiri, T. Manabe, and I. Murata, "Stratospheric ozone and ClO measurements using balloon-borne submillimeter limb sounder," *IEEE Trans. Geosci. Remote Sensing*, vol. 43, no. 6, pp.1258-1265, 2005.
- [3] K. Kikuchi, T. Nishibori, S. Ochiai, H. Ozeki, Y. Irimajiri, Y. Kasai, M. Koike, T. Manabe, K. Mizukoshi, Y. Murayama, T. Nagahama, M. Sano, S. Sato, M. Seta, C. Takahashi, M. Takayanagi, H. Masuko, J. Inatani, M. Suzuki, and M. Shiotani, "Overview and Early Results of the Superconducting Submillimeter-Wave Limb-Emission Sounder (SMILES)," *J. Geophys. Res.*, 115, D23306, doi: 10.1029/2010JD014379, 2010.
- [4] L. Jiang, S. Shiba, T. Shiino, K. Shimbo, N. Sakai, T. Yamakura, Y. Irimajiri, P. G. Ananthasubramanian, H. Maezawa, and S. Yamamoto, "Development of 1.5 THz waveguide NbTiN superconducting hot electron bolometer mixers," *Supercond. Sci. Technol.*, 23 2010.
- [5] S. Kumar, B. S. Williams, S. Kohen, Q. Hu, and J. L. Reno, "Continuous-wave operation of terahertz quantum-cascade lasers above liquid-nitrogen temperature," *Appl. Phys. Lett.*, vol.84, no.14, pp.2494-2496, 2004.
- [6] B. S. Williams, S. Kumar, Q. Hu, and J. L. Reno, "Operation of terahertz quantum-cascade lasers at 164K in pulsed mode and at 117K in continuous-wave mode," *Opt. Express*, vol.13, no.9, pp.3331-3339, May 2005.
- [7] A. L. Betz, R. T. Boreiko, B. S. Williams, S. Kumar, Q. Hu, and J. L. Reno, "Frequency and phase-lock control of a 3 THz quantum cascade laser," *Opt. Lett.*, vol.30, no.14, pp.1837-1839, 2005.
- [8] D. Rabanus, U. U. Graf, M. Philipp, O. Ricken, J. Stutzki, B. Vowinkel, M. C. Wicner, C. Walther, M. Fischer, and J. Faist, "Phase locking of a 1.5 Terahertz quantum cascade laser and use as a local oscillator in a heterodyne HEB receiver," *Opt. Express*, vol.17, no.3, pp.1159-1168, 2009.
- [9] A. W. M. Lee, Q. Qin, S. Kumar, B. S. Williams, Q. Hi, and J. L. Reno, "High-power and high-temperature THz quantum-cascade lasers based on lens-coupled metal-metal waveguides," *Opt. Lett.*, vol.32, no.19, pp.2840-2842, 2007.
- [10] T. Yamakura, "Development of THz band quasi-optical hot-electron bolometer mixer employing superconducting NbTiN microbridge," dissertation, University of Tsukuba, 2010.
- [11] A. R. Kerr, "Suggestions for Revised Definitions of Noise Quantities, Including Quantum Effects," *IEEE Trans. Microw. Theory Tech.*, vol.47, no.3, pp.325-329, 1999.
- [12] J. R. Gao, J. N. Hovenier, Z. Q. Yang, J. J. A. Baselmans, A. Baryshev, M. Hajenius, T. M. Klapwijk, A. J. L. Adam, T. O. Klaassen, B. S. Williams, S. Kumar, Q. Hu, and J. L. Reno, "Terahertz heterodyne receiver based on a quantum cascade laser and superconducting bolometer," *Appl. Phys. Lett.*, 86, 244104, 2005.
- [13] P. Khosropanah, W. Zhang, J. N. Hovenier, J. R. Gao, T. M. Klapwijk, M. I. Amanti, G. Scalari, and J. Faist, "3.4 THz heterodyne receiver using a hot electron bolometer and a distributed feedback quantum cascade laser," *J. of Appl. Phys.*, 104, 113106, 2008.
- [14] J. R. Gao, M. Hajenius, Z. Q. Yang, J. J. Baselmans, P. Khosropanah, R. Barends, and T. M. Klapwijk, "Terahertz Superconducting Hot Electron Bolometer Heterodyne Receivers," *IEEE Trans. On Appl. Superconductivity*, vol.17, no.2, 2007.



## In-orbit Performance and Current Status of the SMILES Mission

K. Kikuchi<sup>1\*</sup>, S. Mizobuchi<sup>1</sup>, T. Nishibori<sup>1</sup>, R. Sato<sup>1</sup>, Y. Irimajiri<sup>2</sup>, S. Ochiai<sup>2</sup>, F. Ohtsubo<sup>3</sup>, K. Mizukoshi<sup>3</sup>,  
H. Ozeki<sup>4</sup>, T. Manabe<sup>5</sup>, and M. Shiotani<sup>6</sup>

*1 Japan Aerospace Exploration Agency, Ibaraki, Japan*

*2 National Institute of Information and Communications Technology, Tokyo, Japan*

*3 Advanced Engineering Services Co. Ltd., Ibaraki, Japan*

*4 Toho University, Chiba, Japan*

*5 Osaka Prefecture University, Osaka, Japan*

*6 Kyoto University, Kyoto, Japan*

\* Contact: kikuchi.kenichi@jaxa.jp, phone +81-50-3362-5580

*Abstract*—In this presentation, we will describe in-orbit performance and current status of the Superconducting Submillimeter-Wave Limb-Emission Sounder (SMILES). Unfortunately the SMILES has stopped atmospheric observation since April 2010 owing to some instrumental failures, but intensive activities for data analysis are still in progress.

The SMILES was launched and attached to the International Space Station (ISS) in September 2009. The SMILES had been conducting atmospheric observations since 12 October 2009 with the aid of a 4 K mechanical cooler and Superconductor-Insulator-Superconductor (SIS) mixers for submillimeter limb-emission sounding in the frequency bands of 624.32-626.32 GHz and 649.12-650.32 GHz. On the basis of the observed spectra, the data processing has been retrieving vertical profiles for the atmospheric minor constituents in the middle atmosphere, such as O<sub>3</sub> with isotopes, HCl, ClO, HO<sub>2</sub>, BrO, and HNO<sub>3</sub>. Results from the SMILES have demonstrated its high potential to observe atmospheric minor constituents in the middle atmosphere.

A notable feature of the SMILES is a high sensitivity of the submillimeter receiver thanks to the SIS technology. The SMILES receiver shows a system noise temperature of <380 K for single sideband operation. The output fluctuation of each spectral channel by radiometric noise is around 0.4 K for each spectrum that acquired every 0.5 s. The measured performance in orbit is consistent with the results of prelaunch tests on the ground and satisfies the specifications.

The SMILES has had troubles in critical subsystems: failure of Gunn diode used in the local oscillator occurred on 21 April 2010, and degradation of cooling power of the Joule-Thomson cryocooler found in June 2010. Although the SMILES terminated observation operation, analysis of the data obtained for a half year is still ongoing. In-orbit calibration and additional ground test results will be implemented in the ground data processing system.

## Operating of the superconducting integrated receiver channel of the TELIS atmospheric sounder.

O. S. Kiselev<sup>1\*</sup>, M. Birk<sup>2</sup>, P. N. Dmitriev<sup>1</sup>, A. B. Ermakov<sup>1</sup>, L. V. Filippenko<sup>1</sup>, H. Golstein<sup>3</sup>, B. van Kuik<sup>3</sup>, A. de Lange<sup>3</sup>, G. De Lange<sup>3</sup>, A. M. Selig<sup>3</sup>, P. Vogt<sup>2</sup>, G. Wagner<sup>2</sup>, and V. P. Koshelets<sup>1</sup>

<sup>1</sup> Kotel'nikov Institute of Radio Engineering and Electronics of Russian Academy of Sciences, Moscow, Russia

<sup>2</sup> DLR German Aerospace Centre, Remote Sensing Technology Institute, D-82234 Wessling, Germany

<sup>3</sup> SRON Netherlands Institute for Space Research, P.O. Box 800, 9700 AV Groningen, the Netherlands

\* Contact: kiselev@hitech.cplire.ru, phone +7-495-629-34-18

**Abstract**— A Superconducting Integrated Receiver (SIR) was proposed more than 10 years ago and has since then been developed up to the point of practical applications. We have demonstrated for the first time the capabilities of the SIR technology for heterodyne spectroscopy both in the laboratory and at remote operation under harsh environmental conditions for atmospheric research. Within a SIR the main components needed for a superconducting heterodyne receiver such as an SIS-mixer with quasi-optical antenna, a Flux-Flow oscillator (FFO) as the local oscillator, and a harmonic mixer to phase-lock the FFO are integrated on a single chip. Light weight and low power consumption combined with broadband operation and nearly quantum limited sensitivity make the SIR a perfect candidate for future airborne and space-borne missions. The noise temperature of the SIR was measured to be as low as 120 K, with an intermediate frequency band of 4 – 8 GHz in double sideband operation; the spectral resolution is well below 1 MHz. The SIR was implemented in the three-channel balloon-borne instrument TELIS (TErahertz and submillimeter LIMb Sounder) that detects spectral emission lines of stratospheric trace gases (like ClO and BrO). These gases even in small quantities can have a significant impact on the atmosphere because they speed up certain chemical processes, such as ozone depletion.

The SIR is very sensitive to external electromagnetic interference and temperature variations, but specially developed shielding, novel design of the SIR itself and sophisticated operating algorithms provide stable operation of the device. During the flight the SIR should perform extremely stable and reliable – some measurements last about an hour. The changing of the LO frequency for next measurement should be as fast as possible (about 1 min).

## Dual-Chip Power Combiner using 300 GHz Tripler with Diamond Heat-Spreaders

Choonsup Lee<sup>1\*</sup>, Lorene Samoska<sup>1</sup>, Robert Lin<sup>1</sup>, Bertrand Thomas<sup>2</sup>, Alain Maestrini<sup>3</sup>, Imran Mehdi<sup>1</sup>

*1 Jet Propulsion Laboratory, California Institute of Technology, Pasadena, CA 91109*

*2 Radiometer Physics GmbH, Meckenheim, Germany*

*3 Universite Pierre et Marie Curie-Paris 6, LERMA, Paris, France*

\* Contact: Choonsup.Lee@jpl.nasa.gov, phone +1-818-393 7140

**Abstract**—Currently several Watts of power in W-band (75-100 GHz) are available attributable to recent advances in GaN-based MMIC power amplifiers. Unfortunately, the current first stage GaAs multiplier in chain driven by W-band amplifier cannot handle that much power because of the elevated temperature problem which limits power handling capability. Therefore, the power handling capability of the first stage multiplier is the limiting factor for more output power at the entire terahertz frequency band in multiplier chain LO sources. Our group had proposed, implemented, and presented ‘diamond heat-spreader’ on the backside of the multiplier in order to reduce the operating temperature of the multiplier and obtained 100 % increase in power handling capability in the past. In this paper, we have applied the multipliers with diamond heat-spreader to a dual-chip power combiner at 300 GHz to obtain additional doubling of the power handling capability of the multipliers by utilizing the power combining technique.

Tests of a dual-chip power combiner with diamond heat-spreader in the range of 260-300 GHz band showed that the conversion efficiency remained flat at approximately 8% up to 470 mW input power, with 37 mW of output power. For the same dual-chip power combiner without diamond heat-spreader, the conversion efficiency drops from 12% to 10 % at 200 mW input power due to heating of the diodes, with 23 mW of output power. 200 mW is the highest input power dual-chip without diamond can tolerate while dual-chip with diamond is able to handle 470 mW input power. It is important to note that these frequency multipliers were not originally designed for diamond heat spreaders, and that optimized design tuned for the additional dielectric material loading to the waveguides should operate with higher conversion efficiency. We will present the measurement results of power sweep and frequency sweep.

# Initial Terahertz Probing of Carbon Nanofiber Composite Coatings as Potential Quasi-Optical THz Shielding and Attenuation Devices

Lei Liu<sup>1\*</sup>, Tao Wang<sup>1</sup>, Abhijit Biswas<sup>1</sup>, and Constantine M. Megaridis<sup>2</sup>

*1 Department of Electrical Engineering, University of Notre Dame\*, Notre Dame, IN 46556*

*2 Department of Mechanical and Industrial Engineering, University of Illinois at Chicago, Chicago, IL 60607*

\* Contact: lliu3@nd.edu, phone +1-574-631-1628

*Abstract*— Electromagnetic waves in the terahertz frequency range (0.1 – 10 THz) have remained the least explored and developed in the entire spectrum, thus creating what is widely known as the “THz gap.” In recent years, there has been an unprecedented growth in the development of terahertz devices, circuits and systems due to their promising applications in astronomy, chemical analysis, biological sensing, imaging and security screening. THz sources based on Schottky diodes and quantum cascade lasers (QCL) currently provide plenty of output power, covering a broad frequency range. Improvements in transistor technology also have enabled the demonstration of THz amplifiers and integrated circuits up to 300 GHz. It is predicted that THz-based communication systems with data rates of 5-10 Gb/s or higher will replace today’s wireless LAN systems in 10 years. With the increasing speed of the above electronic circuits and systems, Electromagnetic interference (EMI) shielding in the THz region is becoming more important. THz EMI shielding may also find applications in security, defense and astronomy to protect information detectable by THz imaging and sensing techniques. In addition, effective THz attenuation devices are required in many quasi-optical systems (e.g. THz spectroscopy and imaging), where not much research has been done to date. Therefore, new innovations in materials and processes for EMI shielding and attenuation of THz electronic devices are of immense interest for a number of advanced technology applications.

In this paper, we report our initial work on THz characterization of carbon nanofiber (CNF) composite coatings using a room temperature frequency domain terahertz spectroscopy and imaging system. The system was developed on the basis of a broadband quasi-optical zero bias Schottky diode detector. The detector was designed to cover the frequency range of 100 GHz to 900 GHz. A responsivity of 300-1000 V/W has been measured, and the noise equivalent power (NEP) is 5-20 pW/ $\sqrt{\text{Hz}}$ . The system was calibrated by measuring Mylar thin films and metal mesh filters. For prototype demonstration, several polymer-based large area CNF coatings containing different CNF/polymer weight ratios were characterized in the frequency range of 190-210 GHz, and 570-630 GHz. A THz shielding effectiveness (SE) of ~ 24 dB, and ~ 32 dB, respectively, were measured for the coating with the highest possible CNF content (~ 14 wt%), in the two examined regions. The coating attenuation level can be modified by varying CNF loading content. Two-dimensional distributions of power attenuation of these coatings at 600 GHz have been measured to evaluate the coating spatial uniformity. A coating uniformity of less than 5% has been demonstrated, and the coatings may have high potential for quasi-optical THz shielding and attenuation applications. These CNF coatings also hold the promise for inkjet-printing of light-weighted, cost-effective and flexible THz quasi-optical components such as grid-polarizers and filters.

# Investigation of a Simple Truncated Waveguide Phase Shifter

N.P. Lourie, D.T. Chuss, R.M. Henry, E.J. Wollack, *Senior Member, IEEE*

**Abstract**— The design, fabrication, and performance of simple phase shifters based upon truncated circular and square waveguide cross-sections are presented. An emphasis is placed upon validation of simple analytical formulae that describe the propagation properties of the structure. A test device was fabricated and tested at 30 GHz. We find that the return loss bandwidth for a given phase shifter volume can be maximized by setting the average of the two cutoff wavelengths in the delay section equal to that of the parent homogenous waveguide structure. The concepts explored and validated here can be directly applied to improving the performance of dual-mode millimeter and sub-millimeter waveguide components.

**Index Terms**— Circuit Synthesis and Modeling, Phase Shifter, Polarization, Waveguide Components

## I. EXTENDED ABSTRACT

In symmetric square and circular waveguides, homogeneous propagation occurs for both polarization states. Truncating the cross-section of the waveguide introduces an asymmetry between the cutoff wavelengths in the structure's dominant modes of propagation. In this phase shifter design approach, the overall phase delay between the two modes is controlled via the degree of asymmetry in the propagation constants and the overall length of the truncated guide used in the structure. For dual-mode phase shifters it is desirable to achieve minimal and balanced reflection performance for both polarizations states. In this paper we propose and validate a design approach that achieves this goal using simple truncated square and circular waveguides as a worked example.

To realize a balanced reflection match for both polarization states, we investigate phase shifters for

which the cutoff wavelength of the parent waveguide is equal to the average of those for the modes propagating in the truncated guide. This can be contrasted with the simplest traditional adiabatic phase shifter design wherein the cutoff wavelength for one mode typically is set equal to that of the parent guide for manufacturing simplicity. As a result, a mismatch occurs between the differing polarizations. In such an adiabatic phase shifter design, the overall length of the phase shifter must be increased in order to mitigate this increase in return loss for one of the polarizations. The proposed matching condition yields propagation constants that are homogeneous on average with respect to the parent guide and enables use of a shorter phase shifter length.

We explore and present calculations for the cutoff wavelengths of truncated square and circular waveguides as a function of the cross-section's degree of truncation. Analytic expressions for the truncated guide's eigenvalues are derived via perturbation theory and compared with numerical simulations. We find that the analytical expressions are of sufficient accuracy to be used to enable design of the structure when used in a simple transmission line circuit model that incorporates the phase shift due to additional impedance matching steps added to the guide cross-section.

Using this approach, we have designed and fabricated a test device based on a truncated circular waveguide design. The test results are compared to a full-wave simulation of the device. The prototype device was found to work as expected given the fabrication tolerances held in manufacture. The concepts explored and validated here can be directly applied to improving the performance of dual-mode millimeter and sub-millimeter waveguide components.

Manuscript received May, 27 2011.

N.P. Lourie is with the National Aeronautics and Space Administration (NASA) Goddard Space Flight Center (GSFC) / ADNET Systems Inc., Greenbelt, MD 20771 USA (e-mail: Nathan.Lourie@gmail.com).

D.T. Chuss is with the NASA GSFC, Code 665, Greenbelt, MD 20771 USA (e-mail: david.t.chuss@nasa.gov).

R.M. Henry is with the NASA GSFC, Code 551, Greenbelt, MD 20771 USA (e-mail: ross.m.henry@nasa.gov).

E.J. Wollack is with the NASA GSFC, Code 665, Greenbelt, MD 20771 USA (email: edward.j.wollack@nasa.gov).

## Advances Towards an ALMA Band-1 Receiver

F.P.Mena<sup>1\*</sup>, N. Reyes<sup>1,2</sup>, P. Zorzi<sup>1</sup>, C. Jarufe<sup>1,2</sup>, J. Pizarro<sup>2</sup>, L. Bronfman<sup>2</sup>, J. May<sup>2</sup>

*1 Electrical Engineering Department, Universidad de Chile, Av. Tupper 2007, Santiago, Chile*

*2 Astronomy Department, Universidad de Chile, Camino El Observatorio 1515, Santiago, Chile*

\* Contact: pmena@ing.uchile.cl, phone +56-2-978 4888

This work received support from the Center of Excellence in Astrophysics and Associated Technologies (PBF 06) and from the ALMA-CONICYT Fund for the Development of Chilean Astronomy (Projects 31080003 and 31080004).

**Abstract**—Despite its low frequency range, band 1 of ALMA (30–45 GHz) presents several challenges for its realization. In particular, the required noise temperature of the system (17 K at 80% of the band) combined with the design of the antenna imposes stringent requirements on low noise amplifiers and focusing optics. A preliminary analysis of the optics sets the specifications of the amplifiers on a maximum noise temperature of 10 K (five times the quantum limit) and a minimum gain of 20 dB. Here we present our recent efforts towards achieving these requirements. Furthermore, we will present the results of construction and characterization of several parts necessary for the future implementation of the receiver.

# Test of a Waveguide Orthomode Transducer for the 385-500 GHz Band

Alessandro Navarrini, Christopher Groppi, Robert Lin and Goutam Chattopadhyay

**Abstract**—We report on the construction and test results of a waveguide Orthomode Transducer (OMT) for the 385-500 GHz band. The OMT is based on a symmetric reverse-coupling structure and consists of two copper alloy blocks in split-block configuration fabricated using numerically controlled (CNC) milling machining. Test results of a first prototype OMT employing standard UG387 flanges at all ports were described at the previous ISSTT Symposium. Here, we report on experimental results of a second OMT version utilizing custom made mini-flanges and much shorter input and output waveguides. This second OMT version is tolerant to misalignment errors of the block halves, has improved performance over the first prototype, and covers a wider band than initially specified. From 325 to 500 GHz the measured input reflection coefficient of the second prototype OMT was less than -10 dB, the transmission was  $\approx -1$  dB, and the isolation was less than -30 dB at room temperature for both polarization channels.

**Index Terms**—Orthomode transducer, polarization splitter, reverse coupling structure, waveguide components.

## I. INTRODUCTION

An Orthomode Transducer (OMT) is a passive device that separates two orthogonal linearly polarized signals within the same frequency band. An OMT has three physical ports but exhibits properties of a four-port device because the input common port, usually a waveguide with a square or circular cross-section, provides two electrical ports that correspond to the independent orthogonal polarized signals. Highly symmetric OMT structures are required to avoid the excitation of higher order modes and achieve broad relative bandwidths (up to 40% or wider.) Only few broadband waveguide OMT designs have been demonstrated to work well at frequencies greater than  $\approx 100$  GHz: the two-fold symmetric Boïfot junction [1]-[4] and its double-ridge variant [5]-[6], *b*) the four-fold symmetric turnstile junction [7]-[9], *c*) and the reverse-coupling waveguide structure [10]-[12]. In [12] we

A. Navarrini is with IRAM (Institut de Radio Astronomie Millimétrique), Saint Martin d'Hères, 38406 FRANCE (phone: +33(0)476-8249-41; fax: +33(0)476-5159-38; e-mail: navarrin@iram.fr).

C. Groppi is with ASU School of Earth and Space Exploration, Tempe, AZ 85287 USA (e-mail: cgroppi@asu.edu).

R. Lin and G. Chattopadhyay are with NASA-Jet Propulsion Laboratory, Pasadena, CA 91109 USA (emails: Robert.H.Lin@jpl.nasa.gov and goutam@jpl.nasa.gov).

reported on test results of a first prototype reverse-coupling 385-500 GHz OMT with standard UG387 flanges; the design of a second OMT version with much shorter input and output waveguides, expected to be more tolerant to fabrication errors was also presented. Here, we report on fabrication and test results of that second OMT version which utilizes custom-made mini-flanges and has much improved performance over the first prototype.

## II. DESIGN

The 385-500 GHz reverse-coupling structure OMT with short input and output waveguides (second version) is shown in Fig. 1. It is based on a 2 mm long square waveguide input (Port 1,  $0.56 \times 0.56$  mm<sup>2</sup>) and two single-mode waveguide outputs: a 4.8 mm long standard WR2.2 waveguide ( $0.56 \times 0.28$  mm<sup>2</sup>) for Pol 2 (Port 3), and a 0.3 mm long oval waveguide with full-radius corners (external cross-section  $0.62 \times 0.28$  mm<sup>2</sup>) for Pol 1 (Port 2). The inner structure of the OMT consists essentially of: *a*) the square waveguide input that transitions to a 2.35 mm long full-height WR2.2 rectangular waveguide through a two-section transformer; the transformer is cascaded with a  $90^\circ$  E-plane rectangular-to-oval waveguide bend; *b*) two symmetric  $90^\circ$  waveguide hybrid couplers on the sidearms utilizing reactively terminated ports; *c*) an E-plane  $180^\circ$  waveguide hybrid (Y-junction) to recombine the out-of-phase signals from the two backward coupling structures. As a comparison, the longer waveguide sections in the first OMT prototype were: 11.3 mm for the

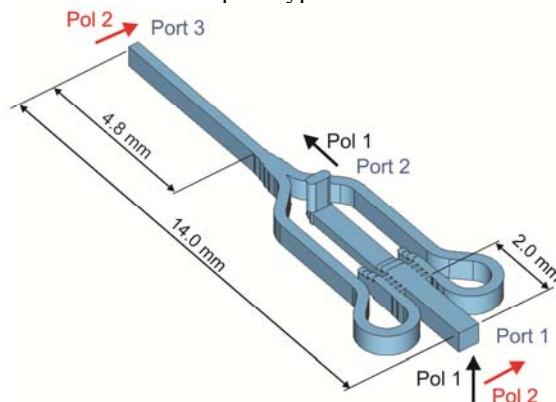


Fig. 1. Waveguide structure of the reverse-coupling OMT (second prototype with mini-flanges at all ports) showing the short square waveguide input (2 mm long) and outputs (0.3 mm long oval waveguide, 4.8 mm WR2.2 waveguide).

square waveguide input, 10.8 mm for the WR2.2 output and 1.0 mm for the oval waveguide output.

Results of the electromagnetic simulation of the OMT of Fig. 1, performed with a commercial software<sup>1</sup>, were presented in [1].

### III. MECHANICAL BLOCKS

The OMT consists of two mechanical blocks and is fabricated by splitting the structure of Fig. 1 along the E-plane of the side-coupled rectangular waveguides. The device has external dimensions 19 x 26 x 28 mm<sup>3</sup> and accepts mini-flanges at all ports. Circular pockets (diameter 20 mm) are machined into the blocks to reduce the waveguide lengths. Photographs of the assembled OMT and of its two unassembled blocks are shown, respectively in Fig. 2 and Fig. 3. The blocks were fabricated at Arizona State University (ASU) in 145 Copper alloy (unplated) using a Kern Micro numerically controlled milling machine. Photographs showing the internal details of the blocks are illustrated in Figs. 4. The blocks were aligned using two precision 1/16" diameter dowel pins. The tolerances for the waveguide channels in the two blocks and of the alignment between the blocks were specified at  $\pm 5 \mu\text{m}$ . The blocks were bolted together by four 4-40 stainless steel screws. The achieved tolerances were all better than  $\pm 3 \mu\text{m}$ .

Four 25.4 mm long waveguide transitions were also

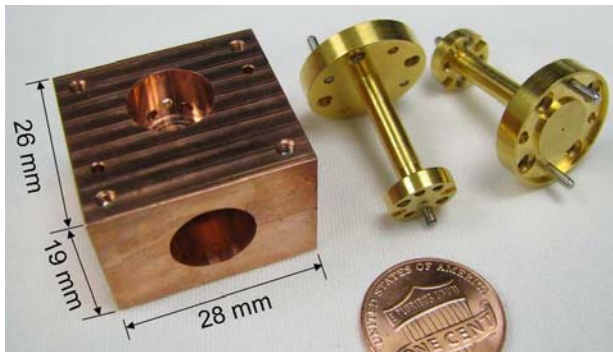


Fig. 2. Photograph of the assembled OMT (second prototype) with custom mini-flanges at all ports. Two of the test transitions with standard UG387 flange at one end and custom mini-flange at the other end are shown on the right.

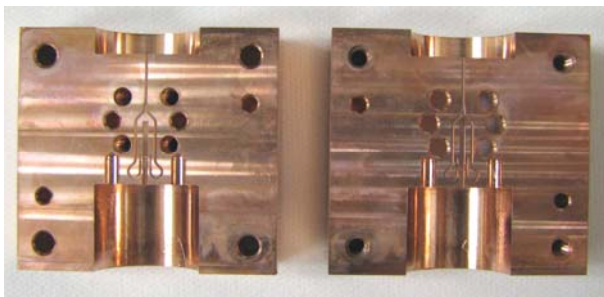


Fig. 3. Photograph of the two unassembled blocks of the OMT showing the internal waveguide circuitry.

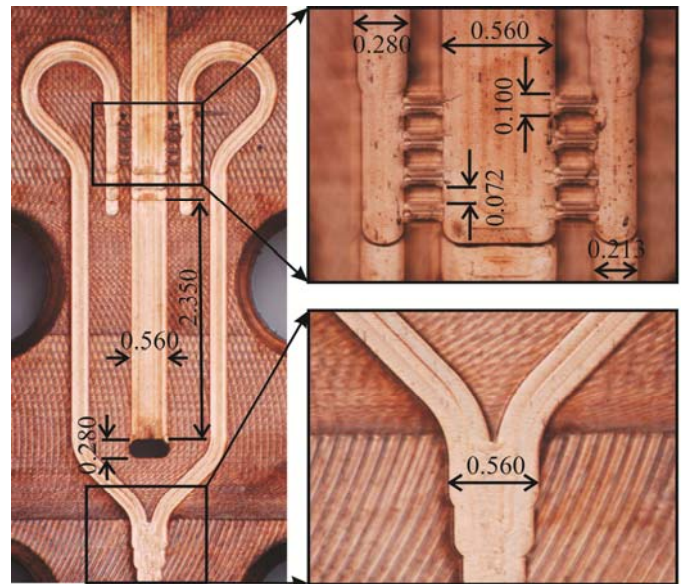


Fig. 4. Photograph of the internal circuitry of one of the two OMT blocks showing the dual-side reverse-coupling waveguide structure (close-up view on the upper right) and the details of the Y-junction power combiner (close-up view on the lower right.) The oval waveguide is visible on the left image.

fabricated<sup>2</sup> to allow testing of this second OMT version: *a*) two identical transitions linearly tapered from 0.56x0.56 mm<sup>2</sup> square waveguide to WR2.2 waveguide (employing custom mini-flange on the square waveguide and standard UG387 on the WR2.2 waveguide), and *b*) two identical straight sections of WR2.2 waveguide (employing custom-made mini-flange at one end and standard UG387 flange at the other end). Two of the test transitions (one of each type) are shown in Fig. 2.

### IV. EXPERIMENTAL RESULTS

The OMT was tested at JPL (Jet Propulsion Laboratory) using a Vector Network Analyser (VNA) consisting of a HP8510C Network Analyser and submillimeter-wave OML test set extensions. The VNA was calibrated at the WR2.2 rectangular waveguides outputs of the extension heads using two-port calibrations with WR2.2 calibration kit. The calibration procedure was used to remove systematic instrumental effects and to calibrate out the response of the instrument up to the chosen calibration planes. Additional measurements of the two pairs of identical back-to-back transitions allowed to calibrate out their individual losses and to derive the S-parameters of the OMT at the physical ports of the device.

A schematic of the Pol 2 transmission test setup is shown in Fig. 5. The square waveguide input of the OMT was attached to the WR2.2 waveguide port of the network analyser through the WR2.2 waveguide-to-square waveguide transition. The transition was oriented to excite the Pol 2 in the OMT. The WR2.2 waveguide output of the OMT was attached to the second WR2.2 waveguide port of the analyser through a straight section of WR2.2 employing a custom mini-flange on the OMT end and UG387 flange on the other end. The oval

<sup>1</sup> CST Microwave Studio, CST AG Bad Nauheimer Str. 1964289, Darmstadt, Germany, <http://www.cst.com>.

<sup>2</sup> Custom Microwave Inc, 24 Boston Ct, Longmont CO 80501 USA.



waveguide of the OMT was terminated with a matched WR2.2 waveguide load through a similar straight WR2.2 waveguide section for flange transition. The transmission measurement of the other polarization channel was obtained with a setup similar to the one in Fig. 5 but with WR2.2 waveguide-to-square waveguide transition rotated by 90° to excite Pol 1 at the OMT input and with waveguide matched load and second port of the analyser swapped at the OMT outputs. A photograph of the transmission test setup of Pol 2, equivalent to that of Fig. 5, is shown on Fig. 6.

All measurements were performed across the frequency band 325-500 GHz. Experimental results are presented in Figs. 7-9, where a vertical line at 385 GHz indicates the nominal lower band edge of the design.

The measured transmissions of the OMT are illustrated in Fig. 7; the values are larger than -2.5 dB across 325-500 GHz with averages of order -1 dB for both polarization channels (the level predicted by the electromagnetic simulation was ~-0.2 dB for Pol 1 and ~-0.6 dB for Pol 2 when using an electrical conductivity  $\sigma=5.8 \cdot 10^7 \Omega^{-1}m^{-1}$ , same as the dc conductivity of Copper at room temperature). The transmissions of individual test transitions are also shown in Fig. 7.

The reflection coefficients at the OMT input were measured by terminating the OMT outputs with WR2.2 matched loads.

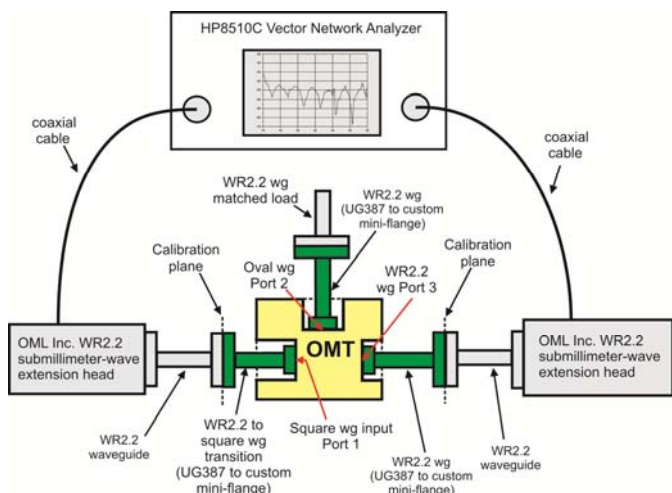


Fig. 5. S-parameter measurement of the OMT with sub-millimeter wave VNA. The particular configuration refers to the transmission measurement of Pol 2.

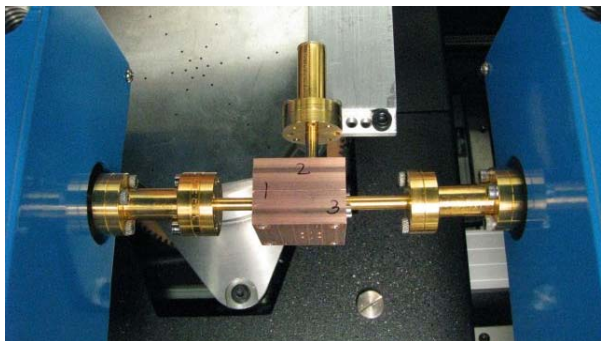


Fig. 6. Photo of the OMT during Pol 2 transmission measurement with the sub-millimeter wave VNA.

The amplitude of the measured reflection is below -10 dB for both polarization channels (Fig. 8.) The effects of reflection from the waveguide test transitions (of order up to -15 dB) could not be removed from these measurements. Therefore, the plots of Fig. 8 provide only an order of magnitude of the OMT input reflection.

An estimate of the isolation was obtained by measuring the transmissions from the OMT output ports with its square waveguide input open to free space. This gives an upper limit of the isolation of the device. The measured isolation is below -30 dB (Fig. 9.)

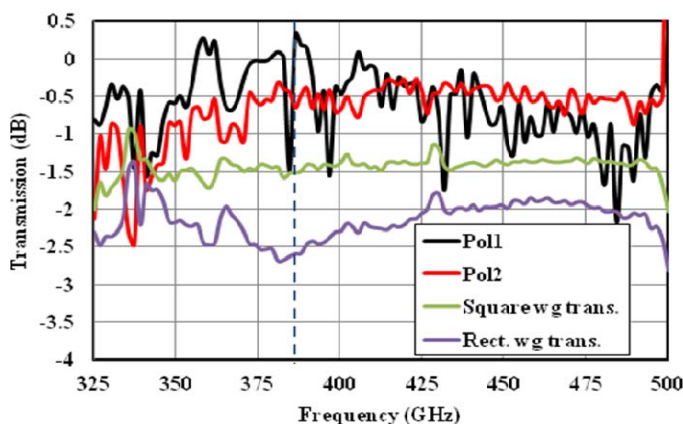


Fig. 7. Measured transmissions of the OMT prototype (at room temperature) and of individual test transitions.

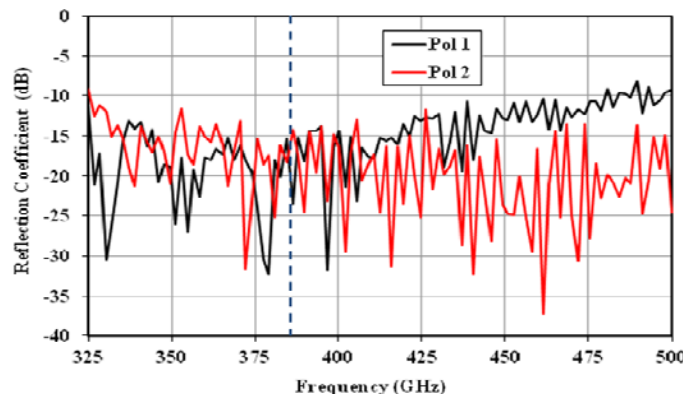


Fig. 8. Measured input reflections of the OMT.

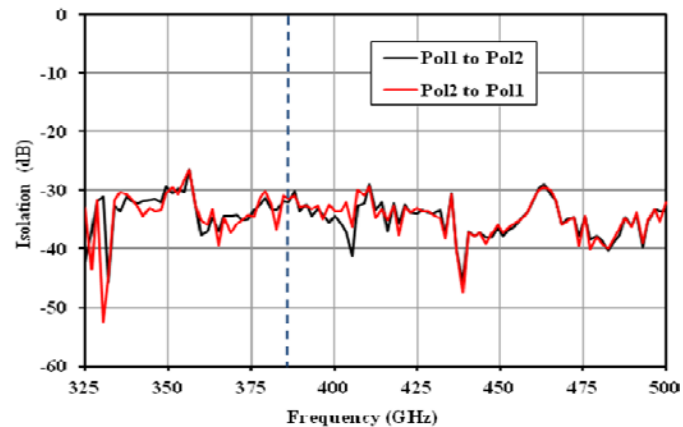


Fig. 9. Measured upper limit of the isolation of the OMT: transmission between output ports with square waveguide input open to free space.

The cross-polarization of the OMT is the transmission from one polarization channel at the square waveguide input to the unwanted output channel when the other two electrical ports of the four electrical ports device are terminated into matched loads. We estimated the cross-polarization of the OMT by using a transmission setup similar to the one in Fig. 5, except that the square waveguide-to-rectangular waveguide transition connected to the VNA port (on the left of Fig. 5) was rotated to excite Pol 1 at the square waveguide OMT input; the transmission to the “unwanted” OMT output in WR2.2 waveguide (Port 3) gives an order of magnitude for the cross-polarization of this polarization channel. The cross-polarization of the OMT second polarization channel was estimated by injecting Pol 2 at the OMT square waveguide and by extracting the signal from the oval waveguide (with WR2.2 port terminated into a matched load). Although this method does not directly measure the OMT cross-polarization (the non-excited polarization channel at the OMT square waveguide is not matched when a rectangular to square waveguide transition is connected at its input) it can be used to provide a good estimate of it. The average values of the OMT measured cross polarization levels were approximately -23 dB across 325-500 GHz for both polarization channels. This is a major improvement over the cross-polarizations of the first OMT prototype [12], whose average values were of order -12 dB and -15 dB.

We found that the adopted measurement method of the OMT cross-polarization was not very accurate because: *a*) it was very sensitive to small imperfections, due to mechanical tolerances, of the custom mini-flanges at the interface between the square waveguides of OMT and test transition, and *b*) the intrinsic cross-polarization of the test WR2.2-to-square waveguide transitions was limited. Therefore, we expect the cross-polarization of the OMT to be actually better than the reported value of  $\sim$ -23 dB.

## V. CONCLUSION

A waveguide OMT based on a reverse-coupling structure with short input and output waveguide was fabricated and tested. The OMT performs well over a wideband, 325-500 GHz, larger than the one of design. The OMT is more tolerant to misalignment errors than a previous prototype version which was based on a much longer square waveguide input and longer WR2.2 output. The second OMT version has insertion losses approximately half of the first prototype and an improved isolation level.

## REFERENCES

- [1] A. M. Boifot, E. Lier, T. Schaug-Pettersen, “Simple and Broadband Orthomode Transducer,” *Proceedings IEE*, vol. 137, n. 6, pp. 396-400.
- [2] E. J. Wollack and W. Grammer, “Symmetric Waveguide Orthomode Junctions,” *Proceedings of the 14<sup>th</sup> International Symposium on Space Terahertz Technology*, Tucson, Arizona, Apr. 2003, pp 169-176.
- [3] G. Narayanan and N. Erickson, “Full-Waveguide Band Orthomode Transducer for the 3 mm and 1mm Bands,” *Proceedings of the 14<sup>th</sup> International Symposium on Space Terahertz Technology*, Tucson, Arizona, Apr. 2003, pp 508-512.

- [4] A. Navarrini and M. Carter, “Design of a Dual Polarization SIS Sideband Separating Receiver Based on Waveguide OMT for the 275-370 GHz Frequency Band,” *Proceedings of the 14<sup>th</sup> International Symposium on Space Terahertz Technology*, Tucson, Arizona, Apr. 2003, pp 159-168.
- [5] G. G. Moorey, P. Axtens, M. Bowen, A. Dunning, R. Gough, G.R. Graves, H. Kanoniuk, “A 77-117 GHz cryogenically cooled receiver for radioastronomy,” *Workshop in Applications of Radio Science (WARS2006)*, Leura, NSW, 15-17 Feb. 2006.
- [6] S. Asayama, “Double-Ridged Orthomode Transducer for ALMA Band 4 receiver,” *Technical Memo of National Astronomical Observatory of Japan NINS*, 27 Feb. 2007.
- [7] A. Navarrini and R. L. Plambeck, “A Turnstile Junction Waveguide Orthomode Transducer,” *IEEE Trans. Microwave Theory Tech.*, vol. 54, n. 1, pp. 272-277, Jan. 2006.
- [8] A. Navarrini A. Bolatto, R. L. Plambeck, “Test of 1 mm Band Turnstile Junction Waveguide Orthomode Transducer”, *Proceedings of the 17<sup>th</sup> International Symposium on Space Terahertz Technology*, Paris, France, May 10-12, 2006.
- [9] G. Pisano, L. Pietranera, K. Isaak, L. Piccirillo, B. Johnson, B. Maffei, S. Melhuish, “A Broadband WR10 Turnstile Junction Orthomode Transducer,” *IEEE Microwave and Wireless Components Letters*, vol. 17, n. 4, April 2007.
- [10] O. A. Peverini, R. Tascone, G. Virone, A. Olivieri, R. Orta, “Orthomode Transducer for Millimeter-Wave Correlation Receivers,” *IEEE Trans. Microwave Theory Tech.*, vol. 54, n. 5, May 2006.
- [11] A. Navarrini, R. Nesti, “Symmetric reverse-coupling waveguide orthomode transducer for the 3 mm band,” *IEEE Trans. Micr. Theory and Tech.*, vol. 57, n. 1, Jan 2009, pp. 80-88.
- [12] A. Navarrini C. Groppi, G. Chattopadhyay, “A Waveguide Orthomode Transducer for 385-500 GHz”, *Proceedings of the 18<sup>th</sup> International Symposium on Space Terahertz Technology*, Oxford, UK, March 23-25, 2010, pp. 328-337.



**Alessandro Navarrini** received the S.M. degree in physics from the University of Florence, Florence, Italy, in 1996, and the Ph.D. degree in electronics and microelectronics from the Université Joseph Fourier, Grenoble, France, in 2002. From 1998 to 2003, he was with the Institut de Radioastronomie Millimétrique (IRAM), Grenoble, France, where he was involved in the development of low-noise superconducting SIS receivers. From 2003 to 2006, he was a Post-Doctoral Fellow with the Radio Astronomy Laboratory, University of California at Berkeley, USA. In 2006 he joined the National Institute for Astrophysics (INAF)–Cagliari Astronomy Observatory, Capoterra, Italy. Since 2010 he has been with the IRAM, Grenoble, France, where he is in charge of the Front-End Group.

# TES Bolometers with High-Frequency Readout Circuit

S. V. Shitov\*

*V.A.Kotel'nikov Institute of Radioengineering and Electronics,  
Russian Academy of Sciences, 125009 Moscow, Russia*

\* Contact: sergey@hitech.cplire.ru, phone +7(495) 629-7432

**Abstract**—The superconductor bolometers based on transition-edge sensing (TES) are nowadays of active interest, since their great potential for ultra-low-noise operation, also in imaging arrays. The small-size TES's are low-impedance devices (approx. 1-10 Ohm), so they are usually matched with SQUID's, which serve as ultra-low-noise current amplifiers. The method of frequency multiplexing has, in theory, a great potential for bolometer arrays. However, due to restricted bandwidth of SQUID's, there is a limit for such frequency division at relatively low frequencies. For this reason quite a number of SQUID's have to serve a large array of detectors that lead to both system complexity/cost and, potentially, to limited calibration accuracy and stability due to variations in regimes/parameters of the multiple SQUID's.

To improve the frequency multiplexing in TES arrays to about factor of 10 along with its easier operation, it is suggested using not SQUID's, but high-frequency low-noise amplifiers in the range of 1-10 GHz. This could result in only one amplifier (only one or two coaxial cables) serves for about 1000 TES detectors of an imaging array. The details of the new concept, which is somewhat similar to MKID's operation, will be presented along with comparison (pro's and con's) to other devices, which can use such high-frequency multiplexing.

# Status of ALMA Band 7 Cartridge Production

S. Mahieu, D. Maier, B. Lazareff, A. Navarrini, G.Celestin, J.Chalain, D. Geoffroy, F.Laslaz, G. Perrin

**Abstract**— The Atacama Large Millimeter/Sub-millimeter Array (ALMA) will be composed of at least 65 high-precision antennas. In this framework, IRAM is responsible for the production (component procurement, assembly and test) of 65 production + 8 spare state-of-the-art receivers, covering the 275–373GHz frequency range, called the ALMA Band 7 cartridges.

Some of the challenging issues that were solved during the design and prototyping of the cartridge, and early experimental results were presented at a previous ISSTT.

The first production cartridge was delivered in Spring 2009. The last receiver (65<sup>th</sup>) has to be provided to the project before the end of 2012.

Currently, half of the production cartridges have been delivered and accepted by the project.

Every single cartridge has to go through thorough preliminary acceptance tests to make sure that they all meet the specifications imposed by the project. In order to achieve such a level of quality with high delivery rate, some product (PA) and quality (QA) assurance processes had to be put in place and fully automated test setups had to be implemented.

We will briefly describe the cartridge, then the PA/QA processes and present the test setups together with the main performances of the production cartridges delivered so far.

## I. INTRODUCTION

IRAM is responsible for the design and production of 73 (including spares) integrated front-end modules for Band 7 (275–373 GHz).

When they were laid down in the early 2000's, the technical specifications of the project were pushing the envelope of the then-current state-of-art. The corresponding challenges were successfully overcome during the design phase and reported in several articles (see [1], [2] and [3] references at the end of this article). At present, well into the production phase, the emphasis has shifted to quality assurance and schedule.

With its background in mm-wave radioastronomy and interferometry, IRAM was in a unique position to meet the technical requirements of the design phase. Performing the series production of 73-off state-of art modules, with tight performance and schedule constraints, was a new type of challenge for a medium size scientific institute, and required to set up an adequate workflow organization and test

instrumentation. The present paper is a brief account of how this was achieved.

## II. BRIEF PRESENTATION OF THE BAND 7 CARTRIDGE

The ALMA front end will consist of a 4-K cryostat with ten plug-in dual polarization receivers called cartridges, covering the frequency range 31 to 950 GHz. A block diagram of the Band 7 cartridge is given in Fig. 1. It includes a cold cartridge assembly (CCA), which was developed and is currently being produced at IRAM, and a warm cartridge assembly (WCA), which is provided to IRAM by the ALMA project for test purposes. An overall view of a production cold cartridge assembly is given in Fig. 2.

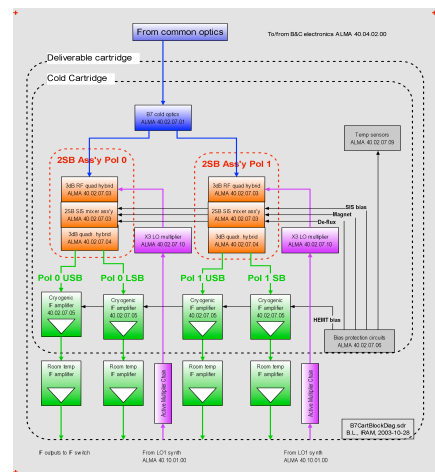


Fig. 1: Band 7 cartridge block diagram.

The cold cartridge assembly consists of three cold stages with operating temperatures of 4K, 15K and 80K and a room temperature baseplate which is the interface between the vacuum and the air. The stages are supported by G10 glass fiber tube spacers. The four plates and G10 tubes constitute the blank cartridge, designed and supplied within the ALMA project by Rutherford Appleton Laboratories (UK).

- The 4 K assembly comprises:
  - The cold optics, consisting of three off-axis elliptical mirrors and a polarization diplexing grid, designed to achieve near-optimum coupling of the two cartridge feedhorns to the telescope within prescribed tolerances;
  - Two dual-sideband (2SB) Superconductor-Insulator-Superconductor (SIS) mixer assemblies, one per polarization, covering the RF band 275-373 GHz. Each 2SB assembly is cascaded with 2x4-8GHz IF low noise amplifiers that provide down converted signals from both upper (USB) and lower sidebands (LSB). These

S. Mahieu<sup>1\*</sup>, D. Maier, A. Navarrini, G.Celestin, J.Chalain, D. Geoffroy, F.Laslaz, G. Perrin are with Institut de Radio Astronomie Millimetrique, IRAM\*, Saint Martin d'Hères, contact: mahieu@iram.fr, phone +33(0)4 76 82 49 61

B. Lazareff is with Institut de Planéotologie et d'Astrophysique de Grenoble (IPAG).

are thermalized to the 4K stage for improved stability and better noise performance.

- The 15K stage only provides thermal shunts for wiring, IF coaxial cables, and local oscillator (LO) waveguides, as well as mechanical (thermally insulated) support for the HEMT amplifiers.
- The 80K stage has one LO tripler per polarization, to multiply the 94.3-121.3 GHz signal coming from a room temperature oscillator to the 283-365GHz LO band. Wiring thermal shunts are also mounted on this stage.
- The 300K baseplate supports the ESD protection board and the IF, DC and LO feedthroughs.

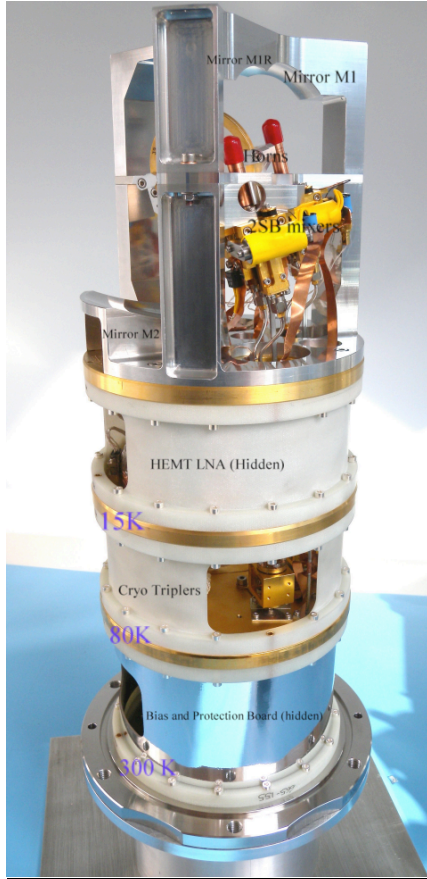


Fig. 2: Complete Production Band 7 Cartridge

### III. COLD CARTRIDGE: FROM COMPONENTS PROCUREMENT TO DELIVERY:

#### A. Procurement Control

Detailed procurement specification documents were written for the main components of the cold cartridge assembly produced outside IRAM (isolators, semi-rigid coax cable, grid, Low Noise Amplifiers, 4 K optics, wire harnesses, ESD protection board). The suppliers were carefully selected based on their know-how and capability to deliver product quality in due time.

#### B. Material and Processes Control

Most of the incoming parts are subject to validation tests, following proper test procedures. Most components are

identified with serial numbers to allow for traceability through incoming/outcoming items record and traveler writing up.

#### C. Band 7 Cartridge Assembly

The cartridges are fully assembled and tested at IRAM. Two parallel assembly lines with laminar flow hoods and ESD protective equipment are in place to achieve the high production rate required by the project. The test system is described in the section F below.

#### D. Validation Tests

After assembly, the cartridges have to undergo time-consuming validation tests on dedicated test setups. This topic is addressed in details in the section III.F below.

#### E. Cartridge Delivery

Finally, each cartridge is delivered to the project to so called integration centers, together with a batch of documents including bill of material (BOM), shipping inspection checklist, full test report, compliance matrix, configured item data list (CIDL) and electronic data files (configuration / tuning parameters and test data).

TABLE I: BAND 7 CARTRIDGE MAIN PERFORMANCE REQUIREMENTS

Property	Required Performance
Mixing scheme	Linearly polarized Sideband Separating Mixer
RF port frequency range	275-373 GHz
LO port frequency range	283-365 GHz
IF bandwidth	4-8 GHz 2SB
SSB receiver noise	<147K over 80% of the RF frequency band <221K at any RF frequency <300K in 370-373GHz extended band
Image band suppression	>-10dB, with allowance: no more than 10% <-10dB no more than 1% <-7dB Globally over all LO settings
Total IF output power integrated over 4-8GHz	-32dBm...-22dBm
IF power variations across 4-8GHz	5dB p-p over any 2GHz window 7dB p-p full band
Large signal gain compression @ 300K input	<5%
Amplitude stability: Allan variance 0.05s...100...300s	4.0E-7, 3.0E-6, respectively
Signal path phase stability	7.1fs over 300s
Aperture efficiency	>80%
Polarization efficiency	99.5% polarization coupling, (equiv<-23dB)
Focus efficiency	>98%
Polarization alignment accuracy	< 2°
Beam squint	1/10 FWHM
Stabilization time from non-operational	< 15 min
Stabilization time from stand by mode	< 1.5 s
Added cartridge mass	< 2.38kg on cold stages
Complete cartridge first eigen-frequency	> 70 Hz

#### F. Non Conformance Control

When a cartridge does not meet a given specification, a non-conformance (NCR) report and a request for weaver

document (RfW) are written for review by the project and keep a record of the discrepancy.

#### IV. AUTOMATED TEST SYSTEMS

##### A. Cartridge Technical Requirements

Each band 7 cartridge must meet given electrical and mechanical specifications as of TABLE I following a test plan and dedicated test procedures.

##### B. Band 7 Cartridge Test System

###### 1) System description

An automated test setup was developed to check in an efficient and timely manner that all of the produced receivers comply with the ALMA specifications (see Fig. 3).

Part of the test system was developed during the pre-production phase (2003-2007) in conjunction with the assembly and delivery of the first eight pre-production cartridges, and test procedures were also refined during the same period.

The first year of the production phase (2008) was dedicated to setting up a second complete cartridge test set that allows for a high rate of cartridge delivery of approximately one every three weeks. A second antenna test range is currently being assembled to further improve the production rate and avoid conflicting needs between the two test setups. The band 7 test system comprises four main parts:

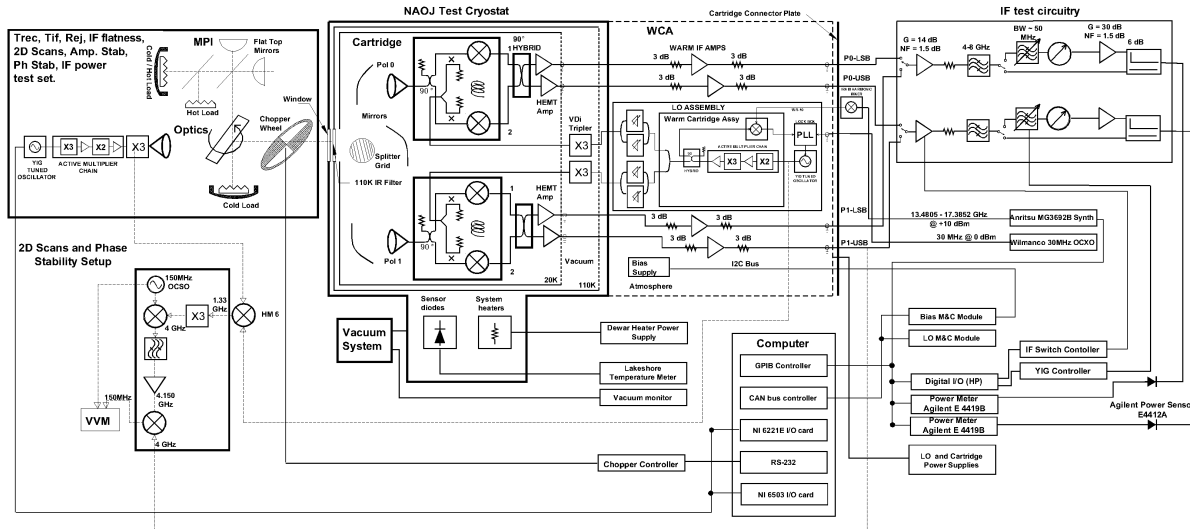


Fig. 3: Band 7 Cartridge Complete Test Setup

The setup involves two monochromatic sources: the local oscillator, and a test signal. The measurement consists of generating a beat note (in the IF band) in two ways: in the mixer, and in an alternate path, generating a reference signal. The relative amplitude and phase of the two beat notes is measured in a commercial vector voltmeter (VVM hereinafter)

This equipment is used to characterize the receiver beam pattern and pointing characteristics of the cartridge (Co-polarization, Cross-polarization, Aperture Efficiency, FWHM, Beam Squint) as well as receiver phase stability at a one second sampling rate. Far field response is derived in post processing by a succession of FFT calculations using a

A single-cartridge test cryostat developed by the National Astronomical Observatory of Japan (NAOJ);

A two IF chain test circuit that incorporates 4-8GHz band-pass filters, amplification stages, computer controlled 50MHz bandwidth YIG filters to sample the 4-8 GHz IF band and pin switches that select polarization channel.

A Martin Puplett Interferometer (MPI, Fig. 3 top left and corner and

Fig. 4 right side) to characterize the cartridge in terms of image band rejection. Few linear motors to swap the cold load with hot load and perform Y factor acquisitions. A rotating grid to characterize the cartridge both for the co and the cross polarizations.

A 2D beam scanner (Fig. 3 top left and corner and

Fig. 4, left side) that records signal amplitude and phase in the near field of the cold cartridge assembly optics. The emitter, based on an ALMA YIG type local oscillator source designed by NRAO, is positioned with the E-field vector at 45° position angle so that beam patterns for the two orthogonal polarization channels – performed simultaneously – share a consistent origin in the X-Y plane, thus allowing the verification of the beam squint specification.

MATLAB-based spreadsheet. Labview based monitor and control software to operate the cartridge test setup bias and control equipment.

###### 1) Monitor and Control Software Design.

All cartridges tests are fully automated and are based on Labview Software platform. Manual intervention is only required to change from one test type (e.g. noise temperature characterization) to another (e.g. image band suppression). Tests that use to take between half a day and one day during the early days of the project are now performed in less than half an hour. Some of the performances like IF signal amplitude stability are verified during night time, when the

laboratory temperature is more stable.

The communication between the warm and cold cartridge with the computer is realized through a Monitor and Control unit, an electronic bias module with CAN interface, and a Labview dedicated software first developed at NRAO. The software was then upgraded at IRAM to allow both full and semi-automation.

Integrated noise temperature measurements over 4-8 GHz are automatically performed at 22 LO frequencies ranging from 283GHz to 365 GHz in 4 GHz steps. The same applies to narrow band (40-50 MHz bandwidth over 4-8 GHz IF bandpass) noise temperature measurements from which the cartridge IF signal flatness across the 4 GHz band pass and in a 2GHz sliding window is derived.

Image band suppression test is itself performed at only five LO frequencies across the IF band of both sidebands.

For all these measurements, the Labview software uses mixer bias voltages and currents look up table created as a result of noise temperature optimization tests. Routines were also developed to refine the optimization if needed.

These mixer bias settings are then subsequently used to fully characterize the receiver as per test plan. The tuning parameters are finally provided to the project under tuning and configuration parameters csv file form.

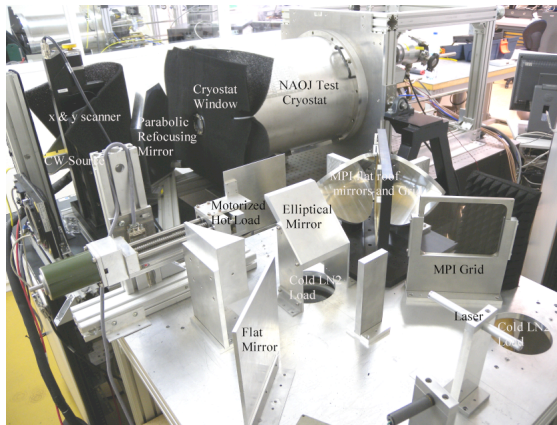


Fig. 4: ALMA Band 7 Cartridge Test Set for Noise Temperature, Image band suppression and beam scanner test set

### V. BAND 7 CARTRIDGE MAIN PERFORMANCES

At the time of writing, 36 cartridges have been assembled, tested and accepted by the project. All of them are meeting the full set of specifications and some of the test results are shown in this section.

#### A. Noise temperature

The Fig. 5 below shows the integrated noise temperature over 4-8 GHz bandpass test results for 36 production cartridges. One can see that the specification is met with comfortable margin.

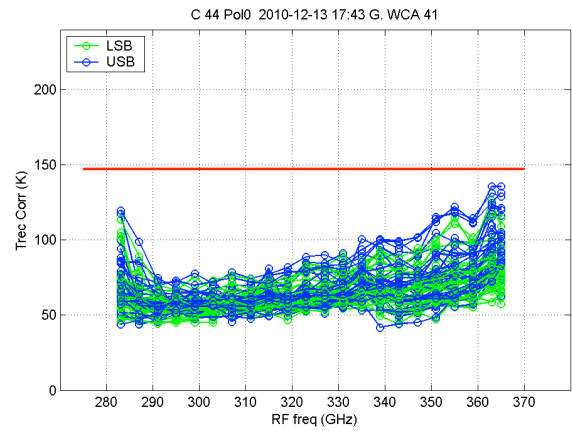


Fig. 5: Total Power Receiver Noise Temperature for 35 production cartridges

#### B. Image band suppression

The Fig. 6 below shows the image band suppression test results for 38 production cartridges. Again, the specification is met.

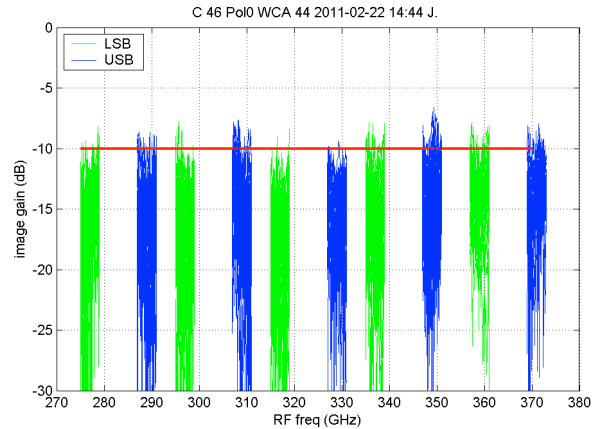


Fig. 6: Pol 0 Image Band Suppression for 38 cartridges

### VI. CONCLUSION

A more industrially minded way of assembling and testing receivers on a larger scale than usually practiced in research institutes has been put in place at IRAM. More than half of the band 7 receivers needed for the Atacama Large Millimeter Array have been produced in a couple of years that meet stringent specifications and deadlines. This has been made possible by the implementation of PA/QA processes and to a large extent, to the automation of the test sets.

### REFERENCES

- [1] S. Claude, "Sideband Separating SIS Mixer for ALMA Band 7, 275-370 GHz", March 2001, ALMA Memo #357.
- [2] D. Maier et al, "The ALMA Band 7 Mixer", in 16<sup>th</sup> International Symposium on Space Terahertz Technology, May 2005, pp. 428-431.
- [3] S. Mahieu et al, "The Band 7 Cartridge (275-373 GHz) for ALMA", in 16<sup>th</sup> International Symposium on Space Terahertz Technology, May 2005, pp.99-104.

## A 230GHz unilateral finline mixer on a silicon substrate

Yangjun Zhou<sup>1\*</sup>, Paul 2<sup>nd</sup> Grimes<sup>1</sup>, G. 3<sup>rd</sup> Yassin<sup>1</sup>, Jamie. 4<sup>th</sup> Leech<sup>1</sup>, Karl, 5<sup>th</sup> Jacobs<sup>2</sup>, Patrick, 6<sup>th</sup>, Puetz<sup>2</sup>

1 University of Oxford, Department of Physics \*, Oxford, OX1 3RH

2 University of Cologne , KOSMA

\* Contact: [Yangjun.zhou@physics.ox.ac.uk](mailto:Yangjun.zhou@physics.ox.ac.uk) phone:0044-018652-83011

**Abstract**— The design and preliminary results from testing the performance of a 230GHz unilateral finline SIS mixer, fabricated on a silicon substrate are presented. The mixer will be employed in the single baseline heterodyne interferometer-GUBBINS (220-GHz Ultra-BroadBand INterferometer for S-Z), which aims to measure the null frequency in the Sunyaev-Zel'dovich spectrum at ~227GHz. The mixer is operated in the frequency range of 180GHz~280GHz with an IF bandwidth of 1-13 GHz. An important feature of this mixer is its ultra-wide IF bandwidth, so as to achieve very high brightness sensitivity in the observation of the galaxy clusters in the faint cosmic microwave background radiation.

This SIS mixer described is deposited on an 80um silicon substrate with the dielectric constant of 11.9. The incoming RF signal from the feed horn is coupled via the waveguide mode to a unilateral finline, which is tapered to a 2.5um slotline. The signal is coupled from the slotline to the microstrip with the aid of two radial stubs. The employment of a silicon substrates gives a slotline impedance of 36Ω , which is ideal for coupling to the microstrip, where the SIS junction is fabricated. Also, the employment of silicon allows the generation of the trenches around the device so that individual devices can be separated from the batch without dicing. A 2-stage notch was fabricated at the front end of the substrate to match the loaded waveguide to the free space. The capacitance of the SIS junction was tuned out using a wide band circuit consisting of two stubs and a 3-stage Chebyshev transformer. This is followed by a 3-stage RF choke to prevent RF signal from leaking into the IF output port.

The mixer chip was fabricated at KOSMA, Cologne using Nb-AIO<sub>x</sub>-Nb tunnel junction defined with E-beam lithography. The device used in this experiment had a normal resistance of 20Ω, a current density of 14KA/cm<sup>2</sup>, an area of 1μm<sup>2</sup> and an intrinsic capacitance of 75fF. Measurement of the mixer performance was done using a local oscillator which gives sufficient power to pump the mixer in the frequency range 200GHz~260GHz using 12μm beam splitter. Measurement of the mixer sensitivity was done using the hot/cold Y-factor method. Uncorrected noise temperature of 75K was obtained at 208GHz, with 30 K contributed by mismatch to the IF system. Future characterization and improvements of the IF system and the measurement with better-tuned devices will also be reported.



# 3.5 THz Quantum Cascade Laser at 70 K as local oscillator

Y. Ren, P.J. de Visser, J.N. Hovenier, W.Zhang, J.R. Gao, T.M. Klapwijk, S.C. Shi, T-Y. Kao, S. Kumar, Q. Hu, and J. L. Reno

**Abstract**—We report a set of measurements to demonstrate a new type of surface emitting distributed feedback (DFB) quantum cascade laser (QCL) operated at 3.5 THz as a local oscillator by pumping a superconducting hot-electron bolometer (HEB) mixer. Based on the Bragg gratings incorporated into the waveguide, the second order DFB surface emitting THz QCL shows single mode emission at 3.555 THz, which is only 4 GHz off from the hydroxyl (OH) line. Because of the radiation being emitted from the surface, the far-field beam is much improved, with a divergent far field beam pattern only in one direction. We also notice that in the far field beam pattern, unlike conventional metal-waveguide QCLs, there are no interference patterns. All these factors make it possible to fully pump a superconducting NbN HEB mixer at 60 K, and even at 70 K based on the estimated power.

**Index Terms**—terahertz, quantum cascade laser, high temperature, far-field beam, hot electron bolometer

## I. INTRODUCTION

The hydroxyl (OH) radical has been identified to be a crucial probe for problems related to the atmosphere such as global warming and ozone destruction. The OH radical emission line at 3.551 THz has been identified as the best candidate for OH profile retrieval because of its brightness and isolation. With a nearly quantum noise limited sensitivity and a ultra high spectral resolution, a heterodyne receiver based on a superconducting NbN hot-electron bolometer (HEB) mixer

The work was partly supported by China Exchange Programme executed by KNAW and CAS, and by the AMSTAR+ project of RadioNet under FP7, and NWO.

Y. Ren is with the Kavli Institute of NanoScience, Delft University of Technology, Lorentzweg 1, 2628 CJ Delft, The Netherlands, with the Purple Mountain Observatory, Chinese Academy of Sciences, Nanjing, China, and with the graduate school, Chinese Academy of Science, Beijing, China, (e-mail: [y.ren@tudelft.nl](mailto:y.ren@tudelft.nl))

P.J. de Visser and J.R. Gao is with the Kavli Institute of NanoScience, Delft University of Technology, Lorentzweg 1, 2628 CJ Delft, The Netherlands, and with the SRON Netherlands Institute for Space Research, Sorbonnelaan 2, 3584 CA Utrecht, The Netherlands ([j.r.gao@tudelft.nl](mailto:j.r.gao@tudelft.nl))

J.N. Hovenier and T.M. Klapwijk are with the Kavli Institute of NanoScience, Delft University of Technology, Lorentzweg 1, 2628 CJ Delft, The Netherlands

W. Zhang and S.C. Shi are with the Purple Mountain Observatory, Chinese Academy of Sciences, Nanjing, China

T-Y. Kao, S. Kumar and Q. Hu are with Department of Electrical Engineering and Computer Science, Massachusetts Institute of Technology, Cambridge, Massachusetts 02139, USA

J.L. Reno is with Center for Integrated Nanotechnologies, Sandia National Laboratories, Albuquerque, NM 87185-0601, USA

will be ideal for detecting the OH line. Since such a mixer has shown a superior sensitivity up to 5.3 THz [1], suitable local oscillators (LO) at this particular frequency become the only obstacle for future development. Solid state LOs based on multipliers have only been demonstrated up to 2.5 THz, but the output power drops severely with frequency due to reduced multiplication efficiency at high frequencies. Also, bulky and power consumptive FIR gas lasers have no strong molecular lines close to this specific frequency.

Based on the quantum well structure, the photon energy of a quantum cascade laser (QCL) is determined by the thickness of the coupled wells and barriers, which makes such a structure ideal for generation of THz radiation. Until now, most of the THz QCLs used as LOs are based on a Fabry-Perot cavity. In order to achieve single mode lasing, the laser has to be narrow and often the width is much smaller than the wavelength. The latter causes a highly divergent beam with even strong interference fringes, which makes it difficult to couple the radiation to any phase sensitive detector like a HEB mixer. However, for a surface emitting DFB THz QCL [2], by incorporating the second order Bragg gratings into the waveguide, a single mode emission is coupled out from the surface. These characteristics make surface emitting DFB QCL that have advantages in both the frequency selection and with less divergent far-field beam. Moreover, due to relative large DC power dissipation of the laser, low temperature operation of QCLs with liquid-helium cooling is impractical for balloon-borne and space missions. Therefore, high temperature operation of the laser with a dry, liquid cryogen-free cooler, such as a pulse tube cryocooler or a Stirling cooler is crucial for instrumental applications.

## II. THz SURFACE EMITTING DFB QCL

The surface emitting DFB QCL used in this experiment is described in Ref. 2. The active region is based on a resonant-phonon depopulation scheme and a metal-metal waveguide is used for modal confinement. By introducing a second-order Bragg grating on the top surface of the waveguide, the radiation is coupled out from the top surface. The DFB grating enables robust single-mode operation over a large operating range. By using a Pi phase-shift in the center of the grating, a single-lobed far beam pattern is obtained.

The QCL is operated on the cold stage of a helium-flow cryostat. The QCL consumes 4 W DC power in continuous wave mode and provides a maximum output power of 1 mW. As to be explained, the QCL working at 70 K can still provide about 25% of its maximum power and is estimated to have

enough power to pump a HEB mixer at its optimal operating point.

### III. MEASUREMENT RESULTS

For the beam pattern measurement, by using a room temperature pyrodetector and two PC controlled stepper motors, the radiation beam was measured in both horizontal and vertical directions spherically.

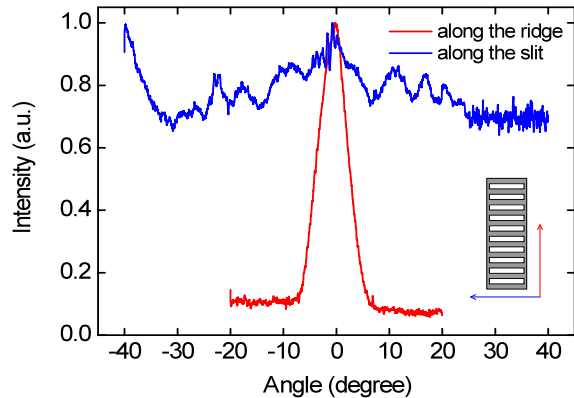


Fig. 1 Measured far-field beam pattern of the surface emitting DFB QCL, where beam pattern measured directly in front of the QCL at a distance of 112 mm.

As shown in Fig. 1a, the radiation beam was measured with a pyrodetector placed at a radial distance of 112 mm. Along the laser's ridge direction, a single-lobed beam was observed, where the full width at half maximum (FWHM) is 7 deg. However, along the laser's slit direction, the beam is highly divergent, which is mainly due to the subwavelength dimension of the waveguide in this direction. Compared with the beam patterns measured from meta-metal waveguide Fabry-Perot type QCLs [3], surface emitting DFB QCL emits a directional beam in one direction. Another advantage is that there are no interference fringes in either direction. These features caused a higher power coupling efficiency from the laser to a HEB mixer, which typically holds a Gaussian beam. For the beam pattern after focused using a HDPE lens, a single-lobed beam is found in both directions, where the divergence is less than 1 deg.

We use a spiral antenna coupled superconducting NbN HEB mixer, which consists of a 2  $\mu\text{m}$  wide, 0.2  $\mu\text{m}$  long, and 5.5 nm thick NbN bridge [1]. The HEB has a low-temperature normal-state resistance ( $R_N$ ) of 83  $\Omega$ , a critical temperature of 9.3 K, and a critical current of 210  $\mu\text{A}$  at 4.2 K.

As shown in Fig. 2, by placing the QCL and the HEB directly face to face, and using a HDPE lens ( $f=50$  mm) to focus the laser's radiation, the current-voltage characteristics of the HEB at different pumping levels are obtained. It is clearly shown that the emission power from the surface emitting DFB QCL working at 60 K is enough to fully pump the HEB (bringing the HEB fully in the normal state). This enables the QCL to be operated as the LO in a heterodyne receiver where a thin Mylar beam splitter is used to reflect the power to a HEB mixer.

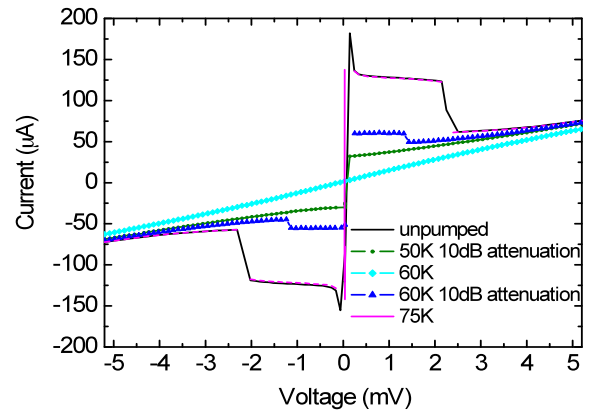


Fig. 2 Current-voltage characteristics of the HEB for different pumping levels caused by different operating temperature of the QCL. In some cases, an attenuation of the LO power is introduced in order to get a proper pumping curve.

Although no pumping measurement data were available at 70 K, we can predict that this laser would be powerful enough to pump the HEB at 70 K by using a thick Mylar Beam splitter or a Martin-Puplett interferometer (MPI). Since the output power of the QCL at 70 K is about half the power generated at 60 K. Based on the value of 530 nW at 60 K, we expect a power of 270 nW at the HEB itself with the QCL at 70 K. This value is more than the optimal LO power (140 nW). Since the beam is still highly divergent in one direction, further improvement can be made by placing the QCL closer to the cryostat window and using a short focal distance lens. The possibility of operating a QCL at 70 K or above is crucial for the application in balloon-borne and space missions because it is technically much easier to have such a cooler in comparison with a cooler for, e.g. 10 K.

### IV. CONCLUSION

In conclusion we have demonstrated using measurements of the beam pattern, spectra characteristics, and pumping a HEB mixer, that the surface emitting DFB QCL working at 3.5 THz can be used as the LO in a heterodyne receiver for the OH line detection. We found that the new laser gives a better beam pattern. The QCL can fully pump a HEB mixer at 60 K, suggesting that there is enough power even at 70 K. We emphasize that operating a QCL at a temperature of 70 K or above is practically important for a real instrument, in particular in space.

### REFERENCES

- [1] W. Zhang, P. Khosropanah, J.R. Gao, E. L. Kollberg, K. S. Yngvesson, T. Bansal, R. Barends, and T. M. Klapwijk, "Quantum noise in a terahertz hot electron bolometer mixer," *Applied Physics Letter* 96, 111113 (2010),
- [2] S. Kumar, B.S. Williams, Q. Qin, A.W.M. Lee, Q. Hu and J. L. Reno, "Surface-emitting distributed feedback terahertz quantum-cascade lasers in metal-metal waveguides," *Opt. Express*, 15,113 (2007)
- [3] A. J.L. Adam, I. Kašalynas, J.N. Hovenier, T.O. Klaassen, J.R. Gao, E.E. Orlova, B.S. Williams, S. Kumar, Q. Hu, and J. L. Reno, "Beam pattern of Terahertz quantum cascade lasers with sub-wavelength cavity dimensions", *Appl. Phys. Lett.* 88, 151105(2006).

## Doped Lead Telluride-Based Alloys – a New Type of Sensitive Detectors of Terahertz Radiation

D.E. Dolzhenko<sup>1</sup>, A.V. Nicorici<sup>2</sup>, L.I. Ryabova<sup>1</sup>, and D.R. Khokhlov<sup>1</sup>

*1 M.V. Lomonosov Moscow State University\*, Moscow 119991, Russia*

*2 Institute of Applied Physics, Moldavian Academy of Sciences, Kishinev MD-2028, Moldova*

\* Contact: khokhlov@mig.phys.msu.ru, phone +7-495-939 1151

*Abstract*— Doping of the lead telluride and related alloys with the group III impurities results in appearance of the unique physical features of a material, such as persistent photoresponse, enhanced responsive quantum efficiency (up to 100 photoelectrons/incident photon), high radiation hardness and many others. We present the physical principles of operation of the photodetecting devices based on the group III-doped IV-VI including the possibilities of a fast quenching of the persistent photoresponse, construction of the focal-plane array, and others. We report on the performance of lead telluride-based single direct detectors. The optical NEP as low as  $6 \cdot 10^{-20}$  W/Hz<sup>1/2</sup> at T=1.57 K has been demonstrated at the wavelength of 350  $\mu$ m. The advantages of terahertz photodetecting systems based on the group III-doped IV-VI are summarized.

## Optical sensitivity measurements in nano-HEB detectors

B. S. Karasik<sup>1\*</sup> and R. Cantor<sup>2</sup>

*1 Jet Propulsion Laboratory, California Institute of Technology\*, Pasadena, CA 91109*

*2 STAR Cryoelectronics, Santa Fe, NM 84508*

\* Contact: boris.s.karasik@jpl.nasa.gov, phone +1 (818) 393-4438

**Abstract**—Recently, an interest to ultrasensitive submillimeter/FIR detectors has been driven due to the astrophysics community's and space agencies' plans to launch telescopes with cryogenically cooled primary mirrors where the thermal emission from the telescope would be largely eliminated. Several concepts of such telescopes (e.g., SAFIR, SPECS, CALISTO, FIRI, SPICA) have been proposed and studied. Moderate resolution spectroscopy would be the most demanding application requiring the detector noise equivalent power (NEP) to be less than  $10^{-19}$  W/Hz<sup>1/2</sup> in the most of the submillimeter/FIR spectral range in order for the photon shot noise to dominate the detector noise. The SPICA mission led by the Japanese space agency is currently seen as the most feasible opportunity to realize such a sensitive astronomical platform. There are two instruments considered for far-IR spectroscopy on SPICA. ESA led SAFARI instrument would use a Fourier Transform Spectrometer in the 30-210  $\mu$ m wavelength range. The detectors for SAFARI should have an NEP =  $3 \times 10^{-19}$  W/Hz<sup>1/2</sup>. Another instrument (BLISS), which is under study in the US, is a grating spectrometer operating in the 35-433  $\mu$ m range. The detector sensitivity goal here (NEP =  $3 \times 10^{-20}$  W/Hz<sup>1/2</sup>) is non-precedent and requires an improvement of the state-of-the-art by 2-3 orders of magnitude.

We have been addressing this sensitive detector needs via development of the superconducting hot-electron nanobolometer (nano-HEB). In this work for the first time, we have measured the optical NEP in twin-slot antenna coupled titanium (Ti) nano-HEBs. The bolometers were  $2\mu\text{m} \times 1\mu\text{m} \times 20\text{nm}$  and  $1\mu\text{m} \times 1\mu\text{m} \times 20\text{nm}$  transition-edge sensor (TES) devices with NbTiN contacts. The measurements were done at  $\lambda = 460$   $\mu$ m using a cryogenic black body radiation source delivering optical power from a fraction of a femtowatt to a few 100s of femtowatts. The detector readout was a dc SQUID with the noise  $\sim 2\text{-}3$  pA/Hz<sup>1/2</sup>. A record low NEP =  $3 \times 10^{-19}$  W/Hz<sup>1/2</sup> at 50 mK has been achieved. The optical efficiency of the tested detector was found to be  $\sim 50\text{-}70\%$ . Along with the results we will discuss the details of the experimental method for determination of the ultralow calibration power and the NEP. The path for getting even lower NEP in the nano-HEB detectors will be discussed as well.

# Low Noise Transition Edge Sensor (TES) for the SAFARI Instrument on SPICA

P. Khosropanah, R.A. Hijmering, M. Ridder, M.A. Lindeman, L. Gottardi, M. Bruijn,  
J. van der Kuur, P.A.J. de Korte, J.R. Gao, H. Hoervers

**Abstract**—We fabricated and characterized a low thermal conductance ( $G$ ) transition edge sensor (TES). The device is based on a superconducting Ti/Au bilayer deposited on a suspended SiN membrane. The critical temperature of the device is 78 mK. The low thermal conductance is realized by using narrow SiN supporting structures. All measurements were performed having the device in a light-tight box, which to a great extent eliminates the loading of the background radiation. We measured the current-voltage (IV) characteristics of the device at different bath temperatures and determine the thermal conductance ( $G$ ) to be equal to 0.13 pW/K. The current noise and complex impedance are also measured at different bias points at a bath temperature of 30 mK. The measured electrical (dark) NEP is  $4.2 \times 10^{-19}$  W/ $\sqrt{\text{Hz}}$ , which is about a factor of 3 higher than what is expected from the thermal conductance that comes out of the IV curves analysis. We also measured the complex impedance of the same device at several bias points. Fitting a simple first order thermal-electrical model to the measured data, we find an effective time constant of about 1-4.5 ms and a heat capacity of 2-3 fJ/K.

**Index Terms**—Transition-edge sensor, TES, far infra-red spectrometer, submm spectrometer, SiN membrane.

## I. INTRODUCTION

SPICA [1] is a Japanese-led mission to fly a 3.5 m diameter SIR telescope with a cryogenically cooled mirror ( $\sim 5$ K). Cooling the optics reduces the background radiation caused by the ambient temperature of the telescope that limits the sensitivity. The loading is then dominated by astrophysical background sources. SAFARI [2] is the European instrument on SPICA. It is an imaging Fourier Transform Spectrometer (FTS) with three bands in the wavelength ranges: 35-60  $\mu\text{m}$ , 60-110  $\mu\text{m}$  and 110-210  $\mu\text{m}$ . The loading in these bands is dominated by emission from the Zodiacal light at a level of 0.3-1 fW [2]. This gives a photon noise equivalent power (NEP) at the detectors of  $1-3 \times 10^{-18}$  W/ $\sqrt{\text{Hz}}$ . We require detectors with electrical NEP at least 3 times lower than the photon noise limit, i.e.  $\leq 3 \times 10^{-19}$  W/ $\sqrt{\text{Hz}}$ . This sensitivity is about 2 orders of magnitude higher than what is required for detectors on a ground based telescope, imposing a great challenge on the detector technology. The requirement for the

response time of the detectors for SAFARI is set to  $\tau \leq 8$  ms, determined by the maximum scanning speed of the FTS mechanism and the downlink bandwidth.

A transition edge sensor (TES) is the selected detector technology for the SAFARI. Silicon nitride suspended structures (although not for TES) were originally developed for ground-based mm-wave observations and have been used in a large number of ground-based and sub-orbital experiments [3]-[6]. Silicon nitride suspended structures were used in the Herschel-SPIRE [7] and the Planck space observatory [8]. All of the detectors in these instruments use bolometer chips that are bonded to the silicon nitride membranes in a hybrid process [9]-[10]. More recently, a number of groups have developed bolometers incorporating silicon nitride thermal isolation combined with TES bolometers (see Ref. [11] and references therein).

In collaboration with several European TES groups, SRON is developing low thermal conductance TES bolometers for SAFARI. These devices are based on a Ti/Au superconducting bilayer as the sensitive element on a suspended silicon nitride membrane.

Previously we reported measurements of a single pixel TES using long diagonal legs [12]. Also the optical test of a similar TES integrated with an absorber was reported [13], where the radiation is coupled to the detector using a conical horn. In order to achieve very low thermal conductance we needed to use 4 very long diagonal legs of 1800  $\mu\text{m}$ . This makes the detector size rather large and therefore not suitable for making arrays with required pixel pitch size for the SAFARI. One solution to overcome this problem is to make ring-like supporting structure [14]. In this paper an alternative approach is taken by having the TES supported by tilted parallel legs.

We present the details of the detector and electrical (dark) characterization, including IVs, noise, impedance data and the analysis.

## II. TES DEVICE

The device under test is based on a Ti/Au (16/60 nm) bilayer, deposited on 0.5  $\mu\text{m}$  thick suspended SiN membrane. The TES area is  $50 \times 50 \mu\text{m}^2$  and the critical temperature ( $T_c$ ) is 78 mK. In order to be able to test this device optically (not reported here), we have an absorber close to the TES, which is an 8 nm thick Ta with an area of  $70 \times 70 \mu\text{m}^2$ . The absorber and the TES are sitting on a  $130 \times 70 \mu\text{m}^2$  SiN island.

Fig. 1 shows a picture of the device. There are 4 SiN supporting legs that are 2  $\mu\text{m}$  wide and 2000  $\mu\text{m}$  long. The

Manuscript received 1 August 2011. This work is supported in part by ESA TRP contract: ITT-1-5922/08/NL/EM TES spectrometer.

P. Khosropanah, M. Ridder, R. Hijmering, J. van der Kuur, L. Gottardi, M. Bruijn, M. Popescu, J. R. Gao, H. Hoervers are with the SRON Netherlands Institute for Space Research, Sorbonnelaan 2, 3584 CA Utrecht, the Netherlands (phone: +31-88877-5600; fax: +31-888-77 5601; email: P.Khosropanah@sron.nl).

J. R. Gao is also with Kavli Institute of NanoScience, Delft University of Technology, Delft, the Netherlands.

electrical contact to the bolometer is realized by 90 nm thick Nb wiring on the top of SiN legs.

Similar devices are fabricated in an array of  $5 \times 5$  with a pitch size of  $840 \mu\text{m}$ , which is required by the SAFARI long wavelength focal plane array (see Fig. 2).

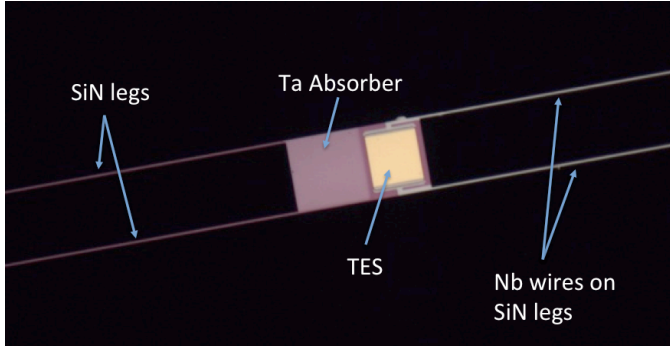


Fig. 1. TES on suspended SiN structure with a spider-web-like design. In the middle of each detector there is a TES and an absorber on a SiN membrane.

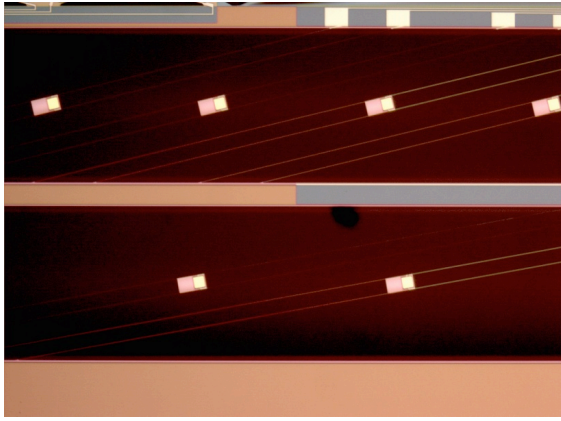


Fig. 2. TES array on suspended SiN structure with tilted parallel legs design. By increasing the tilt angle the leg length increases while the pitch stays the same.

### III. CURRENT-VOLTAGE CHARACTERISTICS

The detector is tested using a Kelvinox dilution fridge with a base temperature of 16 mK. The detector is mounted in a light tight box, which is designed to minimize the background loading due to possible stray light. The electrical wiring into this box goes through a meander path that is filled with Stycast mixed with SiC grains.

The biasing is done by using a  $dc$  current source in parallel with  $5 \text{ m}\Omega$  shunt resistance that simulates a voltage bias. The current in the TES is read out using a SQUID with a closed flux locked loop. Fig. 3 shows a set of measured IV curves at bath temperatures varying from 30 to 70 mK. The  $dc$  power in the transition at each bath temperature is almost constant. Fig. 4 shows the power level as a function of bath temperature.

The heat flow equation for a TES can be written as:

$$P = K(T_C^n - T_{bath}^n), \quad (2)$$

where  $P$  is the bias power applied to the TES;  $K$  a constant that depends on the geometry and material properties of the supporting legs;  $T_C$  the critical temperature of the bilayer; and  $T_{bath}$  the bath temperature. All parameters are known in (2)

except for  $n$  and  $K$ , we can fit (2) to the measured data to find both values. For this device the best fit was obtained using  $n = 2.5$  and  $K = 2.66 \text{ pW/K}^n$ . The fundamental phonon noise in TES can be written as [15]:

$$NEP = \sqrt{\gamma 4k_B T^2 G}, \quad (3)$$

where  $\gamma$  is a number between 0.5 and 1 that accounts for temperature gradient along the supporting legs and in our case is about 0.5,  $k_B$  is the Boltzmann's constant,  $T$  is the temperature of the TES, which is equal to  $T_C$ , and  $G$  is the thermal conductance between the TES and the substrate which can be written as:

$$G = nKT_C^{n-1}. \quad (4)$$

Inserting the values from the fit in Fig. 4 gives a  $G$  of  $0.13 \text{ pW/K}$ , which in turn results in an expected dark NEP of  $1.4 \times 10^{-19} \text{ W}/\sqrt{\text{Hz}}$  using (3).

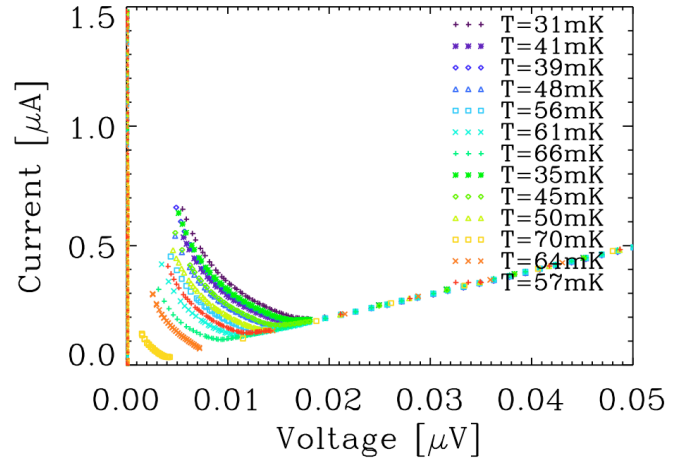


Fig. 3. Calibrated IV curves at different bath temperature.

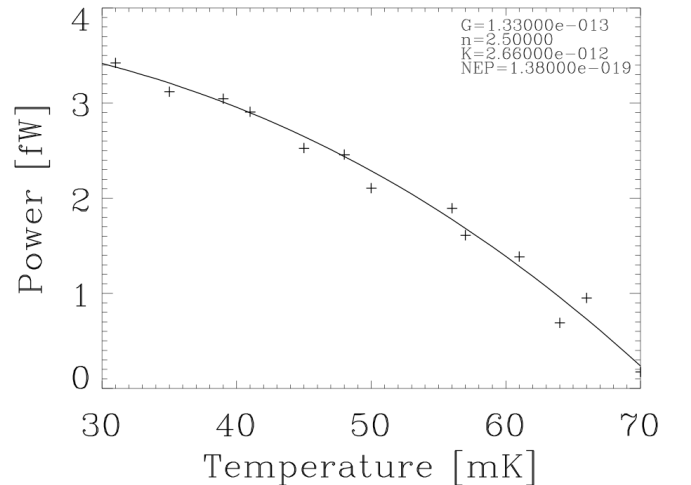


Fig. 4. Power plateaus in the transition as a function of bath temperature.

### IV. NOISE MEASUREMENT

Fig. 5 shows the measured current noise spectra at several bias points in the transition at a bath temperature of 30 mK. The data have a frequency resolution of 1 Hz. Dividing the current noise by the responsivity yields the electrical (dark) NEP at each operating point. The responsivity at low

frequencies can be approximated by  $\frac{1}{I_0(R_0 - R_{Th})}$ , where  $I_0$  is

the bias current,  $R_0$  is the resistance of TES and  $R_{Th}$  is the Thevenin resistance in the bias circuit that is  $R_{series} + R_{shunt}$ . The dark NEP at low frequency at all points in the transition is about  $4.2 \times 10^{-19}$  W/ $\sqrt{\text{Hz}}$ , which is a factor of 3 higher than what we expect from the measured  $G$ . We believe that the main part of this excess noise is due to the thermal fluctuations in the long legs.

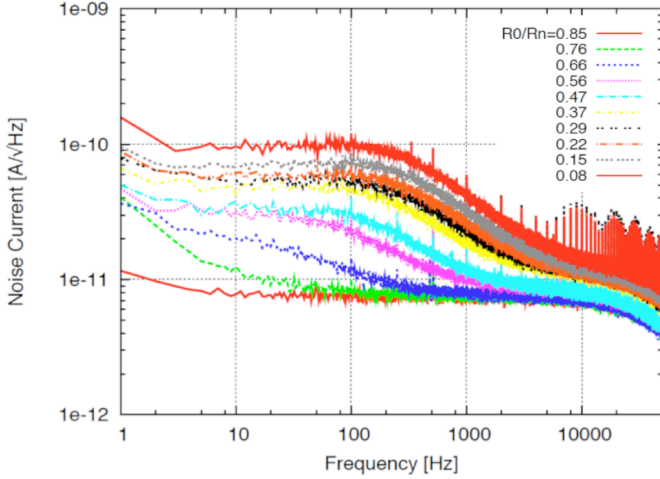


Fig. 5. Noise current spectra measured at a bath temperature of 30 mK in the transition that corresponds to NEP =  $4.2 \times 10^{-19}$  W/ $\sqrt{\text{Hz}}$ .  $R_0$  is the TES resistance at the bias point where the noise was measured and  $R_n$  is the normal state resistance of the device.

## V. TES SPEED

The speed of the device at different bias points is measured by applying a small step current (less than 10% of the bias current) and recording the output signal. Since the signal is small it has to be averaged for over 500 times. The curves are then fit by a first order exponential function that gives the time constant of the response. Fig. 6 shows the measured curves and the fits. The effective time constant varies between 4.5 ms at high in the transition to 1 ms at low in the transition. These numbers are well within SAFARI specifications that require  $\tau \leq 8$  ms.

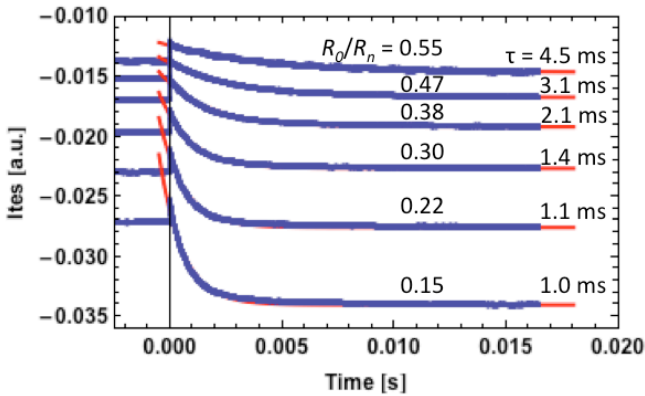


Fig. 6. The response signals (blue curves) to a small current bias step at different bias points. The fits (red curves) are first order exponential decay functions that give the time constants.

## VI. COMPLEX IMPEDANCE MEASUREMENT

For the complex impedance measurements we use a 10 k $\Omega$  resistance as a noise source. This noise is amplified and then added to the  $dc$  bias. Both the input noise signal and the output of the SQUID amplifier are recorded. The complex impedance of TES can be written as:

$$Z_{TES}(j\omega) = \frac{V_{AC}(j\omega)}{R_{loadAC} \cdot I_{TES}(j\omega)} \cdot T(j\omega) - Z_{Th}(j\omega). \quad (4)$$

where

$$Z_{Th}(j\omega) = R_{series} + R_{shunt} + j\omega L. \quad (5)$$

Here  $R_{loadAC}$  is the resistance in series with the noise source,  $R_{series}$  is the series resistance with the TES in the bias circuit,  $R_{shunt}$  is the shunt resistance and  $L$  is the inductance in the bias circuit.  $T(j\omega)$  is the transfer function of the signal lines that is determined experimentally. In order to calculate the  $Z_{TES}(j\omega)$  from (4) and (5), we need to find  $T(j\omega)$  and  $L$ . All other parameters are known. These two can be calculated by using two equations for superconducting and normal state where  $Z_{TES}$  is known. At the superconducting state the  $Z_{TES}(j\omega)$  is simply zero and at the normal state it is the normal resistance of the TES which is 103 m $\Omega$  in this case. The  $L$  obtain from this measurement is 0.5  $\mu\text{H}$ .

Fig. 7 shows measured complex impedance curves different bias points in the transition at a bath temperature of 30 mK. In order to extract the TES parameters from the data we choose a simple, first order model that is described in great detail in Ref. [11]. In this model, the TES is seen as an isolated element with a certain heat capacity  $C$  that is connected to the bath with a low heat conductance  $G$ . In first order our device can be explained with this simple model especially in the low part of the transition where the complex impedance curves are very close to perfect semi-circle. In order to study these devices in greater detail more sophisticated models are needed that accounts for distributed heat capacities and heat conductance through the long legs.

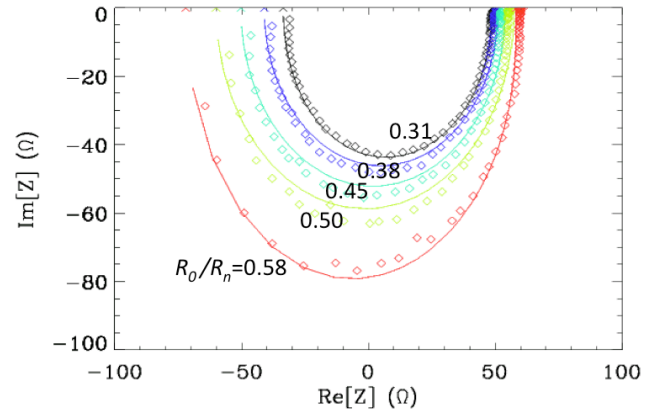


Fig. 7. Measured impedance at 5 points in the transition.  $R_0$  is the TES resistance at the bias point where the impedance is measured and  $R_n$  is the normal state resistance of the device.

Using the electrical and thermal equations, the  $Z_{TES}$  can be written as:

$$Z_{TES} = Z_{\infty} + (Z_{\infty} - Z_0) \cdot \frac{1}{-1 + i\omega\tau_{eff}}. \quad (6)$$

, where  $Z_0$  and  $Z_\infty$  are the impedances at zero and at very high frequency, respectively.  $\tau_{eff}$  is the effective time constant, defined as:

$$\tau_{eff} = \tau_0 \frac{1 + \beta + R_{th} / R_0}{1 + \beta + R_{th} / R_0 + (1 - R_{th} / R_0)L_0}, \quad (7)$$

where  $\tau_0 = C/G$  is the intrinsic time constant and  $L_0$  is the low frequency loop gain that is:  $L_0 = P_0\alpha/GT_0$ . Here  $P_0$  is the *dc* bias power and  $T_0$  is the temperature of TES, which is close to  $T_C$  in the transition.  $\alpha$  is the resistance dependence of the temperature at constant bias current. Similarly  $\beta$  is the resistance dependence of the current at constant temperature. These two are defined as:

$$\alpha = \frac{T_0}{R_0} \left. \frac{\partial R}{\partial T} \right|_{I_0}, \quad \beta = \frac{I_0}{R_0} \left. \frac{\partial R}{\partial I} \right|_{T_0}. \quad (8)$$

In this model  $Z_0$  and  $Z_\infty$  become:

$$Z_0 = R_0 \frac{1 + \beta + L_0}{1 - L_0} \quad (9)$$

$$Z_\infty = R_0(1 + \beta) \quad (10)$$

By choosing the  $Z_0$ ,  $Z_\infty$  and  $\tau_{eff}$  at every bias point, (6) is fitted to the measured data. Knowing  $Z_\infty$  and  $R_0$  we derived  $\beta$  from (10) and using that in (9),  $L_0$  will be known. Knowing the loop gain ( $L_0$ ) and effective time constant ( $\tau_{eff}$ ) and  $\beta$ , we calculate the intrinsic time constant ( $\tau_0$ ) from (7) and since the thermal conductance ( $G$ ) is known from the IV measurement, we can estimate the thermal capacity ( $C$ ) of the device.

Table 1 summarizes the outcome of this analysis for the TES in the transition at bias point where  $R_0/R_n = 0.30$ , which is a preferred operating point for these devices.

TABLE I DEVICE PARAMETERS FROM IMPEDANCE MEASUREMENT

TES parameter	Value
$G$	0.13 pW/K
$C$	2.3 fJ/K
$\tau_0$	17.7 ms
$\tau_{eff}$	1 ms
$L_0$	30
$R_0$	30 m $\Omega$
$P_0$	3.8 fW
$\alpha$	80
$\beta$	0.4

## VII. CONCLUSION

We have fabricated and measured low thermal conductance TES devices as required for SPICA. We measured IV curves at different bath temperatures from 30 to 70 mK while it is mounted in a light-tight box to minimize the background load. The saturation power is 3.8 fW at 30 mK bath temperature. The thermal conductance extracted from the IV curves is 0.13 pW/K that corresponds to phonon noise NEP of  $1.4 \times 10^{-19}$  W/ $\sqrt{\text{Hz}}$ . However our noise measurement shows an electrical (dark) NEP of  $4.2 \times 10^{-19}$  W/ $\sqrt{\text{Hz}}$ . The reason for this

excess noise is under investigation but we believe that the main part of this excess noise is due to the thermal fluctuations in the long legs. The complex impedance data can be relatively well described by a simple, first order model. We derive a heat capacity of 2.3 fJ/K and an effective time constant of about 1 ms when the TES is biased at  $R_0/R_n = 0.30$  in the transition. The speed of the device is well below the specification for SPICA and can be further compromised by lowering the  $G$  to meet the sensitivity requirement.

## ACKNOWLEDGMENT

We would like to thank all our collaborators within ESA-TRP program for fruitful discussions, specially P. Mauskopf, D. Morozov from Cardiff University, S. Withington, D. Goldie, D. Glowacka, A. Velichko from University of Cambridge, A. Murphy, N. Trappe, C. O’Sullivan from National University of Ireland in Maynooth, D. Griffin from Rutherford Appleton Laboratory and B. Leone from ESA.

## REFERENCES

- [1] H. Kaneda, T. Nakagawa, T. Onaka, T. Matsumoto, H. Murakami, K. Enya, H. Kataza, H. Matsuhara, and Y. Y. Yui, “Development of space infrared telescope for the SPICA mission,” in *Optical, Infrared, and Millimeter Space Telescopes*. Edited by Mather, John C. Proceedings of the SPIE, Volume 5487, pp. 991-1000 (2004).
- [2] B. Swinyard, “Esi: the far-infrared instrument for the spica mission,” *Space Telescopes and Instrumentation I: Optical, Infrared, and Millimeter* 6265(1), p. 62650L, SPIE, 2006.
- [3] B. Benson, S. Church, P. Ade, J. Bock, K. Ganga, C. Henson, and K. Thompson, “Measurements of Sunyaev-Zel’dovich effect scaling relations for clusters of galaxies,” *Astrophysical Journal* 617, pp. 829–846, DEC 20 2004.
- [4] G. W. Wilson, J. E. Ausermann, T. A. Perera, K. S. Scott, P. A. R. Ade, J. J. Bock, J. Glenn, S. R. Golwala, S. Kim, Y. Kang, D. Lydon, P. D. Mauskopf, C. R. Predmore, C. M. Roberts, K. Souccar, and M. S. Yun, “The AzTEC mm-wavelength camera,” *Monthly Notices of the Royal Astronomical Society* 386, pp. 807–818, MAY 11 2008.
- [5] F. Piacentini, P. Ade, R. Bhatia, J. Bock, A. Boscaleri, P. Cardoni, B. Crill, P. de Bernardis, H. Del Castillo, G. De Troia, P. Farese, M. Giacometti, E. Hivon, V. Hristov, A. Iacoangeli, A. Lange, S. Masi, P. Mauskopf, L. Miglio, C. Netterfield, P. Palangio, E. Pascale, A. Raccanelli, S. Rao, G. Romeo, J. Ruhl, and F. Scaramuzzi, “The BOOMERANG North America instrument: A balloon-borne bolometric radiometer optimized for measurements of cosmic background radiation anisotropies from 0.degrees 3 to 4 degrees,” *Astrophysical Journal Supplement Series* 138, pp. 315–336, FEB 2002.
- [6] S. Masi, P. A. R. Ade, J. J. Bock, J. R. Bond, J. Borrill, A. Boscaleri, P. Cabella, C. R. Contaldi, B. P. Crill, P. de Bernardis, G. De Gasperis, A. de Oliveira-Costa, G. De Troia, G. Di Stefano, P. Ehlers, E. Hivon, V. Hristov, A. Iacoangeli, A. H. Jaffe, W. C. Jones, T. S. Kisner, A. E. Lange, C. J. MacTavish, C. M. Bettolo, P. Mason, P. D. Mauskopf, T. E. Montroy, F. Nati, L. Nati, P. Natoli, C. B. Netterfield, E. Pascale, F. Piacentini, D. Pogosyan, G. Polenta, S. Prunet, S. Ricciardi, G. Romeo, J. E. Ruhl, P. Santini, M. Tegmark, E. Torbet, M. Veneziani, and N. Vittorio, “Instrument, method, brightness, and polarization maps from the 2003 flight of BOOMERanG,” *Astronomy & Astrophysics* 458, pp. 687–716, NOV 2006.
- [7] M. Griffin, A. Abergel, P. Ade, P. Andr e, J.-P. Baluteau, J. Bock, A. Franceschini, W. Gear, J. Glenn, D. Griffin, K. King, E. Lellouch, D. Naylor, G. Olofsson, I. Perez-Fournon, M. Rowan-Robinson, P. Saraceno, E. Sawyer, A. Smith, B. Swinyard, L. Vigroux, and G. Wright, “Herschel-SPIRE: design, performance, and scientific capabilities,” in *Space Telescopes and Instrumentation I: Optical, Infrared, and Millimeter*. Proceedings of the SPIE, Volume 6265, pp. 62650A (2006).
- [8] J.-M. Lamarre, J. L. Puget, M. Piat, P. A. R. Ade, A. E. Lange, A. Benoit, P. De Bernardis, F. R. Bouchet, J. J. Bock, F. X. Desert,



- R. J. Emery, M. Giard, B. Maffei, J. A. Murphy, J.-P. Torre, R. Bhatia, R. V. Sudiwala, and V. Yourchenko, "Planck high-frequency instrument," in *IR Space Telescopes and Instruments*. Edited by John C. Mather. Proceedings of the SPIE, Volume 4850, pp. 730-739 (2003).
- [9] A. Turner, J. Bock, J. Beeman, J. Glenn, P. Hargrave, V. Hristov, H. Nguyen, F. Rahman, S. Sethuraman, and A. Woodcraft, "Silicon nitride micromesh bolometer array for submillimeter astrophysics," *Applied Optics* 40, pp. 4921-4932, OCT 1 2001.
- [10] P. D. Mauskopf, J. J. Bock, H. del Castillo, W. L. Holzapfel, and A. E. Lange, "Composite infrared bolometers with Si<sub>3</sub>N<sub>4</sub> micromesh absorbers," *Applied Optics* 36, pp. 765-771, Feb. 1997.
- [11] M. A. Lindeman, S. Bandler, R. P. Brekosky, J. A. Chervenak, E. Figueroa-Feliciano, F. M. Finkbeiner, M. J. Li, and C. A. Kilbourne, *Rev. Sci. Instrum.* 75, 1283 2004.
- [12] P. Khosropanah, B. Dirks, J. van der Kuur, M. Ridder, M. Bruijn, M. Popescu, H. Hoevers, J. R. Gao, D. Morozov, and P. Mauskopf, "Low Thermal Conductance Transition Edge Sensor (TES) for SPICA", *AIP Conf. Proc.* 1185, 42 (2009), DOI:10.1063/1.3292369
- [13] D. Morozov, P. D. Mauskopf, P. Ade, M. Bruijn, P. A. J. de Korte, H. Hoevers, M. Ridder, P. Khosropanah, B. Dirks, and J.-R. Gao, "Ultrasensitive TES bolometers for space based FIR astronomy", *AIP Conf. Proc.* 1185, 48 (2009), DOI:10.1063/1.3292385
- [14] P. Khosropanah, B.P.F. Dirks, M. Parra-Borderias, M. Ridder, R. Hijmering, J. van der Kuur, L. Gottardi, M. Bruijn, M. Popescu, J.R. Gao, H. Hoevers, "Transition Edge Sensors (TES) Using a Low-G Spider-Web-Like SiN Supporting Structure," *Applied Superconductivity, IEEE Transactions on*, vol.21, no.3, pp.236-240, June 2011.
- [15] J. Mather, "Bolometer noise: nonequilibrium theory", *Appl. Opt.* 21, 1125-1129 (1982).

## Optical characterization of high sensitivity TES detectors designed for the SPICA/SAFARI 30-60 $\mu\text{m}$ channel

D. Morozov<sup>1\*</sup>, P. D. Mauskopf<sup>1</sup>, P. A. R. Ade<sup>1</sup>, D. Griffin<sup>2</sup>, J.R. Gao<sup>3,4</sup>, H. F. C. Hoevers<sup>3</sup>, P. Khosropanah<sup>3</sup>, R. Hijmering<sup>3</sup>, M. Ridder<sup>3</sup> and M. Bruijn<sup>3</sup>

*1 Cardiff University, School of Physics and Astronomy\*, Cardiff, UK CF24 3AA*

*2 Rutherford Appleton Laboratory, Harwell Science and Innovation Campus, Didcot OX11 0QX*

*3 SRON Netherlands Institute for Space Research, 3584 CA Utrecht, the Netherlands*

*4 Kavli Institute of NanoScience, Delft University of Technology, Lorentzweg 1, 2628 CJ Delft, the Netherlands*

\* Contact: Dmitry.morozov@astro.cf.ac.uk, phone +44-2920-870 159

**Abstract**—High sensitivity TES detectors have been selected as the baseline detector technology for the SAFARI instrument on the SPICA telescope. SAFARI is an imaging Fourier transform spectrometer operating over the wavelength range from 34 – 205  $\mu\text{m}$  (1.5-10 THz). The SAFARI detectors are divided into 3 focal plane units, each covering an octave in wavelength: 34-60, 60-110 and 110-205  $\mu\text{m}$ . The low background environment places a requirement on the sensitivity or noise equivalent power (NEP) of the detectors to be  $\text{NEP}=2\text{-}3 \times 10^{-19} \text{ W}/\sqrt{\text{Hz}}$ . In this paper, we describe the characterization of high-sensitivity TES detectors designed for operation in the short wavelength band of SAFARI from 34-60  $\mu\text{m}$  (5-10 THz). Each detector consists of a TiAu TES thermometer and an optical absorber fabricated from a thin Tantalum (Ta) film deposited on a thermally isolating silicon nitride (SiN) structure. The TES thermometers have transition temperatures of approximately 100 mK and the thermal conductance,  $G$ , varies from  $G = 0.2\text{-}2 \text{ pW/K}$  for different thermal isolation geometries. We measure the NEP for several devices as a function of frequency from the measured noise spectral density and electrical responsivity and routinely obtain values for the  $\text{NEP}=4\text{-}6 \times 10^{-19} \text{ W}/\sqrt{\text{Hz}}$  with time constants of  $< 1 \text{ ms}$ . With these devices, we measure the absorbed optical power and corresponding photon noise from a blackbody source as a function of source temperature through a set of two high pass and two low pass filters defining a pass-band from 5-10 THz. The radiation from the blackbody source is coupled to an integrating cavity containing the TES and absorber using an electroformed conical horn. We find that these detectors have good optical performance and the dependence of absorbed power on blackbody temperature agrees with the values calculated from the combination of the blackbody emission spectrum and the measured filter transmission. The measured photon noise allows a confirmation of the calibration of the measured NEP from the electrical responsivity, a direct measurement of the optical response time of the detector and confirms that the mean energy of the absorbed photons is 5.6 THz.

# Scalable Terahertz-Frequency HEB Mixers

F. Boussaha, J. Kawamura, J. Stern, A. Skalare, V. White

**Abstract**— We are developing low noise waveguide-based heterodyne mixer employing a superconducting NbN hot electron bolometer (HEB) operating around 2.7 THz. The mixer is an NbN nano-bridge integrated with a gold bowtie planar antenna on an ultra-thin silicon substrate of 3  $\mu\text{m}$  thickness. To produce the waveguide embedding circuit for use at such a high frequency, we adopted an original approach combining UV-lithography and micro-plating techniques. The concept was successfully tested at a lower frequency (1.46 THz) where a low noise temperature is achieved. At 2.74 THz, we measured a minimum uncorrected DSB receiver noise temperature of 965 K.

**Index Terms**—Hot Electron Bolometer, waveguide, gold microplating, heterodyne receiver.

## I. INTRODUCTION

JPL is developing waveguide mixers for operation at 1.5 THz [1] for the Stratospheric Terahertz Observatory (STO), a balloon-borne telescope to map a portion of our Galaxy in two key spectroscopic lines [2]. STO will have four spatial pixels per band, representing an incremental improvement from Herschel HIFI [3], which has two in orthogonal polarizations. Future instruments for missions like SOFIA [4] will require an order of magnitude more pixel elements to produce the required science data. Looking ahead to the future, we thus require scalability in terms of both pixel count and frequency. In increasing pixel count, an approach is to produce a filled focal plane array, for example, like a high-frequency version of Supercam, a 64-pixel 0.35 THz camera being built by the University of Arizona. Waveguide mixers offer a compact arrangement as well as the possibilities to implement more sophisticated mixer topology and integration with a local-oscillator source. However, simultaneously increasing the design frequency and pixel count we push conventional machining techniques beyond their practical limits.

Manuscript received August 30, 2011. This research is carried out at the Jet Propulsion Laboratory, California Institute of Technology. The research described is partly supported by Oak Ridge Associated Universities through the NASA Postdoctoral Program (NPP).

F. Boussaha is with Jet Propulsion Laboratory – NASA, 4800 Oak Grove Drive Pasadena CA 91109 USA (phone: 818-354-4488; fax: 818-393-4683; e-mail: faouzi.m.boussaha@jpl.nasa.gov).

J. Kawamura is with Jet Propulsion Laboratory – NASA, 4800 Oak Grove Drive Pasadena CA 91109 USA (phone: 818-393-4779; fax: 818-393-4683; e-mail: jonathan.h.kawamura@jpl.nasa.gov).

J. Stern is with Jet Propulsion Laboratory – NASA, 4800 Oak Grove Drive Pasadena CA 91109 USA (e-mail: jeffrey.a.stern@jpl.nasa.gov).

A. Skalare is with Jet Propulsion Laboratory – NASA, 4800 Oak Grove Drive Pasadena CA 91109 USA (e-mail: anders.skalare@jpl.nasa.gov).

V. White is with Jet Propulsion Laboratory – NASA, 4800 Oak Grove Drive Pasadena CA 91109 USA (e-mail: victor.e.white@jpl.nasa.gov).

Recognizing this, we are investigating a lithographic microplating technique, pioneered for this application, for example, by Chalmers [5]. By utilizing microplating approach, we can mass-produce waveguide circuits with micron-level precision and nanometer wall smoothness. We compare a mixer produced entirely by conventional machining and a duplicate unit whose critical waveguide structures were fabricated using the microplating technique. At 1.5 THz the mixer performance is indistinguishable; both mixers gave a lowest uncorrected DSB receiver noise temperatures of 850 K were measured at around 1.45 THz (more details are presented elsewhere [1]). In this paper, we adopt the microplating technique for a higher frequency operation around 2.7 THz. This allows us to produce numerous waveguide circuits at low cost with excellent reproducibility.

## II. CONCEPT AND DESIGN

Figure 1 depicts the basic mixer circuit utilized in this work. It consists of the mixer chip placed in a channel crossed by a waveguide which couples the RF signal from the feed antenna to the mixer. For producing the mixer chips, we use high-resistive silicon on insulator (SOI) substrate, which is compatible with nitride growth for NbN films [6]. The metallization and the HEB nanobridge are suspended at a distance corresponding to the substrate thickness  $t_{\text{sub}}$  plus an air-cavity depth  $t_{\text{cavity}}$  from the bottom. To realize the mixer block, we use a split-block configuration [7-8] consisting of a section with a feedhorn input ending with a rectangular waveguide (not shown) and a back section with the mixer chip in a waveguide circuit. In Fig. 1, the two pieces are shown to be separated by the XY plane.

The main challenge in manufacturing of the mixer block lies in the producing the channel with the small dimensions that holds the mixer. This can be regarded as the stack of 3 cavities whose dimensions are summarized in table 1. To address this issue, the channel is not machined directly on the back metal piece, but micro-plated onto a silicon wafer using deep-UV photolithography to define the structures. The dimensions of the silicon back-piece are also defined using lithography and deep-trench reactive ion etching. This backpiece is then inserted into a pocket precisely machined in the metal back piece. This approach allows accurate definition of smaller patterns since it is limited by lithography and not the machining technique. A key requirement of this approach is to ensure good alignment between the two pieces of the mixer. This is accomplished by utilizing high precision conventional machining where metrology of several microns can be readily achieved. Another important simplifying aspect of our

approach is that, unlike several previous authors [9-14], we do not use a frame around the mixer chip or beam leads for handling and contacting. This greatly simplifies the fabrication thus increasing yield and reducing fabrication time. Also the use of a frame can make it difficult to thermally heat sink the mixer chip.

### A. HEB mixer device

The mixer in fig. 1 is optimized using HFSS 3D electromagnetic simulator. The mixer chip is made up of a superconducting HEB nanobridge of  $\sim 4$  nm-thick integrated along with a bowtie antenna which converts the waveguide  $TE_{10}$  EM field to RF currents and couples them to the HEB mixer. The antenna is connected to choke filters contacted by IF and DC bias leads. The optimization was carried out with a HEB resistance set to  $80\Omega$ . The silicon substrate is  $22\mu\text{m}$  wide and  $3\mu\text{m}$  thick. The channel into which is inserted the chip is crossed by a half height waveguide (HHWG) of  $78 \times 19 \mu\text{m}$ . The mixers are fabricated on 3-inch diameter SOI wafers. The top Si layer is high resistivity silicon nominally  $3.0 \mu\text{m}$  thick, although the actual wafers were  $2.5 \mu\text{m}$  on a 2 micron oxide layer and a 0.4 mm handle wafer. The NbN films have a sheet resistance of  $1000 \Omega$  and a critical transition temperature of  $T_c > 9$  K with a transition width of 0.5 K. Typical mixer chips were  $1.5$  by  $0.2 \mu\text{m}$  with a resistance of  $80$ - $100 \Omega$ . The fabrication process is described in [15].

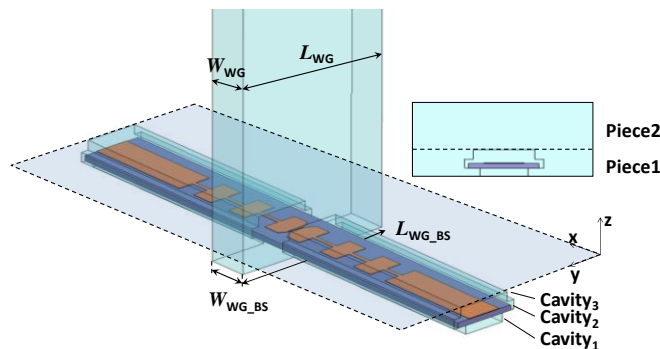


Figure 1: HEB Mixer structure designed at 1.46 THz then scaled up 2.7 THz. The plane XY materializes the mixer split-block concept which consists of a horn piece followed by the waveguide ( $L_{WG}$ ,  $W_{WG}$ ) and a back piece in which is defined a channel crossed by the waveguide backshort ( $L_{WG\_BS}$ ,  $W_{WG\_BS}$ ). The chip is inserted into the channel.

Cavity	t( $\mu\text{m}$ )	w( $\mu\text{m}$ )
1	5	26
2	3.5	40
3	5	26

### B. Mixer block

The 2.7 THz mixer is essentially a scaled version of the 1.46 THz mixer. With the critical dimensions being reduced to nearly half-size (see Table 1), the critical element of the mixer circuit design cannot be readily produced by conventional machining. The mixer block consists of 3 pieces. A metal horn piece, realized by RPG Company [16], has a Pickett Potter

horn ending a section of waveguide, a 2-mm-square silicon chip on which the mixer circuitry is printed and mixer mounted, and a metal back piece with a pocket to receive the silicon chip and an SMA connector on the back side. Figure 2 shows the electron microscope image of the micro-plated channel structure. This part consists of three layers of gold each with a nominal thickness shown in Table 1, crossed by a back short waveguide, with a lateral dimension of  $78 \times 19 \mu\text{m}$ . Each layer is defined by photolithography using GKR 4400 resist followed by a plating step (further fabrication process details are in [17]).

### C. Assembly

The assembly process goes as follows: The chip is slid into the channel so that the center of the antenna is properly aligned in the middle of the waveguide, as shown in Fig. 3-a. Figure 3-b displays a close-up view of an electron micrograph showing how the mixer is precisely aligned in the waveguide. The electrical contact pads are contacted by means of ultrasonic wire bonding.

The silicon piece is inserted into the square pocket and the horn piece is clamped in place. The two sections are aligned to each using steel dowel pins, and the Si piece is aligned mechanically to the back piece by the perimeter of the pocket.

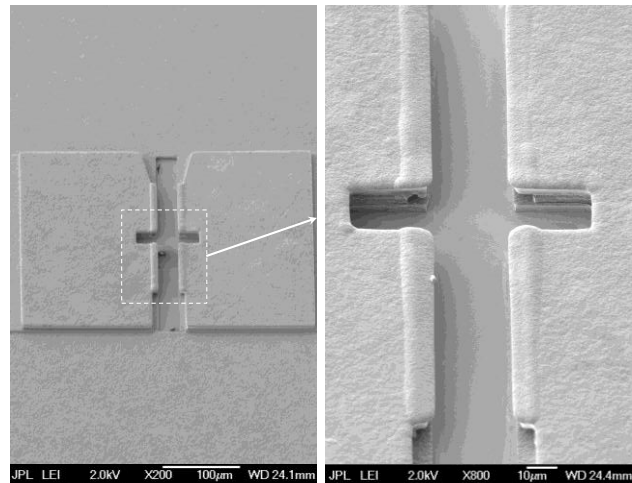


Figure 2: Electron microscope image of the channel structure consisted of stack of 3 gold layers of 5, 4 and 5  $\mu\text{m}$ -thick, respectively and realized by means of the UV-photolithography and the micro-plating technique.

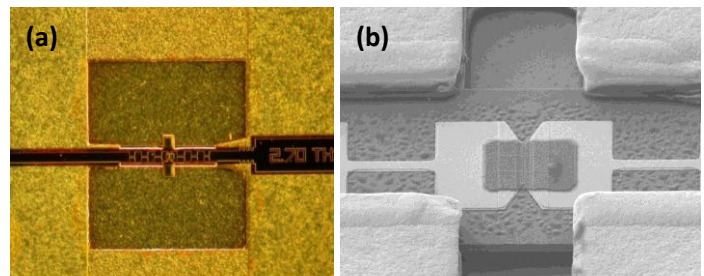


Figure 3: Optical microscope image (a) and electron microscope image (b) of the 2.7 THz mixer chip inserted in the channel. The HEB integrated along with the bowtie antenna is properly aligned in

the waveguide. An SiO<sub>2</sub> passivation layer covers the superconducting HEB nanobridge. The ultra-thin substrate ( $t \approx 2.3 \mu\text{m}$ ) is kept flat by the substrate channel.

The alignment may be verified on an assembled mixer by looking down the feed with a microscope. A circular spring is placed behind the silicon chip to ensure that it maintains physical contact to the horn section during deep cryogenic cooling (see fig. 3).

### III. EXPERIMENT AND MEASUREMENTS

The mixer block is fixed on a 4.2 K cold plate of a liquid helium cryostat. The RF radiation passes the cryostat window, a 1 mm-thick sheet of high-density polyethylene, and the infrared filter, a layer of porous Teflon material on the liquid nitrogen-cooled radiation shield. The output signal at the intermediate frequency is amplified by a cryogenic low noise amplifier with an input noise temperature of 5 K, followed by a room-temperature amplifier and filtered for a final IF bandwidth centered at 1.5 GHz with a detection bandwidth of 500 MHz. The NbN nanobridge mixer device has a width of 2.5 and a length of 0.25  $\mu\text{m}$ , with a normal state resistance of 84  $\Omega$  with a critical current of 120  $\mu\text{A}$ . The current-voltage curves are plotted in Fig. 5.

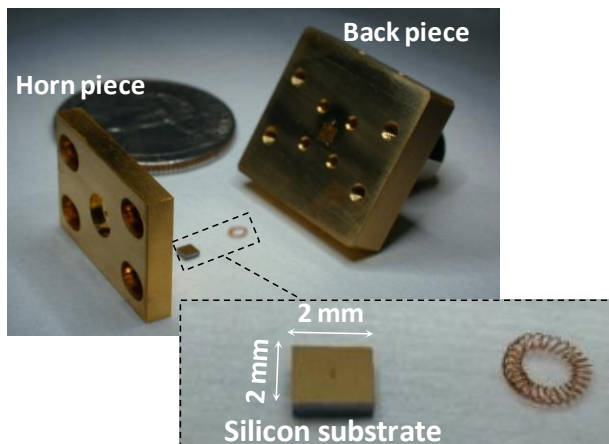


Figure 4: Picture of the mixer split-block consisting of a metal horn piece, a 2-mm square silicon chip holding the mixer, and a metal back piece with an SMA connector on its back side. The spring is placed behind the substrate to exert a force to push the chip against the horn piece.

The sensitivity of mixer is measured by terminating the input of the receiver with room temperature ( $T_{\text{hot}}=295 \text{ K}$ ) and liquid-nitrogen ( $T_{\text{cold}}=77 \text{ K}$ ) temperature loads. A molecular gas laser tuned at a frequency of 2.74 THz was used. The receiver noise temperature is computed using the expression  $T_{\text{rec}}=(T_{\text{eff,hot}}-YT_{\text{eff,cold}})/Y-1$ , where, according to the Callen-Welton formula [18],  $T_{\text{hot}}$  and  $T_{\text{cold}}$  become  $T_{\text{eff,hot}} = 300 \text{ K}$  and  $T_{\text{eff,cold}} = 95 \text{ K}$ , respectively, at 2.74 THz. There is so much LO power margin using the laser that the grid beam splitter angle was set to provide minimum LO port coupling ( $< 1\%$ ). In this set-up we measured a DSB receiver noise temperature of  $965 \pm 30 \text{ K}$  ( $Y$ -factor of  $1.19 \pm 0.005$ ).

These results are comparable to those measured based on

quasi-optical mixer block employing a dielectric lens around 2.7 THz [19-21]. Yet we do not consider these values representing the ultimate sensitivity since it is done without any correction of optical losses. Therefore, we expect an improved noise temperature receiver using a vacuum receiver calibration setup.

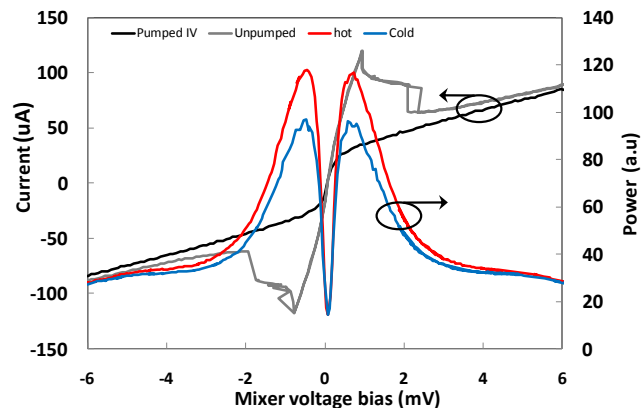


Figure 5: Unpumped and pumped  $I$ - $V$  curves as well as output powers at intermediate frequency (IF) at hot (295K) and cold (77K) load temperatures at 2.74 THz.

### ACKNOWLEDGMENT

This research is carried out at the Jet Propulsion Laboratory, California Institute of Technology. The research described is partly supported by Oak Ridge Associated Universities through the NASA Postdoctoral Program (NPP). We thank P. Bruneau from JPL Space Instruments Shop for the fabrication of metal back pieces and Timothy Crawford from JPL Molecular Spectroscopy team for FTS measurements.

### REFERENCES

- [1] J. Kawamura, A. Skalare, J. Stern, E. Tong, C. Ghroppi, "A 1.5 THz waveguide HEB mixer using Silicon-on Insulator substrates for STO", Proceedings of the 21<sup>th</sup> Int. Symp. Space Terahertz Tech., Oxford - UK, 2010.
- [2] C. Walker et al., "The Stratospheric THz Observatory (STO): 1st Test Flight", Proceedings of the 21<sup>th</sup> Int. Symp. Space Terahertz Tech., Oxford - UK, 2010.
- [3] T. De Graauw, F. P. Helmich, T. G. Phillips, et al. "The Herschel-Heterodyne Instrument for the Far-Infrared (HIFI)", Astronomy & Astrophysics, vol. 518, L6, 2010.
- [4] <http://www.sofia.usra.edu/Sofia/sofia.html>.
- [5] V. Desmaris, D. Meledin, A. Pavolotsky, R. Monje and V. Belitsky "All-metal micromachining for the fabrication of sub-millimetre and THz waveguide components and circuits", J. Micromech. Microeng., Vol. 18, No. 9, 2008.
- [6] B. Guillet, V. Drakinskiy, R. Gunnarsson, O. Arthursson, L. Méchin, S. Cherednichenko, Y. Delorme, J.M. Krieg, "Influence of substrates and buffer layers on the quality of NbN ultra thin film for THz HEB", Proceedings of the 18<sup>th</sup> Int. Symp. Space Terahertz Tech., Groningen, Netherlands, 2008.
- [7] R. Blundell, C. E. Tong, D. C. Papa, R. Leombruno, X. Zhang, S. Paine, J. A. Stern, H. G. Le Duc, "A wideband fixed-tuned SIS receiver for 200 GHz operation", IEEE Trans. Microwave Theory Tech., 43, pp. 933-937, 1995.
- [8] A. Skalare, J. Stern, B. Bumble, F. Maiwald, "Hot-Electron Bolometer Mixers on Silicon-On-Insulator substrates for Terahertz Frequencies", Proceedings of the 16<sup>th</sup> Int. Symp. Space Terahertz Tech., Gothenburg, Sweden, 2005.

- [9] P. Puetz, K. Jacobs, M. Justen, F. Schomaker, M. Schultz, S. Wulff, C. E. Honingh, "NbTiN Hot Electron Bolometer Waveguide Mixers on Si<sub>3</sub>N<sub>4</sub> Membranes at THz Frequencies", IEEE/CSC & ESAS European Superconductivity News Forum (ESNF), No. 15, Jan. 2011.
- [10] D. Dochev, V. Desmaris, D. Meledin, A. Pavolotsky, V. Belitsky, "A Technology Demonstrator for 1.6–2.0 THz Waveguide HEB Receiver with a Novel Mixer Layout", J. Infrared Milli. Terahz. Waves 32:451–465, 2011.
- [11] D. Meledin, A. Pavolotsky, V. Demaris, I. Lapkin, C. Risacher, V. Perez, D. Henke, O. Nystrom, E. Sundin, D. Dochev, M. Pantaleev, M. Strandberg, B. Voronov, G. Goltsman, V. Belitsky, "A 1.3 THz Balanced Waveguide HEB Mixer for APEX Telescope", IEEE Trans. Microw. Theory Tech., vol. 57, Issue 1, pp. 89-98, Jan. 2009.
- [12] P. P. Munoz, S. Bedrof, M. Brandt, T. Tils, N. Honingh, K. Jacobs, "THz Waveguide Mixers with NbTiN HEBs on Silicon Nitrides Membranes", IEEE Microw. Wireless Comp. Lett., Vol. 16, No. 11, Nov. 2006.
- [13] L. Jiang, S. Shiba, K. Shimbo, N. Sakai, T. Yamakura, M. Sugimura, P. G. Ananthasubramanian, H. Maezawa, Y. Irimajiri, and S. Yamamoto, "Development of THz Waveguide NbTiN HEB Mixers", IEEE Tran. Appl. Supercond., vol. 19, no. 3, Jun. 2009.
- [14] L. Jiang, S. Shiba, T. Shiino, K. Shimbo, N. Sakai, T. Yamakura, Y. Irimajira, P. G. Ananthasubramanian, H. Maezawa, and S. Yamamoto, "Development of 1.5 THz Waveguide NbTiN superconducting hot electron bolometer Mixers", Supercond. Sci. Technol. 23 (045025), 2010.
- [15] J. A. Stern, B. Bumble, J. Kawamura and A. Skalare, "Fabrication of terahertz frequency phonon cooled HEB mixers", IEEE Trans. Appl. Supercond., vol. 15, no. 2, pp. 499-502, Jun. 2005.
- [16] Radiometer Physics GmbH, [www.radiometer-physics.de](http://www.radiometer-physics.de).
- [17] F. Boussaha, J. Kawamura, J. Stern, A. Skalare, J. White, "A low noise 2.7 THz waveguide-based NbN HEB mixer", in preparation.
- [18] A. K. Kerr, "Suggestions for revised definitions of noise quantities, including quantum effects", IEEE Trans. Microw. Theory Tech., Vol. 47, Issue 3, pp. 325-329, 1999.
- [19] P. Khosropanah, W. Zhang, J. N. Hovenier, J. R. Gao, T. M. Klapwijk, M. I. Amanti, G. Scalari, J. Faist, "3.4 Thz heterodyne receiver using a hot electron bolometer and a distributed feedback quantum cascade laser", J. of appl. Phys.104, 113106, 2008.
- [20] J. R. Gao, J. N. Hovenier, Z. Q. Yang, J. J. A. Baselmans, A. Baryshev, M. Hajenius, T. M. Klapwijk, A. L. Adam, T. O. Klaassen, B. S. Williams, S. Kumar, Q. Hu, J. L. Reno, "Terahertz heterodyne receiver based on a quantum cascade laser and a superconducting bolometer", Appl. Physic. Lett. 86, 244104, 2005.
- [21] M. Hajenius, P. Khosropanah, J. N. Hovenier, J. R. Gao, T. M. Klapwijk, S. Barbieri, S. Dhillon, P. Filloux, C. Sirtori, D. A. Ritchie and H. E. Beere "Surface plasmon quantum cascade lasers as terahertz local oscillators", Optics Lett., vol. 33, no. 4, February 2008.

# A quasi-optical NbN HEB mixer with 800K DSB noise temperature at 2.5 THz

Y. Delorme<sup>1</sup>, R. Lefèvre<sup>1</sup>, W. Miao<sup>1,3</sup>, A. Féret<sup>1</sup>, W. Zhang<sup>3</sup>, T. Vacelet<sup>1</sup>, F. Dauplay<sup>1</sup>, L. Pelay<sup>1</sup>, J. Spatazza<sup>1</sup>, M. Ba Trung<sup>1</sup>, J.-M. Krieg<sup>1</sup>, Y. Jin<sup>2</sup>, P. Khosropanah<sup>4</sup>, J. R. Gao<sup>4,5</sup> and S. C. Shi<sup>3</sup>

1. *LERMA, Observatoire de Paris, UPMC, CNRS, 75014 Paris, France*

2. *LPN, Laboratoire de Photonique et de Nanostructures, 91460 Marcoussis, France*

3. *Purple Mountain Observatory, NAOC, CAS, Nanjing, Jiangsu 210008, China*

4. *SRON Netherlands Institute for Space Research, 9747 AD Groningen, The Netherlands*

5. *Kavli Institute of Nanoscience, Delft University of Technology, 2628 CJ Delft, The Netherlands*

\* Contact: yan.delorme@obspm.fr, phone +33-1-4051 2042

**Abstract**— This paper presents the heterodyne measurement results of a quasi-optical NbN mixer at 2.5 THz. The HEB device was developed at LERMA in the frame of a CNES research project and the European programme Radionet FP7. It consists of a 2  $\mu\text{m}$  wide, 0.2  $\mu\text{m}$  long and about 3.5 nm thick NbN bridge on a silicon substrate. THz radiation is coupled to the HEB device through a quasi-optical circuit including an integrated spiral antenna and an anti-reflection coated hyper-hemispherical Si lens. The noise temperature measurement was performed at SRON using an optically pumped FIR gas laser as LO and a hot/cold load setup in vacuum to obtain the Y-factor. Two methods have been employed to measure the receiver noise temperature, either by adjusting the LO power at a fixed bias voltage between the hot and cold load to suppress the direct detection effect or by scanning the LO power when the bias voltage is kept constant to overcome the laser power fluctuations and the direct detection. The double sideband receiver noise temperatures obtained by both methods and without any corrections are as low as 800 K at 2.5 THz.

## I. INTRODUCTION

OBSERVING the fundamental transitions of HD and OH in the interstellar medium in the range of 2.5 to 2.7 THz has particular interest for astronomical research since it yields important information about the understanding of the star formation as well as the oxygen and nitrogen chemistries. However, detections of HD and OH so far performed by space missions have suffered from a lack of spectral resolution [1] [2]. The recent development on superconducting Hot Electron Bolometer (HEB) mixers [3] makes it possible to design highly sensitive spectrometers with enough spectral resolution. During the last decade, HEB mixers have been successfully used to detect spectral lines up to 2 THz on ground and space telescopes [4] [5].

We are developing quasi-optical phonon-cooled NbN HEB mixers operating at frequencies between 2-3 THz with the aim of building a heterodyne receiver for CIDRE (Campagne

d'Identification du Deutérium par Détection hÉtérodyne), a balloon experiment at an altitude of 40 km which will be carried out by CNES (Centre National d'Études Spatiales). It consists of carrying a heterodyne receiver mounted on a 80 cm telescope to observe from above most of the earth atmosphere the transitions of OH and HD in the interstellar molecular clouds.

For this mixer development, we have adopted a device fabrication process using direct Au-NbN contact. Excellent DSB noise temperature has been obtained with the realized HEB receiver. We will present in following sections the development and the measurement results of the receiver.

## II. DEVICES DESIGN AND FABRICATION

A quasi-optical design using an extended hemi-spherical silicon lens combined with a planar complementary logarithmic spiral antenna was chosen. The spiral antenna has an impedance nearly frequency independent in a broad frequency range which can be approximately determined by the outer and the inner diameter of the spiral [6]. For this quasi-optical design, we first used full wave electromagnetic solvers ANSYS-HFSS [7] and CST- Microwave Studio [8] to calculate the antenna's input impedance and its radiation pattern by replacing the lens by an infinite dielectric half space. At frequencies around 2.5 THz, the simulated input impedance obtained by both solvers is about 78  $\Omega$  with a reactance around 10  $\Omega$ . To include the lens effect, a hybrid approach combining geometrical and physical optics was used [9] to simulate and optimize the radiation characteristics of the whole integrated lens antenna configuration which still remains difficult to be simulated by full wave electromagnetic solvers.

The key element of a HEB mixer is a microbridge made from an ultra-thin superconductor film. The niobium nitride film used in this work was provided by the Russian company SCONTEL [10]. The film is deposited by magnetron DC reactive sputtering on a high purity silicon substrate. The

details of the NbN film deposition are presented in [11]. The device fabrication process was performed by using the facilities in the clean room of LPN [12]. Previous to this work, excellent receiver noise temperature of 950 K at 2.5 THz has been reported with NbN phonon-cooled HEB mixers processed by adding an additional superconducting interlayer to the Au contact pad [13]. In our process (Fig. 1), the direct Au–NbN contact structure without additional superconducting layer was adopted. The Au layer is deposited on the NbN film

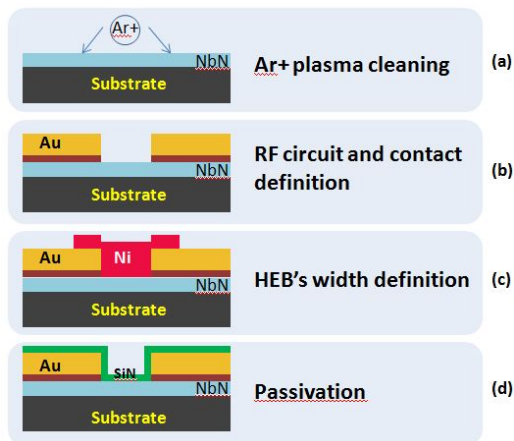


Fig. 1. Flowchart of the NbN HEB fabrication process.

after an in situ cleaning by the argon plasma. A 5 nm titanium layer is used as an adhesion layer. Then a lift-off process is performed on the Au layer to form the HEB's electrodes, the antenna, the transmission lines and the contact pads. The width of the microbridge is determined by reactive ion etching through a mask made of nickel. Finally a dielectric SiN layer

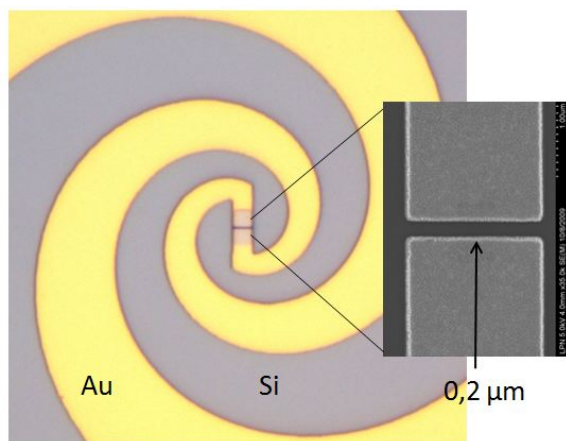


Fig. 2. Scanning electron microscope (SEM) image of a HEB device including the spiral antenna and the NbN bridge. The inset is a close-up of the NbN bridge with a length of 200 nm.

was deposited on the whole substrate for protection.

Fig. 2 shows the fabricated device consisting of a 2  $\mu\text{m}$  wide, 0.2  $\mu\text{m}$  long and 3.5 nm thick NbN bridge which is connected to the spiral antenna's inner terminals made of Au.

The device is then glued on the flat side of a hyper-hemispherical Silicon lens which is mounted into a copper

mixer block to be fixed in the cold plate of a 4.2K liquid helium cryostat. The extended hemispherical lens is coated with a 18  $\mu\text{m}$  thick parylene layer as an antireflection coating which is optimal for 2.5 THz.

The HEB device has a critical current of 260  $\mu\text{A}$  at 4.2K. The critical temperature  $T_c$  is around 9.2 K with a  $\Delta T_c$  about 1.2 K. The DC resistance at room temperature is 74  $\Omega$  which is close to the simulated impedance of the log-spiral antenna (about 78  $\Omega$ ).

### III. EXPERIMENTS AT 2.5 THZ

The mixer's characterization at 2.5 THz was performed at SRON using the Y factor measurement method during a joint measurement campaign carried out in the frame of the European programme FP7 Radionet-Amstar+. Fig. 3 illustrates the measurement setup at SRON. The LO source is an optically pumped far infrared laser adjusted at 2.5 THz. The LO power received by the HEB mixer is regulated by a rotating wire grid. The hot / cold blackbody load set used for the Y factor measurement was built in a vacuum box and attached to the cryostat. Between the mixer block and the hot / cold load there is no window but only a heat filter with 5 THz upper cutoff frequency. The LO and RF (from hot and cold loads) signals are combined by a beamsplitter made of a 3  $\mu\text{m}$  thick Mylar film inside the vacuum box. The use of the vacuum box attached to the cryostat allows to avoid the

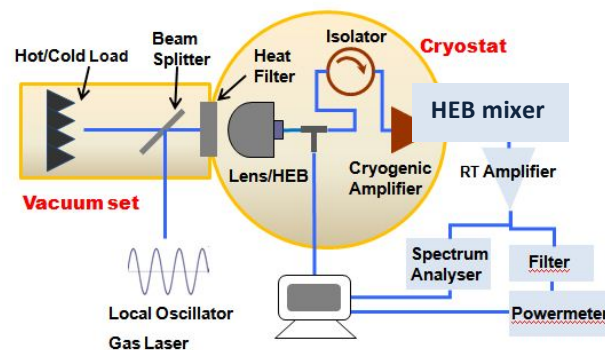


Fig. 3. Illustration of the measurement setup at SRON. The hot/cold loads used for the Y factor measurement and the beam splitter are built in a vacuum unit which is directly attached to the HEB cryostat.

atmospheric absorptions which are significant at 2.5 THz [14]. The HEB mixer's IF output signal is directed, through a bias-T and an isolator, to the input of a Berkshire cryogenic HEMT amplifier with a center frequency at 1.5GHz and followed by two room temperature amplifiers. The IF output power is recorded by a powermeter through a 200 MHz filter and a fast Agilent power head.

The Y factor is given by  $Y = P_{\text{IF}(\text{hot})} / P_{\text{IF}(\text{cold})}$ . The double sideband (DSB) receiver noise temperature is calculated from:  $T_R = (T_{\text{Hot}} - T_{\text{Cold}} * Y) / (Y - 1)$ , where  $T_{\text{Hot}}$  and  $T_{\text{Cold}}$  are respectively the temperatures of the blackbody at 293 K and 77 K with the effective radiation temperature of 297 K and



92 K at 2.5 THz according to the Callen-Welton definition [15].

We first measured the Y factor in the commonly used way by measuring the receiver's IF output power as a function of the HEB's bias voltage. The noise temperature is then derived from the Y factor. During the tests, we noticed a direct detection effect on the IV curves. The pumped IV curve is

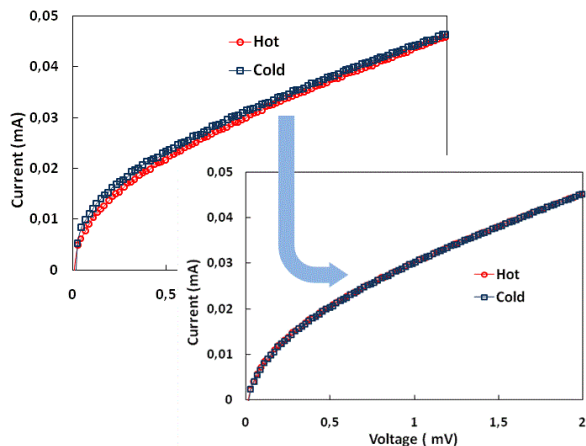


Fig. 4. Current-voltage characteristics of the HEB device responding to the hot and cold load. The direct detection effect (left) was disappeared by adjusting the LO power (right).

slightly changed between hot and cold load (Fig. 4. left). To compensate this effect, the LO power was adjusted to make the IV curves unchanged between hot and cold load measurements (as shown in Fig. 4. right). The degradation of the measured receiver noise temperature caused by the direct detection effect was estimated about 9 % in this experiment.

Fig. 5 shows the measurement results at the optimum LO power. The measured DSB receiver noise temperature presents a relatively broad region of optimal response in its voltage dependence around 0.6 mV, where the lowest noise without correction is as low as 790 K. The LO power absorbed by the HEB and calculated by the isothermal technique is about 280 nW.

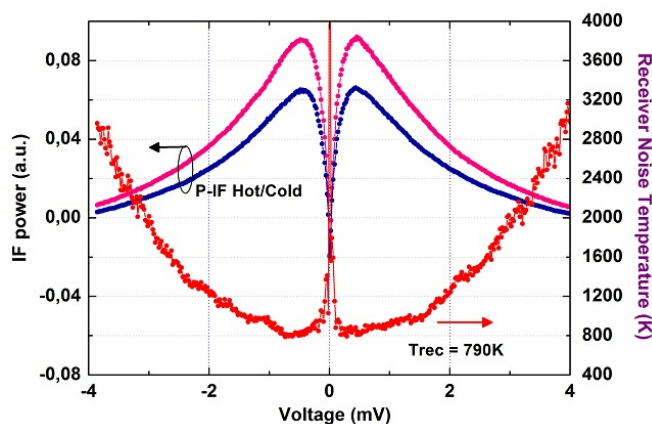


Fig. 5. Measured receiver IF output power (left axis) responding to the hot and cold load at optimal LO power together with the DSB receiver noise temperature (right axis) as a function of bias voltage.

The second measurement method was introduced in order to overcome the influence of the fluctuation of HEB's current on the mixer's sensitivity. This current fluctuation may be caused by the direct detection effect or by the change of LO power due to the laser instability or the air vibrations. This method has been proposed in [16] and consists of measuring, at one fixed bias voltage, the HEB's current and the IF output power for the hot and cold load while the LO power level was changed, from very low to almost fully pumped level. The Y factor is deduced from the fitted curves, i.e. from each pair of fitted lines of hot and cold IF output power. Since the Y factor is calculated for each pair of points  $P_{IF(hot)}$  and  $P_{IF(cold)}$  at exactly the same bias voltage and current, the noise temperature obtained in such a way is then not influenced by either the LO power fluctuations or the direct detection.

Fig. 6 shows the measurement at the optimal bias voltage,

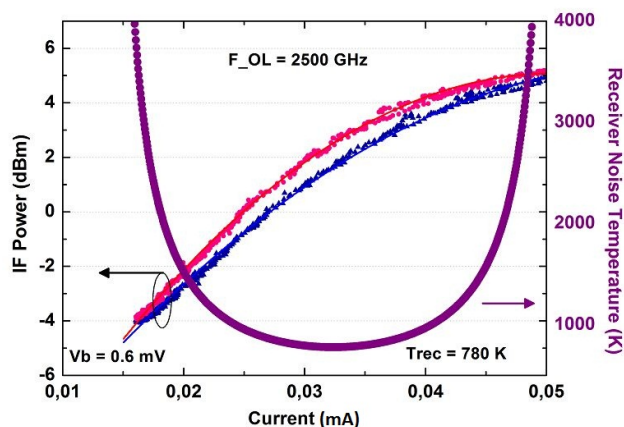


Fig. 6. Measured and fitted IF output power and the deduced noise temperature of the receiver as a function of the mixer's current when the bias voltage is 0.6 mV. The lowest noise temperature is below 800K.

0.6 mV. By the calculation from the fitted curves, we determined the noise temperature corresponding to all LO pumping levels at this bias voltage. The lowest receiver noise is 780K, which is in good agreement with the one measured with the first method.

#### IV. CONCLUSION

We have presented the development of a quasi-optical phonon cooled NbN HEB mixer working at 2.5 THz for CIDRE, a stratospheric balloon experiment. The HEB device was fabricated with a recently developed process using a direct Au-NbN contact structure. With the excellent DSB receiver noise temperature of 800 K measured at 2.5 THz without any corrections, we have shown that HEB devices with a direct Au-NbN contact and processed without using in situ technology are able to offer state-of-the-art sensitivity at THz frequencies.

Multi-pixel configuration is currently under development and experiments with either multiplier chain or cascade quantum laser as THz local oscillator are planned.

## ACKNOWLEDGMENT

This work has been funded by CNES - Centre National d'Etudes Spatiales and the European programme Radionet FP7 – Amstar+.

## REFERENCES

- [1] Caux, E., Ceccarelli, C., Pagani, L., et al, *A&A*, 383, L9, 2002,
- [2] Cernicharo, J., Polehampton, E., and Goicoechea, J.R., *ApJ*, 657, L21, 2007.
- [3] Gerecht, E.; Musante, C.F.; Zhuang, Y.; Yngvesson, K.S.; Gol'tsman, G.N.; Voronov, B.M.; Gershenson, E.M. "NbN hot electron bolometric mixers - a new technology for low-noise THz receivers" *IEEE Trans. on Microwave Theory and Techniques*, vol.47, pp.2519, 1999.
- [4] C. Risacher, D. Meledin, V. Belitsky, and P. Bergman "First 1.3 THz Observations at the APEX Telescope", *Proc. of 20th Symposium on Space Terahertz Technology*, Charlottesville, April, 2009.
- [5] T. de Graauw, F. P. Helmich, T. G. Phillips, J. Stutzki, E. Caux, N. D. Whyborn, P. Dieleman, P. R. Roelfsema et al. "The Herschel-Heterodyne Instrument for the Far-Infrared (HIFI)", *Astronomy & Astrophysics*, Vol. 518, July-August 2010.
- [6] J. D. Dyson, "The equiangular spiral antenna", *IRE Trans. Antennas Propag.*, AP-7, 181-187, 1959.
- [7] High Frequency Structure Simulator, <http://www.ansoft.com>
- [8] Computer Simulation Technology, <http://www.cst.com>
- [9] A. D. Semenov, H. Richter, B. Gunther, H.W. Hubers, and J. Karamarkovic, "Integrated planar antennas at terahertz waves", *Proc. Of 16th International Symposium on Space Terahertz Technology*, Gothenburg, Sweden, pp. 324-328, 2005.
- [10] [www.scontel.ru](http://www.scontel.ru)
- [11] G. N. Gol'tsman, K. Smirnov, P. Kouminov, B. Voronov, N. Kaurova, V. Drakinsky J. Zhang, A. Verevkin, and R. Sobolewski, "Fabrication of Nanostructured Superconducting Single-Photon Detectors", *IEEE Transactions On Applied Superconductivity*, Vol. 13, No. 2, June 2003.
- [12] [www.lpn.cnrs.fr](http://www.lpn.cnrs.fr)
- [13] J. J. A. Baselmans, M. Hajenius, J. R. Gao, T. M. Klapwijk, P. A. J. de Korte, B. Voronov and G. Gol'tsman, "Doubling of sensitivity and bandwidth in phonon cooled hot electron bolometer mixers", *Appl. Phys. Lett.* 84 (11), 2004.
- [14] B. S. Karasik, M. C. Gaidis, W. R. McGrath, B. Bumble, and H. G. LeDuc, "Low noise in a diffusion-cooled hot-electron mixer at 2.5 THz", *Appl. Phys. Lett.* 71 (11), 1997.
- [15] A.R. Kerr, "Suggestions for revised definitions of noise quantities, including quantum effects", *IEEE Trans. MTT.* 47 (3), 1999.
- [16] P. Khosropanah, W. M. Laauwen, M. Hajenius, J.R. Gao, and T. M. Klapwijk, "Sensitivity of a hot electron bolometer heterodyne receiver at 4.3 THz", *19th International Symposium on Space Terahertz Technology*, Groningen, 28-30 April 2008.

# 560 GHz, 664 GHz and 1.2 THz Schottky based MMIC sub-harmonic mixers for planetary atmospheric remote sensing and FMCW radar

Bertrand Thomas<sup>1&2</sup>, Jose Siles<sup>1</sup>, John Gill<sup>1</sup>, Choonsup Lee<sup>1</sup>, Ken Cooper<sup>1</sup>,  
Alain Maestrini<sup>3</sup>, Sam Gulkis<sup>1</sup> and Imran Mehdi<sup>1\*</sup>

<sup>1</sup> NASA Jet Propulsion Laboratory, California Institute of Technology, Pasadena, CA, USA

<sup>2</sup> Radiometer Physics GmbH, Meckenheim, Germany

<sup>3</sup> Université Pierre et Marie Curie-Paris 6, LERMA, Paris, France

\* Contact: Imran.Mehdi@jpl.nasa.gov, phone +1-818-354-2001

**Abstract-** We present here the development of several sub-millimeter wave heterodyne receivers based on MMIC Schottky. First, a 560 GHz heterodyne receiver using MMIC Schottky devices has been developed by JPL. It features a 280 GHz tripler and 560 GHz sub-harmonic mixer integrated in a single block. It exhibits a DSB mixer noise temperature of 1400 K and DSB mixer conversion losses of 7.5 dB at 590 GHz. In addition, a 664 GHz receiver using similar MMIC Schottky devices balanced mixer architecture has been developed. It exhibits good performance with a DSB mixer noise temperature of 2500 K and DSB mixer conversion losses below 10 dB at 670 GHz. Finally, the 1200 GHz channel is under development. It includes an LO source inherited from the HIFI project for the generating enough power at 600 GHz, and a novel 1200 GHz MMIC biasable sub-harmonic mixer that is presented.

## I. INTRODUCTION

Sub-millimeter heterodyne receivers using MMIC semiconductor devices are uniquely suited for long term planetary missions such as EJSM [1], or long term Earth climate monitoring missions such as MetOp SG [2], as they can operate for decades without any active cryogenic cooling. They can give unique insights in the temperature distribution, water vapor content, ice particle sizes, of planets' atmosphere.

Another very interesting application is for FMCW radar for concealed weapons underneath clothing. Indeed, the submillimeter wave range can resolve millimeter scale details at relative long range distances (up to 25-m) thanks to high frequencies and a relative transparency of the atmosphere in certain window channels.

In that context, we present the design, fabrication and test of several sub-millimeter wave receiver front-ends that span in frequency from 520 GHz up to 1300 GHz, using common balanced architecture for all MMIC Schottky components.

First, a 560 GHz receiver has been developed by JPL. It features an integrated 280 GHz MMIC tripler and 560 GHz MMIC sub-harmonic mixer integrated in a single block. In addition, a 664 GHz receiver has been developed. It uses a 332 GHz MMIC tripler and 664 GHz MMIC sub-harmonic mixer (SHM). The receiver architecture and test results are presented. The design, fabrication and tests are presented. The 1200 GHz channel is under development at JPL. The receiver architecture is directly inherited from the HIFI project for the LO

generation at 600 GHz. Using identical MMIC GaAs membrane process, a novel 1200 GHz MMIC sub-harmonic mixer has been designed, and is presented here.

## II. 560 GHz INTEGRATED RECEIVER DEVELOPMENT

An integrated 560 GHz receiver front-end based on MMIC GaAs membrane Schottky diodes fabricated by the Micro Device Laboratory from JPL has been designed fabricated and tested. Both devices have been designed using a combination of 3D-EM simulations (HFSS from Ansys) and linear/non-linear circuit simulations (ADS from Agilent).

### A. Design and fabrication

The 560 GHz receiver channel includes a 280 GHz MMIC tripler using 6 Schottky diodes in series configuration, and a 560 GHz MMIC sub-harmonic mixer using a pair of balanced Schottky diodes. A photo of the integrated receiver is shown in Figure 2 on the bottom.

The design procedure is as following: both the tripler and mixer components are first optimized independently to cover the desired frequency range and exhibit best performances, i.e. best efficiency for the tripler, and best sensitivity for the sub-harmonic mixer. Then the waveguide matching circuit in between these two components is optimized for best coupling efficiency at the desired LO frequency range which is 255 to 300 GHz.

The 280 GHz tripler is based on an earlier design from Maestrini [4]. Simulations have shown that the chip can be kept unchanged and only the waveguide structure is re-optimized to cover the 255-300 GHz band, instead of the initial 265-340 GHz bandwidth. The 560 GHz sub-harmonic mixer is "scaled" from an earlier design at 874 GHz [5], and is biasless. It is estimated that the tripler will output enough LO power to pump the sub-harmonic mixer.

During the design phase, it has been shown that integrating the last stage tripler together with the sub-harmonic mixer presents significant advantages: lower waveguide losses, lower standing waves between both devices as the entire tripler-mixer combination is optimized together, resulting in a flatter and lower pump power required at W-band, a tripler bias voltage

quasi-constant over the frequency range, and less waveguide flanges interfaces required. As shown in Figure 3, only a single W-band UG387 flange is required for LO input, as well as an IF SMA connector. A diagonal horn centered at 560 GHz is integrated into the block for the RF coupling.

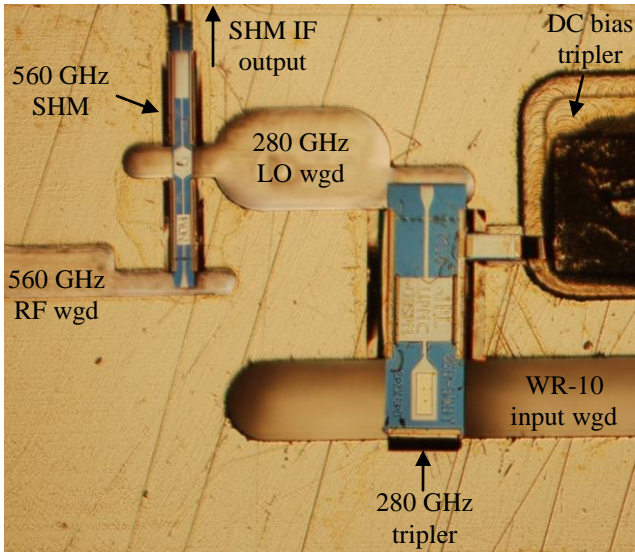


Figure 2: Integrated 560 GHz receiver from JPL, featuring a 280 GHz MMIC tripler and 560 GHz sub-harmonic mixer in a single cavity.

The integrated 280 GHz tripler and 560 GHz sub-harmonic mixer also includes a 2-11 GHz IF impedance transformer circuit and an output K-type glass bead connector. Further integration level is expected by including an IF pre-amplifier inside the block.

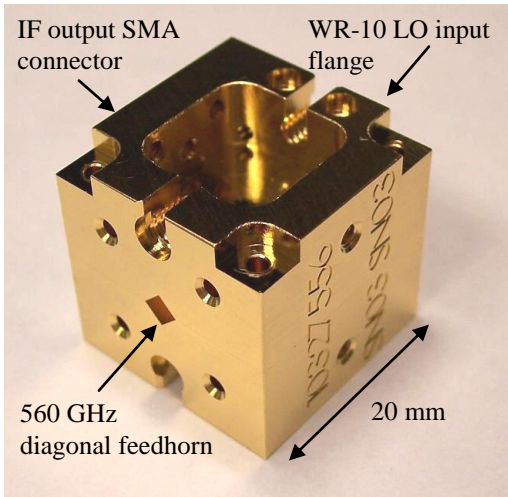


Figure 3: Integrated 560 GHz waveguide block, including a 280 GHz tripler MMIC, a 560 GHz sub-harmonic mixer MMIC, an integral diagonal horn at 560 GHz, and a 2-11 GHz IF matching circuit and connector.

### B. Measurement results

Tests have been performed at room temperature in a vacuum chamber using the procedure described in [6]. The integrated 560 GHz receiver front-end is pumped by a W-band HP source

followed by a W-band power amplifier covering the frequency range 85-103 GHz, with an output power up to 100 mW. A W-band rotary vane attenuator was inserted between the amplifier and the integrated tripler/sub-harmonic mixer to find the best input power.

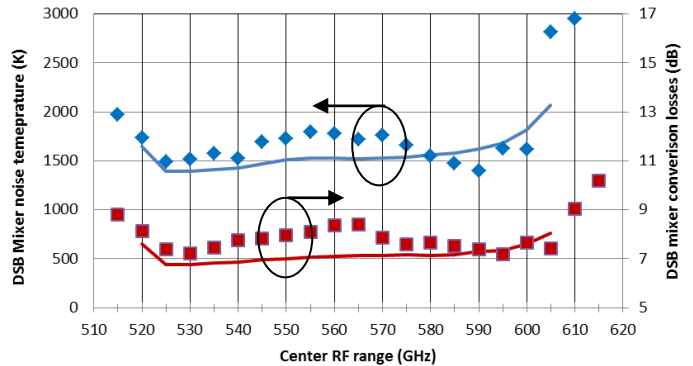


Figure 4: DSB mixer noise temperature and DSB conversion losses measured and simulated of the 560 GHz integrated tripler + sub-harmonic mixer. The IF range is between 4 and 6 GHz.

During the test procedure, the reverse bias voltage of the 280 GHz integrated tripler was kept to a fixed value of 8V for simplicity. It appears that it was nearly optimal over the entire frequency range.

As shown in Figure 4, the best performance obtained are a DSB mixer noise temperature of approximately 1400 K at 590 GHz, corresponding to DSB mixer conversion losses of approximately 7.5 dB. The DSB mixer noise temperature is below 1800 K and conversion losses are below 8.5 dB between 520 GHz and 605 GHz. Figure 4 also shows that the measurement results are in accordance with the simulations. When cooled at a physical temperature of 150 K, the DSB mixer noise temperature improves by 200 to 300 K in average, and the DSB mixer conversion losses remain stable.

The amount of W-band input LO power required to pump the integrated 560 GHz tripler + sub-harmonic mixer is measured separately using a PM4 Erickson calorimeter, between 30 mW at 590 GHz and 80 mW at 530 GHz.

It is important to notice that previously reported performance of this device in [7] is erroneous as a mistake was made in retrieving the DSB mixer conversion losses. The correct performances are presented in Fig.4 of this paper. It should also be noticed that no correction for feed horn losses and IF mismatch is included. The mixer is measured with an isolator at the IF port to remove all influence from the 1<sup>st</sup> LNA in the mixer performance calculation.

### III. 664 GHz RECEIVER DEVELOPMENT

A 664 GHz receiver based on MMIC membrane planar Schottky diodes has been developed. It includes a 332 GHz MMIC Schottky tripler and a 664 GHz sub-harmonic mixer. Both devices have been designed using a combination of 3D-EM simulations (HFSS from Ansys [8]) and non-linear circuit simulations (ADS from Agilent [9]).

### A. Design and fabrication

The 332 GHz tripler is a scale version of the one presented in [4], using a pair of anti-series Schottky diodes. It's a 6-anodes balanced design that includes an on-chip capacitor for DC bias.

The 664 GHz sub-harmonic mixer is based on a series balanced configuration derived from [5], as shown in Fig. 5. Typical DC characteristics of each anode are a series resistance between 17 and 21 Ohms, an ideality factor of 1.32 to 1.35, and a zero voltage capacitance below 1.5 fF.

Figure 6 shows a complete 664 GHz receiver Front-End inside the vacuum test chamber, including a WR-08 isolator, a series of cascaded WR-08 amplifier chains, a 332 GHz tripler and the 664 GHz sub-harmonic mixer.

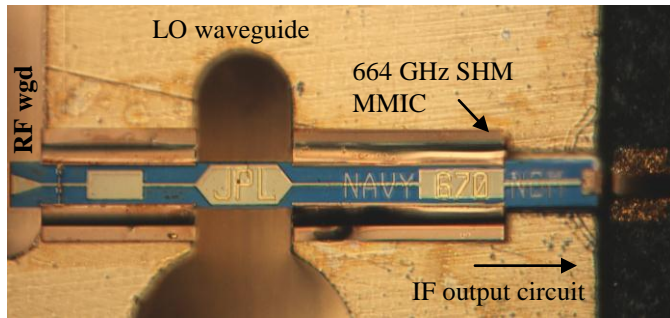


Figure 5: 664 GHz sub-harmonic mixer MMIC mounted inside the lower half of the 664 GHz split-block.

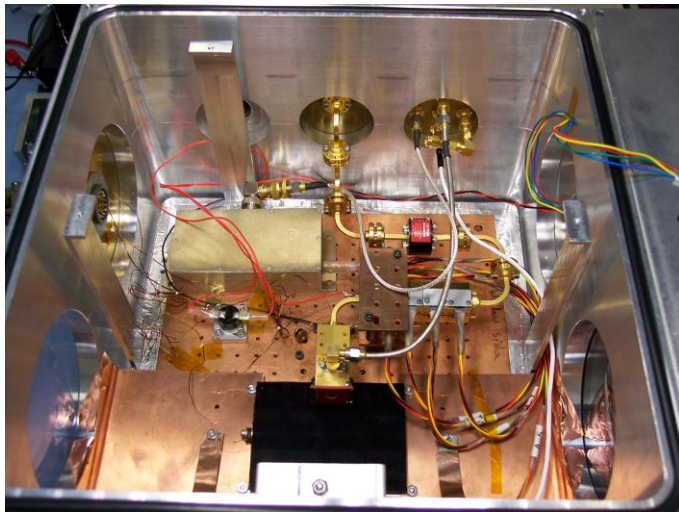


Figure 6: 664 GHz Receiver front-end under test inside the vacuum chamber, including a WR-08 isolator, a series of cascaded WR-08 power amplifiers, a 332 GHz tripler and a 664 GHz sub-harmonic mixer.

### B. Test results

Test results for the 332 GHz MMIC tripler are shown in Figure 7. With a fixed input power ranging 75 mW from the cascaded WR-08 power amplifier stage, the typical output power generated ranges between 6 mW and 10 mW in the frequency range 310-350 GHz, corresponding to an efficiency between 7 % and 13 % in this frequency range. Higher output

powers could be achieved if the maximum output power of the WR-08 amplifier (100 to 140 mW) was used to pump the 332 GHz tripler. However, in our case, a input power of 75 mW for the 332 GHz tripler is more than enough to pump optimally the 664 GHz sub-harmonic mixer.

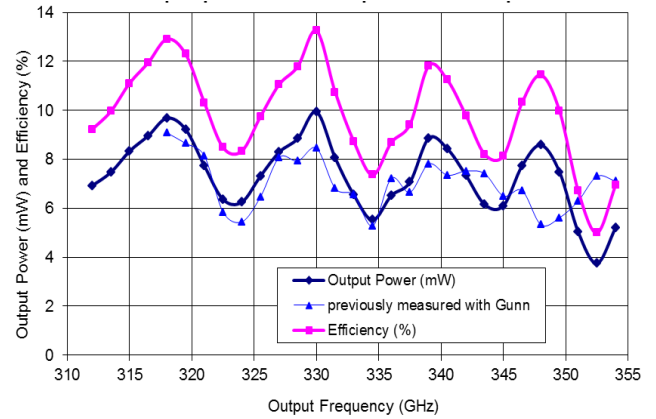


Figure 7: 332 GHz MMIC tripler performance results for a fixed input power of 75 mW between 104 GHz and 118 GHz.

This 332 GHz multiplier source is used to pump the 664 GHz MMIC sub-harmonic mixer. The 664 GHz SHM includes an integral diagonal feedhorn centered and an IF matching circuit from 2-11 GHz. The mixer is tested in the same conditions as previously described [6]. The results are presented in Fig. 8.

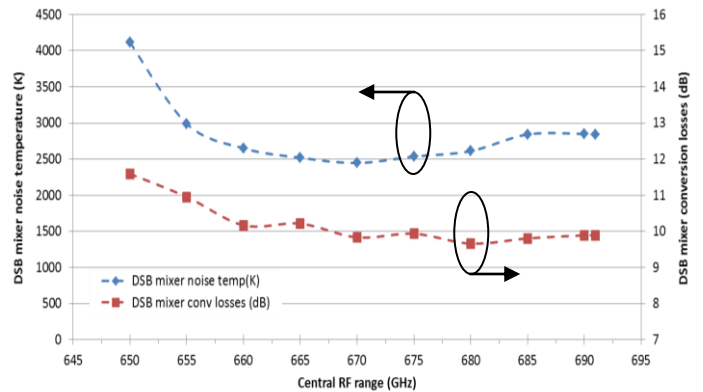


Figure 8: Measured 664 GHz MMIC sub-harmonic mixer performance. The IF range is between 4 GHz and 6 GHz.

As shown in Fig.8, the DSB mixer noise temperature is between 2500 K and 3000 K in average between respectively 655 and 690 GHz. The DSB mixer conversion losses are measured between 9.7 dB and 11 dB in the same frequency range. The amount of LO power necessary to pump the mixer optimally is estimated to be approximately 5 mW. As before, no correction for feed horn losses and IF mismatch is included. The mixer is measured with an isolator at the IF port to remove all influence from the 1<sup>st</sup> LNA.

#### IV. 1.2 THZ RECEIVER CHANNEL

The 1200 GHz channel includes a 600 GHz LO source based on MMIC membrane 200 GHz doubler and 600 GHz tripler as described in [10][11], and a 1100-1300 GHz MMIC membrane biasable sub-harmonic mixer. The 1200 GHz sub-harmonic mixer architecture is scaled from a previous design at 874 GHz, as described in [5]. It's a balanced design similar to the 560 GHz channel mixer described above, with an additional on-chip capacitor in order to forward bias the diodes in series. This feature enables to reduce the amount of LO power required to pump the mixer to 1 or 2 mW.

The 1200 GHz sub-harmonic mixer has been designed and fabricated, as shown in Fig.9. The predicted mixer performance is shown in Figure 10. The design methodology and prediction tools are described in [6].

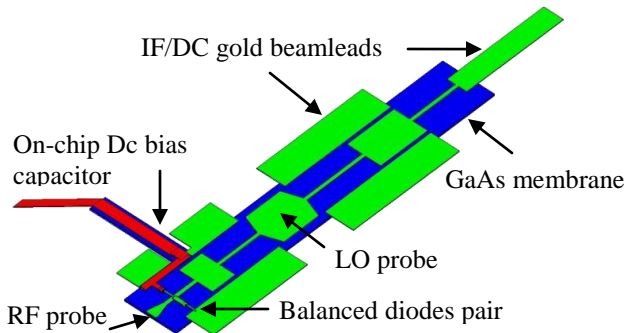


Figure 9: 3D view of the MMIC 1200 GHz sub-harmonic mixer based on MMIC GaAs membrane Schottky diodes, including the on-chip DC bias capacitor (in red).

As shown in Fig. 10, the predicted DSB mixer noise temperature of the mixer is between 4000 and 4500 K at room temperature in the frequency range 1050 to 1280 GHz, corresponding to DSB conversion losses between 12.5 dB and 14 dB approximately.

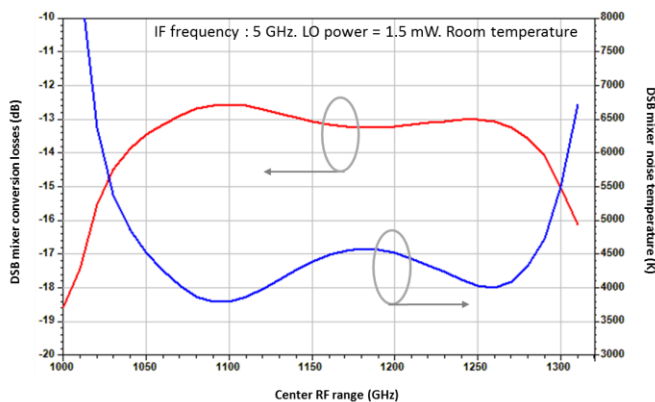


Figure 10: Predicted performance of the MMIC 1200 GHz sub-harmonic mixer at room temperature. IF is fixed to 5 GHz, LO bias is set to 1.5 mW and mixer is DC forward bias to 0.5V per anode.

Test campaign is on-going to measure the performance of the 1200 GHz heterodyne receiver chain.

#### CONCLUSION

Future sub-millimeter wave instruments for the remote sensing of planets' atmospheres such as the Earth, Mars, Jupiter and Saturn will greatly benefit from the recent advances in receiver sensitivity and integration in the 500 to 1200 GHz range, as demonstrated in this paper. The development of MMIC Schottky technology and powerful Local Oscillator sources widely tunable and operating at room temperature are pivotal for THz receiver development.

#### ACKNOWLEDGMENT

The authors wish to thank Dr. Peter Siegel for JPL for his constant support and advices. Mr. Peter Bruneau from the machine shop at JPL is also acknowledged for the high quality blocks manufacturing.

This work has been carried out at the Jet Propulsion Laboratory, California Institute of Technology, under contract from the National Aeronautics and Space Administration.

#### REFERENCES

- [1] P. Hartogh, et al., "Sub-millimeter Wave Instrument for EJSM", EJSM Instrument Workshop, July 2009, Maryland, USA.
- [2] MetOp- Second Generation, Space Requirements Document – SSRD -, ESA MetOp-SG team, MOS-RS-ESA-SYS-0001, January 2011.
- [3] K. B. Cooper, et al., "Penetrating 3-D imaging at 4- and 25-m range using a submillimeter wave radar," *IEEE Trans. Microw. Theory Tech.*, vol. 56, no. 12, pp. 2771–2778, Dec. 2008.
- [4] A. Maestrini, et al., "Multi-Anode Frequency Triplers at Sub-Millimeter Wavelengths", *proceedings of the 16th International Symposium on Space Terahertz Technology*, paper P5-3, Göteborg, Sweden, 2-4 May 2005.
- [5] B. Thomas, et al. "Design of an 874 GHz Biasable Sub-Harmonic Mixer Based on MMIC Membrane Planar Schottky Diodes", *proceedings of the 33rd International Conference on Infrared, Millimeter, and Terahertz Waves*, California Institute of Technology, Pasadena, California, September 15-19, 2008.
- [6] B. Thomas, et al., "THz cooled MMIC Schottky mixer design for the remote sensing of outer planets' atmospheres", *proceedings of the joint 5th ESA Workshop on Millimetre Wave Technology and Applications & 31st ESA Antenna Workshop*, pp. 101-108, ESTEC, Noordwijk, The Netherlands, May 18-20, 2009.
- [7] B. Thomas, J. Gill, C. Lee, R. Lin, S. Sin and I. Mehdi, "An Integrated 520-600 GHz sub-harmonic mixer and tripler combination based on GaAs MMIC membrane planar Schottky diode", *proceedings of the 35th International Conference on Infrared and Millimeter waves, Terahertz Electronics IRMMW-THz 2010*, Rome, Italy, Sept. 10-15, 2010.
- [8] *High Frequency Simulation Software*, v11.0, Ansys Corporation, Pittsburgh, PA, USA.
- [9] *Advanced Design System*, Agilent Technology, Palo Alto, CA, USA.
- [10] E. Schelcht, et al., "A High-Power wideband Cryogenic 200 GHz Schottky 'Substrateless' Multiplier: Modeling, Design and Results", *proceedings of the 9th Int. Conf. on Terahertz Electronics*, Charlottesville, VA, USA, Oct. 2001.
- [11] A. Maestrini, et al., "A 540-640 GHz High Efficiency Four Anode Frequency Tripler", *IEEE Transactions on Microwave Theory and Techniques*, Vol. 53, pp. 2835-2843, September 2005.

# First Results of the Sideband-Separating Mixer for ALMA Band 9 Upgrade

Andrey Khudchenko, Ronald Hesper, Andrey Baryshev, F. Patricio Mena, Gerrit Gerlofma, Tony Zijlstra, Teun M. Klapwijk, Jacob W. Kooi and Marco Spaans

**Abstract**—Last year, the design and implementation details of a new modular sideband-separating mixer block, intended as an upgrade for the current single-ended ALMA Band 9 mixers, were presented at this conference. In high-frequency observation bands like ALMA Band 9 (600–720 GHz), which is strongly influenced by atmospheric noise, employment of sideband-separating mixers can reduce, by roughly a factor of two, the integration time needed to reach a certain signal-to-noise ratio for spectral line observations. Alternatively, in the same integration time, a sufficiently larger selection of sources can be accessed.

Two prototype mixer blocks were produced on a micro milling machine, and equipped with production Band 9 SIS mixer devices that have independently been tested in double-sideband mode.

Here, we present the results of the first measurements, notably, the noise temperature, image rejection, LO pumping balance and IF response. We also present in detail a procedure of the image rejection ratio measurement, which is fast and can be used for single sideband mixers, so that a second IF chain is not required.

**Index Terms**—Image rejection ratio, sideband separating mixers, submillimeter mixers, superconductor-insulator-superconductor junction

## I. INTRODUCTION

THE possibility of reducing the atmospheric noise by a factor of two and increase as result a signal to noise ratio of about 1.4 times is the motivation for ALMA Band 9 mixers upgrade form dual sideband (DSB) to single sideband (SSB) mode.

Manuscript received August 1, 2011. This work was supported in part: by the ESO Band9 Upgrade Study PO-037021; European Community Framework Program 7, Advanced Radio Astronomy in Europe, AMSTAR+, grant agreement no. 227290; Dutch NWO/STW VENI Grant 08119, "Advanced Heterodyne Mixers for THz Applications", Dutch research school for astronomy (NOVA) NOVAIII Grant; Center of Excellence in Astrophysics and Associated Technologies (PBF 06), Chile.

A. Khudchenko and A. Baryshev are with Netherlands Institute for Space Research SRON, Landleven 12, 9747 AD Groningen, The Netherlands, (+31 50 363 4018, A.Khudchenko@sron.nl).

R. Hesper, A. Baryshev, G. Gerlofma and M. Spaans with Kapteyn Astronomical Institute, Landleven 12, 9747 AD Groningen, The Netherlands

P. Mena with Electrical Engineering Department, Universidad de Chile, Av. Tupper 2007, Santiago, Chile

Tony Zijlstra, Teun M. Klapwijk are with Kavli Institute of Nanoscience, Delft University of Technology, Lorentzweg 1, 2628 CJ Delft The Netherlands

J.W. Kooi with California Institute of Technology, MS 320-47 Pasadena, CA 91125, USA is with the National Institute of Standards and Technology, Boulder, CO 80305 USA.

Because the ALMA correlator can only handle 8 GHz of intermediate frequency (IF) bandwidth per polarization, an SSB configuration with 4-12 GHz IF has been chosen [1], rather than a full two sideband (2SB) one, split over two 4 GHz bands. Also, in this way the existing DSB IF chain does not have to be modified for the upgrade, i.e., all the IF components can be reused. The only IF component to be added is one IF hybrid per polarization.

The mechanical design of the SSB receiver was presented in [1]. The manufactured modular block is shown in Fig. 1. There are a few key features in this design. First of all, it is as modular as reasonably possible. Especially the holders containing the junctions are easily separable from the RF hybrid block. The standard single-ended Band 9 junction holders ("back pieces") are used, so that junctions can be tested individually and easily matched. It means that no development of a new junction design is required. The SIS mixers are made in Nb/AlN/Nb technology. The mixer block is also compact: 45x21x53 mm<sup>3</sup> (see Fig. 1), so the upgrade mixers can be retrofitted into the existing optics blocks with minimal reworking.

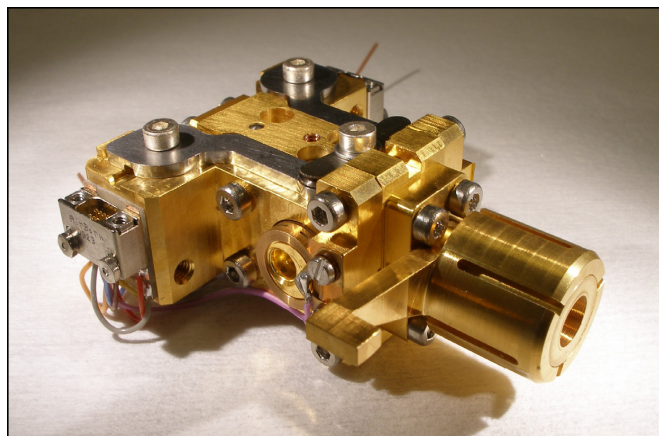


Fig. 1. Photograph of the first SSB mixer. The corrugated RF input horn is on the right, the LO horn is on the back site opposite to it (not visible). One of the standard band 9 mixer back pieces is visible near the center.

In this paper, we present the results of the first measurements performed to characterize this mixer. The properties of the RF hybrid and LO splitter were studied in a direct way, by measuring the balance of pumping levels, both through the LO port and the RF port. Moreover, the frequency response, noise temperature and sideband rejection ratio were also measured. Finally, we describe in detail a new procedure

for measuring the image rejection ratio, which is fast and can be used for a SSB mixer so that a second IF chain is not required.

## II. MIXER CHARACTERIZATION

### A. RF Hybrid

Since the new design uses standard ALMA Band 9 back pieces to hold the SIS junctions, the RF response of each SIS junction can be measured before the installation into the sideband-separating mixer block. A comparison between the frequency responses of the same two SIS mixers in single-ended DSB configuration (production ALMA Band 9 mixer) and in the sideband separating mixer block is presented in Fig. 2. The responses are measured using a Fourier-transform spectrometer. Since the response is measured by way of the mixer bias current, the IF output hybrid does not come into play.

Comparing the spectra taken through the 2SB block (solid lines) with the ones taken with the individual SIS mixer devices (DSB mode, dashed lines) shows that the waveguide structure (consisting of RF hybrid and LO couplers) does not dramatically influence the RF response and covers the required band (600-720 GHz).

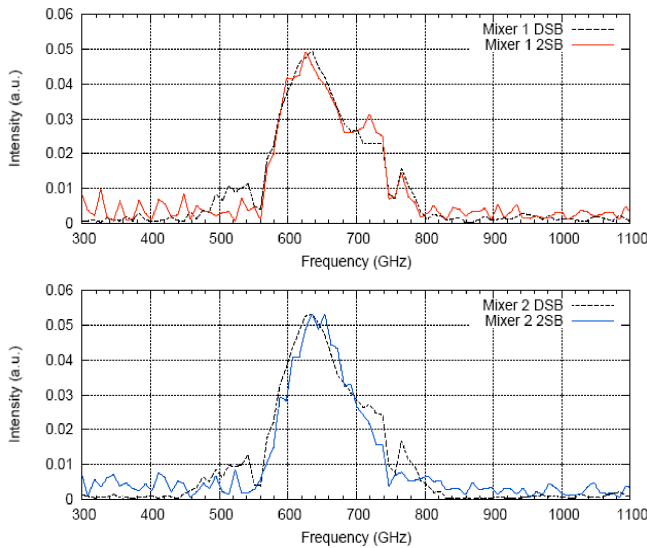


Fig. 2. Direct RF response of the SIS mixers: dashed lines – individual DSB response; solid lines - response of the junctions installed in the 2SB RF hybrid block.

Fig. 3 characterizes the transmission balance of the RF hybrid and LO splitter, measured by injecting the LO signal through, respectively, the RF and LO horns, and measuring the SIS bias current. Since the bias current of a pumped SIS junction at a fixed bias voltage in this regime is proportional to the RF power reaching the junction [2], the ratio of the currents is equal to the power ratio, independent of frequency or absolute LO power.

The curve measured with the signal injected through the LO port shows a periodic frequency-dependent imbalance in the

LO distribution structure (LO splitter, couplers and dummy loads), indicating that standing waves may be present. This imbalance prevents both mixers to be pumped optimally at the same time. However, since around the optimal pumping level the noise performance of an SIS mixer is not very strongly dependent on LO power, deviations of less than about 20% (1 dB) are acceptable. Both the LO and RF coupling ratios, shown in Fig. 3, are within  $\pm 1.5$  dB, which is not too far from that level. However, the real impact should be judged from noise temperature and sideband ratio measurements. Small imbalances can be compensated by adjusting the bias voltages (and thereby the mixer gains) of the individual SIS devices, though possibly with a certain degradation of the noise temperature.

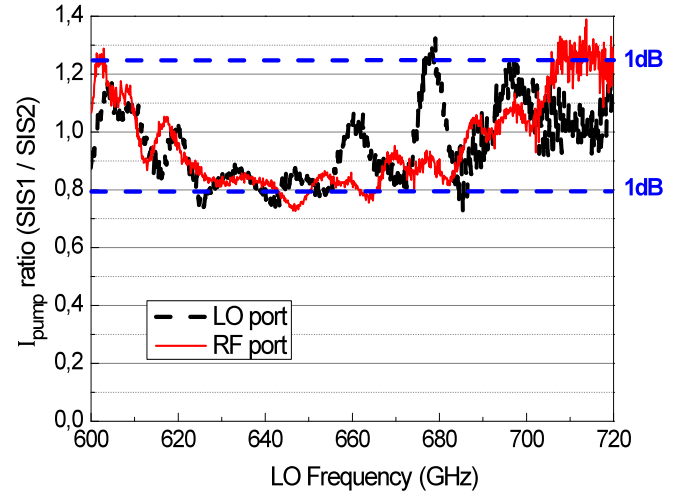


Fig. 3. Pumping balance between the two SIS devices in the mixer block, measured as the ratio of the SIS pumping currents at constant bias voltage while sweeping the LO frequency, both through the RF port and the LO port. Ideally, these ratios should be 1.

### B. IF Hybrid and IF Chain

The preliminary tests of the IF chain were performed with 4-8 GHz cryogenic amplifiers as described in [3]. Here we present results for the 4-12GHz IF chains, based on the Yebes cryogenic amplifiers used in the ALMA Band 9 DSB cartridge. The 90 degree 4-12GHz IF hybrid (provided by Observatorio Astronómico Nacional, Spain [4]) is placed between the SIS junctions and the 4-12 GHz isolators before the amplifiers. The hybrid has an amplitude imbalance less than  $\pm 0.3$  dB and phase imbalance not exceeding  $\pm 2$  degrees, over the 4-12 GHz band.

The performance of the entire IF chain (including the IF microstrip structure on the mixer devices, IF hybrid, isolators and amplifiers) was determined, by using the SIS junctions as noise sources, biasing them at different voltages above the gap (5 and 8 mV in this case). Since the level of the shot noise generated by a SIS junction is known, we can determine the individual noise contributions by measuring the IF output spectra in three (out of four) bias combinations: 5 and 5 mV; 5 and 8 mV; 8 and 5 mV (for the first and the second SIS junctions correspondingly).



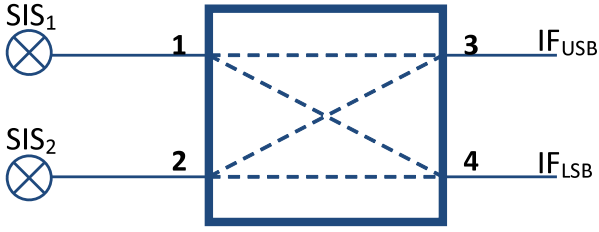


Fig. 4. Block diagram of the IF chains.

The measured IF spectra can be presented in accordance with the diagram in Fig. 4 in the following way (for either IF output):

$$P_{5 \rightarrow 5} = (P_1 G_{31} + P_2 G_{32} + P_N) G_{IF},$$

$$P_{5 \rightarrow 8} = (P_1 G_{31} + K P_2 G_{32} + P_N) G_{IF},$$

$$P_{8 \rightarrow 5} = (K P_1 G_{31} + P_2 G_{32} + P_N) G_{IF},$$

where  $G_{ij}$  is the power gain between ports  $j$  and  $i$ ;  $P_1$  and  $P_2$  are the shot noise powers of the SIS mixers at 5 mV;  $K$  is the factor of shot noise increase when the SIS junction bias is increased from 5 to 8 mV;  $G_{IF}$  is the gain of the IF chain after the hybrid;  $P_N$  is the noise power of the IF amplifiers. The presented equations are valid for both IF chains. By selecting the SIS junctions to have the same gap currents  $I_g$ , we can make  $P_1 = P_2$ . Under this condition the following ratio can be derived:

$$\frac{G_{31}}{G_{32}} = \frac{P_{8 \rightarrow 5} - P_{5 \rightarrow 5}}{P_{5 \rightarrow 8} - P_{5 \rightarrow 5}}$$

which is the ratio of the power gains of the 90 degree (diagonal) branch and the 0 degree one (straight) coming to the USB output. For the LSB output an analog ratio is defined. Both ratios are presented in Fig. 5. The deviation of the ratios from 1 corresponds to imbalance, which will contribute to the total gain balance error determining the final sideband rejection ratio. The current imbalance is not larger than  $\pm 2$  dB, which is an acceptable level for achieving the sideband rejection ratio of 10 dB. This measurement can be used as a tool to estimate the IF chain imbalance and quality of sideband separating receivers.

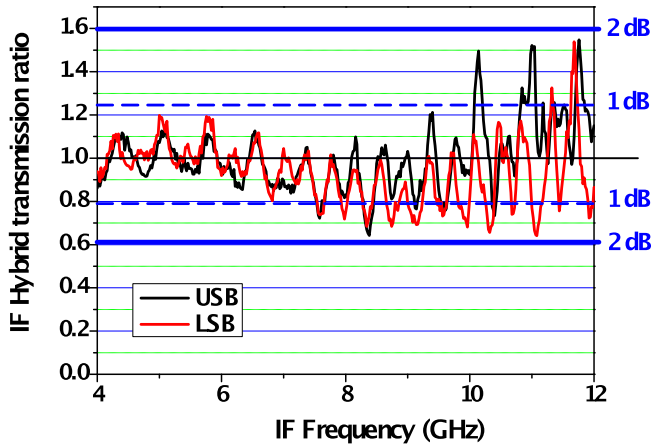


Fig. 5. Ratio of the power transmitted straight and diagonally through the IF hybrid, for both LSB and USB outputs.

The curves in Fig. 5 show a much worse performance than the IF hybrid imbalance determined by manufacturer [4] (2 dB instead of 0.3 dB). This is mainly caused by the transmission ripple of the isolators, and additionally by the interaction of mixers, hybrid and isolators as well as by standing waves between these parts. However, some of these the effects may be exaggerated by the fact that at the used bias points (5 and 8 mV), the output impedances of the SIS devices deviate from their operational design values. In real operation, the mismatches are likely to be smaller.

By biasing both SIS junctions to 5 mV and 8 mV at the same time, the IF noise temperature was determined in the standard way [5][6]. It is in the range from 7 to 12 K in the IF band, as shown in Fig. 6 for one of the IF chains.

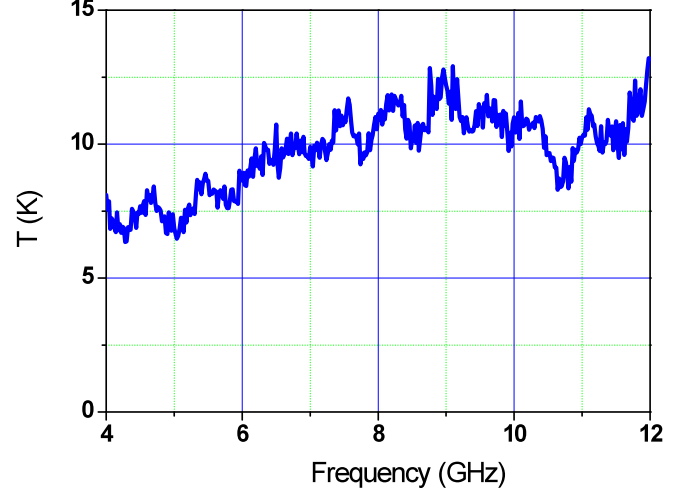


Fig. 6. Noise temperature of the IF chain.

### C. Image Rejection Ratio

The image rejection ratio of a sideband separating receiver is mainly determined by the total amplitude and phase error in the hybrids and all components between them. The diagram in Fig. 7 demonstrates how different combinations of these errors contribute to the image rejection level.

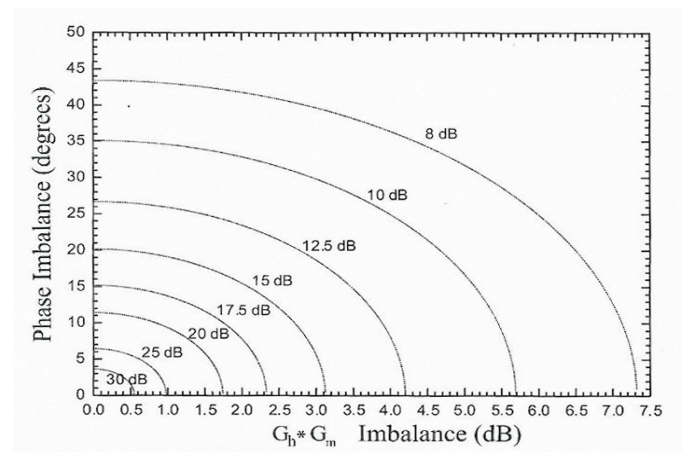


Fig. 7. Theoretical contour lines of equal image rejection as a function of total gain imbalance and total phase imbalance (which include the contributions of RF hybrid, IF hybrid and mixers). Here  $G_h$  and  $G_m$  are the hybrids and mixers gain imbalances, respectively. [7]

According to the pumping balance measurements presented in Fig. 3 and 5, the upper limit of the combined amplitude imbalance is about 3.5 dB.

The joint phase imbalance of the hybrids is a few degrees and consists of  $\pm 2$  degrees for the IF hybrid [4] and  $\pm 2$  degrees for the RF one (based on simulations of the RF hybrid [8]). An additional phase error can appear in case of a length difference between the paths from SIS mixers to IF hybrid input ports. Corresponding cables can be made with a precision of better than 1 mm, which introduces up to 3 degrees phase error for high IF frequencies. All together, phase imbalance should be less than about 7 degrees in total.

Thus, assuming the SIS mixer gains to be equal, the image rejection ratio should be better than 13 dB (according to diagram on Fig. 7). In reality, the gain and phase imbalance of different parts of the receiver may not enhance but compensate each other. Moreover, a compensating amplitude imbalance can be created on purpose by varying the SIS bias voltages, which change the mixer gains.

The ALMA specification for image rejection ratio is 10 dB. We have measured sideband ratio by injecting a test tone RF signal into the upper and lower sidebands. The results for both sidebands are presented in Fig. 8, showing that the image rejection ratio for our mixer is better than 15 dB in the entire range, certainly fitting the ALMA specification. The data presented in Fig. 8 was measured at a fixed bias voltage of 2 mV for both SIS mixers without an additional bias tuning. For the measurements we have used a method described in section III.

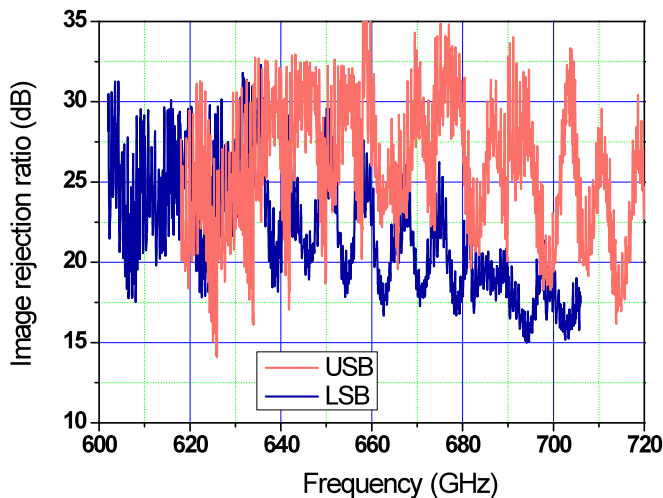


Fig. 8. Image rejection ratio over all RF Band for upper (USB) and lower (LSB) sideband. Each curve consists of 13 IF bands measured for different LO frequencies, spaced 8 GHz apart, yielding a contiguous RF coverage.

#### D. Noise Temperature

The noise temperature, measured for both lower and upper sidebands using the conventional Y-factor method, is presented in Fig. 9. The best noise temperature is about 330 K. Also plotted in Fig. 9 is the DSB noise temperature of one of the individual junctions, converted to a corresponding ideal SSB noise temperature by scaling it with a factor 2. This

way, the shape of the expected curve (in the case of perfect hybrids) can be compared to the actual measurement. Evident from the figure is that the measured data follows the one expected from the DSB data rather closely in shape. However, the overall level of the noise is about 1.8-2 times (2.5 to 3 dB) higher than expected.

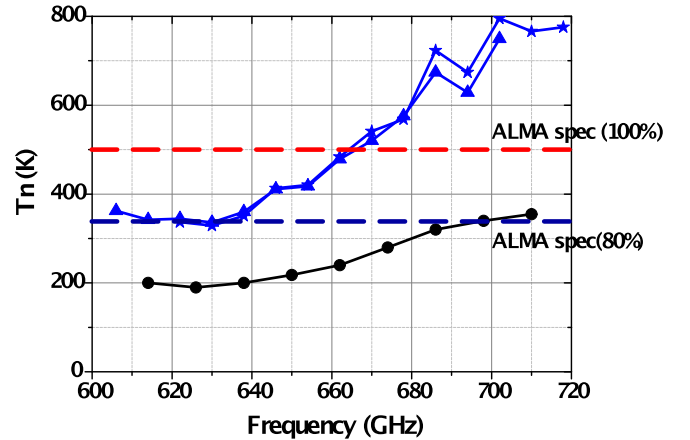


Fig. 9. SSB noise temperature: triangles – lower sideband, stars – upper sideband, circles – the doubled DSB noise temperature of one of the two mixer devices in DSB mode.

The ALMA specifications for single-sideband noise are indicated by the horizontal dashed lines in figure 5: 80% of the band should not exceed 335 K while all points should be below 500 K [9]. In these measurements, the noise temperature is still higher than required.

Additional tests with a standard ALMA Band 9 DSB mixer shows that optics, SIS mixer and IF chain operate properly and do not cause the increase of the observed noise temperature. Therefore, we think that the main reason of the problem is in the RF hybrid block. The frequency independent nature of the noise temperature increase suggests the presence of resistive losses in the waveguide structure. Other defects (mismatches between the blocks, gaps, machining errors) tend to have a strong frequency dependence resulting usually in resonances as demonstrated by electromagnetic simulations. Also, Y-factor measurements through the LO port (instead of the RF port) yield extra losses that scale approximately with the waveguide length. Currently, we are performing an experimental and numerical investigation about the cause of the waveguide losses.

### III. IMAGE REJECTION RATIO MEASUREMENT METHOD

#### A. Standard method

A popular method of measuring the image rejection ratio is described in detail in [10]. Here, it will be referred to as a standard method. In this method the test tone (TT) is alternatively injected into the upper or lower RF sidebands and measured at the upper and lower IF outputs.

The sideband separating receiver is depicted schematically in Fig. 10. In this scheme, the upper and lower sidebands of the RF input signal are considered to enter two distinct ports.

The power gains from each RF port to either IF port are denoted by quantities  $G_{ij}$ . The image rejection ratios are then:

$R_1 = G_{1U}/G_{1L}$  at IF port 1 (USB), and  $R_2 = G_{2L}/G_{2U}$  at IF port 2 (LSB).

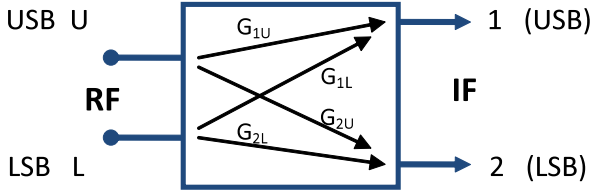


Fig. 10. Power gains of the sideband separating receiver.

$R_1$  and  $R_2$  cannot be measured directly with a test tone RF signal, because at these frequencies it is difficult to determine with sufficient accuracy the relative amplitudes of two RF signals separated in frequency by twice the IF ( $2f_{IF} = 8\text{--}24$  GHz for ALMA receivers). However, the ratios  $M_U = G_{1U}/G_{2U}$  and  $M_L = G_{2L}/G_{1L}$  can be determined experimentally by injecting a test tone at frequencies  $f_{LO} \pm f_{IF}$  and measuring both LSB and USB IF output power. Since the IF output power  $P_{IFi,U} = P_{TT}G_{iU}$ , with  $P_{TT}$  the test tone power, we get

$$M_U = \frac{P_{IF1,U}}{P_{IF2,U}},$$

and similarly for  $M_L$ .

When the ratios  $M_U$  and  $M_L$  are determined,  $R_1$  and  $R_2$  can be shown to be [10]:

$$R_1 = M_U \frac{M_L M_{DSB} - 1}{M_U - M_{DSB}} \quad (1)$$

$$R_2 = M_L \frac{M_U - M_{DSB}}{M_L M_{DSB} - 1} \quad (2)$$

$M_{DSB}$  is defined by the ratio

$$M_{DSB} = \frac{\Delta P_1}{\Delta P_2} = \frac{G_{1U} + G_{1L}}{G_{2U} + G_{2L}} \quad (3)$$

where  $\Delta P_1$  and  $\Delta P_2$  are changes of output power at IF ports 1 and 2, respectively, measured by changing hot and cold loads at the receiver input.

While this method yields accurate results, it has a few disadvantages in our case. In the first place, it requires availability of both sideband outputs, and so it is not usable in an SSB configuration (which we intend for the Band 9 upgrade). Secondly, it requires an accurate calibration of the receiver gains over the IF band for either side band at every LO frequency. This means that at every LO frequency two scans (hot and cold) of over both IF bands have to be performed. This is a rather time-consuming operation, impeding real-time optimization of the image rejection ratio by way of tuning the mixer bias points.

### B. Mixer bias inverting method

Because of the SIS junction's antisymmetric I-V curve, biasing one of the SIS mixers to negative voltages gives an additional  $180^\circ$  phase shift in its IF output signal, compared to a positive bias voltage. Such a phase shift causes switching of the USB and LSB after the IF hybrid. This property can be used to construct another method to measure the image rejection, which, under certain conditions, yields values identical or very close to the standard method.

In this method, we measure the following gain ratios:

$$\bar{R}_1 = G_{1^*L}/G_{1L} \quad \text{and} \quad \bar{R}_2 = G_{2^*U}/G_{2U},$$

Where  $G_{1L}$  is the power gain between RF port L and IF port 1 with both mixers biased positively, and  $G_{1^*L}$  is the same with the inverted bias of one of the SIS mixers. Correspondingly,  $G_{2U}$  and  $G_{2^*U}$  are the same ratios for ports U and 2. It should be noted that  $\bar{R}_1$  and  $\bar{R}_2$  are determined only by inverting the SIS bias voltage, without switching between IF outputs or switching the test tone between two different frequencies (which usually introduces power differences). Results for the bias inverting method ( $\bar{R}_1$  and  $\bar{R}_2$ ) in comparison with ratios determined by the standard method ( $R_1$  and  $R_2$ ) are demonstrated in Fig. 11.

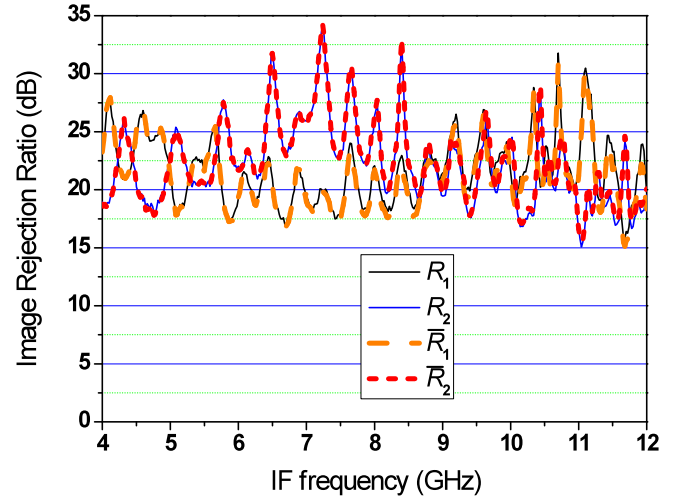


Fig. 11. Image rejection ratio over the entire IF band for a fixed LO frequency (614 GHz). Each curve represents the IF spectrum: solid thin and thick lines corresponds to USB and LSB ratios determined by standard method ( $R_1$  and  $R_2$ ), long and short dashed lines - LSB and USB ratios find by inverted bias method ( $\bar{R}_1$  and  $\bar{R}_2$ ).

The coincidence of  $\bar{R}_1$  with  $R_1$  and  $\bar{R}_2$  with  $R_2$  on Fig. 11 is a clear confirmation that SIS bias inversion method is precise enough and can be used for characterization of the receiver. The difference between the two methods in this case are less than 1.5 dB. However, it has to be noted that  $\bar{R}_1$  and  $R_1$  are not mathematically identical (discussion below will be for  $\bar{R}_1$  and  $R_1$ , but it is analogous for  $\bar{R}_2$  and  $R_2$ ). The reason is that the denominators ( $G_{1L}$ ) of the ratios  $\bar{R}_1$  and  $R_1$  are the

same, but the numerators ( $G_{1U}$  and  $G_{1L}$ ) correspond to different signal paths through the IF and RF hybrids, giving a different combination of phase and amplitude errors. Nevertheless,  $\bar{R}_1$  and  $R_1$  are similar as shown below.

The ratio  $R_1$  is determined by formula (1), which can be simplified as follows. First of all, we will show that  $M_{DSB}$  in our case can be considered as a magnitude of order of 1. The ratio  $M_{DSB}$ , determined by formula (3), can be written as

$$M_{DSB} = \left( \frac{g_{1U} + g_{1L}}{g_{2U} + g_{2L}} \right) \cdot \left( \frac{G_{IF1}}{G_{IF2}} \right), \quad (4)$$

where  $G_{IFi}$  are the power gains of the IF chains and  $g_{i(U,L)} = G_{i(U,L)}/G_{IFi}$  are the power gains from each RF input port to outputs of the IF hybrid. The first factor of the ratio (4) is determined by the balance of the RF and IF hybrids and similarity of the mixers gains. Its value is of the order of 1 because the hybrids have been determined to be balanced within 2 dB (see Fig. 3 and 5) while the SIS mixers have been selected on their similarity in gain performance. The second factor of the equation (4) is the ratio of the IF gains  $G_{IFi}$ , which can be far from 1 in reality. However, it is obvious that SSB-receiver IF gains do not contribute to image rejection ratio. It means that all the  $G_{IF1}$  and  $G_{IF2}$  appearing in the  $M_L$ ,  $M_U$  and  $M_{DSB}$  in (1) or (2) drop out. So, without losing generality, to simplify formula (1) we can consider  $G_{IF1}/G_{IF2} = 1$ , and then  $M_{DSB}$  as a magnitude of order of 1. Taking  $M_U, M_L \gg 1$  and  $M_U \gg M_{DSB}$ , which is correct for image rejections of the order of 10 ( $M_U \sim M_L \sim R_1 \sim R_2$ ), we can write (1) as

$$R_1 \approx M_L M_{DSB} = \frac{G_{2L}}{G_{1L}} M_{DSB}$$

( $M_{DSB}$  is not completely removed on purpose). The precision of this formula is of order of  $1/R_1$  (10% or 0.4 dB for image rejection ratio of 10 dB). Now, to see the difference between  $\bar{R}_1$  and  $R_1$  we have to compare  $G_{1L}$  and the product  $G_{2L} M_{DSB}$ . For both magnitudes the test tone signal is the same, corresponding to RF port L. The output signals are in proper sidebands (not leaking signals) but in different IF ports 1 and 2, which can be equalized by the calibration factor  $M_{DSB}$ , so  $G_{2L} M_{DSB} \approx G_{1L}$ . That bring us finally to  $\bar{R}_1 \approx R_1$ .

A qualitative explanation for the similarity of  $\bar{R}_1$  and  $R_1$  is that the image rejection ratio  $R_I$  is determined mainly by how strong is the leakage from the improper sideband, i.e. by  $G_{1L}$ , which is the same for  $\bar{R}_1$ . The leakage signal amplitude is very sensitive to a small phase or amplitude imbalance in the mixer ( $\sim x^2$ ,  $x \ll 1$ ) while the relative change of the proper sideband signal is much smaller ( $\sim 1 + x^2$ ).  $G_{1L}$  is responsible for the sharp features of the curves  $R_1$  and  $\bar{R}_1$  on Fig. 11.

### C. Optimization of the Image Rejection Ratio

Since the gain of the SIS mixers can be tuned slightly by varying the bias voltage, it is possible to correct for small gain

imbalances in the mixers or hybrids, to optimize the image rejection ratio. Fig. 12 shows the IF output powers (both LSB and USB) obtained when injecting a weak TT signal into USB RF sideband. Frequencies of the TT and LO are fixed. One of the mixers is held at constant bias, while the other is swept over a certain voltage range. It can be seen that the power in the proper sideband (curves 1 and 3) hardly varies, while the power of the rejected sideband (curves 2 and 4) shows a clear minimum, demonstrating that the rejection ratio can be optimized. The best bias points in this respect do not necessarily coincide with those yielding the best noise temperature, however.

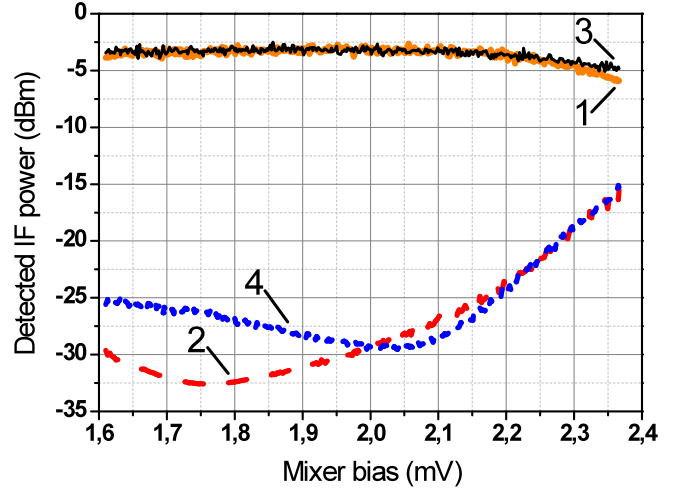


Fig. 12. Dependence of the IF power on the bias voltages of the SIS mixers. The test signal is applied in USB RF sideband. Curves 1 and 2 are the USB and LSB IF powers versus  $SIS_1$  voltage, curves 3 and 4 – USB and LSB IF powers correspondingly versus  $SIS_2$  voltage. Switching of the sidebands is made by inverting the bias voltage of one of the SIS mixers.

## IV. CONCLUSION

We have fabricated and tested a prototype SSB receiver as an upgrade for Band 9. The experimental results are promising. Notably, the image rejection ratio is 15 dB or better in the entire range. The last mixer parameter to be improved to fit ALMA specifications is the noise temperature.

We have also presented in detail the used method for measuring the image rejection ratio. This method is fast, sufficiently precise, gives the possibility of a quick image rejection ratio optimization and works using only one IF sideband.

## ACKNOWLEDGMENT

The authors would like to thank Vincent Pierre Desmaris and Victor Belitsky from Chalmers University (Sweden) and Johan Holstein from University of Groningen (Netherlands) for great support and fruitful collaboration. F. P. Mena would also like thank U. Graf from University of Cologne for his advice in machining of the RF hybrid blocks

## REFERENCES

- [1] R. Hesper, G. Gerlofsma, F. P. Mena, M. Spaans and A. M. Baryshev, "Construction of a Side Band Separating Heterodyne Mixer for Band 9 of ALMA", Proc. 18th. ISSTT, pp. 39-43, 2007.
- [2] J. R. Tucker, M. J., Feldman, "Quantum detection at millimeter wavelength", Rev. Mod. Phys., V. 57., №4., pp. 1055-1113, 1985.
- [3] A. V. Khudchenko, R. Hesper, A. M. Baryshev, G. Gerlofsma, F. P. Mena, T. Zijlstra, Teun Klapwijk, M. Spaans, J. W. Kooi, "Sideband-separating Mixer for 600–720 GHz", Proc. SPIE 7854, 78542R, 2010.
- [4] I. Malo, J. D. Gallego, C. Diez, I. López-Fernández and C. Briso, "Improved Multi-octave 3 dB IF Hybrid for Radio Astronomy Cryogenic Receivers", Proc. 20th. ISSTT, pp. 300-306, 2009.
- [5] D. P. Woody, R.E. Miller and M.J. Wengler, "85-115 GHz receivers for radio astronomy," IEEE Trans. Microwave Theory Tech., vol. MIT-33, pp. 90-95, February, 1985.
- [6] N. B. Dubash, G. Pance and M. J. Wengler, "Photon Noise in the SIS detector", IEEE Trans. Microwave Theory Tech., Vol. 42, №4., pp716-725, 1994.
- [7] J.W. Kooi, "Advanced receivers for submillimeter and far infrared astronomy", PhD thesis, Groningen, 2008, Available: <http://dissertations.ub.rug.nl/FILES/faculties/science/2008/j.w.kooi/ThesisJWK-21Nov2008.pdf>
- [8] F. P. Mena, J. W. Kooi, A. M. Baryshev, C. F. J. Lodewijk, R. Hesper, G. Gerlofsma, T. M. Klapwijk, and W. Wild, "A Sideband-separating Heterodyne Receiver for the 600–720 GHz Band", IEEE Trans. Microwave Theory and Techniques., V. 59., №1., pp. 166-177, 2011.
- [9] W. Wild and J. Payne, "Specifications for the ALMA Front End Assembly", 2000, Available: [http://www.cv.nrao.edu/~awooten/mmalmcal/asac/ALMA\\_rx\\_specs\\_V10.pdf](http://www.cv.nrao.edu/~awooten/mmalmcal/asac/ALMA_rx_specs_V10.pdf)
- [10] A. R. Kerr, S. K. Pan and J. E. Effland, "Sideband Calibration of Millimeter-Wave Receivers", ALMA memo 357, 2001, Available: <http://www.alma.nrao.edu/memos/html-memos/alma357/memo357.pdf>.

## High Sensitivity Waveguide HEB Mixers at 2.5 THz

P. Pütz<sup>1\*</sup>, M. Brasse<sup>1</sup>, J. R. Gao<sup>2,3</sup>, K. Jacobs<sup>1</sup>, M. Justen<sup>1</sup>, P. Khosropanah<sup>2</sup>, W. Miao<sup>4</sup>, M. Schultz<sup>1</sup>, S. C. Shi<sup>4</sup>, W. Zhang<sup>4</sup>, and C. E. Honingh<sup>1</sup>

*1 Kölner Observatorium für Submm Astronomie (KOSMA), 1. Physikalisches Institut, Universität zu Köln, Zùlpicher Str. 77, 50937 Köln, Germany*

*2 SRON Netherlands Institute for Space Research, Landleven 12, 9747 AD Groningen, The Netherlands*

*3 Kavli Institute of Nanoscience, Delft University of Technology, Lorentzweg 1, 2628 CJ Delft, The Netherlands*

*4 Purple Mountain Observatory, National Astronomical Observatories of China, Chinese Academy of Sciences, 2 West Beijing Road, Nanjing, Jiangsu 210008, China*

\* Contact: puetz@ph1.uni-koeln.de, phone +49-221-470 3484

This work was supported by the EU FP7, Advanced Radio Astronomy in Europe, grant agreement no. 227290, by the German Space Agency (DLR), grant 50 OK 0801, through STO by NASA grant number NNX08AG39G, and by the Netherlands-China Exchange Programme executed by KNAW and CAS.

**Abstract**—We present the first successful waveguide HEB mixer in the 2.5 THz frequency band. KOSMA has designed and fabricated the mixer and the RF characterization was performed at 2.523 THz using the FIR gas laser local oscillator and the vacuum hot-cold load with thin Mylar beam splitter at SRON-Groningen. The best uncorrected receiver noise temperature  $T_{rec}(IF, V_{bias})$  measured is 800 K at 1.25 GHz intermediate frequency (IF). This value is comparable with the results of quasi-optical mixers at this frequency. KOSMA develops waveguide HEB mixers for use in focal plane array receivers for the Stratospheric Terahertz Observatory (STO) and the Stratospheric Observatory for Infrared Astronomy (SOFIA).

The mixer consists of a small NbTiN microbridge of 4 nm in thickness, 0.4  $\mu\text{m}$  in length and 1.55  $\mu\text{m}$  in width on a 2  $\mu\text{m}$  SIN membrane substrate that is contacted and mounted to a waveguide mixer block by beam leads. The device shows a noticeable direct-detection response to the loads, which affects evaluation of mixer sensitivity. During each Y factor measurement we therefore adjusted the LO power by means of an attenuator wire-grid in the LO path, keeping the pump level constant as indicated by the HEB bias current. This manual pump level compensation in either direction (for hot or cold load radiation, respectively) was confirmed by identical noise temperatures obtained from successive continuous LO power scans responding to the hot and cold load.

# The experimental demonstration of a low-cost 37-horn focal-plane array consisting of smooth-walled multiple flare-angle horns fabricated by direct drilling

J. Leech\*, B. K. Tan\*, G. Yassin\*, P. Kittara<sup>†</sup> and S. Wangsuya<sup>†</sup>  
\*Department of Physics, University of Oxford, Email: jxl@astro.ox.ac.uk  
<sup>†</sup>Department of Physics, Mahidol University.

**Abstract**—In previous work, we have described novel smooth-walled multiple flare-angle horns designed using a genetic algorithm. A key feature of these horns is that they can be manufactured very rapidly and cheaply in large numbers, by repeated direct drilling into a single plate of aluminium using a shaped machine tool. The rapid manufacturing technique will enable the construction of very low cost focal-plane arrays, offering an alternative to conventional electroformed corrugated horn arrays.

In order to experimentally demonstrate the new technology, we constructed a 230 GHz focal-plane array comprising 37 smooth-walled horns fabricated by direct drilling. We present the measured beam patterns for a large sample of these horns across the array, demonstrating the suitability of our manufacturing techniques for large format arrays. We have measured the cross coupling between adjacent feeds and have shown that it is negligible. We also present high quality beam patterns measured for a much smaller 700 GHz horn, showing the promise of extending this technology to THz frequencies.

## I. INTRODUCTION

The construction of high quality feed horns for mm and sub-mm astronomy has historically been much more challenging than the construction of feed horns at longer wavelengths. The expense and time required to construct these horns is becoming particularly problematic in an era where it is highly desirable to build focal plane array receivers with large numbers of horns for large single dish telescopes. The usual choice of high performance feed horn, the corrugated horn, requires the construction of many azimuthal corrugations per wavelength and becomes expensive and time-consuming to manufacture below wavelengths of around 1 mm. There has therefore been considerable interest [1]–[6] in designing smooth-walled horns that offer performance similar to corrugated horns, but which are much easier to construct at short wavelengths. Large format focal-plane arrays, consisting of many hundreds or even thousands of horns will be essential for maximising the mapping speeds of large single dish telescopes for sub-mm astronomy. Thus the rapid and inexpensive fabrication of large numbers of horns is a critical requirement.

Much recent work [1], [2] has focussed on using the modal matching technique [7] to calculate the far-field beam patterns for horns which are then optimised using a suitable automated

algorithm. The authors of this paper have previously reported using a genetic algorithm (GA) to design Potter horns with a single step or flare-angle discontinuity (Fig. 1 (a)) [3]. We then generalised this approach to design horns with multiple flare-angle discontinuities [4]–[6] leading to designs with significantly higher bandwidths that still have a simple profile which is easy to fabricate at sub-mm wavelengths.

The horns we describe in this paper were designed using a genetic algorithm [8], which mimics the process of natural selection to perform an optimisation by minimising a *cost function*. We have outlined our algorithm and its implementation in detail in [3]–[6]. For our purposes, we chose a simple cost function that is minimised for horns having a high beam circularity and low cross-polarisation [3]. Other cost functions could be used with the same GA, selecting other desirable features in the horn patterns, dependent on the required application — e.g. high beam efficiency, high Gaussianity etc. We have written a suite of design software, incorporating both modal matching and the genetic algorithm, to implement the complete design method. The software can run on single desktop PCs or on multiple CPU Beowulf clusters.

A 230 GHz horn with 2 flare-angle discontinuities (Fig. 1 (b)), designed using the GA with a FWHM beamwidth of 14.6 degrees and a 20% bandwidth is described in [6]. The horn has the following dimensions (in mm):  $R_0 = 0.62$ ,  $R_1 = 1.486$ ,  $R_2 = 1.812$ ,  $R_3 = 3.6524$ ,  $L_1 = 1.479$ ,  $L_2 = 1.212$ ,  $L_3 = 24.0$  (Fig. 1 (b)). The theoretical far-field beam patterns, calculated using modal matching, are shown in Fig. 2.

## II. SINGLE AND DUAL HORN PROTOTYPES

An attractive feature of our multiple flare-angle smooth-walled horns is that their simple interior profiles make them much easier to manufacture than corrugated horns. We have developed a simple technique where the horn is drilled out of an aluminium block using a machine tool (Fig. 1, Bottom) whose cutting edge has been manufactured with the shape of the required interior horn profile. In previous work [4]–[6], we have successfully manufactured and experimentally tested several individual horns using this technique at 230 GHz. In

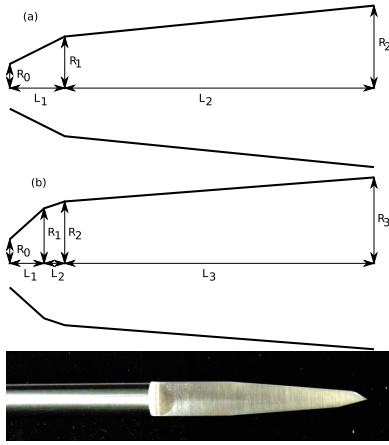


Fig. 1. Top: A schematic diagram of (a) 2-section and (b) 3-section multiple flare-angle horns. Bottom: The high speed steel machine tool used for the fabrication of the drilled horn prototype.

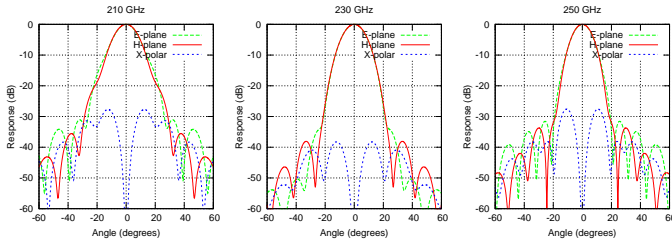


Fig. 2. Theoretical beam patterns (E plane, H-plane and cross-polarisation) calculated using modal matching.

particular, we compared the beam patterns for horns made using conventional electroforming and horns made using the new drilling technique. In both cases the measured beam patterns agreed well with theory with low sidelobes and cross polarisation between 210-250 GHz (20% bandwidth), with little difference between patterns for different horns, validating our new fabrication technique [5].

For focal-plane arrays, it is important to have negligible cross-coupling between two adjacent horns within the array. In order to test this for our horns, we drilled two close packed horns (separation = 8 mm) into a single aluminium block. Using a vector network analyser and a carbon loaded epoxy cone in front of the horns as an absorber we measured the cross coupling between the two horns. We found the measured cross-coupling to be below -67 dB across the operating bandwidth of 210-250 GHz [6]. This result was compatible with that obtained from modelling the cross-coupling of the two horns using Ansoft's HFSS, a full 3-D electromagnetic simulation package. We also measured the far-field beam patterns for each horn in the two-horn block and again found good agreement with the beam patterns calculated using modal matching, with each horn giving very similar beam patterns.

### III. A 37-HORN ARRAY FOR 230 GHz

The high quality beam patterns and low cross-coupling measured for our prototype two-horn array enabled us to proceed confidently with the construction of a larger array

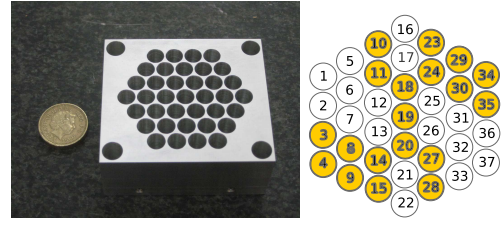


Fig. 3. Left: The 37-horn array prototype, made by repeated drilling into a single block of aluminium. Right: Schematic of the horn array highlighting the sample of 19 horns tested.

with drilled horns of the same design. We constructed a 230 GHz, 37 horn hexagonally close packed array, with a horn spacing of 8 mm, by repeated drilling into a single aluminium plate (Fig. 3, Left). The array was constructed using a standard 5 axis CNC milling machine, taking around two days to manufacture. Making larger arrays with several hundred horns will be a similarly rapid process, once care is taken to accurately align the aluminium plate within the milling machine to ensure good drilling alignment with the axes of the horn and the waveguide machining tools.

After construction of our 37-horn array prototype we measured the far-field patterns of the array directly in the far-field using a cooled bolometer detector in a custom built anechoic chamber. The subset of horns chosen for testing (Fig. 3, Right) was spread across the whole array, enabling us to look for any trends in beam pattern behaviour which might arise from differences in machining tolerances across the array. The experimentally measured beam patterns for a representative sample of 9 of the 19 horns tested are shown in Fig. 4. The measured beam patterns show high beam circularity, low sidelobe levels (below -20 dB) and good agreement with theory for the tested horns. These experimental results show a high degree of beam uniformity across the array, demonstrating the applicability of the direct drilling fabrication technique to future large format focal-plane array receivers. While we saw no obvious trends in beam quality as a function of position within the array, we did notice some E-plane main-beam asymmetry at the high end of the measured bandwidth for two of the nineteen horns tested (horn Nos. 15 & 27 in Fig. 4). We intend to investigate the causes of these asymmetries by splitting the horns in question in half, to examine machining quality near the critical throat region of the horn. We will then model the effect of any measured asymmetrical machining imperfections by simulating these horns using Ansoft's HFSS [6]. We intend to present a full analysis of the machining tolerances required for fabrication of these horns as a function of frequency in a future paper.

### IV. PROTOTYPE HORNS FOR 700 GHz

As well as fabricating complete horn arrays at 230 GHz, we are also extending the technology to sub-mm wavelengths by fabricating horns for a band centre of 700 GHz ( $\lambda = 429 \mu\text{m}$ ). We fabricated three individual horn prototypes, identical to those described above, but scaled by a factor of 0.329 to give



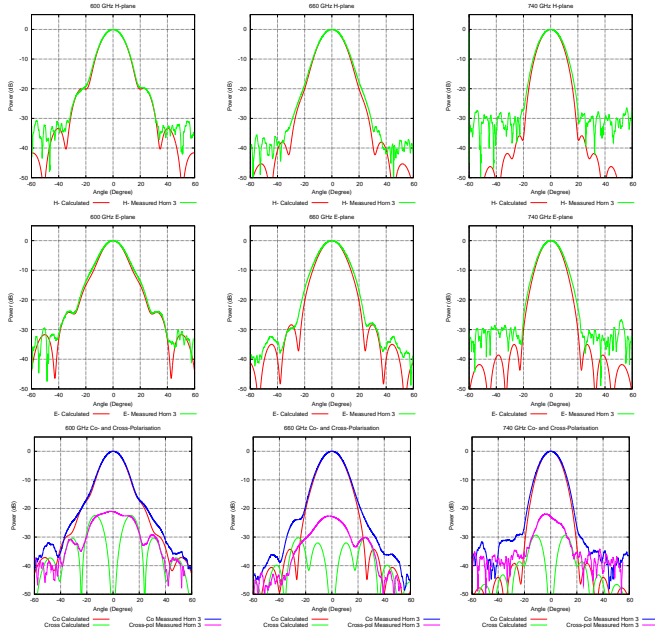


Fig. 5. Experimental and theoretical beam patterns measured for the 700 GHz prototype horn, measured between 600 and 740 GHz. Top: H-plane, Middle: E-plane, Bottom: co-polar and cross polar.

a central frequency of 700 GHz. The cutting tool for horns at these frequencies becomes much smaller, with a maximum radius of 1.2 mm, set by the required aperture of the horn.

We measured the beam patterns of these horns using our far-field test range, between 600 and 740 GHz, the upper frequency measurement being limited by the power available from our LO source (Fig. 5) [9]. The co-polar and cross-polar patterns were measured using a terahertz polarising grid, oriented at 45 degrees to the rotation plane, positioned in front of the cooled bolometric detector. The beam circularity is excellent, the measured sidelobes are below -25 dB and the cross polarisation is below -22 dB across a bandwidth of 140 GHz. We note that the cross polarisations measured will be upper limits, limited by the performance of the polarising grid. These results demonstrate that our horn fabrication technology is effective into the scientifically important high end of the sub-mm wavelength range, with a bandwidth sufficient to cover the entire atmospheric window centred at 660 GHz.

## V. NEW 4-SECTION BROADBAND DESIGNS

The horns in both the 2-horn and 37-horn arrays described above have two flare-angle discontinuities near the throat of the horn, i.e. the horn consists of three conical sections. The horns perform well over a bandwidth of around 20%. Since fabricating these horns we have designed, using the genetic algorithm optimisation software, horns with more flare-angle discontinuities optimised over a greater target bandwidth. These software simulations have been run using the parallelised version of our horn software across 24 CPU cores. We have produced some new designs with good expected performance, including a 700 GHz 4-section design which has an increased fractional bandwidth of 25%. We now intend

to have horn cutting tools with this profile made in order to fabricate and test some prototypes of these extended bandwidth horns.

## VI. CONCLUSION AND FURTHER WORK

We have described multiple flare-angle smooth-walled horns, designed using a genetic algorithm, that are simple and inexpensive to fabricate using direct drilling. The suitability of these horns for use in large format focal-plane arrays has now been demonstrated by fabricating and testing a complete 37-horn prototype array for use at 230 GHz. Horns fabricated and tested at 700 GHz show that the technology scales well to shorter wavelengths. Our future development work will consist of performing a thorough analysis of the machining tolerances required to fabricate these horns at a given wavelength, as well as the design and testing of new broader bandwidth designs incorporating  $> 4$  flare-angle discontinuities.

## ACKNOWLEDGMENT

This work was supported by an STFC follow-on fund grant and by the Keck Institute for Space Studies, at the California Institute of Technology. We thank Bertrand Thomas, Manju Henry, Jeanne Treuttel and M.L. Oldfield at the Rutherford Appleton Laboratories for their help in making beam pattern measurements for the single and dual horn prototypes. We are pursuing the commercialisation of this technology with ISIS Innovation Ltd, the technology transfer company of the University of Oxford.

## REFERENCES

- [1] C. Granet, G. L. James, R. Bolton, and G. Moorey, "A smooth-walled spline-profile horn as an alternative to the corrugated horn for wide band millimeter-wave applications," *IEEE Trans. Antenna Propagat.*, vol. 52(3), pp. 848–854, 2004.
- [2] L. Zeng, C. L. Bennet, D. T. Chuss, and E. J. Wollack, "A low cross-polarization smooth-walled horn with improved bandwidth," *IEEE Trans. Antenna Propagat.*, vol. 58(4), pp. 1383–1387, 2010.
- [3] P. Kittara, A. Jiralucksanawong, G. Yassin, S. Wangsuya, and J. Leech, "The design of Potter horns for THz applications using a genetic algorithm," *International Journal of Infrared and Millimeter Waves*, vol. 28, no. 12, Dec. 2007.
- [4] J. Leech, G. Yassin, B. K. Tan, M. Tacon, P. Kittara, A. Jiralucksanawong, and W. S., "A new, simple method for fabricating high performance sub-mm focal plane arrays by direct machining using shaped drill bits," in *Proceedings of the 20th Int. Symposium Space Terahertz Technology, Charlottesville, VA, USA, 2009.*, 2009.
- [5] J. Leech, B. K. Tan, G. Yassin, P. Kittara, A. Jiralucksanawong, and S. Wangsuya, "Measured performance of a 230 GHz prototype focal-plane feedhorn array made by direct drilling of smooth-walled horns," in *Proceedings of the 21st Int. Symposium Space Terahertz Technology, Oxford, U.K.*, 2010.
- [6] J. Leech, B. K. Tan, G. Yassin, P. Kittara, S. Wangsuya, J. Treuttel, M. Henry, M. L. Oldfield, and P. G. Huggard, "Multiple flare-angle horn feeds for sub-mm astronomy and cosmic microwave background experiments," *Astron. Astrophys.*, vol. 532, pp. A61+, Aug. 2011.
- [7] A. D. Olver, P. J. B. Clarricoats, A. A. Kishk, and L. Shafai, *Microwave horns and feeds*. Bookcraft, Bath., 1994.
- [8] R. Haupt and S. Haupt, *Practical Genetic Algorithms*. Wiley-Interscience Publication., 1998.
- [9] B. K. Tan, J. Leech, G. Yassin, P. Kittara, M. Tacon, S. Wangsuya, and C. Groppi, "High Performance, easy-to-machine terahertz feed horns," Submitted to the *Journal of Infrared, Millimeter and Terahertz waves*, June 2011., 2011.

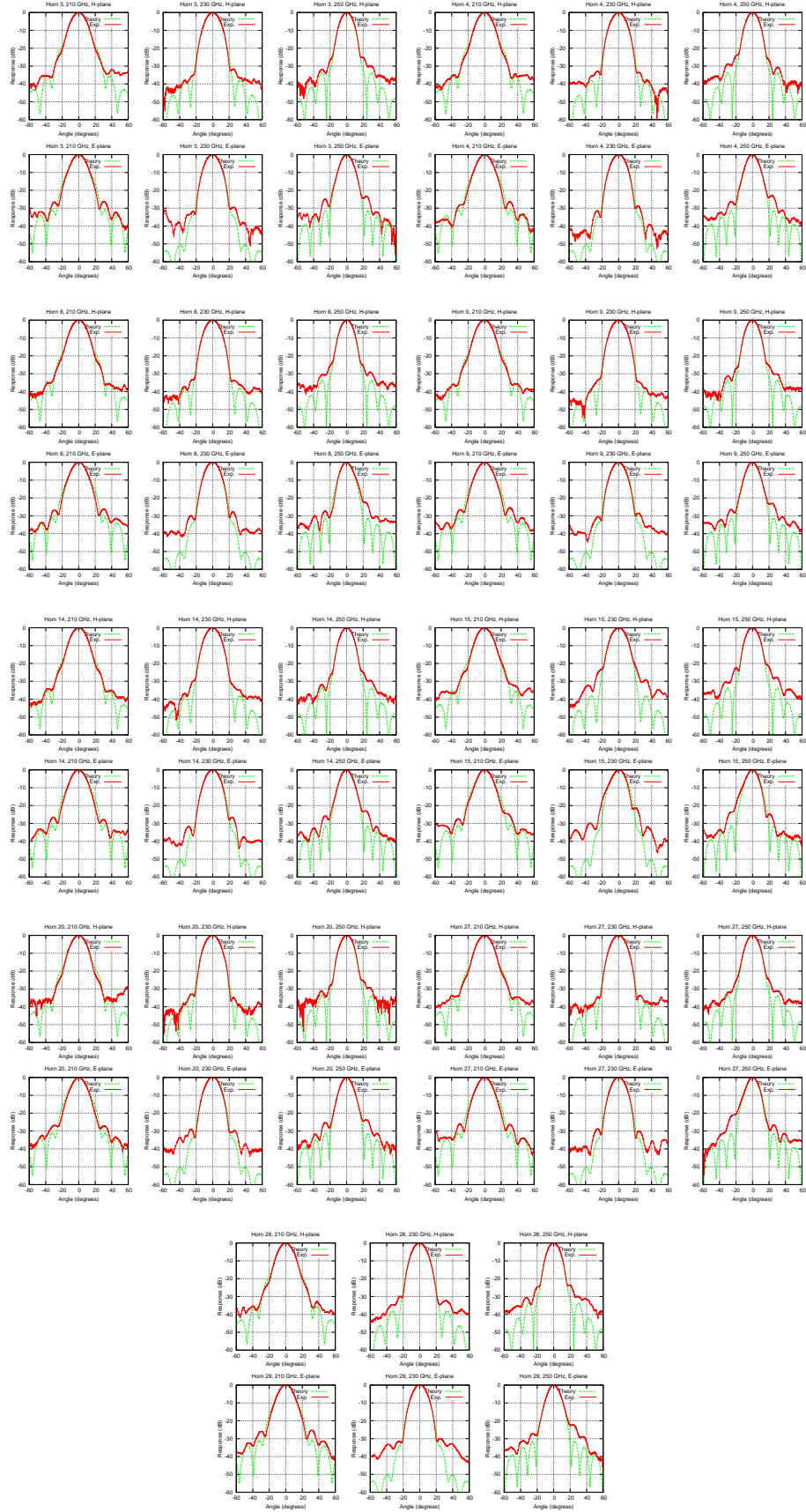


Fig. 4. Experimental and theoretical beam patterns for a sample of horns for the lower half of the array (Horn Nos. 3, 4, 8, 9, 14, 15, 20, 27 and 28). See Fig. 3 for their location within the array.

# Effect of Phase Slippage and Higher Order Beam Modes in a 340GHz Focal Plane Array Optics

Axel.Murk<sup>\*</sup>, Mark Whale, Matthias Renker

*University of Bern, Institute for Applied Physics, CH-3012 Bern, Switzerland*

\* Contact: [murk@iap.unibe.ch](mailto:murk@iap.unibe.ch)

*Abstract*— Focal plane arrays (FPA) are an efficient way to improve the the mapping speed and integration time of single dish observations in radio astronomy and microwave remote sensing. An example is the multi-beam limb sounder STEAMR (Stratosphere-Troposphere Exchange and Climate Monitor Radiometer), which is currently being developed under the lead of the Swedish Space Corporation for the next ESA Earth Explorer Core Mission PREMIER. The instrument consists of a linear array of fourteen 313-355 GHz receivers, which will provide simultaneous observations of the Earth's atmospheric limb at different tangent heights. The STEAMR optics consists of a Ritchey-Chrétien telescope and astigmatic transfer optics which generates the desired elliptical beam profiles with a 2:1 aspect ratio. While these first reflectors M1 to M6 are shared by all fourteen beams of the instrument, the signals are split in the FPA optics by means of a polarizing wire grid and two facet reflector assemblies which are matched to the corrugated feed horns of the receivers. In order to meet the scientific goals of the PREMIER mission it is essential to achieve a high beam efficiency, low sidelobes, high pointing stability and frequency independent performance for each of the fourteen channels.

The overall optical design of STEAMR is described in Whale et al., EuCAP 2011. In this paper, we will focus on the design trade-offs of its focal plane array optics, and in particular on the effect of phase slippage and higher order beam modes on the system performance. The facets of this focal plane array are tightly packed and maintain a relatively high level of truncation in comparison to typical millimetre-wave reflector optics. Specific attention is paid to maximizing the throughput for the array optics. We present results of higher order Gaussian Beam Mode analysis and GRASP Physical Optics simulations for different geometries with both standard and optimized multi-moded corrugated feed horns.

## VNA Measurements in the 0.75-1.1 THz Band

J.L. Hesler\*, K. Hui, B. Foley, S. Durant, and T.W. Crowe

Virginia Diodes Inc., Charlottesville, VA 22902

\* Contact: hesler@vadiodes.com

**Abstract**—The design, development and testing of a state-of-the-art 0.75-1.1 THz Vector Network Analyzer Extender will be presented. The extender consists of a series of multipliers and mixers that are used to extend the frequency of Microwave Vector Network Analyzers (with operating frequency typically below 50 GHz). The transmitter consists of a x27 multiplier chain generating an average output power of -24 dBm over the 0.75-1.1 THz band. This power is then fed into a bi-directional coupler that is used to sample the outgoing wave (reference mixer) and the test signal (measurement mixer). The coupler has an insertion loss of ~ 6 dB, yielding a test port power of -30 dBm typical. The receivers have a harmonic factor of 36, and consist of a multiplier chain driving a harmonic mixer. The conversion loss of these mixers is in the range of 20-25 dB. Transceiver measurements of the VNA system yielded a dynamic range of 60-70 dB over  $\frac{3}{4}$  of the frequency band, with reduced performance at the band edges. The dynamic range measurements were performed with a 10 Hz measurement bandwidth.

The VNA Extender was used to perform calibrated measurements of a variety of one-port and two-port test pieces, using a Short-Open-Load-Thru calibration method. The open circuit was implemented using a  $\frac{1}{4}$ -wave delayed short circuit, and the load was a precision load with expected return loss better than 50 dB. Measurements of a 1" straight waveguide piece indicated a return loss of 25-30 dB typical, with the reflections generated by mechanical misalignments at the waveguide interfaces. The measured insertion loss of the 1" straight waveguide piece matched the theoretical loss with a "roughness" factor of 1.4, which is consistent with losses measured at other bands. Additional measurements will be presented at the symposium.

## A Multibeam 2SB SIS Receiver at 3mm Wavelength

J. Yang<sup>1</sup>, WL. Shan<sup>1</sup>, SC. Shi<sup>1</sup>, QJ. Yao<sup>1</sup>, YX. Zuo<sup>1</sup>, ZH. Lin<sup>1</sup>, SH. Chen<sup>1</sup>, QG. Huang<sup>1</sup>, XG. Zhang<sup>1</sup>, WY. Duan<sup>1</sup>, AQ. Cao<sup>1</sup>, S. Li<sup>1</sup>, Z.Q. Li<sup>1,2</sup>, JQ. Zhong<sup>1,2</sup>, J. Liu<sup>1,2</sup> and K. Liu<sup>1,2</sup>

<sup>1</sup> Purple Mountain Observatory, Chinese Academy of Sciences, Nanjing, China, 210008

<sup>2</sup> Graduate School, Chinese Academy of Sciences, Nanjing, China, 210008

\* Contact: shan@pmo.ac.cn, phone +86-25-8333 2229

**Abstract**—We have developed a 3x3 multi-beam receiver for Delingha millimeter telescope, the major open facility for millimeter-wave radio observation in China. The receiver has been successfully put into observation since the end of 2010 and its considerable enhancement of mapping speed has been proved. The receiver employs 2SB SIS mixers with a typical SSB noise temperature 50K and sideband separation ratio over 10dB in the 85-116GHz frequency range. The SIS mixers have a nearly 50 Ohm output impedance enabling direct connection of the cryogenic low noise amplifier without IF isolator. The nine pixels are pumped by a single LO source distributed by a 2-stage cascaded power dividers realized by 6-branch line directional couplers. The LO is generated by a frequency synthesizer followed by an amplifier-multiplier module providing output power over 10mW across the RF band. The IF band is centered at 2.64GHz with bandwidth 1GHz allowing simultaneously observing three CO lines ( $C^{18}O$ ,  $^{13}CO$  and  $^{12}CO$ ). The nine pixels yield 18 independent IF outputs. Each of them is processed by a digital FFT spectrometer with 200MHz-1GHz reconfigurable bandwidth and 16384 channels. In this symposium the design and the performance of this 2SB multi-beam receiver will be presented in detail.



Fig. 1

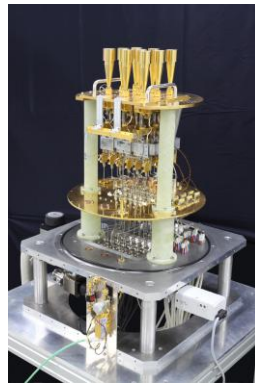


Fig. 2

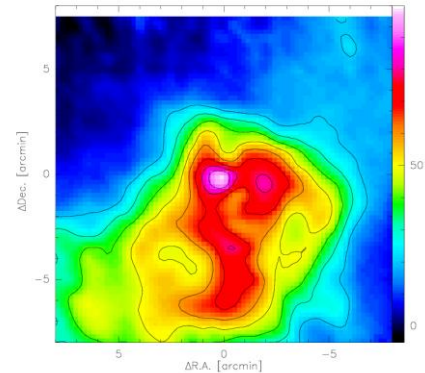


Fig. 3

Fig. 1 The photo of the whole receiver system.

Fig. 2 The photo of the front-end inside Dewar.

Fig. 3 An observation example (S106 12CO J=1-0) using new receiver system.

## Development of the 1.3-1.5 THz Band Superconducting HEB Mixer Receivers for ASTE 10 m Telescope

T. Shiino<sup>1\*</sup>, L. Jiang<sup>2</sup>, R. Furuya<sup>1</sup>, T. Yamaguchi<sup>1</sup>, S. Shiba<sup>1</sup>, T. Sakai<sup>1</sup>, N. Sakai<sup>1</sup>, Y. Watanabe<sup>1</sup>,  
O. Ohguchi<sup>3</sup>, H. Maezawa<sup>3</sup>, T. Yamakura<sup>4</sup>, Y. Irimajiri<sup>5</sup>, S. Yamamoto<sup>1</sup>

*1 The University of Tokyo\*, Hongo, Tokyo, Japan*

*2 Nanjing Forestry University, Nanjing, Jiangsu, China*

*3 Nagoya University, Nagoya, Aichi, Japan*

*4 Tsukuba University, Tsukuba, Ibaraki, Japan*

*5 National Institute of Information and Communications Technology, Koganei, Tokyo, Japan*

\* Contact: shiino@taurus.phys.s.u-tokyo.ac.jp, phone +81-297-5184-2474 24217

**Abstract** In the THz region, there exist many spectral lines of various fundamental atoms, ions and molecules, which give us novel information on chemical and physical state of interstellar clouds including star and planet forming regions. Although observations of these lines have successfully been started with Herschel HIFI, further observations with higher angular resolution from the ground based telescope are still important by utilizing some THz atmospheric windows. With this in mind, we have been developing superconducting HEB (Hot Electron Bolometer) mixers for the THz heterodyne sensing at The University of Tokyo. By use of these mixers, we are preparing a cartridge-type THz heterodyne receiver for the 0.8-0.9 THz and 1.3-1.5 THz bands. This receiver will be installed on ASTE 10 m telescope (Atacama Chili) for molecular line observations in the above regions.

The receiver is the ALMA cartridge type with a single beam. It can observe dual bands (0.9 THz and 1.3-1.5 THz) simultaneously in the DSB mode by using the wire grid. We employ the in-house waveguide HEB mixers for the both bands. Although SIS mixers now show a better performance than HEB mixers at 0.9 THz, we use the HEB mixer to demonstrate observation capability of our HEB mixer. The LO signal is coupled with the RF signal by wire grids placed on the 4 K stage. As for the LO signal source, we use frequency-multiplier chains driven by the microwave synthesizer. We use NbTiN and NbN superconducting films fabricated on a quartz substrate for the HEB mixers. The NbN film formed directly on a quartz substrate does not show high  $T_c$ . Hence, we use the AlN buffer layer between the quartz substrate and the NbN film (Shiino et al. 2010). The thickness of superconducting microbridges is set to be 10.8 nm for NbTiN and 6 nm for NbN. The receiver performance has been measured in the test apparatus. The minimum receiver noise temperatures achieved so far are 450 K for the 0.8 THz NbTiN and NbN mixers, 1050 K for the 1.5 THz NbN mixers, and 570 K for the 1.5 THz NbTiN mixers. The noise performance of the 1.5 THz NbTiN mixer is excellent. The noise temperatures show significant dependence on microbridge size (0.5~3.0  $\mu\text{m}$  width and 0.1~0.4  $\mu\text{m}$  length). We will be able to achieve better noise performance by optimizing the microbridge dimensions carefully.

# Temperature and frequency resolution of a 3.5 THz heterodyne spectrometer using a quantum cascade laser

Y. Ren, J.N. Hovenier, J.R. Gao, T.M. Klapwijk, S.C. Shi, T-Y. Kao, Q. Hu, and J. L. Reno

**Abstract**—Here we characterized the temperature and frequency resolution of a 3.5 THz heterodyne spectrometer based on a quantum cascade laser (QCL) as a local oscillator and a superconducting NbN hot-electron bolometer (HEB) as a mixer. High resolution spectral lines of methanol (CH<sub>3</sub>OH) gas around 3.5 THz were obtained by performing heterodyne spectroscopic measurements. From the measured spectra, we determined the minimal temperature change that could be resolved for the heterodyne receiver in different operation manner. The spectral resolution of the receiver was also addressed.

**Index Terms**—terahertz, quantum cascade laser, high resolution spectroscopy, temperature resolution, frequency resolution

## I. INTRODUCTION

High resolution heterodyne spectroscopy plays a vital role in astronomical observation and atmospheric remote sensing at terahertz (THz) frequencies, due to its high spectral resolution ( $\nu/\Delta\nu > 10^6$ , limited by the local oscillator (LO) and back-end spectrometer, where  $\nu$  is the frequency, and  $\Delta\nu$  is the frequency resolution) and excellent sensitivity (e.g., receiver noise temperature of  $\sim 1000$  K at 3 THz). As the mixer, a superconducting NbN hot-electron bolometer (HEB) has been applied in the HIFI instrument on the Hershel Space Observatory covering the frequency range from 1.4 to 1.9 THz. Recently an HEB mixer has demonstrated superior sensitivity up to 5.3 THz [1]. As the LO, terahertz quantum cascade lasers (QCLs) [2] have shown eminent advantages at

frequencies above 2 THz, based on their high output power, wide emission frequency range and excellent power stability compared to FIR gas lasers. As the development of the heterodyne receiver moves from single pixels to arrays, higher LO power becomes crucial. Therefore, the high output power of a THz QCL appears to be extremely attractive. Recently, several progresses have been made for a THz QCL to be used as the LO, including a noise temperature measurement [3,4], excellent power stability [3] and phase-locking capability [5,6]. Furthermore, as shown in Ref. 7 and 8, heterodyne spectroscopic measurements have also been performed based on a THz QCL as a LO. High resolution molecular spectra were obtained and showed excellent agreement with the modeled ones. All these results suggest that a THz QCL is competent as a LO in a heterodyne receiver above 2 THz. For a heterodyne receiver, both temperature and frequency resolution are of crucial importance since they define the minimum temperature and frequency difference that can be resolved within the integration time [9]. A heterodyne molecular spectroscopic measurement is a direct means to characterize the ultimate performance of a heterodyne receiver in the spectroscopic mode.

In this paper we report on the temperature and frequency resolution of a 3.5 THz heterodyne spectrometer, based on a THz QCL as a LO and a superconducting NbN HEB as a mixer. We observed simultaneously several molecular spectral lines of methanol gas around 3.5 THz. From the measured spectra, the minimal temperature and frequency resolution were determined.

## II. MEASUREMENT SETUP

The LO used in our experiment is designed and fabricated at the MIT group. It is a third-order distributed feedback (DFB) THz QCL [10,11], which is the same one as described in Ref. 8. Our laser consists of 27 periods of gratings with a total length of 1070  $\mu\text{m}$ . It provides a peak emission power of 0.8 mW at a bath temperature of  $\sim 12$  K. Based on the third-order periodic structure with strong refractive contrast gratings, not only is the single mode emission achieved in the DFB laser, but also the radiation power out-coupling from the laser to the free space is considerably improved. Furthermore, the grating structure behaves like a linear phased array antenna, resulting in a low-divergent far field beam. As a result, a higher power coupling efficiency from the QCL to the HEB mixer is obtained in comparison with the use of a metal-metal waveguide Fabry-Perot cavity QCL. Moreover,

This work was partly supported by China Exchange Programme executed by KNAW and CAS, and by the AMSTAR+ project of RadioNet under FP7, and NWO.

Y. Ren is with the Kavli Institute of NanoScience, Delft University of Technology, Lorentzweg 1, 2628 CJ Delft, The Netherlands, with the Purple Mountain Observatory, Chinese Academy of Sciences, Nanjing, China, and with the graduate school, Chinese Academy of Science, Beijing, China, (e-mail: y.ren@tudelft.nl)

J.N. Hovenier and T.M. Klapwijk are with the Kavli Institute of NanoScience, Delft University of Technology, Lorentzweg 1, 2628 CJ Delft, The Netherlands

J.R. Gao is with the Kavli Institute of NanoScience, Delft University of Technology, Lorentzweg 1, 2628 CJ Delft, The Netherlands, and with the SRON Netherlands Institute for Space Research, Sorbonnelaan 2, 3584 CA Utrecht, The Netherlands (j.r.gao@tudelft.nl)

S.C. Shi is with the Purple Mountain Observatory, Chinese Academy of Sciences, Nanjing, China

T-Y. Kao and Q. Hu are with Department of Electrical Engineering and Computer Science, Massachusetts Institute of Technology, Cambridge, Massachusetts 02139, USA

J.L. Reno is with Center for Integrated Nanotechnologies, Sandia National Laboratories, Albuquerque, NM 87185-0601, USA

~1 GHz frequency tuning range is achieved for the LO frequency by varying the bias voltage or the bath temperature of the laser.

The mixer is a spiral antenna coupled superconducting NbN HEB, the same as used in Ref. 1. It is glued to the backside of an elliptical, uncoated Si lens and is operated at 4.2 K.

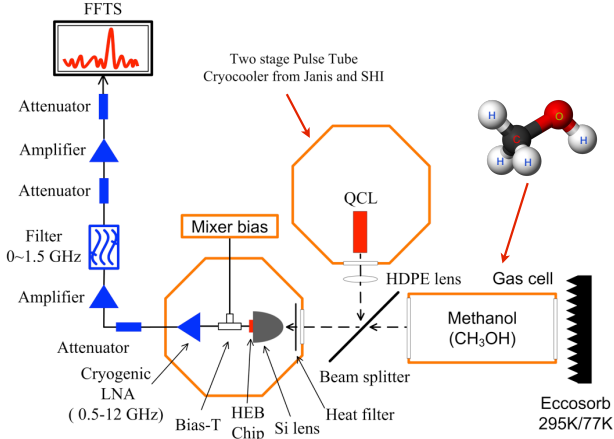


Fig. 1. Schematic view of the heterodyne spectroscopic measurement setup.

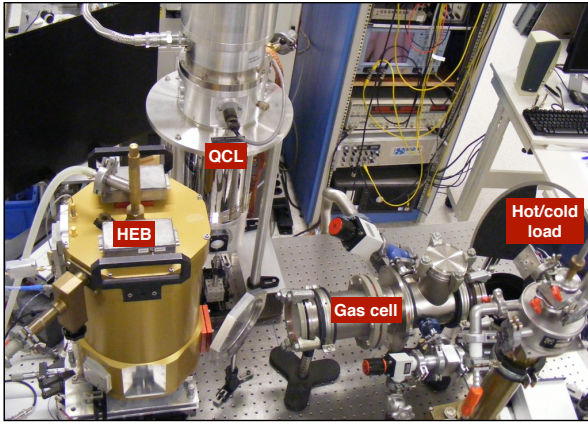


Fig. 2. Picture of the heterodyne spectroscopic measurement setup.

The spectroscopic measurement setup is sketched in Fig.1, which is the same as applied in Ref. 8. The QCL is mounted on the second stage of a pulse tube cryocooler. In order to reduce its mechanical vibration, which causes the instability of the output beam of the QCL and in turn introduces the instability of the HEB receiver, an additional damper is used to minimize the mechanical vibration. The QCL is operated in a free-running mode, namely without any stabilization on its phase and amplitude. The radiation beam from the QCL is focused by a high-density polyethylene (HDPE) lens. The signal source is a combination of a gas cell with a hot load at 295 K and a cold load at 77 K. The gas cell is a 41-cm long cylinder at room temperature and has two 2-mm thick HDPE windows. Methanol ( $\text{CH}_3\text{OH}$ ) gas is chosen since it has abundant absorption lines at this frequency range. The methanol emission lines around 3.5 THz from the gas cell are combined with the QCL's radiation by a 13- $\mu\text{m}$  thick Mylar beam splitter and fed into the HEB mixer. The mixer down-converts the THz spectral lines at  $f_s$  to an intermediate frequency (IF)  $f_{IF}$ . Since the HEB is working in the double

sideband (DSB) mode, both the signal at upper side band (USB)  $f_{USB}=f_{LO}+f_{IF}$  and lower side band (LSB)  $f_{LSB}=f_{LO}-f_{IF}$  will be converted to the same IF frequency range. The IF signal is first amplified using a wide band (0.5-12 GHz) low noise amplifier at 4.2 K, followed by a two-stage room-temperature amplifier with a 1.5 GHz low pass filter used inbetween to define the detection bandwidth. The back-end spectrometer is a Fast Fourier Transform Spectrometer (FFTS) [12], which samples the IF signals in the baseband (0-1.5 GHz) with a spectral resolution of 183 KHz.

### III. MEASUREMENT RESULTS

We start our spectroscopic experiment by characterizing the sensitivity of the entire receiver system. In this case, a band-pass filter centered at 1.4 GHz with 100 MHz bandwidth is used, and a power meter is applied instead of the FFTS. The measured  $T_{DSB,Rec}$  was 3800 K for the case where the hot/cold loads are positioned behind the evacuated gas cell. This noise temperature value is higher than previous reported one [1], which can be attributed to extra losses due to air, the HEB cryostat window as well as the gas cell windows, the non-optimized IF chain, and the direct detection effect.

The same method as in Ref. 9 is applied to measure the spectral lines. With this method three IF power spectra were recorded: (1) the spectrum  $P_{emp,cold}(f)$  when the cold load is behind the evacuated gas cell; (2) the spectrum  $P_{gas,cold}(f)$  when the cold load is behind the filled gas cell; (3) the spectrum  $P_{gas,hot}(f)$  when the hot load is behind the filled gas cell. With the three spectra, the intensity of the molecular emission lines in terms of temperature is calculated using the following expression [9]:

$$T_{gas}(f) = T_{cold} + 2 \cdot (T_{hot} - T_{cold}) \cdot \frac{S_{gas77}(f) - S_{emp77}(f)}{S_{gas300}(f) - S_{emp77}(f)} \quad (1)$$

where Callen-Welton temperature [13] is used to define the effective hot and cold load temperature, and a pre-factor of 2 in Eq.(1) reflects the DSB mode operation of the HEB mixer.

By doing this, a calibrated spectrum within the IF frequency range between 0-1.5 GHz is obtained, as shown in Fig.3. Several methanol spectral lines with different intensity around 3.5 THz were simultaneously observed. For a Dicke-type radiometer, the temperature resolution is given by [9],

$$\Delta T = \sqrt{\frac{(T_A + T_R)^2}{B\tau_A} \frac{1}{d_A} + \frac{(T_{ref} + T_R)^2}{B\tau_{ref}} \frac{1}{d_{ref}}} \quad (2)$$

where  $T_A$  is the effective antenna temperature;  $T_R$  the receiver noise temperature;  $T_{ref}$  the reference signal temperature;  $B$  the detection bandwidth;  $\tau_A$  the integration time for the spectral line signal;  $\tau_{ref}$  the integration time for the reference signal;  $d_A$  and  $d_{ref}$  are the duty cycles of the observation time for the spectral line signal and reference signal, respectively. In our case,  $T_A=300$  K,  $T_R=3800$  K,  $T_{ref}=77$  K,  $B=183$  KHz. For each single spectrum, it takes 3 seconds of integration time. So for a single spectrum,  $\tau_A=\tau_{ref}=3$  sec, and  $d_A=d_{ref}=1/3$ , from which



we expect a  $\Delta T$  of 13.2 K. As shown in Fig.3a, the standard deviation of measured noise level was 13.8 K. We also performed 18 series of the  $P_{\text{gas,cold}}(f)$  spectrum measurement and 21 series of the  $P_{\text{emp,cold}}(f)$  spectrum measurement. The calibrated spectrum was subsequently averaged as plotted in Fig.3b. In the time averaged case,  $\tau_A=3 \text{ sec} \cdot 18$  (18 times average),  $\tau_{\text{ref}}=3 \text{ sec} \cdot 21$  (21 times average),  $d_A=18/(18+21+1)$ ,  $d_{\text{ref}}=21/(18+21+1)$ , from which we expect a  $\Delta T$  of 2.5 K. Our experimental data indicate a temperature resolution of 3.5 K. Then the time averaged spectrum was smoothed to the 1.83-MHz resolution, as plotted in Fig.3c. Since  $B=1.83 \text{ MHz}$ , we expect a  $\Delta T$  of 0.79 K, where our experiment data is 1.44 K. Based on those data, we conclude that the temperature resolution in the single measurement follows the value expected from the radiometer equation. However, a factor of 2 difference was observed for the multiple, time averaged case. For the latter case, as the QCL was operated in the free-running mode, the  $1/f$  noise in the amplitude of the QCL could attribute to the discrepancy between the measured results and the value from the radiometer equation. This effect may relate to the issue of the Allan variance time of the whole receiver system [14]. Since we are doing spectroscopic measurements, so the relevant Allan variance time is a spectroscopic Allan time, which should be much longer than, e.g. 3 sec. However, we do not know the upper limit of the Allan time in our case. To get such information this merits in-depth studies in the future work. The worse temperature resolution for the spectrum below 500 MHz is mainly due to higher noise contribution from the cryogenic amplifier, which is beyond its operating frequency range.

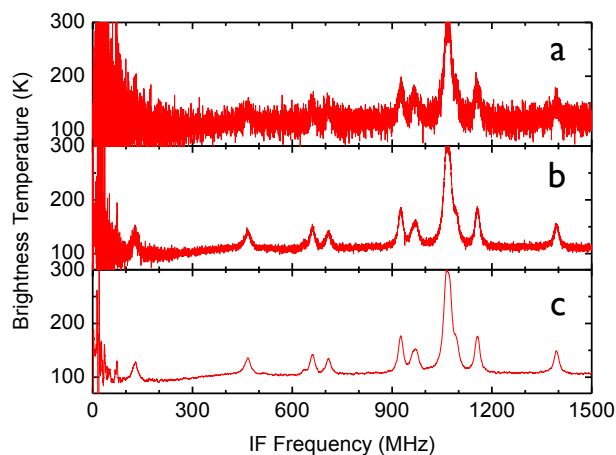


Fig. 3. High resolution methanol ( $\text{CH}_3\text{OH}$ ) emission spectrum measured within the IF frequency range between 0-1.5 GHz. (a) the original spectrum, with 3 seconds integration time for 3 spectrum traces; (b) the time averaged spectrum, where 18 series of the  $P_{\text{gas,cold}}(f)$  spectrum and 21 series of the  $P_{\text{emp,cold}}(f)$  spectrum were averaged; (c) the time and frequency averaged spectrum, the time averaged spectrum was smoothed to the 1.83-MHz resolution.

Also the frequency resolution is crucial for a heterodyne spectrometer. In the current experiment, with the free-running QCL as a LO the narrowest linewidth for the measured methanol spectral line is 11 MHz at a pressure of 0.43 mbar. We inferred that the linewidth of the QCL should be in order

of 1 MHz. The linewidth of this laser has been studied separately and is reported in Ref. 15. In the free-running mode it was found to be around 900 KHz. Together with a 183 KHz resolution FFTS, the frequency resolution of the heterodyne spectrometer increases to 1.1 MHz. This value agrees with that inferred from our experiment. We note that for astronomical observations at THz frequencies, atomic and molecular gases are at lower pressure and lower temperature, resulting in narrow spectral linewidths of  $\sim 1 \text{ MHz}$ . Obviously, to reduce the linewidth, phase or frequency locking of the QCL will be required. As shown in Ref. 15, the linewidth of the QCL is reduced to 17 KHz by locking to a molecular absorption line. This locked linewidth together with the FFTS we used enable a THz heterodyne spectrometer with a frequency resolution of 200 KHz ( $v/\Delta v > 10^7$ ). And the rich molecular absorption lines in combination with the frequency tunability facilitate the frequency locking scheme and hold the advantage for higher frequencies.

#### IV. CONCLUSION

In conclusion, by performing the spectroscopic experiment, we characterize the temperature and frequency resolution of a heterodyne spectrometer at 3.5 THz using a quantum cascade laser as a LO and a NbN HEB as a mixer. The receiver is capable of resolving a temperature change of 3.5 K for the effective brightness temperature of a molecular line and a frequency resolution of 1 MHz when the QCL is operated in the free-running mode. This frequency resolution can be improved to 200 KHz, limited by the back-end spectrometer, by locking the QCL to a molecular absorption line. The receiver is shown to be competent for astronomical and atmospheric applications.

#### REFERENCES

- [1] W. Zhang, P. Khosropanah, J.R. Gao, E. L. Kollberg, K. S. Yngvesson, T. Bansal, R. Barends, and T. M. Klapwijk, "Quantum noise in a terahertz hot electron bolometer mixer," *Applied Physics Letter* **96**, 111113 (2010),
- [2] B. S. Williams, "Terahertz quantum-cascade laser," *Nat. Photonics* **1**, 517 (2007).
- [3] J.R. Gao, J.N. Hovenier, Z.Q. Yang, J.J.A. Baselmans, A. Baryshev, M. Hajenius, T.M. Klapwijk, A.J.L. Adam, T.O. Klaassen, B.S. Williams, S. Kumar, Q.Hu, and J.L. Reno, "Terahertz heterodyne receiver based on a quantum cascade laser and a superconducting bolometer," *Appl. Phys. Lett.* **86**, 244104 (2005).
- [4] H.-W. Hübers, S. G. Pavlov, A. D. Semenov, R. Köhler, L. Mahler, A. Tredicucci, H. E. Beere, D. A. Ritchie, and E. H. Linfield, "Terahertz quantum cascade laser as local oscillator in a heterodyne receiver," *Opt. Express.* **13**, 5890 (2005).
- [5] P. Khosropanah, A. Baryshev, W. Zhang, W. Jellema, J. N. Hovenier, J. R. Gao, T. M. Klapwijk, D. G. Pavelev, B. S. Williams, S. Kumar, Q. Hu, J. L. Reno, B. Klein, and J. L. Hesler, "Phase locking of a 2.7 THz quantum cascade laser to a microwave reference," *Opt. Lett.* **34**, 2958 (2009)
- [6] D. Rabanus, U. U. Graf, M. Philipp, O. Ricken, J. Stutzki, B. Vowinkel, M. C. Wiedner, C. Walther, M. Fischer, and J. Faist, "Phase locking of a 1.5 Terahertz quantum cascade laser and use as a local oscillator in a heterodyne HEB receiver," *Opt. Express* **17**, 1159 (2009).
- [7] Y. Ren, J. N. Hovenier, R. Higgins, J. R. Gao, T. M. Klapwijk, S. C. Shi, A. Bell, B. Klein, B. S. Williams, S. Kumar, Q. Hu, and J. L. Reno, "Terahertz heterodyne spectrometer using a quantum cascade laser," *Appl. Phys. Lett.* **97**, 161105 (2010).

- [8] Y. Ren, J. N. Hovenier, R. Higgins, J. R. Gao, T. M. Klapwijk, S. C. Shi, B. Klein, T.-Y. Kao, Q. Hu, and J. L. Reno, "High-resolution heterodyne spectroscopy using a tunable quantum cascade laser around 3.5 THz," *Appl. Phys. Lett.* **98**, 231109 (2011).
- [9] S. Ryabchun, C.-Y. Tong, S. Paine, Y. Iobanov, R. Blundell, and G. Gol'tsman, "Temperature Resolution of an HEB receiver at 810 GHz," *IEEE Trans. Appl. Supercond.* **19**, 293 (2009).
- [10] M. I. Amanti, M. Fischer, G. Scalari, M. Beck, and J. Faist, "Low-divergence single-mode terahertz quantum cascade laser," *Nat. Photonics* **3**(10), 586–590 (2009).
- [11] M. I. Amanti, G. Scalari, F. Castellano, M. Beck, and J. Faist, "Low divergence Terahertz photonic-wire laser," *Optics Express*, **18**, 6390, (2010)
- [12] B. Klein, I. Krämer, S. Hochgürtel, R. Güsten, A. Bell, K. Meyer, and V. Chetk, "Fast Fourier Transform Spectrometer," *Proceedings of the 20th International Symposium on Space Tera-hertz Technology (ISSTT)*, Charlottesville, (2009).
- [13] H. B. Callen and T. A. Welton, "Irreversibility and Generalized Noise," *Phys. Rev.* **83**, 34 (1951)
- [14] J. W. Kooi, J. J. A. Baselmans, A. Baryshev, R. Schieder, M. Hajenius, J. R. Gao, T. M. Klapwijk, B. Voronov, and G. Gol'tsman, "Stability of heterodyne terahertz receivers", *J. Appl. Phys.* **100**, 064904 (2006)
- [15] Y. Ren, M. Cui, J.N. Hovenier, D.J. Hayton, J.R. Gao, T.M. Klapwijk, S.C. Shi, T.-Y. Kao, Q. Hu, and J. L. Reno, "Frequency locking of a 3.5 THz quantum cascade laser using a gas cell," *Proceedings of the 22th International Symposium on Space Tera-hertz Technology (ISSTT)*, Tucson, (2011).

## Antenna Coupled MKID test camera on APEX telescope: on sky performance

A.M. Baryshev<sup>1,4</sup>, J.J.A. Baselmans<sup>2</sup>, A. Endo<sup>3</sup>, S.J.C. Yates<sup>2</sup>, L. Ferrari<sup>1</sup>, R. Guesten<sup>5</sup>, S. Heyminck<sup>5</sup>, T. Klein<sup>5</sup>, B. Klein<sup>5</sup>, L. Esteras<sup>5</sup>, S. Hoohgurtel<sup>5</sup>, A. Weiss<sup>5</sup>, M. Schuller<sup>5</sup>, T.M. Klapwijk<sup>3</sup>

*1 SRON, Netherlands Institute for Space Research\*, Groningen, 9747 AD, The Netherlands*

*2 Kapteyn Astronomical institute, University of Groningen, Groningen, 9747 AD, The Netherlands*

*3 SRON, Netherlands Institute for Space Research\*, Utrecht, 3584 CA, The Netherlands*

*4 Kavli Institute of NanoScience, Delft University of Technology, Delft, 2628 CJ, The Netherlands*

*5 Max Planck Institute for Radioastronomy, Auf dem Hügel 69, 53121 Bonn, Germany*

\* Contact: a.m.baryshev@sron.nl, phone +31-50-363 8321

**Abstract**—Ateacma Pathfinder Experiment (APEX) telescope is located at 5100m altitude in Aacama desert in Chile. This is a 12m diameter telescope with submm quality surface located at one of the best submm sites on Earth. A large format submm direct detector camera with the goal to cover 15" field of view is being developed. It is based on Microwave Kinetic Inductance Detector (MKID) technology, especially suitable for large pixel count. In order to investigate performance of MKID technology in demanding telescope environment, a small test camera of 72pixels at 350 GHz atmospheric window has been built, and tested at the APEX telescope. Here we report, the camera construction, read out scheme, and results of lab tests and on the sky performance of first successful run. We will also discuss in detail an antenna coupled MKID design.

# The Kilopixel Array Pathfinder Project (KAPPa): A 16 pixel 660 GHz pathfinder instrument with an integrated heterodyne focal plane detector

C. Groppi, C. Wheeler, H. Mani, S. Weinreb, D. Russell, J. Kooi, A. Lichtenberger, C. Walker

**Abstract**—KAPPa (the Kilopixel Array Pathfinder Project) is an effort to develop key technologies to enable the construction of coherent heterodyne focal plane arrays in the terahertz frequency regime with  $\sim 1000$  pixels. The current state-of-the-art pixel count for coherent terahertz focal plane arrays is  $\sim 100$  pixels (the Supercam 350 GHz array with 64 pixels). The leap to  $\sim 1000$  pixels requires several key technological problems to be tackled before the construction of such a focal plane is possible. While the previous generation of arrays used 1D integration of mixer elements into a linear array module, kilopixel instruments will require 2D integration, as has been done with incoherent terahertz and infrared detectors. Over the next three years, the KAPPa project will develop a small (16-pixel) 2D integrated heterodyne focal plane array for the 660 GHz atmospheric window as a technological pathfinder towards future kilopixel heterodyne focal plane arrays in the terahertz frequency regime. KAPPa will use SIS devices fabricated on SOI membranes with beam lead alignment and connection features, designed for high yield and fast installation. A SiGe low noise amplifier with on-chip bias tee will be integrated directly into the mixer block immediately adjacent to each mixer. This amplifier has been designed to yield adequate gain and low noise temperature, while dissipating less than 2mW of power. The SIS and LNA devices will be mounted in a 2D integrated metal micromachined mixer

array consisting of a backshort block containing the SIS device and LNA, and a horn block using drilled smooth-wall feedhorns. Magnetic field will be delivered to the devices via compact, permanent magnets embedded in the horn block. We will also develop cryogenically compatible IF flex circuits to replace individual semi-rigid coaxial lines for IF signal transmission. Once completed, this instrument will demonstrate the critical technologies necessary to construct coherent arrays approaching 1000 pixels for large single-dish THz telescopes like CCAT and SPT.

## I. INTRODUCTION

THE THz spectral regime is one of the last frontiers in both remote sensing and detector development. At this confluence of infrared and radio techniques, two approaches are used to detect THz radiation. Direct detection techniques, similar to those used in the infrared, have been pushed to lower energies to detect THz photons. Photoconductors have been built for astrophysics applications that operate at wavelengths up to  $\sim 200$  microns (e.g. Herschel PACS [1], Spitzer MIPS [2]). For longer wavelength (THz) detection, cryogenic bolometer arrays have been developing at a rapid rate during the last decade. The UK SCUBA2 instrument, with 10,240 pixels at two THz colors (850 microns and 450 microns) is now being commissioned at the 15m James Clerk Maxwell Telescope [3]. This instrument will likely revolutionize astrophysics in the same way its predecessor SCUBA (with 37 pixels at 850 microns and 91 pixels at 450 microns) did a decade ago.

While direct-detection THz focal plane arrays are extremely valuable and have opened a new window on astrophysics, they do have fundamental limitations. Direct detectors do not preserve the relative phase information of arriving photons; therefore they deliver modest spectral resolution. Filters typically define  $\sim 10\%$  imaging bandwidths. Fabry-Perot and grating spectrometers can be constructed and placed in front of the incoherent arrays to disperse the incoming light, but offer modest spectral resolution ( $R < 1000$ - $10,000$ ) and cannot simultaneously spatially and spectrally multiplex. They are therefore primarily used to image thermal emission from dust in astronomical sources. For astronomical and atmospheric applications, there is considerable interest in the behavior of gas species. To disentangle their motions, instruments with high spectral resolutions are required ( $R > 10,000$ ). In

C. Groppi is with the School of Earth and Space Exploration, Arizona State University, Tempe, AZ 85287 USA (phone: 480-965-6436; fax: 480-965-8102; e-mail: [cgroppi@asu.edu](mailto:cgroppi@asu.edu)).

C. Wheeler is with the School of Earth and Space Exploration, Arizona State University, Tempe, AZ 85287 USA (e-mail: [caleb.wheeler@asu.edu](mailto:caleb.wheeler@asu.edu)).

H. Mani is with the School of Earth and Space Exploration, Arizona State University, Tempe, AZ 85287 USA (e-mail: [hamdi.mani@asu.edu](mailto:hamdi.mani@asu.edu)).

S. Weinreb is with the Department of Electrical Engineering, California Institute of Technology, Pasadena, CA 91125 USA (e-mail: [sweinreb@caltech.edu](mailto:sweinreb@caltech.edu)).

D. Russell is with the Department of Electrical Engineering, California Institute of Technology, Pasadena, CA 91125 USA (e-mail: [drussell@caltech.edu](mailto:drussell@caltech.edu)).

J. Kooi is with the Caltech Submillimeter Observatory, California Institute of Technology, Pasadena, CA 91125 USA (e-mail: [kooi@phobos.caltech.edu](mailto:kooi@phobos.caltech.edu)).

A. Lichtenberger is with the department of Electrical and Computer Engineering, University of Virginia, Charlottesville, VA 22904 USA (e-mail: [arthurw@virginia.edu](mailto:arthurw@virginia.edu)).

C. Walker is with the Steward Observatory, University of Arizona, Tucson, AZ 85721 USA (e-mail: [cwalker@as.arizona.edu](mailto:cwalker@as.arizona.edu)).

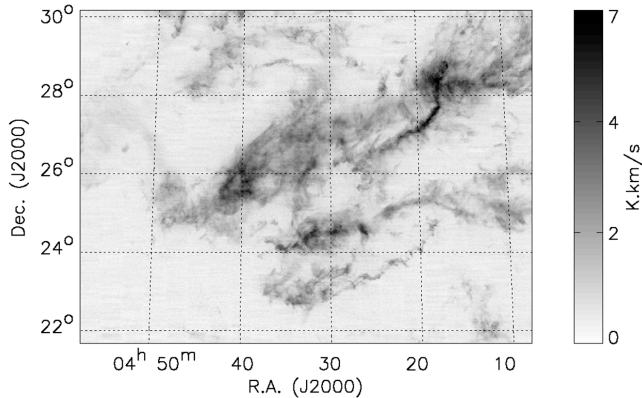


Fig. 1. An integrated intensity image of the Taurus molecular cloud complex covering over 120 square degrees on the sky in the light of the  $^{13}\text{CO}(1-0)$  transition made with the SEQUOIA 32 pixel coherent array [4], [5].

molecular clouds, this gas makes up  $\sim 99\%$  of the material by mass, and is the dominant player in the physics of star and planet formation. Kinematic information extracted from spectra collected using coherent techniques allows the detailed study of gas dynamics, in addition to the chemical information collected from the detection of a particular gas species. Various gas species have emission lines in the terahertz waveband that offer a huge wealth of information. They can be used to determine gas properties of the interstellar medium (ISM), such as mass, kinematics, temperature, density, and chemical composition. Large scale surveys of these lines both in the Milky Way and beyond can be used to help answer long standing questions in astrophysics, such as star formation, the life cycle of the ISM, and the chemical evolution of galaxies. As shown in figure 1, ISM structures like giant molecular clouds can subtend hundreds of square degrees on the sky, and have enormous spatial dynamic ranges spanning cloud size structures down to individual protostellar objects. Imaging these clouds requires focal plane arrays of coherent detectors on large telescopes to achieve the required spatial dynamic range while observing molecular gas line emission with sufficient spectral resolution. In astrophysics and remote sensing applications, the speed of imaging a given area of sky is directly proportional to the number of detectors. An increase of a factor of  $\sim 1000$  in observing efficiency provided by a kilopixel array receiver would revolutionize observational sub-mm/THz astronomy, opening up widefield imaging and dramatically increasing the scientific return of future facilities like CCAT and SPT. Other fields of astronomy went through a similar revolution some time ago. For example, infrared astronomy has graduated from single-pixel technology to arrays consisting of tens of thousands of detectors. The current state-of-the-art pixel count for coherent THz arrays is 64 pixels (i.e. SuperCam) or less. While these instruments are a great leap forward from single pixel detectors, the pixel count is still inadequate for wide field THz imaging of weak spectral lines.

The KAPPA project is developing and testing several solutions to outstanding challenges that must be met if  $\sim 1000$  pixel THz heterodyne arrays are to be realized. The cost and complexity

of such an instrument demand a systematic approach to the solution of these technical challenges before attempting to construct a fully featured science instrument. We are constructing a compact pathfinder instrument with a 16-pixel 2D integrated focal plane at 660 GHz as a vehicle to test technical solutions. These solutions can then be applied to the design and construction of a kilopixel class array receiver. The completed instrument will build on the technology developed for the Supercam project. The instrument will be verified in the laboratory and on the 10m Heinrich Hertz Submillimeter Telescope, making use of existing Supercam [8] infrastructure.

## II. EVOLUTION OF COHERENT THz FOCAL PLANE ARRAYS



Fig. 2. The PoleStar 4-pixel heterodyne array for the 850 GHz band. The mechanical and electrical complexity of modular components limits pixel number.

### A. 0D integrated arrays

Over the course of the past decade, several research groups around the world have constructed heterodyne arrays for astrophysics applications. The majority of these instruments have been constructed by stacking individual mixers in the focal plane (e.g. PoleStar, [9], DesertStar, [10], HARP-B [11], CHAMP+, [12]). While offering dramatically increased imaging speed over single pixel instruments, the mechanical and electrical complexity of this modular architecture has limited arrays to 16 pixels or less. An example of the mechanical and electrical complexity of such instruments is shown in fig. 2. The PoleStar instrument shown here contains only 4 single ended SIS mixers for the 850 GHz band, with associated cryogenic low noise amplifiers and bias electronics. The mechanical and electrical complexity of the system was due largely to the use of discrete cryogenic DC wiring, semi-rigid coaxial cable for intermediate frequency (IF) transmission, and discrete IF amplifiers. In particular, reliability was compromised by the large number of

connectors that required mating and de-mating during construction and maintenance.

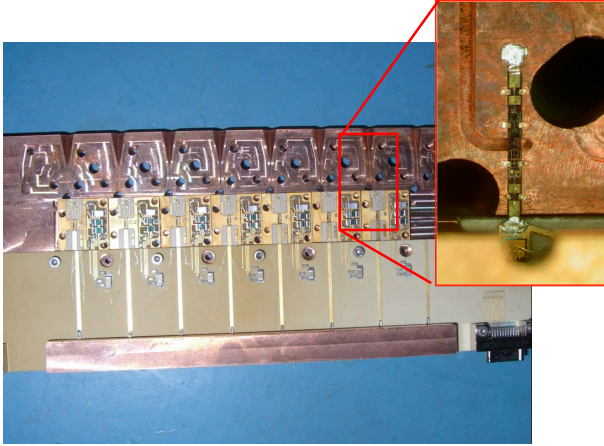


Fig. 3. The Supercam focal plane module with close-up of SIS mixer.

### B. 1D Integrated Arrays

Supercam is a 64 pixel heterodyne array receiver designed to perform observations at 350 GHz. Supercam functionally consists of 3 major parts; 1) a receiver frontend, consisting of optics, mixer arrays and a local oscillator that downconverts the 64 incoming 350 GHz signals from the telescope to microwave frequencies and then amplifies them, 2) an IF processor that further amplifies the microwave signals and downconverts them to baseband (0.1 – 1 GHz), and 3) a digital spectrometer that produces a power spectrum of each of the downconverted microwave signals.

At the heart of the Supercam frontend are eight, 1x8 linear mixer modules cooled to 4K in a closed-cycled cryostat. Each split-block waveguide mixer module integrates eight single-

ended SIS mixers with eight MMIC-based low-noise intermediate frequency IF amplifiers. The mixer module also contains the associated DC and IF wiring and connectors. Blind mate IF and DC connectors allow the mixer modules to be inserted into and removed from the focal plane without disturbing any cryogenic wiring.

The module, shown in fig. 3, combines many advanced features to maximize performance and reliability. The waveguide module was built to micron level tolerances using an in-house micromilling machine. The SIS devices are fabricated on 3-micron thick SOI membranes, with gold beam lead IF and ground contacts. Eight small beam leads on the chip sides self-align the chip into pockets machined in the waveguide block to a tolerance of  $\pm 3$  microns. A single chip can be mounted and bonded directly to the input matching network of the low noise amplifier in  $\sim 15$  minutes. The SIS chips have high enough yield and uniformity that cold testing of devices is not needed before mounting. Devices are pre-selected based on their room temperature resistance and are then mounted and cold tested in the focal plane modules. Chips that are found to fail cold testing can be replaced without disturbing neighboring pixels. Each of the low-noise IF amplifier modules contain a MMIC LNA, LNA/SIS bias network, and input and output matching networks. The IF amplifier module package size is 11mm x 11mm. Each module offers  $\sim 5$ K noise temperature and 30 dB of gain from 2-9 GHz while dissipating only 8 mW of heat. The high performance of these IF amplifier modules together with their low dissipated power is a key development for heterodyne focal plane arrays. An IF amplifier module and test results are shown in fig. 4.

While considerable effort was invested in the design of the IF amplifier modules and electromagnets (needed to suppress the shot noise resulting from Josephson tunneling in the SIS devices) to lower the power dissipation per pixel, the

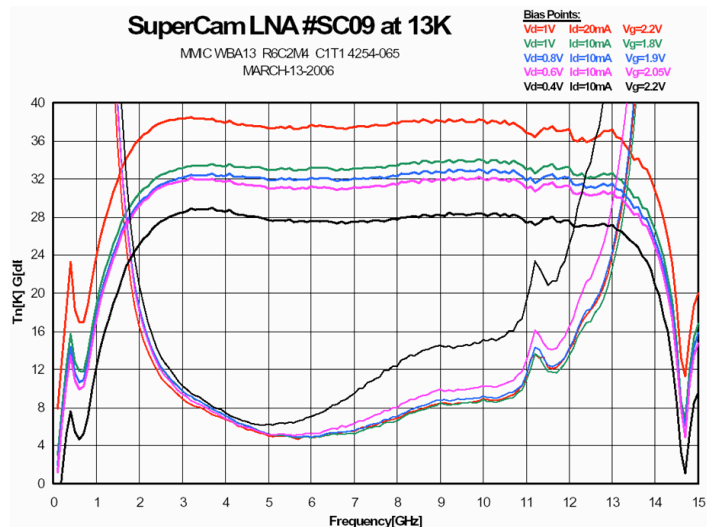
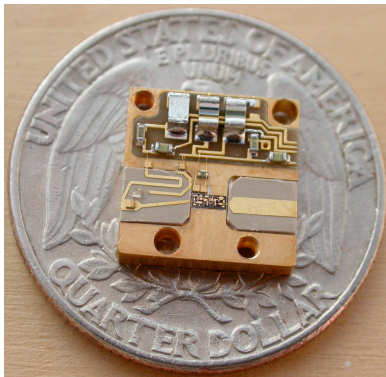


Fig. 4. The Supercam Low Noise Amplifier (LNA) module (left) and test results for 20 mW, 10 mW, 8 mW, 6 mW and 4 mW dissipated power. Noise remains excellent while gain decreases only modestly down to 8 mW power dissipation.

Supercam focal plane still produces over 0.5W of heat at 4K. A commercially available Sumitomo cryocooler with 1.5W capacity at 4.2K is used to cool the focal plane unit. A supplementary CTI cryocooler is employed to cool the 64 IF output cables from the array. This secondary cryocooler permitted standard stainless steel semi-rigid microwave cable to be used for this purpose. The first stages of both coolers are tied to a radiation shield kept at 40K.

LO multiplexing and diplexing is accomplished with a hybrid waveguide/quasi-optical approach. An array of corporate power dividers [13] is employed to split the power from a single Virginia Diodes 350 GHz source 8 ways, feeding splitblock machinable waveguide twists [14]. Additional arrays of corporate power dividers split each of the waveguide twist outputs eight more times before an array of diagonal feedhorns projects the LO beams. A pair of HDPE lenses reimages the array of LO feedhorns to the focal plane of the detectors, using a simple Mylar diplexer for LO injection. The LO power divider has been measured to have ~2 dB loss over an ideal divider. LOs of modest power (<2 mW) are capable of pumping the focal plane array optimally with a 25 micron Mylar diplexer.

### III. CHALLENGES FOR KILOPIXEL ARRAY DEVELOPMENT

During the design phase for Supercam, it became apparent that the expansion of the 0D paradigm of stacking independent mixers in the focal plane would become overwhelmingly complicated and unreliable for ~100 pixel arrays. Similarly, experience with Supercam has shown that the 1D integration of Supercam will also become unwieldy at pixel counts approaching ~1000. We have identified several key areas where technological development is essential to the construction of larger format arrays. These areas and their potential solutions are listed below.

- **Mechanical and Electrical Complexity:** Larger splitblock based 1D integrated arrays will become too unwieldy to fabricate. Separate interconnect sets are still needed for each linear array.

Solution: Use 2D integration.

- **Integration of Detectors with Mixer Module:** 2D integration requires a new method for device mounting as compared to 1D splitblock designs.

Solution: Utilize a vertically stacked 2D metal micromachined mixer architecture.

- **Economical and fast fabrication techniques for waveguide and feeds:** CNC micromachining techniques can make large amounts of waveguide accurately, quickly and economically. Feeds remain difficult to manufacture, especially in large numbers.

Solution: Use a custom tool to directly drill efficient feedhorns in metal.

- **RF and DC interconnects, wire count, and complexity:** At pixel counts of ~1000, individual coaxial transmission lines for each IF signal become overwhelmingly complex and creates an untenable cryogenic heat transfer situation.

Solution: Multi-conductor DC cabling with adequate wire count already exists. Multi-conductor RF ribbon cable and connectors with integral heat sinking should be implemented.

- **LO power availability, multiplexing and injection:** Kilopixel SIS arrays will require power-combining solid-state multiplier based sources to produce enough LO power.

Solution: Several techniques exist for multiplexing LO power and efficiently injecting that power (e.g. phase gratings, Si Etalons)

- **Magnetic field for SIS devices:** ~1000 individually controllable electromagnets are unwieldy and too complicated.

Solution: Use carefully engineered high field permanent magnets instead.

### IV. KAPPA DEMONSTRATION FPU

The KAPPA FPU will be a 16 pixel 2D integrated heterodyne focal plane with integrated SiGe low noise amplifiers (fig. 5). We have chosen the 16-pixel form factor as a reasonable compromise between pixel count (including non-edge pixels) and complexity. The integer multiple of 8 pixels will allow the reuse of Supercam support electronics (bias, IF and spectrometer). Work on the project so far has concentrated on the design and fabrication of components for each pixel cell of the focal plane array. We are reaching completion of the discrete SIS device, and have begun fabrication of test chips to investigate handling and mounting issues. The ultra low power dissipation low noise amplifier chip has been designed, fabricated and tested.

#### A. Focal Plane Architecture

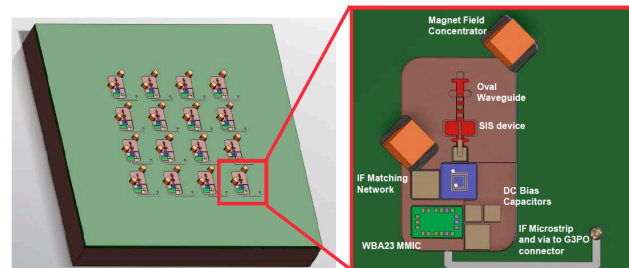


Fig 5. The strawman focal plane array architecture planned for this work. This figure shows the 4x4 detector array at left, with an inset of the detector cell at right.

We have chosen to use discrete SIS detector chips for KAPPA. This extracts the maximum from existing wafer yield, and uses the wafer area most efficiently during fabrication. Experience with Supercam has shown that beamlead based pixels can be assembled in as little as 15 minutes, making assembly of even 1000 discrete detector pixels feasible. Initial focal plane designs, plus the desire to remain compatible with

the Supercam optical system on the HHT, have resulted in the selection of a 6 mm pixel pitch for our prototype array. Since our SIS devices are fabricated on 50mm wafers, the area required for a 4x4 array is very large (almost an entire wafer). This could result in very poor detector array yield and poor uniformity over the large wafer area. Discrete detectors will allow close packing, with hundreds of devices per wafer. With this large number of available devices, variations across the wafer will have a smaller impact on usable chip yield.

The all-metal machined mixer block uses a skeleton printed circuit board to route IF and DC lines. The KAPPA FPU design integrates the SIS device, low noise amplifier MMIC (both discussed below in detail) and associated lumped element components in a pedestal machined into a copper block. A Rogers TMM based printed circuit board with cutouts for the pedestals will carry DC bias lines from edge connectors to each pixel. A microstrip line carries the amplified IF signal to a via, which transfers the IF to a surface mount Corning-Gilbert G3PO blind mate connector on the back side of the PC board. These connectors protrude through holes in the copper block, and mate with an additional PC board made of the same TMM material, also with surface mount G3PO connectors. This arrangement transfers the IF to a different plane to allow easy routing of the IF lines from all pixels without the need to avoid other pixel pedestals or DC traces. These boards will also contain the connectors for attaching to the flex circuits that will be used to route IF and DC signals out of the cryostat.

We will investigate spring contact interposer connectors for both DC and IF flex circuits, but will use direct wirebonding if the interposers do not work as planned. Rather than develop some sort of interconnect at the vacuum wall of the dewar, we will pot the flex circuits directly in epoxy, running them unbroken through the dewar wall. We plan to use a stripline architecture for the flex circuits to avoid interaction with the epoxy potting.

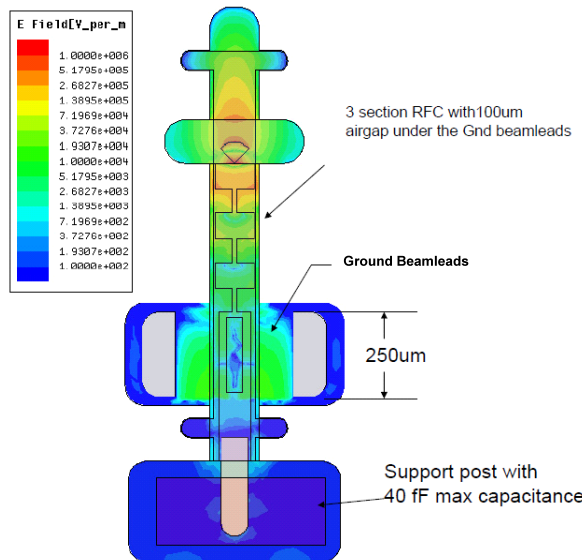


Fig. 6: The SIS device design showing a HFSS simulation of the RF E-field. The choke structure effectively prevents RF leakage.

## B. SIS device

For this project, we have chosen to follow the heritage gained from the Supercam in designing the discrete SIS device. Our experience from Supercam has shown that SIS devices fabricated on SOI membrane are robust and easy to mount. We have refined the Supercam design for this work to improve the ease of mounting and handling while still maintaining optimal performance. We have chosen to baseline a relatively simple single junction design using a traditional AlOx barrier. This will maximize chip yield with the relatively high  $R_n$  required to match to the integrated low noise amplifier discussed below. An AlN barrier would provide wider RF bandwidth, but would require very small junction areas for an  $R_n \sim 30$  as desired. This could reduce chip yield to unacceptable levels. In addition, AlOx barriers provide sufficient bandwidth to cover the 450 micron atmospheric window. Additional bandwidth is not required. The chip will be fabricated on 5 micron thick SOI membrane. EM simulations have shown that this is the thickest SOI permissible without degradation of performance. The SOI membrane will be patterned to provide mechanical alignment tabs for chip mounting. In the Supercam device, we used beam leads for this purpose, but we believe using the silicon itself will result in more robust devices. Beam lead tabs with rounded corners will be used for ground and IF contacts. As with Supercam, the device will use a radial stub waveguide probe with a multi-section RF choke. Unlike Supercam, the IF and ground are on the same side of the probe, eliminating the need for a meandering high impedance line to serve as a ground return path. This meandering line causes resonances that limit the RF bandwidth. These are tolerable for the lower frequency Supercam devices, but not for this work. The IF will be brought out on thin film microstrip fabricated on top of the RF choke structure that serves as the ground plane. This does result in increased potential for reduced chip yield, but does not require any additional layers in the fabrication.

## C. Low Noise Amplifier

KAPPA will integrate a MMIC low noise amplifier directly into the mixer FPU. The amplifier is based on Silicon Germanium (SiGe) technology, and has been designed for ultra-low DC power dissipation. An integral, on chip bias tee used to inject DC bias without a bulky circuit based on discrete components. This amplifier was designed to provide 16 dB of gain and  $\sim 7K$  noise temperature from 0.5-4.5 GHz while consuming only 2 mW of DC power. The devices have been fabricated as part of a wafer run at ST Microelectronics. The first run of devices works as expected; with the exception of somewhat elevated noise at 4K (12K rather than  $\sim 7K$ ). We expect the next generation of chips (now in fabrication) to reduce the noise to the design value.

A simple matching network consisting of a surface mount chip inductor in series with the detector matches the LNA to the SIS device. This results in performance that is not sensitive to SIS device normal resistance from 50-200 ohms. Future generations of this chip can be fabricated to include the matching inductor. This route allows the maximum flexibility to use the chip in the largest number of applications.



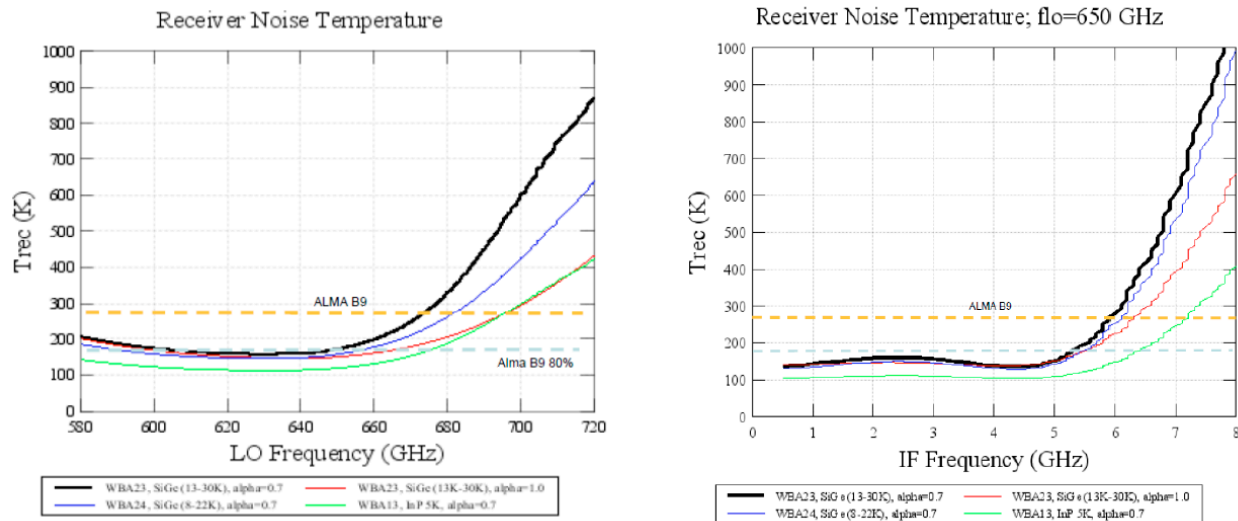


Fig 7. Simulated RF performance of the mixer versus LO frequency (left) and IF frequency, with a LO frequency of 650 GHz (right). The 4 curves show performance for two amplifier designs (the WBA23 is the KAPPA device) and with two LO pumping levels. Alpha=1.0 is optimal pumping, alpha=0.7 is 70% of optimal pumping. The design meets ALMA Band 9 specifications for most of the band using the WBA23 LNA with optimal SIS device pumping.

#### D. Simulated Performance.

We have built a comprehensive performance model of the KAPPA pixel, including estimates for optics loss, SIS device performance, matching network and low noise amplifier. We have assumed a 3% loss at room temperature for the LO diplexer and window, and another 3% loss for IR filtering. We are currently using the measured noise performance of the existing LNAs (12K) in our models. Results are presented in fig. 7. We find that the KAPPA mixer is predicted to meet or exceed ALMA Band 9 noise specifications from below 600 GHz to 695 GHz. The rapid rise at the high end of the band is due to loss in the niobium transmission lines as the RF exceeds the gap frequency of the material. IF performance is predicted to be approximately flat between 0.5 GHz and ~5 GHz. This 4.5 GHz IF bandwidth is more than adequate for almost all wide field imaging science applications (even for extragalactic sources).

#### V. FUTURE WORK

Now that the design and fabrication of the SIS device and LNA are well underway, and a viable design for the focal plane has been designed, we will next concentrate on the design and fabrication of a single pixel test mixer that will allow us to analyze and refine the design for the pixel cell. This single pixel mixer will also be used as a testbed to develop the permanent magnet used to replace tunable electromagnets. The single pixel mixer will allow the use of the well-characterized electromagnet from the Supercam project, and a permanent magnet assembly that has been engineered to deliver the same field as the electromagnet under optimum performance. Our simulations show that commercially available 1.5mm diameter, 1.5mm long cylindrical electromagnets, combined with a simple iron concentrator, can deliver similar fields to the Supercam electromagnet with 20 mA of current in 4500 turns of wire.

#### VI. CONCLUSION

The Kilopixel Array Pathfinder Project (KAPPA) is a project to construct a 16-pixel 2D integrated coherent focal plane unit as a demonstration of necessary technologies needed for the construction of kilopixel class arrays for large terahertz telescopes. The design of KAPPA builds on experience gained building the Supercam 64 beam array, which uses 1D integrated linear detector array modules. The KAPPA focal plane will use beam lead on SOI SIS devices, integrated SiGe MMIC low noise amplifier chips with on-chip bias tees, drilled smooth walled feedhorns, permanent magnets and IF flex circuit cables to solve many of the challenges presented in building very large coherent arrays. We will build and test a single pixel demonstration mixer to verify the performance of the mixer cell before constructing the 16-pixel array. We will then incorporate the lessons learned from this test into the design of the FPU.

#### ACKNOWLEDGMENT

This material is based upon work supported by the National Science Foundation under Grant No. AST-1006148.

#### REFERENCES

- [1] Poglitsch et al. "Herschel Photodetector Array Camera and Spectrometer, Proc. SPIE, 7010, 4, 2008.
- [2] Rieke, G., et al., "The Multiband Imaging Photometer for Spitzer", *ApJSS*, 154, 25, 2004.
- [3] Audley et al. "An update on the SCUBA-2 project", *Proc. SPIE*, 5498, 63, 2004.
- [4] P.F. Goldsmith, M. Heyer, G. Narayanan, R. Snell, D. Li, C. Brunt, "Large-Scale Structure of the Molecular Gas in Taurus Revealed by High Linear Dynamic Range Spectral Line Mapping", *Astrophysical Journal*, vol. 680, 2008, pp. 428-445.
- [5] G. Narayanan, M.H. Heyer, C. Brunt, P.F. Goldsmith, R. Snell, D. Li, "The Five College Radio Astronomy Observatory CO Mapping Survey of the Taurus Molecular Cloud", *Astrophysical Journal Supplement Series*, vol. 177, 2008, pp. 341-361.
- [6] Goldsmith, Paul F., Carpenter, John, Erickson, Neal, Fisher, Rick, Ford, John, Gaier, Todd, Groppi, Chris, Harris, Andy, Heyer, Mark, Kulesa,

- Craig, Lawrence, Charles, Morgan, Matt, Mundy, Lee, Narayanan, Gopal, O'Neil, Karen, Readhead, Tony, Samoska, Lorene, Schloerb Peter, Snell, Ron, Walker, Christopher, Ziurys, Lucy, Coherent Detecto Arrays for Millimeter and Submillimeter Astronomy, Astro2010: Th Astronomy and Astrophysics Decadal Survey, Technology Development Papers, no. 11, 2009
- [7] Kerr, A. R., Barker, Scott, Bryerton. Eric, Crowe, Tom, Erikson, Neal, Fisher, Rick, Goldsmith, Paul, Gottlieb, Carl, Groppi, Chris, Hesler, Jeffrey, Hunter, Todd, Kerr, Tony, Lichtenberger, Arthur, Narayanan, Gopal, Padin, Steve, Pan, S.-K., Russell, Adrian, Srikanth, S., Thaddeus, Pat, Walker, Chris, Webber, John, Weikle, Bobby, Wootten, Al, Ziurys, Lucy, Zmuidzinas, Jonas, In Support of Instrument Technology Development for THz Astronomy, Astro2010: The Astronomy and Astrophysics Decadal Survey, Technology Development Papers, no. 29, 2009.
- [8] Groppi, C.E., Walker, C., Kulesa, C., Golish, D., Kloosterman, J., Weinreb, S., Jones, G., Barden, J., Mani, H., Kuiper, T., Kooi, J., Lichtenberger, A., Cecil, T., Puetz, P., Narayanan, G., Hedden, H., Testing and Integration of Supercam, a 64-Pixel Array Receive for the 350 GHz Atmospheric Window, Millimeter and Submillimeter Detectors and Instrumentation for Astronomy V, Edited by Duncan, William, Holland, Wayne, Withingtonm Stafford, Zmuidzinas, Jonas, Proc. SPIE 7741, 774110X, pp. 1-11, 2010.
- [9] Walker, C. K., Groppi, C., d'Aubigny, C., Kulesa, C., Hungerford, A., Jacobs, K., Graf, U., Schieder, R., & Martin, C., 2001, "PoleSTAR: A 4-Pixel 810 GHz Array Receiver for AST/RO", Proceedings of the 12th International Symposium on Space Terahertz Technology, San Diego, CA, Eds. Mehdi & McGrath, JPL.
- [10] Groppi, C.E., Walker, C.K., Kulesa, C., Golish, D., Hedden, A., Narayanan, G., Lichtenberger, A.W., Kooi, J.W., Graf, U.U., Heyminck, S. "First results from DesertSTAR: a 7-pixel 345-GHz heterodyne array receiver for the Heinrich Hertz Telescope", Proc. SPIE, 5498, 290, 2004.
- [11] Smith, H. et al., "HARP-B: a 350-GHz 16-element focal plane array for the James Clerk Maxwell telescope", Proc. SPIE, 4855, 338, 2003.
- [12] Guesten, R. et al. "Submillimeter heterodyne arrays for APEX", Proc. SPIE 7020, 10, 2008.
- [13] Kerr, A. "Elements for E-Plane Splitblock Waveguide Circuits", ALMA Memo, 381, 2001.
- [14] Ward, J & Chattopadhyay, G, "A 220-320 GHz 90° Polarization Twist for Integrated Waveguide Circuits", MWCL, submitted, 2008.

# The Stratospheric THz Observatory (STO): Preparations for Science Flight

C. Walker<sup>1</sup>, C. Kulesa<sup>1</sup>, J. Kloosterman<sup>1</sup>, T. Cottam<sup>1</sup>, C. Groppi<sup>2</sup>, P. Bernasconi<sup>3</sup>, H. Eaton<sup>3</sup>, N. Rolander<sup>3</sup>, B. Carkhuff<sup>3</sup>, S. Hechtman<sup>3</sup>, J. Gottlieb<sup>3</sup>, D. Neufeld<sup>3</sup>, C. Lisse<sup>3</sup>, A. Stark<sup>4</sup>, D. Hollenbach<sup>5</sup>, J. Kawamura<sup>6</sup>, P. Goldsmith<sup>6</sup>, W. Langer<sup>6</sup>, H. Yorke<sup>6</sup>, J. Sterne<sup>6</sup>, A. Skalare<sup>6</sup>, I. Mehdi<sup>6</sup>, S. Weinreb<sup>7</sup>, J. Kooi<sup>7</sup>, J. Stutzski<sup>8</sup>, U. Graf<sup>8</sup>, C. Honingh<sup>8</sup>, P. Puetz<sup>8</sup>, C. Martin<sup>9</sup>, D. Lesser<sup>9</sup>, Mark Wolfire<sup>10</sup>

<sup>1</sup>Steward Observatory, University of Arizona, Tucson, AZ 85721 USA

<sup>2</sup>School of Earth and Space Exploration, Arizona State University, Tempe, AZ 85287 USA

<sup>3</sup>Johns Hopkins Applied Physics Laboratory, Laurel, MD 20723 USA

<sup>4</sup>Smithsonian Astrophysical Observatory, Cambridge, MA 02138 USA

<sup>5</sup>SETI Institute, Mountain View, CA 94043 USA.

<sup>6</sup>Jet Propulsion Laboratory, Pasadena, CA 91109 USA

<sup>7</sup>California Institute of Technology, Pasadena, CA 91125 USA

<sup>8</sup>University of Cologne, Cologne, D-50937 Germany

<sup>9</sup>Oberlin College, Oberlin, OH 44074 USA.

<sup>10</sup>University of Maryland, College Park, MD 20740 USA

\*Contact: [cwalker@as.arizona.edu](mailto:cwalker@as.arizona.edu), +01-520-621-8783

**Abstract**— The Stratospheric TeraHertz Observatory (STO) is a NASA funded, Long Duration Balloon (LDB) experiment designed to address a key problem in modern astrophysics: understanding the Life Cycle of the Interstellar Medium (ISM). STO will survey a section of the Galactic plane in the dominant interstellar cooling line [C II] (1.9 THz) and the important star formation tracer [N II] (1.46 THz) at ~1 arc minute angular resolution, sufficient to spatially resolve atomic, ionic and molecular clouds at 10 kpc. The science flight instrument package hosts four [CII] and four [NII] HEB receivers. There is also one 492 GHz Schottky receiver for observing the [CI] line. In this paper we discuss preparations for the scheduled Antarctic science flight in December 2011.

## I. INTRODUCTION

STO is a Long Duration Balloon (LDB) experiment designed to address a key problem in modern astrophysics: understanding the Life Cycle of the Interstellar Medium (ISM). During its upcoming science flight STO will survey a section of the Galactic plane in the dominant interstellar cooling line [C II] (1.9 THz), the important star formation tracer [N II] (1.46 THz) and the column density tracer [CI] (0.49 THz) at arcminute angular resolution. On Oct. 15, 2009 STO had its test flight from Ft. Sumner, NM. During its 12 hours at float altitude (~126,000 ft) key components of STO were tested to help ensure the system would meet the objectives of the upcoming ~28 day science flight. STO is the first balloon payload to fly a cryogenic, THz heterodyne receiver system. The science flight will serve as a pathfinder for future 100 day, ultra-long duration (ULDB) NASA missions (e.g. GUSSTO).

## 2. SCIENCE FLIGHT INSTRUMENT

STO itself has three main components; 1) an 80 cm optical telescope, 2) a THz instrument package, and 3) a gondola [1]

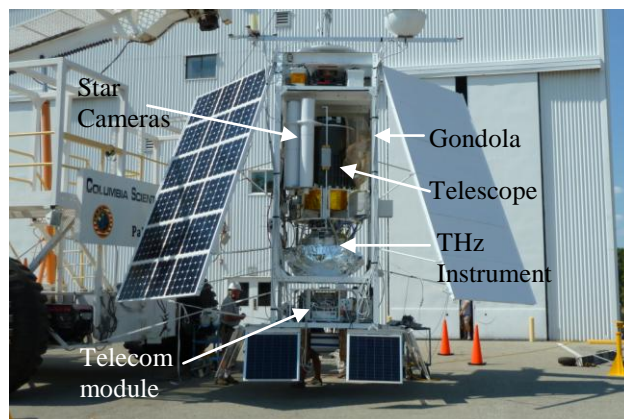


**Figure 1:** STO during its August 15, 2011 hang test in Palestine, TX.

(see Figure 1). Both the telescope and gondola have flown on previous experiments [2,3]. They have been re-optimized for the current mission to include a 3-axis inertial guidance system and wide and narrow field star cameras. Additional solar panels were also added to provide ~1kW of payload power. During the test flight the telescope was able to point and track well within its 15'' design specifications. Figure 1 shows STO in its flight configuration.

STO is scheduled to have its first LDB science flight from McMurdo, Antarctica in December 2011. To achieve the goals of the science flight STO is designed to host two 4-pixel arrays of heterodyne receivers operating at 1.9 THz and 1.46 THz, as well as a room temperature 492 GHz Schottky diode receiver. Niobium superconducting hot electron mixers (similar to those used on *Herschel* – HiFi) provide state-of-the-art noise performance at THz frequencies. These mixers

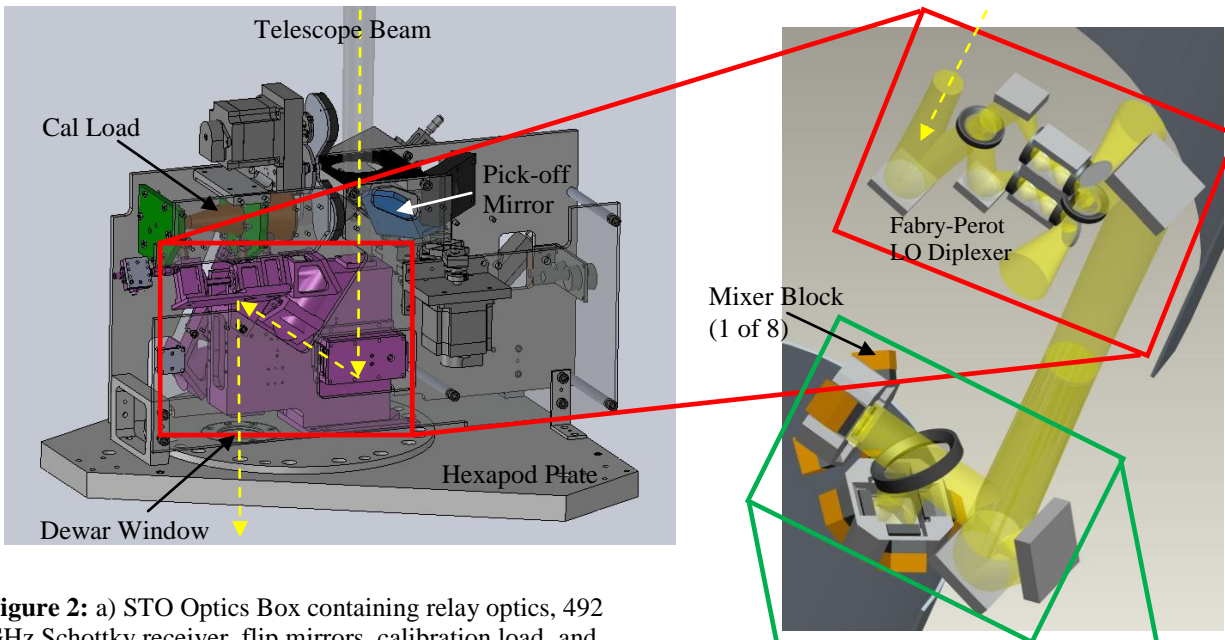


**Figure 2:** a) STO Optics Box containing relay optics, 492 GHz Schottky receiver, flip mirrors, calibration load, and Fabry-Perot ring diplexer. b) Optical assembly of Fabry-Perot

operate just below the transition temperature of niobium at 9K. Therefore, a key component of STO is a cryogenic system designed to maintain the mixers at their operating temperature during flight. For the science flight, a 90 liter liquid helium dewar with a hold time of ~14 days will be used for this purpose.

Between the telescope and the dewar is an Optics Box (see Figure 2a) containing flip mirrors for directing the  $f/17.5$  telescope beam to either a Schottky receiver, calibration load, or Fabry-Perot ring diplexer designed to inject the local oscillator (LO) signal into the telescope beam (see Figure 2b). The Optics Box is mounted to a hexapod plate. The LO beams originate from two solid-state sources (not-shown; one at 1.9 and the other at 1.46 THz) whose output are divided into 4 equal power beams by a Fourier grating. From the diplexer, the combined telescope+LO beams enter the dewar through a 130 mm diameter window and continue to a wire grid located on the 4K cold plate. The grid splits the beams into horizontal and vertical polarizations. The horizontal polarized components proceed to the 1.9 THz mixer array and the vertical components to the 1.46 THz mixer array. Off-axis mirrors convert the telescope beam to match that expected by each mixer's feedhorn. As shown in the figure, each 2x2 mixer array is formed by bolting individual mixers to a common ring. The hot electron bolometer (HEB) mixers for the [NII] arrays are being provided by JPL and the HEB mixers for the [CII] arrays by the University of Cologne. Waveguide technology is being used by both groups to meet the instrument noise and optical coupling requirements. Laboratory measurements indicate the receiver noise temperatures are  $\leq 1500\text{K DSB}$ .

The mixers and cold optics are mounted in a dewar insert (Figure 3). The top of the insert bolts directly to the bottom of the room temperature Fabry-Perot diplexer and forms the

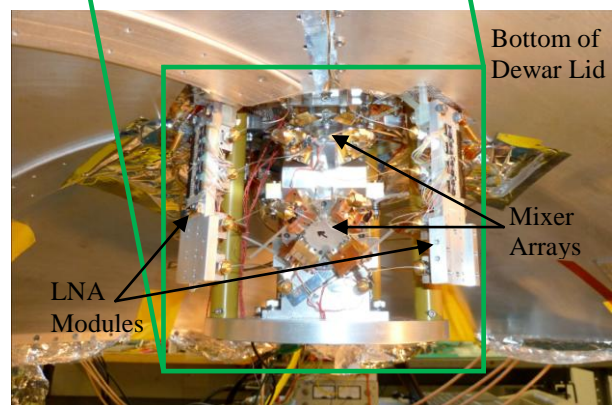


**Figure 3:** STO dewar insert. The telescope beam coming from above is split into orthogonal polarizations by a wire grid and directed into two, 4 pixel mixer arrays. The mixer mounts and cold plate are made from high purity aluminium and thermally strapped to the helium tank (not shown) with flexible S-links.

vacuum seal to the underlying dewar lid. The combined signal+LO beam enters the top of the insert through a resonant, polyethylene vacuum window. Optical alignment between cold and warm optics is maintained by a system of low thermal conductivity, Torlon tubes.

The IF signal for STO has a bandwidth of 1 GHz and is centered at 1.5 GHz, appropriate for low noise operation of our HEBs. The IF output of each mixer is conveyed through 4 cm long, 0.035" diameter coaxial cable to low-noise (~7K), low-power (~5mW) SiGe amplifiers operating at a physical temperature of ~17K. These amplifiers (see Figure 3) were designed and fabricated by Co-I Weinreb at Caltech specifically for STO. After being amplified ~30 dB, the IF signals are brought out of the dewar via coaxial cable to the IF Processor bolted on the frame of the telescope. The IF Processor Box further amplifies the signal from each HEB mixer and provides a DC signal proportional to each pixel's

total power. An Electronics Box, also bolted to the telescope frame, contains a bias card and computer for the receiver frontend. From the IF processor eight coaxial cables (one for

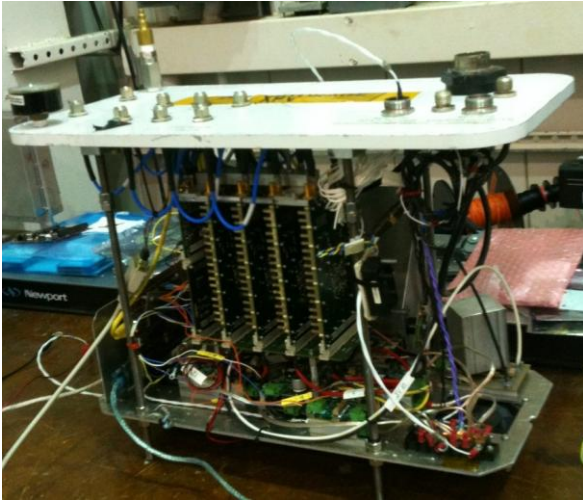


Figure 4: Pressure vessel containing STO flight spectrometer.

each focal plane mixer) carry the amplified IFs up to the pressurized vessel containing the spectrometer (see Figure 4) located at the mezzanine level of the gondola. The pressure vessel contains a single board computer and spectrometer that digitizes and performs FFTs on each of the eight, 1 GHz wide, input signals. The resulting power spectra are read out at  $\sim 1$ Hz, stored in non-volatile flash memory, and made available to the gondola computer via ethernet. From the gondola computer the data is relayed to ground stations on Earth via the TDRSS-1 satellite.

### 3. OBSERVING STRATEGY

STO is capable of performing either Absolute Position Switched (APS) or On-the-Fly (OTF) mapping observations. Pointed observations will be used for calibration, while OTF will be the default observing mode for Galactic Plane Surveys. During a typical OTF scan, STO will begin by taking a reference spectrum well off the Galaxy where the chance of significant emission in the reference (or OFF) position is minimal. The spectrometer is read out continuously as the STO beams cuts through the Galactic Plane. Every  $\sim 10$  sec the Optics Box pick off mirror will swing in for  $\sim 5$  sec. In this position the back of the mirror directs light from an ambient temperature calibration load down into the mixer arrays, while the front of the mirror directs the telescope beam into the 492 GHz Schottky

receiver. When the mirror is swung out, the telescope beam passes through to the diplexer while the Schottky receiver sees the calibration load. By routinely observing the ambient load, the calibration of each observed spectrum can (in principle) be boot strapped to a reference position. Depending on stratospheric wind patterns and payload health, STO could be in flight for up to  $\sim 28$  days.

### 4. CONCLUSION

STO is the first balloon-borne payload designed to perform high resolution spectroscopy at THz frequencies. It will observe the astrophysically important interstellar lines of [CII] (1.9THz), [NII] (1.46THz), and [CI] (0.49THz). The instrumentation used on STO has heritage from Herschel, ODIN, SWAS, and a number of ground-based observatories. We hope the upcoming STO flight will serve as a scientific and technical pathfinder for many other THz missions to come.

### REFERENCES

- [1] Walker, C. K., Kulesa, C. A., Groppi, C. E., Young, E. T., McMahon, T., Bernasconi, P., Lisse, C., Neufeld, D., Hollenbach, D., Kawamura, J., Goldsmith, P., Langer, W., Yorke, H., Sterne, J., Skalare, A., Mehdi, I., Weinreb, S., Kooi, J., Stutzki, J., Graf, U., Honingh, N., Puetz, P., Martin, C., Wolfire, M., "The Stratospheric TeraHertz Observatory" in Proceedings of 19th International Symposium on Space Terahertz Technology, ed. Wolfgang Wild, Groningen, 28-30 April 2008, ([https://www.sron.nl/files/LEA/ISSTT2008/Proceedings\\_ISSTT2008.pdf](https://www.sron.nl/files/LEA/ISSTT2008/Proceedings_ISSTT2008.pdf)), p.28 (2000).
- [2] Bernasconi, P.N., Rust, D. M., Eaton, H. A. C., Murphy, G. A. A., "A Balloon-borne Telescope for high resolution solar imaging and polarimetry", in Airborne Telescope Systems, Ed. By R. K. Melugin, and H. P. Roeser, SPIE Proceedings, 4014, 214 (2000).
- [3] Bernasconi, P.N., Eaton, H. A. C., Foukal, P., and Rust, D. M., "The Solar Bolometric Imager", Adv. Space Res., 33, 1746 (2004).

# A progress update on SuperCam: A 345 GHz, 64-pixel heterodyne imaging spectrometer

Jenna Kloosterman\*, Christopher Groppi<sup>†</sup>, Craig Kulesa\*, Christopher Walker\*, Tiara Cottam\*, Elliott Liggett\*, David Lesser\*, Michael Borden\*, Paul Schickling\*, Dathon Golish\*, Christian d'Aubigny\*, Sander Weinreb<sup>‡</sup>, Glenn Jones<sup>‡</sup>, Joseph Barden<sup>‡</sup>, Hamdi Mani<sup>†</sup>, Tom Kuiper<sup>§</sup>, Jacob Kooi<sup>‡</sup>, Art Lichtenberger<sup>¶</sup>, Thomas Cecil<sup>¶</sup>, Patrick Puetz<sup>||</sup>, Gopal Narayanan\*\*, Abigail Hedden<sup>††</sup>, Xiaoying Xu\*

\*University of Arizona, Tucson, AZ 85721

<sup>†</sup>Arizona State University, Tempe, AZ 85287

<sup>‡</sup>California Institute of Technology, Pasadena, CA 91125

<sup>§</sup>Nasa Jet Propulsion Laboratory, Pasadena, CA 91109

<sup>¶</sup>University of Virginia, Charlottesville, VA 22908

<sup>||</sup>KOSMA, University of Cologne

\*\*University of Massachusetts, Amherst, MA 01003

<sup>††</sup>Army Research Laboratory

Contact: jkloost@email.arizona.edu

**Abstract**—SuperCam is a 345 GHz, 64-pixel heterodyne imaging spectrometer being prepared for installation on the Heinrich Hertz Submillimeter Telescope (HHSMT). In the Fall 2011 the receiver will begin its survey of 500 square degrees of the Galactic plane in  $^{12}\text{CO J=3-2}$ . This large-scale survey will help answer fundamental questions about the formation, physical conditions, and energetics of molecular clouds within the Milky Way. The data set will be available via the web to all interested researchers. By integrating SIS mixer devices with LNAs in 8- 1x8 modules, the size needed for the cryostat and the complexity of internal wiring is significantly reduced. Here we briefly describe SuperCam's operation and report on its status.

## I. INTRODUCTION

SuperCam is a 64 pixel, Superheterodyne Camera designed to operate in the 345 GHz atmospheric window. Its development was motivated by the need to perform large scale, high spectral resolution submillimeter spectroscopy of the interstellar medium (ISM). All 64 pixels have been installed in the cryostat. The cryostat, bias system, IF down-converters and spectrometer are in their final stages of integration. Previously, noise temperature measurements from 32 out of 64 pixels have been presented (1; 2). Here we summarize the instrument design and give an update on SuperCam's progress.

## II. SCIENCE

SuperCam will map 500 square degrees in the Galactic plane between  $0^\circ < l < 90^\circ$  and  $-1 < b < +1$  and all major star-forming regions visible from the HHSMT with 22" spatial resolution and 0.3 km/s velocity resolution. This survey has been outlined in black in Figure 1. By combining the results of SuperCam surveys in  $^{12}\text{CO J=3-2}$  and  $^{13}\text{CO J=3-2}$  with existing CO J=1-0 surveys, a complete excitation temperature map of the survey region can be constructed. Additionally, the SuperCam survey will improve upon the spatial resolution of

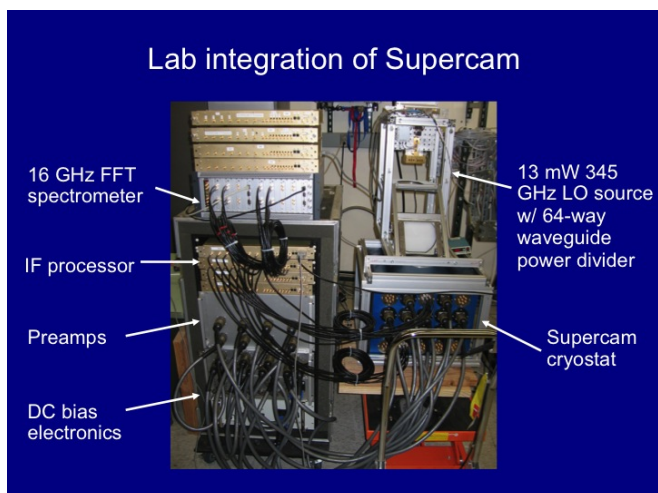


Fig. 2. Photograph of SuperCam cryostat, LO, and electronics for all 64 pixels.

existing Galactic Plane surveys by a factor  $>10$ . The depth of the survey is sufficient to detect CO to a level consistent with  $A_\nu \sim 1$ , detecting all CO that has formed in-situ (1).

## III. INSTRUMENT DESCRIPTION

SuperCam is composed of several subsystems; optics, cryogenics, and electronics. A recent photograph of SuperCam is shown in Figure 2. A block diagram of the instrument is provided in Figure 3. Each subsystem is discussed below.

### A. Cryostat

The cryostat was constructed by Universal Cryogenics in Tucson, AZ. Light passes through an AR coated crystalline quartz vacuum window and 40K GoreTex GR IR filter before

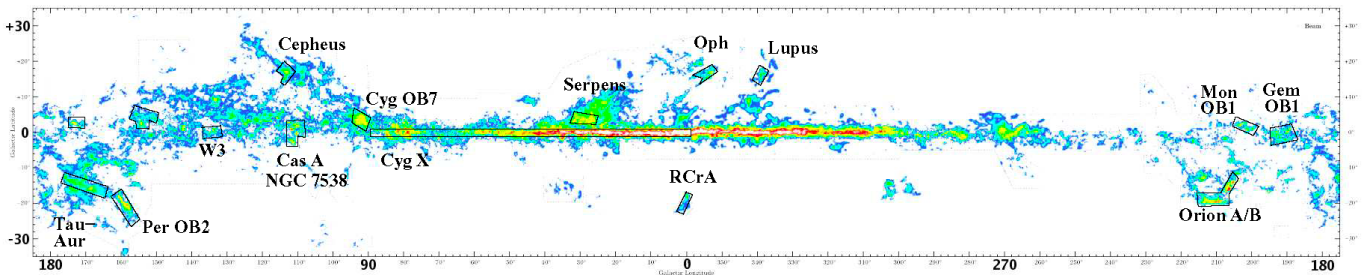


Fig. 1. The 500 square degree SuperCam Galactic Plane Survey from the HHSMT has been outlined in black. The survey will Nyquist sample the galactic plane from  $0^\circ < l < 90^\circ$ ,  $-1^\circ < b < +1^\circ$  and all major star forming regions visible from the HHSMT.

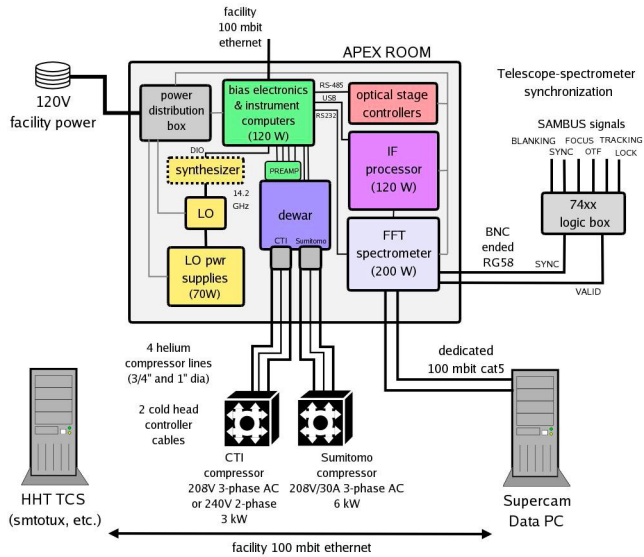


Fig. 3. A block diagram of SuperCam. The cryostat, pre-amplifier electronics, bias electronics, LO, IF downconverters, spectrometer, power supplies, control computers will reside in the HHSMT's Apex room, located just behind the 10 m dish.

illuminating the 4K mixer array. SuperCam uses a CTI-350 coldhead and a Sumitomo SRDK-415DP cryocooler. The CTI-350 supplements cooling of the 40K shield and provides 12K heat sinking for the 64 stainless steel semi-rigid IF cables leading from the mixer array to the vacuum bulkhead. The Sumitomo refrigerator cools the eight, 1x8 mixer array blocks to 4K (1).

### B. Mixer Arrays

SuperCam uses eight 1x8 mixer modules made of 145 copper alloy, shown in Figure 4. The mixer modules were fabricated at the University of Arizona with a Kern MMP micromilling machine. Each module integrates 8 SIS devices with LNAs. The SIS devices have been optimized to work between 320-380 GHz. The modules use stainless steel guide pins and screws for proper alignment and thermal conductivity. A diagonal feedhorn array bolts to the front (2).

Inside each pixel, waveguide directs the incoming signal around a 90° curve to the SIS junction suspended above the stripline channel. Its design includes a quarter wave backshort.

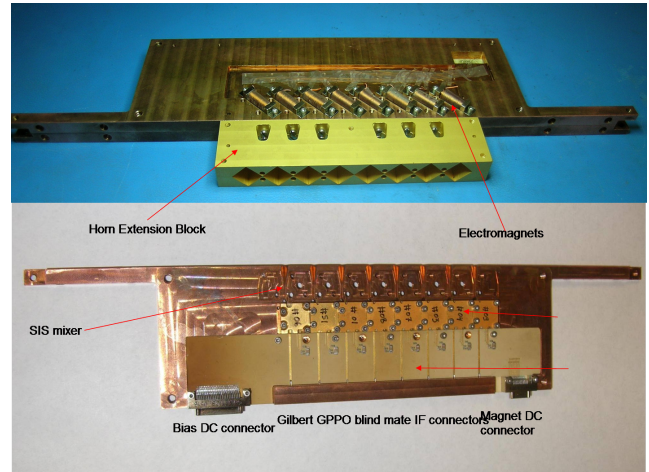


Fig. 4. A fully assembled mixer module (top) and a mixer module with the top covers removed (bottom).

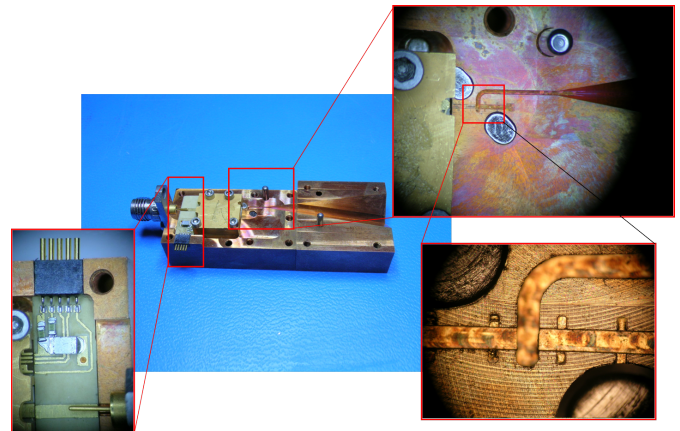


Fig. 5. A single pixel showing an enlarged SIS device and MMIC amplifier.

The output 5 GHz IF signal of each SIS device is immediately directed into a MMIC LNA. One pixel is shown in Figure 5. The amplified IF signal is then conveyed via semi-rigid coax to a vacuum flange. Outside the dewar each IF signal is downconverted to baseband in an IF Processor Box. Each of the 8 IF Processor Boxes downconverts the IFs from a 1x8 mixer array. Both the MMIC modules and IF downconversion boxes were designed and built at Caltech by Sander Weinreb's

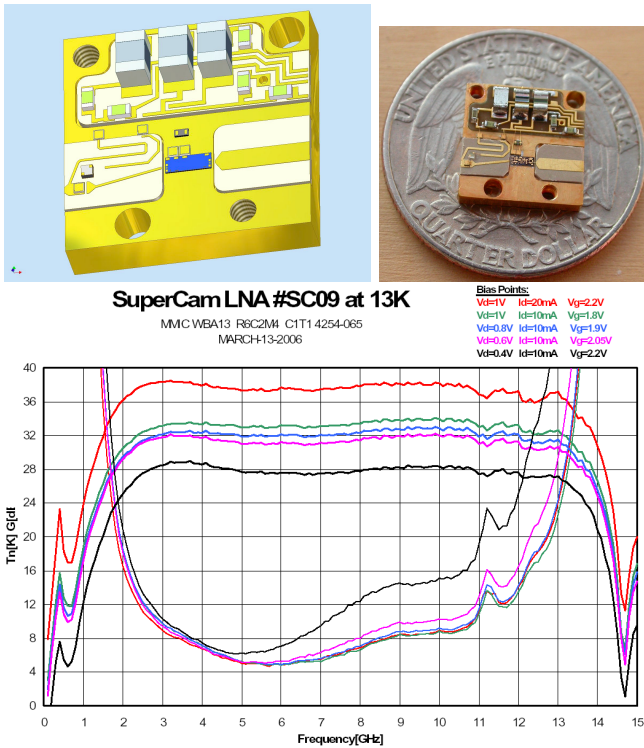


Fig. 6. A CAD drawing of MMIC amplifier drawing alongside its photograph (top) and its measured performance in a 13 K bath temperature along several bias points (bottom).

group. Figure 6 contains a CAD drawing of a MMIC amplifier in the top left panel. In the top right panel a photograph of an actual MMIC is shown with a quarter that has been placed for size comparison. The bottom figure shows the performance of a typical MMIC with measured gain and noise data at 4mW through 20mW power dissipation. The noise remains unchanged down to 6mW (1; 2). Tests have shown that these amplifiers are stable in the integrated configuration and do not overheat the SIS devices (3). With only 8mW of power, the IF modules achieve a  $\sim 5$  K noise and 32dB of gain (1; 2).

### C. Local Oscillator

A Virginia Diode, Inc. multiplier chain consisting of a chain of a single quadrupler and three subsequent doublers provides LO signal to the mixers. The output power of the multiplier chain is divided into 64 beams using a waveguide power divider and transmitted via an array of 64 diagonal feedhorns to an identical feedhorn array attached to the mixer modules in the cryostat. The LO power divider was machined at the University of Arizona using a Kern MMP micromilling machine. The signal is uniformly spread to each pixel on the  $\sim 10\%$  level (1; 2).

### D. IF Bias System

The IF bias system controls the SIS bias voltage, electromagnetic current, and the biasing of the LNA gate and drain stages. The electronics are contained in two boxes, the pre-amplifier box and the bias box as seen in Figure 2. The

pre-amp box was designed and built at the University of Massachusetts. The bias box was designed and constructed at the University of Arizona.

There are 8 bias cards. Each card provides all the required bias signals for a 1x8 mixer subarray. Each card has its own Technological System TS-7200 single-board-computer. The TS-7200 runs a TCP/IP socket server that provides all I/O to each board via Ethernet. To connect to the socket server a variety of clients can be used; including a graphical user interface (GUI), a script interface, or an interactive command line.

### E. IF Processors

The warm IF Processor boxes downconvert each SuperCam IF signal to baseband for input into the spectrometer. The system consists of 8 printed circuit boards, each handling 8 SuperCam channels. There are switchable filters for the 250 MHz and 500 MHz bandwidth modes of the spectrometer (1; 2)

### F. Spectrometer

Recent advances in the speeds of analog-to-digital converters (ADCs) and field programmable gate arrays (FPGAs) have enabled Omnisys AB of Sweden to build the SuperCam spectrometer in a single box. These advances have driven down the costs of spectrometers, which would have consumed the entire instrument budget in the past. A total of 8 boards are used each constructed with 4 ADCs that feed into a single Virtex 4 SX55 FPGA. A single board is shown in the top left of Figure 7. Each board can process either four 500MHz bandwidth signals or two 1GHz bandwidth signals in real time. Power consumption is 25 W per board. The FPGAs are easily reconfigurable and the spectrometer can be expanded to increase bandwidth. The spectrometer connects to the outside world via Ethernet (1; 2).

In its current configuration the spectrometer can process 64x250 MHz IF signals, 32x500 MHz IF signals, or 16x1 GHz IF signals. In the 64x250 MHz configuration the upper and lower sidebands signals are power combined. The Allan time with the IF downconverters is  $\sim 250$ s, top right of Figure 7 (1; 2). The bottom of Figure 7 is a picture of the spectrometer in its entirety.

### G. Optics

The SuperCam optics were designed to convert an  $f/13.8$  beam, the beam after the HHSMT secondary mirror, to a  $\sim f/6$  beam. Smaller  $f/\#$ 's reduce the overall size of the instrument. The optics will be mounted in the Apex room of the HHSMT along with the cryostat and all of the electronic equipment (1; 2).

The optics system consists of 7 mirrors; 5 flat mirrors and 2 curved mirrors mounted to a steel support structure. The mirrors are made from nickel plated, aluminum. They were polished to near-optical quality to permit laser alignment. The polishing process utilized smaller and smaller grit sizes (down to  $1\mu\text{m}$ ) until a laser beam could be reflected with minimal speckling.



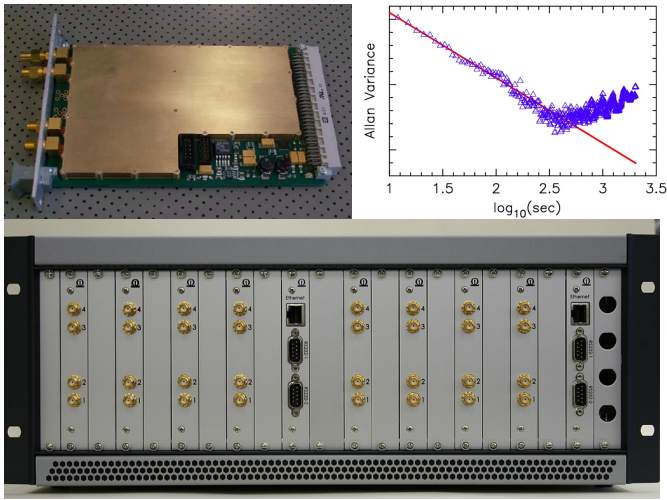


Fig. 7. A single spectrometer board (top left), the Allan Variance (top right), and the total SuperCam spectrometer (bottom).

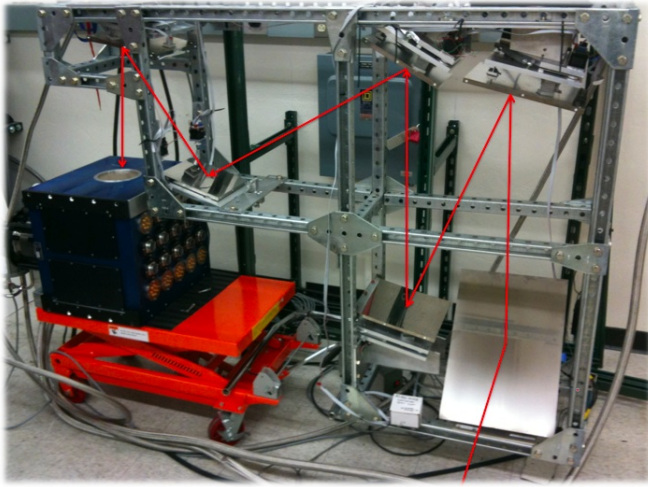


Fig. 8. The optical support structure in the lab at the University of Arizona with the optical path of the light drawn in. Mirror 1 is the pickoff mirror from the tertiary and is not pictured.

Initial alignment of the mirrors is performed mechanically with a FARO portable coordinate measuring arm (to be discussed in a separate paper) and then by laser. To facilitate alignment, each of the mirrors is mounted on a motorized, tip-tilt stage. A photograph of the optical system is provided in Figure 8. The optical path is indicated in red.

#### IV. LABORATORY RESULTS AND CURRENT STATUS

We have completed the fabrication and full assembly of all 64 pixels. These are installed in the SuperCam cryostat, shown in figure 9 with their diagonal feedhorns. After cooling the cryostat to 4 K, there are currently 52 live devices, 64 working LNAs, and 59 working magnets. The bias and pre-amp boxes have been fully tested and all 64 channels are working. The aluminum mirrors have been nickel-plated and polished to optical quality. Additionally, the optical support structure has been assembled with all mirrors and is currently

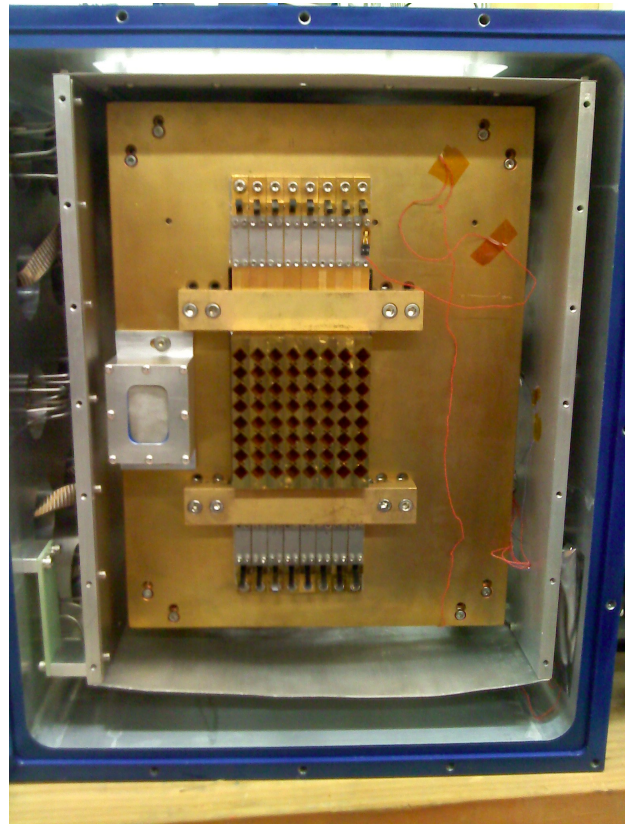


Fig. 9. All 64 pixels installed in the SuperCam cryostat.

undergoing alignment. The LO has been attached and is being aligned to provide power evenly to all 64 pixels. An end-to-end test has been performed on 8 pixels using a 345 GHz test signal. Each pixel simultaneously detects the tone. These results are shown in Figure 10. Preparations in the apex room of the HHSMT are underway for SuperCam to be installed this coming fall.

#### V. CONCLUSIONS

SuperCam is a leap forward in the realization of a fully integrated heterodyne array for THz astronomy. The 64 pixel SuperCam imaging spectrometer is now fully assembled and is undergoing performance tests. SuperCam will be installed on the HHSMT in Fall 2011. Once installed, SuperCam will be initially used to survey the Milky Way in the  $^{12}\text{CO } J=3 \rightarrow 2$  line. These maps will provide new, valuable insights into the life cycle of the ISM and the inner working of our Galaxy.

#### ACKNOWLEDGMENTS

SuperCam is supported by the NSF Major Research Instrumentation Program, Award AST- 0421499.

#### REFERENCES

- [1] C. Groppi, C. Walker, C. Kulesa, D. Golish, J. Kloosterman, S. Weinreb, G. Jones, J. Bardin, H. Mani, T. Kuiper, J. Kooi, A. Lichtenberger, T. Cecil, P. Puetz,

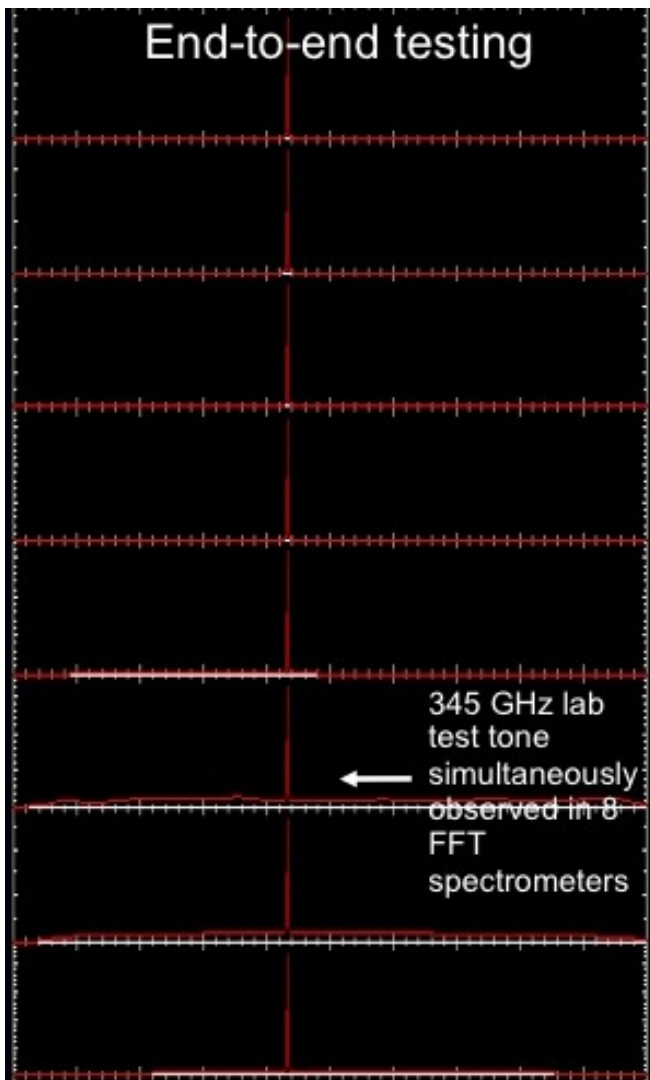


Fig. 10. 8 simultaneous spectra from an end-to-end test using a 345 GHz test signal.

- G. Narayanan, and A. Hedden, "Test and integration results from SuperCam: a 64-pixel array receiver for the 350 GHz atmospheric window," in *Society of Photo-Optical Instrumentation Engineers (SPIE) Conference Series*, ser. Presented at the Society of Photo-Optical Instrumentation Engineers (SPIE) Conference, vol. 7741, Jul. 2010.
- [2] C. Groppi, C. Walker, C. Kulesa, D. Golish, J. Kloosterman, S. Weinreb, G. Jones, J. Barden, H. Mani, T. Kuiper, J. Kooi, and A. Lichtenberger, "Testing and Integration of SuperCam, a 64-Pixel Array Receiver for the 350 GHz Atmospheric Window," in *Twenty-First International Symposium on Space Terahertz Technology*, Mar. 2010, pp. 368–373.
- [3] P. Pütz, A. Hedden, P. Gensheimer, D. Golish, C. E. Groppi, C. Kulesa, G. Narayanan, A. Lichtenberger, J. W. Kooi, N. Wadefalk, S. Weinreb, and C. K. Walker, "345 GHz Prototype SIS Mixer with Integrated Mmic Lna," *International Journal of Infrared and Millimeter Waves*,

# HEAT: The High Elevation Antarctic Terahertz Telescope

Craig Kulesa<sup>1</sup>, Christopher Walker<sup>1</sup>, Abram Young<sup>2</sup>, John Storey<sup>3</sup>, Michael Ashley<sup>3</sup>

(1) University of Arizona, 933 N. Cherry Ave. Tucson, AZ, 85721, USA

(2) Teravision Inc., 1815 W Gardner Lane, Tucson, AZ 85705, USA

(3) The University of New South Wales, Dept. of Astrophysics & Optics, School of Physics, University of New South Wales, NSW, 2052, Australia

\* Contact: ckulesa@as.arizona.edu, phone 1-520-965-6540

*Abstract*— KAPPA (the Kilopixel Array Pathfinder Project) is an effort to develop key technologies to enable the construction of coherent heterodyne focal plane arrays in the terahertz frequency regime with ~1000 pixels. The current state-of-the-art pixel count for coherent terahertz focal plane arrays is ~100 pixels (the Supercam 350 GHz array with 64 pixels). The leap to ~1000 pixels requires several key technological problems to be tackled before the construction of such a focal plane is possible. While the previous generation of arrays used 1D integration of mixer elements into a linear array module, kilopixel instruments will require 2D integration, as has been done with incoherent terahertz and infrared detectors. Over the next three years, the KAPPA project will develop a small (16-pixel) 2D integrated heterodyne focal plane array for the 660 GHz atmospheric window as a technological pathfinder towards future kilopixel heterodyne focal plane arrays in the terahertz frequency regime. KAPPA will use SIS devices fabricated on SOI membranes with beam lead alignment and connection features, designed for high yield and fast installation. A SiGe low noise amplifier with on-chip bias tee will be integrated directly into the mixer block immediately adjacent to each mixer. This amplifier has been designed to yield adequate gain and low noise temperature, while dissipating less than 2mW of power. The SIS and LNA devices will be mounted in a 2D integrated metal micromachined mixer array consisting of a backshort block containing the SIS device and LNA, and a horn block using drilled smooth-wall feedhorns. Magnetic field will be delivered to the devices via compact, permanent magnets embedded in the horn block. We will also develop cryogenically compatible IF flex circuits to replace individual semi-rigid coaxial lines for IF signal transmission. Once completed, this instrument will demonstrate the critical technologies necessary to construct coherent arrays approaching 1000 pixels for large single-dish THz telescopes like CCAT and SPT.

# Balanced Receiver Development for the Caltech Submillimeter Observatory

J. W. Kooi, R. A. Chamberlin, R. Monje, B. Force, D. Miller, and T. G. Phillips.

**Abstract**—The Caltech Submillimeter Observatory (CSO) is located on top of Mauna Kea, Hawaii, at an altitude of 4.2 km. The existing suite of facility heterodyne receivers covering the submillimeter band is rapidly aging and in need of replacement. To facilitate deep integrations and automated spectral line surveys, a family of remote programmable, synthesized, dual-frequency balanced receivers covering the astronomical important 180–720 GHz atmospheric windows is in an advanced stage of development. Installation of the first set of receivers is expected in the Summer of 2012.

Dual-frequency observation will be an important mode of operation offered by the new facility instrumentation. Two band observations are accomplished by separating the H and V polarizations of the incoming signal and routing them via folded optics to the appropriate polarization sensitive balanced mixer. Scientifically this observation mode facilitates pointing for the higher receiver band under mediocre weather conditions and a doubling of scientific throughput (2 x 4 GHz) under good weather conditions.

## I. INTRODUCTION

Although different in detail and configuration, advanced receiver designs are now featured prominently in, for example, the Heterodyne Instrument for the Far-Infrared (HIFI) on the Herschel satellite [1], ALMA [2], the Plateau de Bure interferometer (IRAM) [3], the Atacama Pathfinder EXperiment (APEX) [4], and the Harvard-Smithsonian Submillimeter Array (SMA) [5].

To upgrade the heterodyne facility instrumentation at the CSO, four tunerless balanced-input waveguide receivers have been constructed to cover the 180-720 GHz frequency range [6]. The new suite of submillimeter receivers will be installed in the Nasmyth focus of the 10.4 m diameter telescope and will soon allow observations in the 230/460 GHz and 345/660 GHz atmospheric windows. The IF bandwidth of the CSO receivers will increase from the current 1 GHz to 4 GHz (though in principle 12 GHz is possible). Balanced configurations were chosen for their inherent local oscillator (LO) amplitude noise cancellation properties, facilitating the use of synthesizer-driven LO chains. It was also judged to be an optimal compromise between scientific merit and finite funding, offering the very stable performance needed to meet the desired science requirements. Unique to the CSO, wide RF bandwidth is favored [7], allowing the same science to be done with fewer instruments. In all the upgrade covers ALMA band 5b–9.

This work is supported in part by NSF grant # AST-0838261.

J. W. Kooi, R. Chamberlin, R. Monje, B. Force, D. Miller, and T. G. Phillips are with the Submillimeter Astronomy and Instrumentation Group, California Institute of Technology, Pasadena, CA 91125, USA. e-mail: kooi@submm.caltech.edu.

To maximize the RF bandwidth, we explore the use of high-current-density AlN-barrier SIS technology in combination with a broad bandwidth full-height waveguide to thin-film microstrip transition [8]. Compared to AlO<sub>x</sub>-barriers, advantages of AlN tunnel barriers are a low  $\omega$ RC product (increased RF bandwidth) and enhanced chemical robustness. Even if optimal RF bandwidth is not a requirement, a low  $\omega$ RC product provides a more homogeneous frequency response and increased tolerance to errors in device fabrication.

To process the required IF bandwidth, the CSO has acquired a Fast Fourier Transformer Spectrometer (FFTS) from Omnisys Instruments, Sweden [9]. This spectrometer facilitates 8 GHz of processing bandwidth with a resolution of 268 KHz/channel, or 3724 channels/GHz. The 8 GHz Omnisys FFTS comes in a 19 inch rack and has two built-in IF processor modules (4-8 GHz each), an embedded controller module, a synchronization module, and power supply.

In this paper we describe the instrument suite and discuss the development of a wide variety of technologies. Particular attention is given to the challenge of providing synthesized LO coverage from 180-720 GHz with minimal latency.

## II. THE SINGLE-BALANCED MIXER

In principle, a single balanced mixer can be formed by connecting two reverse biased (SIS) mixers to a 180° or 90° input hybrid [10]. Consider a 90° (quadrature) hybrid with a noise signal  $V_n(t) = \sum C_k \cos(\omega_k t + \theta_k)$  over all  $k$  superimposed on the incident LO signal. The amplitude(s)  $C_k$  and phase(s)  $\theta_k$  may be determined from Fourier analyses of  $V_n(t)$ . At the output ports of the 90° (quadrature) hybrid we then have

$$v_1(t) = [V_{lo}\tau \sin(\omega_{lo}t) + V_n\tau \sin(\omega_n t)] - V_{rf}\rho \cos(\omega_{rf}t) \quad (1)$$

and

$$v_2(t) = V_{rf}\tau \sin(\omega_{rf}t) - [V_{lo}\rho \cos(\omega_{lo}t) + V_n\rho \cos(\omega_n t)]. \quad (2)$$

$\omega_n$  represents the frequency components  $\sum C_k \cos(\omega_k t + \theta_k)$ . After some mathematical treatment [11] the noise reduction for a balanced mixer is obtained as

$$NR(dB) = -20 \cdot \log \left[ 1 - \sqrt{G_m} G_h \cos(\Delta\varphi) \right]. \quad (3)$$

Here  $\sqrt{G_m}$  represents the mixer gain imbalance,  $G_h$  the RF hybrid imbalance, and  $\cos(\Delta\varphi)$  the phase error of the RF

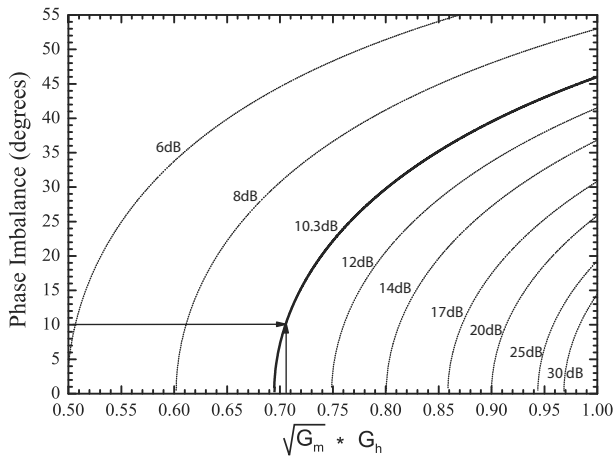


Fig. 1. Amplitude rejection of a balanced mixer relative to an ideal single-ended mixer. Given a realized quadrature hybrid imbalance ( $G_h \geq 0.75$ ), mixer gain (power) imbalance of 0.5 dB ((Sec. III-B), and a differential phase error of  $10^\circ$ , we can expect an amplitude noise rejection of  $\geq 10$  dB over the traditional single-ended mixer.

hybrid, device placement, wirebond length, and IF summing node.

If the mixers are biased symmetric (rather than antisymmetric), then in the case of a perfectly balanced mixer a doubling of the LO amplitude noise (at the IF summing node) would result [12]

$$NR'(dB) = -20 \cdot \log \left[ 1 + \sqrt{G_m G_h} \cos(\Delta\varphi) \right]. \quad (4)$$

Fig. 1 illustrates the balanced mixer noise reduction as a function of gain and phase imbalance.

### III. CSO NASMYTH FOCUS RECEIVER LAYOUT

The receiver configuration consists of two cryostats, one of which will house the 180–280 GHz / 380–520 GHz balanced mixers, the other the 280–420 GHz / 580–720 GHz balanced mixers

To supply the needed LO pump power, planar multiplier sources [13] are mounted inside the cryostat and connected to the 15 K stage. This allows for a more compact optical configuration, improves reliability of the multipliers, and reduces thermal noise. We estimate that each SIS junction requires roughly  $1/2 \mu\text{W}$  of LO pump power ( $\alpha = eV_{lo}/h\nu \sim 0.7$  on average). And since two SIS junctions are used as part of the RF tuning design we require  $\sim 1.5\text{--}2 \mu\text{W}$  of LO power at the mixer LO input port, including waveguide loss in the mixer block.

In Fig. 2 we show the 230 GHz and 460 GHz balanced mixer, LO hardware, and optical components on the 4 K LHe work surface.

#### A. Integrated IF and Wilkinson in-phase summing node

In a mixer configuration, the active device is typically terminated into a desired IF load impedance, the bias lines EMI-filtered and injected via a bias Tee, and the IF output dc-isolated (Fig. 3). The balanced mixer has the additional

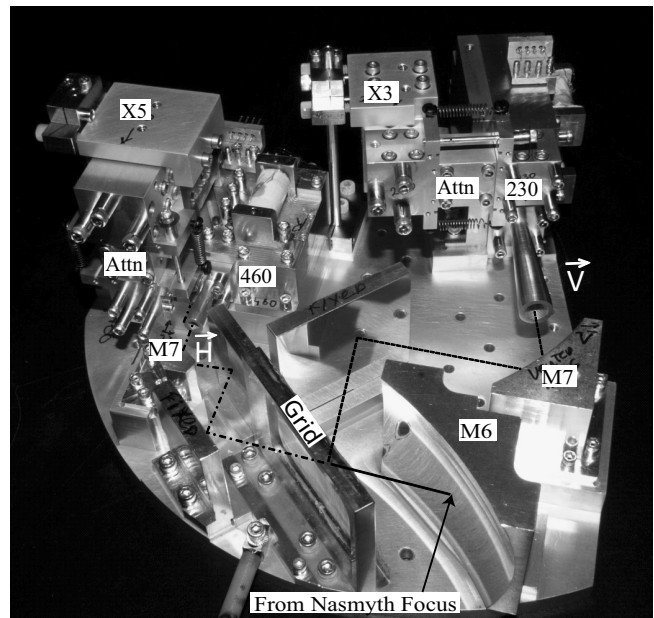


Fig. 2. 230/460 GHz focal plane unit (FPU) with associated balanced mixer blocks, multiplier hardware, and optics.

constraint that the IF signals need to be combined either in phase, or  $180^\circ$  out of phase, putting tight limits on the allowed phase error ( $< 5^\circ$ ). Since in our application the SIS junctions will be biased antisymmetric we conveniently combine the bias-Tees, electrical isolation of the IF port, band pass filters, IF matching networks, and an in-phase Wilkinson power combiner [14] on a single planar circuit. The  $100 \Omega$  balancing resistor of the Wilkinson power combiner (Fig. 3b) is a 1% laser trimmed thinfilm NiCr resistor, lithographically deposited on a  $635 \mu\text{m}$  thick Alumina ( $\epsilon_r=9.8$ ) circuit board [15].

The IF bandpass filter is comprised of a set of parallel

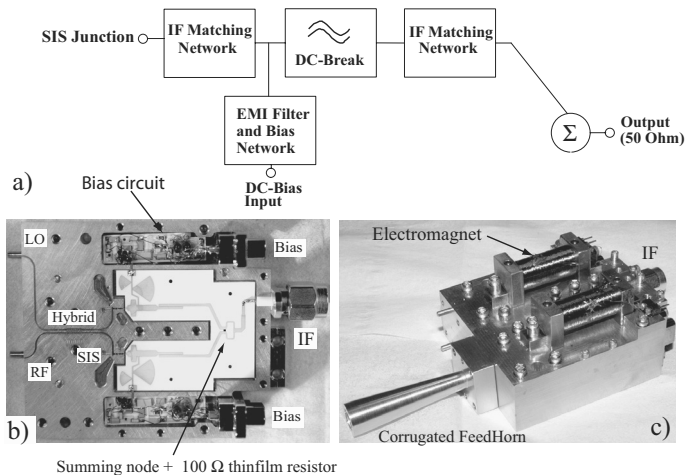


Fig. 3. a) Balanced mixer block layout. b) The IF board is entirely planar (alumina), and combines the IF match, dc-break, bias Tee, EMI filter, and Wilkinson in-phase power combiner. The E-field component of the incoming signal is horizontally polarized along the waveguide split. c) Josephson noise suppression in the SIS tunnel junctions is accomplished by two independent electromagnets.

coupled suspended microstrip lines [16]. For this filter to work, the ground plane directly underneath the filter has been removed, and the IF board positioned on top of a machined cutout (resonant cavity). There are several discontinuities in this structure. When combined, they form the bandpass filter poles. The advantages are; simplicity of design (only one lithography step), accurate knowledge of the phase, and reliability. The disadvantage is its size,  $\lambda_g/4$  ( $\sim 6$  mm at 6 GHz).

*B. High current density SIS junctions with integrated IF matching*

To facilitate the CSO heterodyne upgrade a suite of high-current-density AlN-barrier niobium SIS junctions (4 bands) have been fabricated by JPL [6]. These devices have the advantage of increasing the mixer instantaneous RF bandwidth while minimizing absorption loss in the mixer normal or superconducting thinfilm front-end RF matching network.

The junction designs employ twin-SIS junctions with a  $R_n A$  product of  $7.6 \Omega \cdot \mu\text{m}^2$  ( $J_c=25$  kA/cm<sup>2</sup> current density). Supermix [17], a flexible software library for high-frequency superconducting circuit simulation, was used in the design process.

IV. SYNTHESIZED LOCAL OSCILLATOR (186–720 GHz)

The CSO suite of balanced receivers will employ a dual-synthesizer LO configuration operating at a baseband frequency of 20–35 GHz (Fig. 4). This setup, shown in Fig. 4, facilitates remote and automated observations, frequency agile performance, and ease of operation. The commercial synthesizers [18] connect via 2.5 m length low loss coaxial cables [19] to a pair of magnetically shielded signal conditioning “mu-Boxes”. Each mu-Box contains a medium power amplifier (P<sub>sat</sub> = +25 dBm) [20], a tunable Yttrium-Iron-Garnet (YIG) 4-pole bandpass filter [21] for removal of low level spurious content, a 20 dB directional coupler and zero bias detector diode for the purpose of signal monitoring/calibration,

TABLE I  
MULTIPLICATION FACTORS OF THE CSO SYNTHESIZED LO

Frequency	PMW [24]	VDI [13]	Total Multiplication
186-280 GHz	×3	×3	×9
280-420 GHz	×3	×2×2	×12
400-520 GHz	×3	×5	×15
580-720 GHz	×3	×3×3	×27

a 3 dB power splitter, and two Ditom K<sub>a</sub>-band isolators [22]. The input signal to the YIG is approximately +22 dBm. The isolated output ports ( $\sim +11$  dBm) route the filtered carrier signal via 30 cm & 1.4 m coaxial lines to a second signal conditioning box, known as the “mm-Wave” box.

Like the mu-Box, the mm-Wave signal conditioning box also contains medium power amplifiers [20]. These also are run into saturation (+25 dBm) thereby reducing amplitude noise on the carrier. Fourier harmonics from the resulting clipped sinusoidal waveform are removed by means of a 35 GHz 17-pole low pass filter (LPF) [23]. The measured in-band signal loss of the lowpass filter at 35 GHz is  $\sim 1.75$  dB. At 40 GHz the attenuation has increased to  $\sim 23$  dB. In large part due to frequency dependent variations in the saturated output power of the mm-wave medium power amplifiers, the available signal level to drive broad bandwidth passive triplers [24] ranges from +20 dBm to +22 dBm. The output of the passive triplers is either WR-12 or WR-10 waveguide (TE<sub>10</sub> mode), depending on the frequency band. Given the 17 dB conversion loss of the triplers and 1 dB waveguide loss, this translates into a (measured) input signal level at the WR-11 power amplifiers (see section: IV-A) of 1–2 mW.

Following the WR-11 balanced power amplifier there is a “Frequency Dependent Attenuator” (section: IV-B) which is designed to provide an optimum (safe) drive level for the VDI [13] passive multipliers (Table I) at the 15 K work surface of the cryostat. Finally, to inject the 186–720 GHz submillimeter LO signal into the balanced mixers while providing a suitable level of attenuation and thermal break, a cooled waveguide attenuator is employed (section IV-C).

At frequencies below 210 GHz and 320 GHz there is the possibility that harmonics at the high end of the frequency band will be amplified by the WR-11 power amplifier, and thus be incident along with the intended carrier frequency on the final multipliers. To eliminate this possibility a set of waveguide lowpass filters has been designed [25] and procured [26]. The mm-Wave boxes are designed to facilitate insertion of the lowpass filters in the LO path as needed.

Important science considerations to the operation of the synthesized LO, and in particular the YIG tracking filter, are the rate at which the YIG tuning parameters (due to drift/hysteresis) need to be updated and the settling time after a retune. For additional information on the design and operation we refer to [11].

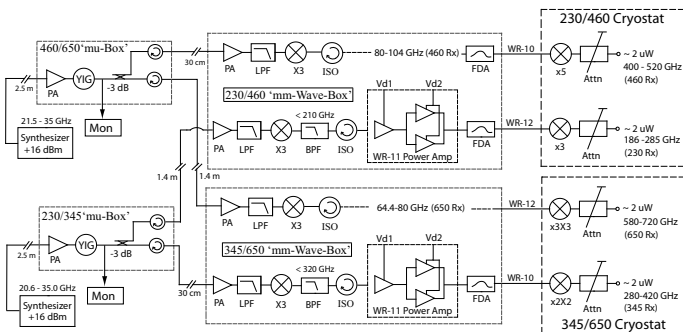


Fig. 4. CSO dual-frequency synthesized local oscillator layout. At the input of the mu-Box the baseband frequency of 20–35 GHz (K<sub>a</sub>-band) is amplified and drives the medium power amplifier into saturation. The LO signal is filtered by the YIG to remove low level spurious and harmonic content, passively multiplied (X3) to 63–105 GHz, once again amplified (WR-11 waveguide power amplifiers), signal conditioned (FDA), and finally injected into the cryostat where the carrier signal is multiplied up to the final submillimeter frequency (186–720 GHz) and injected into the balanced mixers via a cooled attenuator. Spectral line observations below 186 GHz will need to be in the mixer lower side band.

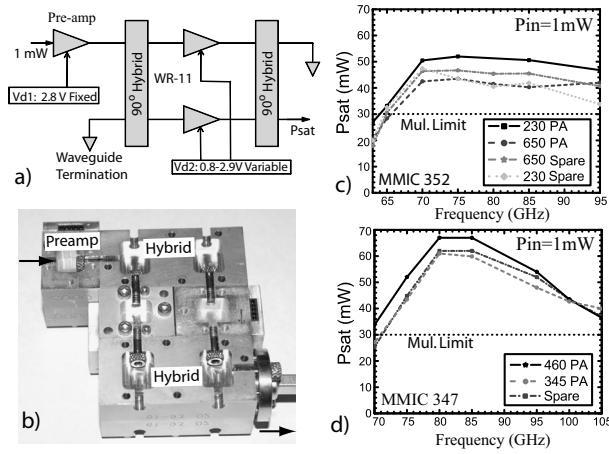


Fig. 5. a) Pre-amp & balanced power amplifier setup. The pre-amp is fixed biased at  $\sim 2.8$  V and drives two variable bias gain modules in a balanced configuration. b) Assembled power amplifier. The measured RF loss in the quadrature hybrids is  $\sim 1$  dB. c) Measured output power of the MMIC 352 configuration. This chain is used to drive the 230 & 650 GHz submillimeter multipliers. d) Measured output power of the MMIC 347 configuration which is used to drive the 345 & 460 GHz submillimeter multipliers. See also Table I. The input power level requirement is  $\geq 1$  mW. Note the individual variation.

A. 63–105 GHz waveguide power amplifiers

The output signals of the (passive) millimeter wave triplers [24] have to be amplified before they can be routed into the cryostat and drive the final submillimeter multipliers [13] (Fig. 4). This amplification is achieved with custom designed balanced power amplifiers (PAs). Every PA consist of three WR-11 gain modules, each of which houses a medium power monolithic microwave integrated circuit (MMIC) [27] originally developed for HIFI [28], the high resolution instrument on Herschel [29].

The use of balanced amplifiers has the advantage that RF power is combined, and reflected power terminated into a (internal) load [30]. This is particularly important as the input- and output return loss (IRL/ORL) of the MMIC chips can be as high as  $-4$  dB at the (extended) band edges. The balanced configuration has a measured ORL of  $\leq -17$  dB thereby minimizing standing waves at the output port. To minimize reflections of the single-ended input pre-amp we employ full-waveguide band WR-12 & WR-10 isolators [31]. With this configuration, and the pre-amp module fixed biased at 2.8 V, the output of the balanced amplifiers was measured to be in saturation over the entire range of usable drain voltages (0.8–2.9 V). The latter being very important in minimizing LO AM-carrier noise.

B. Frequency dependent attenuators

The balanced power amplifiers of section IV-A, though extended in RF bandwidth, have significant variation in saturated output power ( $\sim 4$  dB). This characteristic is problematic when driving submillimeter multipliers with typical input power level requirements of  $\leq 30$  mW. To constrain the available RF power to safe levels (Fig. 5c, d) it was decided to provide hardware limits by means of “Frequency Dependent Attenuators” or FDAs. This is opposed to software limits with

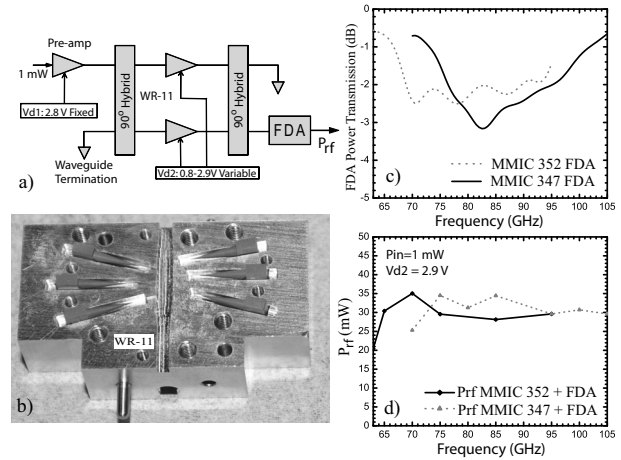


Fig. 6. a) Pre-amp & balanced power amplifier setup including a “frequency dependent Attenuator” (FDA). b) Photograph of the (E-plane) split block showing the six frequency tuned branches with waveguide absorbers. c) Calculated power transmission through the FDA. d) Measured output power,  $P_{rf}$ . The measured output return loss is  $< -18$  dB.

safety tables, as is the case with HIFI [28]. The result is shown in Fig. 6.

C. LO injection

The final LO multipliers [13] are mounted to the cryostat LHe temperature cold work surface while thermally strapped to an intermediate 15 K cold stage. This is done for stability reasons (curtail mechanical modulation of the LO-mixer standing wave [32], [33], [34]) and to minimize thermal heat loading on the LHe reservoir (multipliers have a low conversion efficiency and most of the RF power is converted into heat). For the CSO Nasmyth receivers, injection of the LO signals quasi-optically from outside the dewar was never an option as this required new and larger cryostats, both of which were beyond the scope of the upgrade effort. Since the LO signal is injected via waveguide (Fig 4) a vacuum block at the cryostat entrance is needed. For this we use 0.27 mm thick Mica ( $\epsilon_r=2.54-2.58$ ) [35], building on ALMA Band 9 [36] development. A dc-break is also provided at this junction to avoid ground loops.

To connect the LO signal from the (final) multiplier output to the input port of the balanced mixer a number of technical criteria have to be satisfied: First, there has to be an in-line (course) attenuator to set the LO power to an appropriate level. Second, there needs to be a thermal break between the 15 K multiplier and 4 K mixer. Third, flange adaptors are needed on both the multiplier and balanced mixer ports. And finally, the whole configuration has to be compact to minimize RF loss and fit the limited workspace. Fig. 7 shows the final arrangement.

The attenuator is formed by inserting a  $50 \mu\text{m}$  resistive card into the waveguide. For this we use an ‘Erickson’ style calorimeter [13] in automated synchronous detection mode by switching the balanced power amplifier (section IV-A) On/Off at an appropriate speed ( $\sim 30$  s). The calorimeter Allan variance response time [33] was improved by mounting it

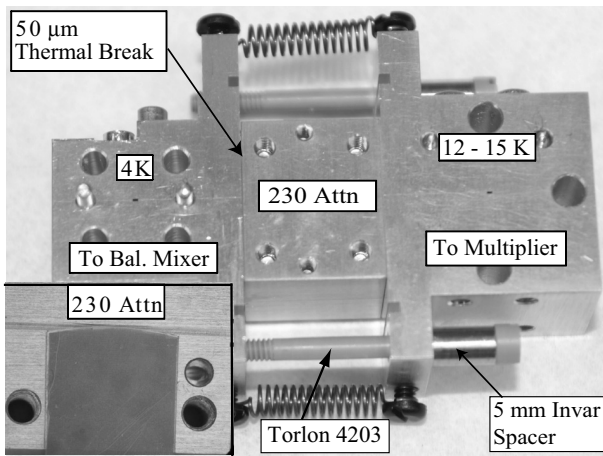


Fig. 7. 230 GHz ‘cooled’ waveguide attenuator, thermal break, and flange adaptor. The overall size of the unit is 4.9 cm x 1.9 cm x 1.4 cm. The attenuator is formed by manually inserting a 50  $\mu\text{m}$  resistive card (inset) into the split-block waveguide. See text for details.

to a copper baseplate with neoprene insulation throughout, providing a rms noise level of  $\sim 0.1 \mu\text{W}$ .

The thermal break is accomplished via a 50  $\mu\text{m}$  airgap, formed by eight  $1 \times 1$  mm Kapton spacers, located at the perimeter of the attenuator and mixer block interface. Torlon 4203 #4 screws in combination with insulated SS springs hold the blocks together. Torlon was chosen for its very low thermal conductivity at 4 K and high strength. The two SS springs in Fig.7 provide a constant tension and long thermal path. Specially designed 5 mm invar spacers compensate for the difference in thermal contraction between the gold plated brass blocks and Torlon screws. To minimize RF loss in the thermal break, a quarter wave (circular) RF choke is incorporated in the waveguide flange on both sides of the break. To verify the integrity of the thermal break an Ohm meter may be used. It should be noted that the multiplier efficiency is expected to improve upon cooling by approximately 25–40%.

## V. SENSITIVITY

A single-ended ‘Technology Demonstration Receiver’ (Trex) covering the important 275–425 GHz atmospheric windows was installed at the CSO in 2007 [7]. Trex is in active use and offers an unprecedented 43% RF bandwidth, nearly 50% wider than the ALMA band 7 275–373 GHz specification [37]. The Trex instrument has proven itself to be an extremely useful testbed for the many new and exciting technologies outlined in this paper.

In Fig. 8 we show the simulated balanced receiver and mixer noise temperature from 180–720 GHz in 4 waveguide bands. To derive a realistic estimate for the balanced receiver noise, we used the measured optics losses of the existing CSO receivers minus LO thermal noise. Superimposed in the plot are the measured results of the single-ended ‘Technology Demonstration Receiver’. From the discussions it is evident that the primary advantage of the balanced receiver is not sensitivity, but rather LO amplitude and spurious noise suppression (stability) and efficient use of local oscillator power [38] [39].

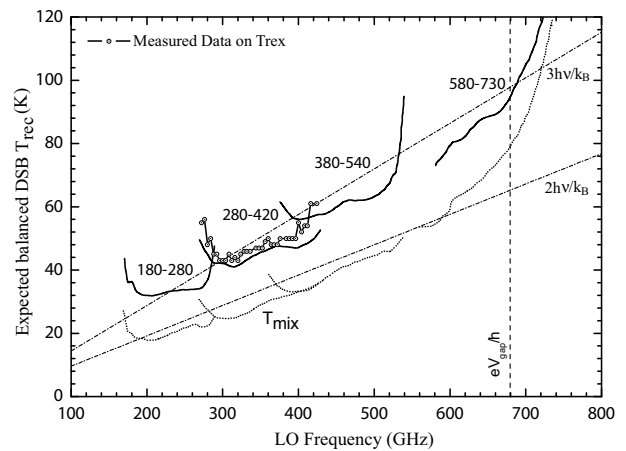


Fig. 8. Estimated double sideband receiver noise temperatures for the new suite of balanced mixers. The noise estimate was calculated by Supermix [17], and includes a realistic optics & IF model. The LO noise contribution should be negligible owing to the noise rejection properties of the balanced mixers (calculated to be  $\geq 10$  dB), and the cooled LO/attenuator. The balanced mixer noise follows the  $2h\nu/k_B$  line and is useful to estimate receiver temperatures for different IF and optics configurations.

## VI. CONCLUSION

The facility receivers of the CSO are being replaced with fully synthesized, dual-frequency, tunerless, 4–8 GHz IF bandwidth state-of-the-art versions. At their heart, the new Nasmyth heterodyne instrumentation will consist of four balanced mixers designed to cover the 180–720 GHz atmospheric frequency range (ALMA B5b–B9). Design and fabrication of the many individual components, e.g. low noise amplifiers, SIS junctions, mixer blocks, corrugated feedhorns, optics, synthesized LO etc. is now complete with assembly and characterization in full swing.

To facilitate automated tuning procedures, remote observations, spectral line surveys, frequency agility, ease of operation, and enhanced scientific throughput (scripting), the receivers and local oscillators will be under full synthesizer and computer control. Furthermore, to accommodate the  $2 \times 4$  GHz IF bandwidth, the CSO has recently installed an 8 GHz Fast Fourier Transformer Spectrometer (FFTS) with a channel resolution of 268 KHz.

## VII. ACKNOWLEDGEMENTS

We wish to thank Marty Gould of Zen Machine & Scientific Instruments for his mechanical advice and machining expertise, John Pierson of the Jet Propulsion Laboratory for his assistance with the medium power amplifiers modules, James Parker for assembly of the many LO related components, Kevin Cooper for setting up the data acquisition network, and Jeff Groseth for help with the Cryogenics and laboratory work. We also wish to thank Pat Nelson for rewiring of the Cryostat and the CSO day-crew for their logistic support over the years. Finally we wish to thank Prof. J. Zmuidzinas of Caltech and the former CASIMIR program for providing the  $K_\alpha$ -band synthesizers and Fast Fourier Transform Spectrometers (FFTS).



## REFERENCES

- [1] [Online]. Available: <http://www.sron.nl/divisions/lea/hifi/>
- [2] [Online]. Available: <http://www.alma.info/>
- [3] [Online]. Available: <http://iram.fr/>
- [4] [Online]. Available: <http://www.apex-telescope.org/>
- [5] [Online]. Available: <http://sma-www.harvard.edu/>
- [6] J. W. Kooi, A. Kovács, B. Bumble, G. Chattopadhyay, M. L. Edgar, S. Kaye, R. LeDuc, J. Zmuidzinas, and T. G. Phillips "Heterodyne Instrumentation Upgrade at the Caltech Submillimeter Observatory" *Proc. SPIE*, Vol. 5498, pp 332-348, Jun., 2004.
- [7] J. W. Kooi, A. Kovács, M. C. Sumner, G. Chattopadhyay, R. Ceria, D. Miller, B. Bumble, R. LeDuc, J. A. Stern, and T. G. Phillips, "A 275-425 GHz Tunerless Waveguide Receiver Based on AlN SIS Technology", *IEEE Trans. Microwave Theory and Techniques*, Vol. 55, No. 10, pp. 2086-2096, Oct. (2007).
- [8] J. W. Kooi, G. Chattopadhyay, S. Withington, F. Rice, J. Zmuidzinas, C. K. Walker, and G. Yassin, "A Full-Height Waveguide to Thin-Film Microstrip Transition with Exceptional RF Bandwidth and Coupling Efficiency" *Int J. IR and MM Waves*, Vol. 24, No. 3, Sept, (2003).
- [9] Omnisys Instruments AB. August Barks gata 6B, SE-421 32 Västra Frölunda SWEDEN [Online]. Available: <http://www.omnisys.se>
- [10] S. A. Maas, *Microwave Mixers*, 2<sup>nd</sup> Edition.
- [11] J. W. Kooi, R. A. Chamberlin, R. Monje, B. Force, D. Miller, and T. G. Phillips "Balanced Receiver Technology Development" Submitted to IEEE Trans on Terahertz Science and Technology, Jan, (2012).
- [12] M. P. Westig, K. Jacobs, J. Stutzki, M. Schultz, M. Justen, and C. E. Honingh, "Balanced superconductorinsulatorsuperconductor mixer on a 9  $\mu\text{m}$  silicon membrane" *Supercond. Sci. Technol.* Vol. 24, No. 8, Aug, 2011.
- [13] Virginia Diodes Inc., 979 Second Street, S.E. Suite 309, Charlottesville, VA 22902. [Online]. Available: <http://vadiodes.com/>
- [14] E. J. Wilkinson, "An N-way Hybrid Power Divider", *IRE, Microwave Theory and Techniques*, Vol MTT-13, pp. 116-118, Jan. (1960).
- [15] American Technical Ceramics, One Norden Lane, Huntington Station, NY 11746, USA.
- [16] W. Menzel, L. Zhu, K. Wu, and F. Bögelsack "On the design of novel compact broadband planar filters," *IEEE Trans. Microwave Theory Tech.*, Vol. 51, no. 2, pp. 364-370, Feb. (2003).
- [17] J. Ward, F. Rice and J. Zmuidzinas, "Supermix: a flexible software library for high-frequency circuit simulation, including SIS mixers and superconducting components", *10<sup>th</sup> Int. Symp. on Space Terahertz Tech.*, University of Virginia, Charlottesville, VA, Mar. (1999).
- [18] Anritsu Company, "model: MG3690B", 490 Jarvis Drive, Morgan Hill, CA 95037-2809. [Online]. Available: <http://www.anritsu.com/en-US/Products-Solutions/Test-Measurement/RF-Microwave/Signal-Generators>
- [19] Micro-coax Inc., "UFB142A", 206 Jones Blvd., Pottstown, PA 19464-3465. [Online]. Available: <http://www.micro-coax.com>
- [20] Norden Millimeter Inc. "Model: N09-2414", 5441 Merchant Circle, Suite C, Placerville, Ca 95667. [Online]. Available: <http://www.nordengroup.com/index.html>
- [21] Micro Lambda Wireless Inc., "Model: MLFP-41840RS", 46515 Landing Pkwy., Fremont, CA 94538-6421. [Online]. Available: <http://www.microlambdawireless.com>
- [22] Ditom Microwave Inc., "Model: D3I2004", 7592 N. Maroa Ave., Suite 103 Fresno, CA 93711. [Online]. Available: <http://www.ditom.com>
- [23] Marki Microwave Inc., "Model: FX0069", 215 Vineyard Court, Morgan Hill, CA 95037. [Online]. Available: <http://www.markimicrowave.com>
- [24] Pacific Millimeter Products, Inc., "Models: E3, E3+, W3, W3+", 64 Lookout Mountain Circuit, Golden, Co 80401. [Online]. Available: <http://pacificmillimeterproducts.lbu.com/index.html>
- [25] Ansoft Corporation, Four Station Square, Suite 200, Pittsburgh, PA 15219-1119.
- [26] Zen Machine and Scientific Instruments, 1568 Steamboatvalley Rd, Lyons, CO 80540.
- [27] H. Wang, L. Samoska, T. Gaier, A. Peralta, H-H. Liao, Y.C. Leong, S. Weinreb, Y.C. Chen, M. Nishimoto, and R. Lai, "Power-amplifier modules covering 70 – 113 GHz using MMICs," *IEEE Trans. Microwave Theory & Tech.*, Vol. 49, pp. 9 V16, Jan. 2001.
- [28] Th. de Graauw, F. P. Helmich, T. G. Phillips, J. Stutzki, E. Caux, N. D. Whyborn, P. Dieleman, P. R. Roelfsema, H. Aarts, R. Assendorp, R. Bachiller, W. Baechtold, A. Barcia, D. A. Beintema, V. Belitsky, A. O. Benz, R. Bieber, A. Boogert, C. Borys, B. Bumble, P. Caïs, M. Caris, P. Cerulli-Irelli, G. Chattopadhyay, S. Cherednichenko, M. Ciechanowicz, O. Coeur-Joly, C. Comito, A. Cros, A. de Jonge, G. de Lange, B. Delforges, Y. Delorme, T. den Boggende, J.-M. Desbat, C. Diez-González, A. M. Di Giorgio, L. Dubbeldam, K. Edwards, M. Eggens, N. Erickson, J. Evers, M. Fich, T. Finn, B. Franke, T. Gaier, C. Gal, J. R. Gao, J.-D. Gallego, S. Gauffre, J. J. Gill, S. Glenz, H. Golstein, H. Goulooze, T. Günsing, R. Güsten, P. Hartogh, W. A. Hatch, R. Higgins, E. C. Honingh, R. Huisman, B. D. Jackson, H. Jacobs, K. Jacobs, C. Jarchow, H. Javadi, W. Jellema, M. Justen, A. Karpov, C. Kasemann, J. Kawamura, G. Keizer, D. Kester, T. M. Klapwijk, Th. Klein, E. Kollberg, J. Kooi, P.-P. Kooiman, B. Kopf, M. Krause, J.-M. Krieg, C. Kramer, B. Kruizenga, T. Kuhn, W. Laauwen, R. Lai, B. Larsson, H. G. Leduc, C. Leinz, R. H. Lin, R. Liseau, G. S. Liu, A. Loose, I. López-Fernandez, S. Lord, W. Luinge, A. Marston, J. Martín-Pintado, A. Maestrini, F. W. Maiwald, C. McCoey, I. Mehdi, A. Megej, M. Melchior, L. Meinsma, H. Merkel, M. Michalska, C. Monstein, D. Moratschke, P. Morris, H. Müller, J. A. Murphy, A. Naber, E. Natale, W. Nowosielski, F. Nuzzolo, M. Olberg, M. Olbrich, R. Orfei, P. Orleanski, V. Ossenkopf, T. Peacock, J. C. Pearson, I. Peron, S. Phillip-May, L. Piazzo, P. Planesas, M. Rataj, L. Ravera, C. Risacher, M. Salez, L. Samoska, P. Saraceno, R. Schieder, E. Schlecht, F. Schlöder, F. Schmülling, M. Schultz, K. Schuster, O. Siebertz, H. Smit, R. Szczerba, R. Shipman, E. Steinmetz, J. A. Stern, M. Stokroos, R. Teipen, D. Teysier, T. Tils, N. Trappe, C. van Baaren, B.-J. van Leeuwen, H. van de Stadt, H. Visser, K. J. Wildeman, C. K. Wafelbakker, J. S. Ward, P. Wesselius, W. Wild, S. Wulff, H.-J. Wunsch, X. Tielens, P. Zaal, H. Zirath, J. Zmuidzinas, and F. Zwart, "The Herschel-Heterodyne Instrument for the Far-Infrared (HIFI)," *Astronomy & Astrophysics* 518, L6, 2010.
- [29] G. L. Pilbratt, J. R. Riedinger, T. Passvogel, G. Crone, D. Doyle, U. Gageur, A. M. Heras, C. Jewell, L. Metcalfe, S. Ott, and M. Schmidt, "Herschel Space Observatory. An ESA facility for far-infrared and submillimetre astronomy", *Astronomy & Astrophysics* 518, L1, 2010.
- [30] A. R. Kerr, H. Moseley, E. Wollack, W. Grammer, G. Reiland, R. Henry, K.P. Stewart, "MF-112 AND MF-116: Compact Waveguide Loads And FTS Measurements At Room Temperature And 5 K", *NRAO*, Charlottesville, VA, ALMA Memo 494, Mar. 14, 2004.
- [31] Millitech Inc. 29 Industrial Dr. East, Northhampton MA 01060. [Online]. Available: <http://www.millitech.com>
- [32] J. W. Kooi, G. Chattopadhyay, M. Thielman, T.G. Phillips, and R. Schieder, "Noise Stability of SIS Receivers," *Int J. IR and MM Waves*, Vol. 21, No. 5, pp. 689-716, May, 2000.
- [33] R. Schieder, and C. Kramer, "Optimization of Heterodyne Observations using Allan Variance Measurements", *Astron. Astrophys* 373, pp. 746-756, Jul., 2001.
- [34] J. W. Kooi, J. J. A. Baselmans, A. Baryshev, R. Schieder, M. Hajenius, J. R. Gao, T. M. Klapwijk, B. Voronov, and G. Gol'tsman, "Stability of Heterodyne Terahertz Receivers", *Journal of Applied Physics*, Vol. 100, 064904, Sep. (2006).
- [35] P. F. Goldsmith, *QuasiOptical Systems*, Piscataway, NJ: IEEE Press, 1998.
- [36] R. Hesper, B. D. Jackson, A. M. Baryshev, J. Adema, K. Wielinga, M. Kroug, T. Zijlstra, G. Gerlofsma, M. Bekema, K. Keizer, H. Schaeffer, J. Barkhof, F. P. Mena, A. Kooops, R. Rivas, T. M. Klapwijk, and W. Wild, "Design and development of a 600-720 GHz receiver cartridge for ALMA Band 9," in *Proc. 16<sup>th</sup> Int. Symposium on Space Terahertz Technology*, 2005, pp.110.
- [37] D. Maier, A. Barbier, B. Lazareff, and K. F. Schuster, "The Alma Band 7 Mixer", *Proc. 16<sup>th</sup> Int. Symposium on Space Terahertz Technology*, Chalmers, Göteborg, Sweden, May, 2005, S08-02.
- [38] P. D. Strum "Crystal Checker for Balanced Mixers" *IEEE Trans. Microwave Theory and Techniques*, Vol. 2, No. 2, pp. 10-15, Jul. (1954).
- [39] Y. Serizawa, Y. Sekimoto, T. Ito, W. Shan, T. Kamba, N. Satou, M. Kamikura "A 385-500 GHz Balanced Mixer with a Waveguide Quadrature Hybrid Coupler" *17<sup>th</sup> Int. Symp. on Space Terahertz Tech.*, Paris, France, May 10-12. (2006).

temp

## Next Generation of Hot-Electron Bolometer Mixers for Future Heterodyne Missions

S. Ryabchun\*, M. Finkel, I. Tretyakov, A. Maslennikova, N. Kaurova, B. Voronov, and G. Gol'tsman  
*Department of Physics and Information Technology, Moscow State Pedagogical University, Moscow, Russia*

\* Contact: sryabchun@rplab.ru, phone +7-499-246 1202

**Abstract**— At frequencies well above 1 THz the only type of receiver with so far unmatched performance is the hot-electron bolometer (HEB) receiver, which has offered excellent noise characteristics ( $5h\nu/k$ ), a wide gain bandwidth, and also requires much less local oscillator (LO) power than Schottky diodes. In 2009 the Herschel space telescope was successfully launched with an HEB receiver on board for observations in the terahertz range. The next two big projects that will require HEB receivers are SOFIA, a joint project between NASA and the German Aerospace Center (DRL), and Millimetron, a project of the Russian Aerospace Center.

We present the results of the noise temperature, gain bandwidth and absorbed LO power measurements on new generation NbN HEB mixers with simultaneous phonon and diffusion cooling of the hot electrons. At 4.2 K the HEB receiver driven by a 2.5-THz gas discharge laser offered an uncorrected noise temperature of about 600 K ( $5h\nu/k$ ). Such an unprecedentedly low value of the noise temperature results from the reduction of radio frequency loss at the interface between the mixing element and the contact pads due to the use of the *in situ* (without breaking vacuum) deposition technology. We have also found that the noise temperature remains almost constant across an intermediate frequency range of 1-7 GHz. Measurements near the superconducting transition have shown that the mixer time constant decreases with its length, following the predictions of the model of the HEB mixer with simultaneous phonon and diffusion cooling of the hot electrons. The model also predicts, in agreement with experiment, that the LO power required to drive the mixer to the low-noise operating point becomes independent of the mixer length when it becomes shorter than the thermal healing length.

# Performance of a 700 GHz Unilateral Finline SIS Mixer

Boon-Kok Tan\*, Ghassan Yassin\*, Paul Grimes\*, Karl Jacobs† and Christopher Groppi ‡

\*Department of Physics University of Oxford, United Kingdom.

Email: tanbk@astro.ox.ac.uk

†KOSMA, I. Physikalisches Institut, University of Cologne, Germany.

‡ASU School of Earth and Space Exploration PO Box 871404 Tempe, USA.

**Abstract**—We present a novel design and the measured performance for a superconductor-insulator-superconductor (SIS) mixer, operating near the superconducting gap of niobium (Nb), in the frequency range of 600–700 GHz.

A key feature of the mixer design is the employment of a unilateral finline taper to provide smooth transition from the high-impedance waveguide mode to the low-impedance of planar circuits suitable for the operation of SIS tunnel junction. This geometry of the transition can be electromagnetically modelled and optimised to give a short mixer chip with wide RF bandwidth. The finline taper and all the superconducting transmission lines are integrated on-chip and deposited on a 60  $\mu\text{m}$  thick quartz substrate. This results in an extremely simple mixer block design, comprising a feed horn and a straight waveguide section; no backshort or any mechanical tuning structure is needed.

In this paper, we describe the design of the mixer chip, including full electromagnetic simulations of the passive circuits, combined with the heterodyne mixer gain and noise temperature predictions. We have tested the mixer performance from 595 GHz to 702 GHz and measured best receiver noise temperature of 145 K at 600 GHz, corrected for a beam splitter of 75  $\mu\text{m}$  thickness. The need for a thick beam splitter was caused by the lack of sufficient power from the local oscillator (LO) which was optimised between 630–720 GHz and because our mixer was tuned low as a result of larger than designed tunnel junction. Nevertheless, our investigation has demonstrated that superconducting finline mixers work well at high frequencies and have several advantages over other designs, in particular simple mixer block and large substrate for integration of planar circuits.

**Index Terms**—SIS mixers, Submillimeter wave receivers, On-chip integration, Planar circuit

## I. INTRODUCTION

We have previously reported the successful operation of antipodal finline SIS mixers at millimetre and submillimetre frequencies [1], [2], [3], [4], [5] with performance comparable to other mixer designs. These mixers have important advantages as a result of fully integrated transmission lines on a large substrate. This yields a simple mixer block design, without a backshort or mechanical tuners, and plenty of space on the substrate for elegant integrating of planar circuits such as sideband separation or balanced designs.

These advantages become particularly attractive at high frequencies, where tolerances on manufacturing high performance mixer blocks becomes stringent. Antipodal finline

mixers however, employ a long section of gradually overlapping fins to form the microstrip. Since the overlapping fins are only separated by 400 nm of oxide, the manufacturing of this section is difficult and makes the mixer chip rather long. The mixer chip described in this paper employs an alternative design based on a unilateral finline taper which transforms the waveguide into a slotline. Once the width of the slot becomes small enough to lower the impedance, a transition to a microstrip or coplanar waveguide (CPW) becomes straightforward [6]. As we shall see later, this retains all the advantages of the finline mixer mentioned above, and yet yields a much shorter mixer chip which helps to reduce RF losses and provides many more devices on the wafer. Moreover, the simple geometry enables full wave simulation of the mixer chip and removes the difficulty of fabricating the antipodal section.

The design of the unilateral finline mixer chip has already been reported [7], [8], hence it will only be briefly mentioned in this paper. In particular, we will show how to obtain a good match between the RF source and the device over a large range of frequencies. We will also give detailed reporting of the experimental investigation carried out to study the gain and noise temperature performance of the new mixer. The experimental results will be analysed using the CalTech package *SuperMix*<sup>1</sup> [9], in conjunction with the Ansoft High Frequency Structure Simulator (HFSS).

## II. MIXER DESIGN

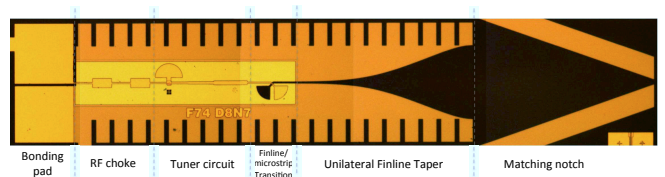


Fig. 1. Overview of a 700 GHz unilateral finline mixer chip with a direct finline-to-microstrip transition on a 60  $\mu\text{m}$  quartz substrate, showing the transition stubs, tuning circuit and the RF choke. The SIS tunnel junction is located at the microstrip below the half-moon stub.

The concept of the unilateral mixer chip design is shown in Fig. 1. It comprises a triangular matching notch in the

<sup>1</sup>A quantum mixing software package written by a Caltech research group to study the behaviour of SIS mixers.

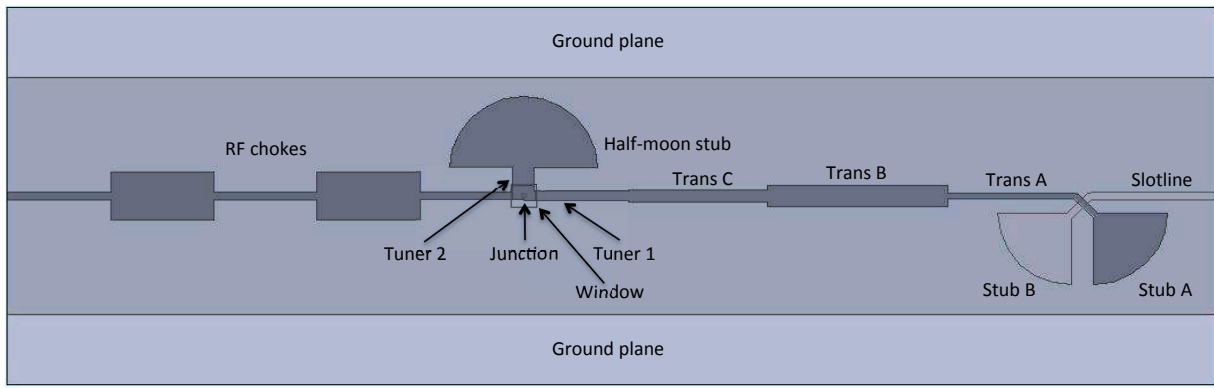


Fig. 2. Enlarged drawing of the planar circuitry consisting the slotline-to-microstrip transition, tuning circuit and the RF chokes.

substrate, a unilateral finline taper, a finline-to-microstrip transition, a tuning circuit, a four-sections RF choke and two IF bonding pads. Our mixers are designed to work with a circular Nb/AIO<sub>x</sub>/Nb SIS tunnel junction with an area of 1 μm<sup>2</sup>. This corresponds to a normal resistance of approximately 20 Ω and junction capacitance of 75 fF. The Nb ground plane film (250 nm thick) which form the finline is separated from the Nb wiring film (400 nm thick) forming the microstrip by a 475 nm silicon monoxide (SiO) insulating layer. The entire structure is deposited on one side of a 60 μm quartz substrate.

The finline taper transforms RF power from the waveguide mode into a slotline over a wide RF bandwidth. The profile of the taper is carefully calculated to obtain the shortest possible taper without limiting the bandwidth [10]. The final design is checked with Ansoft HFSS for a full 3-D electromagnetic simulation, including the effect of superconductivity surface impedance. The impedance of the loaded waveguide is matched to the free space via a simple triangular quarter-wavelength notch, which turns out to be sufficient for quartz substrates. For substrates with higher dielectric constant, multiple notch transformers should be used. The slotline width needs to be tapered to approximately 2.5 μm in order to reduce the characteristic impedance to the values suitable for CPW or microstrip (~20–30 Ω).

The transition from the slotline to microstrip is realised through direct coupling of power across the dielectric layer, as shown in Fig. 2. Both the slotline and the microstrip are connected to 90° radial stubs, each has a radius of approximately λ<sub>g</sub>/4. At the crossing plane, the slotline radial stub appears as an open-circuit, whilst the microstrip radial stub appears as a short-circuit. This combination forces the RF signal to propagate from the slotline to the microstrip with minimum mismatch losses. This direct transition also has all the different layers clearly separated, avoiding potential shorting during fabrication.

The mixer planar transmission lines include 4 components: two inductive strips, a multi-section transformer and an RF choke. The two inductive strips, one in series to the junction and one in parallel, are used to tune out the junction capacitance at two slightly different frequencies. This provides two deep dips in the return loss (see Fig. 3) around the centre

frequency in the matching diagram and thus broadens the RF bandwidth [7], [8]. The multi-section transformer is used to match the impedance of this sub-circuit to the output of the slotline-to-microstrip transition. Finally, an RF choke is placed after the tunnel junction to prevent RF signal from leaking into the IF path.

The various components used in our mixer design were optimised using the Ansoft Designer and HFSS. The profile of the finline taper was calculated using our own software, *FinSynth* [10], which synthesises and analyses the tapers using the Optimum Taper Method (OTM). To verify the heterodyne mixing performance of the designed mixer, we exported the scattering matrix of the various components optimised by HFSS into *SuperMix* to construct a full rigorous mixer model.

### III. MIXER SIMULATIONS

Following the design of the individual components, an HFSS model of the combined circuits was created in order to analyse the complete mixer chip structure. This took into account the effect of all interfaces, making sure the combination of various parts do not introduce anomalies in the final performance of the mixer design. Fig. 3 (a) shows the return loss and insertion loss of the complete RF design generated by HFSS. As can be seen, the electromagnetic simulator predicts an RF bandwidth of ~100 GHz centred at 650 GHz. The power coupled to the junction is better than -0.5 dB within the entire operating bandwidth.

In Fig. 3 (b), we show an example of the calculations of *SuperMix* using the complete mixer model. The mixer chip S-parameters were imported from HFSS. These predictions match well with the HFSS output, verifying the integrity of our mixer design across a wide RF bandwidth. It can be seen that the RF gain and noise temperature are reasonably flat across the band. The simulation in Fig. 3 (b) shows clearly the effects of losses above the superconducting gap voltage, where the mixer conversion gain starts to deteriorate rapidly above 670 GHz.

### IV. DEVICE FABRICATION

Our mixer chips were fabricated at KOSMA, University of Cologne processing facility, by Dr. Paul Grimes. The Nb-AIO<sub>x</sub>-Nb trilayer was deposited at the same time as the rest

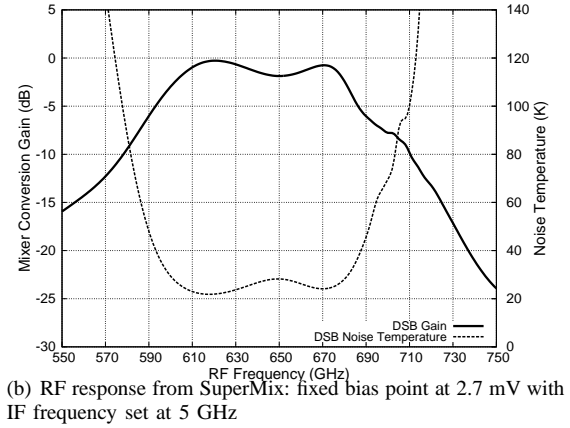
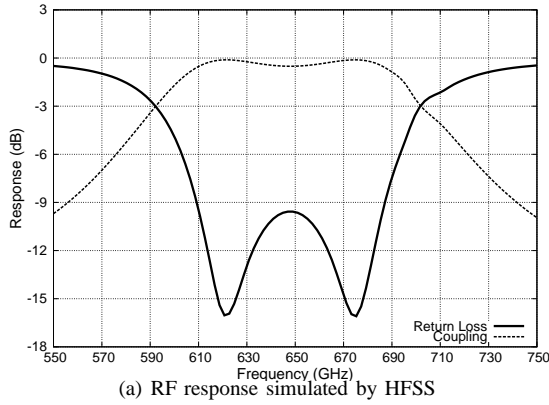


Fig. 3. (a) HFSS simulation showing broadband tuning of about 100 GHz centred at 650 GHz. (b) SuperMix simulation showing the predicted heterodyne performance of the mixer chip.

of the planar transmission lines. The mixer design assumed junctions with current density of  $\sim 14000$  A/cm<sup>2</sup> and an area of  $1 \mu\text{m}^2$ . With these parameters and the tuning circuit dimensions, the mixer would have given good performance from 600 GHz to 700 GHz. However, impedance recovery performed to find the position of the resonance frequency and close inspection of the pumped IV curve, indicated that the tuning was shifted to below 600 GHz. Considering that the normal resistance of the junction came below the design value of  $20 \Omega$ , the low tuning frequency could be explained by a larger than designed tunnel junction area. This conclusion was supported by HFSS simulations which showed that an increase in the junction capacitance narrows down the operating bandwidth and shifts the tuning range downwards in frequency. The *SuperMix* model constructed earlier but with a larger junction area showed similar behaviour to the HFSS model. Unfortunately, our LO did not produce much power below 610 GHz, hence thick beam splitter needed to be used. Due to the broadband tuning design however, the performance did not deteriorate substantially at the high frequency end.

## V. RESULTS AND ANALYSIS

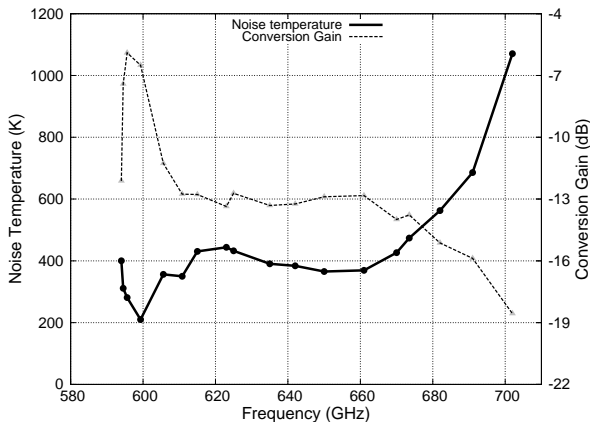


Fig. 4. Measured conversion gain and noise temperature against frequency for the tested unilateral finline mixer over the operating bandwidth.

The Y-factor of the mixer was measured over the frequency range where the LO power was sufficient to pump the device to an acceptable level. In Fig. 4, we show the measured gain and double-sideband (DSB) receiver noise temperature as a function of frequency between 595–702 GHz. These values represent the raw uncorrected data of the receiver, which includes the optical, the transmission line and the IF conversion loss, in particular the losses incurred by the  $75 \mu\text{m}$  beam splitter used to pump the mixer near 600 GHz.

The best noise temperature was measured at 600 GHz,

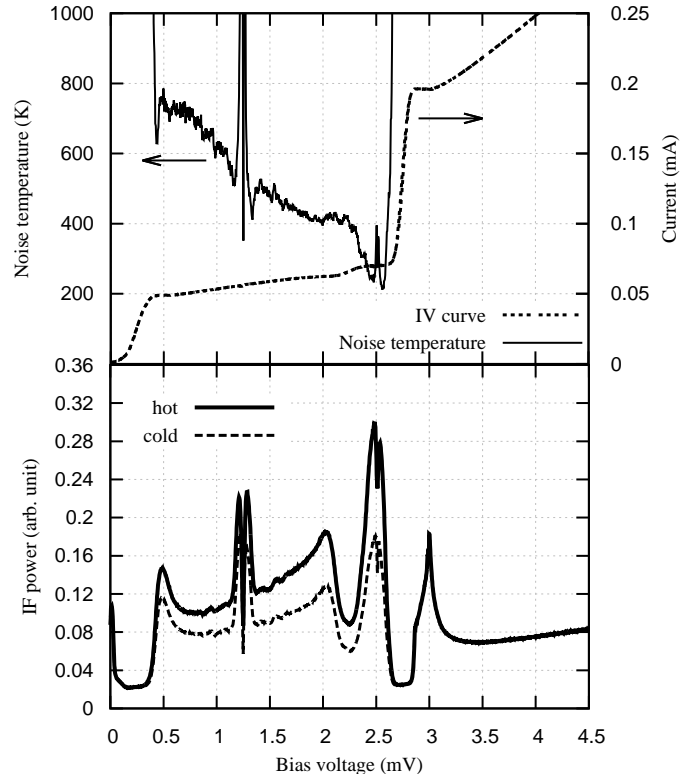


Fig. 5. IV characteristic of the tested mixer irradiated with a 600 GHz RF signal. The noise temperature curve is calculated using the measured hot and cold loaded IF curve.

significantly lower in frequency than the designed tuning central band (650 GHz), for reasons we explained in the previous section. As we have indicated above, we were unable to test the mixer below 600 GHz as a result of lack of LO power. Nevertheless, the tuning double dips are clearly seen in the plot and seem to be located around 600 GHz and 650 GHz. The uncorrected noise temperature below the superconducting gap was measured below 400 K. This is well above what can be achieved by modern mixers at these frequencies but is consistent with the behaviour of an untuned mixer. This argument can be supported by the result at 600 GHz where the noise temperature dropped to 145 K if corrected against the beam splitter thickness, and yet included all the other noise contributions.

In Fig. 5, we have plotted in the upper frame, the pumped IV curve and the noise temperature as a function of the biased voltage at 600 GHz. In the lower frame, we show the hot and cold IF response used to generate the noise temperature plotted above. The Shapiro steps can clearly be seen on top of the photon steps, indicating an incomplete suppression of Josephson pairs current. The Josephson features can be further suppressed by increasing the magnetic field across the junction, but would result in a slight suppression of the superconducting gap. The best noise temperature values are obtained at bias voltage values close to the superconducting gap, which can clearly be seen from the IF conversion plots.

## VI. CONCLUSION

We have designed and tested a 700 GHz unilateral finline SIS mixer in the frequency range of 595–702 GHz. The mixer chip was fully modelled using a combination of HFSS and *SuperMix*. The measured performance agreed with the software predictions but was degraded at the high frequency end by a significantly larger than designed tunnel junction. The best uncorrected receiver noise temperature of 210 K was measured at 600 GHz using a 75  $\mu\text{m}$  thick beam splitter, and remained reasonably low for the entire frequency range. The experimental investigation and data analysis indicate that the unilateral finline mixer should yield noise temperature of 100–150 K between 600–700 GHz. This performance, in addition to the large substrate area and simple mixer block, makes it attractive for designing balanced and single sideband mixers at THz frequencies.

## ACKNOWLEDGMENT

This project is partially funded by AMSTAR+ of RadioNet and an STFC follow-on-fund grant. The D.Phil. study of Boon-Kok Tan at the University of Oxford is funded by the Royal Family of Malaysia under the King's Scholarship.

## REFERENCES

- [1] G. Yassin, R. Padman, S. Withington, K. Jacobs, and S. Wulff, "Broadband 230 GHz finline mixer for astronomical imaging arrays." *Electronics Letters*, vol. 33, pp. 498–500, Mar. 1997.
- [2] G. Yassin, S. Withington, M. Buffey, K. Jacobs, and S. Wulff, "A 350-GHz SIS antipodal finline mixer," *IEEE Transactions on Microwave Theory Techniques*, vol. 48, pp. 662–669, Apr. 2000.

- [3] P. Kittara, "The development of a 700 GHz SIS mixer with Nb finline devices: Nonlinear mixer theory, design techniques and experimental investigation," Ph.D. dissertation, University of Cambridge, United Kingdom, 2002.
- [4] P. Kittara, P. Grimes, G. Yassin, S. Withington, K. Jacobs, and S. Wulff, "A 700-GHz SIS Antipodal Finline Mixer Fed by a Pickett-Potter Horn-Reflector Antenna," *IEEE Transactions on Microwave Theory Techniques*, vol. 52, pp. 2352–2360, Oct. 2004.
- [5] P. Grimes, G. Yassin, K. Jacobs, and S. Withington, "A 700 GHz single chip balanced SIS mixer," in *Sixteenth International Symposium on Space Terahertz Technology, held May 2-4, 2005 at Chalmers University of Technology, Göteborg, Sweden.*, p.46-52, May 2005, pp. 46–52.
- [6] G. Yassin, P. K. Grimes, O. King, and C. E. North, "Waveguide-to-planar circuit transition for millimetre-wave detectors," *Electronics Letters*, vol. 44, no. 14, pp. 866–867, 2008.
- [7] B.-K. Tan, G. Yassin, P. Grimes, J. Leech, K. Jacobs, S. Withington, M. Tacon, and C. Groppi, "A 700 GHz unilateral finline SIS mixer fed by a multi-flare angle smooth-walled horn," W. S. Holland and J. Zmuidzinas, Eds., vol. 7741, no. 1. SPIE, 2010, p. 774110. [Online]. Available: <http://link.aip.org/link/?PSI/7741/774110/1>
- [8] B.-K. Tan, G. Yassin, P. Grimes, and K. Jacobs, "Designs of Broadband Unilateral Finline SIS Mixers Employing 15  $\mu\text{m}$  Silicon-On-Insulator Substrate at THz Frequencies," in *Twenty-First International Symposium on Space Terahertz Technology*, Mar. 2010, pp. 204–211.
- [9] J. Ward, F. Rice, G. Chattopadhyay, and J. Zmuidzinas, "SuperMix: A Flexible Software Library for High-Frequency Circuit Simulation, Including SIS Mixers And Superconducting Elements," in *Proceedings of the Tenth International Symposium on Space Terahertz Technology, held March 16-18, 1999, at the University of Virginia, Charlottesville, VA USA. Organized by University of Virginia, Applied Electrophysics Laboratory. Organizing committee: Thomas W. Crowe and Robert M. Weikle. 1999, p.268*, T. W. Crowe & R. M. Weikle, Ed., Mar. 1999, pp. 268–+.
- [10] C. North, G. Yassin, and P. Grimes, "Rigorous Analysis and Design of Finline Tapers for High Performance Millimetre and Submillimetre Detectors," in *Seventeenth International Symposium on Space Terahertz Technology, held May 10-12, 2006 at Observatoire de Paris, LERMA, Paris, France.*, p.284-287, A. Hedden, M. Reese, D. Santavica, L. Frunzio, D. Prober, P. Piitz, C. Groppi, & C. Walker, Ed., May 2006, pp. 284–287.

# 670 GHz Schottky Diode Based Subharmonic Mixer with CPW Circuits and 70 GHz IF

Goutam Chattopadhyay<sup>1\*</sup>, Erich Schlecht<sup>1</sup>, Choonsup Lee<sup>1</sup>, John Gill<sup>1</sup>, Robert Lin<sup>1</sup>, Seth Sin<sup>1</sup>, Imran Mehdi<sup>1</sup>, William Deal<sup>2</sup>, Kowk K. Loi<sup>2</sup>, Peta Nam<sup>2</sup>, and Bryan Rodriguez<sup>2</sup>

<sup>1</sup> Jet Propulsion Laboratory, California Institute of Technology\*, Pasadena, CA 91109

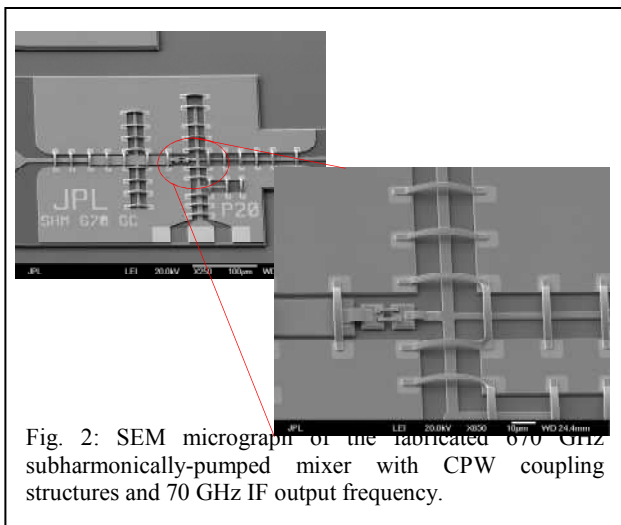
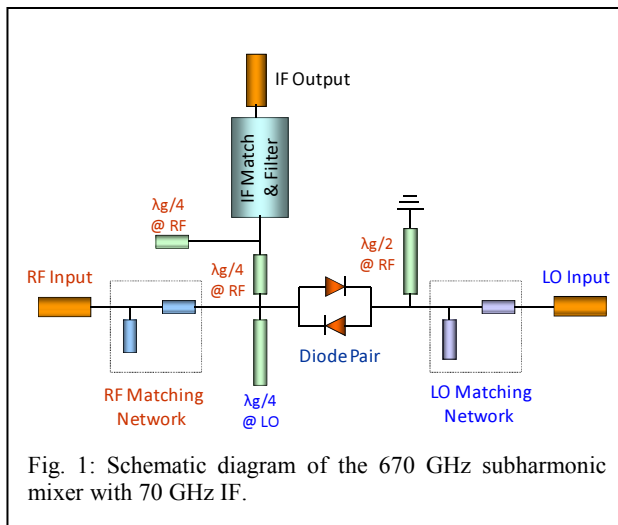
<sup>2</sup> Northrop Grumman Aerospace Systems, 1 Space Park, Redondo Beach, CA 90278

\* Contact: goutam@jpl.nasa.gov, phone +1-818-393-7779

**Abstract**—Gallium Arsenide (GaAs) based sub-harmonically pumped Schottky diode mixers offer a number of advantages for array implementation in a heterodyne receiver system. Since the radio frequency (RF) and local oscillator (LO) signals are far apart, system design becomes much simpler. JPL has developed a planar GaAs Schottky diode process that results in very low parasitic modes that have cutoff frequencies in the tens of terahertz. This technology enables robust implementation of monolithic mixer and frequency multiplier circuits well into the terahertz frequency range. Using optical and e-beam lithography and conventional epitaxial layer design with innovative GaAs membrane topologies and metal beam leads JPL is able to design high performance terahertz circuits with high fidelity.

However, all these mixers use metal waveguide structures for housing. Mixers in metal machined waveguides are difficult to incorporate in integrated multi-pixel heterodyne array receivers for spectroscopic and imaging applications at terahertz frequencies. Moreover, the recent developments of terahertz transistors with sufficient gain provide an opportunity, for the first time, to have integrated amplifiers followed by Schottky diode mixers in a heterodyne receiver at these frequencies. Since the amplifiers are developed on a planar coplanar waveguide (CPW) coupled architecture, it is useful to design the mixers on similar CPW coupled transmission lines to facilitate integrated multi-pixel array implementation.

We have designed and developed a coplanar waveguide (CPW) based subharmonically-pumped mixer working at 670 GHz using GaAs Schottky diodes. The specific system design required an IF frequency of 70 GHz, posing a substantial design challenge. To the best of our knowledge, this is the first time CPW-based Schottky diode mixers have been designed at these frequencies. In this design, shown in Fig. 1, RF and LO signals are coupled to a anti-parallel diode pair using grounded CPW lines on a 25-micron thick GaAs substrate with air-bridges and vias to cancel substrate modes. In this design we used LO and RF matching networks as well as appropriate CPW stubs to short out LO and RF frequencies at appropriate locations. Fig. 2 shows a SEM micrograph of a fabricated device. We measured 16-18 dB of conversion loss for these mixers at 670 GHz RF and 70 GHz IF. Compared to waveguide mixers, these results are inferior. However, we believe that the performance can be improved if we use a low frequency IF output frequency.



Acknowledgement: The research described herein was carried out at the Jet Propulsion Laboratory, California Institute of Technology, Pasadena, CA, under contract with National Aeronautics and Space Administration. This work was supported by the DARPA THz Electronics Program and Army Research Laboratory under the DARPA contract no. HR0011-09-C-0062. The views, opinions, and/or findings contained in this article/presentation are those of the author/presenter and should not be interpreted as representing the official views or policies, either expressed or implied, of the Defense Advanced Research Projects Agency or the Department of Defense.

The authors would like to thank Dr. John Albrecht and Dr. Mark Rosker of DARPA, and Dr. Alfred Hung of ARL.



# Cryogenic MMIC Low Noise Amplifiers for W-Band and Beyond

Lorene A. Samoska *Senior Member, IEEE*, Sarah Church, Kieran Cleary, Andy Fung, Todd C. Gaier, Pekka Kangaslahti, Richard Lai, *Fellow, IEEE*, Judy M. Lau, Gerry Mei, Rodrigo Reeves, Matthew M. Sieth, and Patricia Voll

**Abstract**—We discuss results of low noise amplifier Monolithic Millimeter-wave Integrated Circuits (MMICs), which were designed for specific frequencies in the range of 70-200 GHz. We report on room temperature and cryogenic noise performance for a variety of circuits. The designs utilize Northrop Grumman Corporation's (NGC) 35 nm gate length InP HEMT technology. Some of the lowest reported noise figures to date have been observed with this process at cryogenic temperatures.

**Index Terms**—MMIC LNAs, InP HEMT, cryogenic low noise amplifiers, multi-chip modules

## I. INTRODUCTION

IN this work, we describe our recent results from cryogenic testing of low noise Monolithic Millimeter-wave Integrated Circuit (MMIC) amplifiers for a range of frequencies including 70-200 GHz. The MMICs were fabricated at Northrop Grumman Corporation (NGC) using 35 nm gate length InP HEMT technology on a 50  $\mu\text{m}$  thick InP substrate. Some of the lowest reported cryogenic noise figures for any HEMT amplifiers have been observed with this process, including 22K noise at 85 GHz [1].

Unprecedented noise figures have been observed with this short gate length process, and this is due in part to the improvements made in device performance in terms of extremely high transistor cutoff frequencies. Major breakthroughs have been accomplished in the past few years in InP HEMTs and MMICs, permitting high gain MMIC amplifiers well over 400 GHz [2-5]. A very useful

Manuscript received August 1, 2011. This work was carried out in part by the Jet Propulsion Laboratory, California Institute of Technology, under a contract with the National Aeronautics and Space Administration. This work was sponsored in part by the W. M. Keck Institute for Space Studies. This work was also sponsored in part by NSF grant AST-090585.

Lorene A. Samoska, Andy Fung, Todd C. Gaier, and Pekka Kangaslahti are with the Jet Propulsion Laboratory, California Institute of Technology, Pasadena, CA 91109 USA (phone: 818-354-0849; fax: 818-393-4683; e-mail: lorene.samoska@jpl.nasa.gov).

Sarah Church, Matthew M. Sieth, and Patricia Voll are with Stanford University Department of Physics and Kavli Institute for Particle Astrophysics and Cosmology, Stanford, CA 94305 USA. (email: schurch@stanford.edu).

Judy M. Lau was with Stanford University Department of Physics and Kavli Institute for Particle Astrophysics and Cosmology, Stanford, CA 94305 USA. She is now with Theranos, Palo Alto, CA 94304 USA.

Kieran Cleary, and Rodrigo Reeves are with the California Institute of Technology, Pasadena, CA USA. (email: kcleary@astro.caltech.edu).

Gerry Mei and Richard Lai are with Northrop Grumman Corporation, Redondo Beach, CA 90278 USA (e-mail: Richard.lai@ngc.com).

consequence of these high frequency transistors are their higher gain, and lower noise, found at lower frequencies such as W-Band (75-110 GHz), and G-Band (140-220 GHz).

InP HEMTs have extremely high electron mobilities, particularly when cooled to cryogenic temperatures. A factor of 7-10 improvement in noise temperature has been experimentally observed when cooling these HEMT MMIC amplifiers from 300K to 20K ambient. Advantages of MMIC LNA receivers include operation at 20K, well above the temperature required for superconducting detectors, which are a competing technology used for radio astronomy and remote sensing. Inexpensive cryocooler options are more readily available for 20K cooling as compared to 4K cooling. MMICs are also well-suited for large arrays.

Some examples of MMIC-based receivers incorporating front-end LNAs are the Q/U Imaging Experiment (QUIET) telescope, a 91 element, 90 GHz array which has operated in Chile for study of polarization of the cosmic microwave background radiation in astrophysics [6-8]. The CARMA [9] receivers in Owens Valley, CA utilize cryogenic MMIC amplifier front ends. MMIC amplifiers are being used and proposed for the Green Bank Telescope [10] for spectroscopic studies. The Planck receivers for the Low Frequency Instrument also utilize cryogenic MMIC low noise amplifiers [11].

## II. DESCRIPTION OF CIRCUITS

### A. Individual MMICs

The InP MMIC chip designs utilize microstrip transmission lines, on-chip metal-insulator-metal (MIM) capacitors, thin film resistors, and thru-substrate vias, and employ a common-source configuration. We will report on data from MMIC amplifiers having two and three gain stages. We packaged several MMIC amplifiers in waveguide housings and tested them at room temperature and at 20K ambient. A W-band design having two-stages of gain is shown in Fig. 1. Typical room temperature gain for this chip is about 10-15 dB from 75-105 GHz. A three-stage design reported in [1] has as much as 30 dB of gain at room temperature from 60-90 GHz. A third amplifier developed for G-Band was described in [12, 13], and has 15-20 dB of gain from 140-220 GHz. The G-Band amplifier chip photo is shown in Fig. 2.

### B. Multi-Chip MMIC Receiver Module

We have also designed and fabricated a multi-chip MMIC receiver module for 140-180 GHz [14, 15]. The heterodyne module includes a waveguide RF input, MMIC LNAs, a GaAs

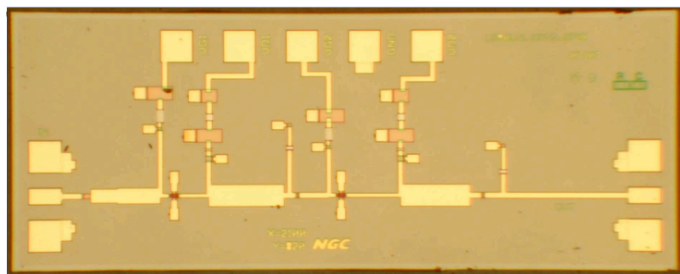


Fig. 1. MMIC LNA designed for W-Band having two gain stages in a common source configuration.

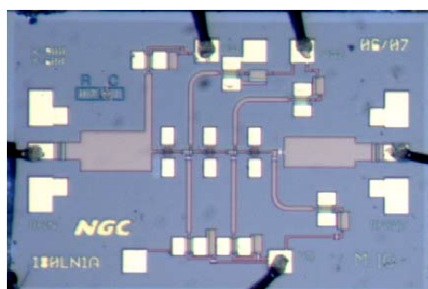


Fig. 2. MMIC LNA designed for G-Band having three gain stages (from [13]).

Schottky diode subharmonic mixer chip, and bandpass filters in a miniature compact waveguide housing suitable for scaling to large arrays. A photo showing the interior of the module, with the chip cavities, LNAs, mixer, filter, DC bias boards, DC feedthrus, and waveguide inputs and outputs is shown in Fig. 3. The split-block module is shown in Fig. 4, with the fully assembled multichip receiver module shown with a penny for scale. Cryogenic receivers built with these amplifiers may be useful for observations of the polarization of the cosmic microwave background and for spectroscopic surveys.

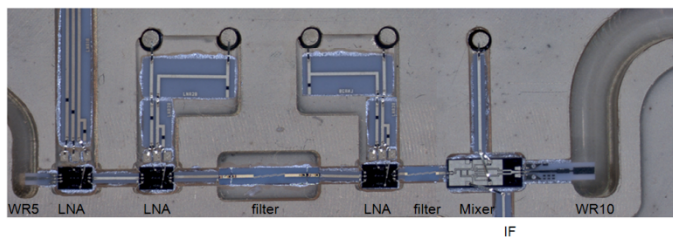


Fig. 3. Multi-chip MMIC module for G-Band, interior showing chips and waveguides.

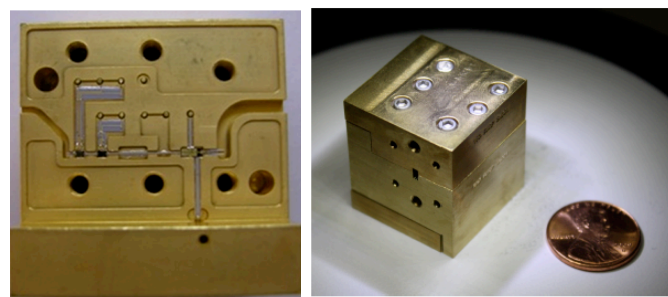


Fig. 4. Multi-chip MMIC Module for G-Band, split-block view at left, and fully assembled module with penny for scale at right.

### III. MEASURED RESULTS

#### A. Individual MMIC Modules: Results

We have performed room temperature and cryogenic noise testing of the MMIC modules using the Y-factor method, with a room temperature and a 77K load made of Eccosorb AN-72 (from Emerson & Cummings). In W-Band, we have measured the two-stage MMIC LNA of Fig. 1 to have a noise temperature of typically 220K-250K at room temperature. In the case of one LNA having HEMTs with an InAs channel composition, a minimum noise of 180 K is observed at 95 GHz, with gain greater than 15 dB up to 103 GHz. The data are shown in Fig. 5.

The schematic of the cryogenic test set, indicating the MMIC LNA modules inside a dewar at 20K, is shown in Fig. 6. The horn is separated from the load by a 1 mil thick mylar window. In addition to cryogenic measurements with a 295K and 77K load using the horn and window, we also employed a second method using a heated load, cooled in the dewar and having a hot and cold temperature of 50K and 30K, respectively. This was done to ensure that the noise power of the 295K load was not causing saturation effects in the LNAs in the horn and window method. Noise powers were measured after amplifying the signal from the mixer with IF amplifiers and a bandpass filter with a power meter. Both measurement methods agreed to within a few K.

When the two-stage LNA (having  $\text{In}_{0.75}\text{Ga}_{0.25}\text{As}$  channel HEMTs) of Fig. 1 was cooled to 20K ambient temperature, we measured a receiver noise temperature  $T_{\text{rec}}$  of 36K at 90 GHz. Comparison between MMICs having  $\text{In}_{0.75}\text{Ga}_{0.25}\text{As}$  channel HEMTs and InAs channel HEMTs for the same chip design showed improvement in noise temperature ( $T_{\text{amp}}$ ) in the InAs case with less than 40K from 76-101 GHz as shown in Fig. 5. We calibrated our backend noise contribution to the LNA noise, and calculated the corrected amplifier noise temperature to be 27K at 90 GHz. The data from the two-stage LNAs, having both InAs channel HEMTs, and  $\text{In}_{0.75}\text{Ga}_{0.25}\text{As}$  channel HEMTs, are plotted along with the data from the three-stage amplifier of Ref. 1, and the results are shown in Fig. 7.

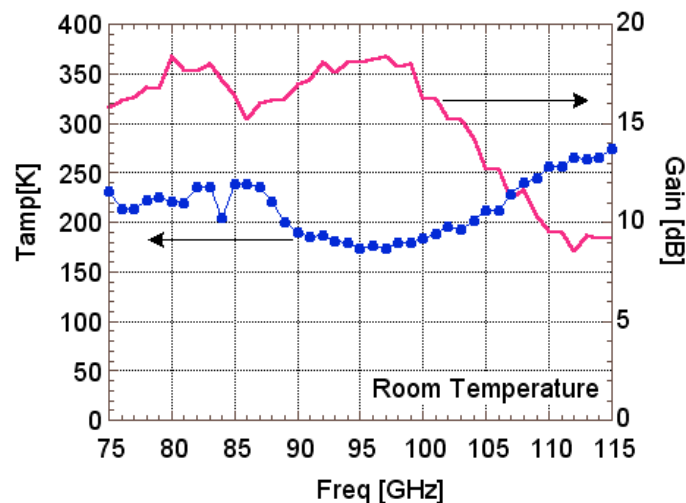


Fig. 5. Room temperature noise and gain measurement of the W-Band LNA shown in Fig. 1, having an InAs channel composition in the HEMTs.

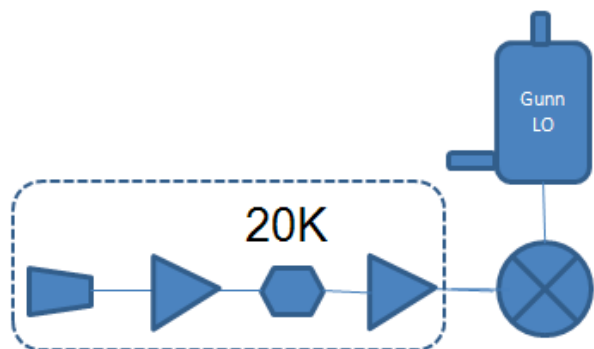


Fig. 6. Schematic of test set for noise figure measurements. Horn, LNA, cryogenic low-loss isolator, and second LNA are cooled to 20K in a dewar, while a room temperature mixer (with Gunn source for local oscillator) is used for down-conversion of the power signal in Y-factor measurements.

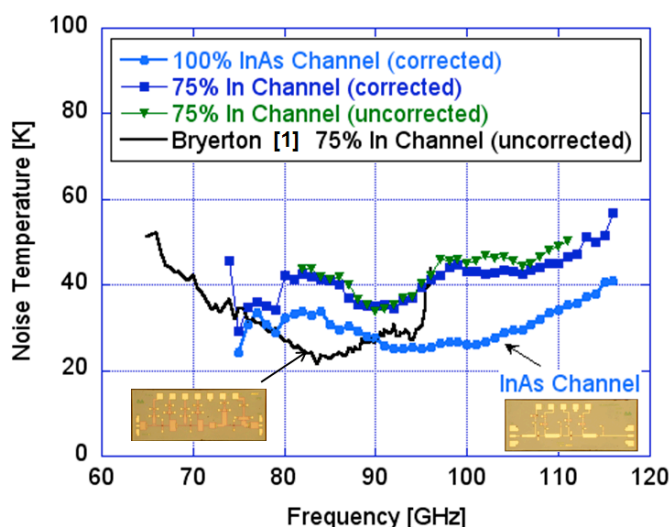


Fig. 7. Comparison of noise temperature in W-Band of different LNA blocks when cooled to 20K ambient temperature. Included are the design of Fig. 1 fabricated using InAs channel HEMTs, as well as  $\text{In}_{0.75}\text{Ga}_{0.25}\text{As}$  channel HEMTs. Also included are the data from Bryerton *et al.* in Ref. 1 using  $\text{In}_{0.75}\text{Ga}_{0.25}\text{As}$  channel HEMTs.

In addition to the W-Band results, we also measured the G-Band amplifier module discussed in Ref. 11, having the chip shown in Fig. 2. For the test, as in the schematic of Fig. 6, two LNAs were cooled in the dewar to 20K, with a WR5 horn in front of the first LNA. In this case, no low-loss cryogenic isolator was available between the LNAs. Using the same cryogenic test dewar with a 295K and 77K load, and 1 mil thick mylar window, we downconverted the noise power with an appropriate mixer for G-Band. The noise temperature of the G-Band amplifier of Fig. 2 is shown in Fig. 8. The amplifier noise was corrected for the backend noise contribution. We observed a minimum corrected amplifier noise temperature of 63K at 164 GHz. This result represents the lowest noise temperature obtained for a MMIC LNA module when cooled to 20K in G-Band to date.

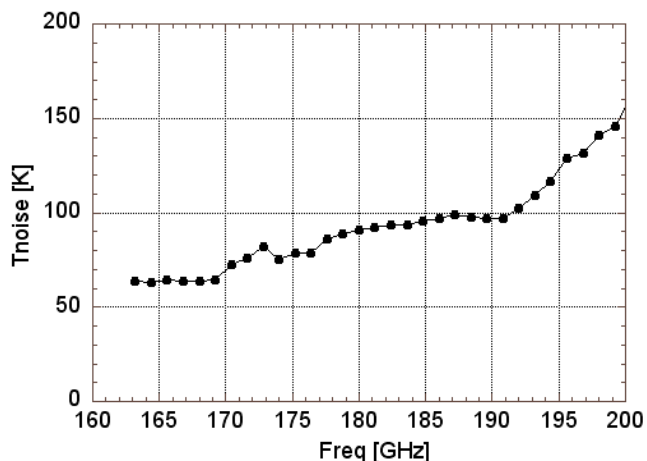


Fig. 8. Measured cryogenic noise of G-Band LNA from reference [12, 13].

### B. Multi-Chip MMIC Receiver Module: Results

A photo of the G-Band multi-chip receiver module, described in Figs. 3 and 4, is shown in Fig. 9, with the local oscillator applied at the WR10 waveguide port, and a WR5 horn at the input. At room temperature, we have observed a receiver noise temperature of as low as 390K at 166 GHz. We have also performed cryogenic testing at 20K using a dewar with a 1 mil mylar window, and a 295K and 77K external load. Results from cryogenic testing indicate record performance for the HEMT MMIC superheterodyne receiver module: we have observed a receiver noise temperature of 58K at 166 GHz and less than 70 K between 162-174 GHz [15]. In Fig. 10, we plot the noise of the G-Band superheterodyne receiver module, alongside the G-Band amplifier module of Fig. 8 (which was corrected for backend noise contribution). The superheterodyne receiver module was not corrected for backend noise contribution from the mixer, since it contains an integrated mixer chip inside the module. The results of the two plots compare favorably, indicating that the receiver module has sufficient LNA gain to overcome the conversion loss of the mixer inside. The amplifier-only module has lower noise above 180 GHz than the multi-chip

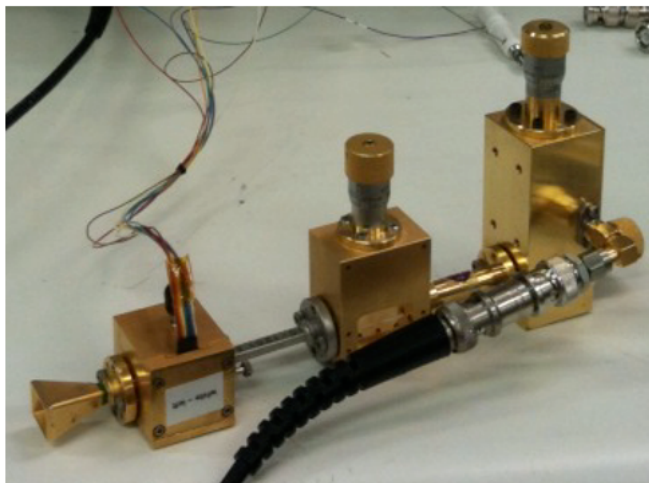


Fig. 9. Photo of the G-Band receiver module, with local oscillator applied at room temperature.

receiver module. This is due to the bandpass filter in the multi-chip receiver module, which was intended to block out the  $H_2O$  line at 183 GHz for future measurements of the cosmic microwave background radiation.

Both of the G-Band modules contained MMIC LNAs having  $In_{0.75}Ga_{0.25}As$  channel HEMTs. We hope to achieve even better performance using InAs channel HEMTs. Testing is currently underway of new MMIC amplifiers having InAs channel HEMTs.

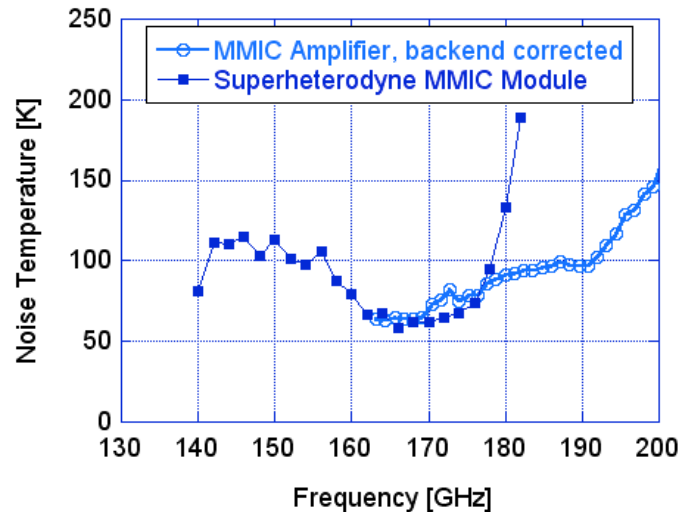


Fig. 10. Cryogenic noise performance vs. frequency for the multi-chip MMIC super heterodyne receiver module, plotted with the data for a single LNA module (from Fig. 8), obtained at 20K ambient temperature. A minimum noise temperature of 62K is achieved at 164 GHz.

#### IV. CONCLUSION

In summary, we have designed several LNAs to cover various parts of W-Band. Wafers with InAs channel HEMTs and those with  $In_{0.75}Ga_{0.25}As$  channel HEMTs were fabricated alongside, and we have measured identical chip designs from both wafers. A noise temperature of less than 40K is possible across W-Band with a two-stage LNA design, and a minimum noise in the mid-20K range was observed experimentally. In addition, we have tested a G-Band LNA and a multichip G-Band receiver module. Both G-Band modules obtained record performance of approximately 62K at 164 GHz.

#### ACKNOWLEDGMENT

We would like to acknowledge the expertise of Ms. Mary Soria and Ms. Heather Owen for amplifier and module micro-assembly. We would also like to thank Drs. Sander Weinreb and Anthony Readhead of the California Institute of Technology, Drs. Michael Seiffert and Charles Lawrence of the Jet Propulsion Laboratory, and Dr. Eric Bryerton of the National Radio Astronomy Observatory for helpful discussions.

#### REFERENCES

- [1] E. W. Bryerton, X. B. Mei, Y. M. Kim, W. Deal, W. Yoshida, M. Lange, J. Uyeda, M. Morgan, and R. Lai, "A W-Band Low Noise Amplifier with 22K Noise Temperature," *2009 IEEE MTT-S Int. Microwave Symp. Dig.*, June 2009, Charlottesville, VA, pp. 681-684.
- [2] L. Samoska, A. Fung, D. Pukala, P. Kangaslahti, R. Lai, S. Sarkozy, X. B. Mei, and G. Boll, "On-Wafer Measurements of S-MMIC Amplifiers from 400-500 GHz," *2011 IEEE MTT-S Int. Microw. Symp. Dig.*, Baltimore, MD, June, 2011.
- [3] W. R. Deal, K. Leong, X. B. Mei, S. Sarkozy, V. Radisic, J. Lee, P. H. Liu, W. Yoshida, J. Zhou, and M. Lange, "Scaling of InP HEMT Cascade Integrated Circuits to THz Frequencies," *IEEE Compound Semiconductor IC Symp.*, Oct., 2010, pp. 1-4.
- [4] A. Tessmann, A. Leuther, R. Loesch, M. Seelmann-Eggebert, H. Massler, "A Metamorphic HEMT S-MMIC Amplifier with 16.1 dB Gain at 460 GHz," *IEEE Compound Semiconductor IC Symp.*, Monterey, CA, Oct., 2010, pp. 1-4.
- [5] L. A. Samoska, "An Overview of Solid State Integrated Circuit Amplifiers in the Submillimeter-wave and THz Regime," to appear in *IEEE Transactions on Terahertz Science and Technology*, Vol. 1, Sept. 2011.
- [6] C. Bischoff, A. Brizius, I. Buder, Y. Chinone, K. Cleary, R. N. Dumoulin, A. Kusaka, R. Monsalve, S. K. Ness, L. B. Newburgh, R. Reeves, K. M. Smith, I. K. Wehus, J. A. Zuntz, J. T. L. Zwart, L. Bronfman, R. Bustos, S. E. Church, C. Dickinson, H. K. Eriksen, P. G. Ferreira, T. Gaier, J. O. Gundersen, M. Hasegawa, M. Hazumi, K. M. Huffenberger, M. E. Jones, P. Kangaslahti, D. J. Kapner, C. R. Lawrence, M. Limon, J. May, J. J. McMahon, A. D. Miller, H. Nguyen, G. W. Nixon, T. J. Pearson, L. Piccirillo, S. J. E. Radford, A. C. S. Readhead, J. L. Richards, D. Samteben, M. Seiffert, M. C. Shepherd, S. T. Staggs, O. Tajima, K. L. Thompson, K. Vanderlinde, R. Williamson, and B. Winstein, "First Season QUIET Observations: Measurements of CMB Polarization Power Spectra at 43 GHz in the Multipole Range  $25 \leq l \leq 475$ ," submitted to *Astrophysical Journal*, 2010.
- [7] Todd Gaier, Charles R. Lawrence, Michael D. Seiffert, Mary M. Wells, Pekka Kangaslahti, Douglas Dawson "Amplifier arrays for CMB polarization," *New Astronomy Reviews*, 47, 1167 (2003).
- [8] P. Kangaslahti, T. Gaier, M. Seiffert, S. Weinreb, D. Harding, D. Dawson, M. Soria, C. Lawrence, B. Hooberman, A. Miller, "Planar Polarimetry Receivers for Large Imaging Arrays at Q-band", *IEEE MTT-S, International Microwave Symposium Digest*, 89 (2006).
- [9] CARMA website: <http://www.mmarray.org/>
- [10] Green Bank Telescope website: <http://www.gb.nrao.edu/>
- [11] Bersanelli, M., ..., Seiffert, M., et al. (113 co-authors), "Planck pre-launch status: Design and description of the Low Frequency Instrument," *Astronomy & Astrophysics*, 520, A4 (2010).
- [12] P. Kangaslahti, D. Pukala, T. Gaier, W. Deal, X. Mei, R. Lai, "Low Noise Amplifier for 180 GHz Frequency Band," *2008 IEEE MTT-S Int. Microwave Symp. Dig.*, June 2008, Charlottesville, VA, pp. 681-684.
- [13] P. Kangaslahti, "Recent developments in 180 GHz MMIC LNA and receiver technology" *Proc. 11th Specialist Meeting on Microwave Radiometry and Remote Sensing of the Environment MicroRad2010*, March, 2010, pp 272–275.
- [14] P. Voll, J. M. Lau, M. Sieth, S. E. Church, L. A. Samoska, P. Kangaslahti, T. C. Gaier, D. Van Winkle, and S. Tantawi, "Development of a 150 GHz MMIC Module Prototype for Large-Scale CMB Radiation Experiments," *Proc. of SPIE Millimeter, Submillimeter, and Far-Infrared Detectors and Instrumentation for Astronomy V*, Vol. 7741, June, 2010, San Diego, CA, pp. 77412J-77412J-10.
- [15] P. Voll, L. Samoska, S. Church, J. Lau, M. Sieth, T. Gaier, P. Kangaslahti, M. Soria, S. Tantawi, and D. Van Winkle, "A G-Band Cryogenic MMIC Heterodyne Receiver Module for Astrophysical Applications," to be presented at the *European Microwave Conference*, Manchester UK, Oct., 2011.

# Upgrade of EMIR's Band 3 and Band 4 Mixers

D. Maier, J. Reverdy, D. Billon-Pierron, and A. Barbier

**Abstract**— The Eight Mixer Receiver (EMIR) is a multi-band millimeter wave receiver installed since 2009 at the 30m telescope of the Institut de RadioAstronomie Millimétrique (IRAM) at Pico Veleta in Spain. In autumn 2011, Band 3 and Band 4 will be equipped with state-of-the-art sideband-separating mixers with 8 GHz IF bandwidth.

For Band 3 a sideband-separating mixer has been developed within the European project AMSTAR+ in order to replace the currently employed single-sideband mixer. The new mixer has a twice as large IF bandwidth than the current one thus doubling the continuum sensitivity of the receiver.

The mixer currently installed in Band 4 will simply be upgraded to 8 GHz IF bandwidth by changing its IF components.

**Index Terms**—millimeter wave receiver, sideband-separating mixers, SIS mixers, wide IF band

## I. INTRODUCTION

IN spring 2009 IRAM installed its Eight Mixer Receiver (EMIR) at the 30m telescope at Pico Veleta in Spain [1]. Since then EMIR observes successfully in four frequency bands centered around 100, 150, 230, and 305 GHz, respectively. The characteristics of its mixers are summarized in Table 1.

TABLE 1: CHARACTERISTICS OF EMIR MIXERS.

Band	Frequency	Mixer Type	IF Band
1	83–116 GHz	2SB	4–12 GHz
2	129–174 GHz	SSB	4–8 GHz
3	200–268 GHz	SSB	4–8 GHz
4	260–354 GHz	2SB	4–8 GHz

Bands 2 and 3 still employ single-sideband mixers using a movable backshort in the waveguide behind the mixer chip to tune out the image sideband and delivering one IF output of 4–8 GHz [2], [3], whereas current state-of-the-art receivers employ sideband-separating (2SB) mixers with two IF outputs and twice as large IF bands [4], [5]. EMIR's Band 1 is already equipped with such a sideband-separating mixer, which has been developed within the European project AMSTAR [6], [7]. Band 4 finally, is equipped with a sideband-separating mixer with 4–8 GHz IF bandwidth, which has been originally developed for the ALMA Band 7 cartridge [8] and tuned down

Manuscript received July 31, 2011. This work was supported in part by the European Union through the Radionet program.

D. Maier, J.Reverdy, D. Billon-Pierron, and A. Barbier are with the Institut de RadioAstronomie Millimétrique, Saint Martin d'Hères, France (corresponding author: +33 4 76 82 49 16; fax: +33 4 76 51 59 38; e-mail: maier@iram.fr).

in frequency to join the Band 3 frequency range.

## II. BAND 3 UPGRADE

### A. 2SB Mixer Assembly

Within the European project AMSTAR+, follow-up project of AMSTAR, we designed a 230 GHz sideband-separating mixer to be employed in focal plane array receivers [9]. For this mixer RF quadrature coupler, two LO couplers, LO splitter as well as two DSB mixers have been combined into one unit and realized as one E-plane split-block (see Figure 1). Since this mixer has been designed having in view its future use for a focal plane array receiver, the IF outputs have been placed at the back of the mixer block, allowing the signal path to go straight through the block, so that the mixers can be plugged onto a feedhorn array and be followed in-line by the IF chain. The LO input has been moved to the top of the mixer block by adding an H-bend into the LO injection path [10]. For a detailed description of the design of the waveguide components see [9].

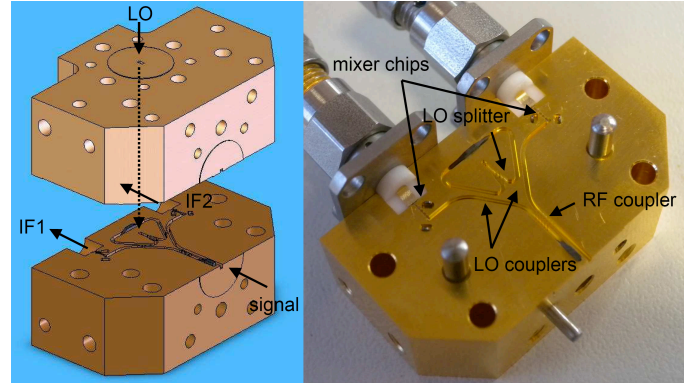


**Figure 1: Left: Schematic view of the E-plane split-block combining waveguide couplers, LO splitter, and DSB mixers. Right: Photograph of one half of the split-block with mounted loads, mixer chips, and IF connectors.**

The distance of the IF outputs has been adjusted to the inputs of the employed IF coupler [11], so that the hybrid can be mounted directly onto the mixer block.

### B. DSB Mixer

A detailed description of the DSB mixer design is given in [9]. The mixing element is a superconductor-insulator-superconductor (SIS) tunnel junction, which is deposited together with a superconducting circuit onto a quartz substrate. The role of this circuit is to compensate the junction's capacitance and to provide a match to the RF input and the IF

output. Figure 2 shows a photograph of the mixer chip mounted into the RF coupler/mixer block. The dimensions of such a chip are  $2.4 \times 0.26 \times 0.08$  mm<sup>3</sup>. These devices are fabricated by IRAM's SIS group [12].

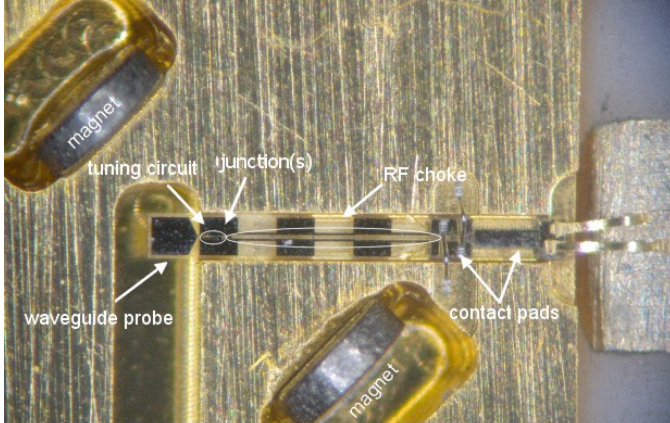


**Figure 2: Mixer chip mounted into the RF coupler/mixer block.**

A close-up of the tuning structure is shown in Figure 3. A parallel inductance consisting of a coplanar waveguide compensates the capacitance of the  $10 \mu\text{m}^2$  junction and the following capacitance provides the virtual ground. The impedance of this structure is matched to the probe impedance by a quarter-wavelength transformer.

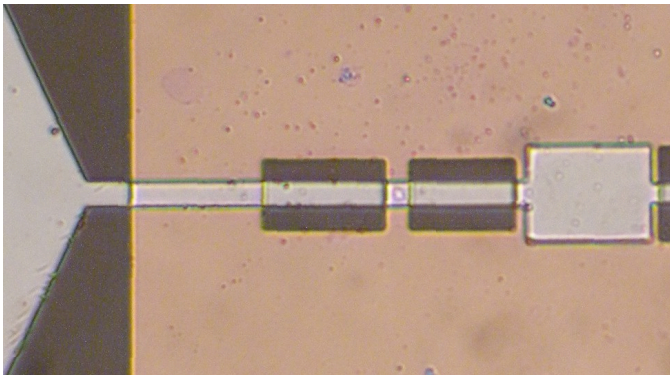


**Figure 3: Close-up of the tuning structure.**

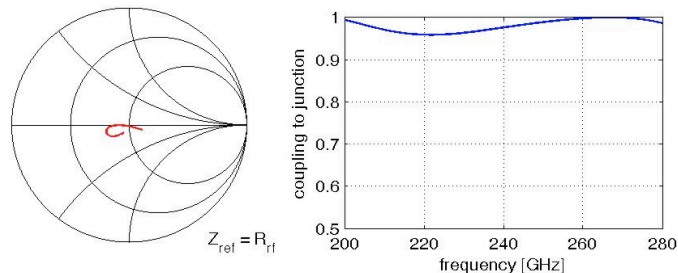


**Figure 4: Left: Embedding impedance of the junction for frequencies between 200 and 280 GHz. Right: Fraction of power coupled to the junction.**

The achieved matching to the junction is quite homogenous over the whole frequency range as can be seen by the junction's embedding impedance plotted in the Smith chart in Figure 4 (left). The power coupled to the junction lies above

96% (see Figure 4, right).

### C. Mixer Performances

Two mixers for the installation on-site as well as spare mixers have been fabricated and fully characterized by measuring noise temperatures and image rejections in the 4–12 GHz IF band for LO frequencies between 210 and 270. The results of one mixer are shown in Figure 5. As can be seen, the achieved noise temperatures are very good over the whole frequency range. The obtained image rejection is almost always better than  $-10$  dB.

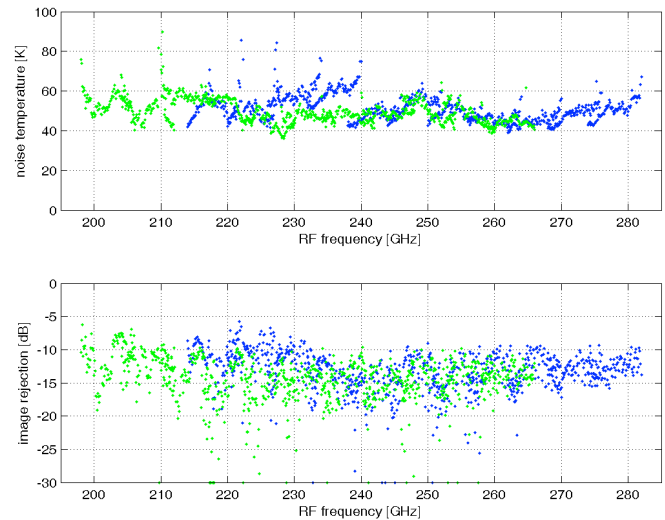


**Figure 5: Noise (above) and image rejection (below) of one Band 3 sideband-separating mixer measured in the IF band for LO frequencies between 210 and 270 GHz. LSB measurements are plotted in green, USB results are shown in blue.**

## III. BAND 4 UPGRADE

### A. Current Mixer

The mixer currently installed in Band 4 of EMIR is a modification of a mixer initially designed for the ALMA Band 7 cartridge [8], [13]. Since this mixer has been designed having in view a small series production, a modular approach has been chosen, which allows testing of the different parts prior to integration. Only the waveguide couplers have been realized as one E-plane split-block, so that the block as a whole can be characterized using a vector network analyzer. The DSB mixers are separate units, which can be tested individually and which are then selected according to their performances for integration into a 2SB mixer. The employed IF hybrid coupler is commercially available [14]. A photograph of a Band 4 2SB mixer assembly is shown in Figure 6.

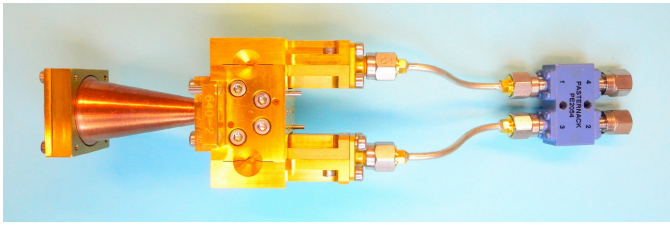


**Figure 6: Photograph of the EMIR Band 4 Mixer.**

The ALMA mixer has been adapted to the lower frequency range of Band 4 by changing the RF coupler and increasing the size, and thus the capacitance, of the junctions.

### B. Upgrade to 4-12 GHz IF Band

As 8 GHz IF bandwidth is more and more attractive, we tested this mixer for the larger IF band. These tests have been carried out with a mixer of the ALMA Band 7 production by replacing the commercial IF coupler [14] with the same coupler used for the Band 3 mixer and developed for frequencies from 4–12 GHz [11].

The conclusion of these mixer tests was that the existing Band 4 receivers could be easily upgraded to the twice as large IF band by simply changing its IF components.

And since the new Band 3 mixers work up to at least 280 GHz, there is no need anymore for the use of the frequency shifted Band 4 mixers. The new Band 4 mixers will therefore work for the initially designed frequency range of 275–373 GHz with a 4–12 GHz IF band.

### C. Mixer Performances

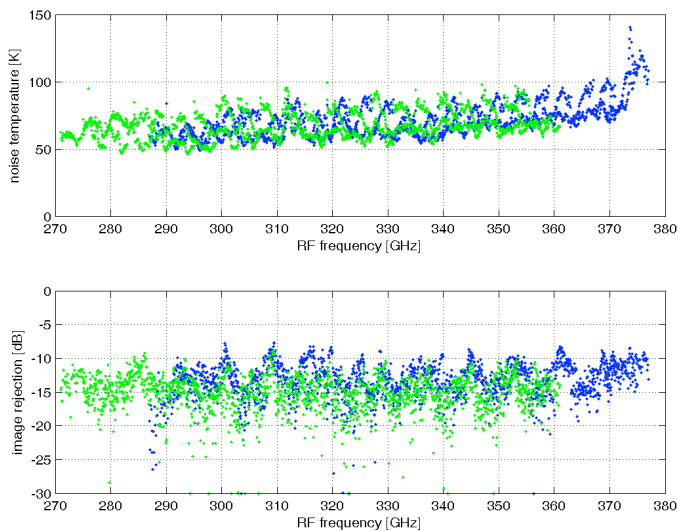


**Figure 7: Noise (above) and image rejection (below) of one Band 4 sideband-separating mixer measured in the IF band for LO frequencies between 283 and 365 GHz. LSB measurements are plotted in green, USB results are shown in blue.**

Mixers have been fabricated and characterized. Just as for Band 3, noise temperatures and image rejections have been measured in the 4–12 GHz IF band for LO frequencies between 283 and 365 GHz. The achieved noise temperatures

over the RF band are very good as can be seen in the plot in Figure 7, above. The obtained image rejections are quite below  $-10$  dB (see Figure 7, below).

## IV. CONCLUSION

A sideband-separating mixer with wide IF band has been successfully developed for EMIR Band 3. It covers an RF frequency range of 200–280 GHz and shows very good noise temperatures over the whole RF band. Achieved image rejections are better than  $-10$  dB. This mixer increases the Band 3 frequency range and replacing the old SSB mixer with 4 GHz IF band by this mixer will double the continuum sensitivity of the receiver and increase the flexibility of line observations.

The current Band 4 mixer has been upgraded to larger IF bandwidths and its RF frequency range has been shifted to higher frequencies. The new mixers will cover RF frequencies from 275 to 365 GHz with an IF band of 4–12 GHz.

The upgrade of both bands will take place in autumn 2011 allowing observations with the improved system in winter 2011/2012.

## REFERENCES

- [1] M. Carter et al., “The EMIR Multi-band mm-Wave Receiver for the IRAM 30m Telescope”, to be published
- [2] A. Navarrini and B. Lazareff, “Design of a 129–174 GHz SSB SIS mixer for Band 2 of New Generation Receiver of IRAM PdB Interferometer” in Proc. 14th Int. Symp. On Space Terahertz Technology, pp. 450-452, 22-24 April 2003, Tucson, Arizona, USA
- [3] D. Maier, S. Devoluy, M. Schicke, and K.F. Schuster, “230 GHz SSB SIS mixer for band 3 of the new generation receivers for the Plateau de Bure interferometer” in Proc. 16th Int. Symp. On Space Terahertz Technology, pp. 33-36, 2-4 May 2005, Göteborg, Sweden
- [4] A.R. Kerr, S.-K. Pan, E.F. Lauria, A.W. Lichtenberger, J. Zhang, M.W. Pospieszalski, N. Horner, G.A. Ediss, J.E. Effland, R.L. Groves, “The ALMA Band 6 (211–275 GHz) Sideband-Separating SIS Mixer-Preamp” in Proc. 15th Int. Symp. On Space Terahertz Technology, pp. 55-61, 27-29 April 2004, Northampton, Massachusetts, USA
- [5] F.P. Mena, J.W. Kooi, A.M. Baryshev, C.F. Lodewijk, T. Zijlstra, R. Hesper, G. Gerlofsma, T.M. Klapwijk, and W. Wild, “Design and Performance of a 600–720 GHz Sideband-Separating Receiver Using AlOx und AlN SIS Junctions”, IEEE-MTT, vol. 59, pp. 166-177, 2011
- [6] D. Maier, D. Billon-Pierron, J. Reverdy, and M. Schicke, “100 GHz sideband separating mixer with wide IF band” in Proc. 18th Int. Symp. On Space Terahertz Technology, pp. 260-263, 21-23 March 2007, Pasadena, California, USA
- [7] D. Maier, D. Billon-Pierron, J. Reverdy, and M. Schicke, “100 GHz sideband separating mixer with wide IF band: First Results” in Proc. 19th Int. Symp. On Space Terahertz Technology, pp. 93-96, 28-30 April 2008, Groningen, The Netherlands
- [8] D. Maier, A. Barbier, B. Lazareff, and K.F. Schuster, “The ALMA band 7 mixer” in Proc. 16th Int. Symp. On Space Terahertz Technology, pp. 428-431, 2-4 May 2005, Göteborg, Sweden
- [9] D. Maier, “230 GHz sideband-separating mixer array” in Proc. 20th Int. Symp. On Space Terahertz Technology, pp. 14-18, 20-22 April 2009, Charlottesville, Virginia, USA
- [10] A.R. Kerr, “Elements for E-Plane Split-Block Waveguide Circuits”, ALMA Memo 381
- [11] I. Malo-Gomez, J.D. Gallego-Puyol, C. Diez-Gonzales, I. López-Fernández, C. Briso-Rodríguez, “Cryogenic Hybrid Coupler for Ultra-Low-Noise Radio Astronomy Balanced Amplifiers”, IEEE MTT-57, pp. 3239-3245, 2009
- [12] I. Péron, P. Pasturel, and K.F. Schuster, “Fabrication of SIS junctions for space borne submillimeter wave mixers using negative resist e-beam lithography”, IEEE Trans. Appl. Supercond., Vol. 11, pp. 377-380, March 2001

- [13] S. Mahieu, B. Lazareff, D. Maier, M. Carter, AL. Fontana, and S. Claude, "The Band 7 Cartridge (275-373 GHz) for ALMA" in Proc. 16th Int. Symp. On Space Terahertz Technology, pp. 99-104, 2-4 May 2005, Göteborg, Sweden
- [14] Pasternack Enterprises, Inc. USA, Model PE2054



# A Low VSWR 340 GHz 2SB Schottky Receiver for Earth Observation Applications

Peter J. Sobis, *Student Member, IEEE*, Anders Emrich, and Jan Stake, *Senior Member, IEEE*

**Abstract**—A waveguide integrated 2SB Schottky receiver operating in the 320-360 GHz band with a performance similar to state-of-the-art DSB Schottky mixers is demonstrated. The unique receiver topology utilizes a low RF and LO VSWR design leading to better mixer performance and superior response for the radiometer system in general. On average a 15 dB SBR is measured over the RF band and a LO return loss of 15 dB broadband.

**Index Terms**—Submillimeter wave technology, schottky diode, receivers, radiometers, subharmonic mixers, sideband separating mixers, dual sideband receivers, image rejection mixers

## I. INTRODUCTION

WE report on the development of a fully integrated 2SB receiver designed for the STEAMR instrument [1], operating at 320-360 GHz. STEAMR is a part of the ESA PREMIER Earth explorer core mission and will provide tomographic limb viewing of the upper troposphere and lower stratosphere UT-LS range from 6 km to 28 km, and will consist of an array of 14-16 receivers with DSB or SSB capability. The receivers will operate at a fixed LO frequency of about 170 GHz with a total IF bandwidth of 12 GHz from 4 to 16 GHz. The instantaneous IF frequency coverage will thus be larger than 192 GHz and we are close to the submillimeter wave range also in IF bandwidth, not only RF frequency.

This work was carried out in the GigaHertz Centre in a joint project in part financed by Swedish Governmental Agency of Innovation Systems (VINNOVA), Chalmers University of Technology, Wasa Millimeter Wave AB, Omnisys Instruments AB and SP Technical Research Institute of Sweden. The work was also supported in part by the Swedish Research Council (VR) under grant no. 2005-2855.

P. J. Sobis is with Omnisys Instruments AB and with the Gigahertz Centre, Terahertz and Millimeter wave Laboratory, Department of Microtechnology and Nanoscience (MC2), Chalmers University of Technology, SE-412 96 Göteborg, Sweden (e-mail: peter.sobis@chalmers.se).

J. Stake, is with the Gigahertz Centre, Terahertz and Millimeter wave Laboratory, Department of Microtechnology and Nanoscience (MC2) Chalmers University of Technology, SE-412 96, Göteborg, Sweden.

A. Emrich is with Omnisys Instruments AB, August Barks gata 6B, SE-421 32 V.F., Sweden.

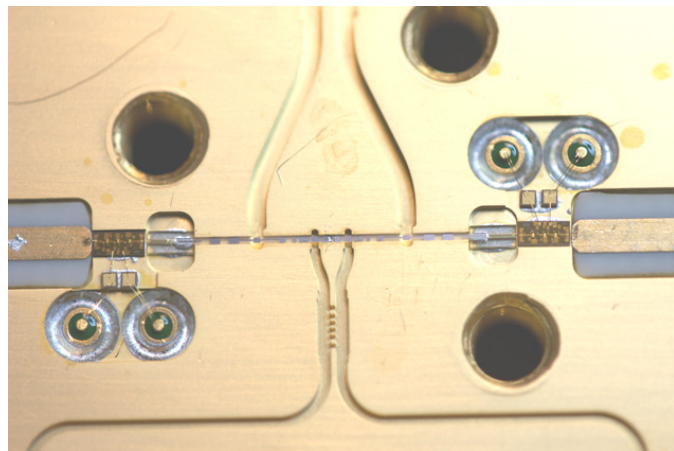


Fig. 1. Front-End receiver module assembly.

## II. DESIGN

The unique receiver design exhibits low LO and RF port voltage standing wave ratio as quadrature feeding is employed, see [2-8], of two subharmonic Schottky diode DSB mixers. In the first prototype module commercial IF LNA's with a 1.8 dB minimum noise figure have been integrated to the receiver I and Q paths. The approach of LNA embedding has two advantages, it improves the flatness and bandwidth of the IF response and provides a flexible way for tuning the image rejection by external IF networks, without affecting the receiver sensitivity.

## III. RESULT

Several modules, both SSB and DSB, have been fabricated and tested using both commercial and in house developed Schottky diodes. Results have been consistent and repeatable for all the assembled units, with an optimum 2SB receiver noise below 2800 K(SSB) including the contribution from the RF hybrid termination, and with an estimated DSB mixer noise and conversion loss of 800 K(DSB) and 8 dB(SSB) respectively including all system losses. Thus, the 2SB mixer is found to operate at similar performance as the DSB mixers. The measured sideband ratio was typically around 15 dB without any compensation of the IQ-imbalance and the typical LO input return loss was measured to about 15 dB broadband.

#### IV. CONCLUSIONS

High performance waveguide integrated sideband separating Schottky receivers can now for the first time be considered for THz applications, enabling new measurement techniques and instrument concepts.

#### ACKNOWLEDGMENT

We would like to acknowledge Professor Victor Belitsky for helpful discussions regarding sideband separating mixer topologies, and Carl-Magnus Kihlman for the excellent work of machining the waveguide splitblock modules, both are with Chalmers University of Technology.

#### REFERENCES

- [1] ESA SP-1313/5 Candidate Earth Explorer Core Missions – Reports for Assessment: PREMIER – Process Exploration through Measurements of Infrared and millimetre-wave Emitted Radiation, 2008, ISBN 978-92-9221-406-7, ISSN 0379-6566.
- [2] V.Vassilev, V.Belitsky and R.Booth, "A New Sideband Separation SIS Mixer for ALMA," Proceedings of SPIE, Vol. 4015, 2000.
- [3] P.Sobis, J.Stake and A.Emrich, "Towards a THz Sideband Separating Subharmonic Schottky Mixer," GigaHertz Symposium 2008, Chalmers University of Technology, Göteborg, Sweden, p. 46, Mar. 2008.
- [4] P.Sobis, J.Stake and A.Emrich, "Towards a THz Sideband Separating Subharmonic Schottky Mixer," 19th International Symposium on Space Terahertz Technology, ISSTT 2008, Groningen, the Netherlands, April 2008.
- [5] P.Sobis, J.Stake and A.Emrich, "A 170 GHz 45° Hybrid for Submillimeter Wave Sideband Separating Subharmonic Mixers," IEEE Microwave and Wireless Components Letters, vol.18, no.10, pp.680-682, Oct. 2008.
- [6] Bhushan Billade, Victor Belitsky, Alexey Pavolotsky, Igor Lapkin, Jacob Kooi, "ALMA Band 5 (163-211 GHz) Sideband Separation Mixer Design", the Proceedings of the 20th International Symposium on Space Terahertz Technology, pp. 19 - 23, Charlottesville, USA, April 20-22, 2009.
- [7] P.Sobis, A.Olsen, J.Vukusic, V.Drakinskiy, S.Cherednichenko, A.Emrich and J.Stake, "Compact 340 GHz Receiver Front-Ends," 20th International Symposium on Space Terahertz Technology, ISSTT 2009, Charlottesville, VA, USA, pp.183-189, Apr. 2009.
- [8] P. Sobis, A. Emrich and M. Hjorth, "STEAMR Receiver Chain," 20th International Symposium on Space Terahertz Technology, ISSTT 2009, Charlottesville, VA, USA, pp.320-325, Apr. 2009.

**Peter Sobis** (S'05) was born in Göteborg, Sweden in 1978. He received the degrees of M.Sc. in electrical engineering and Licentiate in THz electronics from Chalmers University of Technology, Göteborg, Sweden in 2003 and 2010, respectively.

In 2003 he joined Anaren Microwave Inc. and the Space and Defense department in Syracuse NY, working as a microwave design engineer mainly with planar passive components for beamforming networks and various power distribution networks. In 2004 he joined Omnisys Instruments AB developing radiometer components and subsystems. In 2006 he started his Ph.D studies in THz Front-Ends in an industrial collaboration project between Omnisys Instruments AB and Chalmers University of Technology. His current research involves Schottky based THz systems, measurement techniques and the development of multifunctional chips and integrated modules for terrestrial and space born applications.

**Anders Emrich** was born in Uddevalla, Sweden in 1962. He received the degrees of M.Sc. and Ph.D. in electrical engineering from Chalmers University of Technology, Göteborg, Sweden in 1985 and 1992, respectively.

In 1992, he started Omnisys Instruments AB together with Stefan Andersson and was responsible for several subsystems for the ODIN radiometer payload and many development contracts towards ESA/ESTEC.

Omnisys has been engaged in research collaborations with Chalmers University of Technology and other research institutes and universities. He is currently co-supervisor for three Ph.D. students at Chalmers. He has been responsible for the development and production of the 183 GHz Water Vapor Radiometer (58 units) for ALMA, the GAS radio interferometer demonstrator (ESA contract) and the STEAMR instrument for the ESA PREMIER mission (14 x 340 GHz receivers).

**Jan Stake** (S'95–M'00–SM'06) was born in Uddevalla, Sweden in 1971. He received the degrees of M.Sc. in electrical engineering and Ph.D. in microwave electronics from Chalmers University of Technology, Göteborg, Sweden in 1994 and 1999, respectively.

In 1997 he was a research assistant at the University of Virginia, Charlottesville, USA. From 1999 to 2001, he was a Research Fellow in the millimetre wave group at the Rutherford Appleton Laboratory, UK, working on HBV diode multiplier circuits for submillimeter-wave signal generation. He then joined Saab Combitech Systems AB as a Senior System Consultant, where he worked as an RF/microwave engineer until 2003. From 2000 to 2006, he held different academic positions at Chalmers and was also Head of the Nanofabrication Laboratory at MC2 between 2003 and 2006. During the summer 2007, he was a visiting professor in the Submillimeter Wave Advanced Technology (SWAT) group at Caltech/JPL, Pasadena, USA. He is currently Professor and Head of the Terahertz and Millimetre Wave Laboratory at the department of Microtechnology and Nanoscience (MC2), Chalmers, Göteborg, Sweden. His research involves sources and detectors for terahertz frequencies, high frequency semiconductor devices, graphene electronics, terahertz techniques and applications. He is also co-founder of Wasa Millimeter Wave AB.

# Frequency locking of a 3.5 THz quantum cascade laser using a gas cell

Y. Ren, J.N. Hovenier, M. Cui, D.J. Hayton, J.R. Gao, T.M. Klapwijk, S.C. Shi, T-Y. Kao, Q. Hu, and J. L. Reno

**Abstract**—We report a frequency locking experiment of a 3.5 THz third-order distributed feedback quantum cascade laser (QCL) by using a molecular absorption line of methanol (CH<sub>3</sub>OH) gas. With the help of the absorption line, the frequency noise of the QCL is transformed into measurable amplitude fluctuation. We first present the study of the noise of the THz QCL with the contribution from both the frequency and amplitude domain, by using a NbN superconducting hot-electron bolometer as a power detector. We then present the frequency locking measurement with a lock-in amplifier registering the derivate curve of the absorption line and a proportional-integral-derivative (PID) controller generating the feedback signal. The linewidth of the QCL in the free-running mode was found to be around 900 KHz. This linewidth is reduced to below 17 KHz (full width at half maximum) with a Gaussian-like shape when the control loop is active. Because of the frequency stabilization the noise power spectral density of the QCL shows a reduction of more than 20 dB at frequencies below 30 Hz.

**Index Terms**—terahertz, quantum cascade laser, frequency stabilization, heterodyne, and local oscillator

## I. INTRODUCTION

In the terahertz (THz) frequency range, a high resolution heterodyne spectrometer is of crucial importance for astronomical observation and atmospheric remote sensing applications, based on its high spectral resolution and superior sensitivity. As the mixer, a superconducting NbN hot-electron

This work was partly supported by China Exchange Programme executed by KNAW and CAS, and by the AMSTAR+ project of RadioNet under FP7, and NWO.

Y. Ren is with the Kavli Institute of NanoScience, Delft University of Technology, Lorentzweg 1, 2628 CJ Delft, The Netherlands, with the Purple Mountain Observatory, Chinese Academy of Sciences, Nanjing, China, and with the graduate school, Chinese Academy of Science, Beijing, China, (e-mail: y.ren@tudelft.nl)

J.N. Hovenier and T.M. Klapwijk are with the Kavli Institute of NanoScience, Delft University of Technology, Lorentzweg 1, 2628 CJ Delft, The Netherlands

M. Cui and D.J. Hayton are with the SRON Netherlands Institute for Space Research, Sorbonnelaan 2, 3584 CA Utrecht, The Netherlands

J.R. Gao is with the Kavli Institute of NanoScience, Delft University of Technology, Lorentzweg 1, 2628 CJ Delft, The Netherlands, and with the SRON Netherlands Institute for Space Research, Sorbonnelaan 2, 3584 CA Utrecht, The Netherlands (j.r.gao@tudelft.nl)

S.C. Shi is with the Purple Mountain Observatory, Chinese Academy of Sciences, Nanjing, China

T-Y. Kao and Q. Hu are with Department of Electrical Engineering and Computer Science, Massachusetts Institute of Technology, Cambridge, Massachusetts 02139, USA

J.L. Reno is with Center for Integrated Nanotechnologies, Sandia National Laboratories, Albuquerque, NM 87185-0601, USA

bolometer (HEB) mixer has demonstrated excellent sensitivity up to 5.3 THz [1]. As the local oscillator (LO), terahertz quantum cascade lasers (QCLs) [2] have shown advantages at frequency above 2 THz, based on their single mode emission, wide frequency operating range, high output power and long term stability. Several progresses have been made for a THz QCL to be used as the local oscillator (LO) in a heterodyne receiver, including a noise temperature measurement [3,4] and a heterodyne spectroscopy measurement [5,6]. Since the spectral resolution is governed by the back-end spectrometer as well as the LO, a narrow linewidth LO is demanded for a high resolution heterodyne spectrometer, especially for application in astronomical observation, where atomic and molecular gases are at lower pressure and lower temperature, resulting in narrow spectral linewidths. For a quantum cascade laser, due to its fast non-radiative process, which strongly suppress the noise associated with spontaneous emission, the intrinsic linewidth can be as narrow as 1~10 KHz [7,8]. However, due to external jitters, which is caused by noise from the bias current source and temperature fluctuations, a practical linewidth for a free-running THz QCL is much larger, typically is 1 MHz or larger within 1 sec integration time [9,10].

Phase locking a QCL to a reference source means to control the phase of the laser radiation field precisely [11], which is to stabilize the frequency and to transfer the line profile of the reference to the laser. In the case of frequency-locking, the QCL's average frequency is fixed, but its linewidth remains equal to its intrinsic linewidth. Recently, several demonstrations have been given to lock a THz QCL to an external signal source [10, 12], where both frequency and phase of the laser are stabilized. However, in this way, additional signal source and mixer are required, which complicates the instrument and is difficult to implement especially at frequency above 3 THz because of the lack of suitable reference sources. Recently an alternative stabilization scheme for a THz QCL is demonstrated based on a molecular resonance serving as the frequency reference [13], by additionally using only a power detector and a gas cell. In this approach, a liquid-He cooled detector was applied and a locked linewidth of 300 KHz was achieved. It is worth noting that this locked linewidth is still much larger than the intrinsic linewidth of a THz QCL, which indicates that this technique was not fully understood yet.

Here we report our frequency stabilization measurement of a 3.5 THz quantum cascade laser to a molecular absorption line. We used a superconducting NbN HEB as power detector.

The derivative curve of the absorption profile was used as the reference signal for frequency locking. We report, in comparison with the work in Ref. 13, the frequency locking experiment not only for a much higher frequency QCL, but also achieving a much narrower locked linewidth.

## II. MEASUREMENT SETUP

The measurement setup is described schematically in Fig.1. A single mode, third-order distributed feedback (DFB) QCL [14,15] emitting at 3.5 THz is used. As demonstrated in Ref.6, by using the third-order periodic structure with strong refractive index contrast gratings, not only can single mode emission be achieved, but also a single spot, less divergent far-field beam is obtained. Furthermore, by electric tuning the bias voltage of the QCL, a tuning range of 1 GHz was achieved for the 3rd DFB QCL as a LO in a heterodyne spectroscopic measurement. The laser, based on a 10- $\mu\text{m}$  thick active region, consists of 27 periods of gratings with a total length of 1070  $\mu\text{m}$ . The QCL is mounted on the second stage of a pulse tube cryocooler without further temperature stabilization, where the temperature rises up to 12 K and stays at the same value during the laser operation. The beam from the QCL passes through a high-density polyethylene (HDPE) window of the cooler and is focused with a HDPE lens ( $f=26.5\text{mm}$ ). The beam is then guided through a gas cell by a 13- $\mu\text{m}$  thick Mylar beam splitter. The gas cell is a 41-cm long cylinder at room temperature and has two 2-mm thick HDPE windows. Methanol ( $\text{CH}_3\text{OH}$ ) gas is chosen since it contains abundant absorption lines in the terahertz frequency range. The transmitted signal is detected by a superconducting NbN hot-electron bolometer working at liquid helium temperature as a direct power detector whereby we benefit from a low NEP ( $10^{-12}$ - $10^{-13}$   $\text{W}/\text{Hz}^{1/2}$  [16]) and high speed of response (40 psec). The absorption spectrum is measured while the HEB is operated with a constant bias voltage, where the current level of the HEB is a measure of the transmitted THz power through the gas cell.

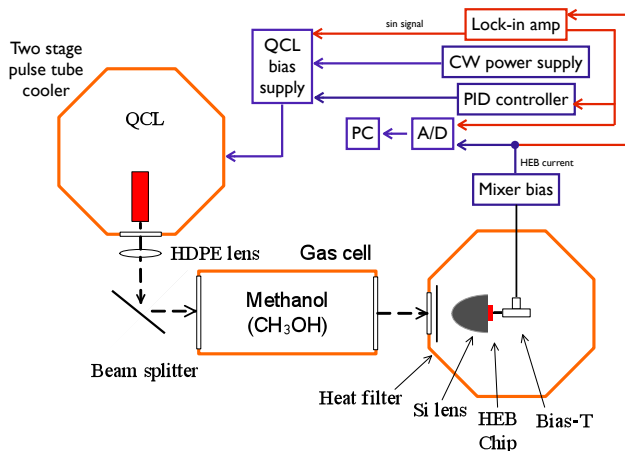


Fig. 1. Schematic view of the frequency locking experiment setup

For the bias circuit of the QCL, a summing circuit is used. It combines three input signals to independently control the bias voltage of the laser. The first input is the DC bias supply for

the laser, which is used to set the DC operating point for the laser. The second input is an AC modulation signal and the third one is the control signal from the feedback loop. A sinusoidal modulation signal at around 1 KHz with relative small amplitude ( $< 0.1\%$  compared with the DC bias point for the laser) was used. By feeding the HEB current to a lock-in amplifier, the derivative signal of the absorption spectrum is obtained. A proportional-integral-derivative (PID) controller is used to actively lock this derivative signal to absolute zero value, and a compensate signal is fed back to the bias circuit of the QCL. By doing this, the QCL frequency could be stabilized at the central frequency of the absorption line.

## III. MEASUREMENT RESULTS

### A. Characterization of the QCL's frequency noise

As shown in Fig.2, methanol absorption lines were observed by making direct absorption spectroscopic measurement [17]. By increasing the bias voltage of the QCL, the laser's emission power gets higher, as a result the HEB current decreases. Since the QCL voltage determines the emitting frequency, the frequency of the QCL decreases with the increase of the bias voltage. By sweeping a frequency range of 1 GHz, two methanol absorption lines at around 3.5 THz were observed.

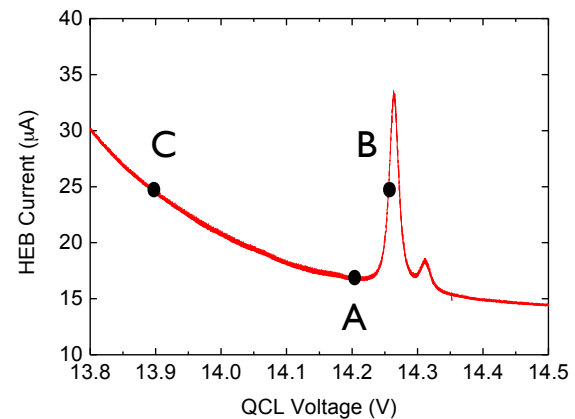


Fig. 2. HEB current measured as a function of QCL voltage that varies QCL frequency. The methanol gas is at 1.1 mbar. The points A, B and C indicate the measurement points for monitoring the HEB current variation, where point A and C contain the contribution from only the HEB noise and the laser intensity noise, but point B contains the HEB noise, laser intensity noise and also laser frequency noise contribution.

In order to study the frequency noise of the QCL, we monitor the HEB current fluctuation at different working points as shown in Fig.3. The measured current within 10 seconds is plotted and also the current noise power spectral density is calculated for each case. The intrinsic HEB current data were measured when the HEB detector was operated at a high voltage bias (3 mV) without LO power, where the HEB detector behaves like a normal resistor. From the noise power spectral density result, we observed the contribution from the laser amplitude noise as well as from the laser frequency noise for different working points. As shown, the extra noise for point A and C arises from the laser amplitude noise, which

locates mainly at the frequencies lower than 100 Hz. While for point B, the extra noise represents the contribution from the QCL frequency noise, and it contributes up to 1 KHz. Please notice that the roll-off of the spectral density above 1 KHz is due to a low pass filter used for the HEB current readout circuit.

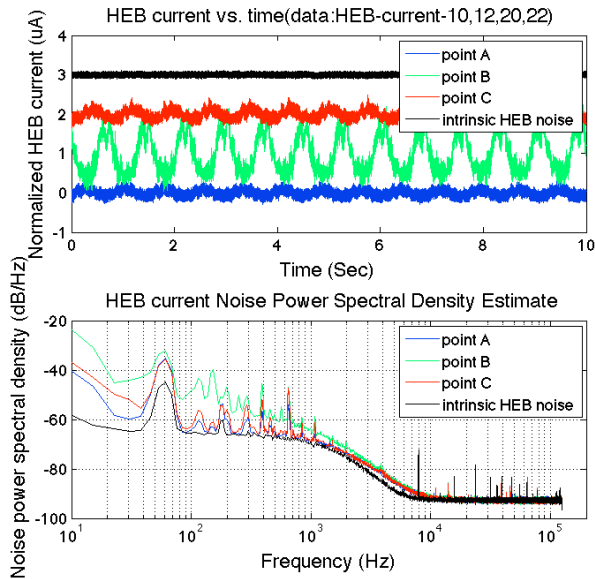


Fig. 3. HEB current measured at different working points as a function of time within 10 sec, and the absolute value is normalized. The lower plot shows the current noise power spectral density of the measured HEB current for each working point.

### B. Frequency stabilization by using a methanol absorption line

Fig.4 shows the measured methanol absorption line at 3.5 THz, and a derivate signal from the lock-in amplifier. Around the absorption peak point, the linear range of the error signal indicates the feedback locking range. The error signal is used for the PID control loop, where a feedback signal is generated and fed to the bias circuit of the QCL in order to yield a stabilized error signal.

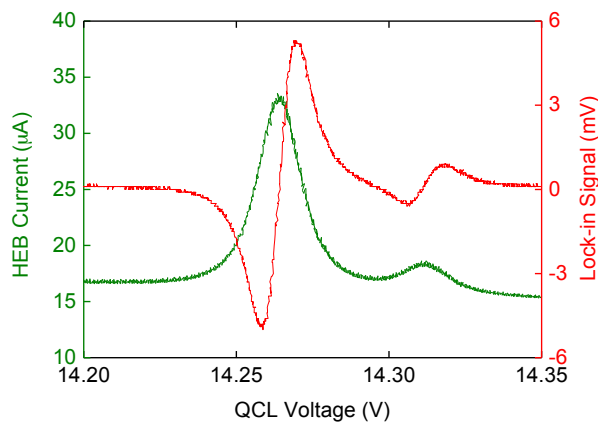
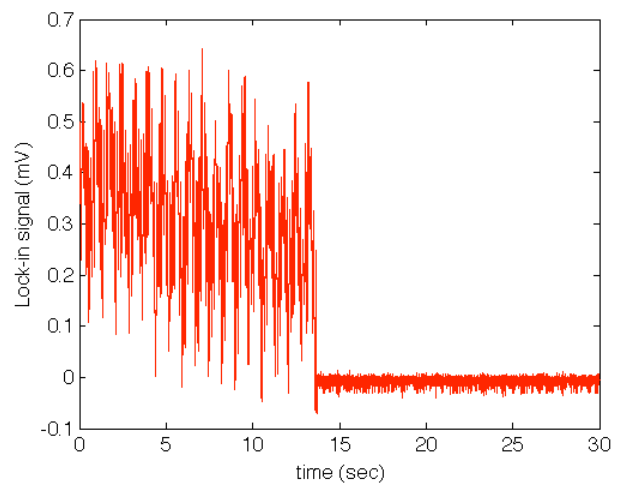
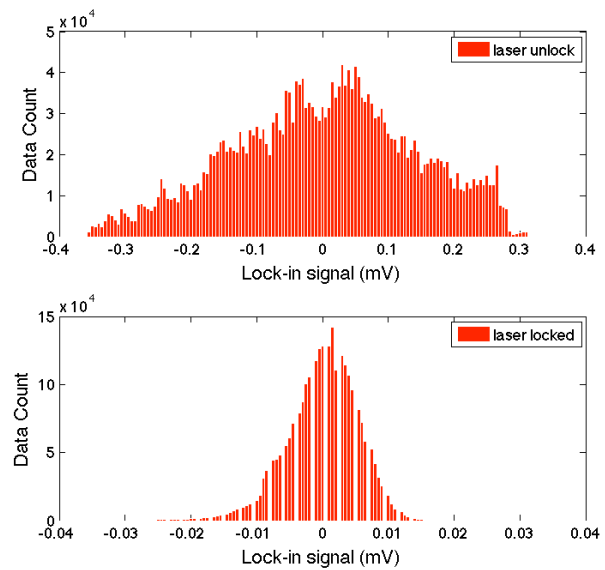


Fig. 4. Absorption profile of the methanol absorption line at 1.1mbar and the error signal was measured using the lock-in amplifier. The voltage window (linear range for the lock-in signal) used for the lock-in loop is around 8mV.

Fig.5. For the unlocked state, the 1 Hz variation is related to the temperature fluctuation and mechanical vibration of the pulse tube cooler. And the long term drifting is due to the non-stability of QCL emission power while operating in the cryocooler. After the PID feedback loop is in active, the error signal is well stabilized to zero value. Also, the error signal data variation is plotted in Fig.5b for both the unlocked state and locked state for the laser during a 10 sec integration time. It is shown that the error signal data variation after the frequency locking is improved by a factor of 55. Furthermore, from the noise power spectral density of the error signal as shown in Fig.6, a noise suppression of over 20dB is achieved below 30 Hz. This relatively small bandwidth is due to the 30 millisecond time constant used in the lock-in amplifier. A further improvement can be done by increasing the bandwidth of the entire feedback loop bandwidth.



a



b

Fig.5 (a) error signal in the unlocked and locked state measured as a function of time. (b) error signal value distribution in the unlocked and locked state during 10 sec integration time.

The laser frequency stabilization result is demonstrated in

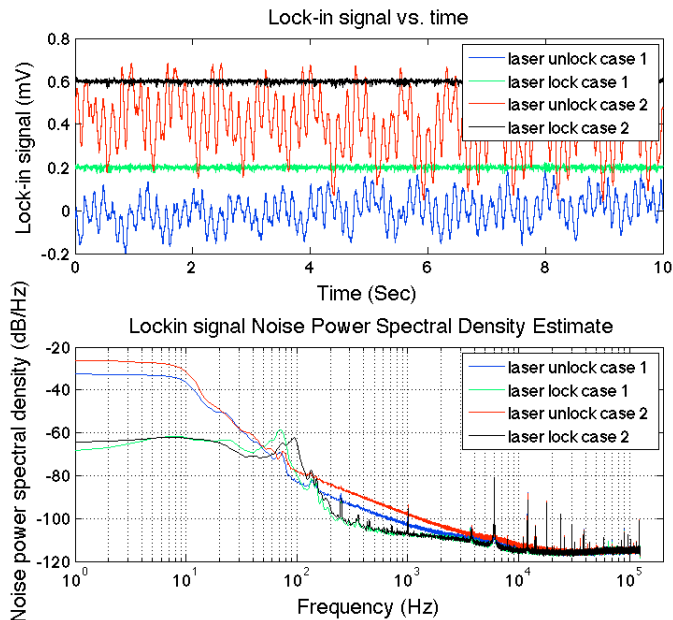


Fig.6 Noise power spectral density of the error signal for two unlocked and locked states, where different P.I.D parameters are used for the feedback loop.

### C. Laser linewidth estimation

The laser linewidth after frequency-locking is estimated by transforming the variation of the error signal into the frequency domain. The error signal is transformed into the QCL bias voltage variation using the linear relationship between these two signals as shown in Fig.4. To do so, two different methods were used to calculate the correspondence between QCL frequency and the bias voltage. First, from the previous heterodyne spectroscopic experiment [6], the frequency tuning coefficient of this QCL at different operating points was obtained. In this way, we calculated a free running laser linewidth within the range of 443-962 KHz, and when the laser is locked, the linewidth in a range of 8-17 KHz. The uncertainty in the linewidth is caused by the uncertainty in the frequency tuning coefficient of the QCL, which is bias point dependent. Secondly, by knowing the methanol gas pressure broadening coefficient at 3.5 THz [6], a sets of methanol absorption lines at different gas pressure were measured. In this way the error signal is also transformed to the frequency domain. With this method, we obtained a free running laser linewidth of 558-798 KHz and the linewidth of 10~14 KHz for the locked state. In the 2<sup>nd</sup> case, the linewidth uncertainty is determined by the accuracy of the gas pressure calibration. It is really important to note that although we applied two different approaches, we obtained similar linewidth results.

As been found in Ref. 13, the temperature fluctuation of the cryocooler will also introduce the linewidth broadening to the QCL, since the emission frequency is related to the bath temperature of the laser. We monitored the bath temperature fluctuation with a Si diode on the cold stage of the cryocooler and a Pt-1000 thermistor on the cooper block near the laser, where less than 30 mK bath temperature variation of the QCL was measured. With a temperature tuning coefficient of -33 MHz/K obtained from Ref. 6, a free running linewidth of less

than 1 MHz for the QCL is expected, which is in agreement with our measurement data. Furthermore, we notice that our frequency locked linewidth is constant with published results in the literature, which was either 30 KHz measured by a heterodyne technique [9] in a very short period of 3 ms or 6.3 KHz obtained in a frequency locking measurement [18].

## IV. CONCLUSION

In conclusion, we succeeded in frequency locking a 3.5 THz quantum cascade laser by using a methanol absorption line as the frequency reference. Two different methods were applied for determining the linewidth where similar linewidth results were obtained. The locked linewidth of the QCL is found to be below 17 KHz with a Gaussian-like shape. Our experiment indicates that this frequency locking scheme is robust and has advantages for QCL at higher frequencies. A future development is to replace the HEB detector in our experiment with other power detectors working at a relatively high temperature (e.g. 77 K or above) and using a small sized gas cell. So, this frequency locking scheme will be competent for practical instrument.

## V. ACKNOWLEDGEMENT:

The authors thank S. Bartalini from Istituto Nazionale di Ottica (INO) – CNR for his extremely helpful discussions and suggestions for our experiment.

## REFERENCES

- [1] W. Zhang, P. Khosropanah, J.R. Gao, E. L. Kollberg, K. S. Yngvesson, T. Bansal, R. Barends, and T. M. Klapwijk, "Quantum noise in a terahertz hot electron bolometer mixer," *Applied Physics Letter* **96**, 111113 (2010).
- [2] B. S. Williams, "Terahertz quantum-cascade laser," *Nat. Photonics* **1**, 517 (2007).
- [3] J.R. Gao, J.N. Hovenier, Z.Q. Yang, J.J.A. Baselmans, A. Baryshev, M. Hajenius, T.M. Klapwijk, A.J.L. Adam, T.O. Klaassen, B.S. Williams, S. Kumar, Q.Hu, and J.L. Reno, "Terahertz heterodyne receiver based on a quantum cascade laser and a superconducting bolometer," *Appl. Phys. Lett.* **86**, 244104 (2005).
- [4] H.-W. Hübers, S. G. Pavlov, A. D. Semenov, R. Köhler, L. Mahler, A. Tredicucci, H. E. Beere, D. A. Ritchie, and E. H. Linfield, "Terahertz quantum cascade laser as local oscillator in a heterodyne receiver," *Opt. Express.* **13**, 5890 (2005).
- [5] Y. Ren, J. N. Hovenier, R. Higgins, J. R. Gao, T. M. Klapwijk, S. C. Shi, A. Bell, B. Klein, B. S. Williams, S. Kumar, Q. Hu, and J. L. Reno, "Terahertz heterodyne spectrometer using a quantum cascade laser," *Appl. Phys. Lett.* **97**, 161105 (2010).
- [6] Y. Ren, J. N. Hovenier, R. Higgins, J. R. Gao, T. M. Klapwijk, S. C. Shi, B. Klein, T.-Y. Kao, Q. Hu, and J. L. Reno, "High-resolution heterodyne spectroscopy using a tunable quantum cascade laser around 3.5 THz," *Appl. Phys. Lett.* **98**, 231109 (2011).
- [7] M. Yamanishi, T. Edamura, K. Fujita, N. Akikusa, and H. Kan, "Theory of the Intrinsic Linewidth of Quantum-Cascade Lasers: Hidden Reason for the Narrow Linewidth and Line-Broadening by Thermal Photons," *IEEE J. Quantum Electron.* **44**(1), 12 (2008).
- [8] S. Bartalini, S. Borri, P. Cancio, A. Castrillo, I. Galli, G. Giusfredi, D. Mazzotti, L. Gianfrani, and P. De Natale, "Observing the Intrinsic Linewidth of a Quantum-Cascade Laser: Beyond the Schawlow-Townes Limit," *Phys. Rev. Lett.* **104**, 083904 (2010)
- [9] A. Barkan, F. K. Tittel, D. M. Mittleman, R. Dengler, P. H. Siegel, G. Scalari, L. Ajili, J. Faist, H. E. Beere, E. H. Linfield, A. G. Davies, and D. A. Ritchie, "Linewidth and tuning characteristics of terahertz quantum cascade lasers," *Opt. Lett.* **29**, 575 (2004).

- [10] P. Khosropanah, A. Baryshev, W. Zhang, W. Jellema, J. N. Hovenier, J. R. Gao, T. M. Klapwijk, D. G. Paveliev, B. S. Williams, S. Kumar, Q. Hu, J. L. Reno, B. Klein, and J. L. Hesler, "Phase locking of a 2.7 THz quantum cascade laser to a microwave reference," *Opt. Lett.* 34, 2958 (2009)
- [11] Miao Zhu and John L. Hall, "Stabilization of optical phase/frequency of a laser system: application to a commercial dye laser with an external stabilizer," *J. Opt. Soc. Am. B* 10, 802-816 (1993)
- [12] D. Rabanus, U. U. Graf, M. Philipp, O. Ricken, J. Stutzki, B. Vowinkel, M. C. Wiedner, C. Walther, M. Fischer, and J. Faist, "Phase locking of a 1.5 Terahertz quantum cascade laser and use as a local oscillator in a heterodyne HEB receiver," *Opt. Express* 17, 1159 (2009).
- [13] H. Richter, S. G. Pavlov, A. D. Semenov, L. Mahler, A. Tredicucci, H. E. Beere, D. A. Ritchie, and H.-W. Hübers, "Submegahertz frequency stabilization of a terahertz quantum cascade laser to a molecular absorption line," *Appl. Phys. Lett.* 96, 071112 (2010)
- [14] M. I. Amanti, M. Fischer, G. Scalari, M. Beck, and J. Faist, "Low-divergence single-mode terahertz quantum cascade laser," *Nat. Photonics* 3(10), 586-590 (2009).
- [15] M. I. Amanti, G. Scalari, F. Castellano, M. Beck, and J. Faist, "Low divergence Terahertz photonic-wire laser," *Optics Express*, 18, 6390, (2010)
- [16] Ren Yuan, Miao Wei, Yao Qi-Jun, Zhang Wen and Shi Sheng-Cai, "Terahertz Direct Detection Characteristics of a Superconducting NbN Bolometer," *Chinese Phys. Lett.* 28 010702 (2011).
- [17] H. -W. Hübers, S. G. Pavlov, H. Richter, A. D. Semenov, L. Mahler, A. Tredicucci, H. E. Beere, and D. A. Ritchie, "High-resolution gas phase spectroscopy with a distributed feedback terahertz quantum cascade laser," *Appl. Phys. Lett.* 89, 061115 (2006).
- [18] A. Baryshev, J. N. Hovenier, A. J. L. Adam, I. Kašalynas, J. R. Gao, T. O. Klaassen, B. S. Williams, S. Kumar, Q. Hu, and J. L. Reno, "Phase locking and spectral linewidth of a two-mode terahertz quantum cascade laser," *Appl. Phys. Lett.* 89, 031115 (2006).

## High power room temperature, compact, narrow line THz source as a local oscillator for THz receivers

M. Scheller<sup>1,2</sup>, J. Yarborough<sup>1,3</sup>, A. Young<sup>4</sup>, J. Moloney<sup>1,3</sup>, C. d'Aubigny<sup>4,5</sup>, M. Fallahi<sup>1,3</sup>, M. Koch<sup>1,2</sup>, S. Koch<sup>1,2</sup>, C. Walker<sup>5</sup>

(1) Desert Beam Technologies LLC, 3542 N Geronimo Avenue, Tucson, AZ 85705, USA

(2) Fachbereich Physik, Philipps-Universität Marburg, Renthof 5, 35037 Marburg, Germany

(3) College of Optical Sciences, University of Arizona, 1630 E University Boulevard, Tucson, AZ, 85721, USA

(4) TeraVision Inc. 1815 W. Gardner Lane, Tucson, AZ, 85705, USA

(5) Steward Observatory, University of Arizona, 933 N. Cherry Ave. Tucson, AZ, 85721, USA

\* Contact: cdaubign@teravision-inc.com, phone 1-520-621-6540

**Abstract**—We present a continuous wave terahertz source based on intracavity difference frequency generation within a dual color vertical external cavity surface emitting laser. Using a nonlinear crystal with a surface emitting phase matching scheme allows for high conversion efficiencies. Due to the tunability of the dual mode spacing, the entire spectral range of the terahertz gap can be covered. The terahertz output scales quadratically with the intracavity intensity, potentially allowing for terahertz intensities in the range of 10s of milliwatts and beyond. This source has already shown great promise as a high power THz local oscillator. We present initial testing results and remaining the challenges.



# Solid-State LO Sources for Greater than 2THz

T.W. Crowe, J.L. Hesler, S.A. Retzloff, C. Pouzou, G.S. Schoenthal  
Virginia Diodes Inc., Charlottesville, VA, USA

**Abstract**—Over the last several years, VDI has been developing THz sources based on microwave frequency amplifiers and a cascaded series of frequency multipliers. These are intended to be used as local oscillator sources for astronomical receivers, such as those on the SOFIA airborne observatory. In 2010 a 1.9 THz source with greater than ten microwatts output at room temperature was presented at this conference. VDI has now completed the initial development of similar sources for use at 2.5 and 2.7 THz. The measured output power is about 3 microwatts and is sufficient to fully pump an HEB mixer.

This effort required the development of improved millimeter-wave varactor multipliers with better thermal grounding for greater power handling, the optimization of the THz multipliers for operation at low power levels and the development of improved assembly and testing techniques. This paper discusses some of the challenges of achieving useful sources at such high frequency and reviews the results that have been achieved to date, with emphasis on the new 2.51THz source that has recently been used on the SOFIA aircraft for astronomical observations.

**Index Terms**—Terahertz sources, frequency multipliers, radio astronomy.

## I. INTRODUCTION

THE needs of the radio astronomy community have long driven the development of terahertz technology. The relatively recent development of high quality HEB mixers for use in the frequency range above 1 THz is presently enabling the development of low noise, high spectroscopic resolution heterodyne receivers for investigations of the dynamics of molecular clouds, particularly in star forming regions. The primary benefit of these new mixers is their greatly reduced local oscillator (LO) power requirement. Even after the inclusion of significant losses in the LO coupling to the HEB element, a power level of only a few microwatts is considered sufficient in the 1-3THz frequency range. This low level enables the use of sources based on high-quality microwave oscillators followed by amplifier-multiplier chains (AMCs). These sources offer very high quality signals with broad frequency tuning. Developing a commercial source for these LO systems has been the primary goal of this project.

## II. PREVIOUS DEVELOPMENT OF A 1.9THz SOURCE

At the 2010 ISSTT meeting, VDI presented the results for a 1.9THz source that was developed for use on the German Receiver for Astronomy at Terahertz Frequencies (GREAT) [1,2]. A simple block diagram of this source is depicted in Fig.

1. The signal from the user supplied synthesizer is coupled into the AMC via a coaxial line. This signal is first frequency doubled and then amplified in a commercially available component [3]. A series of three VDI varactor doublers then increases the frequency. The varactor doublers are selected because of their high efficiency and power handling. The power from the final doubler is then coupled into the integrated x9 frequency multiplier. This final component consists of two frequency triplers that are integrated into a single housing. This integration eliminates a high frequency flange and reduces the intervening length of lossy waveguide between the triplers. A diagonal horn antenna is machined into the housing to couple the output power into free-space (~25dBi). The power generated by this source is shown in Fig. 2.

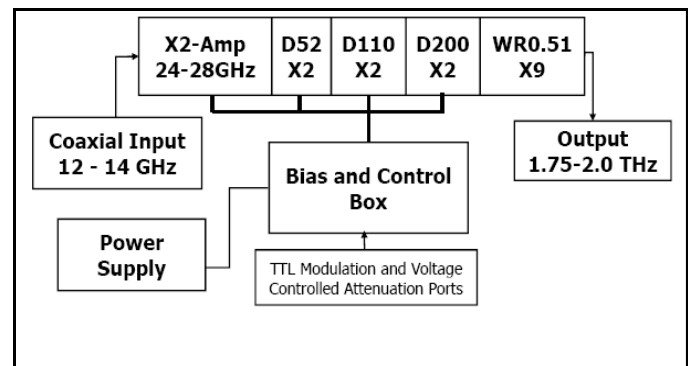


Fig. 1: A simple block diagram of the 1.9THz source.

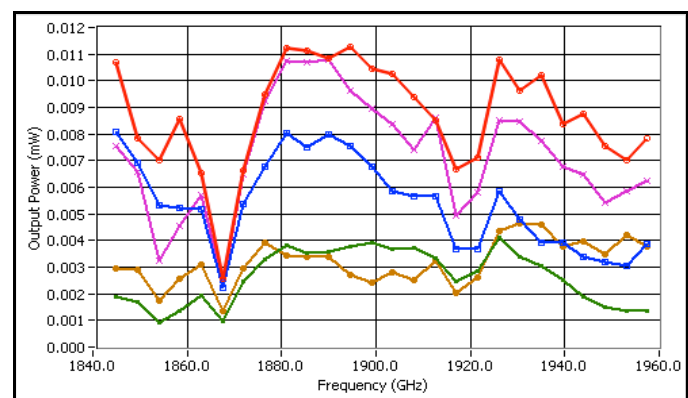


Fig. 2: The measured power from the 1.9THz source, using several different builds of the final WR0.51x3 frequency tripler. The variation is due to both design changes and the quality of the assembly.

### III. EXTENSION OF THE TECHNOLOGY TO >2THz

#### A. The High-Power Driver Modules

For the 2.7 THz source, it was decided to maintain the same system design, while increasing the operating frequency of all of the components. Fortunately, excellent power amplifiers are readily available in the 34-40GHz frequency range [3], and VDI had previously developed varactor doubler designs for the required frequency bands. However, the power handling of these doublers was found to be insufficient. Specifically, the best previous power generated near 300GHz was of order 20-25mW, whereas a level approaching 50mW was used to pump the x9 multiplier to 1.9THz.

One method to significantly increase the power of the frequency multipliers is to employ in-phase power combining. Essentially, a waveguide splitter is used to share the available input power between two identical frequency multiplier circuits, and the output powers are then recombined in waveguide. Provided the two paths are identical, the output power will be combined in-phase, yielding a power increase of about 3dB. However, for this effort VDI decided to initially focus on improving the power handling of the varactor doubler designs through the improvement of the electrical and thermal circuits. Once the power is maximized in this manner, power combining can then be implemented in future research.

Typical performance of the varactor multiplier chains is depicted in Fig. 3. In order to ensure coverage of the full frequency range desired (~2.5-2.75THz), two driver chains were developed to pump the final broadband x9 multiplier. As is shown in the figure, the goal power level was achieved, although without much margin.

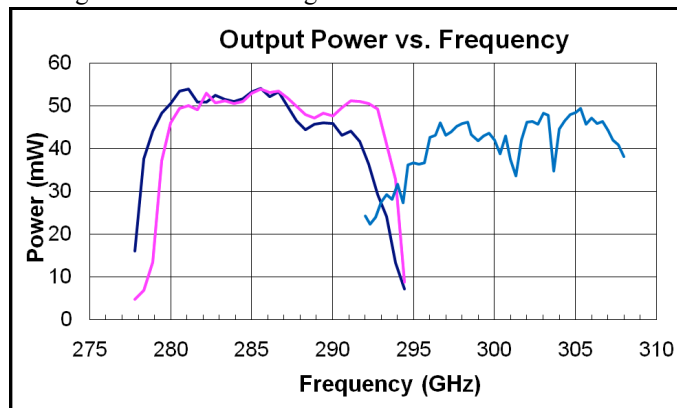


Fig. 3: The measured power from the two driver chains ( $xnAmpx2x2x2$ ) that were developed for sources at ~2.5 and 2.7THz. The goal power level of ~50mW was achieved without waveguide power combining.

#### B. The THz x9 Multiplier

The VDI THz sources use an integrated x9 multiplier, as described above. However, during development a discrete tripler to the WR1.0 waveguide band was first developed and tested. The measured power from this tripler is depicted in Fig. 4. The results were quite good, with power levels of greater than 0.5mW across much of the frequency band. Further, it should be expected that the power coupled to the

final tripler may be significantly greater when the two units are integrated in close proximity within a single housing, since this will significantly reduce the waveguide and atmospheric losses.

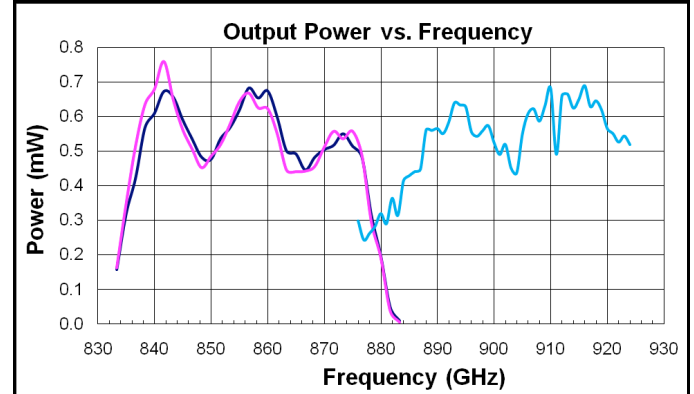


Fig. 4: The measured power from the WR1.0x3 frequency tripler when driven by the power levels shown in Fig. 3.

The final x9 multiplier is shown in Fig. 5, on the right-hand side of the image. The integrated diode circuits for the final tripler were fabricated in the VDI cleanroom facility. The anode area was of order 0.5 square microns and the circuit thickness was less than 10 microns. However, the circuits were relatively easy to handle and once proper assembly procedures were developed, the component yield was acceptably high.

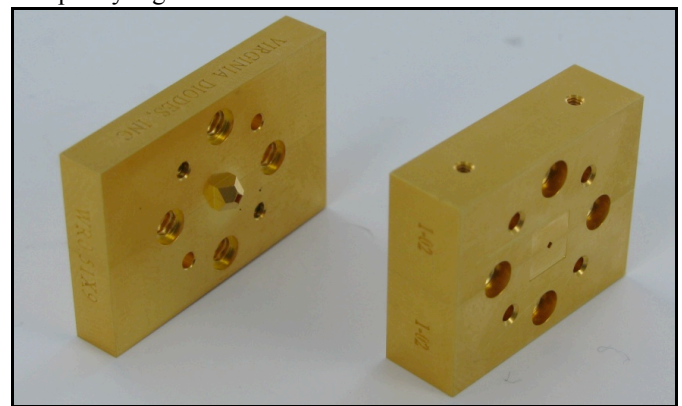


Fig. 5: The VDI x9 multipliers to the WR0.51 (left) and WR0.34 waveguide bands. Each component has an integrated diagonal horn antenna (~25dBi). In the case of the lower frequency x9, the horn protrudes from the housing.

The test results presented at the conference are shown in Fig. 6. These measurements were performed with a VDI-Erickson PM4 Power Meter at room temperature in an open-air environment. The maximum power level was about 2uW, and the tuning band of each system was about 100GHz. Since these measurements were made without any special humidity control and with significant path length between the horn antenna and the absorbing element of the power meter, it is clear that the power generated is likely significantly greater than shown. In fact the general structure of the curves, including the deep trough at 2.65THz is largely explained by the expected atmospheric losses.

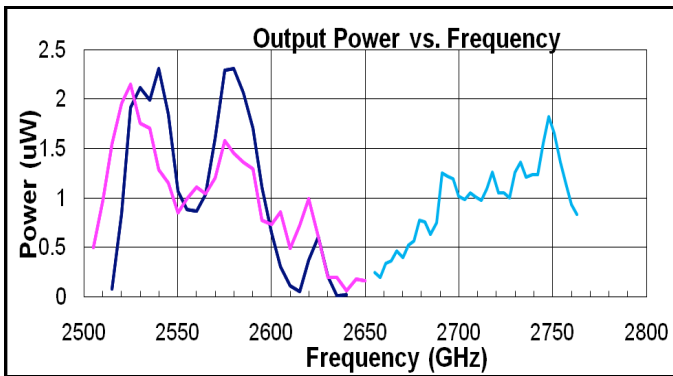


Fig. 6: The measured power from the VDI-WR0.34x9 components, as presented at the ISSTT in April 2011.

IV. LO SOURCE INTEGRATION AND TESTING FOR GREAT

The development of these sources was supported by the Max Planck Institute for Radioastronomy for use on the GREAT instrument. Two systems were delivered in April of 2011 for integration into GREAT. An image of the 2.67THz module is shown in Fig. 7. It should be noted that these sources use no tuners, neither mechanical nor electrical. Rather the frequency is set simply by adjusting the input signal from the synthesizer. Also, the only bias required is for the power amplifier and the three varactor doublers, and these values are all fixed. The frequency triplers do not require external bias.

Both sources were subsequently shown to have sufficient power to fully pump the HEB mixers developed by the University of Cologne [4].

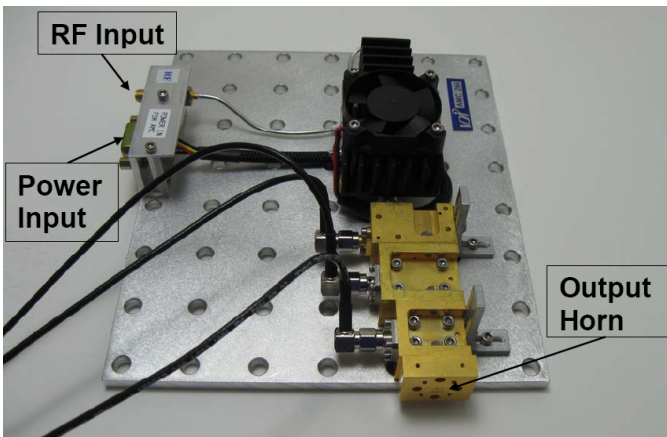


Fig. 7: An image of the VDI 2.67THz AMC module that was integrated into the GREAT instrument for flights on SOFIA.

V. DIGEST UPDATE

The two VDI sources were flown on SOFIA in July of 2011, when the 16OH line was successfully detected [5]. After that flight, VDI had an opportunity to upgrade the 2.5THz source with the specific goal of re-tuning the system for measurement of the isotopic 18OH line at ~2.51THz. During this period VDI was also able to test the system over a greater operating band. The resulting data is shown in Fig. 8, which also

includes a graph showing relative atmospheric losses, which map very well the structure of the measured data. This upgraded source was successfully flown again on GREAT/SOFIA in November 2011, resulting in the successful detection of the 18OH line [5].

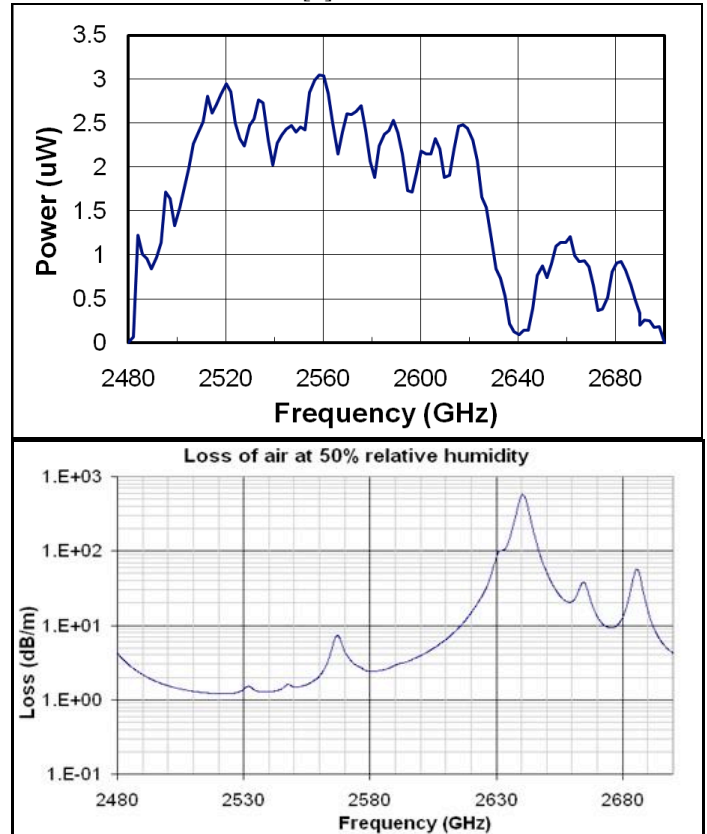


Fig. 8: The measured power of the improved 2.5THz source measured across a broader frequency band. A graph of atmospheric absorption is also shown, which correlates well with the structure of the measured power. This shows clearly the effect of the atmospheric losses on these measurements.

VI. CONCLUSION & DISCUSSION

This work has shown that all-solid-state sources can be developed for applications well above 2THz. The sources described here are based on high quality microwave oscillators and amplifier-multiplier chains. The resulting peak power is in the range of 3uW near 2.5THz, which is sufficient to fully pump HEB mixers. Further, this power is measured at room temperature in an open laboratory environment without any attempt to reduce atmospheric absorption. Significantly more power is available if the source is placed in an evacuated chamber and/or cryogenically cooled. Additional power will also be achieved when power combining is implemented in the high power varactor multipliers. This is particularly true since the THz multipliers are known to be under-pumped, and therefore their efficiency will increase with greater input power.

Most importantly these new sources are frequency agile and have excellent frequency stability, since they are referenced to the input synthesizer. In fact, the VDI source has shown some 200GHz tuning bandwidth with no adjustment other than the

setting of the synthesizer frequency.

These results, as well as similar results reported by another group at the symposium [6], yield confidence that this technology can meet the immediate needs of the radio astronomy community, including the development of instruments for the important [OI] line at 4.7THz and array receivers in throughout 1-3 THz band.

#### ACKNOWLEDGMENT

The development of the THz sources was supported by the Max Planck institute for Radioastronomy in Bonn Germany. The core technology, including the frequency multipliers and the basic system design, was supported by a series of SBIR contracts, including from DARPA (W31P4Q-08-C-0267) and NASA (NAS5-02107 & NNG07CA13C).

#### REFERENCES

- 
- [1] S. Heyminck, R. Güsten, U. Graf, J. Stutzki, P. Hartogh, H.-W. Hübers, O. Ricken, B. Klein, "GREAT: ready for early science aboard SOFIA," Proc. 20<sup>th</sup> Intl. Symp. Space THz Techn., pp. 315-317, Charlottesville, VA, April 2009.
  - [2] <http://www.mpifr-bonn.mpg.de/public/pr/pr-great-mar2011-en.html>
  - [3] Spacek Labs Inc., 212 East Gutierrez Street, Santa Barbara, California USA 93101, sales@spaceklabs.com.
  - [4] P. Pütz, C.E. Honingh, K. Jacobs, M. Justen, F. Schomaker, M. Schultz, S. Wulff, J. Stutzki, J., "Hot electron bolometer waveguide mixers for 1 to 3 THz," IR, MM and THz Waves, pp. 1-2, Sept. 2010.
  - [5] Dr. R. Guesten, Max Planck Institute for Radioastronomy, Bonn, Germany, private communication.
  - [6] A. Maestrini, I. Mehdi, J.V. Siles, J. Ward, R. Lin, B. Thomas, C. Lee, J. Gill, G. Chattopadhyay, E. Schlecht, J. Pearson, and P. Siegel, "First Demonstration of a Tunable Electronic Source in the 2.5 to 2.7 THz Range, In Press, IEEE Trans. Terahertz Science Techn., 2011.

# Toward a Terahertz Local Oscillator for SOFIA Based on a Quantum-Cascade Laser

H. Richter<sup>1\*</sup>, S. G. Pavlov<sup>1</sup>, A. D. Semenov<sup>1</sup>, M. Wienold<sup>2</sup>, L. Schrottke<sup>2</sup>, M. Giehler<sup>2</sup>, R. Hey<sup>2</sup>,  
H. T. Grahn<sup>2</sup>, and H.-W. Hübers<sup>1,3</sup>

*1 Institute of Planetary Research, German Aerospace Center (DLR), Rutherfordstr. 2,  
12489 Berlin, Germany\**

*2 Paul-Drude-Institut für Festkörperelektronik, Hausvogteiplatz 5–7, 10117 Berlin, Germany*

*3 Institut für Optik und Atomare Physik, Technische Universität Berlin, Hardenbergstraße 36,  
10623 Berlin, Germany*

\* Contact: heiko.richter@dlr.de, phone +49-30-67055697

This work is funded by the European Commission through the ProFIT program of the Investitionsbank Berlin.

**Abstract**— Heterodyne spectroscopy of molecular rotational lines and atomic fine-structure lines is a powerful tool in astronomy and planetary research. It allows for studying the chemical composition, the evolution, and the dynamical behaviour of astronomical objects, such as molecular clouds and star-forming regions. For frequencies beyond 2 THz, SOFIA, the Stratospheric Observatory for Infrared Astronomy, is currently the only platform which allows for heterodyne spectroscopy at these frequencies. A major challenge for heterodyne receivers operating at such high frequencies is the local oscillator (LO), which not only has to provide coherent radiation of certain quality, but also to operate in the specific environment of an airborne observatory. THz quantum-cascade lasers (QCLs) have the potential to comply with these requirements.

We report on the development of a compact LO for operation on board of SOFIA, namely for the GREAT (German Receiver for Astronomy at Terahertz Frequencies) heterodyne receiver. The LO combines a QCL with a compact, low-input-power Stirling cooler. Two QCLs operating at 3.1 and 4.7 THz have been investigated. Both are based on a two-miniband design and have been developed for continuous-wave operation, high output powers, and low electrical pump powers [1]. Efficient carrier injection is achieved by resonant longitudinal-optical phonon scattering. At the same time, the operating voltage can be kept below 6 V. The amount of generated heat complies with the cooling capacity of the Stirling cooler of 7 W at 65 K with 240 W of electrical input power. Special care has been taken to achieve a good thermal coupling between the QCL and the cold finger of the cryostat. The whole system weighs less than 15 kg including cooler, power supplies etc. [2]. We will present the performance of the lasers in the cryocooler with respect to output power and beam profiles. Frequency stabilization to below 300 kHz full width at half maximum is achieved by locking to a molecular absorption line [3]. Finally, we will discuss the integration of a 4.7-THz QCL-based LO into GREAT.

[1] M. Wienold, L. Schrottke, M. Giehler, R. Hey, W. Anders, and H. T. Grahn, *Electron. Lett.* **45**, 1030–1031 (2009).

[2] H. Richter, M. Greiner-Bär, S. G. Pavlov, A. D. Semenov, M. Wienold, L. Schrottke, M. Giehler, R. Hey, H. T. Grahn, and H.-W. Hübers, *Opt. Express* **18**, 10177–10187 (2010).

[3] H. Richter, S. G. Pavlov, A. D. Semenov, L. Mahler, A. Tredicucci, H. E. Beere, D. A. Ritchie, and H.-W. Hübers, *Appl. Phys. Lett.* **96**, 071112 (2010).

## Verification of Spectral Purity in the HIFI Local Oscillator

J. Pearson<sup>1\*</sup>, David Teyssier<sup>2</sup>, F. Maiwald<sup>1</sup>, J. Ward<sup>3</sup>, R. Lin<sup>1</sup>, I. Mehdi<sup>1</sup>, Jacob Kooi<sup>4</sup>, Thomas Klein<sup>5</sup>,  
Christian Leinz<sup>5</sup>, William Jellema<sup>6</sup>, Christophe Risacher<sup>6</sup>

*1 Jet Propulsion Laboratory, California Institute of Technology, 4800 Oak Grove Drive, Pasadena, CA, 91109, USA*

*2 European Space Astronomy Centre (ESAC), P.O. Box 78, 28691 Villanueva de la Cañada, Madrid - Spain*

*3 Raytheon Company, Fort Wayne, Indiana, USA*

*4 California Institute of Technology, Pasadena, CA, 91125, USA*

*5 MPIfR Max-Planck-Institut für Radioastronomie, Auf dem Hügel 69, D-53121 Bonn, Germany*

*6 SRON Netherlands Institute for Space Research, P.O. Box 800, 9700 AV Groningen, The Netherlands*

\* Contact: [John.Pearson@jpl.nasa.gov](mailto:John.Pearson@jpl.nasa.gov), phone +1-818-354-6822

This work was sponsored by NASA.

**Abstract**—Many high efficiency varactor diode multipliers rectify a small amount of RF input power and act as a charge pump into the bias network. If the phase and the frequency of the pumped charge resonates with the bias circuit it will result in a forced parametric oscillation, which is as spectrally pure as the fundamental input signal. In HIFI these oscillations were observed in half the local oscillator bands over a range of output frequencies up to 50 GHz wide. The oscillation at the resonant bias network frequency results in AM side bands on the carrier. After several subsequent multiplier stages one or more sidebands can exceed the carrier signal. This effect can not be detected in a Y-factor measurement. It is also extremely hard to detect in the pumped SIS mixer IV curve due to the relatively small frequency offset of the extra LO frequencies, so determination of the mixer response usually requires spectroscopic measurements.

These oscillations have been observed in half of the HIFI local oscillator bands. We describe a method for detecting and suppressing of parametric oscillations by reviewing the pumped IV curves of the multiplier as function of input power and bias. This has successfully been used to mitigate the oscillations in HIFI band 1 and 5. Further studies need to be done to provide design criteria to prevent parametric oscillations in varactor multipliers.

# Characterizing the Full Spatial Optical Behaviour of Power Detectors Using an Interferometric Technique

Christopher N. Thomas, and Stafford Withington

**Abstract**—An experimental method is presented for characterizing the full optical behaviour of few-mode power detectors. The technique involves illuminating the detector with a pair of coherent sources. When the phase of one source is rotated relative to the other, the detector output displays a fringe. Measurement of the complex amplitude of this fringe allows an element of a two-point optical response function to be recovered. By repeating the process for different source positions and orientations, the full two-point response function can be mapped out. From this function it is possible to obtain the full spatial form of each of the modes of the field in which the detector is incoherently sensitive to power, along with the responsivity to the power carried in each of these modes. We describe a scanning system assembled for performing such measurements at frequencies in the range 195 - 270 GHz. Results will be presented for measurements made on a detector that was stopped down to simulate a few mode planar absorber.

## I. INTRODUCTION

Incoherent detectors are used widely in astronomy at THz frequencies, where they provide high sensitivities over large bandwidths. Science requirements in areas such as spaceborne astronomy are driving the need for better optical characterisation of these devices. The characterisation of coherent detectors, such as heterodyne receivers, is a much better understood process. Coherent detectors are responsive to the complex amplitude of a single mode of the incident field. The amplitude, phase and polarisation of this mode can be mapped out using techniques such as near-field scanning[1] or microwave holography[2]. Incoherent detectors, or power detectors as we will refer to them, measure the energy flux of an incident field. In contrast with coherent detectors, a power detector can be independently responsive to the power arriving in several natural optical modes simultaneously. At present, usually only the intensity and polarisation of the overall response is measured. However, this gives an incomplete picture of the behaviour and cannot, for example, be used to calculate how the detector will couple power from an optical system. To fully characterize a device the individual spatial forms of all the natural modes must be determined, along with the responsivity of the detector output to power arriving in each of them.

In this paper we will present the first experimental demonstration of a two-source, interferometric, scheme for characterizing the full optical behaviour of a power detector from power measurements alone. In section II we will outline the formalism developed by Withington[3] and Saklatvala[4] for

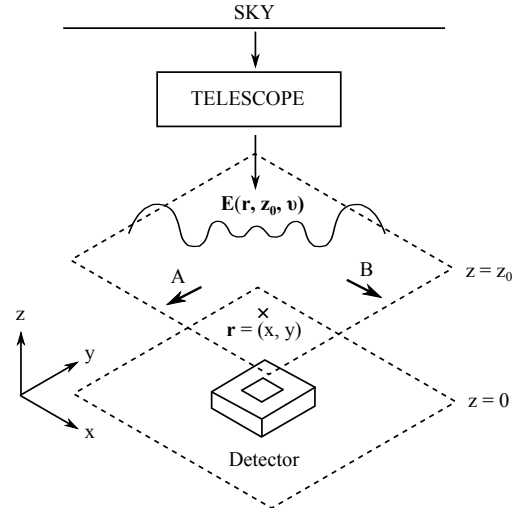


Fig. 1. Diagram illustrating the characterisation of the optical behaviour of a power detector. Over the surface  $z = z_0$ , at each frequency there exists a set of field modes  $\{\mathbf{U}_n(\mathbf{r}, z_0, \nu)\}$  in which the detector is independently sensitive to power with responsivity  $\{\alpha_n(\nu)\}$ .

describing the optical behaviour of power detectors. Here it will be shown that a device's behaviour can be characterised either in terms of its natural modes or, equivalently, in terms of a two-point dyadic response function. Section III will outline a scheme for recovering elements of this response function using a pair of phase-locked coherent sources. In section IV we will describe a demonstration system for performing measurements of this type in the frequency range 195 - 270 GHz. Finally, in section V we will present data taken at 240 GHz for a TK Instruments Absolute Power Meter, the window of which was stopped down to a  $15 \text{ mm} \times 15 \text{ mm}$  in order to simulate a few-mode planar absorber.

## II. CHARACTERIZING THE OPTICAL BEHAVIOUR OF POWER DETECTOR

The optical behaviour of power detectors has been discussed in detail by Withington[3] and Saklatvala[4]. A summary of their main results will be provided here. Consider a power detector being illuminated by a temporally-stationary field, as shown in figure 1. At each radiation frequency  $\nu$ , it is possible to identify a set of modes  $\{\mathbf{U}_n(\mathbf{r}, z_0, \nu)\}$  of the electric field over a plane  $z = z_0$  in which the detector is independently responsive to power. We will refer to this set as the *natural optical modes* of the detector at  $\nu$ . Assume the output of the detector varies as  $\alpha_n(\nu)$  with the square-modulus of the amplitude of the mode in the incident; i.e. the

$\alpha_n(\omega)$  is proportional the responsivity of the detector output to power arriving in that field mode. Letting  $\mathbf{E}(\mathbf{r}, z_0, \nu)$  denote the electric field incident over the plane as a function of the frequency, the detector output  $P$  is given by

$$P = \int_0^\infty \sum_n \alpha_n(\nu) \left| \int \mathbf{U}_n^*(\mathbf{r}, z_0, \nu) \cdot \mathbf{E}(\mathbf{r}, z_0, \nu) d^2\mathbf{r} \right|^2 d\nu. \quad (1)$$

If the incident field is spatially partially-coherent, then the expected value of the output is found by taking the ensemble average  $\langle \rangle$  of (1). By algebraic manipulation,  $\langle P \rangle$  can be put into the dyadic form

$$\langle P \rangle = \int_0^\infty \int_{z_0} \int_{z_0} \bar{\mathcal{D}}^\dagger(\mathbf{r}_1, \mathbf{r}_2, \nu) \cdot \bar{\mathcal{E}}(\mathbf{r}_1, \mathbf{r}_2, \nu) d^2\mathbf{r}_1 d^2\mathbf{r}_2 d\nu, \quad (2)$$

where the following definitions have been made:

$$\bar{\mathcal{E}}(\mathbf{r}_1, \mathbf{r}_2, \nu) = \langle \mathbf{E}(\mathbf{r}, z_0, \nu) \mathbf{E}^*(\mathbf{r}, z_0, \nu) \rangle \quad (3)$$

$$\bar{\mathcal{D}}(\mathbf{r}_1, \mathbf{r}_2, \nu) = \sum \alpha_n(\nu) \mathbf{U}_n(\mathbf{r}, z_0, \nu) \mathbf{U}_n^*(\mathbf{r}, z_0, \nu). \quad (4)$$

$\bar{\mathcal{E}}(\mathbf{r}_1, \mathbf{r}_2, \nu)$  is the second-order correlation function of the electric field and encodes the state of spatial coherence of the incident field. The second dyadic,  $\bar{\mathcal{D}}(\mathbf{r}_1, \mathbf{r}_2, \nu)$ , incorporates all the information about the optical behaviour of the detector. We shall refer to it subsequently as the Detector Response Function (DRF). It is the DRF that can be recovered directly by experiment, as will be described in the next section. It follows from (4) that the natural modes of the detector may then be found by a diagonalization procedure. A useful physical picture of the DRF is as the second order correlation function of the state of coherence of the field to which the detector is sensitive. The detector output depends on the amplitude of component of the incident field that projects into this state. This projection operation is described by (2).

Once the DRF has been measured on one plane, its form on another plane can be computed using partially-coherent optics. It is straightforward to show that the DRF propagates through space in the same way as the second order correlations in a partially coherent field [5]. This can be done in particularly elegant and computationally efficient way by propagating the natural modes individually, then re-assembling the DRF by superposing the transformed fields together according to (4)[6]. Similarly, the full spatial sensitivity of the detector on the sky when it is placed on a focal plane can be found by back-scattering the DRF through the telescope. This is unlikely to be a unitary process, in which case the natural modes of the detector will no longer diagonalize the dyadic response function on the sky. Instead, the transformed response function and the new set of natural modes should be thought of as those of the complete instrument.

### III. MEASURING THE DETECTOR RESPONSE FUNCTION

The detector response function at a particular frequency can be measured using a pair of monochromatic sources, phase-locked together at a controllable phase angle  $\Delta\phi$ . For clarity of discussion, we will assume each source generates a point-like excitation of the electric field on  $z = z_0$ . However, it is a

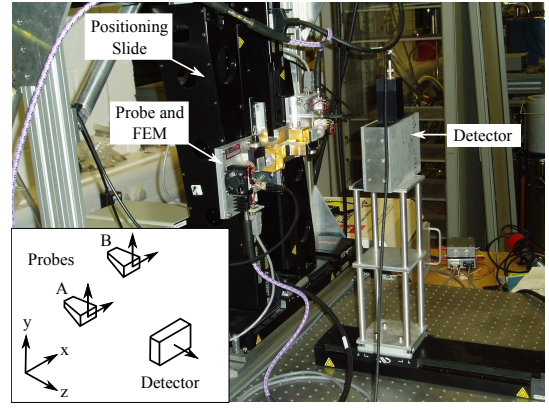


Fig. 2. Photograph of the demonstration system.

straightforward to account for the true form of the probe field. The illuminating field is given by

$$\mathbf{E}(\mathbf{r}, z_0, \nu) = [E_a \hat{\mathbf{p}}_a \delta(\mathbf{r} - \mathbf{r}_a) + E_b e^{i\Delta\phi} \hat{\mathbf{p}}_b \delta(\mathbf{r} - \mathbf{r}_b)] \delta(\nu - \nu_0). \quad (5)$$

Substituting (5) into (2), we find that the detector output is

$$\begin{aligned} \langle P \rangle = & |E_a|^2 \hat{\mathbf{p}}_a \cdot \bar{\mathcal{D}}(\mathbf{r}_a, \mathbf{r}_a, \nu_0) \cdot \hat{\mathbf{p}}_a \\ & + |E_b|^2 \hat{\mathbf{p}}_b \cdot \bar{\mathcal{D}}(\mathbf{r}_b, \mathbf{r}_b, \nu_0) \cdot \hat{\mathbf{p}}_b \\ & + 2\text{Re}[E_a^* E_b e^{i\Delta\phi} \hat{\mathbf{p}}_a \cdot \bar{\mathcal{D}}(\mathbf{r}_a, \mathbf{r}_b, \nu_0) \cdot \hat{\mathbf{p}}_b]. \end{aligned} \quad (6)$$

To obtain this expression, use has been made of the Hermiticity of the DRF,  $\bar{\mathcal{D}}(\mathbf{r}_a, \mathbf{r}_b, \nu_0) = \bar{\mathcal{D}}^\dagger(\mathbf{r}_b, \mathbf{r}_a, \nu_0)$ , which follows from (4). (6) shows that as the phase angle  $\Delta\phi$  between the sources is rotated, the detector output will show a fringe pattern. Provided  $E_a$ ,  $E_b$  and  $\Delta\phi$  are known, it is possible to infer  $\hat{\mathbf{p}}_a \cdot \bar{\mathcal{D}}(\mathbf{r}_a, \mathbf{r}_b, \nu_0) \cdot \hat{\mathbf{p}}_b$  from the amplitude and phase shift of the fringe. Measurements of  $\hat{\mathbf{p}}_a \cdot \bar{\mathcal{D}}(\mathbf{r}_a, \mathbf{r}_a, \nu_0) \cdot \hat{\mathbf{p}}_a$  and  $\hat{\mathbf{p}}_b \cdot \bar{\mathcal{D}}(\mathbf{r}_b, \mathbf{r}_b, \nu_0) \cdot \hat{\mathbf{p}}_b$  can be made by switching each source off alternately. By repeating the process for different source positions and polarisations,  $\bar{\mathcal{D}}(\mathbf{r}_a, \mathbf{r}_b, \nu_0)$  can be mapped out in full.

In most cases it will be possible to reconstruct the full DRF without having to explore all possible source configurations. It is only necessary to take sufficient measurements to account for the number of degrees of freedom in the DRF, as determined numerically by (4) or physically by the degree of spatial coherence. One way of achieving this is to project the DRF into a finite set of appropriate basis functions: for example, a set of Gauss-Hermite modes. In an experiment, the estimates of the projection coefficients could be updated each time a certain amount of new data is taken. Data taking would stop when the estimates have converged and the error is at a desired level.

### IV. EXPERIMENTAL SYSTEM

A demonstration system has been assembled for making measurements on power detectors over the frequency range 195 - 270 GHz, which is shown in figure 2. Figure 3 is a block diagram of the major components of the scanning system. The sources are a pair of rectangular waveguide probes. These are moved independently around the  $(x, y)$ -plane by a set of four computer-controlled slides. Both probes



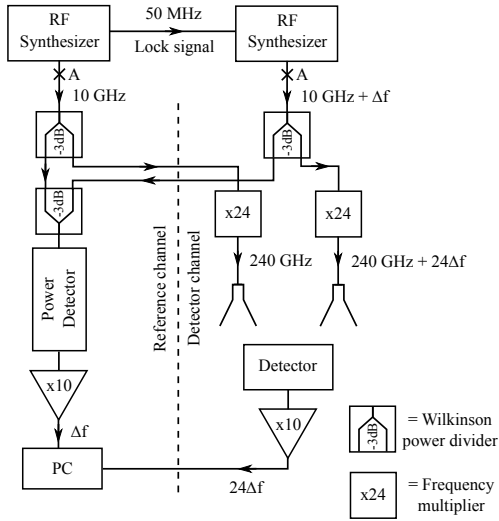


Fig. 3. Block diagram showing the major components of the scanning system.

are driven in the TE01 mode by a pair of phase-locked RF synthesizers operating at 8.1 - 11.25 GHz through separate  $\times 24$  multipliers from Virginia Diodes. They are orientated so the resulting electric field is  $y$ -polarised. The multipliers are mounted on the slides and are connected to the synthesizers through amplitude- and phase-stable cables to minimize errors from cable flexure. Absolute values of  $E_a$  and  $E_b$  were not measured. Instead, consistent system settings were used to facilitate the comparison of  $\hat{\mathbf{y}} \cdot \bar{\mathbf{D}}(\mathbf{r}_a, \mathbf{r}_b, \nu_0) \cdot \hat{\mathbf{y}}$  between different data sets.

The phase angle between the sources was made to rotate by setting the synthesizers at slightly different frequencies  $f_a$  and  $f_b$ . This causes the phase angle between the sources to rotate at a frequency  $\Delta\nu = 24|f_a - f_b|$ , generating a temporal fringe pattern in the detector output at the same frequency (right-hand side of figure 3). A phase reference was provided by superposing the outputs of the synthesizers and then detecting the envelope of the combined signal using an Agilent 8471E power detector (left-hand side of figure 3). A Wilkinson splitter was used as the combiner. The resultant signal has frequency  $\Delta f = |f_a - f_b|$  and its phase is locked to  $\Delta\phi$  at the synthesizer level. Before it can be used as a reference for the phase shift of the detector fringe, the frequency of the reference must be multiplied by a factor of 24.

Characterisation measurements were made on a TK Instruments Absolute Power Meter. This was mounted on a fifth computer-controlled slide, allowing the distance from the probes to be changed. The front window of the detector was stopped down to a 15 mm  $\times$  15 mm aperture to simulate a few-mode detector; while the rear window was blanked-off to minimise interference from stray light. The SNR of the fringe measurement was found to be greatest for  $\Delta\nu \approx 8$  Hz. The frequency of the corresponding phase reference is 0.333Hz, which is too small for the signal frequency to be multiplied up easily electronically. This prevented us from using a lock-in amplifier to measure the complex fringe amplitude. A software based scheme was adopted instead, which involved logging

both the detector output and phase reference to computer for each source arrangement. In post-processing, fringe models were fitted to the signals using the Bayesian method from Chapter 4 of [7]. This requires an accurate value for  $\Delta f$ , which was derived from the reference channel using a Gaussian-windowed discrete Fourier transform. The fitted phase shift for the reference,  $\phi_r$ , and detector output,  $\phi_f$ , were then used to find the phase shift of the detector fringe,  $\phi_d = \phi_f - 24\phi_r$ .

The degree of contamination of the data from multi-path reflections within the apparatus was reduced mainly by spatial averaging. Each of the data points in section V is an average over the  $z$ -direction, based on 10 measurements at points over a range of  $\pm\lambda$ . Each measurement was based on a 20 s fringe recording made at a sampling rate of 1 kHz. The stated errors in the average amplitude and phase are the standard error in the mean of each quantity over the 10 measurements. As an additional measure to reduce contamination, absorber was applied to the detector aperture plate to disrupt the main reflection path.

Measurements of  $E_a^* E_b \hat{\mathbf{y}} \cdot \bar{\mathbf{D}}(\mathbf{r}_a, \mathbf{r}_b, \nu_0) \cdot \hat{\mathbf{y}}$  with  $\mathbf{r}_a = \mathbf{r}_b$  cannot be made directly, as it is impossible to overlap the probes. Instead, single-source-scans were made with each probe in turn. By taking the square root of the product of these traces, it follows from (6) that a measurement with the correct factor of  $|E_a||E_b|$  can be obtained. The sensitivity of the single-source measurements was improved by inserting switches at A in figure 3 to modulate the probe output at 8 Hz. To account for the effect of the insertion loss of the switch, the data was for each probe was rescaled using an on-axis measurement made using a chopper wheel to modulate the signal.

## V. RESULTS

The probes were aligned vertically ( $y$ -direction) with the centre of the aperture on a plane  $153 \pm 1$  mm from the aperture plane. Measurements were then made of the variation of the DRF in the horizontal direction ( $x$ -direction) at 240 GHz. This data is shown in figures 4 and 5. As part of the analysis, we decided to see how well the data could be modelled by assuming the DRF of the detector is uniform, unpolarized and spatially incoherent over the aperture. With these assumptions, the detector output is given by

$$\langle P \rangle \propto \int |\mathbf{E}(\mathbf{r}, z_0, \nu)|^2 d^2\mathbf{r}, \quad (7)$$

where the integral is taken over the aperture. An approximate form for the electric field at the detector plane is

$$\begin{aligned} \mathbf{E}(\mathbf{r}, 0, \nu) = & \frac{1}{r_a} E_a \sqrt{g(\theta_a)} \hat{\mathbf{y}} e^{-ik_0 x \sin \theta_a} \\ & + \frac{1}{r_b} E_b \sqrt{g(\theta_b)} \hat{\mathbf{y}} e^{-ik_0 x \sin \theta_b} e^{2\pi i |\Delta\nu| t}, \end{aligned} \quad (8)$$

where  $k_0$  is the angular wave number of the radiation and  $(r, \theta)$  are the radial distance and zenith angle of the probes at the aperture centre.  $E_a$  and  $E_b$  are complex amplitudes and  $g(\theta)$  is the gain pattern of the horn in the plane. By propagating the TE01 mode to the far-field using plane wave methods, it can be shown that

$$g(\theta) \propto \frac{wh(\cos \theta \cos(\pi w \sin \theta / \lambda))^2}{\lambda^2 [\pi^2 - (2\pi w \sin \theta / \lambda)^2]^2}, \quad (9)$$

where  $\lambda$  is the wavelength of the radiation and  $w$  and  $h$  are the horizontal and vertical dimensions of the probe aperture. Assume the aperture has side length  $p$ . Substituting (8) into (7), we find the complex amplitude  $C$  of the detector fringe is expected to have the form

$$C = 2\alpha p^2 |E_a| |E_b| \left[ \frac{g(\theta_a)}{r_a} \right] \left[ \frac{g(\theta_b)}{r_b} \right] \times \exp[i(\Delta\psi - \Delta\nu [k_0(r_a - r_b) + \phi_a - \phi_b]/|\Delta\nu|)] \times \text{sinc} \left[ \frac{p}{\lambda} (\sin \theta_a - \sin \theta_b) \right], \quad (10)$$

where  $\Delta\nu = \nu_b - \nu_a$ ;  $\phi_a$  and  $\phi_b$  are the arguments of  $E_a$  and  $E_b$ ;  $\alpha$  and  $\Delta\psi$  account for the readout electronics. In each plot, the solid lines show a least square fit of this model to the data assuming  $E_a$ ,  $E_b$ ,  $\alpha$  and  $\Delta\psi$  as unknowns.

Figures 4(a) and 4(b) are plots of the amplitude and phase of the fringe as a function of  $x_a$  with  $x_b = 0$  mm. The amplitude points have been normalised to the value on-axis ( $x_a = x_b = 0$  mm) calculated using the model fit. For clarity, the error bars on the amplitude data are not shown. They are on the order of  $\pm 0.01$  on all points. The phase values have been corrected for the fitted values of  $\phi_a$ ,  $\phi_b$  and  $\Delta\psi$ . Excellent agreement is observed between the model and the data. The fitted value for the separation of the source and detector planes was 152 mm, which is close to the measured value of  $153 \pm 1$  mm. Figure 5 shows similar amplitude plots for different values of  $x_b$ . All of the plots have been normalised to the experimentally measured fringe amplitude at  $x_a = x_b = 0$  mm. Each line of best fit was calculated by fitting the model to the corresponding set of data, rather than attempting a global fit. It can be seen from the data that the model fits begin to worsen at high  $x_b$ . This may either be a failure in the model for the horn gain, or a failure in the assumption that the response over the aperture is uniform. For example, at high angles we may begin to see the effect of reflections at the internal window in the detector. Additionally, the peaks on the curves fitted to the  $x_b \neq 0$  data sets should all lie on the envelope function  $x_a = x_b$ . The fact they do not is most likely a result of issues with the calibration of the single-source scans.

## VI. CONCLUSIONS

We have demonstrated an interferometric technique for characterizing the full optical behaviour of multi-mode power detectors. The detector under test is illuminated with a pair of phase-locked, monochromatic, sources. When the phase angle between the sources is rotated, the detector output traces out a fringe pattern. From the complex amplitude of the fringe we can determine the value of the Detector Response Function (DRF) at the source positions. By repeating the procedure for different source positions, the DRF can be mapped out in full. Measurements of both the fringe amplitude and phase were made on a stopped down detector at 240 GHz. The data collected was found to be well described by model that assumes the DRF is spatially incoherent over the aperture.

The basic experimental scheme described here is applicable at all wavelengths with suitable modification. For example, a measurement at optical wavelengths might use laser-fibre

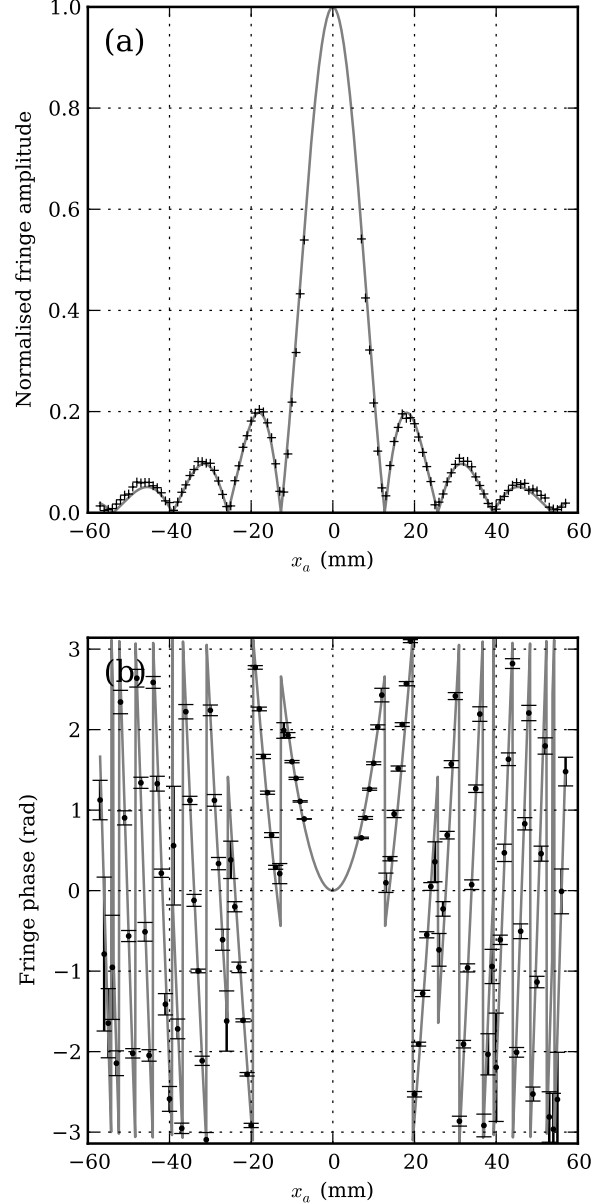


Fig. 4. Fringe amplitude (a) and phase (b) as a function of the  $x$ -coordinate of source A with source B fixed on the center axis of the detector. The fringe amplitude is normalised to the value at  $x_a = x_b = 0$  mm, as calculated using the model fit. The phase shifts  $\phi_a$ ,  $\phi_b$  and  $\Delta\psi$  have been subtracted off the phase data. The solid line shows the model fit. Radiation frequency = 240 GHz.

probes and micrometer stages in place of slides. Other realizations of the same experiment are also possible. Much of the current design was influenced by the need to make measurements on a slow, room-temperature, detector. Cryogenic astronomical detectors are much faster and have much greater sensitivity, so a simplified read-out scheme could be adopted.

Although the emphasis in this paper has been on detector characterisation, we also envisage the scheme having application in other fields of research. A near-field version of the scheme might, for example, be useful for measuring non-local conduction effects and microstructure in thin conducting films.

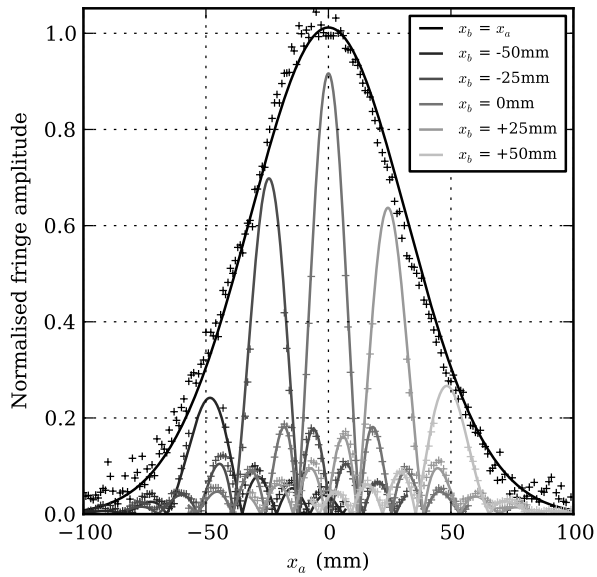


Fig. 5. Fringe amplitude (a) and phase (b) as a function of the  $x$ -coordinate of source A with source B in different positions. The fringe amplitude is normalised to the value at  $x_a = x_b = 0$  mm measured using a chopper wheel and the single sources. The phase shifts  $\phi_a$ ,  $\phi_b$  and  $\Delta\psi$  have been subtracted off the phase data. The solid line shows the model fit to each data set. Radiation frequency = 240 GHz.

## REFERENCES

- [1] A. Yaghjian, "An overview of near-field antenna measurements," *Antennas and Propagation, IEEE Transactions on*, vol. 34, no. 1, pp. 30–45, 1986.
- [2] J. Bennett, A. Anderson, P. McInnes, and A. Whitaker, "Microwave holographic metrology of large reflector antennas," *Antennas and Propagation, IEEE Transactions on*, vol. 24, no. 3, pp. 295–303, 1976.
- [3] S. Withington and G. Saklatvala, "Characterizing the behaviour of partially coherent detectors through spatio-temporal modes," *Journal of Optics A: Pure and Applied Optics*, vol. 9, p. 626, 2007.
- [4] G. Saklatvala, S. Withington, and M. Hobson, "Coupled-mode theory for infrared and submillimeter wave detectors," *JOSA A*, vol. 24, no. 3, pp. 764–775, 2007.
- [5] C. Thomas, S. Withington, D. Chuss, E. Wollack, and S. Moseley, "Modeling the intensity and polarization response of planar bolometric detectors," *JOSA A*, vol. 27, no. 5, pp. 1219–1231, 2010.
- [6] H. Liu, G. Mu, and L. Lin, "Propagation theories of partially coherent electromagnetic fields based on coherent or separated-coordinate mode decomposition," *JOSA A*, vol. 23, no. 9, pp. 2208–2218, 2006.
- [7] G. Bretthorst, *Bayesian spectrum analysis and parameter estimation*. Citeseer, 1988, vol. 1.

## Development of Silicon Based Integrated Receivers

C. Jung<sup>a</sup>, B. Thomas<sup>a,b</sup>, C. Lee<sup>a</sup>, A. Peralta<sup>a</sup>, G. Chattopadhyay<sup>a</sup>, J. Gill<sup>a</sup>, R. Lin<sup>a</sup> and I. Mehdi<sup>a</sup>

<sup>a</sup> NASA-Jet Propulsion Laboratory, California Institute of Technology  
4800 Oak Grove Drive, Pasadena, CA 91109, USA

<sup>b</sup> Radiometer Physics GmbH  
Birkenmaarstraße 10, 53340 Meckenheim, Germany

\* Contact: Cecile.d.jung@jpl.nasa.gov, phone +1-818-354-1658

**Abstract**— Submillimeter heterodyne instruments have played a critical role in addressing some of the fundamental questions regarding galaxy evolution as well as enhancing our understanding of the planet that we live on. To make these instruments compatible on small platforms for the study of the outer planets, it is essential to make them low-mass and low-volume. At JPL, we have developed over the years a world-class expertise in fabricating GaAs Schottky diode based integrated circuits for sub-millimeter and THz applications. Normally, the mixer and the multiplier chips are packaged in separate metal-machined waveguide blocks and then mated together to form part of the receiver front end. We now can utilize technologies from the semiconductor micro-fabrication arena to design and fabricate super-compact receiver packages. One way to make highly integrated, compact, and low-mass receiver front-end is to make the waveguide in silicon where the power amplifiers, multipliers, and mixer chips can be integrated in a single silicon micromachined block (Figure 1). We have developed DRIE processes to etch silicon wafers (Figure 2) and using these techniques, we have designed, fabricated and characterized an integrated receiver architecture called Radiometer-On-a-Chip (ROC). The stacking of micro-machined silicon wafers allows for the 3-dimensional integration of the W-band power amplifier, a 280 GHz tripler and a 560 GHz sub-harmonic mixer in an extremely compact package. Preliminary results give a DSB mixer noise temperature of 4860 K and DSB mixer conversion losses of 12.15 dB at 542 GHz and they demonstrate that Si micromachining technology can be used for building THz components and systems.

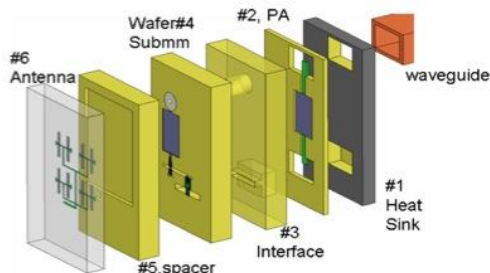


Fig 1: Stack of 6 different Si wafers to provide functionality of a single-pixel receiver front end.

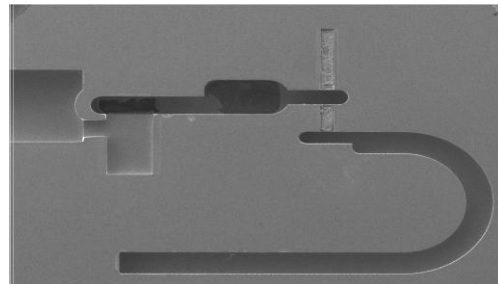


Fig 2: SEM picture of Si-etched cavities and waveguides for the 560GHz Radiometer-On-A-Chip architecture.

*The research described here is supported by Oak Ridge Associated Universities through the NASA Postdoctoral Program (NPP). This is carried out by the Jet Propulsion Laboratory, California Institute of Technology.*